Insights into West Antarctica`s Geology and Late Pleistocene Ice Sheet Behaviour from Isotopic Sedimentary Provenance Studies

Patric Simões Pereira

Imperial College London

The Grantham Institute for Climate Change and the Environment &

The Department of Earth Science and Engineering

Thesis submitted for the degree of Doctor of Philosophy (Ph.D.), 2018

Declaration of Originality

I declare that the contents of this thesis are completely my own, and that any work of others, published or otherwise, is fully and correctly acknowledged.

Patric Simões Pereira

To Alexandre and Sara

Acknowledgments

First and foremost, I wish to express my deepest gratitude to my advisors Tina van de Flierdt and Claus-Dieter Hillenbrand for the unreserved support and guidance, enthusiasm and scientific rigour which they shared throughout my research work. You have been tremendous mentors for me and I cannot thank you enough for allowing me to grow as a research scientist.

I wish to thank the Kristian Gerhard Jebsen Foundation and the Grantham Institute for Climate Change and the Environment for their wonderful support, and for providing funding and opportunities to further myself over the course of my PhD.

I also wish to express my thanks to the entire MAGIC group, and especially to Barry Coles and Katharina Kreissig for keeping the labs running at all times and ensuring that I could conduct my research in the best possible conditions. My special appreciation also goes to Martin Mangler and Rachel Bertram for the incountable shared times in the lab, and David Wilson and Susan Little for always offering a helping hand (or simply a chat) when needed. Special thanks also goes to all my colleagues and friends at Imperial as well as the captain, crew and colleagues of the RV Polarstern expedition PS104 in early 2017.

During this journey, my time in London was made enjoyable in large part due to the many friends that became part of my life. Special thanks goes to Alberto Padoan, Alessandro Piccininno, Nima Subramaniam, Martina Zambelli, Olivia Wei, Debashis Puhan, Xiaxi Cheng, Domagoj Margan, Bhavani Esapathi, Raph Zufferey, Luciano L. Fedele and the list goes on.

A huge thanks goes as well to all my friends across the channel for their conscious or unconscious support throughout my PhD. This includes, but is not limited to David Mike Fries, Jeremy Brossier, Jeanne Vidal, Valentin Basch, Jeanne Mercier, Mark Melichar, Joseph Vallone, Sandrine Roy, Yann Plard, Hugo Nguyen, Marie-Eva Epin and many others.

Sofia Dall'Orso, you owe a very special thanks for your unending support, encouragement and patience during this journey. I thank you for always and incessantly believing in me, especially in the moments when I failed to do so.

Finally, I would like to thank my family for their continued support throughout this time, and specially my sister for always being there and always counting on me.

Abstract

A fundamental question in Antarctic glaciology and climate change research is whether the West Antarctic Ice Sheet (WAIS) has experienced complete or partial disintegration during the late Pleistocene. Direct geological evidence for its past evolution is scarce, preventing improved predictions on its future behaviour. To this end, I investigated the provenance of late Pleistocene (1.1 Myrs) to modern detrital marine sediments deposited off West Antarctica using strontium and neodymium isotopic compositions of fine-grained (<63μm) sediments and $^{40}Ar/^{39}Ar$ ages on ice-rafted (>150μm) hornblende and biotite grains. Bedrock characteristics inferred from the sedimentary records can ultimately be tied to the location of eroding ice through time, and hence constrain ice dynamics in a novel way.

My key findings are as follows:

1) isotopic and geochemical fingerprints of seafloor surface sediments in the Pacific sector of West Antarctica are varied enough to distinguish different ice drainage sectors on the continent and interpret the results in terms of varying subglacial geology and sediment transports pathways

2) the provenance of glaciogenic detritus delivered by the Pine Island and Thwaites Glaciers, which drain the WAIS into the Amundsen Sea, are significantly distinct from each other and reveal little to no provenance change since the Last Glacial Maximum

3) the sediment eroded by the WAIS in the Amundsen Sea area fluctuated in composition in pace with eccentricity between 1.1 and 0.2 Ma, but lacks evidence for substantial retreat from the modern ice margin

4) the sediment eroded during the peak of the last interglacial (~130 ka) suggests a significant retreat or even 'ungrounding' of the WAIS its Amundsen Sea sector.

Overall, my new data show the promise of the approach chosen. Future work, from additional locations and using complementary methods, such as multivariate analysis, is needed to derive a more complete history of the WAIS.

Table of Content

List of Figures

List of Tables

Chapter 1

Introduction

1.1. A short history of the Antarctic ice sheet

Large continental-scale ice sheets play an essential role in Earth's climate system and understanding their future behaviour under changing climatic conditions is therefore of societal importance. Knowledge on the geological past of ice sheets is crucial to test and inform model-based predictions of the behaviour of ice sheets under future climate change. However, finding direct geological evidence of the state of ice sheets in the past remains a major scientific challenge, as ice sheets tend to overprint their own history in the proximal marine sedimentary record, while records preserved on the continent itself are largely covered by ice.

The initiation of continental-scale glaciation occurred during the Eocene-Oligocene transition (~34 Ma). A two-stepped excursion of +1.0‰ in oxygen isotope compositions of benthic foraminifera (e.g. Zachos et al., 2001, 2008; Coxall et al., 2005; Miller et al., 2005; Scher et al., 2011) shows significant global changes in continental ice volume and bottom water temperature. Direct evidence for the onset of Antarctic glaciation during this time comes from the sudden appearance of ice-rafted debris (IRD) and changes in clay mineral assemblages around the Antarctic continent (Kennett, 1977; Ehrmann and Mackensen, 1992; Zachos et al., 1992). The formation of a large-scale Antarctic ice sheet was contemporary with cooling of deep-sea temperatures (e.g. Lear et al., 2004, 2008), major restructuring of Southern Ocean plankton ecosystems (Houben et al., 2013) and a general decrease in atmospheric CO_2 from ~1000 ppm during the late Eocene to ~400 ppm during the late Oligocene (Pagani et al., 2011; Zhang et al., 2013). The cause for significant ice growth is assumed to be related to gradual modification in Earth's boundary conditions, such as changes in continental geography and bathymetry, opening of oceanic gateways and fluctuations in atmospheric greenhouse gases (see Zachos et al., 2001; and references within). For instance, two widely cited hypotheses invoke opening of critical oceanic gateways and a decline in atmospheric CO_2 levels. Opening and widening of the Tasmanian and Drake Passage gateways could have resulted in the thermal isolation and subsequent cooling of Antarctica (e.g. Kennett and Shackleton, 1976; Scher and Martin, 2006). A general decline in Cenozoic atmospheric CO_2 levels, on the other hand, could have passed a threshold corresponding to 2.5 to 3 times of preindustrial atmospheric CO_2 levels, instigating positive feedbacks that led to rapid ice sheet expansion (DeConto and Pollard, 2003).

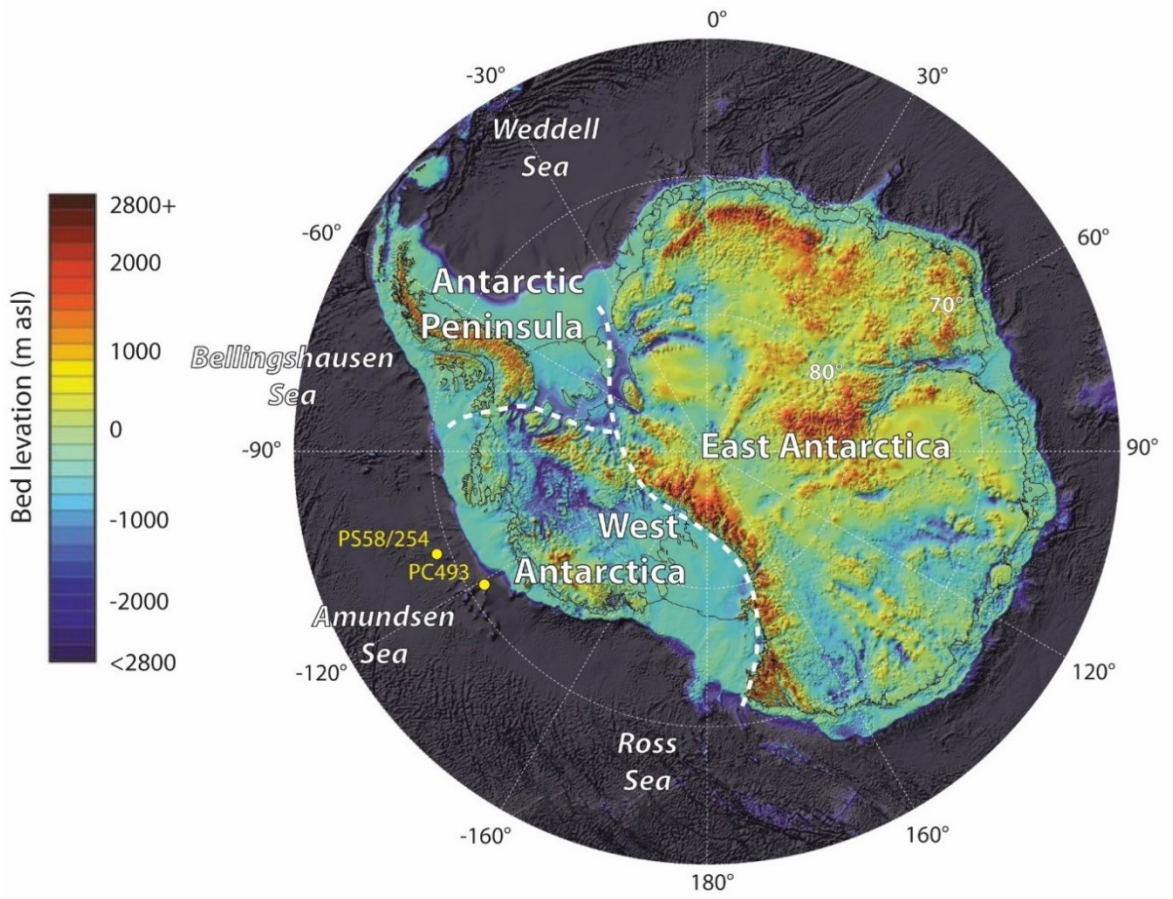

Figure 1.1. Map of Antarctica showing bed elevation from BEDMAP2 (Fretwell et al., 2013) in meters above sea level (m asl), with the boundaries between the West Antarctic Ice Sheet, East Antarctic Ice Sheet and the Antarctic Peninsula Ice Sheet (white dashed lines), and locations of major study sites within this thesis (yellow circles).

Antarctic ice extent fluctuated since the Eocene-Oligocene transition, paced by orbital oscillations with frequencies of ~20 kyrs, 41 kyrs, 100 kyrs and 400 kyrs at various times (Naish et al., 2009; Patterson et al., 2014; Galeotti et al., 2016; Levy et al., 2016). The last pronounced change in the periodicity of worldwide climate records occurred between 1.2 and 0.6 Ma. During the so-called Mid Pleistocene Transition (MPT), weaker (smaller benthic $\delta^{18}O$ amplitude) cycles with a ~40 kyr cyclicity gave way to stronger (greater benthic $\delta^{18}O$ amplitude) cycles with a periodicity of ~100 kyrs (Elderfield et al., 2012; Past Interglacials Working Group of PAGES, 2016; and references therein). Ice core data do not reach far enough back to capture this transition, but show that the climate oscillated through eight glacial cycles over the last 800 kyrs. CO_2 levels varied by ~100 ppm between glacial and interglacial stages (Lüthi et al., 2008), accompanied by fluctuations in local atmospheric temperature in Antarctica of ~14 °C, which parallel ocean records of temperature and ice volume (Jouzel et al., 2007).

While the large East Antarctic Ice Sheet (EAIS), which holds enough freshwater to raise global sea level by ~53 m, was probably the main reason for sea level fluctuations in the earlier parts of the Cenozoic and Neogene, the smaller West Antarctic Ice Sheet (WAIS) (Figure 1.1), which holds enough ice to raise sea-level by ~3.3 to 4.3 meters (Bamber et al., 2009; Fretwell et al., 2013), is suggested to be vulnerable even under only slightly warmer temperature conditions of late Pleistocene interglacials. The first warning that the WAIS may be "uniquely unstable and vulnerable" and that it may have experienced "catastrophic disintegration" in the past was formulated in a historical paper by Mercer (1968). The assumed instability of the WAIS is based on the fact that it is grounded on bedrock that lies well below sea-level and that deepens further inland (up to ~2500 meters below sea-level, see Fretwell et al., 2013), so that any initial retreat of the groundling line towards deeper ocean water will lead to more thinning and retreat (Weertman, 1974; Schoof, 2007; Katz and Worster, 2010). At present, mass loss of this marine-based ice sheet is attributed to melting of floating ice shelves by upwelling of relatively warm Circumpolar Deep Water (CDW) (Walker et al., 2007, 2013; Jenkins et al., 2010, 2016), which further leads to extensive thinning of ice shelves (Rignot and Jacobs, 2002; Pritchard et al., 2012), increased ice speed and discharge (Rignot et al., 2008; Joughin et al., 2010; Mouginot et al., 2014) and fast grounding line retreat (Joughin et al., 2010; Tinto and Bell, 2011)(Figure 1.2).

Multi-proxy data, including magnesium(Mg)/calcium(Ca) ratios of calcareous shells of benthic foraminifera as a proxy for paleo-bottom-water temperature show that the CDW was the main driver behind the intense deglaciation that occurred in the Amundsen Sea sector of West Antarctica ~10,400 years to 7,500 years ago, and again since the 1940s (Hillenbrand et al., 2017; Smith et al., 2017). Since John Mercer's first warning, sea level reconstructions, sedimentological investigations and modelling studies have suggested that the WAIS underwent large waxing and waning during the Pleistocene (Scherer et al., 1998; Hillenbrand et al., 2009; Kopp et al., 2009; Pollard and DeConto, 2009; Holden et al., 2011; Vaughan et al., 2011; O'Leary et al., 2013; Pollard et al., 2015; DeConto and Pollard, 2016; Tigchelaar et al., 2018). However, most of these studies only provide indirect evidence for WAIS retreat (cf. Chapters 4 and 5), and therefore necessitate the development of new approaches to investigate the evolution of the WAIS during the late Pleistocene.

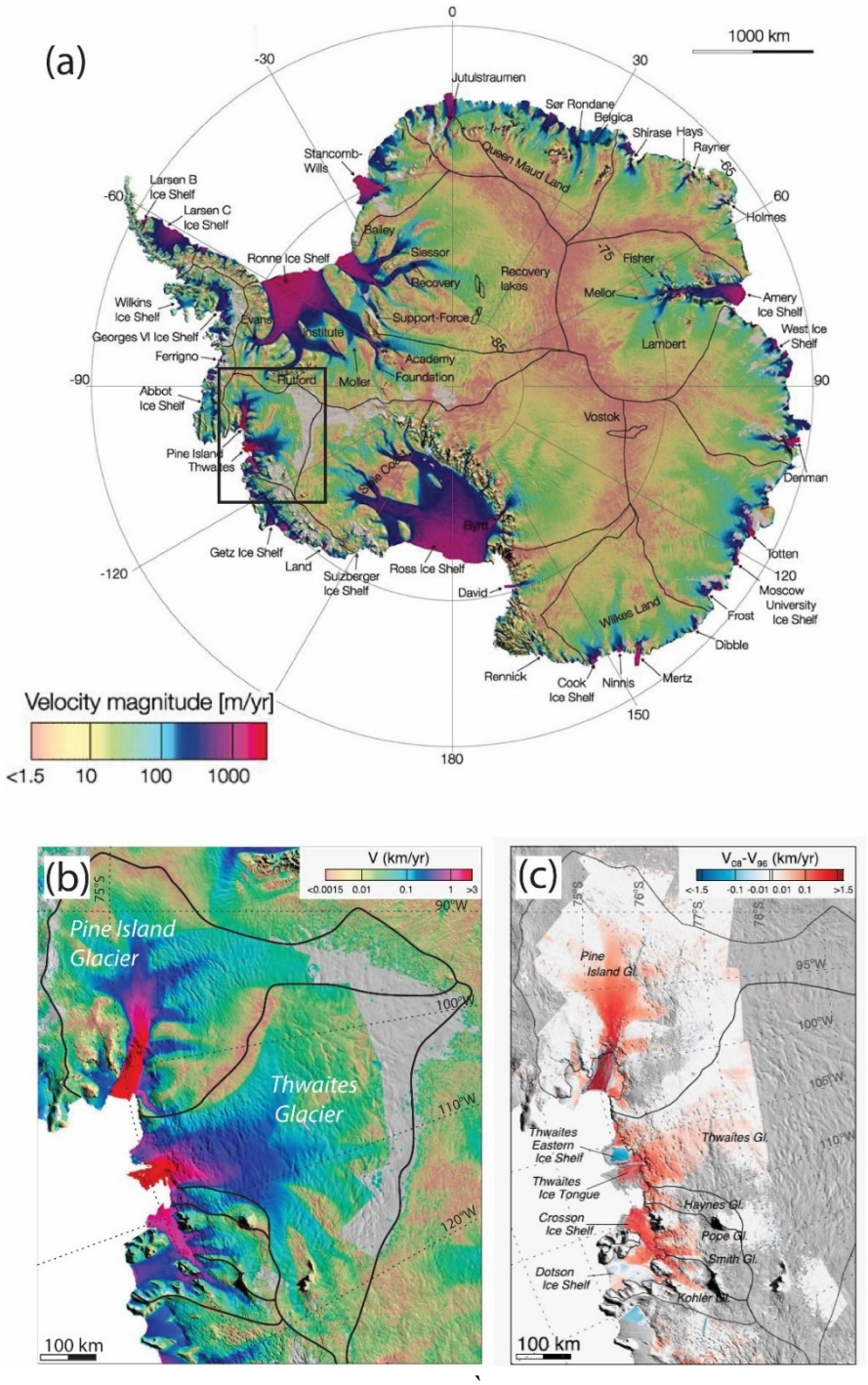

Figure 1.2. (a) Ice flow speed of the Antarctic Ice Sheet derived from various satellite observations between 2007 and 2009 (modified from Rignot et al., 2011). Black frame show location in 'b' and 'c'; (b) ice flow speed of ice streams draining the West Antarctic Ice Sheet into the Amundsen Sea derived using satellite observations between 1996 and 2013 (modified from Mouginot et al., 2014); (c) change in flow speed between 2008 and 1996 (modified from Mouginot et al., 2014). All figures are color coded on a logarithmic scale and overlaid on a MODIS mosaic of Antarctica.

1.2. Provenance of glaciomarine sediments

A powerful way to reconstruct past stability of ice sheets is to investigate the provenance of glaciomarine sediments by means of radiogenic isotope fingerprinting and dating (Licht and Hemming, 2017). As glaciogenic material is transported by flowing ice or subglacial meltwater from the continent towards the ice margin, it carries with it a geochemical imprint of its geological source. This detrital material is then deposited offshore as glacial diamict, by calving detritus-laden icebergs, or by wind or tidal currents (e.g. Diekmann and Kuhn, 1999; c.f. Section 1.3). Investigating isotopic and geochemical characteristics of glacially eroded detritus deposited offshore can thus provide insights into geologic composition of ice-covered bedrock (e.g. Pierce et al., 2011, 2014; Simões Pereira et a., 2018) and further provide insights into past ice sheet stability (e.g. Goldstein and Hemming, 2003; Williams et al. 2010; Colville et al. 2011). This approach has been successfully applied in the North Atlantic. For instance, investigation of the source of IRD deposited in the late Pleistocene revealed the portions of Northern Hemisphere ice sheets that endured significant destabilization (Grousset et al., 1993; Gwiazda et al., 1996; Hemming et al., 1998, 2000, 2003; Hemming, 2004; Hemming and Hajdas, 2003; Peck et al., 2007; Downing et al., 2013), while isotopic fingerprints of fine-grained sediments provided further insights on past extents of these ice sheets (e.g. Farmer et al., 2003; Colville et al., 2011; Reyes et al., 2014). Such isotopic provenance studies in downcore records have so far been comparatively underexploited in the Southern Ocean. The first successful attempts to link the geochemical provenance of modern circum-Antarctic glaciomarine sediments with Antarctic geology were described by Walter et al. (2000), Roy et al. (2007), van de Flierdt et al. (2007) and Hemming et al. (2007), and later by Flowerdew et al. (2012), Pierce et al. (2011, 2014) and Simões Pereira et al. (2018). Since then, isotopic provenance studies have mostly focused on glacial till samples from the Ross Sea sector (Farmer et al., 2006; Licht and Palmer, 2013; Licht et al., 2014; Welke et al., 2016) and downcore records from the Weddell Sea region (Carter et al., 2017) and off East Antarctica (Williams et al., 2010; Tochilin et al., 2012; Cook et al., 2013, 2014, 2017; Pierce et al., 2017; Bertram et al., 2018; Wilson et al., 2018).

Around Antarctica, analysis of the long-lived radiogenic rubidium-strontium (Rb-Sr) and samarium-neodymium (Sm-Nd) isotope systems in fine-grained (<63μm) detrital glaciomarine sediments have been shown to be particularly valuable to trace the provenance of glaciomarine sediment. During mantle extraction (i.e. rock formation), different levels of

compatibility between coupled parent and daughter elements lead to different enrichments in the crust and mantle, which subsequently leads to the acquisition of distinct radiogenic isotope compositions depending on age and lithology. To utilise Sr and Nd isotope fingerprints as proxies for provenance, it is important to exclude major fractionation during low-temperature processes such as weathering and mineral sorting (i.e. grain-size effects). While Sm and Nd are shown to be largely unaffected by such processes given their nearly equal incorporation in most rock-forming minerals (e.g. Garçon et al., 2013), Rb and Sr are more readily fractionated in rock-forming minerals and are hence more easily affected by grain-size effects or weathering (Dasch, 1969; Eisenhauer et al. 1999; Blum and Erel, 2003). However, when correlated with Nd isotopes, Sr isotope records can provide a useful mean to trace provenance of source terrains (Goldstein and Hemming, 2003).

An additional tracer that has shown to be particularly valuable for deciphering the provenance of glaciomarine sediments is the application of $^{40}Ar/^{39}Ar$ dating on individual ice-rafted mineral grains such as hornblende and biotite grains (Hemming, 2004). Both minerals occur as major rock-forming constituents in a variety of lithologies. The advantage of applying the dual dating approach on hornblende and biotite grains is based on the fact that these minerals occur in varying amounts in different rock types. Additionally, hornblende and biotite minerals have different closure temperatures for argon of ~550°C and ~300°C, respectively (Harrison, 1982; Harrison et al., 1985) and hence reflect different points on the cooling path following a major extrusive or tectono-metamorphic event. In general, radiochronological investigations of rock-forming mineral systems retain information on the thermal history of their source rocks (e.g. Hodges et al., 2003) and are hence extremely valuable in reconstructing source locations of IRD deposited offshore, particularly where continental sources are characterized by complex tectonic and metamorphic histories.

For my thesis, I primary looked at Sr and Nd isotope fingerprints of fine-grained sediments and $^{40}Ar/^{39}Ar$ ages on hornblende and biotite grains deposited offshore of West Antarctica in order to study the evolution of the WAIS during the late Pleistocene. The working hypothesis I follow is that a significant WAIS retreat caused erosion in and sediment supply from distinct geological source regions to the offshore by shifting the location of subglacial erosion further inland. Changes in the sediment supply and provenance in turn should be recorded in offshore marine records proximal to the ice sheet. I primarily focused on sediments deposited in the Amundsen Sea, which lies in the Pacific sector the Southern Ocean. The portion of the WAIS that drains into the Amundsen Sea has been identified as the "weak underbelly of the WAIS" (Hughes, 1981; Vaughan et al., 2006), meaning that any large retreat

in this ice sheet is likely to have initiated in this sector. To this end, I first examined the overall fingerprint of glacially eroded sediments off West Antarctica, and more specifically in the Amundsen Sea, before investigating the provenance signature of two continuous and well-dated sediment records retrieved from the Amundsen Sea at site PS58/254 (69°19°S, 108°27°W, water depth 4014 m) collected during RV Polarstern cruise ANT-XVIII/5a in 2001 and site PC493 (71°08°S, 119°55°W, water depth 2077 m) collected during RV James Clark Ross cruise JR179 in 2008 (Figure 1.1).

1.3. Glaciological background

Successful application of sedimentary provenance analysis in glaciomarine sediments ultimately requires an understanding on the processes by which glacial debris is produced, entrained and deposited to the marine realm. Glaciers and ice sheets are among the most effective agents of mechanical erosion on Earth, carrying large amount of glacial debris of various grain sizes (silt, sand, gravel, boulders) up to several hundreds of kilometres from their source area to their depositional site. The purpose of the following sections is to provide a brief description of the processes relevant for interpreting sedimentary provenance of glaciomarine sediments (compiled from Bennett and Glasser, 2009 and Benn and Evans, 2010).

Glacial erosion

The process by which ice detaches and entrains rock and sediment as it flows along glaciated environments is known as glacial erosion. Glacial debris is largely produced subglacially though mechanical weathering of the bedrock or substrate, or by remobilization of unconsolidated layer of sediment in the subglacial environment. Subglacial erosion can be defined by two principal processes: glacial abrasion and glacial plucking. Glacial abrasion is the process by which basal rock particles are moved across a bedrock surface, causing erosion of the bed primary through scouring or polishing. Glacial plucking occurs when ice removes large rock fragments (greater than 1 cm) from its bed. The presence of fractures within the geological structure is primordial for glacial plucking. Fractures within the bedrock may be an inherent structure of the geological structure or may have pre-existed before the advance of the glacier, or could have been formed in-situ by freeze-thaw weathering processes or as ice flow above it. In general, glacial erosion is more effective in areas where ice is warm-based and basal melting is strong, and is limited where the ice is cold-based, and basal melting is absent.

Debris entrainment in glacial systems

Debris can enter glaciers or ice streams either at the surface of the ice (supraglacially) or at the bed of the glacial system (subglacially). Supraglacial sources are often delivered to the surface of the ice by gravitational processes in areas where ice is surrounded by valley walls or protruding nunataks, either through rock falling from adjacent cliffs or avalanches. Deposition of far-travelled ash falls or meteorites may also contribute for the overall supraglacial sediment load, but generally accounts for a small fraction of it. The basal portion of a glacier distinguishes itself from the overlying ice as it is subjective to various processes that enhances subglacial debris entrainment processes near the bed. In summary, the formation of debris-rich basal ice happens through processes such as regelation (pressure melting and refreezing), glaciohydraulic supercooling (advection and freezing of meltwater at a temperature below its freezing pint), net adfreezing (accumulation of basal ice by cyclic shifts in basal thermal regime), or ice deformation around rock joints. Basal debris can further be entrained and lifted from the glacier bed to higher elevation in the ice column of a glacier or ice sheet (englacial position) through compressive deformation, which generally occurring near the ice margin, i.e. englacial thrusting. Sediment evacuation by subglacial drainage systems result in further debris entrainment below the ice cover. This process tend to dominate the sediment outflux of most temperate glaciers and ice caps, either in form of suspended load in the drainage system or as bedload carried along the channel floor (e.g. Alley et al., 1997).

Sedimentation in marine envrionments

Glacial detritus can be deposited in the marine realm through several main key processes as described in the following. Sediments may be deposited directly at the glacier front by melting of supraglacial and englacial debris incorporated in the ice at the glacier front. Another path by which sediments are evacuated from a glacier or ice sheet is through sediment-laden icebergs which calve from the glacier front. As icebergs move along the open ocean, they gradually melt, causing the 'rain-out' of glacial debris and deposition to the ocean floor. Icebergs calved from ice shelves generally carry little to no debris within them as debris tends to melt from the base of the ice shelf prior to calving. As mentioned in the previous section, sediment-laden water may also cause the release of debris from the base of the ice to the open ocean. Fresh meltwater generally enters the ocean as an overflow plume given its low density, but occasionally occurs as an underflow when the density of meltwater is altered (heavier) due to high concentration of sediments. Suspended material will then eventually settle out to the

ocean floor. Finally, resedimentation by gravity flows may occur when sediments deposited on steep slopes become unstable and are redistributed to the ocean floor. Other minor or localised factors such as rock fall and mass flow, re-mobilisation by iceberg scour, current reworking may also influence marine sedimentation, particularly in polar environments.

1.4. Thesis Aim and Objectives

The central aim of this thesis is to advance our understanding on the evolution of the WAIS during the late Pleistocene, i.e. past ~1.1 million years. Specific objectives are as follows:

i) Examine if modern seafloor surface sediments around West Antarctica show sufficient geochemical (i.e. isotopic) variability to distinguish various West Antarctic ice drainage sectors and allow interpretation in terms of geology and sediment transport pathways.
ii) Characterize the fingerprint of glaciogenic sediments delivered by the two largest West Antarctic glaciers draining into the Amundsen Sea, i.e. the Pine Island Glacier and Thwaites Glacier.
iii) Reconstruct the detrital provenance of two sediment cores from the Amundsen Sea spanning the past 1.1 Myrs. Can results constrain the behaviour of the late Pleistocene WAIS in the Amundsen Sea sector?
iv) Investigate whether a major disintegration or collapse of the WAIS occurred during the peak of the last interglacial period, Marine Isotope Stage 5e.

1.5. Thesis Outline

This thesis is divided into four main chapters that address the individual objectives outlined above, and utilise the tools of (isotope) geochemistry (major and trace element geochemistry, Sr and Nd isotopic compositions, $^{40}Ar/^{39}Ar$ ages of hornblende and biotite grains) to reconstruct the sedimentary provenance of glaciomarine sediments.

Chapter 2 describes the first comprehensive isotopic provenance study for ice proximal seafloor surface sediments deposited off West Antarctica. New data allows to differentiate five major ice drainage regions in West Antarctica, namely the Antarctic Peninsula, Bellingshausen

Sea, Amundsen Sea, Wrigley Gulf-Hobbs Coast, and Sulzberger Bay. Geochemical composition of marine detrital sediment can be interpreted in terms of geology under ice drainages and sediment transport pathways (i.e. fine-grained vs IRD fraction) offshore. Fine-grained sediments in the Amundsen Sea Embayment are generally carried along bathymetric troughs which incise the continental shelf, while the transport pathway of IRD is largely driven by ocean surface currents. Chapter 2 is a modified version of a paper published earlier this year in Earth-Science Reviews (Appendix 1).

Chapter 3 provides a detailed provenance analysis of sediments deposited in Pine Island Bay, Amundsen Sea. In a multi-proxy approach, isotopic (Sr, Nd, Ar) and geochemical (major and trace element compositions) results are combined with data on bulk and clay mineral assemblages as well as rock magnetic properties of marine sediments in front of Pine Island and Thwaites Glaciers. The new data reveal large changes in the isotopic fingerprint of seafloor surface sediments depending on their proximity to the Pine Island and Thwaites Glaciers. Glaciogenic sediments delivered by these two glaciers are clearly distinct from each other and can be interpreted in terms of varying geology below the ice drainages. This observation opens the possibility that retreat in both glacial systems may be traced back in time. In a first step towards this direction, recent subglacial to deglacial sediment layers were analysed, and revealed that sedimentary sequences deposited in the flowline of the Pine Island and Thwaites ice streams since the Last Glacial Maximum remained largely unchanged.

Chapter 4 describes the first radiogenic isotope provenance study of detrital downcore sediments proximal to the West Antarctic ice sheet from sites PS58/254 and PC493. Sediments deposited at both sites between 1.1 and 0.2 Ma show similar Sr and Nd isotopic compositions to modern sediments deposited in the eastern and western Amundsen Sea shelf (see Chapter 2), indicating northward sediment transport from the shelf to the continental rise and slope. Site PS58/254 shows clear fluctuation in the detrital Sr isotope composition over the last 1.1 Ma in pace with eccentricity. The Nd isotope record shows similar, although less pronounced, eccentricity-driven oscillations. Strontium and Nd isotopic compositions at site PC493 do not show pronounced glacial-interglacial changes, which is explained by the relatively homogenous geology cropping out in the hinterland. The IRD signal at site PS58/254 record proximal sources originating from the Amundsen Sea coast during glacial and interglacial periods, with additional supply of IRD sourced from the westernmost sector of the Amundsen Sea coast (i.e. Wrigley Gulf-Hobbs Coast) during interglacials. Increased IRD contribution with a westerly source during interglacials is explained by southward migration of the westerlies, shifting the position of the southern boundary of the Antarctic Circumpolar Current

(ACC) south of site PS58/254. At Site PC493, less variability in the provenance of IRD is observed. Glacial and interglacial grains have their source in the eastern Amundsen Sea coast. This observation shows that this westward flowing coastal current remained predominant at site PC493 during glacial and interglacial periods. Overall, the data in this chapter do not provide evidence for significant WAIS retreat between 1.1 and 0.2 Ma, but suggest a relatively stable late Pleistocene WAIS oscillating in pace with eccentricity.

Chapter 5 focuses on the transition from Marine Isotope Stage (MIS) 6, the penultimate glaciation, to MIS 5, the last interglacial, at sites PS58/254 and PC493 in the Amundsen Sea. The data presented in this chapter cover the past 200 kyrs. Similar to the IRD data in Chapter 4, changes in the provenance of IRD at both sites suggest southward migration of the westerlies and the southern boundary of the Antarctic Circumpolar Current during interglacial MIS 5. However, the most striking feature in the provenance data presented in this Chapter is an abrupt excursion in Nd isotopic compositions towards higher values at, or shortly after, Termination II (~130 ka). This abrupt shift in Nd isotopic compositions is explained by significant WAIS grounding line retreat over this period. Large grounding line retreat, or even "ungrounding" of the base of the WAIS from the Pine Island Glacier and Thwaites Glacier basins temporally decreased or ceased sediment supply from these sectors, resulting in a loss of the characteristic fingerprints described in Chapter 3. Continued supply of detritus from local areas where ice remained grounded, can explain the observed increase in Nd isotopic compositions. Although the extent of the ice retreat remains unconstrained, the data provide evidence for MIS 5e being the interglacial that witnessed the largest retreat of the grounding line in the Amundsen Sea sector during the late Pleistocene.

Chapter 2

Geochemical fingerprints of glacially eroded bedrock from West Antarctica: Detrital thermochronology, radiogenic isotope systematics and trace element geochemistry in Late Holocene glacial-marine sediments

Modified from: Simões Pereira, P., van de Flierdt, T., Hemming, S.R., Hammond, S.J., Kuhn, G., Brachfeld, S., Doherty, C., Hillenbrand, C.-D., 2018. Geochemical fingerprints of glacially eroded bedrock from West Antarctica: detrital thermochronology, radiogenic isotope systematics and trace element geochemistry in Late Holocene glacial-marine sediments. *Earth-Science Reviews* 182, 204-232.

Chapter Summary

Geochemical provenance studies of glacial-marine sediments provide a powerful approach to describe subglacial geology, sediment transport pathways, and past ice sheet dynamics. The marine-based West Antarctic Ice Sheet (WAIS) is considered highly vulnerable to ocean warming and sea level rise that is likely to cause its rapid and irreversible retreat. Studies of its past response to climate change are hence essential for projecting its future behaviour. The application of radiogenic and trace element provenance studies for past ice sheet reconstructions requires surveying the geographic variability of geochemical compositions of glaciomarine sediments. In this study, we characterize the provenance of the detrital fraction of 67 Late Holocene marine sediment samples collected off the Pacific margin of West Antarctica (60°W to 160°W), including $^{40}Ar/^{39}Ar$ ages of individual hornblende and biotite grains (>150μm), as well as strontium (Sr) and neodymium (Nd) isotope and trace element composition of the fine-grained (<63μm) sediment fraction. Overall, this approach allows differentiating West Antarctica into five source regions: the Antarctic Peninsula, Bellingshausen Sea, Amundsen Sea, Wrigley Gulf-Hobbs Coast and Sulzberger Bay. Minor geochemical variability is found within each individual sector due to local variability in onland geology. $^{40}Ar/^{39}Ar$ ages of iceberg-rafted hornblende and biotite grains record primarily Carboniferous to Late Quaternary ages (~0 to 380 Ma), with a notable age peak of ~100 Ma, associated with plutonic intrusions or deformation events during the mid-Cretaceous. Permian-Jurassic $^{40}Ar/^{39}Ar$ ages are widespread in the Amundsen Sea sector, marking episodes of large-volume magmatism along the long-lived continental margin. Metasedimentary rocks and Late Cenozoic alkali basalts in West Antarctica cannot be detected using detrital hornblende and biotite $^{40}Ar/^{39}Ar$ ages due to the absence or small grain-size (i.e. <150μm) of these minerals in such rocks. These sources can however be readily recognized by their fine-grained geochemical composition. In addition, geographic trends in the provenance from proximal to distal sites provide insights into major sediment transport pathways. While the transport of fine-grained detritus follows bathymetric cross-shelf troughs, the distribution of iceberg-rafted grains shows influence by transport in the Antarctic Coastal Current (ACC). Our study provides the first systematic geochemical characterisation of sediment provenance off West Antarctica, and highlights the importance of combining multiple provenance approaches in different size fractions of glacial-marine sediments, and paves the way to investigate past WAIS dynamics.

2.1. Introduction

The West Antarctic Ice Sheet (WAIS) holds enough ice to raise global sea-level by 4.3 m if completely melted (Fretwell et al., 2013). Its base rests largely on surfaces of bedrock and sedimentary strata that are well below sea level with an inland-deepening slope, making the WAIS vulnerable to changing environmental conditions (e.g. Oppenheimer, 1998), particularly to ocean warming and sea-level rise via the marine ice sheet instability hypothesis (e.g. Rignot and Jacobs, 2002; Schoof, 2007; Katz and Worster, 2010; Jacobs et al., 2011; Joughin and Alley, 2011; Pritchard et al., 2012) and/or marine ice cliff instability (DeConto and Pollard, 2016; Wise et al., 2017). This vulnerability is confirmed by modern observational data, which show thinning of ice shelves, acceleration of ice stream flow, and overall mass loss in the Pacific sector of the WAIS (Payne et al., 2004; Rignot et al., 2008; Pritchard et al., 2009, 2012; Shepherd et al., 2012; Mouginot et al., 2014). Most of the current retreat occurs in the Amundsen Sea sector, which drains approximately ~35% of the WAIS. High rates of mass loss originate from the Pine Island and Thwaites Glaciers, with potential collapse being hypothesised to occur in as little as ~400 years (Oppenheimer, 1998 and references therein; Vaughan et al., 2011; Joughin et al., 2014). The proposed mechanism for collapse is an irreversible retreat of the grounding line (Schoof, 2007; Katz and Worster, 2010), facilitated by the landward dipping bed under the WAIS. Thereby, the bathymetric setting of the continental shelf may trigger initial retreat by allowing relatively warm Circumpolar Deep Water that is upwelling onto the shelf to enter sub-ice shelf cavities through cross-shelf troughs carved by past ice stream advances (e.g. Walker et al, 2007; 2013; Jenkins et al., 2010, 2016).

While modern and historical processes leading to ice-sheet loss are increasingly well studied and understood (e.g. Hillenbrand et al. 2017; Smith et al., 2017; Turner et al., 2017), reconstructions of the past stability of the WAIS are still sparse (e.g. Scherer et al., 1998; Hillenbrand et al., 2002, 2009a; Pollard and DeConto, 2009; Naish et al., 2009; Vaughan et al., 2011). One promising tool to learn about past ice stability has been to study the provenance of marine detrital sediments. Radiogenic isotope fingerprinting and dating has been successfully applied to reconstruct ice sheet history in the Northern Hemisphere (e.g. Gwiazda et al., 1996; Hemming et al., 1998, Hemming and Hajdas, 2003; Peck et al., 2007; Downing et al., 2013; Reyes et al., 2014) and around East Antarctica (e.g. Williams et al., 2010; Pierce et al., 2011, 2014, 2017; Cook et al., 2013, 2014, 2017). Geochemical (i.e. radiogenic isotope composition) studies of glacially derived sediments with a West Antarctic provenance have so far been

restricted to the Ross Sea (Farmer et al., 2006; Licht and Palmer, 2013; Licht et al., 2014), glacial till samples from distinct ice streams (Farmer and Licht, 2016; Licht et al., 2014; Welke et al., 2016), and only a few marine sediment core top analyses along the West Antarctic margin (Walter et al., 2000; Roy et al., 2007; van de Flierdt et., 2007; Hemming et al., 2007).

In this study, we close this gap and describe the detailed geochemical provenance of glacially derived Late Holocene sediments along the Pacific margin of West Antarctica. Our primary motivation is to identify isotopic and geochemical fingerprints for individual WAIS sectors, and to characterize its subglacial geology building on the pioneering work of Roy et al. (2007), van de Flierdt et al. (2007) and Hemming et al. (2007). Paramount to such studies is the knowledge of the geological history of the exposed and subglacial bedrock (Figs. 2.1, 2.2) and its overall geochemical variability. Outcrop studies, integrated with airborne and field geophysical campaigns have significantly increased our knowledge of the hidden bedrock below the Antarctic Ice Sheet (e.g. Ferraccioli et al., 2009; Smith et al., 2013; Jordan et al., 2013a,b; Aitken et al., 2014). Investigations of sediments that are shed from Antarctica can also contribute to understanding subglacial geology as well as providing the groundwork for using this approach to document the past history of the ice sheets. Here we present results on the geochemical signature of 67 surface sediment samples using $^{40}Ar/^{39}Ar$ ages of individual hornblende and biotite grains (>150µm or >63µm), and Sr and Nd isotope ratios and trace element compositions of the fine-grained fraction (<63µm). We present these results in the context of published studies of the geology and geochemistry of West Antarctica from field observations and geophysical investigations. By combining different provenance tools, we characterize source sectors of glaciogenic detritus, a vital precondition for unravelling the history of the WAIS by tracing down-core provenance changes in marine sediment records. We place a particular emphasis on the Amundsen Sea sector, and relate our new sediment provenance results to specific ice drainage signatures, as well as pathways and transport mechanisms that may deliver sediments to their sites of deposition.

2.2. Regional Framework of West Antarctica

2.2.1. Tectonic history

The Antarctic continent preserves a geological record from ~3.5 Ga to present. Most known Precambrian rocks are found in East Antarctica (see Boger, 2011 for a recent review),

while West Antarctica generally has a younger, largely Phanerozoic, geological history. West Antarctica consists of four micro-continental blocks: the Antarctic Peninsula, Ellsworth-Whitmore Mountains, Thurston Island and Marie Byrd Land (Dalziel and Elliot, 1982) (Figs. 2.1, 2.2).

The 'birth' of West Antarctica is largely associated with the onset of the accretionary Terra Australis (Ross) Orogeny (~510 Ma). The Terra Australis Orogeny took place after suturing of West Gondwana (South American and South African shields) and the Australo-Antarctic plates (Kuunga Orogen), which shifted the locus of active subduction from between the pre-collision complexes of Gondwana towards the Proto-Pacific margin (Cawood, 2005). This orogenic event resulted in deformation of passive margin sediments, formation of back-arc basins with quiescent sedimentation (Ellsworth-Whitmore Mountains, Figure 2.1), and led to arc-type plutonism and subsequent crustal accretion onto the Gondwana margin (Cawood, 2005; Boger, 2011).

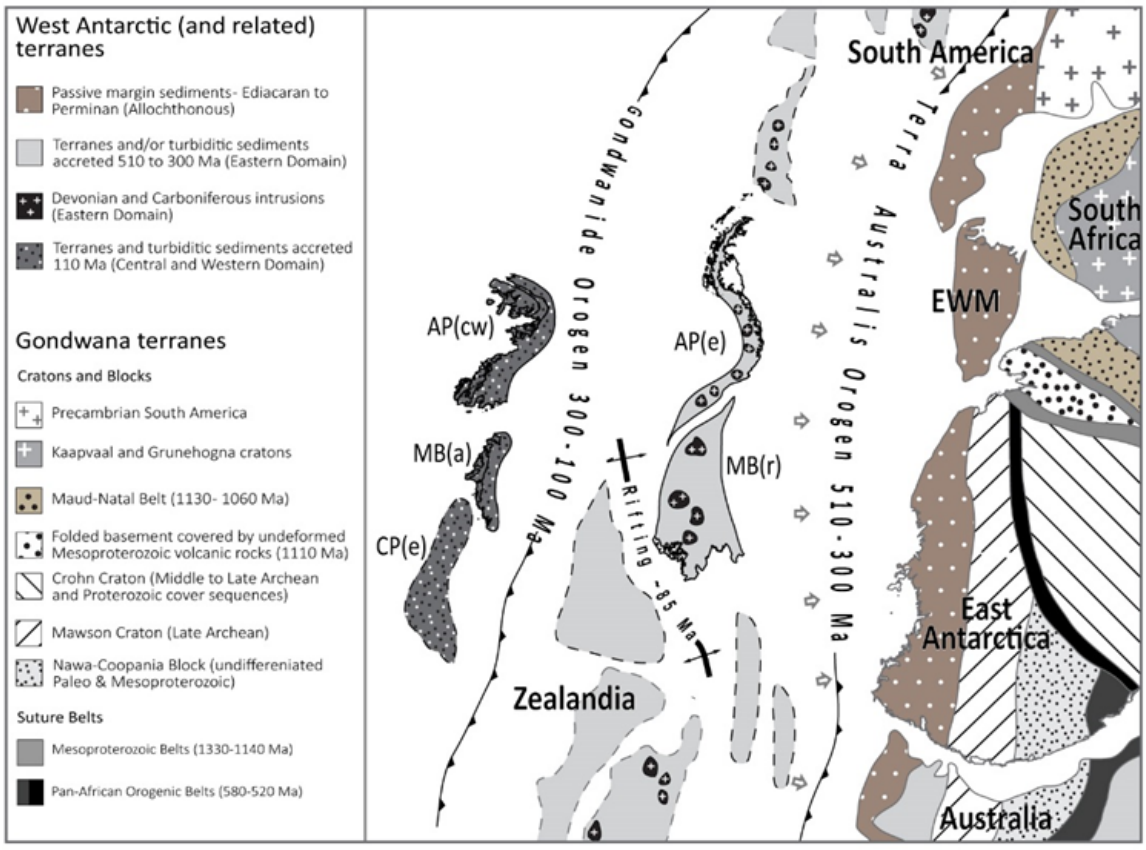

Figure 2.1. Tectonic reconstruction of West Antarctica during the Early Palaeozoic to Cretaceous (modified from Boger, 2011). AP – Antarctic Peninsula, MB(a) – Amundsen Province of Marie Byrd Land, related to the Central Domain, MB(r) – Ross Province of Marie Byrd Land, related to the Eastern Domain, CP – Campbell Plateau. Indices: e – Eastern Domain, c – Central Domain, w – Western Domain.

Convergence along the Pacific margin of Gondwana led to deposition and subsequent accretion of Cambrian-Ordovician turbiditic sequences, and intrusion of Devonian-Carboniferous (~375–345 Ma) granitoids. Relicts of these Early Palaeozoic rocks are found in the Ross province of Marie Byrd Land (Pankhurst et al., 1998; Mukasa and Dalziel, 2000), on Thurston Island (Pankhurst et al., 1993; Riley et al., 2017) and in the Eastern Domain of the Antarctic Peninsula (Millar et al., 2002), considered as the innermost and oldest arc-terranes in West Antarctica (Vaughan and Storey, 2000) (Figs. 2.1, 2.2).

During the late Carboniferous, collision of Gondwana with Laurentia terminated the Terra Australis Orogeny, which was followed by the Gondwanide Orogeny (Figure 2.1). This transition marked the initiation of a series of magmatic arc terranes, largely calc-alkaline granodiorite, diorite, and monzogranite intrusions in the Central Domain (Amundsen Province) of Marie Byrd Land and in the Central Domain of the Antarctic Peninsula during the Late Palaeozoic-Mesozoic. Notable episodes of magmatism occurred during the late Triassic-early Jurassic (236-199 Ma), mid-Jurassic (~180-160 Ma) and Early to Late Cretaceous (~140-80 Ma) (Leat et al., 1995; Storey et al., 1996). Though initially disconnected from Antarctica, these terranes became accreted to the continent by the end of the Cretaceous.

The outermost terrane belt in West Antarctica, the Western Domain of the Antarctic Peninsula (Vaughan and Storey, 2000) is composed of Carboniferous to Late Cretaceous accretionary sedimentary rocks such as those found on Alexander Island (Figure 2.2). This terrane accreted to the West Antarctic margin by 103 – 107 Ma, leading to back-arc plutonism and metamorphism of the Western and Central Domain in the mid-Cretaceous (Wendt et al., 2008; Vaughan et al., 2012a).

Gondwana break-up led to extensive extrusion of Jurassic volcanic rocks documented by outcrops in the Antarctic Peninsula, and resulted in rifting away of Zealandia in the Cretaceous (Weaver et al., 1992; Pankhurst et al., 2000; Korhonen et al., 2010). Plutonism on West Antarctica continued until the Cenozoic with a diachronous eastward cessation of subduction (Larter and Barker, 1991; Leat et al., 1995; Larter et al., 2002; Cunningham et al., 2002; Mukasa and Dalziel, 2000). This was followed and accompanied by the extrusion of the widespread Late Cenozoic alkali basalts (e.g. Futa and LeMasurier, 1983; Hole and LeMasurier, 1994), which crop out extensively in central West Antarctica, especially the Marie Byrd Land volcanic province (e.g. LeMasurier and Rex, 1991).

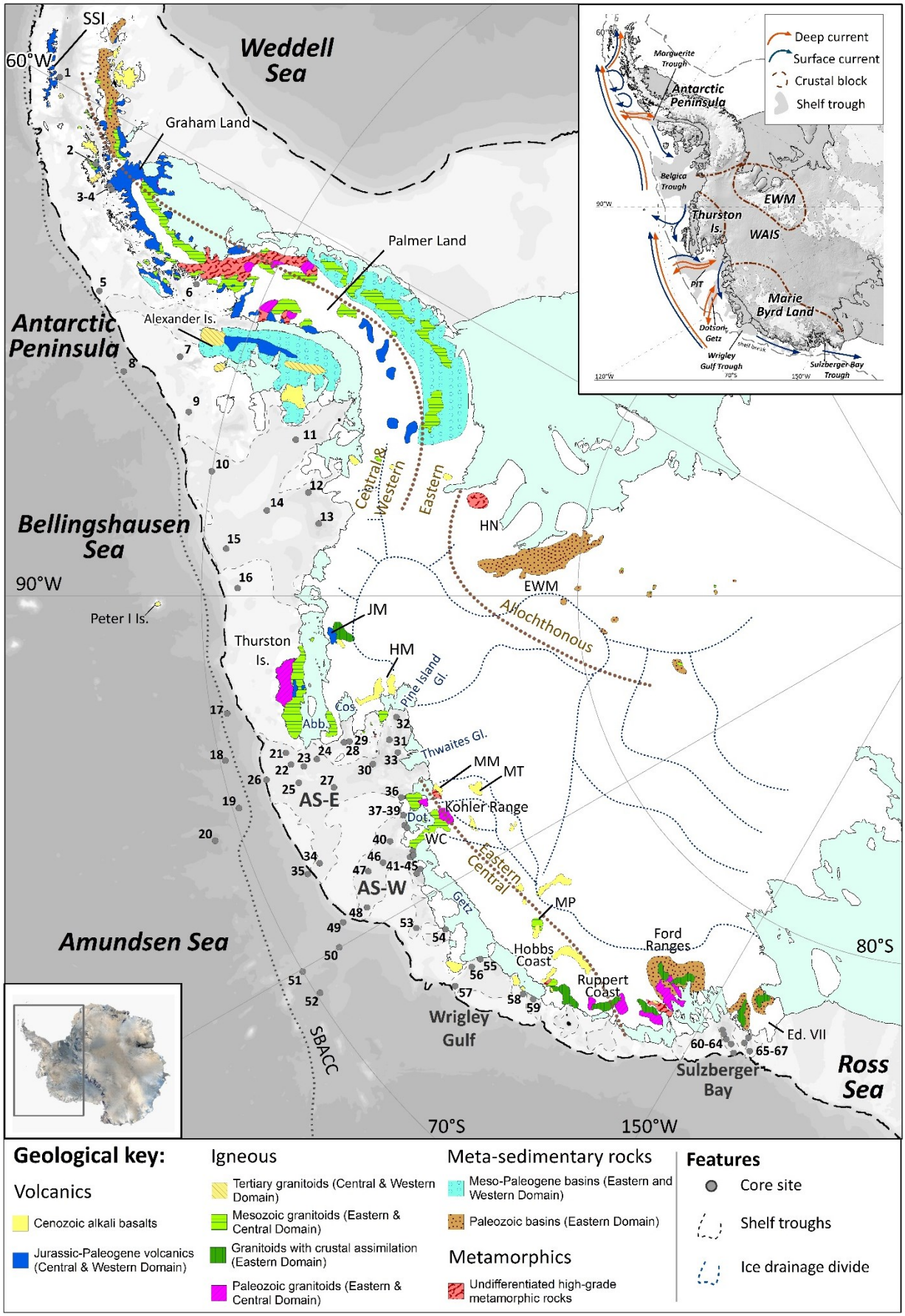

(caption on next page)

Figure 2.2. Simplified geological map of West Antarctica, including major geological units discussed in the text (Futa and LeMasurier, 1983; Storey et al., 1988; Pankhurst et al., 1993; McCarron and Smellie, 1998; Mukasa and Dalziel, 2000; Ferraccioli et al., 2002; Korhonen et al., 2010; Burton-Johnson and Riley, 2015). Thin blue dotted lines on the continent represent divides between major ice drainage basins, and brown dotted lines mark approximate boundaries between tectonic domains (Pankhurst et al., 1998; Vaughan and Storey, 2000). Grey dashed line on the continental shelf outlines bathymetric troughs, dashed black lines indicate the approximate location of the shelf break, and dotted line offshore marks position of the Southern Boundary of the Antarctic Circumpolar Current (SBACC; Orsi et al., 1995). Sites of surface sediments analysed in this study are shown as grey circles and numbers refer to their position in Table 2.1. Abbreviations: Abb – Abbot Ice Shelf; AS: Amundsen Sea; Cos – Cosgrove Ice Shelf; Dot – Dotson Ice Shelf; Ed. VII – Edward VII Peninsula: EWM – Ellsworth-Whitmore Mountains; FR – Ford Ranges; JM – Jones Mts; HN – Haag Nunataks; HM – Hudson Mts ; MM – Mt Murphy; MP – Mount Petras; MT – Mt Takahe; SSI – South Shetland Islands.; TI – Thurston Island; WAIS – West Antarctic Ice Sheet; WC – Walgreen Coast. Inset: Digital elevation model of Antarctica (Bamber et al., 2009) with major crustal blocks of West Antarctica (Dalziel and Elliot, 1982). White contours denote bedrock above modern sea-level (Fretwell et al., 2013). Blue arrows denote main surface ocean currents (Gladstone et al., 2001; Assmann et al., 2005; Murphy et al., 2013) and orange arrows denote deep (i.e. down to ca. 1000 m water depth) currents (Holland et al., 2010; Assmann et al., 2013; Murphy et al., 2013; Ha et al., 2014). Palaeo-ice streams are shown in grey.

2.2.2. Oceanography

The dominant oceanographic feature off (West) Antarctica is the eastward flowing ACC, which is driven by the West Wind Drift, creating a clockwise flow around the Antarctic continent (Orsi et al., 1995; Sokolov and Rintoul, 2009). In the eastern Pacific sector of West Antarctica the Southern Boundary of the ACC (SBACC) follows approximately the shelf break (Sokolov and Rintoul, 2009), but the SBACC runs slightly north of it in the eastern Amundsen Sea and deviates further away from the continent towards the Ross Sea (Orsi et al., 1995; Walker et al., 2013) (Figure 2.2). Wind stress and buoyancy forcing drive the westward flowing Antarctic Coastal Current, which spans the area between the SBACC and the coast (e.g. Stammerjohn et al., 2015; Kim et al., 2016a), creating a westward flowing surface current

(Figure 2.2). This general circulation pattern is complicated by local winds and large cyclonic gyres, such as in the Bellingshausen Sea (Figure 2.2) and the Ross Sea. On the shelf of the Bellingshausen Sea, for instance, significant quantities of icebergs initially drift westwards with the coastal current but are then directed northwards near Thurston Island eventually joining the eastward flowing ACC (Gladstone et al., 2001; Sokolov and Rintoul, 2009). In the Pacific sector of the Southern Ocean, deep warm water upwells onto the continental shelf (Figure 2.2 inset), locally protrudes towards the coast via bathymetric cross-shelf troughs, which were eroded by WAIS advances during past ice ages, and causes the bases of floating ice shelves to melt (e.g. Walker et al., 2007; Thoma et al., 2008; Jenkins et al., 2010; Arneborg et al., 2012; Randall-Goodwin et al., 2015). In the Amundsen Sea Embayment (ASE) the resulting glacial meltwater is detected in the mid-layer of the water column at about 400-500 m and flows northward along incised troughs towards the shelf break (e.g. Kim et al., 2016b).

The velocities of ocean currents measured and/or modelled in the surface and deep waters of our study area are on average ca. ≤5 cm/s, with a maximum of 22 cm/s (Assmann et al. 2005; Wåhlin et al., 2010, 2012, 2013, 2016; Jacobs et al., 2011, 2013; Arneborg et al., 2012; Carvajal et al., 2013; Walker et al., 2013; Ducklow et al., 2015; Kim et al., 2015; Randall-Goodwin et al., 2015). Exceptions to this are the westward flowing Antarctic Coastal Current in front of the Dotson Ice Shelf, and a local current within the Amundsen Polyna. The former current reaches a speed up to 40 cm/s in a narrow layer at 70 m water depth (Kim et al., 2016a), but this speed decreases to below 22 cm/s when integrated over the entire water column (Randall-Goodwin et al., 2015). The latter Amundsen Polynya current is characterized by a flow speed ≤27 cm/s detected at 430 m water depth north of the Dotson and westernmost Getz ice shelves (Kim et al., 2016a). These velocities will become important when discussing transport pathways of detrital mineral grains later on.

2.3. Approach and samples

2.3.1. Approach to provenance fingerprinting

Analysis of the provenance of marine detrital sediments requires the consideration of a variety of glaciological and geological factors (see review by Licht and Hemming, 2017). Glacial influence on provenance records is exerted by preferential subglacial erosion of specific substrates. Glacial-marine transport and depositional processes in the ocean can furthermore

introduce sorting and hence affect mineral assemblages in sediments. Geologically, onland bedrock needs to provide sufficient geochemical heterogeneity in order to produce distinct isotopic fingerprints. In addition, different rock types and mineral components are prone to be disproportionately represented in different grain-size fractions. Plutonic and high-grade metamorphic rocks, for instance, are rich in coarse-grained minerals, and are therefore likely to be over-represented in the coarse fraction of marine sediments. In contrast, sedimentary rocks consist of recycled continental material, and typically show a finer texture as well as depletion in minerals that are less resistant to chemical and physical weathering, such as hornblende and biotite (e.g. Pierce et al., 2014). Erosion of sedimentary rocks would lead to enrichment of these minerals in the fine fraction of glacial-marine sediments.

To limit the risk of neglecting or over-representing a particular rock type, we apply different geochemical tracers and analyse two different size-fractions of the same sediment sample. We investigate $^{40}Ar/^{39}Ar$ ages of ice-rafted (>150μm) hornblende and biotite grains, as well as Sr and Nd isotope and trace element compositions of fine-grained (<63μm) detritus. Dating of individual grains from marine sediments has been shown to provide powerful insights into the thermo-metamorphic history of the parent rocks. In the Southern Ocean, detailed studies on the provenance of East Antarctic glacial-marine sediments have shed light on previously documented as well as undiscovered geological provinces below the ice (e.g. Roy et al., 2007; Cook et al., 2014, 2017; Pierce et al., 2014, 2017). Even though most studies so far have focused on $^{40}Ar/^{39}Ar$ analysis of hornblende grains, recent work has elegantly demonstrated how biotite can provide complementary information on source rock metamorphism (Pierce et al., 2011, 2014). Both minerals are major rock-forming constituents and are present in a variety of lithologies. The advantage of using the dual dating approach relies on the fact that different lithologies might contain different amounts of hornblende and biotite grains. Additionally, hornblende and biotite minerals have different closure temperatures for argon of ~550°C and ~300°C, respectively (Harrison, 1982; Harrison et al., 1985) and hence reflect different points on the cooling path following a major extrusive or tectono-metamorphic event. The distinct attributes between both chronometers can be exploited to extract information on the source rock, only if both minerals originate from the same source. In the marine environment, however, selective transport pathways may compromise such coupling. Critical factors to consider are ocean current speeds, which determine the grain sizes and types of detrital mineral grains being eroded, transported, or deposited and hydraulic equivalence (i.e settling behaviour) of the different mineral types, which determines preferential transport and deposition of one mineral grain type over another.

In order to overcome the potential bias created by using mineral tracers, which rely on the existence of rocks containing these minerals, we also chose to investigate Sr and Nd isotopic compositions and trace element geochemistry of fine-grained detritus. Fine-grained material can be eroded from any type of geology, and its radiogenic isotope composition depends on the age and lithology of the source formation (Taylor and McLennan, 1995). Hence, fine-grained Sr and Nd isotopic compositions have the potential to record an integrated signature of bedrock eroded under an ice stream or ice margin (Hemming et al., 1998; Farmer et al., 2003, 2006; Colville et al., 2011; Pierce et al., 2011; Cook et al., 2013; 2017; Farmer and Licht, 2016). Samarium (Sm) and Nd are not fractionated during continental erosion due to their nearly equal incorporation in most rock forming minerals. Neodymium model ages, based on the long-lived ^{147}Sm to ^{143}Nd decay system, are thus effective at reconstructing the mantle extraction age of precursor material of sediments (Goldstein and Hemming, 2003). Different minerals tend to have very similar Sm/Nd ratios (e.g. Bayon et al., 2009, Garçon et al., 2013, Rickli et al., 2014), making it unlikely that Nd isotopic compositions in sediments are majorly influenced by sedimentary sorting and/or weathering. In contrast, comminution of minerals with variable rubidium(Rb)/Sr ratios can produce grain-size effects in the $^{87}Sr/^{86}Sr$ ratio, particularly due to the enrichment of clay minerals and biotite in the fine-grained fraction (e.g. Eisenhauer et al., 1999; Goldstein and Hemming, 2003). Additionally, $^{87}Sr/^{86}Sr$ ratios can be fractionated during continental weathering due to the different solubility of the parent isotope ^{87}Rb compared to the daughter isotope ^{87}Sr (e.g. Blum and Erel, 1997).

2.3.2. Samples and site selection

For this study, we selected 67 proximal to distal seafloor surface sediment samples from the Pacific margin of West Antarctica. In total, 59 samples were provided from core repositories of the British Antarctic Survey (Cambridge), the Alfred-Wegener Institute for Polar and Marine Research (Bremerhaven), and the Antarctic Marine Geology Research Facility at the Florida State University (formerly at Tallahassee, FL). We additionally complemented our sample selection by eight samples previously studied by Roy et al. (2007), which we picked for $^{40}Ar/^{39}Ar$ age analysis of biotite grains, not carried out in the original study. Table 2.1 provides a full description of the site locations and water depths, coring devices, and sample depths. Sites proximal to individual major ice streams were selected to identify the geochemical fingerprint of each ice drainage basin and therefore to constrain subglacial geology (Figure 2.2). Distal sites were selected to test whether provenance

signatures from the terminus of an active ice stream can be traced offshore, with the future goal to reconstruct ice history through time by analysing downcore records. Most sampling sites are located in the ASE, the modern-day locus of major ice stream retreat (e.g. Rignot et al., 2008, 2014), and proposed site of substantial WAIS retreat in the past (e.g. Vaughan et al., 2011).

Most sediment samples used in this study are seafloor surface samples collected with box and multiple corers, and thus are of modern or at least Late Holocene age, which has been confirmed by AMS ^{14}C dating and/or ^{210}Pb analyses for several of these samples (Hillenbrand et al., 2010a,b, 2013; Smith et al., 2011, 2014). Other samples were chosen solely due to their geographical position. Even though no chronological constraints were available for some of those samples, e.g. shelf samples from Sulzberger Bay, the stratigraphic position of these samples near the seafloor surface assures that they are most likely not older than Late Holocene, which is evident from AMS ^{14}C ages of such samples in the Bellingshausen, Amundsen and Ross Seas and on the western Antarctic Peninsula margin (The RAISED Consortium, 2014). We followed this approach to avoid the potential influence of past changes in erosion or sediment transport/deposition on the provenance of the studied sediments.

As detailed in section 2.2, current speeds in the study area are typically ≤22 cm/s. This flow velocity is too low to move sand particles (≥63 µm), which would require current speeds exceeding 26-29 cm/s (e.g. McCave et al., 2017). Large sheeted (flaky) biotite grains have a hydraulic equivalence to smaller (bulky) hornblende grains according to Komar et al. (1984) and Garzanti et al. (2008, 2009). These studies concluded that coarse grained (>150µm) biotite grains are hydraulically equivalent to quartz grains with a size exceeding ~75µm. Such grains would not be moved by the ocean currents typical for the West Antarctic margin, allowing interpretation of biotite grains >150µm as subglacial debris, which was released by grounded ice directly at the coast or transported by icebergs further offshore, alongside hornblende grains >150µm. Several samples, however, have been picked for hornblende and biotite grains from the 63-150µm fraction due to a low amount of grains in these samples. Due to the weak ocean currents in the study area, bulky hornblende grains from the 63 – 150µm fraction are likely unaffected by hydrodynamic sorting and provide the same lithologic information as the coarser >150µm size fraction. Sediment samples from sites 13 and 41 (Table 2.1, Figure 2.2) were, however, picked for biotite grains from the 63 – 150µm fraction only. These results will hence be discussed separately (i.e. potential for selective mineral transport by ocean currents).

Table 2.1. $^{40}Ar/^{39}Ar$ ages analysed in ice-rafted (>150μm or >63μm) hornblende and biotite grains from surface sediments off West Antarctica

Core Site	Site location	Core depth (cm)	Sector [a]	Size fraction	Gear	Lat	Long	Water depth (m)	Hornblende grains[b]	Biotite grains[b]	Reference
1	DF86-48	28-34	AP		piston corer	-62.68	-59.74	1234			
2	DF85-53	39-44	AP	>150μm	piston corer	-64.56	-63.16	201	**55**		this study
3	PD88-111 Grab37	Surface	AP		surface grab	-65.14	-63.97	240			
4	PD88-111 Grab41	Surface	AP		surface grab	-65.23	-64.09	200			
5	ELT05-22	4-6	AP	>150μm	piston corer	-65.95	-70.25	373	**91**	**7**	Roy et al., 2007; this study
6	DF85-82	28-33	AP	>150μm	piston corer	-68.24	-67.50	275	**39**		this study
7	PS2524-1	0-1	AP		box corer	-68.49	-72.72	458			
8	ELT05-20	2-4	AP	>150μm	trigger core	-67.18	-74.78	2926	**37**	**7**	Roy et al., 2007; this study
9	BC470	0-2	BS		box corer	-69.09	-76.39	670			
10	ELT42-09	0-2	BS	>150μm	piston corer	-69.99	-80.39	567	**30**	**19**	Roy et al., 2007; this study
11	BC361	0-1	BS	>150μm	box corer	-71.99	-76.55	633	**38**	**38**	this study
12	GC362	0-1	BS		box corer	-72.60	-80.83	846			
13	BC364	0-1	BS	63μm-2mm	box corer	-72.98	-83.44	1010		**20**	this study
14	BC369	0-2	BS	150μm-2mm	box corer	-71.58	-82.86	587	**47**	**44**	this study
15	BC459	0-1	BS	>150μm	box corer	-70.61	-86.25	676	**61**	**46**	this study
16	PS2543-3	0-1	BS		multi-corer	-70.95	-89.36	537			
17	ELT11-19	0-2	AS-E	>150μm	trigger corer	-70.42	-99.25	3808	**63**	**16**	Roy et al., 2007; this study
18	ELT11-18	2-4	AS-E	>150μm	piston corer	-70.14	-102.82	3786	**24**	**5**	Roy et al., 2007; this study
19	ELT11-17	2-4	AS-E	>150μm	trigger corer	-70.17	-106.64	3456	**6**	**5**	Roy et al., 2007; this study
20	PS58/254-2	0-2	AS-E	>150μm	multi-corer	-69.31	-108.45	4016	**14**	**7**	this study
21	PS75/192-2	0-1	AS-E		giant box corer	-71.74	-103.33	793			
22	PS69/255-3	0-1	AS-E	150μm-2mm	giant box corer	-71.80	-104.36	654	**31**		this study
23	PS69/251-1	0-1	AS-E		giant box corer	-72.11	-104.81	573			
24	DF85-109	11-17	AS-E	>150μm	piston corer	-72.49	-104.48	567	**30**		this study
25	BC451	0-1	AS-E	150μm-2mm	box corer	-71.87	-106.04	568	**49**	**51**	this study
26	BC455	0-1	AS-E	>150μm	box corer	-71.07	-105.08	807	**54**	**44**	this study
27	BC485	0-3	AS-E	150μm-2mm	box corer	-72.73	-107.29	692	**15**	**26**	this study
28	DF85 96-1	83-88	AS-E	>150μm	piston corer	-73.30	-103.62	786	**30**		this study

(table continues on next page)

29	PS69/299-1	0-1	AS-E	150µm-2mm	giant box corer	-73.44	-103.65	718	**24**	**57**	this study
30	BC482	0-2	AS-E		box corer	-73.89	-106.27	1113			
31	BC476	0-2	AS-E		box corer	-74.48	-104.42	1120			
32	PS75/159-1	0-1	AS-E	63µm-2mm	gravity corer	-74.80	-102.36	1046	**1**		this study
33	PS75/168-1	0-1	AS-E	63µm-2mm	gravity corer	-74.61	-105.87	652	**9**		this study
34	BC442	0-1	AS-E	150µm-2mm	box corer	-71.68	-113.01	608	**47**	**53**	this study
35	BC443	0-1	AS-E	150µm-2mm	box corer	-71.28	-113.46	1789	**55**	**39**	this study
36	PS69/281-3	0-1	AS-W		giant box corer	-74.33	-110.21	213			
37	NBP07-02 SMG6	Surface	AS-W		surface grab	-74.21	-111.90	343			
38	BC420	0-2	AS-W	>150µm	box corer	-74.14	-112.86	806	**24**	**15**	this study
39	NBP00-01 KC24	13-19	AS-W		kasten corer	-74.17	-113.18	301			
40	BC421	0-1	AS-W	>150µm	box corer	-73.62	-113.71	833	**32**	**21**	this study
41	BC412	0-1	AS-W	63µm-2mm	box corer	-73.92	-115.86	1128	**19**	**33**	this study
42	NBP00-01 PC22	5-10	AS-W		piston corer	-74.06	-115.46	1171			
43	NBP00-01 KC21	5-10	AS-W	>150µm	kasten corer	-74.03	-115.84	1049	**35**		this study
44	NBP07-02 SMG5	Surface	AS-W		surface grab	-74.02	-117.30	350			
45	PS69/275-2	0-1	AS-W	>150µm	giant box corer	-73.89	-117.55	1517	**11**	**37**	this study
46	BC407	0-2	AS-W	>150µm	box corer	-73.21	-115.24	815	**6**	**18**	this study
47	PS69/283-5	0-1	AS-W	150µm-2mm	giant box corer	-72.76	-115.38	612	**52**	**44**	this study
48	BC431	0-1	AS-W	>150µm	box corer	-72.30	-118.16	512	**45**	**42**	this study
49	BC433	0-1	AS-W	150µm-2mm	box corer	-71.56	-118.31	1722	**43**	**41**	this study
50	BC492	0-1	AS-W	>150µm	box corer	-71.15	-119.96	2073		**26**	this study
51	ELT33-12	2-6	AS-W	>150µm	piston corer	-70.00	-120.17	2615	**27**	**18**	Roy et al., 2007; this study
52	ELT33-11	0-2	AS-W	>63µm	piston corer	-70.10	-122.26	3639	**10**		Roy et al., 2007
53	PS2545-1	0-1	AS-W		giant box corer	-73.16	-121.95	636			
54	NBP00-01 KC17	7-13	AS-W		kasten corer	-73.79	-123.53	891			
55	NBP99-02 PC21	8-13	WH	>150µm	piston corer	-74.08	-127.79	702	**9**	**5**	this study
56	NBP99-02 TC23	0-3	WH		trigger corer	-73.78	-127.86	726			
57	NBP00-01 PC14	1-3	WH	>150µm	piston corer	-73.11	-128.32	591	**51**		this study
58	PS75/133-1	0-1	WH	>150µm	giant box corer	-74.34	-133.08	474	**19**	**40**	this study
59	PS75/130-2	0-1	WH	>150µm	giant box corer	-74.45	-134.15	793	**22**	**40**	this study

(table continues on next page)

60	DF83-III BC28	2-4	SB	>63µm	box corer	-76.83	-152.48	1024	**18**	this study
61	NBP96-01 PC12	0-3	SB		piston corer	-76.74	-152.85	881		
62	NBP96-01 TC13	0-3	SB		trigger corer	-76.65	-153.36	739		
63	NBP99-02 Grab20	Surface	SB		surface grab	-76.41	-154.82	458		
64	DF83 PC31	0-3	SB	>63µm	piston corer	-76.60	-154.10	713	**5**	this study
65	DF83-III BC26A	1-3	SB	>63µm	box corer	-76.95	-155.62	1353	**3**	this study
66	NBP96-01 JTC11	0-3	SB		trigger corer	-76.78	-155.44	392		
67	DF83-III BC33	3.5-5.5	SB		box corer	-76.63	-156.40	770		

a) AP: Antarctic Peninsula sector, BS: Bellingshausen Sea, AS-E: eastern Amundsen Sea, AS-W: western Amundsen Sea, WH: Wrigley Gulf-Hobbs Coast, SB: Sulzberger Bay

b) See Appendix Table 2.1 for complete dataset

2.4. Analytical procedures

Sediment samples were freeze-dried, weighed, and wet sieved through a 63-micron sieve. The sand fraction (>63μm) was subsequently dry sieved at 150μm to obtain the >150μm fraction (Table 2.1). The fine-grained (<63μm) fraction was separated by gravitational settling, after which the clear supernatant was discarded, and sediment was dried in an oven at 60°C. Approximately 1g of <63μm sediment was leached with buffered acetic acid to remove calcium carbonate, followed by 0.02M hydroxylamine hydrochloride solution to extract Fe-Mn oxyhydroxide coatings (Rutberg et al., 2000). Finally, the dried residue from leaching was thoroughly homogenised using an agate mortar.

Hornblende and biotite grains were hand-picked from the coarse (>150μm) fraction for $^{40}Ar/^{39}Ar$ age analysis on 43 of the 67 samples. Picking was extended to include the >63μm fraction only if too few grains were available in the >150μm fraction. Eight samples were exclusively picked from the 63-150μm fraction, of which seven were picked for hornblende grains and two for biotite grains (Table 2.1; Appendix Table 2.1). Fresh (i.e. glassy or black) grains were hand-picked from the coarse fraction with weathering being relatively minor or negligible (see also Licht and Hemming, 2017). Single grains and monitor standards (Fish Canyon sanidine) were irradiated at the USGS reactor in Denver, CO. Calibration for the neutron flux was based on J-values calculated to normalize Fish Canyon sanidine ages to 28.201+/- 0.046 Ma (Kuiper et al., 2008). $^{40}Ar/^{39}Ar$ ages were calculated from measurements of gas released using a single-step CO_2 laser fusion at the Argon Geochronology for the Earth Sciences (AGES) laboratory at Lamont-Doherty Earth Observatory. Argon isotope ratios were corrected for atmospheric argon ($^{40}Ar/^{36}Ar$ = 298.6, Lee et al., 2006), procedural blanks and mass discrimination from frequent measurements of blanks and air pipettes. Nuclear interference corrections were made based on the values reported by Dalrymple et al. (1981).

Radiogenic isotope (Sr, Nd) and trace element analyses were carried out on two separate aliquots (~50mg) from the residual and leached (i.e. detrital) <63μm sediment fraction. Aliquots were weighed into pre-cleaned Savillex vials and dissolved in a mixture of HF (2ml), HNO_3 (1ml) and $HClO_4$ (0.8ml) for three to four days on a hotplate until no visible particles remained. After digestion, one set of aliquots were dried and taken up in acid for the three-stage ion exchange chromatography in preparation for Sr and Nd isotope analysis. The Sr fraction was extracted from the sample matrix using Eichrom's Sr Spec resin in HNO3 medium (similar to Hemming et al., 2007, modified from Pin and Bassin, 1992). The sample matrix was

collected from this step and rare earth elements (REEs) were subsequently separated from the sample matrix using a cation exchange resin (AG50W-X8) in HCl medium (following the specific method of Struve et al., 2016). The Nd fraction was subsequently separated from the other REEs using Ln-Spec resin in HCl medium (modified after Pin and Zalduegui, 1997).

Dried Sr cuts were re-dissolved in 6M HCl, loaded as 1µl aliquots on degassed tungsten filaments, and covered by 1µl of $TaCl_5$ activator solution. Strontium isotopes were measured using a Trition Thermal Ionisation Mass Spectrometer (TIMS) in the Mass Spectrometry and Isotope Geochemistry laboratories at Imperial College London (MAGIC). Measured $^{87}Sr/^{86}Sr$ ratios were corrected for mass bias using an exponential law and assuming an $^{88}Sr/^{86}Sr$ ratio of 8.375. Repeated SRM987 standard measurements over the duration of three months yielded an $^{87}Sr/^{86}Sr$ ratio of 0.710261 ± 13 (2 S.D., n=31), in agreement with the published value for SRM987 of 0.710252 ± 13 (2 S.D., n=88; Weis et al., 2006). Strontium blanks were typically below 200pg (n=5), except for one batch that yielded a blank of 460pg Sr.

Neodymium isotope ratios were analysed on a Nu Plasma HR MC-ICP-MS in the MAGIC laboratories. Neodymium isotope ratios were corrected for instrumental mass bias using a $^{146}Nd/^{144}Nd$ ratio of 0.7219 and an exponential law. Measured $^{143}Nd/^{144}Nd$ ratios for all samples are reported after correcting for the average JNdi $^{143}Nd/^{144}Nd$ ratio of the session to the accepted value of 0.512115 (Tanaka et al., 2000). Blanks for the Nd procedure were typically below 10pg (n=3) but always below 40pg (n=1). Repeat measurements of the USGS BCR-2 standard over multiple runs during the course of this study yielded $^{143}Nd/^{144}Nd$ ratios of 0.512637 ± 14 (2 S.D., n=43) and $^{87}Sr/^{86}Sr$ ratios of 0.705011 ± 13 (2 S.D., n=12), in agreement with published values of by Weis et al. (2006).

Aliquots for trace element analysis were dried and transported to the Open University in Milton Keynes, and made up to a 1000-fold dilution of the original sample weight with MQ H_2O, such that the final solutions were in a 0.45 M HNO3 matrix. Trace element analyses were conducted at the Open University, using an Agilent 8800 ICP-QQQ. The ICP-QQQ has a collision / reaction (ORS) cell, which allows for targeted removal of interference ions. Most elements reported here are measured using no gas (if interferences are not an issue) or He gas in the collision reaction cell, with the exception of the REE, which were measured in mass shift mode, using O_2 in the cell. Analyses were calibrated against five USGS reference materials (BIR-1, W-2, DNC-1, BHVO-2, AGV-1) at the start of each measurement session. An internal standard was added on line to monitor and correct for instrument drift. In addition, a monitor block, consisting of the reference material BCR-2, a repeated unknown, and a nitric solution, was run every five to seven unknowns, to assess the drift correction and monitor the precision

and accuracy of analyses. Oxide formation (measured as CeO^+/Ce^+) was kept low at <1.0% in no gas, or <0.6% in He gas mode, and doubly charged species (Ce^{++}/Ce^+) at <1.5% and <1.0%, respectively. Detection limits of trace elements were typically 2–50ppt in solution for light elements and ≤2ppt for mid to heavy elements (Rb – U). Overall, precision on repeated BCR-2 standard measurements (n=12) was usually below 5%, while accuracy checks were below 10% (except for Ti at 18%).

2.5. Results

2.5.1. $^{40}Ar/^{39}Ar$ ages of individual hornblende and biotite grains

$^{40}Ar/^{39}Ar$ ages for 1281 hornblende and 864 biotite grains are reported in Table 2.1 and Appendix Table 2.1, and illustrated in Figure 2.3 for each geographical sector. From east to west, the sectors are: Antarctic Peninsula (AP sector, 60-75°W), Bellingshausen Sea (BS sector, 75-90°W), Amundsen Sea (AS sector, 90-125°W), Wrigley Gulf-Hobbs Coast (WH sector, 125-150°W) and Sulzberger Bay (SB sector, 150-160°W). Our results include 178 hornblende $^{40}Ar/^{39}Ar$ ages previously reported by Roy et al. (2007).

2.5.1.1. Antarctic Peninsula (AP, 60-75°W, core sites 1-8)

In the AP sector we find a continuous hornblende $^{40}Ar/^{39}Ar$ age spectrum from 0 to ~320 Ma with three major peaks at 14 Ma, 55 Ma and ~90 Ma, and some scattered older grains of ~480-1000 Ma and ~1600-2000 Ma (n=222; Figure 2.3a). Significantly fewer biotite grains (n=14) were analysed for $^{40}Ar/^{39}Ar$ ages (Table 2.1). Three minor age clusters occur in the 23–83 Ma age interval, with three peak ages of ~27 Ma, ~50 Ma and ~77 Ma (Figure 3b). Two single grains record ages of 360-380 Ma.

2.5.1.2. Bellingshausen Sea (BS, 75-90°W, core sites 9-16)

In the BS sector a continuous hornblende $^{40}Ar/^{39}Ar$ age spectrum spans from 0–260 Ma, but with a dominant cluster between ~75 and 140 Ma, a peak of ~110 Ma, and one older

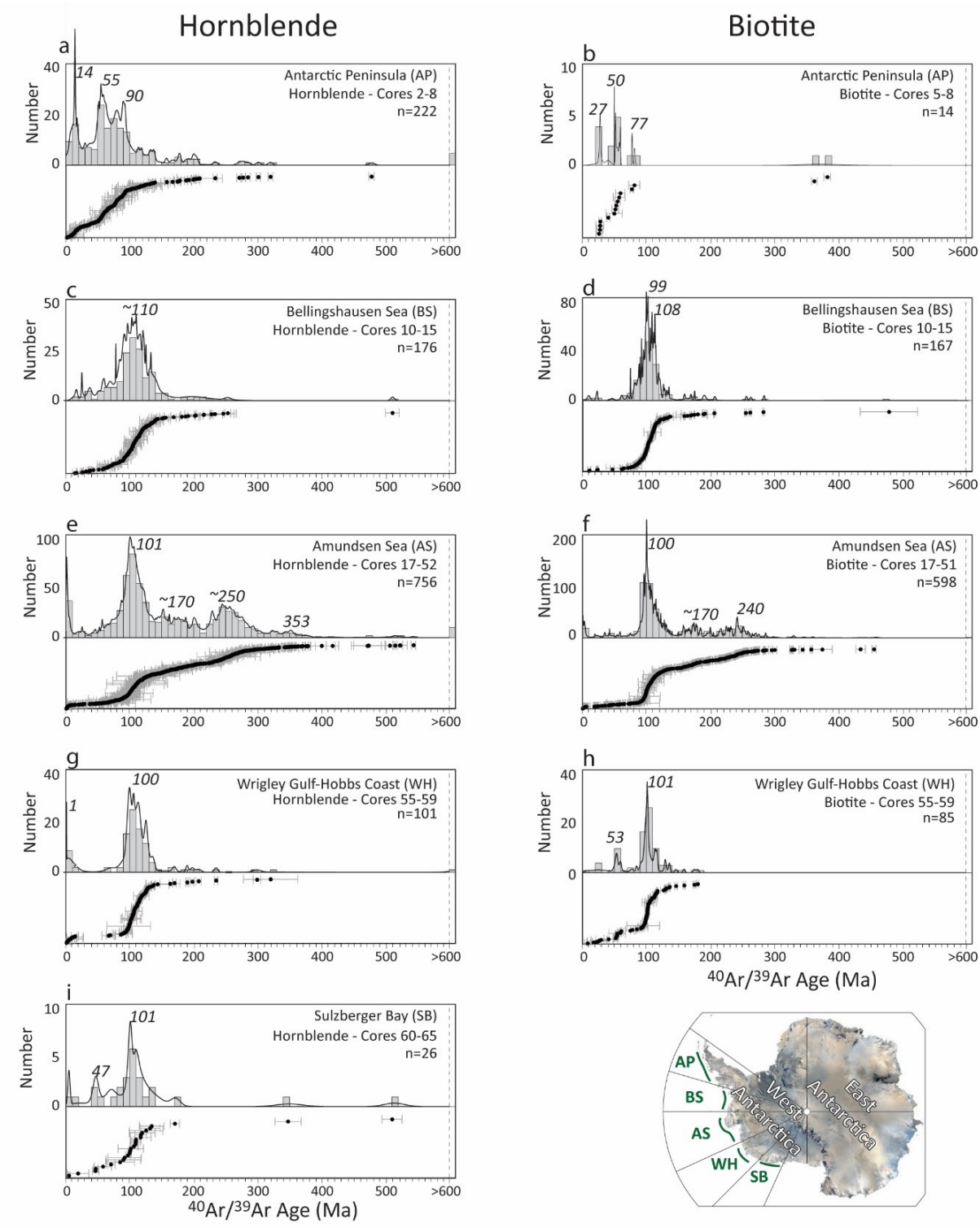

Figure 2.3. $^{40}Ar/^{39}Ar$ ages of hornblende and biotite grains from five sectors off the Pacific margin of West Antarctica. Histograms are produced using 10 Ma as bin intervals. Probability density plots (ISOPLOT4.15; Ludwig et al., 2003) are superimposed, and individual ages are shown with uncertainties in the lower panel. Results include previously analysed $^{40}Ar/^{39}Ar$ ages of hornblende grains from Roy et al. (2007) (see Table 2.1).

grain at 510 Ma (n=176; Figure 2.3c). Biotite $^{40}Ar/^{39}Ar$ ages (n=167) yield a similar age range, predominantly from 0 to ~280 Ma, with the majority of grain ages in the interval between 75 and 135 Ma, and with peaks at ~99 Ma and ~108 Ma. One older grain dates back to 480 Ma (Figure 2.3d). The finer sand size-fraction (63 − 150μm) of site 13 was picked for biotite grains, and hence the $^{40}Ar/^{39}Ar$ ages for this sample could be influenced by ocean current transport because biotite grains of this size can be affected by relatively weak ocean currents with flow speeds as observed in the Bellingshausen Sea. However, age distribution observed at site 13 shows no pattern deviating from that of other core samples in the BS sector, with the majority of the ages ranging from 94-120 Ma (Appendix Table 2.1).

2.5.1.3. Amundsen Sea (AS, 90-125°W, core sites 17-54)

The AS sector is the main focus of this study and a total of 756 hornblende grains and 598 biotite grain ages are reported for this sector. A continuous hornblende $^{40}Ar/^{39}Ar$ age spectrum from 0 to ~380 Ma shows two noticeable peaks at ~101 Ma and ~250 Ma. A significant number of grains with ages ranging from 140 to ~210 Ma are found, which are notably absent from the other sectors. A minor age peak is observed at ~353 Ma. Though significantly smaller in number, older hornblende grains also appear in these sediments (n=20), with age clusters of 400-550 Ma, 640-800 Ma, 1120-1360 Ma, 1700-1850 Ma and 2600-2800 Ma (Figure 2.3e, Appendix Table 2.1). Biotite $^{40}Ar/^{39}Ar$ ages (n=598) spread from 0 to ~300 Ma, with a prominent peak at ~100 Ma, and secondary peaks at ~170 and 240 Ma. Nine older grains yield ages of ~330-375 Ma, ~450 and 890 Ma (Figure 2.3f). The apparent modern (~0 Ma) age peaks observed in both minerals in the AS sector seem suspicious as the corresponding grains were primarily picked from core 49 situated on the upper continental slope, and are not detected in other sectors (Figure 2.2). Biotite grains from site 41 were picked from a smaller size-fraction (Table 2.1) and hence could potentially be influenced by ocean current transport due to fast flow speeds detected off the Dotson Ice Shelf (Kim et al., 2016a). However, $^{40}Ar/^{39}Ar$ ages from this sample do not reveal any pattern deviating from that of $^{40}Ar/^{39}Ar$ ages in nearby core samples (Appendix Table 2.1). We hence consider differential sorting of biotite and hornblende mineral grains of the same size fraction to be negligible in our study area.

2.5.1.4. Wrigley Gulf-Hobbs Coast (WH, 125-150°W, core sites 55-59)

A total of 101 hornblende ages obtained from the WH sector record well defined $^{40}Ar/^{39}Ar$ ages with populations around 0-20 Ma and 65-140 Ma, and age probability peaks at ~0 Ma and ~100 Ma as well as three scattered ages of ~210 Ma, 300 Ma and 610 Ma (Figure 2.3g). Biotite $^{40}Ar/^{39}Ar$ ages (n= 85) cover a similar age range from 0 to ~150 Ma, with some scattered ages of ~180 Ma, but the dominant age probability peak at 101 Ma is slightly older than the one defined by the hornblende grains. A second minor age peak is detected around ~53 Ma, which is absent in the hornblende age spectrum (Figure 2.3h).

2.5.1.5. Sulzberger Bay (SB, 150-160°W, cores 60-67)

Most hornblende $^{40}Ar/^{39}Ar$ ages (n= 26) from the SB sector range from 0 to ~135 Ma, and show a well-defined age probability peak at ~100 Ma. Minor age peaks occur at ~48 Ma and ~5 Ma and three individual grains yield ages of ~170 Ma, 350 Ma and 510 Ma (Figure 2.3i). No biotite grains were picked/analysed from this sector.

2.5.2. Neodymium and strontium isotope composition of fine-grained detrital sediments

In total, 63 and 51 samples were analysed for their detrital Nd and Sr isotopic composition respectively. The Nd isotope results are expressed as epsilon values (ε_{Nd}), which denotes the deviation from a chondritic value of 0.512638 in parts per 10,000 (Jacobsen and Wasserburg, 1980). Neodymium and Sr isotope results from the study of Roy et al. (2007) on eight additional distal samples are included in the following results and subsequent discussion (Table 2.2).

Overall, detrital continental margin sediments off West Antarctica have Nd isotopic compositions ranging from -12 to +2 and $^{87}Sr/^{86}Sr$ ratios from 0.7493 to 0.7057 (Figure 2.4, Table 2.2). The values are anti-correlated as expected from global trends, and are distinct for individual sectors. The highest Nd isotope values and the lowest Sr isotope ratios are found in the WH sector (ε_{Nd} = -0.5 to 1.3, $^{87}Sr/^{86}Sr$ = 0.7056 to 0.7061), in the westernmost sample from the AS sector (site 54; ε_{Nd} = 0.3) and in the easternmost samples from the AP sector (site 1 and 3-5: ε_{Nd} = 0.9 to 2.2; $^{87}Sr/^{86}Sr$ ~0.7053). The other end of the data range is defined by samples from SB, i.e. offshore from western Marie Byrd Land (Figure 2.2), with Nd isotopic

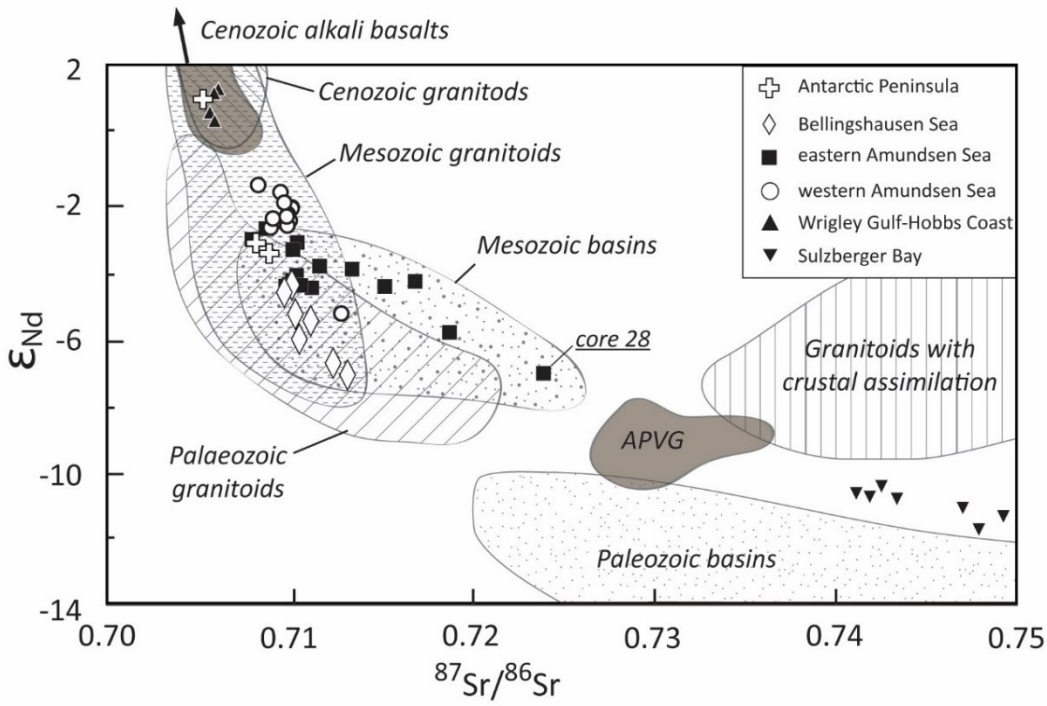

Figure 2.4. Neodymium (Nd) and strontium (Sr) isotopic compositions of detrital surface sediments along the Pacific margin of West Antarctica. Marine sediment data are displayed as symbols according to geographical sectors defined in Table 2.1 (only samples where both Nd and Sr isotope ratios were measured are shown). Isotopic compositions of major bedrock outcrops on land are compiled from the literature (see Appendix Table 2.2) and correspond to the units displayed in Figure 2.2 (Note: For simplicity data from high-grade metamorphic rocks are not displayed). APVG = Antarctic Peninsula Volcanic Group.

compositions of -11.9 to -10.6 and $^{87}Sr/^{86}Sr$ = 0.7411 to 0.7493. Detrital shelf sediments from the AS sector reveal intermediate values, but with distinctly different values in the eastern and western AS. In the eastern AS, lower Nd and higher radiogenic Sr values (ε_{Nd} ~-7.3, $^{87}Sr/^{86}Sr$ ~ 0.7240) are found in a sample taken in front of Pine Island Glacier (site 32, Table 2.2, Figure 2.2). Along the eastern flank of the AS sector the isotopic fingerprints of the samples change systematically northwards across the shelf to higher Nd and lower Sr isotopic compositions (site 20: ε_{Nd} ~-3.3, $^{87}Sr/^{86}Sr$ ~ 0.7079). A uniform signature is observed in the western AS sector, where shelf sediments yield Nd and Sr isotopic compositions of ε_{Nd} ~-2.9 to -1.7 and $^{87}Sr/^{86}Sr$ ~0.7082 to 0.7101 (n=17), except sample from site 39 proximal to Dotson Ice Shelf (ε_{Nd} = 0.4; $^{87}Sr/^{86}Sr$ was not measured) and site 51 on the lower continental slope ε_{Nd} ~-5.5; $^{87}Sr/^{86}Sr$ = 0.7128). Detrital surface sediments from the BS extend from the values recorded in the western AS and on the eastern AS shelf towards lower Nd and higher Sr values, along

Table 2.2. Strontium and neodymium isotope compositions of the detrital fraction (<63μm) and clay mineral assemblages (<2μm) of surface sediments off West Antarctica

			Radiogenic signature								Clay mineral assemblages				
Core Site	**Site location**	**Sector [a]**	**$^{87}Rb/^{86}Sr$ [b]**	**$^{87}Sr/^{86}Sr$ (±2 S.E.)**	**$^{147}Sm/^{144}Nd$ [b]**	**$^{143}Nd/^{144}Nd$ (±2 S.E.)**	**ε_{Nd}**	**± 2 S.D. [c]**	**T_{DM} (Ma) [d]**	**Ref.[e]**	**Ill (%)**	**Sme (%)**	**Kln (%)**	**Chl (%)**	**Ref.[e]**
1	DF86-48*	AP				0.512751 ± 8	2.20	0.36							
2	DF85-53	AP													
3	PD88-111 Grab37*	AP				0.512725 ± 9	1.69	0.36							
4	PD88-111 Grab41*	AP				0.512719 ± 9	1.57	0.36							
5	ELT05-22	AP		0.705281 ± 5	0.1366	0.512685 ± 10	0.92		920	2,3					
6	DF85-82	AP													
7	ELT05-20	AP		0.708198 ± 7	0.1341	0.512469 ± 18	-3.30		1304	2,3					
8	PS2524-1	AP	1.423	0.708926 ± 5	0.1179	0.512453 ± 8	-3.61	0.21	1109	1	58	8	0	34	4
9	BC470	BS	1.628	0.710100 ± 4	0.1179	0.512405 ± 8	-4.55	0.28	1185	1					
10	ELT42-09	BS			0.1255	0.512420 ± 9	-4.25		1261	2					
11	BC361	BS	1.706	0.709714 ± 5	0.1160	0.512392 ± 16	-4.80	0.32	1183	1	44	20	5	31	5
12	GC362	BS	1.920	0.711165 ± 5	0.1173	0.512349 ± 6	-5.64	0.29	1267	1	52	19	6	23	5
13	BC364	BS	1.846	0.713189 ± 5	0.1142	0.512267 ± 6	-7.24	0.30	1353	1	66	7	2	25	5
14	BC369	BS	1.547	0.710320 ± 4	0.1152	0.512359 ± 9	-5.44	0.24	1224	1	46	20	3	30	5
15	BC459	BS	1.399	0.710539 ± 4	0.1136	0.512321 ± 10	-6.18	0.28	1262	1	52	16	6	26	6 (GC372)
16	PS2543-3	BS	1.889	0.712397 ± 5	0.1123	0.512285 ± 7	-6.89	0.21	1301	1	59	14	4	23	4
17	ELT11-19	AS-E		0.707928 ± 6	0.1271	0.512470 ± 10	-3.28		1197	2,3					
18	ELT11-18	AS-E		0.709790 ± 5	0.1213	0.512399 ± 5	-4.66		1239	2,3					
19	ELT11-17	AS-E		0.710616 ± 8	0.1257	0.512400 ± 16	-4.64		1299	2,3					
20	PS58/254-2	AS-E	1.658	0.708704 ± 4	0.1185	0.512486 ± 6	-2.96	0.30	1064	1	33	38	12	17	7
21	PS75/192-2	AS-E	1.726	0.710162 ± 5	0.1127	0.512408 ± 8	-4.49	0.21	1121	1					
22	PS69/255-3	AS-E	1.541	0.709971 ± 5	0.1135	0.512402 ± 8	-4.61	0.24	1139	1	41	27	14	18	7
23	PS69/251-1	AS-E	2.041	0.711226 ± 6	0.1123	0.512396 ± 8	-4.71	0.21	1133	1	41	25	16	18	7
24	DF85-109	AS-E													

(table continues on next page)

25	BC451	AS-E	2.255	0.711652 ± 5	0.1131	0.512429 ± 10	-4.07	0.28	1092	1	46	23	16	14	7
26	BC455	AS-E	1.703	0.710384 ± 5	0.1117	0.512415 ± 9	-4.34	0.28	1099	1	45	24	16	15	7
	duplicate sample[f]			*0.710365 ± 5*		*0.512415 ± 7*	*-4.35*	*0.16*							
27	BC485	AS-E	2.789	0.713436 ± 4	0.1141	0.512425 ± 9	-4.16	0.28	1110	1	46	19	19	15	7
28	DF85 96-1	AS-E													
29	PS69/299-1	AS-E	1.193	0.707947 ± 5	0.1118	0.512470 ± 8	-3.28	0.24	1018	1	41	26	7	25	7
30	BC482	AS-E	3.303	0.715235 ± 4	0.1118	0.512399 ± 9	-4.67	0.28	1125	1	44	19	23	15	7
31	BC476	AS-E	3.903	0.718795 ± 6	0.1116	0.512329 ± 10	-6.03	0.28	1226	1	52	16	17	16	7
32	PS75/159-1	AS-E	4.659	0.723959 ± 5	0.1100	0.512267 ± 8	-7.24	0.21	1299	1					
33	PS75/168-1	AS-E	3.557	0.716904 ± 6	0.1096	0.512406 ± 8	-4.52	0.21	1090	1	50	13	21	16	7 (PS69/292-3)
34	BC442	AS-E	1.946	0.710417 ± 4	0.1131	0.512465 ± 9	-3.37	0.28	1039	1	47	18	19	16	7
35	BC443	AS-E	1.712	0.710181 ± 5	0.1135	0.512454 ± 8	-3.58	0.28	1059	1	47	20	18	16	7
36	PS69/281-3	AS-W	2.058	0.709504 ± 6	0.1116	0.512542 ± 8	-1.87	0.28	909	1	42	14	29	15	7
37	NBP07-02*	AS-W				0.512512 ± 8	-2.46	0.32							
38	BC420	AS-W	2.084	0.710125 ± 5	0.1167	0.512519 ± 6	-2.32	0.29	992	1	47	13	18	22	7
39	NBP00-01 KC24*	AS-W				0.512660 ± 9	0.43	0.37							
40	BC421	AS-W	2.205	0.710011 ± 5	0.1124	0.512499 ± 8	-2.71	0.28	981	1	43	22	19	16	7
41	BC412	AS-W	2.109	0.709682 ± 5	0.1148	0.512496 ± 9	-2.76	0.28	1008	1	40	21	20	19	7
42	NBP00-01 PC22*	AS-W				0.512517 ± 10	-2.35	0.29							
43	NBP00-01 KC21*	AS-W				0.512495 ± 8	-2.79	0.29							
44	NBP07-02*	AS-W				0.512486 ± 8	-2.97	0.32							
45	PS69/275-2	AS-W	2.446	0.710115 ± 5	0.1144	0.512517 ± 8	-2.35	0.29	973	1	43	20	20	16	7
46	BC407	AS-W	2.275	0.709903 ± 4	0.1134	0.512509 ± 7	-2.52	0.24	975	1	43	18	22	18	7
	duplicate sample			*0.710041 ± 5*		*0.512504 ± 9*	*-2.62*	*0.21*							
47	PS69/283-5	AS-W	2.180	0.709881 ± 4	0.1133	0.512492 ± 7	-2.86	0.20	1000	1	43	20	19	18	7
48	BC431	AS-W	1.746	0.708959 ± 4	0.1136	0.512488 ± 8	-2.92	0.28	1008	1	46	17	19	18	7
49	BC433	AS-W	1.848	0.709845 ± 4	0.1128	0.512505 ± 7	-2.59	0.28	976	1	43	17	21	18	7
50	BC492	AS-W	1.697	0.709711 ± 5	0.114	0.512526 ± 7	-2.18	0.29	954	1					
51	ELT33-12	AS-W		0.712846 ± 6	0.1188	0.512358 ± 8	-5.46		1272	2,3					
52	ELT33-11	AS-W		0.709086 ± 6	0.1187	0.512502 ± 10	-2.65		1040	2,3					
53	PS2545-1	AS-W	1.809	0.708276 ± 7	0.1144	0.512553 ± 8	-1.66	0.21	918	1	39	28	23	10	4

(table continues on next page)

54	NBP00-01 KC17*	WH				0.512653 ± 8	0.29	0.32								
55	NBP99-02 PC21*	WH				0.512610 ± 7	-0.54	0.32								
56	NBP99-02 TC23	WH	1.012	0.705656 ± 5	0.1156	0.512667 ± 10	0.57	0.24	752	1	37	27	20	17	1	
57	NBP00-01 PC14	WH	1.045	0.705917 ± 4	0.1155	0.512654 ± 9	0.32	0.24	770	1	37	25	20	18	1	
58	PS75/133-1	WH	1.081	0.706122 ± 4	0.1151	0.512703 ± 8	1.26	0.30	693	1	36	28	14	21	1	
59	PS75/130-2	WH	0.891	0.705889 ± 4	0.1158	0.512697 ± 5	1.14	0.29	707	1						
60	DF83-III BC28	SB	7.142	0.741188 ± 4	0.1133	0.512085 ± 8	-10.79	0.24	1616	1						
61	NBP96-01 PC12	SB	7.492	0.743425 ± 4	0.1131	0.512077 ± 9	-10.95	0.24	1623	1						
62	NBP96-01 TC13	SB	8.265	0.747045 ± 5	0.1127	0.512063 ± 8	-11.22	0.24	1639	1						
63	NBP99-02 Grab20	SB				0.512058 ± 7	-11.31	0.32								
64	DF83 PC31	SB	8.324	0.747928 ± 5	0.1129	0.512030 ± 8	-11.86	0.24	1691	1						
65	DF83-III BC26A	SB	8.010	0.742576 ± 4	0.1119	0.512096 ± 9	-10.58	0.24	1576	1						
66	NBP96-01 JTC11	SB	8.224	0.749275 ± 4	0.1118	0.512050 ± 10	-11.47	0.24	1643	1						
	duplicate sample			*0.749534 ± 6*		*0.512633 ± 8*	*-11.52*	*0.16*								
67	DF83-III BC33	SB	7.976	0.741931 ± 4	0.1128	0.512080 ± 8	-10.89	0.24	1616	1						

a) see Table 2.1

b) calculated from elemental composition of the same sample (Table 2.3)

c) standard deviation based on the reproducibility of the $^{143}Nd/^{144}Nd$ ratio of the JNdi standard during each run: 0.512224 ±14 (n=24), 0.512116 ±12 (n=17), 0.512144 ± 12 (n=13), 0.512157 ± 10 (n=12), 0.512106 ± 12 (n=32), 0.512149 ± 11 (n=27) and 0.512142 ± (n=16).

d) Nd model ages relative to present depleted mantle (DM) using a one-stage evolution model: $^{147}Sm/^{144}Nd$= 0.2136; $^{143}Nd/^{144}Nd$=0.51315

e) (1) this study; (2) Roy et al., 2007; (3) Hemming et al., 2007; (4) Hillenbrand et al., 2002; (5) Hillenbrand et al., 2009; (6) Hillenbrand et al., 2010; (7) Ehrmann et al., 2011

f) *duplicate sample* values represent full procedural replicates of sample powders (i.e. from digestion, through ion exchange chromatography, to mass spectrometry).

*) Samples denoted with a star were analysed at L-DEO for their Nd isotopic composition using similar methodologies to those described in the main text, but run on a AXIOM MC-ICP-MS (see van de Flierdt et al., 2008, for more details on methodology).

steeper slope (ε_{Nd} = -7.3 to -4.2, $^{87}Sr/^{86}Sr$ = 0.7097 to 0.7132, n=8; Figure 2.4). General anti-correlation of Nd and Sr isotopes in fine-grained detrital sediments off West Antarctica, in addition to the extremely uniform values observed in the western AS from ice proximal to ice distal (ocean) locations, indicate that both isotope systematics are predominantly governed by provenance and not by sedimentary sorting or weathering. I further carried out additional leaching tests using a different leaching reagents on several samples to test the robustness of our (neodymium isotope) data to trace provenance. The tests reveal good agreement between sediments leached with the new procedure and our standard method (i.e. section 2.4), with (almost) similar neodymium isotopic compositions within the error, showing that our data reliably measures to the detrital signature of the sediments (cf. Appendix Figure 2.1 and Appendix Table 2.3).

2.5.3. Trace element composition of fine-grained detrital sediments

Trace element compositions, including full REE patterns, were analysed on the <63µm fraction of 44 detrital seafloor sediment samples. The data are reported in Table 2.3 and are illustrated in mid-ocean ridge basalt (MORB)-normalized spider diagrams (Figure 2.5).

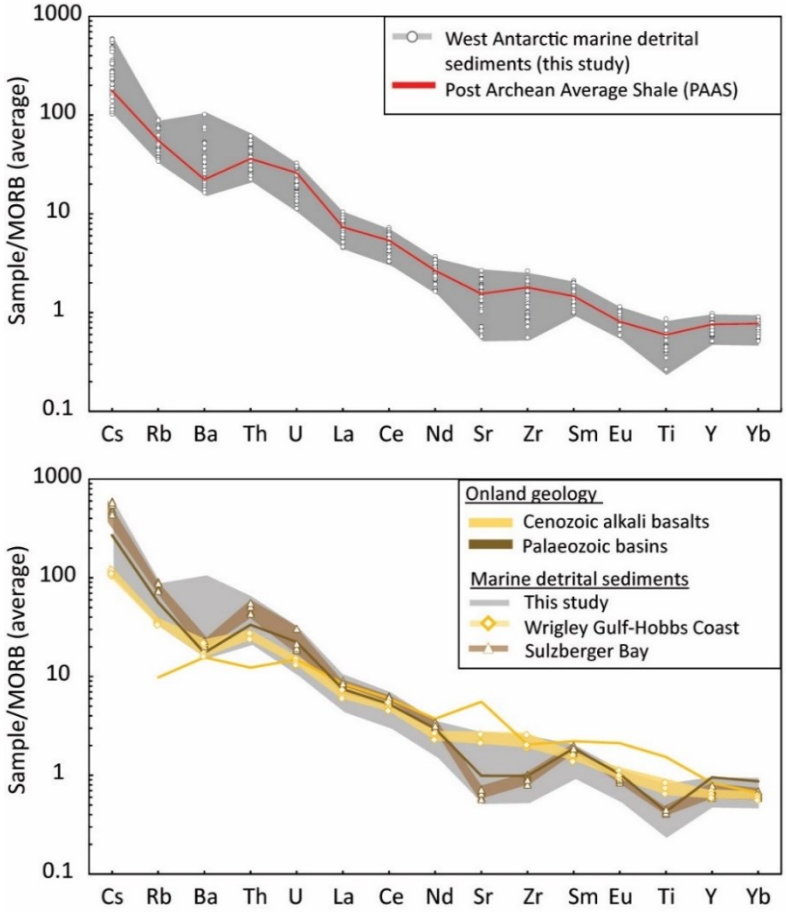

(Caption on next page)

Figure 2.5. a) Trace element compositions of fine-grained (<63μm) detrital surface sediments along the Pacific margin of West Antarctica, normalized to average mid-ocean ridge basalts and arranged in order of incompatibility (Gale et al., 2013). Individual sample results are indicated by white circles in the upper graphs, while the red line denotes the composition of the Post-Archean Average Shale (PAAS, McLennan, 2001). The grey field denotes marine sediment samples from this study. b) Sediments from the Wrigley Gulf-Hobbs Coast sector are now shown as diamonds connected by a yellow line, and sediments from Sulzberger Bay are shown as triangles connected by a brown line. The grey field denotes samples from the Antarctic Peninsula (AP), Bellingshausen Sea (BS) and Amundsen Sea (AS) sectors. The patterns for these two groups are similar to onland results obtained for Late Cenozoic alkali basalts (yellow line; Futa and LeMasurier, 1983; Hart et al., 1997) and Palaeozoic meta-sedimentary rocks (brown line; Korhonen et al., 2010), respectively.

Overall, detrital sediments show compositions comparable to Post-Archean Average Shale (PAAS) (McLennan, 2001). Some elements, however, deviate from PAAS. Zirconium (Zr) concentrations show considerable scatter (Figure 2.5), while the elemental ratio of the two high-field strength elements Zr and yttrium (Y) are high in sediments from the WH sector (Zr/Y ~10.5) and low in sediments from the SB sector (Zr/Y ~4) as well as in sediments proximal to Pine Island and Thwaites Glaciers (Zr/Y ~5). Similarly, high Sr over thorium (Th) ratios of 25 – 30 are observed in WH, at site 29 on the AS (Sr/Th ~25) and in the AP sector (site 8, Sr/Th ~27), with the latter sector being mostly characterized by very low thorium (Table 2.3). The ratio of Th over scandium (Sc), which generally describes the relative contribution of basic and felsic rocks (Taylor and McLennan, 2001), is elevated in the samples from sites 32 and 33 proximal to Pine Island and Thwaites Glaciers (1.5-2.0), but low in WH (~0.8-1), sites 8 to 11 from the AP and BS sectors (0.6-0.8) and in one distal sample from site 20 in the AS sector (0.6). Europium anomalies are moderately negative (Eu/Eu* = 0.5-0.9) in most samples, and correlate well with Th/Sc (r^2= 0.67; Figure 2.6) and Sr/Th ratios (r^2= 0.87) (Table 2.3).

2.6. Provenance of glacial-marine sediments

In this section we evaluate the provenance signature of coarse and fine-grained detrital sediment from the seafloor in conjunction with onshore geochemical (Sr and Nd isotope values)

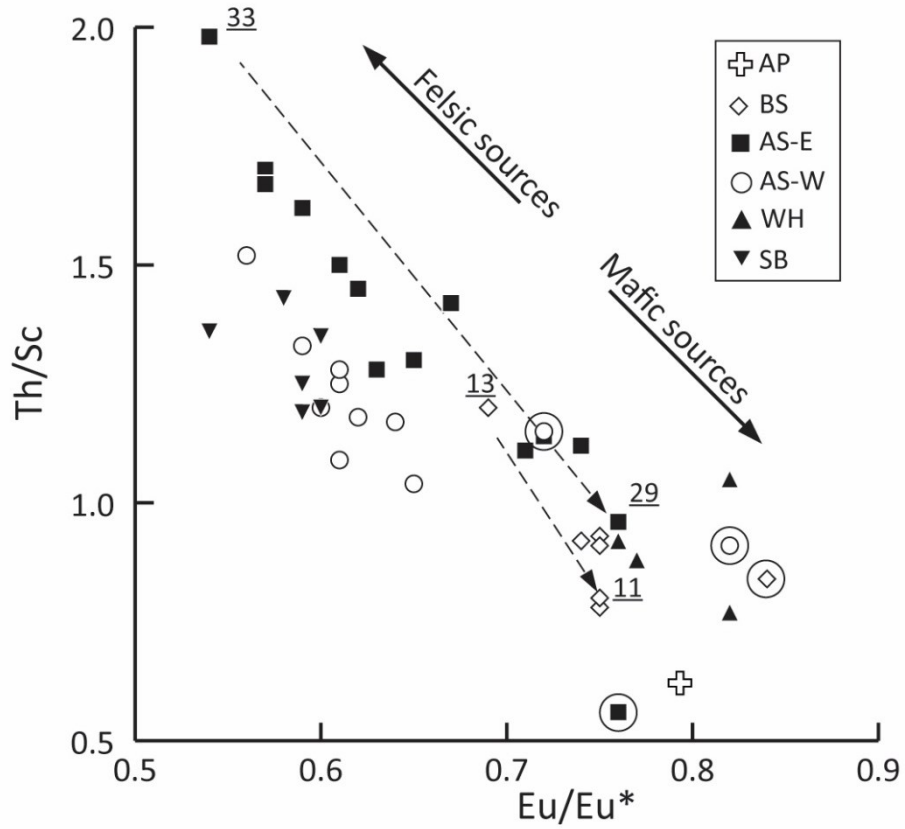

Figure 2.6. Diagram of Th/Sc vs Eu/Eu* compositions of surface sediments along the Pacific margin of West Antarctica. Circled samples denote sediments with positive cerium anomalies ($Ce/Ce^{*}>1.1$), indicating minor redox processes affecting the sediments or their sources. Numbers indicate core sites of samples, which are discussed in more detail in the main text. Abbreviations: AP – Antarctic Peninsula, BS – Bellingshausen Sea, AS-E – eastern Amundsen Sea, AS-W – western Amundsen Sea, WH – Wrigley Gulf – Hobbs Coast, SB – Sulzberger Bay.

---

and geochronological data (K-Ar and $^{40}Ar/^{39}Ar$ ages on hornblende, biotite, mica grains and whole rock samples, U/Pb zircon ages, and Rb-Sr whole rock ages) compiled from the literature (Table 2.2). Knowledge of the regional tectonic history of West Antarctica is a prerequisite in order to relate offshore $^{40}Ar/^{39}Ar$ mineral ages to bedrock sources, particularly in areas where $^{40}Ar/^{39}Ar$ cooling ages are scarce and comparison with other geochronological data is required. Overall, offshore $^{40}Ar/^{39}Ar$ ages match those reported for outcrops onland, recording largely the erosion of syn-tectonic Palaeozoic to Cenozoic plutons emplaced onto the former magmatic arc along the Gondwana margin, with distinctive thermal age peaks at ~245 Ma, ~170 Ma, ~100 Ma and 50-90 Ma. Onshore U-Pb ages on zircons on crystalline bedrock are sparse, but fall in the range of our offshore $^{40}Ar/^{39}Ar$ data, reflecting West Antarctica's active margin

settings. In addition to the thermochronological ages, fine-grained Sr and Nd isotope and trace element fingerprints from the <63μm sediment fraction record an integrated signal of the erosion of major outcropping lithologies. The observed fingerprint in marine sediments allows to distinguish between glaciomarine sediments supplied by five major source sectors on West Antarctica. The integrated signal allows furthermore to identify erosion of volcanic and sedimentary rocks, which are inherently difficult to detect using hornblende and biotite $^{40}Ar/^{39}Ar$ ages (i.e. 'mineralogical or grain-size biases').

2.6.1. Antarctic Peninsula (AP)

2.6.1.1. Provenance of ice-rafted detritus

Outcrops of young Late Cretaceous (<90 Ma) to Cenozoic igneous rocks have been documented on the Antarctic Peninsula, especially along the western coasts of Graham and Palmer Land and on Alexander Island (Leat et al., 1995; McCarron and Smellie, 1998; Ryan, 2005; Figure 2.2, Appendix Table 2.2), recording the latest stage of the eastward-propagating cessation of ocean crust subduction under the Antarctic plate. Of particular interest are igneous rocks of ~12-14 Ma (particularly of hornblende-bearing mafic dykes), 20-21, 47-68 Ma and ~85 Ma, which crop out along the coast of Marguerite Bay on the west side of the Antarctic Peninsula, and at the northern tip of Alexander Island (Figure 2.2 e.g. Ryan, 2007; Appendix Table 2.2), and which could explain the majority of the mineral grain ages observed in the shelf sediments. The extensively outcropping metasedimentary rocks of Carboniferous to Cretaceous age on Alexander Island are depleted in amphiboles and micas (Pierce et al., 2014) and hence not captured in the offshore $^{40}Ar/^{39}Ar$ age record. The signature of these sedimentary rocks is however observed by qualitative petrographic analysis and fine-grained Sr and Nd isotope fingerprints. In particular, site 8 sediments contain quarzitic clasts (quartz, feldspars), fine-grained dark lithic clasts (mudstone?), and lithic clasts with a fine-grained pink matrix. This is consistent with erosion of the meta-sedimentary formation on Alexander Island, which is largely composed of feldspathic sandstone, siltstone and black mudstones (Burn, 1984), as well as igneous rocks (lava, tuffs) similar to the Tertiary volcanics present on the island (Care, 1983).

2.6.1.2. Provenance of fine-grained detritus

Outcrops of Cretaceous to Cenozoic plutonic and volcanic (<97 Ma) rocks are characterised by radiogenic Nd and Sr isotopic compositions (ε_{Nd} ~-2 to 5; $^{87}Sr/^{86}Sr$ ~0.703-0.708; Pankhurst et al., 1988; McCarron and Smellie, 1998; Riley et al., 2001, 2003; Ryan, 2005), which are distinct from Jurassic to Cretaceous granitoids in the Antarctic Peninsula and the Amundsen Sea region (ε_{Nd}: -8 to 0; $^{87}Sr/^{86}Sr$ ~0.703-0.715) (Figure 2.4; Appendix Table 2.2). The Antarctic Peninsula Volcanic Group and/or nearby granitoids hence seem to be the likely source for the fine-grained detritus with relatively radiogenic values observed at site 1-4, most proximal to the Graham Land coast (Figure 2.2; Table 2.2). Sites 7 and 8 are located near to the Alexander Island, where extensive occurrences of arkosic sedimentary rocks (Figure 2.2, Doubleday et al., 1993) are characterized by less radiogenic Nd isotope values (ε_{Nd}: -8 to -3; Figure 2.3; Adams et al., 2005). The agreement between onshore data and our new offshore data indicate a local source for the marine sediments in the AP sector. We note, however, that a mixture between the granitic and volcanic rocks, which crop out on Alexander Island, could yield a similar isotopic fingerprint.

2.6.2. Bellingshausen Sea (BS)

2.6.2.1. Provenance of ice-rafted detritus

Bedrock exposures along the BS coast are extremely rare (Figure 2.2) and limited to outcrops of some Cretaceous igneous rocks (Rb-Sr whole rock ages of 113 to 128 Ma; Pankhurst and Rowley, 1991) and Miocene-Quaternary volcanic rocks (Smellie, 1999; Hathway, 2001). Aeromagnetic investigations detected the 'Pacific Margin Anomaly' in the coastal region flanking the BS, notably in its eastern sector (Ferraccioli et al., 2006), which has been linked to mafic and intermediate basement rocks $^{40}Ar/^{39}Ar$ dated at 129-141 Ma by (Maslanyi and Storey, 1990; Vaughan et al., 1998). Hornblende and biotite $^{40}Ar/^{39}Ar$ ages, extracted from our marine sediment samples, record a dominant age interval of 74 to ~140 Ma with well-defined age peaks of ~110 Ma and ~99-108 Ma, respectively. Onland source rock candidates for such ages are mid-Cretaceous felsic plutons intruding metasedimentary rocks in eastern Palmer Land (Figure 2.2; $^{40}Ar/^{39}Ar$ dated to 95-119 Ma; Vaughan et al., 2012b), and/or older terranes which have been affected by the amphibolite-grade thermo-metamorphic Palmer Land event at 103-107 Ma (Wendt et al., 2008; Vaughan et al., 2012a). We suggest that this

Palmer Land thermal event potentially affected large parts of the coast around the Bellingshausen Sea. Supporting evidence for this idea comes from the absence of mafic intrusion ages (i.e. Pacific Margin Anomaly; 129-141 Ma) in the sedimentary record of the eastern BS sector. Furthermore, distinctively different geologies along the eastern and western coasts of the Bellingshausen Sea seem not to be reflected in the iceberg-rafted component of the offshore sediments, which show a narrow range of $^{40}Ar/^{39}Ar$ age populations in both hornblende and biotite grains between sites 11 and 13 indicating regional thermal resetting (Table 2.2; Figure 2.2).

2.6.2.2. Provenance of fine-grained detritus

Surface sediments in the BS are characterized by lower Nd isotopic composition for a given $^{87}Sr/^{86}Sr$ value compared to the other sectors (ε_{Nd} = -7.3 to -4.2, $^{87}Sr/^{86}Sr$ = 0.7097 to 0.7132; Figure 2.4). Volcanic rocks of the Antarctic Peninsula Volcanic Group, situated inland of the BS coast (Figs. 2, 4), could provide the less radiogenic Nd isotopic compositions, but are Jurassic in age (~160-190 Ma) and have high $^{87}Sr/^{86}Sr$ values (Riley et al., 2001). The Cenozoic alkali basalts have very high Nd and low Sr isotope values and thus are unlikely to explain the observed signature in the shelf sediments (Figure 2.4). Furthermore, clay mineral data from shelf sediments in the BS sector (Table 2.2) make it unlikely that volcanic source rock from along the BS coast contribute significantly to the observed provenance of the glacial-marine sediments, because enhanced smectite contents (indicative of supply of volcanic detritus) are restricted to samples from the easternmost BS sector along the west coast of Alexander Island (Hillenbrand et al., 2009b). More negative ε_{Nd} values, as well as felsic trace element patterns (high Th/Sc, Eu/Eu* and low Sr/Zr and Zr/Y), are consistent indicators of a more evolved source (e.g. McLennan et al., 1993), notably in the western BS sector. This observation is in agreement with the clay mineral composition of marine sediments along the southern coast of the BS (Hillenbrand et al., 2009b), which is characterised by high illite and low smectite contents (sites 11 to 12), indicating a granitic or gneissic source (Figure 2.5). Felsic bedrock in the southern hinterland of the BS has indeed been inferred from aeromagnetic observations, with ilmenite-rich intrusions in the west contrasting with magnetite-rich counterparts to the east responsible for the Pacific Margin Anomaly (Ferraccioli et al., 2006).

Table 2.3. Trace element composition of detrital <63µm surface sediments off West Antarctica (in ppm)

Core Site	Site location	Sector[a]	Li	Sc	Ti	V	Cr	Mn	Co	Ni	Cu	Zn	Rb	Sr	Y	Zr	Cs	Ba	La	Ce	Pr	Nd	Sm	Eu	Gd	Tb	Dy	Ho	Er	Yb	Lu
8	PS2524-1	AP	54	15	4123	108	50	661	12	21	34	137	**122**	**247**	21	84	5	634	22.8	50.6	5.4	**20.9**	**4.1**	0.9	3.5	0.6	3.3	0.7	2.1	1.9	0.3
9	BC470	BSE	47	14	3954	90	44	542	9	17	16	144	**120**	**213**	23	96	6	966	26.8	57.7	6.1	**23.6**	**4.6**	1.0	3.9	0.6	3.6	0.8	2.2	2.2	0.3
11	BC361	BSE	40	15	4115	94	43	612	11	18	23	131	**129**	**218**	22	98	6	883	27.5	59.7	6.0	**23.3**	**4.5**	1.0	3.8	0.6	3.5	0.7	2.1	2.2	0.3
12	GC362	BSE	40	14	4151	90	42	634	11	22	22	128	**146**	**220**	25	101	6	1131	31.0	65.0	6.7	**25.8**	**5.0**	1.1	4.2	0.7	3.9	0.8	2.3	2.4	0.4
13	BC364	BSE	19	8	2675	51	31	418	6	16	21	72	**108**	**169**	19	65	3	566	24.3	50.1	5.3	**20.1**	**3.8**	0.8	3.2	0.5	3.0	0.6	1.8	1.9	0.3
14	BC369	BSE	41	14	4329	85	40	596	10	19	23	125	**133**	**249**	24	108	6	1568	30.7	66.0	6.8	**26.1**	**5.0**	1.1	4.2	0.7	3.8	0.8	2.3	2.2	0.3
15	BC459	BSE	32	13	4300	74	37	523	8	13	19	95	**118**	**245**	25	116	5	1312	34.3	70.7	7.7	**29.0**	**5.5**	1.1	4.5	0.7	4.0	0.8	2.4	2.5	0.4
16	PS2543-3	BSE	33	11	3511	70	36	559	10	27	19	101	**148**	**226**	23	96	5	748	32.0	69.7	7.0	**26.8**	**5.0**	1.1	4.1	0.6	3.8	0.8	2.3	2.1	0.3
20	PS58/254-2	ASE-E	36	19	4528	90	51	546	11	25	105	125	**109**	**190**	19	146	5	646	23.0	52.8	5.2	**19.8**	**3.9**	0.8	3.2	0.5	3.0	0.6	1.8	1.9	0.3
21	PS75/192-2	ASE-E	38	12	4677	80	41	468	9	15	20	103	**137**	**231**	25	146	6	1025	35.5	76.3	7.8	**29.4**	**5.5**	1.1	4.5	0.7	4.0	0.8	2.4	2.4	0.4
22	PS69/255-3	ASE-E	38	13	4781	79	45	470	9	17	22	96	**140**	**263**	26	152	6	1343	34.9	76.8	8.1	**30.7**	**5.8**	1.1	4.7	0.7	4.2	0.9	2.6	2.5	0.4
23	PS69/251-1	ASE-E	39	12	4759	79	41	479	9	16	20	103	**148**	**209**	28	163	7	727	38.4	82.3	8.4	**31.8**	**5.9**	1.1	4.8	0.8	4.4	0.9	2.7	2.5	0.4
25	BC451	ASE-E	42	14	4884	86	49	521	10	19	24	113	**165**	**211**	29	181	9	1032	41.2	90.4	9.3	**34.8**	**6.5**	1.1	5.2	0.8	4.7	1.0	2.8	2.9	0.4
26	BC455	ASE-E	36	13	4755	81	48	480	9	16	24	101	**144**	**245**	27	178	7	1540	40.1	84.6	8.8	**33.1**	**6.1**	1.1	4.9	0.8	4.4	0.9	2.6	2.6	0.4
	duplicate sample[b]		*37*	*12*	*4569*	*81*	*45*	*483*	*9*	*15*	*24*	*100*	***142***	***250***	*28*	*195*	*6*	*1514*	*40.3*	*85.7*	*8.8*	***33.4***	***6.2***	*1.2*	*5.1*	*0.8*	*4.6*	*0.9*	*2.7*	*2.7*	*0.4*
27	BC485	ASE-E	47	14	4924	89	49	544	11	21	27	124	**180**	**187**	32	194	11	979	46.0	98.5	10.1	**37.5**	**7.1**	1.2	5.7	0.9	5.2	1.1	3.1	3.1	0.5
29	PS69/299-1	ASE-E	31	13	4393	88	50	564	10	16	18	107	**127**	**308**	21	111	5	662	31.1	65.8	6.9	**26.8**	**4.9**	1.1	4.0	0.6	3.6	0.7	2.1	2.1	0.3
30	BC482	ASE-E	43	11	4284	74	41	509	9	20	23	102	**159**	**139**	26	144	10	676	38.7	80.3	8.4	**31.6**	**5.8**	1.0	4.6	0.7	4.1	0.9	2.4	2.5	0.4
31	BC476	ASE-E	50	14	4745	84	54	521	11	23	24	112	**203**	**150**	30	137	12	732	47.0	96.7	10.3	**38.6**	**7.1**	1.2	5.7	0.9	5.0	1.0	3.0	3.0	0.4
32	PS75/159-1	ASE-E	58	13	4624	81	53	474	10	24	18	101	**213**	**133**	30	134	12	711	44.5	91.9	9.8	**36.8**	**6.7**	1.2	5.5	0.9	5.0	1.0	3.0	2.8	0.4
33	PS75/168-1	ASE-E	58	13	5404	83	47	506	10	19	15	109	**210**	**171**	36	210	12	615	55.0	113.1	12.0	**44.5**	**8.1**	1.3	6.6	1.0	6.0	1.2	3.5	3.3	0.5
34	BC442	ASE-E	42	13	5684	90	52	489	11	21	24	117	**151**	**224**	29	219	8	1101	42.7	92.6	9.5	**35.6**	**6.7**	1.2	5.3	0.8	4.8	1.0	2.8	2.9	0.4
35	BC443	ASE-E	41	14	5319	86	51	507	11	21	35	113	**146**	**247**	29	197	8	2080	40.6	88.7	8.9	**33.7**	**6.3**	1.2	5.2	0.8	4.6	1.0	2.7	2.8	0.4
36	PS69/281-3	ASE-W	48	13	5832	94	46	574	14	23	19	128	**163**	**230**	34	263	11	598	50.9	104.5	11.1	**41.9**	**7.7**	1.3	6.2	1.0	5.7	1.1	3.2	3.0	0.5
38	BC420	ASE-W	47	17	6113	119	62	762	16	28	25	134	**152**	**211**	31	200	9	664	41.7	88.7	9.3	**35.3**	**6.8**	1.2	5.5	0.9	5.1	1.1	3.0	3.0	0.4
40	BC421	ASE-W	48	16	5613	106	57	608	13	24	28	140	**152**	**200**	28	202	9	641	41.6	87.8	9.1	**34.6**	**6.4**	1.2	5.3	0.8	4.6	0.9	2.7	2.7	0.4
41	BC412	ASE-W	49	14	5395	111	50	722	14	25	33	141	**146**	**201**	28	179	9	658	40.4	85.6	9.2	**35.2**	**6.7**	1.2	5.4	0.8	4.6	1.0	2.6	2.6	0.4
45	PS69/275-2	ASE-W	57	15	5561	120	53	542	13	26	37	179	**165**	**195**	29	214	11	747	43.5	95.1	9.6	**36.1**	**6.8**	1.2	5.4	0.8	4.8	1.0	2.8	2.7	0.4
46	BC407	ASE-W	58	15	5815	116	53	687	14	26	27	175	**155**	**198**	28	192	10	622	41.1	90.8	9.4	**36.0**	**6.7**	1.2	5.5	0.9	4.8	1.0	2.8	2.6	0.4
	duplicate sample		*61*	*15*	*5709*	*116*	*53*	*659*	*14*	*26*	*26*	*170*	***159***	***187***	*28*	*194*	*9*	*597*	*41.8*	*90.2*	*9.1*	***34.7***	***6.5***	*1.2*	*5.3*	*0.8*	*4.7*	*0.9*	*2.7*	*2.6*	*0.4*
47	PS69/283-5	ASE-W	50	14	5819	101	52	608	13	26	28	149	**152**	**202**	27	211	9	595	40.2	90.2	9.0	**33.9**	**6.4**	1.2	5.1	0.8	4.6	0.9	2.7	2.5	0.4
48	BC431	ASE-W	43	15	5726	103	53	610	14	24	27	130	**146**	**241**	26	194	8	799	40.1	88.7	8.9	**33.9**	**6.4**	1.2	5.1	0.8	4.4	0.9	2.5	2.6	0.4
49	BC433	ASE-W	46	15	5503	98	44	592	12	22	41	139	**152**	**238**	29	252	9	2212	42.3	98.4	9.2	**34.6**	**6.5**	1.2	5.2	0.8	4.8	1.0	2.8	2.8	0.4
50	BC492	ASE-W	43	15	5259	93	47	581	12	22	48	129	**141**	**240**	26	235	8	2972	36.7	88.1	8.1	**30.2**	**5.7**	1.1	4.6	0.7	4.2	0.9	2.5	2.5	0.4
53	PS2545-1	ASE-W	54	14	5868	98	47	667	14	27	37	160	**146**	**233**	25	174	8	546	36.5	80.2	8.1	**30.7**	**5.8**	1.1	4.7	0.7	4.1	0.8	2.4	2.3	0.3
56	NBP99-02 TC23	WG	25	13	8695	94	64	593	16	25	23	125	**98**	**281**	22	243	4	479	32.3	71.0	7.4	**28.3**	**5.4**	1.3	4.6	0.7	4.1	0.8	2.3	2.1	0.3
57	NBP00-01 PC14	WG	31	13	7712	91	59	629	14	24	27	126	**103**	**284**	24	237	4	513	34.3	77.1	7.5	**29.0**	**5.5**	1.3	4.7	0.7	4.2	0.8	2.4	2.2	0.3
58	PS75/133-1	WG	31	11	6716	76	45	600	10	18	16	114	**107**	**287**	26	308	4	653	37.9	82.9	8.5	**32.8**	**6.2**	1.5	5.0	0.8	4.3	0.9	2.4	2.3	0.3
59	PS75/130-2	WG	32	12	6736	94	52	674	15	24	19	113	**106**	**344**	22	227	4	618	35.3	75.2	7.8	**30.2**	**5.8**	1.3	4.6	0.7	3.9	0.8	2.2	2.1	0.3
60	DF83-III BC28	SBE	76	15	4522	98	78	380	13	34	22	115	**219**	**89**	26	119	17	588	42.5	88.6	9.6	**36.9**	**6.9**	1.2	5.4	0.8	4.5	0.9	2.6	2.5	0.4
61	NBP96-01 PC12	SBE	71	15	4516	98	81	378	13	35	21	129	**223**	**87**	26	117	17	617	42.9	90.7	9.8	**37.5**	**7.0**	1.2	5.4	0.8	4.5	0.9	2.6	2.5	0.4
62	NBP96-01 TC13	SBE	71	15	4302	102	83	365	13	35	22	115	**219**	**77**	23	110	16	593	43.0	89.4	9.7	**37.2**	**6.9**	1.2	5.2	0.7	4.0	0.8	2.3	2.2	0.3
64	DF83 PC31	SBE	66	14	4100	98	81	329	12	32	22	108	**212**	**74**	23	111	15	568	42.2	88.9	9.6	**36.7**	**6.9**	1.2	5.2	0.8	4.1	0.8	2.3	2.4	0.3
65	DF83-III BC26A	SBE	81	16	4343	104	81	392	13	32	23	119	**257**	**93**	22	96	20	674	40.3	84.7	9.1	**34.8**	**6.4**	1.1	4.9	0.7	3.9	0.8	2.2	2.1	0.3
66	NBP96-01 JTC11	SBE	81	16	4474	101	79	374	13	31	22	109	**258**	**91**	25	94	19	620	45.5	95.7	10.7	**40.5**	**7.5**	1.1	5.6	0.8	4.5	0.9	2.5	2.3	0.3
	duplicate sample		*97*	*15*	*4212*	*101*	*74*	*391*	*12*	*31*	*23*	*113*	***262***	***85***	*29*	*108*	*19*	*592*	*48.2*	*100.8*	*10.8*	***41.1***	***7.6***	*1.2*	*6.0*	*0.9*	*4.8*	*1.0*	*2.7*	*2.5*	*0.4*
67	DF83-III BC33	SBE	78	16	4518	101	80	385	13	33	21	119	**254**	**92**	23	106	20	669	44.3	92.2	10.1	**38.2**	**7.1**	1.1	5.3	0.8	4.3	0.9	2.4	2.3	0.4

(table continues on next page)

Table 2.3. (*continued***)**

Core Site	Site location	Sector[a]	Hf	Pb	Th	U	Sr/Th	Sr/Zr	Zr/Y	Th/Sc	Ce/Ce*	Eu/Eu*
8	PS2524-1	AP	2.2	11.4	9.0	1.7	27.35	2.95	3.98	0.60	1.05	0.77
9	BC470	BSE	2.6	11.9	11.0	1.9	19.42	2.21	4.26	0.78	1.04	0.71
11	BC361	BSE	2.8	18.0	11.7	1.8	18.61	2.22	4.45	0.80	1.06	0.73
12	GC362	BSE	2.7	20.3	13.3	1.9	16.52	2.19	4.01	0.92	1.03	0.70
13	BC364	BSE	1.8	15.1	10.1	1.3	16.73	2.59	3.48	1.20	1.02	0.70
14	BC369	BSE	3.0	17.0	11.7	1.9	21.23	2.31	4.56	0.84	1.05	0.73
15	BC459	BSE	3.2	17.1	12.0	2.0	20.40	2.11	4.64	0.93	1.00	0.69
16	PS2543-3	BSE	2.6	24.8	10.2	1.6	22.14	2.36	4.18	0.91	1.07	0.75
20	PS58/254-2	ASE-E	3.4	20.1	10.5	1.5	18.03	1.30	7.71	0.56	1.11	0.72
21	PS75/192-2	ASE-E	3.7	18.1	13.5	2.2	17.13	1.58	5.83	1.11	1.06	0.69
22	PS69/255-3	ASE-E	4.2	19.4	14.1	2.4	18.63	1.72	5.90	1.12	1.05	0.67
23	PS69/251-1	ASE-E	4.2	21.0	15.6	2.5	13.45	1.29	5.85	1.30	1.06	0.64
25	BC451	ASE-E	4.6	26.0	19.7	2.8	10.73	1.17	6.29	1.45	1.06	0.60
26	BC455	ASE-E	4.7	21.0	18.4	2.6	13.35	1.38	6.57	1.42	1.03	0.61
	duplicate sample		*4.9*	*21.8*	*15.0*	*2.5*						
27	BC485	ASE-E	4.8	28.0	22.8	3.5	8.21	0.96	6.08	1.62	1.05	0.57
29	PS69/299-1	ASE-E	3.0	18.8	12.5	2.0	24.56	2.79	5.15	0.96	1.03	0.76
30	BC482	ASE-E	3.8	24.2	19.5	2.8	7.14	0.97	5.63	1.70	1.02	0.57
31	BC476	ASE-E	3.9	27.6	23.9	3.5	6.30	1.10	4.50	1.67	1.01	0.59
32	PS75/159-1	ASE-E	3.6	27.1	19.6	3.1	6.79	0.99	4.46	1.50	1.01	0.60
33	PS75/168-1	ASE-E	5.1	30.6	24.8	3.6	6.90	0.81	5.84	1.98	1.01	0.54
34	BC442	ASE-E	5.5	24.2	17.2	2.6	13.07	1.02	7.50	1.28	1.06	0.63
35	BC443	ASE-E	5.0	22.1	15.7	2.5	15.75	1.26	6.87	1.14	1.07	0.63
36	PS69/281-3	ASE-W	6.4	33.0	19.9	3.1	11.55	0.88	7.68	1.52	1.01	0.58
38	BC420	ASE-W	4.8	28.0	18.7	2.7	11.25	1.05	6.46	1.09	1.03	0.62
40	BC421	ASE-W	5.0	28.3	19.5	2.8	10.23	0.99	7.09	1.25	1.04	0.61
41	BC412	ASE-W	4.7	32.9	18.5	2.6	10.85	1.12	6.39	1.28	1.02	0.61
45	PS69/275-2	ASE-W	5.2	28.8	20.5	3.9	9.52	0.91	7.26	1.33	1.07	0.58
46	BC407	ASE-W	4.7	33.8	17.9	3.1	11.04	1.03	6.74	1.20	1.06	0.60
	duplicate sample		*4.6*	*32.9*	*17.1*	*2.9*						
47	PS69/283-5	ASE-W	5.1	30.8	16.8	2.5	12.05	0.96	7.94	1.18	1.09	0.62
48	BC431	ASE-W	4.9	29.4	17.8	2.4	13.59	1.25	7.33	1.17	1.08	0.64
49	BC433	ASE-W	6.0	24.7	16.9	2.4	14.03	0.94	8.64	1.15	1.15	0.63
50	BC492	ASE-W	5.7	20.6	14.0	2.1	17.15	1.02	9.18	0.91	1.18	0.65
53	PS2545-1	ASE-W	4.2	27.4	15.1	2.2	15.40	1.34	6.98	1.04	1.07	0.63
56	NBP99-02 TC23	WG	5.6	20.7	9.9	1.6	28.42	1.16	10.88	0.77	1.06	0.82
57	NBP00-01 PC14	WG	5.4	24.5	11.3	1.7	25.07	1.20	9.76	0.88	1.10	0.77
58	PS75/133-1	WG	6.9	18.6	11.2	1.8	25.63	0.93	11.82	1.05	1.06	0.82
59	PS75/130-2	WG	4.9	20.0	11.2	1.6	30.79	1.52	10.31	0.92	1.04	0.77
60	DF83-III BC28	SBE	3.2	17.7	17.7	2.2	5.03	0.75	4.61	1.20	1.01	0.60
61	NBP96-01 PC12	SBE	3.2	22.7	18.1	2.3	4.78	0.74	4.49	1.19	1.02	0.60
62	NBP96-01 TC13	SBE	3.0	18.1	18.3	2.3	4.20	0.70	4.77	1.19	1.01	0.59
64	DF83 PC31	SBE	3.1	19.3	17.5	2.2	4.24	0.67	4.76	1.25	1.02	0.61
65	DF83-III BC26A	SBE	2.7	19.5	21.4	2.4	4.35	0.97	4.40	1.35	1.01	0.58
66	NBP96-01 JTC11	SBE	2.7	20.5	21.7	3.6	4.21	0.97	3.75	1.36	1.00	0.54
	duplicate sample		*2.9*	*23.2*	*20.6*	*2.3*						
67	DF83-III BC33	SBE	3.0	17.9	22.4	2.6	4.12	0.88	4.50	1.43	1.00	0.56

a) see Table 2.1

b) *duplicate sample* values represent full procedural replicates of sample powders (i.e. from digestion).

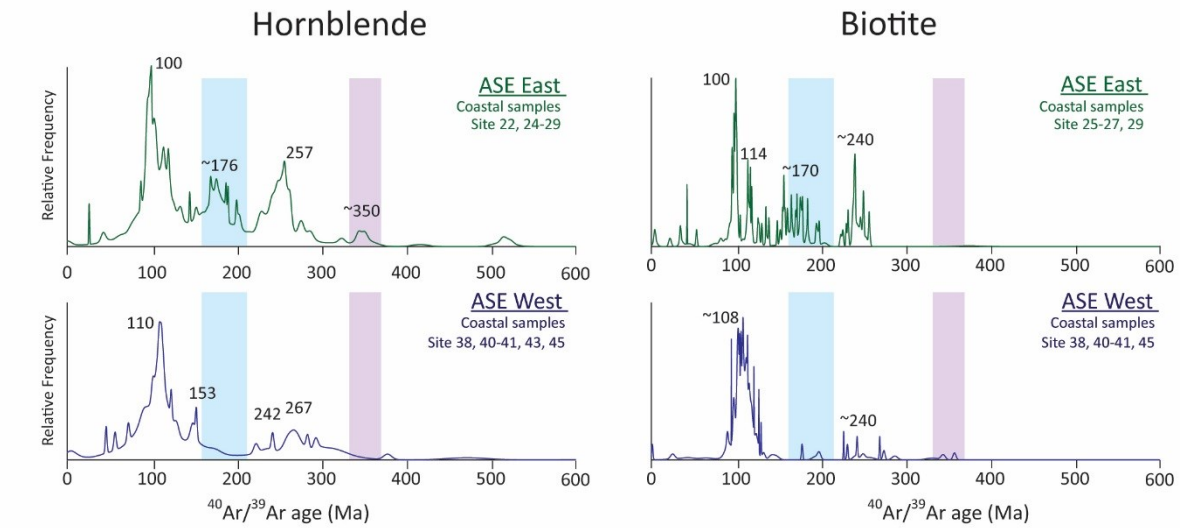

Figure 2.7. Relative frequency of $^{40}Ar/^{39}Ar$ ages on hornblende and biotite grains from proximal locations in the Amundsen Sea Embayment (ASE). Upper panel displays results for the eastern ASE (sites 22 and 24-29) and lower panel displays results for the western ASE (sites 38, 40-41 and 45). Note the presence of a significant population of hornblende grains with ages of ~140-210 Ma (blue shading) and ~350 Ma (purple shading) in the eastern ASE and their absence from the western ASE.

2.6.3. Amundsen Sea

2.6.3.1. Provenance of ice-rafted detritus

Ice-rafted hornblende and biotite grains in sediments from the AS are distinct from other sectors on the Pacific margin of West Antarctica because of the significant presence of $^{40}Ar/^{39}Ar$ ages >140 Ma (Figure 2.3e,f). Predominant hornblende age peaks are ~100-110 Ma, ~140-210 Ma, ~250 Ma and ~350 Ma, and ~100-110 Ma, ~170 and ~240 Ma for biotite grains (Figure 2.7). Similar age populations have been detected in coastal outcrops of mainly calc-alkaline igneous and metaigneous granitoid rocks around the ASE by using a variety of dating methods (Pankhurst et al., 1993; 1998; Mukasa and Dalziel, 2000; Kipf et al., 2012; Riley et al., 2017; Appendix Table 2.2).

In detail, sites proximal to the coast reveal a different provenance between the Walgreen Coast in the western AS, and the coast extending from Thurston Island towards Pine Island Bay in the eastern AS (Figure 2.2). Sites 22 and 24-29 along the eastern AS coast are characterized by a large number of grains with ages from 140-210 Ma, while grains from sites proximal to the Walgreen Coast (sites 38, 40-41 and 45) lack such ages (Figure 2.7). Ice-rafted

debris (IRD) supplied by icebergs calved from of the Abbot and Cosgrove Ice Shelves (Figure 2.2), as well as from Pine Island and/or Thwaites Glaciers (sites 31-32) are likely sources for the observed $^{40}Ar/^{39}Ar$ ages of 140-210 Ma. The unique geological signature of the Thurston Island block, with its characteristic Jurassic ages, was already specified by Pankhurst et al. (1993), based on biotite and hornblende K-Ar ages (~150 Ma) and is also present in our offshore record.

Peak Cretaceous ages for both hornblende and biotite grains are slightly but distinctively (~10 Ma) different between the eastern and western ASE (Figure 2.7). Hornblende and biotite grains supplied from the Walgreen Coast (western ASE) record ages of 108-110 Ma, while erosion along the eastern ASE coast sheds grains with a pronounced ~100 Ma age peak (Figure 2.7). This difference in mineral age population between the western and eastern Amundsen Sea sectors can be related to the diachronous eastward cessation of subduction, and therefore a progression of calc-alkaline magmatism from Marie Byrd Land towards Thurston Island (Mukasa and Dalziel, 2000). Finally, a minor ~353 Ma age peak is visible in ice-rafted hornblende grains, particularly at sites 18, 22 and 25-27 proximal to Thurston Island, but not in biotite grains (Figs. 2.2, 2.7; Appendix Table 2.1). Matching ages can be identified onland from a granodioritic orthogneiss formation cropping out on the eastern side of Thurston Island, which has been dated by zircon U-Pb to ~349 Ma (Riley et al., 2017). Material from these outcrops could either be carried by icebergs into the eastern AS sector via the Antarctic Coastal Current, or similar outcrops could be located below ice streams feeding the Abbot Ice Shelf, which eventually calves into the eastern ASE.

Rocks cropping out along the Walgreen Coast have Cretaceous (~100-130 Ma, zircon U-Pb and $^{40}Ar/^{39}Ar$ plateau) and Late Palaeozoic ages (~250 Ma and ~350-500 Ma, zircon U-Pb) (Pankhurst et al., 1998; Mukasa and Dalziel, 2000; Kipf et al., 2012). These ages are mostly found in the grains of the proximal offshore sediments, except for the 350-500 Ma age interval, which may be absent due to the limited onshore occurrence of rocks of that age and the limited amount of grains analysed in the marine sediments.

One striking observation when comparing the geological map (Figure 2.2) with the marine detrital mineral grain ages (Figure 2.3) is the notable absence of ages that can be related to outcropping Late Cenozoic alkali basalt volcanoes (e.g. Hudson Mountains, Mount Murphy and Mount Takahe, Figure 2.2), with the exception of site 49 from the continental slope. Explanations for this observation could either involve the limited extent of such lithologies below the erosive ice drainage compared to the igneous batholith, or the fact that hornblende

and biotite grains are not present or are too fine-grained to be detected in the coarse (i.e. >150μm) fraction of marine samples, and hence not reflected in the $^{40}Ar/^{39}Ar$ age spectrum.

2.6.3.2. Provenance of fine-grained detritus

Similar to the $^{40}Ar/^{39}Ar$ ages of the ice-rafted grains, the Sr and Nd isotopic composition of the fine-grained sediments in the AS can be separated into an eastern and western sub-sector, broadly delimited by the extent of the Pine Island and Cosgrove-Abbot troughs in the East and the Dotson-Getz Trough in the West, which are incised into the continental shelf (Larter et al., 2014; Figs. 2.2, 2.4). Sediments in the western AS are characterized by a very homogeneous Sr and Nd isotope signature (ε_{Nd} ~-2.9 to -1.8 and $^{87}Sr/^{86}Sr$ ~0.7082 to 0.7101), which correlates with the isotopic signature of Mesozoic granites and granodiorites observed in coastal outcrops (Figs. 2.4, 2.9). We note that sites 36 to 45 are located proximal to the Dotson Ice Shelf and various parts of the Getz Ice Shelf along the Walgreen Coast. The glaciers feeding into these ice shelves drain distinct, separate basins, but nevertheless the offshore sediment samples record very similar Sr and Nd isotope fingerprints. Site 39 marks an exception to this general pattern (Figs. 2.2, 2.9), because it is characterized by distinctively higher ε_{Nd} values, potentially due to a much localised source. Supply of material eroded from Palaeozoic granites seems to be a minor contributor to the fine-grained detritus, similar to what was observed for the IRD fraction from sites in this area.

In the eastern AS, sediment recovered just in front of Pine Island Glacier (site 31) shows a different and distinct radiogenic isotope fingerprint (ε_{Nd} = -7.2; $^{87}Sr/^{86}Sr$ = 0.7240; Table 2.2). This unradiogenic signature is unlikely to be related to proximal outcropping young volcanic rocks, which have more radiogenic (higher) ε_{Nd} and lower Sr isotope ratios (ε_{Nd} ~5; $^{87}Sr/^{86}Sr$ ~0.703; Hart et al., 1997). Seismic reflection and airborne potential field data provide evidence for a mixed bed below Pine Island Glacier, consisting of unconsolidated and consolidated sedimentary strata, basement rocks and igneous intrusives (Smith et al., 2013). Rocks similar to the Palaeozoic sedimentary outcrops on western Marie Byrd Land could be one candidate to contribute to the observed signature (Figure 2.4). Petrographic studies on coarse-grained clasts (>2mm) in seafloor surface sediments in a nearby core (PS75/215-1), however, found a largely granitic source for this IRD (Lindow et al., 2016). It is unclear whether the IRD originated from below Pine Island Glacier or from granitic islands cropping out in Pine Island Bay. Overall, given the presence of igneous basement and granitic IRD in shelf sediments proximal to Pine

Island Glacier, we suggest that the distinctively low ε_{Nd} values and high $^{87}Sr/^{86}Sr$ ratios in fine-grained detrital sediments at site 32 represent a significant input from evolved granites, which experienced significant crustal assimilation during mantle extraction (Figure 2.4), or sedimentary infill eroded from this source. Such granites crop out further inland in the Jones Mountains and in the Ellsworth-Whitmore Mountains (Figure 2.2, Pankhurst et al., 1993; Millar and Pankhurst, 1987). This interpretation is further supported by trace metal compositions showing low Th/Sc and Eu/Eu* (Figure 2.6), and high Th/Zr ratios (see Table 2.3 for values). Such ratios are indicative of felsic rocks such as evolved granites or granites that encountered more crustal assimilation (e.g. McLennan et al., 1993).

Along the eastern flank of the AS sector, ε_{Nd} values become consistently lower with increasing distance from inner Pine Island Bay, while $^{87}Sr/^{86}Sr$ values become higher, and eventually overlap with the composition of the local Mesozoic granites (Figs. 2.4, 2.9). A logical interpretation of this pattern is increasing input of material from the eastern coast of the ASE (between Thurston Island and Pine Island Glacier), where extensive Mesozoic granites are exposed (Figs. 2.4 and 2.9).

2.6.4. Wrigley Gulf-Hobbs Coast

2.6.4.1. Provenance of ice-rafted detritus

The Hobbs Coast is characterized by granitoid outcrops with zircon U-Pb ages of ~115 Ma at Mt. Petras (Figs. 2.2, 2.8), and similar ages elsewhere along the Ruppert Coast in migmatitic, anorogenic, and I-type granitoids (Mukasa and Dalziel, 2000). This age is well reflected in the $^{40}Ar/^{39}Ar$ ages of coarse hornblende and biotite grains in marine sediments from the WH sector with a dominance of ages between 90 and 130 Ma, and slightly younger peak ages of ~100 Ma and ~101 Ma, respectively (Figure 2.3g,h). Older Palaeozoic granitoids crop out along the Ruppert Coast and in the Ford Ranges. It is however, unlikely that such rocks are present below the drainage basin of the western Getz Ice Shelf, as they are rich in hornblende and biotite grains recording undisturbed K-Ar mineral ages of 324-375 Ma (Adams, 1987), which we do not find in the age population of our grains. A secondary biotite $^{40}Ar/^{39}Ar$ age peak of ~53 Ma detected at site 58 is more difficult to explain, as rocks of suitable ages are unknown from the local geology. Previous studies on IRD from sites 58 and 59 have focused on apatite fission track (AFT) thermochronology (Spiegel et al., 2016) and found widespread AFT ages of 60 to 80 Ma. AFT thermochronology is based on the analysis of lattice damage

caused by the spontaneous fission of radiogenic ^{238}U. This method has a lower closure temperature of ~120°C, and Spiegel et al. (2016) correlated AFT ages of 60 to 80 Ma with Cretaceous granitoids, which makes them an unlikely source for ~53 Ma old biotite grains. Basement rocks with (post-) Miocene AFT cooling ages (~20 Ma) on the other hand were interpreted by Spiegel et al. (2016) to reflect an unknown source under the Getz Ice Shelf drainage basin. This source is not found in proximal outcrops, but is likely to be composed of granitic and/or diorite material given the petrographic data on IRD (>2mm) from the same site. These rocks could account for our observed ~53 Ma $^{40}Ar/^{39}Ar$ age in the biotite population.

A small number of young hornblende ages (<10 Ma, n=9) are found in the detrital sediments, tracing the erosion of young alkali basalts. Erosion of these volcanic rocks is further confirmed by petrographic IRD analysis carried out by Spiegel et al. (2016), revealing the contribution of ~40% from volcanogenic clasts that can be associated with the local alkali basalts. Given the extent of outcropping Cenozoic volcanic rocks in the hinterland of the WH sector (Figure 2.2), the relative absence of a significant young age peak in our data signifies that these volcanic rocks are likely to contain hornblende and biotite grains that are too small to be detected in coarse marine samples (i.e picked from >150μm fraction).

2.6.4.2. Provenance of fine-grained detritus

The fine-grained detritus of the WH sector (and site 54 in the western AS, Figure 2.2) has high ε_{Nd} values and low $^{87}Sr/^{86}Sr$ ratios (Figure 2.4), which can be explained by the two major lithologies cropping out along the Hobbs and Ruppert Coasts, the Late Cenozoic alkali basalts and Cretaceous calc-alkaline granites (Figure 2.2). Mixing calculations between these two end-members suggests a ~30% contribution from alkali basalts and ~70% contribution from Cretaceous granites to the sediments (average Mesozoic granitoids vs. average Late Cenozoic alkali basalts, Appendix Table 2.2). This assessment is in agreement with the petrographic IRD analysis by Spiegel et al. (2016) and further supported by trace element compositions of our detrital sediment samples, which indicate a mixture between a Mesozoic granitic end-member and Cenozoic alkali basalts (Figure 2.4). In detail, high Sr/Th (~28) and Zr/Y ratios (~10.5; Table 3) and slightly elevated Eu/Eu* ratios relative to the other studied sectors (~0.8) are all consistent with a significant contribution from mafic alkali basalts to the detrital composition of the seafloor sediments.

2.6.5. Sulzberger Bay

2.6.5.1. Provenance of ice-rafted debris

During the mid-Cretaceous, rifting of Zealandia from western Marie Byrd Land led to the intrusion of extensive anorogenic granitoids with K-Ar ages of ~98-105 Ma (Richard et al., 1994; Adams et al., 1995). These rocks are predominantly exposed in the Ford Ranges and on Edward VII Peninsula, where they crop out alongside Palaeozoic granodiorites (i.e. Ford Granodiorite Suite) and Cambrian-Ordovician metasedimentary rocks (i.e. Swanson Formation) (Weaver et al., 1992; Adams et al., 1995, Figure 2.2). The Ford Granodiorite Suite contains coarse hornblende and biotite grains with zircon U-Pb and K-Ar hornblende and biotite ages of 320-370 Ma (Adams, 1987; Pankhurst et al., 1998). Predominant hornblende $^{40}Ar/^{39}Ar$ ages of 90 to 130 Ma (peak age: ~100 Ma; n=26) in marine sediments in SB indicate limited erosion from the Ford Granodiorite Suite, with the exception of two grains with ages of 347 Ma and 510 Ma (Appendix Table 2.1). A more likely source for the IRD in the SB sector is hence Edward VII Peninsula (Figure 2.2). This conclusion seems in contrast to aeromagnetic investigations of the area, which inferred a larger extent for the Ford Granodiorite Suite on Edward VII Peninsula (Ferraccioli et al., 2002). Overall, however, our age distribution is in agreement with the ages of local A-type granites, the thermal overprinting ages and the absence of hornblende grains in the sedimentary Swanson Formation (Adams et al., 1995, see Pierce et al. 2014, for a discussion on durability of hornblende grains in the sedimentary cycle), which crops out extensively on Edward VII Peninsula.

2.6.5.2. Provenance of fine-grained sediments

In contrast to the IRD signature, low Nd (ε_{Nd}: -11.9 to -10.5) and high Sr isotope values ($^{87}Sr/^{86}Sr$: 0.7411 to 0.7493) in the fine-grained detritus in the SB sector show a strong affinity to the metasedimentary Swanson Formation (ε_{Nd}: -13.4 to -10.5 and $^{87}Sr/^{86}Sr$: 0.7264 to 0.7618) (Pankhurst et al., 1998; Korhonen et al., 2010; Figure 2.3). In detail, Nd isotopic compositions are slightly higher and Nd model ages are slightly younger (~1600 Ma, Table 2.2) than documented for the Swanson Formation on land (1650-1800 Ma; Appendix Table 2.2). An additional source is therefore needed to explain the observed signatures, which is readily found in the local A-type granites intruding the Swanson Formation on Edward VII Peninsula (Weaver et al., 1992). A mixture between Palaeozoic sediments from the Swanson

Formation and Cretaceous anorogenic granitoids in the marine detrital sediments from the SB sector is further suggested by low Sr/Th ratios (4-5) and characteristic low Eu anomalies (Eu/Eu* ~ 0.6), and is consistent with coarse and fine-grained geochemical signatures in marine sediments from the area.

2.7. Comparison of different provenance proxies

2.7.1. $^{40}Ar/^{39}Ar$ ages in hornblende vs biotite grains

Combined analyses of $^{40}Ar/^{39}Ar$ ages from hornblende and biotite grains in detrital sediments allows for more detailed provenance analysis due to the different closure temperatures of both minerals (~550°C and 300°C, respectively). In the case of East Antarctica, partial or total resetting of lower temperature thermochronometers has been observed in several sectors. For example, in detrital sediments from the Wilkes Land sector (90°E to 135°E), a characteristic ~1494 Ma peak age is found in hornblende grains, but is absent from the biotite grains. This observation has been linked to partial resetting of biotite grain ages during the Grenville orogeny (Pierce et al., 2014).

In West Antarctica, coastal geology is dominated by Andean-style plutonism of Permian or younger age, resulting in large diorite, granodiorite, monzogranite and syenite intrusions, which in many cases are not overprinted by any major younger tectono-metamorphic events (except for the regional Palmer Land Event at 103-107 Ma). If marine sediment sites are proximal enough to the continental source areas, which carry both large hornblende and biotite grains, as is the case for many of the West Antarctic plutonites, and if the erosional pathway from source to sink does not separate the two mineral phases by differential current sorting, combined biotite-hornblende $^{40}Ar/^{39}Ar$ data sets may be used to broadly support provenance interpretations by inferred cooling rates. We think that a case can be made as large parts of our data set meet these criteria. Overall, probability peaks of hornblende grain ages are similar to or slightly older than those of biotite grains around West Antarctica (Figure 2.3). Both minerals record a dominant Cretaceous age peak (100-110 Ma) in all sectors, apart from the AP sector (Figure 2.3). This age interval is particularly well defined in most of the sectors and peak ages between both mineral systems vary by as little as ~2 Ma in the detrital marine sediments (e.g. AS sector; Figure 2.7). Because magmatic activity has been largely episodic (e.g. Pankhurst et al., 1993; Leat et al., 1995), we suggest that these

ages point towards regional sources from the same lithological unit (i.e. batholith). Derived cooling rates for the Cretaceous source rocks would be extremely fast (~>100°C per million years between 550 and 350°C). To our knowledge, there are no detailed investigations on the cooling rates of Cretaceous I-type granitoids from West Antarctica. Concordant ages between zircon U-Pb ages, and reliable $^{40}Ar/^{39}Ar$, K-Ar and Rb-Sr data have nonetheless been observed for intrusive I-type granites on Palmer Land (Pankhurst and Rowley, 1991; Flowerdew et al., 2005; Vaughan et al., 2012b). Thermochronological investigations on Cretaceous A-type granites in the Ford Ranges ('Byrd Coast Granites'; Figure 2.2) have revealed cooling rates of >100°C/Ma, associated with granitic intrusion into the shallow crust (Richard et al., 1994). In South America, the emplacement of large Cretaceous plutonic rocks was coeval with the build-up of the Cretaceous batholith on West Antarctica. The mid-Cretaceous plutonic complex in the Coastal Range of central Chile show similar rapid cooling of gabbro to granodiorite suites (93 to 95 Ma based on coupled $^{40}Ar/^{39}Ar$ hornblende, biotite and plagioclase ages), and similar crystallization ages of the same batholith (95-97 Ma; zircon U-Pb ages; Parada et al., 2005; Ferrando et al., 2014). Another comparison can be made for the eastern AS, where detrital hornblende grains yield well-defined ages of ~257 Ma and biotite grains record a younger age of 240 Ma (Figure 2.7). This age difference would imply an approximate cooling rate of ~15°C per million years for the Permian-Triassic source rocks. This result is consistent with cooling rates of similarly aged dioritic to granodioritic rocks from Thurston Island (~12.5°C/Ma based on K/Ar and $^{40}Ar/^{39}Ar$ on hornblende and biotite; Pankhurst et al., 1993) and calc-alkaline diorites of the Median Batholith in New Zealand (~20°C per million years, Mortimer et al., 1999), which formed the continuation of the Amundsen Sea province prior to the onset of rifting (Bradshaw et al., 1997; Vaughan and Storey, 2000). Offshore from the Walgreen Coast, pre-Cretaceous (>140 Ma) biotite grains are relatively rare compared to hornblende grains (Figure 2.7). This observation is explained either by the presence of intermediate to mafic sources which carry more hornblende than biotite (i.e. granodiorite and diorite; Pierce et al., 2014), or by thermal resetting of biotite ages during the Cretaceous. Permian diorite and granodiorite outcrops of ~243 Ma and ~283 Ma (zircon U-Pb, Mukasa and Dalziel, 2000) have been identified in the Kohler Range, which is fed by ice streams flowing towards the Walgreen Coast, and could hence indicate a (minor) mineralogical bias towards biotite in the area.

In several locations, a marked distinction between the two chronometers is observed in the offshore record. In addition to the previously mentioned exotic biotite ages of ~53 Ma in the WH sector, hornblende ages of ~350 Ma, which are absent in the biotite record, were found in the eastern AS sector (Figure 2.7). Comparison with the proximal geology relate these ages

to the emplacement of a granodioritic-orthogneiss on Thurston Island (Rb-Sr whole rock: ~309 Ma, Pankhurst et al., 1993; zircon U-Pb: ~349 Ma, Riley et al., 2017). These gneisses show evidence for realignment and recrystallization of biotite crystals, indicating that a thermal event is likely to have affected the cooling ages of these crystals, possibly during later intrusions of the widespread Permian-Triassic plutonic rocks (~240 Ma).

2.7.2. Fine-grained sediment provenance derived from radiogenic isotopes and trace elements versus clay mineralogy

Along the Pacific margin of West Antarctica, most of the previous provenance work has focussed on the analysis of mineral assemblages in the clay fraction (<2μm), which was published by Hillenbrand and Ehrmann (2002), Hillenbrand et al. (2003, 2009b) and Ehrmann et al. (2011). In this study, we expanded the existing clay mineral data set by analysing additional samples from the Wrigley Gulf-Hobbs Coast sector (Table 2.2). We here show that the combined study of clay mineralogy and fine-grained sediment fingerprints provides complimentary information on their onshore source.

In the AP and BS sectors, high illite content in shelf sediments (45-70 %) has been found offshore from the eastern tip of Alexander Island, as well as in the western part of the BS sector (Table 2.2; Hillenbrand and Ehrmann 2002; Hillenbrand et al., 2003). The high abundance of illite in these areas was suggested to originate from granitic and gneissic sources. Assumption of a granitic-gneissic source on Alexander Island is based on the presence of plutonic rocks in the eastern part of the island (i.e. the Rouen Mountains; Care, 1983) and the dominance of quartz-mica schistose/gneissic pebbles believed to be derived from the Rouen Mts. in subglacial tills recovered in cores from the nearby shelf (Kennedy and Anderson, 1989). However, erosion of these Tertiary rocks would produce a more radiogenic isotopic fingerprint in the fine-grained material of site 6 than what is observed (ε_{Nd} ~ 2 and $^{87}Sr/^{86}Sr$ ~ 0.705; McCarron and Smellie, 1998) (Figure 2.4). We suggest that the extensively outcropping accretionary sedimentary rocks on Alexander Island (LeMay Formation), which was shown to have high illite content (e.g. Underwood and Pickering, 1996) and Nd isotope values of ~ -8 to -3 (Figure 2.4), are the more likely source rocks for the fine-grained fraction.

The trace element fingerprint (e.g. Th/Sc, Eu/Eu*) of shelf sediments in the BS reveals a mafic eastern sector and a felsic western sector (Figure 2.6). This finding is confirmed by the clay mineral composition of the sediments that contain up to 66% illite and only 7% smectite

in the western part of this sector, while in the eastern part of the sector 44% illite and 20% smectite are found (Hillenbrand et al, 2009b). In addition, these observations agree with geophysical surveys, which suggested a felsic composition of the hinterland of the western BS (i.e. Central Domain Eastern Zone; Ferraccioli et al., 2006). Shelf sediments further offshore record a mixed signature between these end-members (Hillenbrand et al, 2009b), which is consistent with our new data. For example, site 15 (ε_{Nd} = -6.2, Th/Sc = 0.93 and illite = 52%) shows detrital contribution from both end-members (Tables 2.2, 2.3). Based on the clay mineral assemblage in the BS, Hillenbrand et al. (2003) proposed sediment material being carried northward by wind- and tide-driven currents without significant influence of the westward-driven coastal current. This fits with our observations, implying a similar sediment transport for the fine-grained sediment (<63μm).

In the AS sector, high kaolinite content in shelf sediments (up to 30 %) has been suggested to originate from pre-Oligocene sedimentary rocks beneath the Pine Island and Thwaites Glaciers (Hillenbrand et al., 2003; Ehrmann et al., 2011), probably sourced from the Byrd Subglacial Basin (Figure 2.2). Such sedimentary rocks do not crop out in the hinterland of the AS (Figure 2.2), making their geochemical signature elusive. The comparison between clay mineralogy and the fine-grained geochemistry yields clear correlations between kaolinite content and trace elements (not shown in figures). For example, hafnium (Hf), zirconium (Zr), and Nd exhibit a positive correlation with kaolinite content (r^2= 0.67, 0.62 and 0.62, respectively), while a negative correlation can be observed between kaolinite content and Sr/Zr ratios (r^2= 0.83). In general, kaolinite is associated with chemical weathering of bedrock under warm and humid conditions (Biscaye, 1965), and if it is found in Antarctica today, it is assumed to be derived from pre-Oligocene sedimentary strata as it cannot form under glacial conditions (e.g. Ehrmann et al., 1992). High Field Strength Elements (HFSEs) such as Zr or Hf, on the other hand, tend to be immobile during chemical weathering and remain in the residues of weathering while lithophile elements (i.e. Sr) are preferentially leached away. Hence, it is tempting to suggest that correlation between kaolinite and Sr/Zr is related to the presence of weathered outcrops in the hinterland. However, we do not observe a relationship between kaolinite and $^{87}Sr/^{86}Sr$ ratios, making glacial weathering a less likely candidate, and instead favour a provenance change as an explanation for Sr concentrations and isotopic compositions.

2.8. Geochemical signature of ice drainage basins and influence of marine sediment transport

Detailed geochemical characterization of the sediment provenance offshore from individual ice drainage basins gives valuable information on the integrated signature of subglacial geology and dispersal of glacially eroded detritus onto the shelf and further into the deep sea. It also provides the necessary modern day understanding how to use provenance analyses for palaeo-ice sheet reconstructions from marine down-core records (e.g. for East Antarctica; Cook et al., 2013, 2017; Pierce et al., 2017). The relatively young geological history of West Antarctica means that individual ice drainage basins will show less pronounced geochemical differences when compared to East Antarctica (e.g. Pierce et al., 2011, 2014) or the North Atlantic (e.g. Hemming, 2004). For instance, Pb analyses of K-feldspars grains have been shown to be a valuable tool for distinguishing erosional inputs from West and East Antarctic source terranes (Flowerdew et al., 2012). However, Pb isotopic values are remarkably uniform on West Antarctica due to the exclusively mantle-derived sources for the exposed crystalline bedrock (Mukasa and Dalziel, 2000; Flowerdew et al., 2012). Our multi-proxy approach nevertheless allows us to distinguish distinct ice drainage basins within West Antarctica as well as sediment transport pathways.

2.8.1. Coarse-grained detrital sediment signature and potential transport pathways

The modern IRD in the Southern Ocean is supplied by melting of calved icebergs. Ice-rafting has been described as the main mechanism for the transport of coarse detritus from the Antarctic continent to the pelagic realm as ocean currents can only transport finer sediments (e.g. Diekmann and Kuhn, 1999). The westward flowing Antarctic Coastal Current is of particular relevance, as it dominates the transport of icebergs in proximity to the coast (e.g. Stammerjohn et al., 2015; Kim et al., 2016a; Figure 2.8). We find a strong contrast in IRD provenance patterns between the AP and the BS sectors (Figs. 2.3, 2.8). Relatively young ages observed in the AP sector are sourced from the west coast of the Antarctic Peninsula, where outcrops of magmatic rocks of Late Cretaceous to Cenozoic ages produced by the eastward migration of the active subduction of the (proto-) Pacific plate under West Antarctica during that time are widespread (Leat et al., 1995). This can be explained by the fact that most icebergs from the Antarctic Peninsula are deflected northwards into the ACC by cyclonic gyres on the

shelf before reaching the BS sector (e.g. Hofmann et al, 1996; Smith et al., 1999; cf. Hillenbrand et al., 2003) (Figure 2.8).

In the BS sector, the $^{40}Ar/^{39}Ar$ hornblende and biotite ages are relatively uniform in proximal and distal sediments and record sources with a strong mid-Cretaceous thermo-metamorphic event related to suturing between the western/central domains with the eastern domain of the Antarctic Peninsula (Figure 2.1). These ages are not found in the AP sector. A large cyclonic gyre in the southern Bellingshausen Sea deflects the coastal current along the eastern flank of Thurston Island (~95°W) (Gladstone et al., 2001; Assmann et al., 2005; cf. Hillenbrand et al., 2003), injecting most of the icebergs into the ACC. Some westward IRD transport may also occur within the Antarctic Coastal Current, but this is difficult to trace due to the ubiquitous nature of mid-Cretaceous thermochronological ages around West Antarctica (Figure 2.8, Appendix Table 2.1).

Most of the outcrops in the AS sector are located around Thurston Island and along the Walgreen Coast, where ice streams are feeding into the Abbott and Cosgrove and the Dotson and Getz ice shelves, respectively (Figure 2.2). Proximal ice-rafted grains in these two areas show similar mid-Cretaceous and Permian-Triassic ages (~100 Ma and ~250 Ma), but are distinct from the other sectors by the presence of grains with Jurassic ages (140-210 Ma), which mainly occur offshore from the Abbott and Cosgrove ice shelves (Figs. 2.7, 2.8). Although the numbers of grains analysed in samples just offshore from Pine Island Glacier (n=1) and Thwaites Glacier (n=9) are low, they also include grains of Jurassic ages (Appendix Table 2.1). This shows that the main source for Jurassic hornblende and biotite grains to the AS sector (and off West Antarctica) originates from the Cosgrove and Abbott ice shelves and from the Pine Island and Thwaites Glaciers. In addition, surface currents in the ASE are influenced by the Antarctic Coastal Current. This current is overall weak (~ 1.0 cm s-1) within the embayment, but appears strongest near the coastline (Assmann et al., 2005; Stammerjohn et al., 2015; Kim et al., 2016a). We observe Jurassic grains at sites on the continental slope and rise offshore from Dotson-Getz Trough (sites 50-52). We suggest that icebergs that drift generally westwards within the ASE (e.g. Mazur et al., 2017) transport the Jurassic grains from the eastern ASE to these locations, which are all situated south of the southern boundary of the ACC (Figs. 2.2, 2.8).

In general, IRD in samples from the continental slope and rise in the Amundsen Sea shows a larger age population (~30-80 Ma) than IRD on the continental shelf (Figure 2.8). This feature is particularly pronounced around 70°S latitude. Source areas for grains of this age

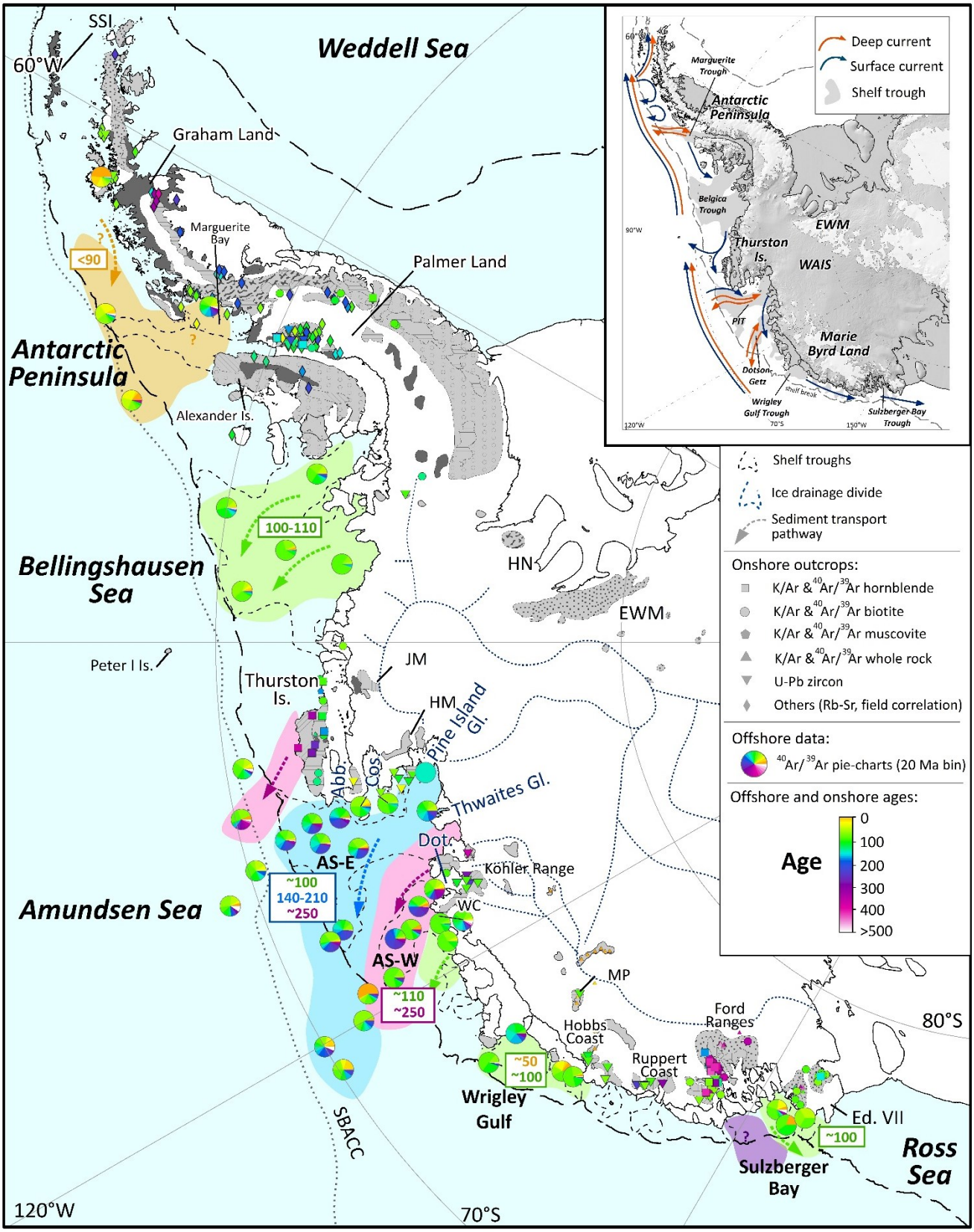

(caption on next page)

Figure 2.8. Distribution of thermochronological ages in offshore sediments and terrestrial outcrops of West Antarctica. $^{40}Ar/^{39}Ar$ ages of ice-rafted hornblende and biotite grains are presented as pie charts in 20 Ma increments. Outcrop ages are displayed with different symbols depending on the type of mineral and the method applied (see Appendix Table 2.2). Simplified geology is shown in grey-scale after Figure 2.2. Thick dashed black lines indicate the approximate location of the shelf break. Coloured dashed arrows and underlying colour field denote major ice-rafted debris transport pathways. Abbreviations and inlet figure are the same as for Figure 2.2.

range could be either the western AP or the Hobbs Coast (sites 58-59) (Figs. 2.3, 2.8), both of which would require iceberg drift in opposing directions. Support for an AP provenance comes from petrographic observations on Plio-Pleistocene ice-rafted cobbles at DSDP Leg 35 Site 324 (located offshore from site 17) that show a provenance from Alexander Island (Tucholke et al., 1976; Veevers and Saeed, 2013). An argument against a far-travelled signal from the AP, however, is the lack of significant numbers of hornblende and biotite grains of this age range in the BS, as well as the existence of the large gyre in the BS, which carries most of the icebergs north-east towards the ACC (e.g. Assmann et al., 2005) (Figure 2.8). Oceanographic observations indicate that sites at around 70°S in the Amundsen Sea are located within the eastward flow of the ACC (Orsi et al., 1995; Stammerjohn et al., 2015). This suggests that the source of the ~30-80 Ma old grains at the corresponding sites lies to the west. Indeed, our samples from the Hobbs Coast shelf show a well-defined ~50 Ma age peak, which indicates this area as the potential source for these young detrital grains (Figure 2.3h). The corresponding sites are located proximal to the westernmost Getz Ice Shelf. While the ~54 Ma age is unknown from onshore outcrops, it could represent a hidden source under the ice (cf. Spiegel et al. 2016). At present, icebergs calving from the westernmost Getz Ice Shelf drift westwards with the Antarctic Coastal Current towards the Ross Sea and are injected into the ACC offshore from Sulzberger Bay (Merino et al., 2016; Tournadre et al., 2016).

2.8.2. Fine-grained detrital sediment signature and potential transport pathways

In the modern Southern Ocean, coarse grained terrigenous debris is typically transported by icebergs, which follow wind-driven surface currents. Fine-grained sediments are also transported by these icebergs, but suspended particulates can additionally be

transported by meltwater plumes, tidal, thermohaline, and geostrophic currents, as well as gravitational downslope processes such as turbidity currents (e.g. Aitken and Bell, 1998; Pudsey and Camerlenghi, 1998; Diekmann and Kuhn, 1999). Similar to the sand provenance signature, the geochemical fingerprint of the studied proximal fine-grained glacial-marine sediments off West Antarctica matches the nearby coastal geology very well, excluding a significant contribution of dust, which plays a more important role for the deposition of fine-grained detritus in the Sub-Antarctic Pacific sector of the Southern Ocean (e.g. Lamy et al., 2014). The fingerprint of sediments can be traced offshore, revealing the transport pathway of fine grains across the continental shelves.

In the AP sector, similarities in the radiogenic isotope fingerprint of site 7 on the shelf and site 8 located on the continental rise suggest seaward transport of detrital particles originating from the metasedimentary rocks on Alexander Island (Table 2.2, Figure 2.9). Such a transport pathway across the western Antarctic Peninsula continental shelf has been described before for fine-grained terrigenous detritus (Hillenbrand and Ehrmann, 2002). In the BS, proximal sites denote felsic and mafic sources in both its western and eastern parts, consistent with aeromagnetic observations in the area (Ferraccioli et al., 2006; Bingham et al., 2002). Following the Belgica palaeo-ice stream Trough northwards, sediments record a mixing signature between these two areas, which has previously been attributed by wind- and tidal-driven currents (Hillenbrand et al., 2003, 2009).

A good example of bathymetrically constrained dispersal of fine-grained detritus is observed in the AS sector. Provenance of sediments proximal to the Pine Island and Thwaites Glaciers is distinct, pointing to a felsic source or igneous rock with a geochemical signature of enhanced crustal assimilation underneath these two major ice drainage basins. Progressive northward change in sediment provenance along the eastern AS requires that sediment with this distinct fingerprint is transported northwards, and diluted along the way with Palaeozoic-Mesozoic source rocks along the eastern flank of the ASE (Figure 2.9). The fact that samples from Dotson-Getz Trough show a uniform fine-grained fingerprint indicates that no significant cross shelf transport of fine-grained particles from further east or west occurred, as this would be recognizable in the radiogenic isotope signature of the samples. A candidate for the observed undiluted northward sediment transport is the northward return flow of upwelled Circumpolar Deep Water, after interacting with the base of the ice shelves, as Antarctic Surface Water (Jenkins et al., 2016). Observation from autonomous underwater vehicles found melt-laden outflow from ice shelves in the ASE to carry suspended sediment, which is sourced from the sediment-laden base of the ice shelves (Jenkins et al., 2016; Miles et al, 2016). This sediment-

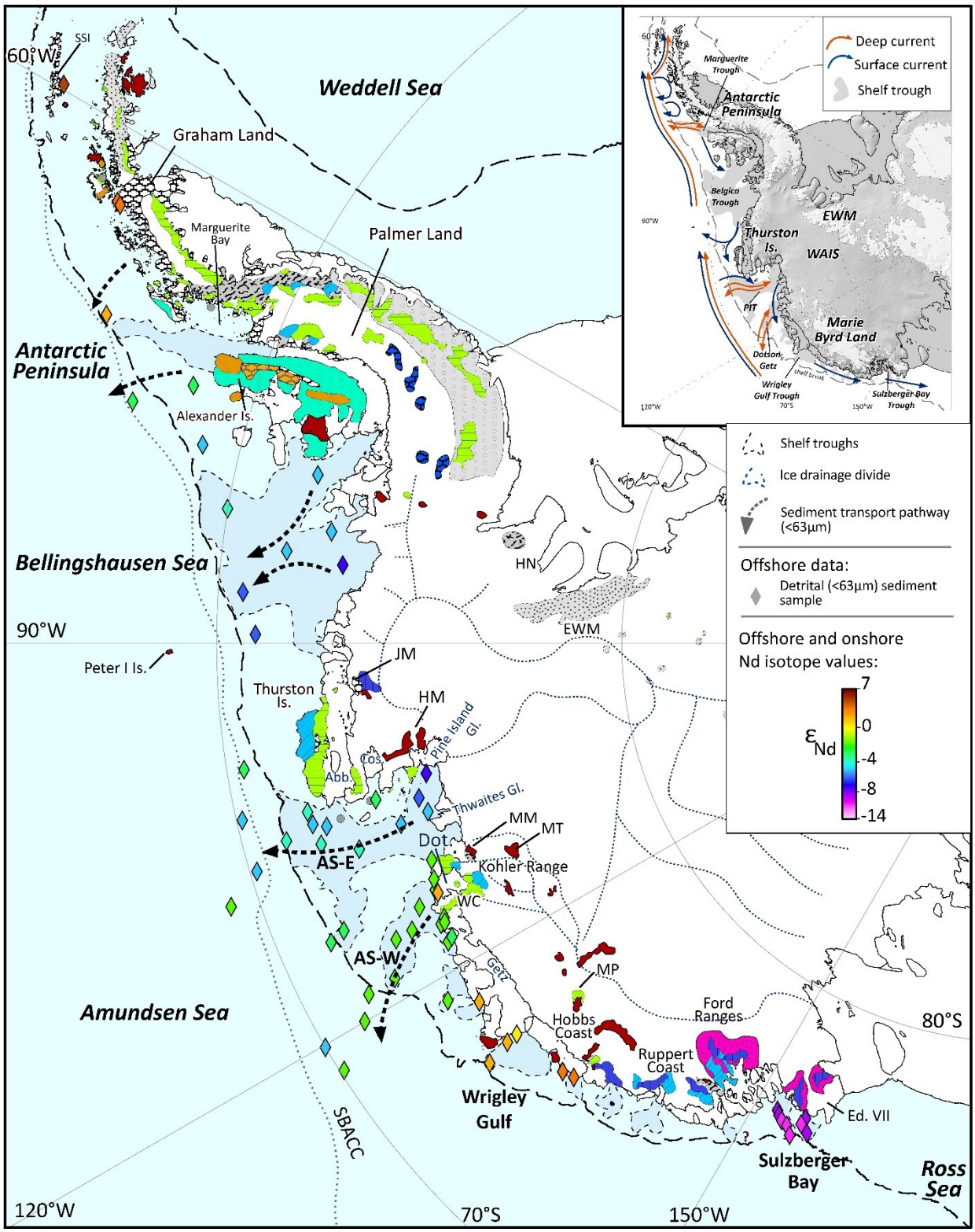

(caption on next page)

Figure 2.9. Distribution of Nd isotope composition (ε_{Nd}) in marine sediments and terrestrial rocks. The geology is based on Figure 2.2. Note: Colour scheme for outcrops is based on the average Nd isotopic composition of the lithology (see Appendix Table 2.2 for data assimilated from the literature). Geological units which could not be assigned a Nd isotope fingerprint are shown in grey. Two different colours were assigned to the Antarctic Peninsula Volcanic Group depending on the regional geochemical variation of these rocks (e.g. Riley et al., 2001, see Table S2 and text). Dashed black lines delineate the approximate location of the shelf break. Black dashed arrows denote major fine-grained (<63μm) transport pathways. Abbreviations and inlet figure same as for Figure 2.2.

---

laden meltwater reaches the mid-depths of the water column and is transported northwards along the bathymetric troughs (e.g. Kim et al., 2016b). Release of this suspended particulate matter occurs notably along its main transport pathway, explaining the consistent provenance signatures of fine-grained sediment along the cross-shelf troughs in the ASE.

2.8.3. The geochemical fingerprint of West Antarctic provenance regions in the Pacific sector of the Southern Ocean

An integrated provenance approach allows for a characterization of subglacial sources from individual ice drainage basins along the Pacific margin of West Antarctica. Figure 2.10 presents provenance characteristics compiled from our new data set and previously published studies for five different West Antarctic sectors. An erosional source from the Antarctic Peninsula is best identified by a predominance of $^{40}Ar/^{39}Ar$ ages spanning 30-90 Ma in coarse-grained IRD and a very radiogenic fingerprint of fine-grained detrital sediments (ε_{Nd} up to +0.9 and $^{87}Sr/^{86}Sr$ ratios down to 0.705). The only other West Antarctic area that exhibits similar characteristics is the Hobbs Coast, where most biotite and hornblende $^{40}Ar/^{39}Ar$ ages are, however, older (90-140 Ma) and Nd model ages are younger (700 to 770 Ma). Both areas are also relatively far apart from each other, which should not impede their respective identification in down-core studies on marine sediment cores collected proximal to these source regions. The Bellingshausen Sea sector shows a predominance of IRD $^{40}Ar/^{39}Ar$ ages around ~110 Ma, which are similar to those from the Wrigley Gulf-Hobbs Coast sector (~100 Ma), but the fine-grained detritus in the former sector has lower Nd values and higher $^{87}Sr/^{86}Sr$ ratios (ε_{Nd} = -4.3 to -7.2; $^{87}Sr/^{86}Sr$ = 0.710-0.713), as well as significantly older Nd model ages (1180-1350 Ma).

The oldest protolith ages in West Antarctica are indicated by Nd model ages of 1570 to 1700 Ma in Sulzberger Bay, which also stands out by the unradiogenic isotope fingerprint of fine-grained detrital sediments (ε_{Nd} <-10.6; $^{87}Sr/^{86}Sr$ > 0.741).

Finally, a more detailed picture starts emerging for the Amundsen Sea sector, the locus of major glacial ice loss in Antarctica today. While both the eastern and western AS sub-sectors are characterized by hornblende and biotite ages of ~110 Ma and 240-260 Ma, ages of 140 to 210 Ma are more prevalent in the eastern ASE. Furthermore, source rocks to the eastern ASE seem to extend to older Nd model ages (up to 1300 Ma, ε_{Nd} = -7.2) than in the western ASE (900-1000 Ma, ε_{Nd} = -1.7 to -2.9). Further studies are required to reveal whether this observation points to a distinct bedrock source under Pine Island Glacier, a result with major implications for tracing past WAIS retreat and collapse.

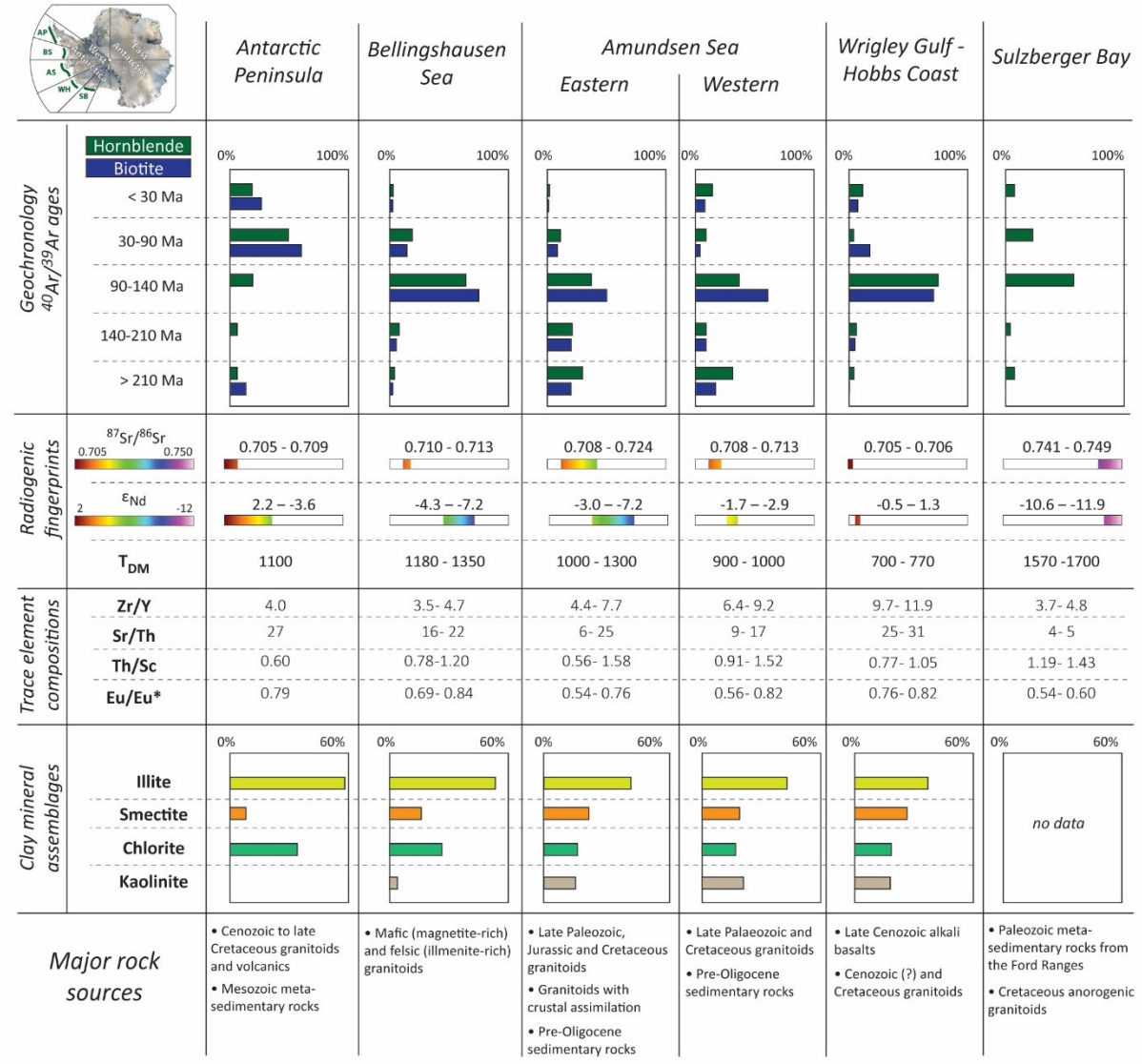

(caption on next page)

Figure 2.10. Summary figure of geochemical and clay mineralogical provenance characteristics of different sectors along the Pacific margin of West Antarctica as derived from analyses of detrital marine sediments. Clay mineral assemblages are taken from Hillenbrand and Ehrmann (2002), Hillenbrand et al. (2003, 2009b) and Ehrmann et al. (2011), and major terrestrial rock sources are compiled from the literature (see text for further details).

2.9. Conclusions

We here report for the first time a detailed geochemical approach to unraveling different provenance sectors along the Pacific margin of West Antarctica. By investigating the fingerprints of fine-grained terrigenous detritus and coarse-grained ice-rafted debris in ice-sheet proximal to distal marine sediments of Late Holocene age, we draw the following conclusions:

Thermochronological $^{40}Ar/^{39}Ar$ dating on individual mineral grains highlights the Phanerozoic history of West Antarctica. Hornblende and biotite ages can be readily associated with extensively outcropping granites and granodiorites and allow us to distinguish the following sectors: Antarctic Peninsula (~52 and ~74 Ma), Bellingshausen Sea, Wrigley Gulf-Hobbs Coast and Sulzberger Bay sectors (~100-110 Ma) and Amundsen Sea sector (~100-110 Ma and ~140 to 360 Ma). $^{40}Ar/^{39}Ar$ dating of hornblende and biotite grains is less suitable for detecting Late Cenozoic alkali basalts and metasedimentary units around West Antarctica (i.e. mineralogical or grain-size bias).

Strontium and Nd isotopic compositions in fine-grained detrital sediments match the coastal geology, and observed geochemical variability can be readily related to genetic and lithological differences in source rocks. Data range from radiogenic values around the (young) Antarctic Peninsula (ε_{Nd} = -3.6 to +0.9; $^{87}Sr/^{86}Sr$ = 0.705-0.709) to less radiogenic values around the Sulzberger Bay, where mantle extraction ages point to a much older protolith (up to 1700 Ma). An exciting finding is a potentially distinct geological source (i.e. Cretaceous granites that experienced extensive crustal assimilation) beneath Pine Island Glacier, which was identified in the radiogenic isotope composition of fine-grained sediments near its calving front. While major Palaeozoic to Mesozoic geological units in West Antarctica are identified in the provenance of the marine sediments, the fine fraction analyses prove particularly useful

in detecting Late Cenozoic alkali basalts and metasedimentary rocks, as well as distinguishing A-type granites and granites with pronounced crustal assimilation signatures.

Despite an overall small variation of trace element compositions in marine detrital sediments off West Antarctica, they nevertheless complement isotopic provenance analyses and are broadly indicative of mafic and felsic source rocks. Significant variability within individual ice drainage basins may prove useful for provenance studies on the local to regional scale, as indicated by contrasting hinterland geology between the eastern and western Bellingshausen Sea, the eastern and western Amundsen Sea embayment, Wrigley Gulf-Hobbs Coast and Sulzberger Bay.

Combined provenance studies on different size fractions of detrital sediments enable monitoring of modern sediment transport pathways. For example, the occurrence of ~140-210 Ma old ice-rafted grains in the western Amundsen Sea sector, which originate from the eastern coast of the Amundsen Sea Embayment, highlights the modern pathway of wind-driven iceberg trajectories within the area. On the other hand, fine-grained sediments can additionally be transported by currents, as exemplified by an evolving radiogenic isotope signature from Pine Island Bay towards the shelf break.

Our study highlights the importance of integrated studies for identifying the geochemical fingerprints of individual ice drainage basins around West Antarctica. Such modern-day studies do not only provide the basis for any attempts to reconstruct ice drainage patterns and ice sheet extent in West Antarctica during the past, but also allow valuable insights into the geology under the ice.

Statement of Contribution

The work presented here was part of a collaborative effort to which the author, Tina van de Flierdt (Imperial College, UK) and Claus-Dieter Hillenbrand (BAS, UK) contributed to the initial idea. Claus-Dieter Hillenbrand, Gerhard Kuhn (AWI, Germany), Tina van de Flierdt, Sidney R. Hemming (L-DEO, Columbia University, US) and Carys P. Cook supplied the sample material. Sidney R. Hemming conducted the $^{40}Ar/^{39}Ar$ measurements on hornblende and biotite minerals. Sam J. Hammond (Open University, UK) provided support with the trace element analysis. Stefanie Brachfeld (Montclair State University, US) and Cathleen Doherty (Rutgers University, US) provided some of the $^{40}Ar/^{39}Ar$ hornblende and biotite, and neodymium isotope data. Werner Ehrman is acknowledge for providing clay contents for the Wrigley Gulf-Hobbs Coast samples.

Chapter 3

Fingerprinting the sediment provenance of West Antarctica`s weak underbelly: Pine Island Glacier and Thwaites Glacier

Chapter Summary

This chapter presents the first multi-proxy provenance study on sediments deposited in Pine Island Bay (PIB), Amundsen Sea. The main objective is to characterize the fingerprints of glaciogenic sediments supplied by Pine Island and Thwaites Glaciers. Identifying the presence or absence of the fingerprint of these two glaciers in downcore sedimentary records allows for reconstructing the state of the West Antarctic Ice Sheet (WAIS) in the past. Hence, seafloor surface sediments at 24 sites were investigated for their fine-grained isotopic (Sr, Nd) and geochemical compositions, bulk and clay mineral assemblages, rock magnetic properties and $^{40}Ar/^{39}Ar$ ages of individual iceberg-rafted hornblende and biotite grains in order to provide a comprehensive compilation of the various provenance signatures.

Seafloor surface sediment samples from PIB show a consistent distinction in their isotopic signature between sediments deposited proximal to Pine Island Glacier, including below its ice shelf, and those deposited proximal to Thwaites Glacier. Similar distinction is observed in the clay mineral assemblages and rock magnetic data. The large range of provenance change in combination with the geographical position of the sampling sites indicates that Pine Island and Thwaites Glaciers deliver sediments with a distinct fingerprint which originates from the distinct geology below the two catchments. Furthermore, iceberg-rafted (IRD) hornblende and biotite grains in the surface sediments at a core site proximal to Pine Island Glacier show a significant $^{40}Ar/^{39}Ar$ age population of 170-270 Ma, which is distinct from the IRD signal at sites proximal to Thwaites Glacier because these are characterised by ages of <40 Ma and ~110 to 330 Ma, with a major age peak at 115 Ma. Our data show that the IRD signals of Pine Island and Thwaites Glaciers are not carried over long distances across the Amundsen Sea shelf, as they become overprinted by the IRD provenance signal of other ice streams located further north.

We further investigated 19 downcore sediment samples from 11 sites, which targeted facies recording a subglacial to deglacial-transitional setting. Overall, the provenance of the downcore samples is very similar to the provenance of the modern surface samples. The largest variation, however, occurs near the Crosson Ice Shelf and the Northern Ice Shelf. We suggest that erosion of glaciers draining into these ice shelves today may have been enhanced during glacial times with the basal conditions in their ice drainage basins changing from warm-based (thicker ice) at the Last Glacial Maximum (LGM; ca. 19-25 ka BP) to cold-based (thiner ice) during the Holocene. Thermal conditions below Pine Island Glacier and Thwaites Glacier

remained similar between the LGM and the Holocene, hence provenance of sedimentary sequences in the flow direction of these ice streams remained largely unchanged.

3.1. Introduction

The WAIS is considered capable of rapid future and past collapse resulting in up to 4.3 m of global sea level rise (Fretwell et al., 2013). Of particular interest are Pine Island Glacier (PIG) and Thwaites Glacier, whose combined drainage basins are often referred to as the "weak underbelly" of the WAIS, the portion that is most susceptible for rapid collapse (Weertman, 1974; Mercer; 1978; Thomas et al., 1979; Hughes, 1981), although its exact extent has recently been refined to comprise Thwaites Glacier alone (Vaughan et al., 2006; Holt et al., 2006; Scambos et al., 2017). The catchments of both glaciers are large, low-lying (i.e. marine-based) basins draining approximately 20% of the WAIS into PIB in the south-eastern Amundsen Sea (Figure 3.1). They have only small buttressing ice shelves that are in contact with relatively warm ocean water and are grounded on a bed that deepens further inland, with no physiographic barriers further upstream observed in the Thwaites Glacier catchment (e.g. Joughin et al., 2009, 2014). Any destabilization in this sector has the potential to result in a self-sustained retreat of the grounding line further inland (e.g. Schoof, 2007; Joughin and Alley, 2011; Rignot et al., 2014), eventually reaching the low-lying Bentley Subglacial Trench and Byrd Subglacial Basin (Kleman and Applegate, 2014; Feldmann and Levermann, 2015, Figure 3.1). Numerical studies have shown that the Pine Island and Thwaites Glaciers basins may have collapsed at several times over the last 5 Ma (e.g. Pollard and DeConto, 2009, 2016), but direct geological evidence for such destabilization during the Late Quaternary remains elusive (e.g. Hillenbrand et al., 2009a) and is mainly based on far-field data, such as sea-level records (e.g. Dutton et al., 2015).

A powerful way in which to study past retreat of low-lying portions of an ice drainage basin is to examine mineralogical or geochemical provenance of glaciomarine sediments deposited at the periphery of the ice sheet (e.g. Ehrmann et al., 1992, 2011; Diekmann and Kuhn, 1999; Hillenbrand et al. 2003, 2009b; Pierce et al., 2011; 2014; Simões Pereira et al., 2018). As material is eroded by ice and entrained to the ice margin, it carries with it the lithological and geochemical signature of its source rocks. Glaciogenic detritus is released into the marine realm by calving of sediment-laden icebergs and/or meltwater plumes. The icebergs and suspension load are then transported further offshore by currents before the ice-rafted

debris (IRD) and fine-grained detritus are released at the deposition site by progressive iceberg melting or suspension settling (e.g. Diekmann and Kuhn, 2002). If glaciogenic detritus deposited on the seafloor possesses distinct mineralogical and/or geochemical characteristics that allow to trace it back to its continental source, then investigating temporal changes in the provenance of this material could indicate past changes in the ice sheet, such as ice sheet extent and basal conditions, as well as changes in the climate controlled weathering regime (e.g. Ehrmann et al., 1992; Hillenbrand and Ehrmann, 2002; Hillenbrand et al., 2009b; Basak and Martin, 2013; Cook et al., 2013). Isotopic provenance fingerprints of coarse-grained (>150μm) IRD and fine-grained (<63μm) detrital material in particular has allowed to investigate past destabilization of marine-based portions of an ice sheet during periods of particular warmth. In the Northern Hemisphere, geochemical provenance studies of IRD allowed to specify portions of the Laurentide Ice Sheet that underwent collapse during the so-called "Heinrich events" (Heinrich, 1988; Grousset et al., 1993; Gwiazda et al., 1996; Hemming et al., 1998; Farmer et al., 2003; Hemming, 2004). In the Southern Ocean, a marine sedimentary record presented evidence for massive iceberg discharge by the East Antarctic Ice Sheet during the late Miocene and early Pliocene, as observed in far-travelled ice-rafted hornblende grains originating from a source area located ~1500 km to the east of the depositional site (Williams et al., 2010). Similarly, Pliocene changes in the isotopic provenance of fine-grained (<63μm) detrital material deposited offshore from the marine-based portion of the East Antarctic Ice Sheet above the Wilkes Subglacial Basin were related to fluctuation of the eroding ice margin during several glacial and interglacial stages (Cook et al., 2013). An important prerequisite for applying such provenance studies back in time is, however, the knowledge of the geochemical fingerprint of the source areas (Pierce et al., 2011, 2014; Simões Pereira et al., 2018).

In this study, we build upon the first isotopic and geochemical surveys of glaciomarine seafloor sediments in the Pacific sector of the Southern Ocean (Hemming et al., 2007; Roy et al., 2007; van de Flierdt et al., 2007; Simões Pereira et al., 2018) and investigate seafloor surface sediments and sediment cores that were deposited in PIB. We here analyse strontium (Sr) and neodymium (Nd) isotope and major and trace element compositions of fine-grained (<63μm) detrital sediments, as well as $^{40}Ar/^{39}Ar$ dates of individual ice-rafted (>150μm) hornblende and biotite grains. We further complement isotopic and geochemical analyses by examining the clay (<2μm) and bulk mineral assemblages, as well as rock magnetic properties of the bulk sample. Our study provides the first comprehensive multi-proxy provenance characterization of glaciomarine sediments in the Amundsen Sea, offering a framework to which study WAIS instabilities back in time.

3.2. Study area, sample sites and sample selection

We investigated the provenance signature of seafloor surface samples and downcore sedimentary sequences recovered from 24 sites in PIB (Table 3.1; Figure 3.1). Three cores were retrieved from below the Central PIG Ice Shelf and 21 from the seasonal open marine shelf. All these sample sites were targeted because of their proximity to PIG and Thwaites Glacier, as well as to smaller ice streams, such as Lucchitta Glacier and an unnamed glacier that flow through the Hudson Mountains and feed into the Northern Ice Shelf (Rignot, 2002; Johnson et al., 2014), which was connected to the Central (PIG) Ice Shelf until 2015 (Jeong et al., 2016), and Haynes Glacier, Pope and Smith Glaciers which drain into the Crosson Ice Shelf (Rignot et al., 2014; Scheuchl et al., 2016) (Figure 3.1; Figure simplified to show Smith Glacier only). For the purpose of this chapter and based on their geographical locations, we divide the studied sites into four groups: PIG sub-ice shelf (n=4), eastern PIB (n=8), central PIB (n=3) and western PIB (n=9) (Table 3.1, Figs. 3.1, 3.2). Sub-ice shelf sediments were deposited on a prominent ridge below the central PIG Ice Shelf and were retrieved with a hand-operated percussion corer after drilling through the ice shelf (Smith et al., 2017). The recovered cores are characterized by two lithological facies (Figure 3.3). The lower facies is a stratified to homogenous terrigenous gravelly to sandy mud deposited by melt-out of glaciogenic detritus from the ice-shelf base, current transport and mass flows proximal to grounded ice, while the upper facies consists of a thin unit of laminated to homogenous terrigenous mud deposited in an ocean cavity below the ice shelf (Smith et al., 2017).

Offshore sediment samples were collected during RV Polarstern cruises ANT-XXIII/4 (Gohl, 2006), ANT-XXVI/3 (Gohl, 2010) and PS104 (Gohl, 2017), during RV Nathaniel B. Palmer cruises NBP99-02 (1999), NBP00-01 (2000) and NBP07-02 (2007), during RRS James Clark Ross cruise JR179 (Enderlein & Larter, 2008) and during USCGC Glacier cruise Deep Freeze 85 using gravity corer, (giant) box corer, piston corer and sample grab (Table 3.1). The seafloor surface sediments (n=21) consist of laminated to homogenous or bioturbated terrigenous muds or poorly sorted silty and sandy muds, similar to the upper facies sediments in the sub-ice shelf cores and core top sediments described from offshore sites elsewhere in PIB (Kirshner et al., 2012; Hillenbrand et al., 2013; Nitsche et al., 2013; Smith et al. 2014; Witus et al., 2014). These sediments were deposited via suspension settling from meltwater plumes and IRD melt-out in a seasonal open-marine or permanently sea-ice and/or ice shelf covered environment distal to the grounding line (cf. Ehrmann et al, 2011; Kirshner et al., 2012;

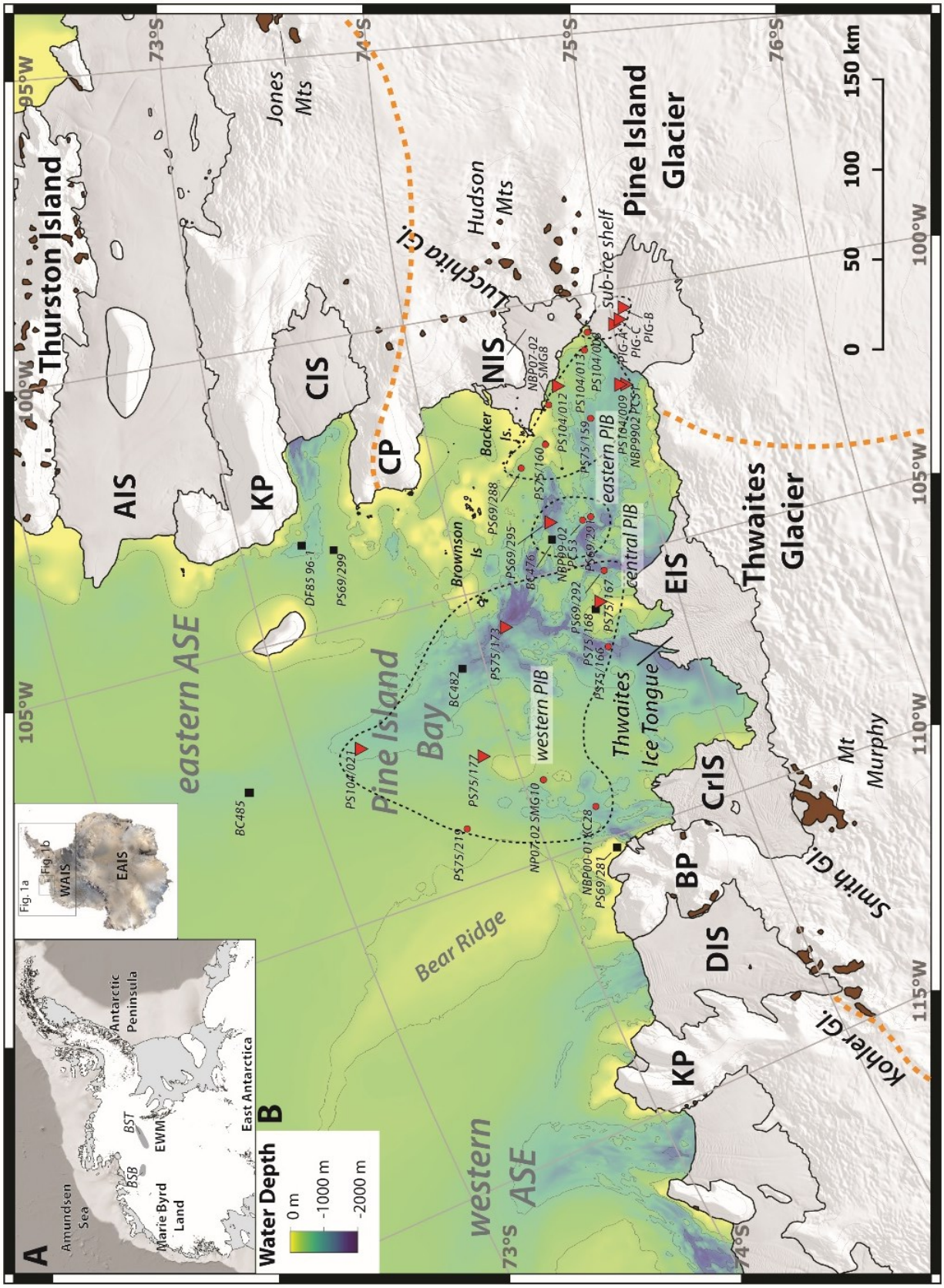

(caption on next page)

Figure 3.1. a) Overview map of West Antarctica, b) Bathymetric map of the Amundsen Sea Embayment (Arndt et al., 2013) with Pine Island Bay and the surrounding coast (Mosaic of Antarctica; Scambos et al., 2007). Red circles indicate locations of seafloor surface sediment samples analysed for this study and red triangles indicate sediment cores for which sedimentary sequences were investigated for this study (corresponding expeditions are given in Table 3.1). Black squares mark sites of cores which were previously analysed and are discussed in the main text. Black stippled lines outline the geographical grouping of core sites mentioned in the text. Thick orange stippled lines indicate positions of ice divides within the West Antarctic Ice Sheet (Zwally et al., 2012). Abbreviations: AIS: Abbott Ice Shelf; BP: Bear Peninsula; CIS: Cosgrove Ice Shelf: CP: Canisteo Peninsula; CrIS: Crosson Ice shelf; DIS: Dotson Ice Shelf; EAIS: East Antarctic Ice Sheet; EWM: Ellsworth-Whitmore Mountains; KP: Kings Peninsula; MP: Martin Peninsula; NIS: Northern Ice Shelf; WAIS: West Antarctic Ice Sheet.

Hillenbrand et al., 2013; Smith et al. 2014; Kuhn et al., 2017). We infer a modern, or at least late Holocene age for the near surface sediments (<6 cm core depth; except NBP99-02 53PC: 24-29 cm) based on their stratigraphic position near the seabed surface and on AMS ^{14}C and ^{210}Pb dating on several sediment records from the same lithological unit in the Amundsen Sea (Hillenbrand et al., 2013; Witus et al., 2014; Smith et al., 2017).

Downcore samples targeting subglacial and deglacial-transitional sediments were taken from a total of eleven cores, including three sediment cores recently recovered during expedition PS104 (PS104/009-1, PS104/012-2 and PS104/021-1) and two previously unpublished sediment cores (PS75/173-1 and PS75/177-1) (Figure 3.1; Table 3.1). Site PS104/009-1 contains a homogenous sandy muddy diamicton at its base which is overlain by moderately to strongly laminated and stratified muds to sandy muds that are slightly bioturbated near the core top (Appendix Figure 3.2). Similarly, core PS104/021-1 consists of a homogenous diamicton at its base and moderately laminated to slightly bioturbated muds above, which are separated by a layer of homogenous muddy to gravelly sand. Core PS104/012-2 comprises a massive muddy diamicton at its base and a thick sequence of laminated to stratified muddy sand, sandy mud and mud on top, which are sandwiching a succession of structureless muddy sand to sandy mud and muddy diamicton (Appendix Figure 3.2). Core PS75/173-1 consists of muds alternating with lenses of (gravelly) sand at the base, which is separated by a thin layer of sandy gravel from the overlying mud unit. Similarly, the

base of PS75/177-1 contains a unit of mud alternating with (sandy) silt at the base and a mud unit at the top. The former unit encompasses a segment of muddy diamicton and a segment of sandy gravel (Figure 3.3; Appendix Figure 3.2). Stratigraphies for all other sediment cores, including bibliographic source information, are summarized in Table 3.1 and Figure 3.3.

We base our interpretation of depositional environments of the newly investigated sedimentary sequences from cruises ANT-XXVI/3 and PS104 on previous sedimentological studies in the Amundsen Sea, including PIB (Ehrmann et al., 2011; Kirschner et al., 2012; Hillenbrand et al., 2013, 2017; Smith et al., 2014, 2017; Witus et al., 2014; Kuhn et al., 2017). The lithological facies for the offshore sedimentary sequences, from which the downcore samples (n=19) were taken, and their interpretation are given in Table 3.1. Overall, sedimentary sequences deposited in PIB comprise up to three different facies: (i) a soft diamicton at the base, covered by (ii) a transitional unit of sandy-gravelly mud to muddy-gravelly sand, and (iii) an occasionally bioturbated, predominantly terrigenous mud near the seafloor surface (Figure 3.3). Diamictons were deposited as a subglacial deformation till below a grounded ice stream, a glaciomarine diamicton molten out from the base of an ice shelf proximal to the grounding line, an iceberg-rafted diamicton, an iceberg turbate generated by the reworking of pre-existing seabed sediments by keels of grounded icebergs or as a glaciogenic debris flow at the flank of a topographic high (e.g. Hillenbrand et al. 2003; Smith et al., 2014, and references therein). The deglacial-transitional unit typically characterises the transition from subglacial to glaciomarine conditions, usually indicating deposition under a thin ice shelf or permanent sea-ice cover distal from the grounding line. Its lithological facies is more varied, but generally consists of moderately stratified mud alternating with layers of silt and sandy silt (Facies MSi) and/or sand and gravelly sand (Facies MSa) (Hillenbrand et al., 2013). The depositional environment of the upper unit corresponds to that of the surface sediments described above. We did not carry out additional chronological analyses on the investigated sediments. However, the lithological facies of the studied sediment cores together with the published chronologies available for cores from PIB and elsewhere on the Amundsen Sea and Antarctic shelves permit to interpret our downcore provenance data in terms of changes in WAIS configuration.

Table 3.1. Lithology, depositional process and strontium and neodymium isotopic composition of sediments from the Pine Island Bay

ID	Core Site[a]	Core depth [cm]	Gear[b]	Cruise expedition	Lat	Long	Water depth (m)	Coarse (>63µm) fraction	Fine (<63µm) fraction	Area	Lithology[c]	Depositional process	Ref.[d]	$^{143}Nd/^{144}Nd$	2 S.E.	ε_{Nd}	2SD	$^{87}Sr/^{86}Sr$	2 S.E.
1−1	PIG-B	2	PerC	n.a.	-75.12	-100.36	740			sub-ice shelf PIG	M	Sub-ice shelf	1	0.512213	0.000009	-8.29	0.21	0.726553	0.000007
1−2	*PIG-B*	*52*									GS	Deglacial/transitional	1	*0.512180*	*0.000010*	*-8.93*	*0.21*	*0.728300*	*0.000006*
2−1	PIG-A	2	PerC	n.a.	-75.07	-100.74	760			sub-ice shelf PIG	M	Sub-ice shelf	1	0.512199	0.000012	-8.55	0.51	0.730518	0.000008
2−2	*PIG-A*	*48*									GS	Deglacial/transitional	1	*0.512171*	*0.000010*	*-9.11*	*0.21*	*0.731158*	*0.000007*
2−3	*PIG-A*	*84*									GS	Deglacial/transitional	1	*0.512149*	*0.000014*	*-9.54*	*0.51*	*0.731690*	*0.000007*
3−1	PIG-C	2	PerC	n.a.	-75.05	-100.82	820			sub-ice shelf PIG	M	Sub-ice shelf	1	0.512174	0.000017	-9.05	0.21	0.728822	0.000006
3−2	*PIG-C*	*28*									GS	Deglacial/transitional	1	*0.512169*	*0.000011*	*-9.15*	*0.51*	*0.731478*	*0.000006*
	duplicate sample [e]							8	92									0.731464	0.000009
4	PS104/008(-2)	3.5	GC	ANT-XXXII/3	-74.87	-100.71	698	5	95	sub-ice shelf PIG	M	Open-marine	2	0.512216	0.000011	-8.24	0.26	0.723985	0.000006
5	PS104/013(-2)	5	GC	ANT-XXXII/3	-74.84	-101.04	545	14	86	eastern PIB	M	Open-marine	2	0.512266	0.000013	-7.25	0.26	0.718398	0.000006
6−1	PS104/012(-2)	5	GC	ANT-XXXII/3	-74.68	-101.62	358	*49*	*51*	eastern PIB	M	Open-marine	2	0.512257	0.000011	-7.44	0.26	0.722623	0.000007
6−2	*PS104/012(-2)*	*153*						*46*	*54*		*M*	Open-marine	2	*0.512472*	*0.000021*	*-3.23*	*0.51*	*0.711910*	*0.000009*
6−3	*PS104/012(-2)*	*173*						*34*	*66*		*mD*	*Debris-flow ?*	2	*0.512431*	*0.000008*	*-4.03*	*0.21*	*0.711025*	*0.000008*
6−4	*PS104/012(-2)*	*253*						*35*	*65*		*M*	*Debris-flow ?*	2					*0.710894*	*0.000007*
6−5	*PS104/012(-2)*	*313*									*mD*	*Subglacial*	2	*0.512407*	*0.000010*	*-4.50*	*0.51*	*0.712564*	*0.000007*
7−1	NBP99-02 PC51	17-22	PC	NBP99-02	-74.96	-101.85	998			eastern PIB	M	Open-marine	3, 4	0.512231	0.000013	-7.94	0.36		
7−2	*NBP99-02 PC51*	*30-38*									M	Open-marine	3, 4	*0.512253*	*0.000006*	*-7.51*	*0.32*		
8−1	PS104/009(-1)	6	GC	ANT-XXXII/3	-74.99	-101.87	989	10	90	eastern PIB	M	Open-marine	2	0.512294	0.000010	-6.71	0.28	0.722533	0.000008
8−2	*PS104/009(-1)*	*223*						*3*	*97*		*M*	Open-marine	2	*0.512269*	*0.000010*	*-7.20*	*0.21*	*0.722424*	*0.000008*
8−3	*PS104/009(-1)*	*265*						*50*	*50*		*mD*	*Subglacial*	*2*	*0.512296*	*0.000011*	*-6.67*	*0.51*	*0.720531*	*0.000008*
8−4	*PS104/009(-1)*	*505*						*43*	*57*		*mD*	*Subglacial*	*2*	*0.512296*	*0.000009*	*-6.68*	*0.21*	*0.721115*	*0.000007*
9	NBP07-02 SMG8	Surface	grab	NBP07-02	-74.62	-101.92	438			eastern PIB	M	Open-marine	based on 4	0.512531	0.000007	-2.08	0.32		
10	PS75/159(-1)[f]	0-1	GC	ANT-XXVI/3	-74.80	-102.36	1046	0	100	eastern PIB	M	Open-marine	5, 6	0.512267	0.000008	-7.24	0.21	0.723959	0.000005
11	PS75/160(-1)	1	GC	ANT-XXVI/3	-74.56	-102.62	336	32	68	eastern PIB	M	Open-marine	4	0.512284	0.000009	-6.91	0.26	0.718102	0.000007
12	PS69/288(-3)	4	GC	ANT-XXIII/3	-74.42	-102.99	772	1	99	eastern PIB	M	Open-marine	6, 7	0.512272	0.000011	-7.15	0.26	0.721267	0.000007
13−1	PS69/295(-1)	4	GC	ANT-XXIII/4	-74.48	-104.10	1151	1	99	central PIB	M	Open-marine	7	0.512335	0.000010	-5.91	0.26	0.717354	0.000007
13−2	PS69/295(-1)	*375*						*53*	*47*		*MSa*	Deglacial/transitional	7	*0.512327*	*0.000010*	*-6.07*	*0.21*	*0.713774*	*0.000008*
13−3	PS69/295(-1)	*474*						*40*	*60*		*mD*	*Subglacial*	*7*	*0.512328*	*0.000009*	*-6.04*	*0.21*	*0.716413*	*0.000006*
14	PS69/291(-1)	7	GC	ANT-XXIII/4	-74.69	-104.16	1023	*1*	*99*	central PIB	M	Open-marine	6	0.512314	0.000010	-6.32	0.26	0.719121	0.000006
15	NBP99-02 53PC	*24-29*			-74.67	-104.34				central PIB	M	Open-marine	3, 4						
16	PS69/292(-2)	3	GC	ANT-XXIII/4	-74.68	-105.19	1407	0	100	western PIB	M	Open-marine	6	0.512387	0.000010	-4.89	0.28	0.716554	0.000006
17−1	PS75/167(-1)[f]	5	GC	ANT-XXVI/3	-74.62	-105.80	526	23	77	western PIB	M	Open-marine	4	0.512406	0.000008	-4.52	0.21	0.716904	0.000006
17−2	*PS75/167(-1)*	*818*						*1*	*99*		*MSa*	Deglacial/transitional	4	*0.512309*	*0.000016*	*-6.41*	*0.51*	*0.722327*	*0.000008*
18	PS75/166(-3)	6	GC	ANT-XXVI/3	-74.60	-106.64	1385	0	100	western PIB	M	Open-marine	6	0.512461	0.000011	-3.44	0.28	0.712849	0.000006
19−1	PS75/173(-1)	5	GC	ANT-XXVI/3	-74.14	-105.73	1507	1	99	western PIB	M	Open-marine	2	0.512380	0.000011	-5.03	0.26	0.714694	0.000006
19−2	PS75/173(-1)	*195*						*11*	*89*		*MSa*	Deglacial/transitional	2	*0.512353*	*0.000019*	*-5.56*	*0.51*	*0.715615*	*0.000007*
20−1	PS75/177(-1)	5	GKG	ANT-XXVI/3	-73.85	-107.88	740	2	98	western PIB	M	Open-marine	2	0.512395	0.000008	-4.74	0.28	0.716112	0.000007
20−2	*PS75/177(-1)*	*300*						*2*	*98*		*MSi*	Deglacial/transitional	2	*0.512526*	*0.000009*	*-2.19*	*0.21*	*0.709917*	*0.000010*
21	PS75/219(-2)	3	GKG	ANT-XXVI/3	-73.67	-109.00	458	23	77	western PIB	M	Open-marine	2	0.512401	0.000011	-4.63	0.26	0.714902	0.000006
22−1	PS104/021(-1)	5	GC	ANT-XXXII/3	-73.30	-107.11	882	2	98	western PIB	M	Open-marine	2	0.512400	0.000012	-4.64	0.26	0.715925	0.000006
22−2	*PS104/021(-1)*	*77*						*53*	*47*		*GS*	Deglacial/transitional	2	*0.512463*	*0.000013*	*-3.41*	*0.51*	*0.712328*	*0.000008*
22−3	*PS104/021(-1)*	*103*						*47*	*53*		*mD*	*Subglacial*	2	*0.512452*	*0.000020*	*-3.62*	*0.51*	*0.712327*	*0.014049*
23	NBP07-02 SMG10	Surface	grab	NBP07-02	-74.10	-108.61	730			western PIB	M	Open-marine	based on 4	0.512462	0.000007	-3.43	0.32		
24	NBP00-01 KC28	9-14	GC	NBP00-01	-74.30	-109.36	1012			western PIB	M	Open-marine	based on 4	0.512518	0.000006	-2.34	0.36		

(Table continues on next page)

Table 3.1. (*continued*)

a) *italic*: sedimentary sequences deposited below the upper muddy unit of of the sediment core

b) PerC: percussion corer; GC: gravity corer; PC: piston corer; grab: Smith-Mcintyre Grab; GKG: giant box corer

c) M: mud; GS: Gravelly sand to sandy gravel; mD: muddy diamicton; MSa: Mud alternating with lenses of sand/gravelly sand; MSi: mud alternating with lenses of silt/sandy silt

d) (1) Smith et al., 2017; (2) Hillenbrand, pers. comm.; (3) Description of sediments recovered by RV Nathaniel B. Palmer 99-02 (http://arf.fsu.edu/publications/documents/NBP_1999_02.pdf; accessed 08/2018); (4) Hillenbrand et al., 2013; (5) Nitsche et al., 2013; (6) Kuhn et al., 2017; (7) Smith et al., 2014

e) Duplicate sample values represent full procedural replicates of sample powders (i.e. from digestion).

f) Neodymium and strontium isotopic data is from Chapter 2 (i.e. Simões Pereira et al, 2018)

3.3. Methods

We applied a multi-proxy toolbox using Sr and Nd isotopic, and major and trace metal compositions of the fine-grained fraction (<63μm), $^{40}Ar/^{39}Ar$ dates on ice-rafted (>150μm) hornblende and biotite grains, mineral composition of the clay (<2μm) and bulk sediment fractions, and rock magnetic parameters. Tables 3.1 and Appendix Tables 3.1, 3.2, 3.3 and 3.4 show results of the different methods that were applied to each sample.

As erosion occurs basically everywhere below the ice, isotopic and geochemical provenance signatures of fine-grained detritus may represent an integrated average fingerprint of glacial detritus eroded by the ice along its flow line (e.g. Pierce et al., 2011). Ice-rafted hornblende and biotite grains, on the other hand, may be mainly sourced from bedrock located at the ice margin. Subglacial erosion depends on substrate erodibility, basal ice velocity, ice thickness and the basal thermal regime (e.g. Jamieson et al., 2010), with the latter three factors favouring subglacial erosion in the downstream sections of modern ice streams around the fringes of the WAIS, where flow velocity (e.g. Rignot et al., 2011) and basal melting (e.g. Pattyn 2010) are highest whilst the ice is relatively thin (e.g. Fretwell et al., 2013). The differences in closure temperature of hornblende and biotite grains (~550 and 300°C, respectively) and their different fertility in certain lithologies, i.e. different source rocks might contain different amounts of hornblende and biotite (Pierce et al., 2014), make them useful tracers to characterise subglacial provenance. Bulk and clay mineral assemblages can provide further constraints on the mineralogy of the source rocks (Neumann and Ehrmann, 2000, 2001; Ehrmann et al., 1992, 2011), while rock magnetic properties allow to determine the magnetic state, as well as the relative concentrations of magnetic minerals in the sediments (e.g. Frederichs et al., 1999).

3.3.1. Strontium and neodymium isotope composition

Bulk sediment samples (~10cc) were freeze-dried and sieved into <63μm, 63-150μm and >150μm fractions. An aliquot (~500mg) of the fine-grained (<63μm) fraction was leached to remove the biogenic carbonate using buffered acetic acid, and sequentially the authigenic ferromanganese coatings using 0.02M hydroxylamine hydrochloride, following the procedure by Rutberg et al. (2000), based on Chester and Hughes (1967). Biogenic opal is not an important carrier of trace elements (Collier and Edmond, 1984) and therefore no further removal of opal was undertaken. For instance, strontium and Nd concentration in biogenic opal are generally very low (~5 ppm and ~3 ppm, respectively; Grousset et al., 1998), therefore opal-bound Sr and Nd are unlikely to exert a large influence in our provenance results (Bayon et al., 2002). After homogenization, approximately ~50mg of the residual (detrital) fraction were weighted into Savillex beakers and dissolved using 2ml of HF (27M), 1ml of HNO_3 (15M) and 0.8ml of $HClO_4$ (20M) mixing solution for 3-4 days on a hotplate until no visible particle remained. The purified Sr and Nd fractions were extracted using a three-stage ion-exchange chromatography. The sample was first loaded onto a column with cation-exchange resin AG50W-X8 to separate Sr and the rare earth elements (including Nd) from the sample matrix. The Sr fraction was purified using Eichrom`s Sr spec (Cook, 2013; modified from Pin and Bassin, 1992), while Nd was extracted from the other rare earth elements using Ln-Spec resin (Cook, 2013; modified from Pin and Zalduegui, 1997).

Dried Sr cuts were re-dissolved in 10μl HCl, and an 1μl aliquot was loaded onto a degassed tungsten filament with 1μl of $TaCl_5$ activator solution. Strontium isotope ratios were measured on a thermal-ionisation mass spectrometer (TIMS) at the MAGIC laboratories at Imperial College. Raw $^{87}Sr/^{86}Sr$ ratios were corrected for mass bias by normalizing to an $^{88}Sr/^{86}Sr$ ratio of 8.375 using an exponential law. ^{87}Rb was kept below 100 ppm of the measured ^{87}Sr beam, except sub-ice shelf core sample PIG-C (28 cm) which was measured with an average rubidium-87 contribution of 236 ppm, varying from 800 ppm to <50 ppm over the course of the measurement with no influence on the raw $^{87}Sr/^{86}Sr$ ratio. Strontium isotope measurements were carried out over a period of 3 months. Reported $^{87}Sr/^{86}Sr$ ratios were corrected for the slight offset in the measured $^{87}Sr/^{86}Sr$ ratio of SRM987 standard value of 0.710250 ± 0.000010 2.S.D. (n=39, collected between February 2017 and January 2018) to the accepted value of 0.710252 ± 0.000013 (Weis et al., 2006), for the sake of consistency over the period of this PhD project. Three procedural BCR-2 standards gave an $^{87}Sr/^{86}Sr$ value of 0.705015 ± 0.000010 2.S.D. (n=3), which conforms to the accepted value of 0.705013 ±

0.000010 2.S.D. (Weis et al., 2006). Three batches gave procedural blanks of ~100pg, 104pg and ~900pg.

Neodymium isotope composition was measured on a Nu Instruments multi-collector inductively coupled plasma mass spectrometer (MC-ICP-MS) in the MAGIC facilities. The Nd isotope ratios were obtained after correcting for instrumental mass bias using a 146Nd/144Nd ratio of 0.7129 and an exponential law. Four batches were measured over a period of three months. For three batches, reported $^{143}Nd/^{144}Nd$ ratios were corrected for the average JNdi value of the run (0.512137 ± 0.000011, n=20; 0.512119 ± 0.000015, n=28; 0.512117 ± 0.000013, n=17; 0.512124 ± 0.000016, n=21) to the accepted value of 0.512115 (Tanaka et al., 2000). For one batch, we applied a standard-sample bracketing method (sample analysed between two standards) due to a drift in the observed JNdi $^{143}Nd/^{144}Nd$ ratio. Reported standard deviation on this batch is based on the largest BCR-2 $^{143}Nd/^{144}Nd$ offset to the accepted value of 512638 ± 0.000015 (Weis et al., 2006). Inter-batch comparison of repeated samples shows values that are the same within their respective error bars. Neodymium blank contribution to the smallest total sample Nd amount was below 0.12% (n=2). One batch gave a blank contribution of 0.46% (1.2ng) but mass balance calculation showed minimal offset from the measured value well within the reported error.

3.3.2. Major and trace element composition

An additional split (~50mg) of the leached <63μm residual was retrieved for major and trace element composition analysis and digested using 2ml HF (27M), 1ml HNO_3 (15M) and 0.8ml $HClO_4$ (28M) for 3-4 days on a hotplate until the complete sample went into solution. Solution was converted into nitric and samples were taken to the Open University in Milton Keynes. Analysis of major and trace element composition were performed on an Agilent 8800 ICP-QQQ inductively coupled plasma mass spectrometer, with an integrated collision/reaction cell to remove targeted interference ions. Most elements were measured with no gas or He gas in the collision reaction cell, except for rare earth elements measured with O2. Oxide formation (CeO^+/Ce^+) was kept below 1.0% and 0.6% in no gas and He gas mode, respectively, and doubly charged species (Ce^{2+}/Ce^+) was kept below 1.5% and 1.0%, respectively. Analyses were standardized against five USGS reference materials, in addition to an internal standard to correct for instrument drift. Detection limits of light trace elements were typically 2–50ppt in solution, while mid to heavy trace elements (Rb-U) were ≤2ppt. Repeated BCR-2 standard measurements (n=11) indicate an overall precision for trace elements below 5% with accuracy

being below 10%, while checks on major elements produced 5% precision and accuracy, respectively.

3.3.3. $^{40}Ar/^{39}Ar$ ages of iceberg-rafted hornblende and biotite grains

As fine-grained detrital material <63μm can be transported by ocean currents, wind and ice-rafting, we picked hornblende and biotite grains (n=150) from the coarse fraction >150μm of surface sediments from 7 core sites (Appendix Table 3.1) to ensure that these grains were transported and deposited by icebergs or an ice shelf but no other processes. Sample and monitor (Fish Canyon sanidine) grains were irradiated at the TRIGA reactor at the USGS in Denver, Colorado. The neutron flux was calibrated using J-values calculated to normalize Fish Canyon sanidine grains to 28.201 ± 0.046 Ma (Kuiper et al., 2008). $^{40}Ar/^{39}Ar$ age measurements were carried out using single-step CO_2 laser-fusion at the Lamont-Doherty Earth Observatory Argon Geochronology for the Earth Sciences (AGES) laboratory, after correcting for atmospheric argon ($^{40}Ar/^{36}Ar$ = 298.6; Lee et al., 2006), procedural blanks, mass discrimination and nuclear interferences (Dalrymple et al., 1981).

3.3.4. Bulk and clay mineralogy

Sediment samples (~10cc) were freeze-dried at the Alfred-Wegener Institute for Polar and Marine Research (Bremerhaven, Germany) and sent to the Institute for Geophysics and Geology at the University of Leipzig for sample processing and bulk mineral investigations. An aliquot of the dried sediment sample (~1 mg) was mixed with an internal corundum standard (~0.2 g) and homogenized using an agate mortar under acetone. Samples then were mounted on small aluminium tiles, producing randomly-oriented pressed-slides, and X-rayed from 2° to 50° 2Θ (0.005° 2Θ/s) using the diffractometer Rigaku New Miniflex with CoKα radiation. We used the software "MacDiff" (Petschick, 2001) to assess bulk mineral diffractogram patterns. Diffractograms were adjusted to the corundum peak (3.479 Å), and contents of quartz (4.25 Å), K-feldspar (3.23 Å), plagioclase (3.19 Å), total feldspar (combined areas of feldspar peaks at 3.24 Å, 3.21 Å and 3.18 Å), pyroxene (2.89-2.98 Å), hornblende (8.4 Å) and halite (2.82 Å) were estimated by normalizing peak intensities (of quartz, K-feldspar, plagioclase) and peak areas (of total feldspar, pyroxene, hornblende, halite) to the peak intensity and area of corundum, respectively.

Sediment sample processing and analysis for clay mineral assemblages were performed at the University of Leipzig, following standard procedures (see Ehrmann et al., 1992, 2011, and references therein). A split (~1g) of the fine-grained (<63μm) sample (sieved during sample processing for Sr and Nd isotope analysis, Section 3.3.1) was repeatedly leached with acetic acid (10%) and H_2O_2 to remove carbonate and the organic fraction. The clay fraction (<2μm) was separated from the remaining sample in settling tubes after being mixed with an internal MoS_2 standard at a ratio of 0.4 to 1. The suspended material was rapidly filtered through a 0.2μm membrane filter to obtain a texturally oriented aggregate, then dried and fixed on small aluminium tiles with exposure to ethylene glycol vapour (60°C for 18h) before X-ray analysis. Clay diffractograms were obtained using a Rigaku New Miniflex diffractometer with CoKa radiation (30kV, 15 mA), and irradiated in the range of 3-40° 2Θ (at 0.02° 2Θ steps/4s integration time), and again in the range of 27.5-30.5° 2Θ (0.01° 2Θ steps/4s integration time) to better discriminate the kaolinite (002) peak from the chlorite (004) peak. Diffractograms were assessed using "MacDiff" (Petschick, 2001). Diffraction patterns were adjusted for the MoS2 peak (6.15 Å) and clay groups were identified based on their basal reflections at 16.5 Å for smectite (after glycolisation), at 10 Å for illite, 3.58 Å for kaolinite and 3.54 Å for chlorite. Semi-quantitative analyses were measured using empirically determined weighing factor on the integrated peak areas of the different clay mineral groups (Biscaye, 1964, 1965).

3.3.5. Rock magnetic analyses

Samples for rock magnetic investigations were collected in small oriented cubes of 6.2cm^3 pressed into the split core section. Low-field magnetic susceptibility (MS), the median destructive field (MDF), anhysteretic (ARM) and isothermal (IRM) remanent magnetization were measured with an automated 2G SQUID Rock Magnetometer at the Department of Earth Sciences, University of Bremen. While the remanent magnetization of virtually all minerals contributes to the measured MS, ARM usually quantifies the content of fine-grained (<1μm) single-domain (SD) magnetite (Frederichs et al., 1999). IRM_{100mT} (here term IRM) is dependent on the content of coarser-grained magnetite, meaning that the ratio ARM_{100mT}/IRM_{100mT} can be used as a magneto-granulometric index. Saturated IRM (SIRM) and high IRM (HIRM) provides estimates of the contents of anti-ferromagnetic minerals, such as hematite and goethite. The S-ratio ($S=0.5[(-IRM_{-300mT}/SIRM)+1]$ represents the ratio of low to high-coercivity magnetic minerals (e.g. magnetite vs hematite) (Bloemendal et al., 1992).

3.4. Results

3.4.1. Provenance signature of Late Holocene sediments

3.4.1.1. Fine-grained sediment provenance

Tables 3.1 and Appendices 3.2 and 3.3 show the results of our radiogenic (Sr, Nd) isotope, major and trace element and clay mineral analyses on the 24 seafloor surface sediments from PIB. This dataset included previously analysed clay mineral contents of the PIG sub-ice shelf cores (Smith et al., 2017; Smith, pers. comm.) as well as previously published Sr and Nd isotope and trace element compositions of seafloor surface sediments at sites PS75/159-1 and PS75/168-1 (Simões Pereira et al., 2018), the latter core site being located near site PS75/167-1. The tables include Sr and Nd, trace element and clay contents of four samples (western PIB: n=3; central PIB: n=1) previously analysed by Ehrmann et al. (2011) and Simões Pereira et al. (2018), which we include in the following results and discussion.

Overall, the radiogenic, geochemical and clay mineral provenance signatures of sediments in PIB fall between two end-members: the sub-ice shelf sediments beneath the Central PIG Ice Shelf and site PS75/166-3 located directly offshore from the Thwaites Ice Tongue, which is sometimes referred to as Thwaites Glacier Tongue (Figure 3.2). The PIG sub-ice shelf samples record the lowest Nd and highest Sr isotope values from PIB (ε_{Nd}: -9.1 to -8.3; $^{87}Sr/^{86}Sr$: 0.7265 to 0.7305). These sample have low smectite contents (~7%) and zirconium(Zr)/titanium(Ti) ratios (0.028 to 0.030), as well as high K_2O/Al_2O_3 ratios (0.26 to 0.28). Across the shelf, we observe a general change from eastern PIB towards western PIB in the radiogenic, geochemical and clay mineral compositions. Neodymium isotope compositions become progressively more radiogenic with increasing distance from PIG (ε_{Nd} eastern PIB: -8.3 to -6.7; ε_{Nd} central PIB: -6.0 to -5.9; ε_{Nd} western PIB: -5.1 to -2.3), with the exception of site NBP07-02 SMG8 located in eastern PIB (-2.1). As expected, $^{87}Sr/^{86}Sr$ ratios show the opposite change (eastern PIB: 0.7240 to 0.7181; central PIB: 0.7191 to 0.7173; western PIB: 0.7169 to 0.7128). In general, kaolinite contents are comparatively low in eastern and central PIB (<20%), except at site PS104/009-1 close to PIG (26%; Figure 3.1), and increase towards the western PIB (>20%). Smectite contents remain low in eastern PIB in the vicinity of PIG (<10%), but gradually increase towards central PIB (10-13%) and western PIB (9-20%). Similar trends are observed in the Zr/Ti ratios (eastern PIB: 0.026-0.030, central PIB: 0.029-0.031, and western PIB: 0.034-0.042).

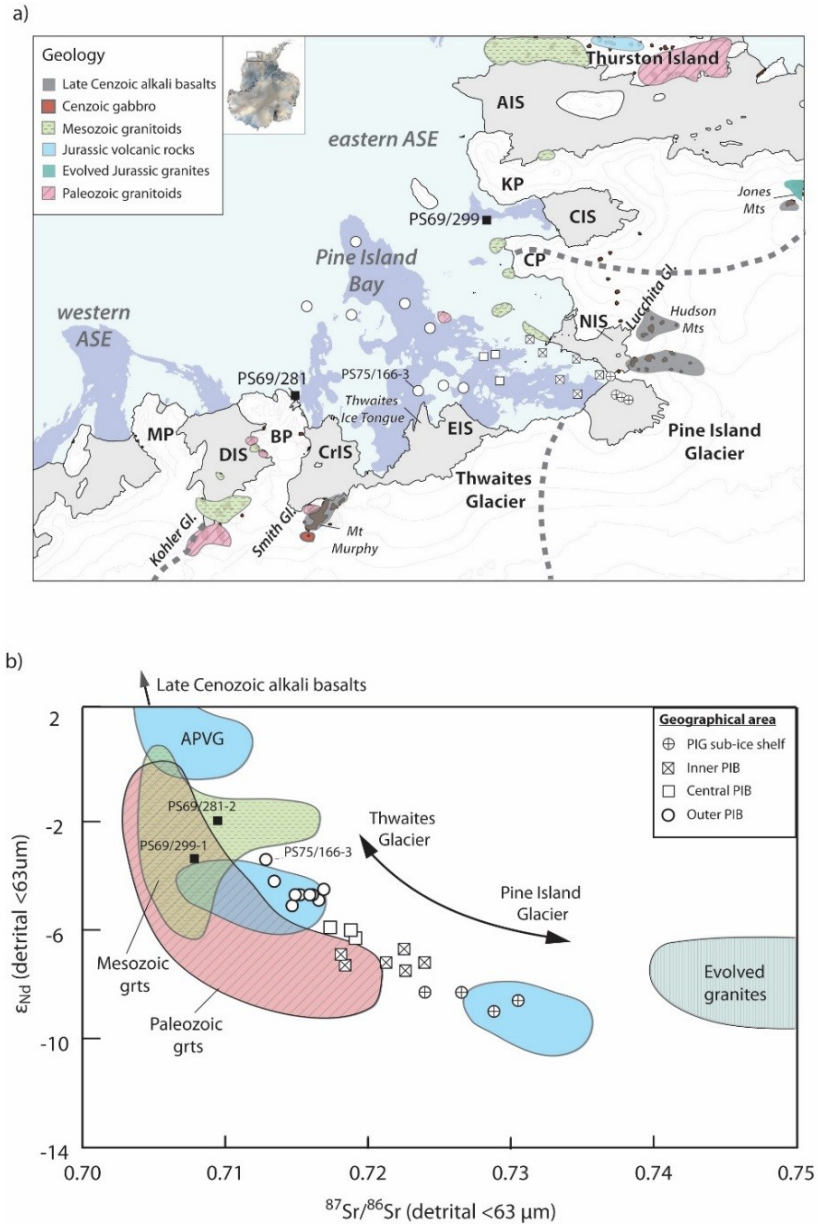

Figure 3.2. (a) Simplified geological map of the coast in the Amundsen Sea sector of West Antarctica. Dark blue shading highlights shelf water depths below 750 m (Arndt et al., 2013). Grey stippled lines mark ice drainage divides (Zwally et al., 2012). Geological information is based on: Pankhurst et al., 1993, 1998; Hole et al., 1994; Mukasa et al., 2000; Rocchi et al., 2006; Kipf et al., 2012. (b) Neodymium and strontium isotope compositions of fine-grained (<63µm) detritus of seafloor surface sediments from Pine Island Bay. Symbols represent sites from different geographical areas, as described in Table 3.1 (only samples analysed for both Nd and Sr isotope ratios are shown). Coloured fields outline the overall Sr and Nd isotope compositions of the major geological units reported from the Amundsen Sea sector. Colour of the fields is related to 'a'. Isotopic composition shown for the volcanic rocks include sources from the Antarctic Peninsula. Isotopic data are from: Pankhurst et al., 1993; Riley et al., 2003, 2010, 2018; Futa and LeMasurier, 1983.

3.4.1.2. Provenance of ice-rafted hornblende and biotite grains

A total of 150 hornblende and biotite grains from eastern PIB (n=29), central PIB (n=61) and western PIB (n=60) were $^{40}Ar/^{39}Ar$ dated, adding to the ages on 10 hornblende grains from site PS75/159-1 (n=1; eastern PIB) and PS75/168-1 (n=9; western PIB) previously published by Simões Pereira et al. (2018). Results are summarized in Figure 3.4 and shown in Appendix Table 3.1. IRD at site PS104/009-1 from eastern PIB is characterised by ages between 170 and 270 Ma (n=24), together with five ages at 2 Ma, 6 Ma, 141 Ma, 313 Ma and 543 Ma. In central PIB, IRD from sites PS69/291-1, PS69/295-1 and NBP99-02 PC53 shows a large age population ranging from 90 to 160 Ma (n=56), with a maximum between 90 and 120 Ma, and a minor age population ranging from 180 to 270 Ma (n=9). The IRD at central PIB sites contains several grains younger than 60 Ma (n=5). IRD at sites from western PIB (PS75/173-1 and PS75/177-1) contains a high number of hornblende and biotite grains with ages ranging from 110 Ma to 380 Ma (n=45), with a peak between 110 and 130 Ma. These sites further contain 6 IRD grains younger than 40 Ma.

Hornblende and biotite grains have been observed in all seafloor surface sediment samples. Overall, we do not observe a distinct age distribution between the two mineral systems (Appendix Figure 3.2) for ages exceeding 40 Ma. The only exception to this observation comes from core PS75/173-1, with biotite ages of 110-200 Ma and hornblende ages of 250-380 Ma. Other sites from western PIB (i.e. PS75/177-1) show presence of hornblende and biotite grains in the 110-200 Ma and 250-380 Ma age interval, respectively. Hence, and in addition to the relatively low number of grains analysed (n=17), we suppose that the distinct age distribution observed at site PS75/173-1 is coincidental and does not bear any geological meaning. Grains younger than 40 Ma from all core sites are, however, predominantly composed of hornblende (10 grains out of 11; Appendix Figure 3.2).

3.4.1.3. Rock magnetic and bulk mineral data

Surface sediments from western PIB are characterized by higher fine-grained (SD) magnetite contents (ARM >200mA/m; n=7) compared to eastern PIB (ARM <200mA/m; n=6), except at site PS104/012-2 (ARM=257mA/m) (Figure 3.5, Appendix Table 3.4). The highest fine-grained magnetite content is recorded at site PS75/166-3 located offshore from Thwaites Ice Tongue in western PIB (ARM = 326 mA/m). Similarly, high coercivity minerals such as goethite or hematite are largest in seafloor surface sediments proximal to the Eastern Ice Shelf

of Thwaites Glacier (PS75/167-1) and Thwaites Ice Tongue (PS75/166-3) and at site PS104/012-2 offshore from the Northern ice shelf in eastern PIB (HIRM >680 mA/m). Furthermore, these three sites are characterized by high magnetite concentrations ($IRM_{@100mT}$ > 14,000 mA/m). Other rock magnetic parameters (i.e. MDF, $ARM_{@100mT}/IRM_{@100mT}$, S-ratio) do not display any particular geographical trend (Appendix Table 3.4) and are not further discussed.

Bulk mineralogy of surface sediment samples from PIB shows no clear geographical trend (Appendix Table 3.3). In the absence of any geographical variability, I further normalized peak areas of feldspar (Fsp) and pyroxene (Px) to the peak intensity of quartz (Qtz). If we exclude samples containing ≥10% coarse fraction (>63μm) (PS104/012-2, PS104/009-1, PS75/167-1 and PS75/219-2), we observe a slight shift from low Px/Qtz (0.5-0.7)(Figure 3.5) and Fsp/Qtz (1.4-2.7) ratios in eastern PIB toward higher ratios in central PIB (~0.8 and ~2.4) and western PIB (0.8-1.0 and 2.4-3.3).

3.4.2. Provenance of deglacial-transitional and subglacial sediments

Sediments of the lower (sandy/gravelly sandy mud) facies in the sub-ice shelf cores PIG-A, PIG-B and PIG-C were deposited proximal to the grounding line and record slightly lower ε_{Nd} values (up to -9.5) and higher $^{87}Sr/^{86}Sr$ ratios (up to 0.7317) compared to the surface samples (Figure 3.3). Clay mineral contents in this facies sediments are relatively uniform with, for instance, smectite contents varying between 4 and 6%.

The downcore ε_{Nd} signature of the fine-grained sediments co-varies largely with smectite content in all records. The largest variation between the downcore and surface samples occurs at site PS104/012-2 off the Northern Ice Shelf in eastern PIB, with ε_{Nd} increasing up to -3.2 units and $^{87}Sr/^{86}Sr$ ratios decreasing to 0.7109 further downcore. The isotopic provenance change in this core correlates with higher downcore contents of smectite (up to 43%) and ferromagnesian oxides and small cations (i.e. Fe_2O_3, Ti, Mg, Sc, V, Ca, Sr; Appendix Table 3.1), which all indicate input from volcanic sources (e.g. Bhatia and Crook, 1986; Ehrmann et al., 1992). The lower section of this sediment core consists of an alternation of sandy mud to muddy sand and muddy diamictons. I interpret the diamicton at the core base as subglacial till and the upper diamicton, which was deposited on a muddy sand to sandy mud unit as a glaciogenic debris-flow, which was deposited when the grounding line was more proximal to the site. This interpretation needs to be confirmed by additional sedimentological analyses.

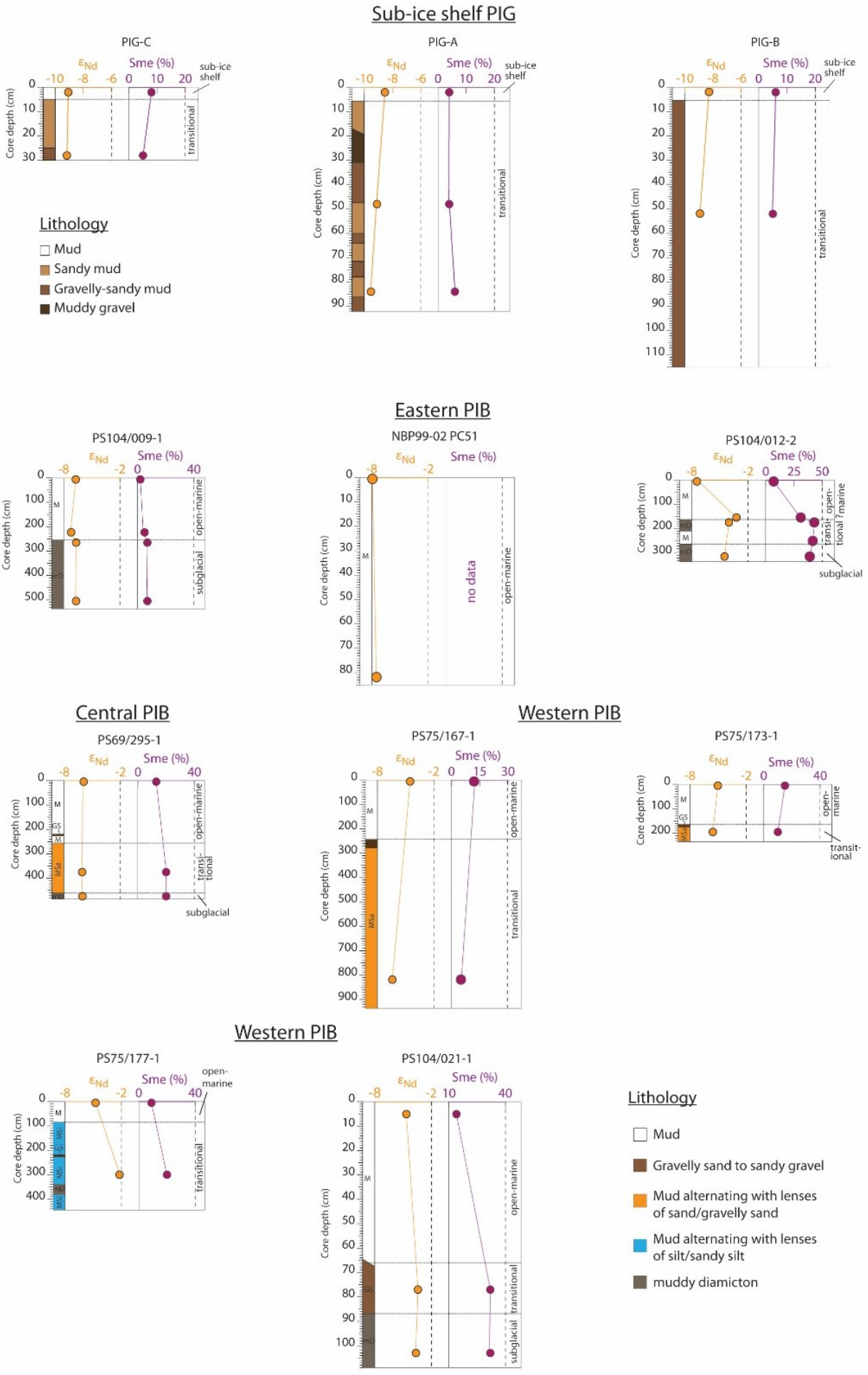

(caption on next page)

Figure 3.3. Lithology, depositional environment and fine-grained (Nd) isotopic and smectite compositions of sub-ice shelf cores from below the Central Pine Island Glacier (PIG) Ice Shelf (lithology and depositional environments from Smith et al., 2017) and offshore sediment cores from the eastern, central and western Pine Island Bay (PIB) (lithology and depositional environments from Hillenbrand et al., 2013; Witus et al., 2014; Kuhn et al., 2017; Hillenbrand, unpublished).

Other sites from eastern PIB (i.e. NBP99-02 PC51 and PS104/009-1) show only minor downcore changes in provenance, with ε_{Nd} varying by ≤0.5 units and clay contents by ≤5% (Figure 3.3). In central PIB, site PS69/295-1 is characterized by three facies reflecting the increasing distance of the core site from the grounding line (subglacial diamicton, transitional, open-marine). This site has, however, relatively uniform ε_{Nd} values (~-6) and $^{87}Sr/^{86}Sr$ ratios (0.7138-0.7173), and shows a slight downcore increase in smectite contents (up to 20%), as well as in several ferromagnesian element ratios (i.e. MgO/Al_2O_3, Co/Yb)(Appendix Table 3.2). In western PIB, the transitional sediments at sites PS75/167-1 and PS75/173-1, which consist of muds alternating with layers of sand, are characterized by slightly lower ε_{Nd} values (-6.2 and -5.5, respectively) and higher $^{87}Sr/^{86}Sr$ ratios (0.7223 and 0.7156, respectively) compared to the surface samples. Smectite contents of these transitional sediments record a slight downcore decrease to 5% and 10%, respectively. In contrast, transitional sediments at sites PS75/177-1 and PS104/021-1 show an opposite trend, recording elevated ε_{Nd} values (-2.2 and ~-3.5, respectively) and lower $^{87}Sr/^{86}Sr$ ratios (0.7099 and ~0.7123, respectively) in the surface sediments, together with a downcore increase in smectite (20% and 32%). The subglacial sediments at site PS104/021-1 have a similar geochemical and clay mineralogical provenance as the transitional sediments at this location.

Qtz/Std, Px/Std and Fsp/Std ratios in the transitional and subglacial sediments of the studied cores are similar or higher when compared to the surface samples (Appendix Table 3.3). We do, however, not observe any particular correlation between these ratios and other provenance tracers. The magnetic properties of these sediments show presence of coarser magnetite grain-sizes (lower ARM_{100mT}/IRM_{100mT} ratio). In addition, most of these sediments show an increase in low and high coercivity (e.g. more magnetite and more, goethite respectively), except at site PS75/167-3 and PS104/021-1 in western PIB. In general, however, all rock magnetic properties of the transitional and subglacial sediments show an increase in their values compared to the surface samples (Appendix Table 3.4).

3.5. Late Holocene detrital sediment provenance in Pine Island Bay

3.5.1. Source characterization of the sediments

3.5.1.1. Geochemical and clay mineralogical provenance signature of fine-grained detritus

Glacially eroded fine-grained detritus supplied by PIG has a distinct provenance fingerprint, which allows to differentiate glaciomarine sediments from this ice drainage basin (i.e. low ε_{Nd}, high $^{87}Sr/^{86}Sr$, low smectite) from sediments originating from other catchments. This specific signature characterises surface and downcore sediments below the Central PIG Ice Shelf (Figure 3.2, 3.6). Based on the isotopic composition of surface sediments deposited at site PS75/159-1, Simões Pereira et al. (2018) suggested that the substrate below the PIG drainage basin is composed of a mix of locally outcropping evolved Jurassic granites and Palaeozoic-Mesozoic granites. Proximal outcrops for the evolved Jurassic granites are found in both the Jones Mountains (Figure 3.2) and the Ellsworth-Whitmore Mountains (Figure 3.1, inset; Craddock et al., 2017), while Palaeozoic-Mesozoic granitoids are widespread along the Amundsen Sea coast (Pankhurst et al., 1993, 1998; Mukasa and Dalziel, 2000; Kipf et al., 2012). Sedimentary basins below PIG have been concluded from seismic reflection and airborne geophysical investigations (Jordan et al., 2010; Smith et al., 2013; Muto et al., 2016) and were also observed below many other ice streams elsewhere in Antarctica (e,g, Anandakrishnan et al., 1998; Bell et al., 1998; Bingham et al., 2012; Jordan et al., 2013). Our data provide further support for the previous interpretations because the Sr and Nd isotope signature of the PIG sub-ice shelf samples is less radiogenic (i.e. lower ε_{Nd}) compared to that of the offshore sediments and falls in between the signatures of the evolved Jurassic granites and Palaeozoic-Mesozoic granitoids (Figure 3.2), therefore suggesting that sediments representing a mixture of these two sources are present under PIG. In detail, the Sr and Nd isotope signatures of the sub-ice sediments overlap with the signature of Jurassic volcanic rocks, which crop out on Thurston Island and the Jones Mountains (Figure 3.2; Pankhurst et al., 1993; Riley et al., 2003, 2017), but also in the Antarctic Peninsula. These volcanic rocks show different geochemical signatures depending on their geographical occurrence, with the least radiogenic volcanics cropping out in the Antarctic Peninsula (Mt Poster formation; Riley et al., 2001). Since these rocks are genetically linked, we need to consider the former rocks as a potential provenance source. Smectite, which is produced by weathering of volcanic detritus (Singer, 1984; Ehrmann et al., 1992) is, however, low at the PIG sub-ice shelf sites, arguing against a predominantly volcanic source.

We observe a change in the radiogenic provenance signature between the PIG sub-ice shelf and eastern PIB sediments (ε_{Nd}: ~-8.6 to ~-6.8; $^{87}Sr/^{86}Sr$: 0.7286 to 0.7216), while clay mineral assemblages remain relatively uniform (e.g. smectite: ~6%; kaolinite: 16 to 18%) (Figure 3.6). Clay is typically a minor product of glacial erosion and usually reflects the erosive signature of subglacial sedimentary strata (Tulaczyk et al., 1998; Licht and Hemming, 2017), while silt-sized glacial flour is produced through comminution by ice crushing (e.g. Boulton, 1996). Glaciers flowing into the Northern Ice Shelf hence supply silt-sized detritus with higher ε_{Nd} values compared to the PIG sub-ice shelf sediments. Local sources are post-Miocene volcanic rock cropping out in the Hudson Mountains (Hole and LeMasurier, 1994), and/or Palaeozoic to Mesozoic granitic rocks cropping out locally in the Backer and Brownson islands and on Canisteo Peninsula and King Peninsula (Pankhurst et al., 1998)(Figure 3.1, 3.5). Low smectite, in addition to low ferromagnesian ratios (MgO/Al_2O_3, Fe_2O_3/Al_2O_3, Co/Yb) and ε_{Nd} values in the eastern PIB sediments argue against predominantly volcanic sources. This in turn indicates that most of the substrate below glaciers feeding into the Northern Ice Shelf is composed of non-volcanic rocks (i.e. granitic) sources.

Kaolinite supplied to PIB is mainly sourced from Thwaites Glacier (Ehrmann et al., 2011), which is may derived from erosion of pre-Oligocene sedimentary rocks in the Byrd Subglacial Basin and/or Bentley Subglacial Trench in the WAIS interior (Hillenbrand et al., 2003). Our data shows that the Thwaites Glacier is also a major source of smectite, as indicated by high smectite contents in sediments deposited in western PIB, which are as high as 20% at site PS75/166-3 located directly offshore from the Thwaites Ice Tongue. Sources for this clay mineral are typically volcanic rocks which crop out extensively in the Thwaites Glacier ice drainage basin (Behrendt, 2013; van Wyk de Vries et al., 2017).

3.5.1.2. Sources for iceberg-rafted hornblende and biotite grains

The $^{40}Ar/^{39}Ar$ hornblende and biotite age populations at sites PS104/009-1 and PS75/159-1 in eastern PIB record notable Jurassic to Triassic (~180 – 250 Ma) cooling ages (Figure 3.4). The younger ages match those of Jurassic granites cropping out in the Jones Mountains (183 Ma K-Ar muscovite; Pankhurst et al., 1993), on the Brownson Islands (194 Ma U-Pb zircon; Mukasa and Dalziel, 2000) and in the Ellsworth-Whitmore Mountains (~170-210 Ma K-Ar whole rock and U-Pb zircon; Craddock et al., 2017; not shown in figures). Triassic magmatic intrusions (~200-250 Ma; obtained by various dating methods) are well

recorded on Thurston Island (Pankhurst et al., 1993), along the Walgreen Coast (Mukasa and Dalziel, 2000; Kipf et al., 2012), and as inherited U-Pb zircon ages in the Jurassic intrusions of the Ellsworth-Whitmore Mountains (Craddock et al., 2017). The geology below the PIG catchment is most likely related to these evolved and juvenile (i.e. low crustal assimilation) Jurassic-Triassic granitoids, possibly granite-granodiorite-tonalites as Triassic ages are observed in both hornblende and biotite grains. The observed ages record events that represent the break-up of Gondwana, which caused a shift from Triassic arc-related intrusions towards mafic intrusions and extrusions, and Jurassic granite intrusions with evolved (high crustal assimilation) geochemical signatures. Surprising is the low number of IRD grains younger than 140 Ma in our record (only a few grains <10 Ma), despite this age population being well recorded in every other sector around PIB (Figure 3.4), indicating absence of a mid-Cetaceous orogenic belt below the PIG ice drainage basin. The ages from eastern PIB contrast with those recorded in central and western PIB, which show well-defined age peaks at 100 & 115 Ma, and 115 & 130 Ma, respectively. We relate the ~100 Ma age peak in central PIB to a source originating from the coast further north, given that the ages match the previously observed $^{40}Ar/^{39}Ar$ age peak offshore from the Cosgrove Ice Shelf (Figure 3.4). However, given the proximity of the central and eastern PIB sites to Thwaites Glacier, we assign the dominant ~115 Ma age peak to a source in the Thwaites Glacier catchment. Igneous rocks with similar crystallization and/or cooling ages crop out along the western Walgreen Coast (Figure 3.4; Pankhurst et al., 1993; Mukasa et al., 2000; Kipf et al., 2012).

The mid-Cretaceous is characterized by emplacement of huge granodiorite-tonalite batholiths along the active margin of West Gondwana (i.e. magmatic flare-ups; Vaughan and Livermore, 2005; Riley et al., 2018). In the Antarctic Peninsula, at least three episodic flare-ups occurred between 100-130 Ma based on U-Pb zircon data on igneous intrusions (i.e. U-Pb zircon: 102-108 Ma, 113-118 Ma and 126-130 Ma; Flowerdew et al., 2005; Riley et al., 2018), which was caused by plate reconfiguration or plume-lithosphere interaction. Our $^{40}Ar/^{39}Ar$ age record from PIB fits these mid-Cretaceous plume events and suggests that similar episodic flare-ups in the Amundsen Sea sector may be genetically related to the Antarctic Peninsula. Cretaceous granites in the Antarctic Peninsula were emplaced over 10 Ma, with some emplaced over a much shorter time interval of <100,000 yrs (Riley et al., 2018). Relatively rapid exhumation can explain the relatively good agreement between the $^{40}Ar/^{39}Ar$ ages of iceberg-

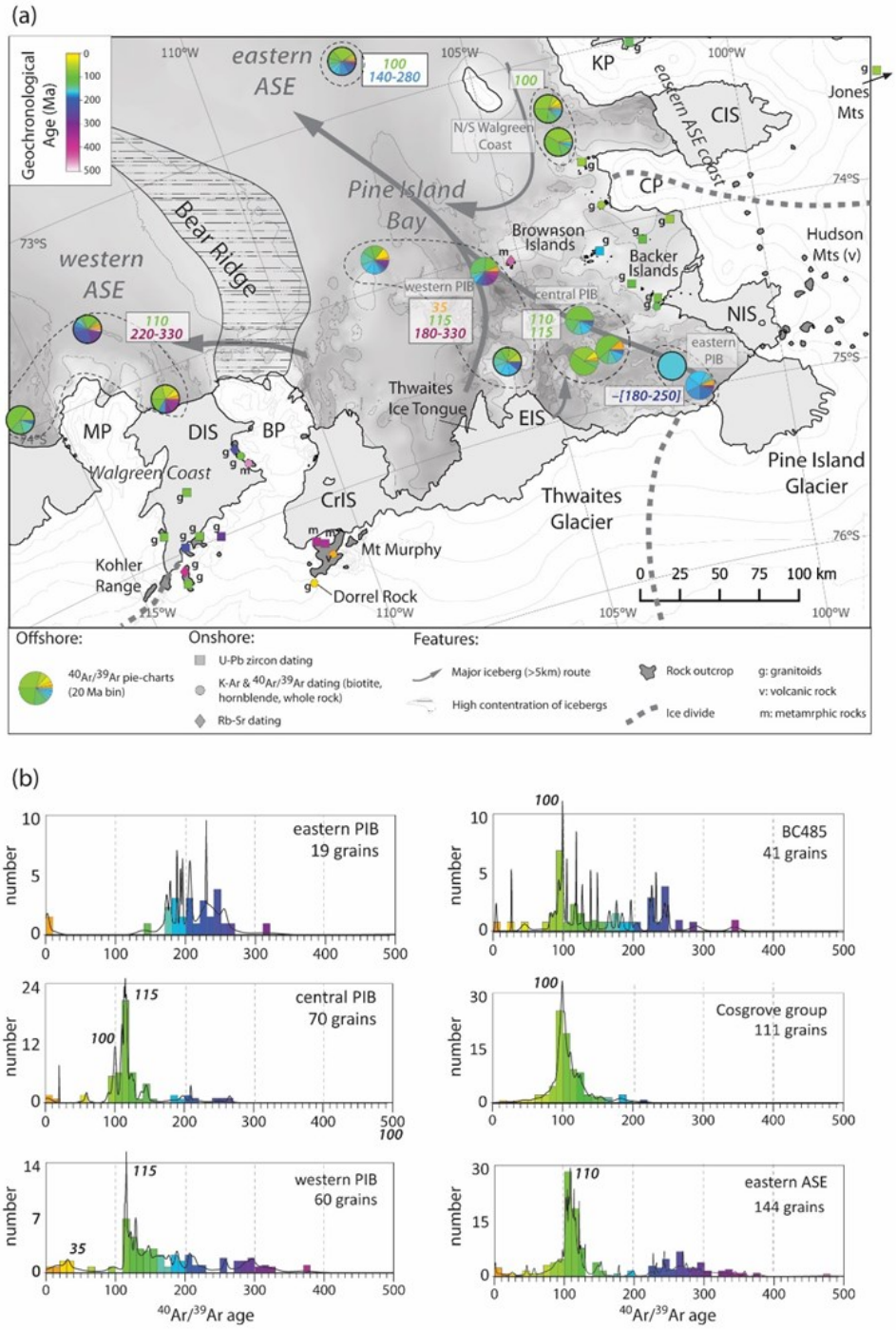

Figure 3.4. (a) Distribution of thermochronological $^{40}Ar/^{39}Ar$ dates on iceberg-rafted (>150μm) hornblende and biotite grains in seafloor surface sediments from the Amundsen Sea Embayment. Age populations are shown as pie-charts with a 20 Ma age bins. Transport pathways of large (>5km) icebergs recorded between 2006 and 2012 are taken from Kalén (2017). Areas of high iceberg concentrations are from Mazur et al. (2017). Black thin stippled lines outline the groupings of the core sites. Black circles around pie-charts highlight data previously published by Simões Pereira et al. (2018). Terrestrial geochronological data

(caption continues on next page)

Figure 3.4. (*continued*) are taken from Futa and LeMasurier, 1983; Pankhurst et al. (1993; 1998), Mukasa and Dalziel (2000), Wilch and McIntosh (2000), Kipf et al. (2012) (b) $^{40}Ar/^{39}Ar$ age histograms (10 Ma age bins) of IRD hornblende and biotite grains by geographical area. Colour coding is the same as in 'a'. Bathymetry is show in greyscale after Figure 3.1.

---

rafted hornblende and biotite grains (representing onshore outcrop cooling ages) and U-Pb zircon crystallization ages recorded onshore, despite the three systems having distinct closure temperatures of >900°C, ~550°C and 300°C.

The ~35 Ma $^{40}Ar/^{39}Ar$ age peak from western PIB is related to the Dorrel Rock gabbro intrusive complex cropping out in a single nunatak at Mt. Murphy at the western Walgreen Coast (Figure 3.4; Rocchi et al., 2006). Occurrence of these ages in IRD from western PIB coincides with the appearance of 280 – 330 Ma old grains, with these ages also being observed in onshore outcrops from the western Walgreen Coast (~283-353 Ma; e.g. Kipf et al., 2012) and in IRD from the western Amundsen Sea Embayment (Figure 3.4; Simões Pereira et al., 2018). Overall, we associate the <40 Ma ages, which are mainly observed in hornblende grains, to outcrops of Late Cenozoic alkali basalts or gabbroic rocks (similar to the Dorrel Rock gabbro). Airborne aeromagnetic investigations show two strong magnetic anomalies in the ice drainage basin of Thwaites Glacier (Bingham et al., 2012; Golynsky et al., 2018; Appendix Figure 3.3). In the Antarctic Peninsula similar anomalies have been related to outcrops of gabbro-tonalite-granodiorite (Vaughan et al., 1998). High geothermal flux (and basal melting) occurs near or above the magnetic anomalies in the Thwaites Glacier catchment (Schroeder et al., 2014) and suggests a relatively young age for the mafic rocks causing the anomalies, which according to their magnetic signature are most likely intrusions (pers. comm. F. Ferraccioli, 17/07/2018). A gabbro source would also explain the mineralogical composition of our IRD. Hornblende and biotite grains are generally depleted or too fine-grained in basalts to be detected in the coarse-grained (>150μm) hornblende and biotite record offshore (Cook et al., 2017; Simões Pereira et al., 2018). Gabbroic rocks, on the other hand, are coarse-grained and usually contain higher concentrations of hornblende compared to biotite (Pierce et al., 2014), explaining the higher number of hornblende grains <40 Ma old over biotite grains of the same age. Erosion of gabbro can, in addition to existing volcanic rocks which are known to sit below the Thwaites Glacier ice drainage (van Wyk de Vries et al., 2017) but which are not detected in our IRD signal, account for high magnetite and pyroxene contents combined with high feldspar contents in the western PIB sediments.

3.5.1.3. Bulk mineralogy and rock magnetic sediment provenance

Physical grain-size distribution in the bulk samples may exert a strong influence on bulk mineralogical and rock magnetic data (e.g. Brachfeld et al., 2003; Hillenbrand et al., 2010). For our samples, we found that comparing the bulk mineralogical and rock magnetic signatures of sediments containing less than 10% sand and gravel allows for a better provenance characterization (Figure 3.5). Bulk surface samples from western PIB have, for instance, higher pyroxene and fine-grained magnetite contents compared to eastern PIB samples, indicating erosion of mafic (i.e. pyroxene rich) bedrock below Thwaites Glacier. Likely mafic sources are volcanic rocks which crop out extensively in the ice drainage basin of Thwaites Glacier (van Wyk de Vries et al., 2017). Thwaites Glacier is also a major source for high-coercivity minerals such as goethite and/or hematite (Figure 3.5). These two antiferrimagnetic minerals are commonly found in soils and sedimentary rocks (Liu et al., 2012). In our study area, kaolinite contents correlate to some extent with HIRM (r^2=0.6), supporting the presence of pre-Oligocene sedimentary strata in the Thwaites Glacier catchment.

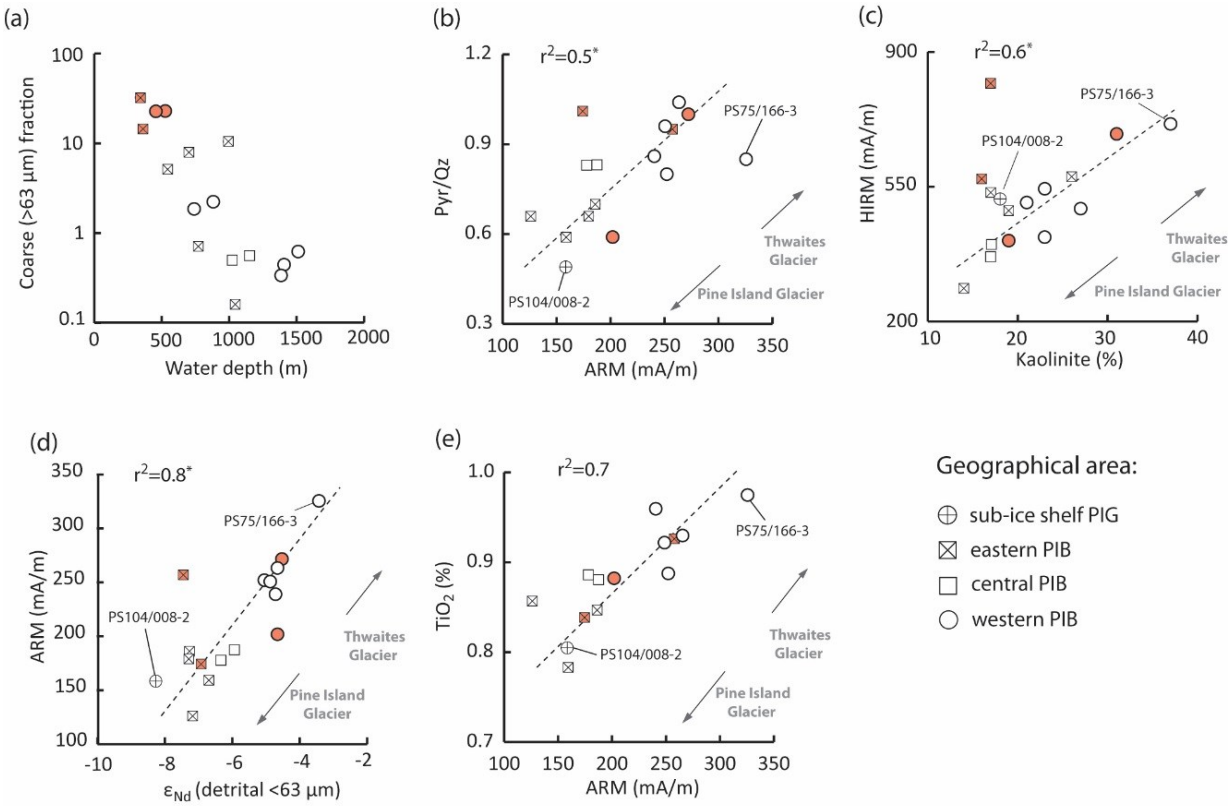

(caption on next page)

Figure 3.5. Relationships between rock magnetic, geochemical and mineralogical parameters of detrital seafloor surface sediments from the Central Pine Island Glacier (PIG) Ice Shelf and eastern, central and western Pine Island Bay (PIB), showing (a) percentage of coarse (>63μm) fraction of sediments vs water depth of core sites; (b) pyroxene/quartz (Px/Qtz) ratio in bulk sediment vs ARM (proxy for fine-grained magnetite content); (c) HIRM (proxy for goethite/hematite content) vs kaolinite content in clay fraction; (d) ARM (fine-grained magnetite content) vs ε_{Nd} value of fine fraction, and (e) ARM (fine-grained magnetite) vs TiO_2 content of fine fraction. Symbols assign samples to particular geographic groups on the shelf (Table 3.1). Red symbols highlight samples with >10 wt.% sand and gravel fraction, and deposited at water depths below 525 m (see text). (*) r^2 was calculated excluding the latter samples.

3.5.2. Comparison between provenance proxies

The Sr and Nd isotope fingerprint of detrital fine-grained (<63μm) surface sediments in PIB co-varies with clay (<2μm) mineral content, and hence suggests a similar sediment transport pathway for both size-fractions mainly originating from sources in the Pine Island Glacier and Thwaites Glacier catchments (Figure 3.6). This holds true for smaller grain sizes, too because fine-grained (SD) magnetite, which is is generally smaller than 1μm (Dekkers, 2001), shows a strong correlation with the Nd isotope signal (r^2=0.8; Figure 3.5) and clay mineral content (e.g. r^2=0.8 for illite). The main transport of the fine-grained detritus in PIB is by sediment-laden meltwater plumes originating either from the grounding line or melting of sediment-rich basal ice at the ice shelf base which is carried offshore by meltwater outflow (Jenkins et al., 2010; Nakayama et al., 2013; Witus et al., 2014; Naveira-Garabato et al., 2017; Kimura et al., 2017; Smith et al., 2017).

Low-coercivity minerals in the PIB sediments are composed of Ti-magnetite, as indicated by the correlation between the ARM signal and TiO_2 (Figure 3.5). Ti-magnetite is mainly supplied by Thwaites Glacier. This is in agreement with high concentrations of particulate iron in the water column just downstream of Thwaites Ice Tongue, which is an area generally riddled by a large number of drifting and grounded icebergs (Planquette et al., 2013; Stammerjohn et al., 2015). Melting and calving of icebergs from the Crosson Ice Shelf or the icebergs originating from further east (Mazur et al., 2017) are suggested as the main sources for the particulate iron in the water column (Planquette et al., 2013). We here suggest that

icebergs calved from Thwaites Glacier (Thwaites Ice Tongue and Eastern Ice Shelf) are the main source, given the high magnetic signal in the nearby core sites.

We observe consistent trends in the provenance signal between iceberg-rafted ($^{40}Ar/^{39}Ar$ ages of hornblende and biotite grains) and fine grained (ε_{Nd}, smectite/illite) detritus in the sediments from inner, central and western PIB (Figure 3.7). The peak spanning 110-170 Ma in the IRD age populations becomes more pronounced from inner towards western PIB while the peak spanning 170-270 Ma becomes less pronounced. This trend correlates with an increase of smectite/illite ratios and ε_{Nd} values from inner to western PIB. Moreover, grains >270 Ma grains are more abundant in western PIB compared to inner and central PIB. These

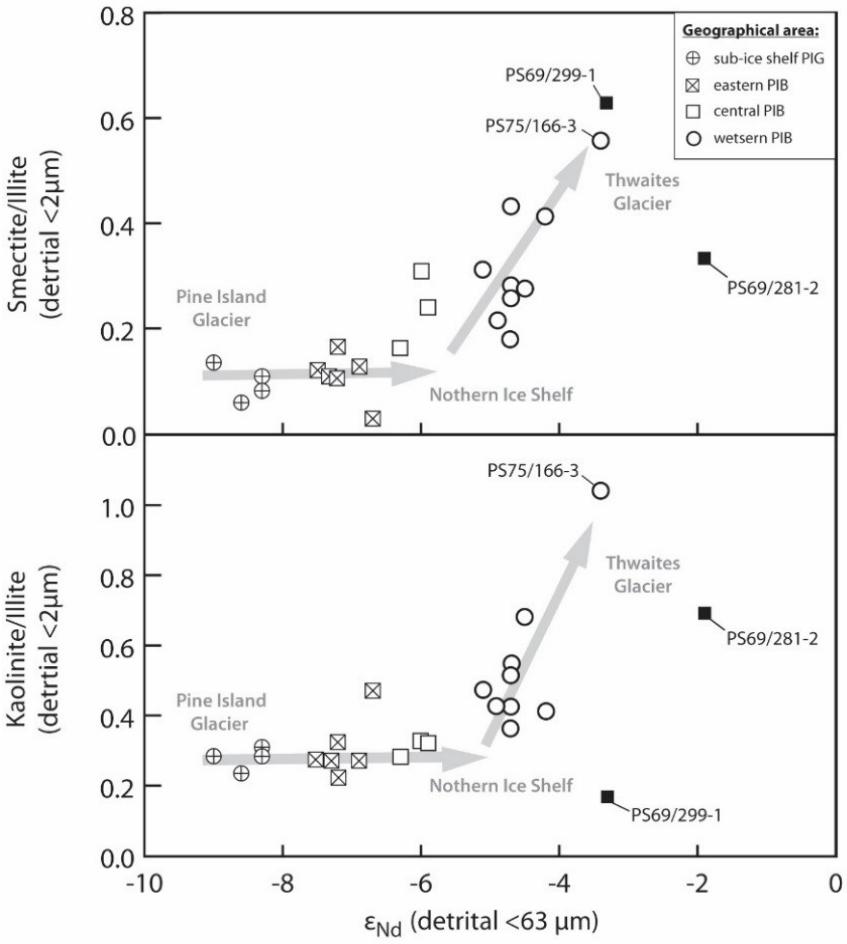

Figure 3.6. Neodymium isotope composition vs (a) smectite/illite and (B) kaolinite/illite ratios in detrital seafloor surface sediments from Pine Island Bay, West Antarctica. Symbols assign samples to particular geographic groups on the shelf (Table 3.1). Clay mineral ratios and ε_{Nd} values include data from Ehrmann et al. (2011) and Simões Pereira et al. (2018) (Table 2.2; cf. Chapter 2). Note: Clay mineral contents are relatively uniform in sub-ice shelf samples and samples eastern PIB (proximal to Pine Island Glacier) and change in a westerly direction towards a composition similar to that at site PS75/166-3 (proximal to Thwaites Glacier).

trends indicate a similar sediment delivery route for the fine-grained and iceberg-rafted detritus, with additional input from other sources along the transport pathway. Sediment mixing between the Pine Island and Thwaites glacier systems occurs mainly in western PIB, explaining the shift in $^{40}Ar/^{39}Ar$ age populations and fine-grained provenance signatures in an E-W direction eastern PIB. This trend is not observed at core sites located further to the north (i.e. BC485, PS69/299-1), indicating a more complex mixture of sediment including additional supply from sources along the eastern Amundsen Sea Embayment coast (Figs. 3.4, 3.7).

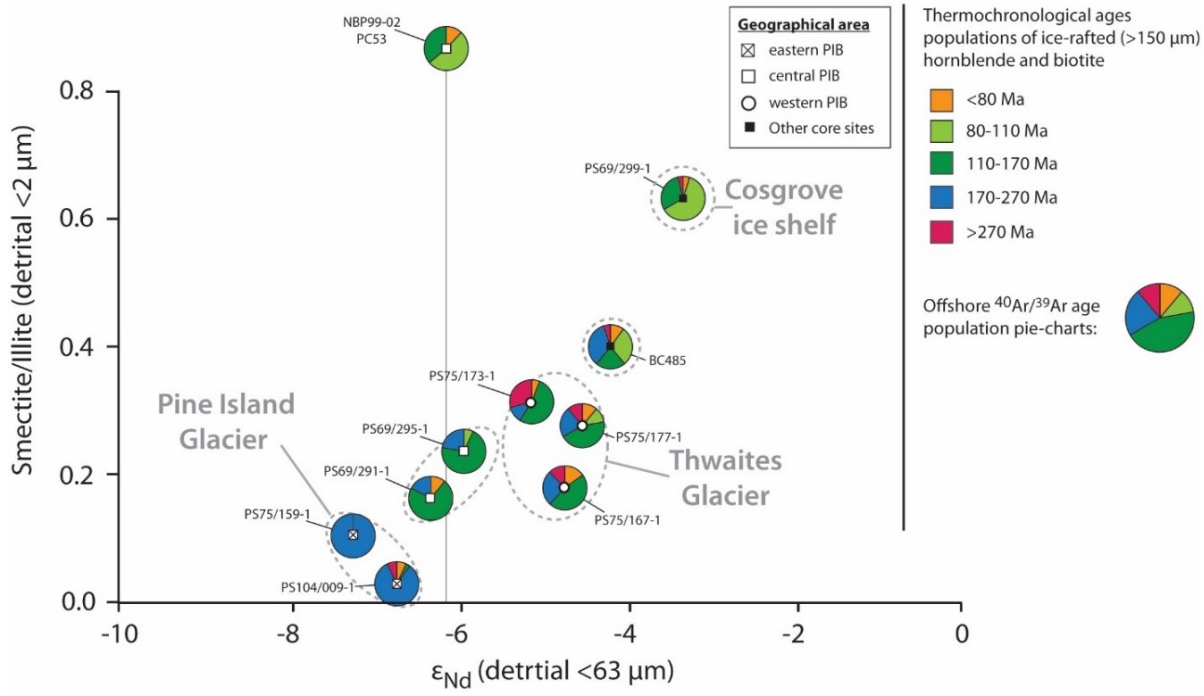

Figure 3.7. Neodymium isotope composition vs (a) smectite/illite and (B) kaolinite/illite ratios in detrital seafloor surface sediments from Pine Island Bay, West Antarctica. Symbols assign samples to particular geographic groups on the shelf (Table 3.1). Clay mineral ratios and ε_{Nd} values include data from Ehrmann et al. (2011) and Simões Pereira et al. (2018) (Table 2.2, cf. Chapter 2). Note: Clay mineral contents are relatively uniform in sub-ice shelf samples and samples eastern PIB (proximal to Pine Island Glacier) and change in a westerly direction towards a composition similar to that at site PS75/166-3 (proximal to Thwaites Glacier).

3.5.3. Limited distribution of IRD supplied by Pine Island Glacier and Thwaites Glacier across the Amundsen Sea shelf?

The central Pine Island ice shelf extended further seaward during and prior to the 21st century (Kellogg and Kellogg, 1987; Rignot, 2002; Steig et al., 2012), covering site PS104/008-2 until 2015 (Jeong et al., 2016; Arndt et al., 2018). Therefore, IRD at the surface of core PS104/008-2 was likely delivered by melt out of debris from the base of the ice shelf. The IRD provenance signal of PIG (170-270 Ma old hornblende and biotite grains) is less pronounced in western PIB (less than 22%; Figure 3.7) and becomes overprinted by 115 Ma and ~280-350 Ma old grains originating from Thwaites Glacier. Core site BC485 is located north of western PIB and in the mid-shelf section of Pine Island Trough (Figure 3.4). The $^{40}Ar/^{39}Ar$ age population of IRD from site BC485 is characterised by a dominant peak at ~100 Ma with only a very minor peak at ~118 Ma (Simões Pereira et al., 2018), requiring an additional (and major) source other than Pine Island and Thwaites Glaciers. The ~100 Ma age peak is likely sourced from the eastern coast of the Amundsen Sea Embayment which can be inferred from the $^{40}Ar/^{39}Ar$ ages of iceberg-rafted hornblende and biotite grains deposited at sites PS69/299-1 and DF85 96-1 offshore from the Cosgrove Ice Shelf (Figure 3.5; Simões Pereira et al., 2018). As for sea-ice flows, the westward iceberg drift from the eastern Amundsen Sea Embayment coast is caused by the prevailing easterly winds over the shelf (e.g. Assmann et al.; 2005; Stammerjohn et al., 2015; Mazur et al., 2017). Westward drift of deep-keeled icebergs originating from eastern PIB is temporarily halted at Bear Ridge (Stammerjohn et al., 2015;Mazur et al., 2017), which is a prominent shallow bathymetric feature extending from Bear Peninsula northwards to ~72.5 °S (Nitsche et al., 2007; Gohl et al., 2013; Figure 3.4). Kalén (2017) tracked the drift of icebergs with an average size of 20 km2 and estimated keel depths between 200 and 400m in the Amundsen Sea Embayment between 2006 and 2012. The author found that icebergs calved from PIG seemed to be driven by NW-directed currents following the bathymetric contours of the eastern Bear Ridge flank to at least 73°S before being deflected westwards, while icebergs calved from the large iceberg B-22 (which had calved from the Thwaites Ice Tongue in 2002, e.g. Stammerjohn et al., 2015; St-Laurent et al., 2017) drifted directly westwards with the Antarctic Coastal Current across Bear Ridge. During the time interval analysed by Kalén (2017) iceberg B-22 was grounded north of the Thwaites Ice Tongue, with a large fast ice tongue attached that extended northwards from B-22 (Stammerjohn et al., 2015). These huge ice mass probably had a strong impact on the drift of

icebergs calved from PIG. Therefore, it is unclear whether the tracks of icebergs calved from PIG reported by Kalén (2017) are representative for the long-term record.

Our data suggest that IRD sourced from Pine Island and Thwaites Glaciers is not carried over long distances in the Amundsen Sea Embayment. This is shown by a muted PIG provenance signal in IRD from central and western PIB, and a muted Thwaites Glacier provenance signal in IRD from site BC485 and at other middle and outer shelf sites in the Amundsen Sea Embayment (Simões Pereira et al., 2018). In general, Antarctic ice shelves produce large tabular icebergs, which tend to carry only minor quantities of IRD because most of the basal debris melts out at the grounding line, where the base of the ice gets into contact with relatively warm ocean water (e.g. Anderson, 1999; Williams et al., 2010). We suggest that the eastern Amundsen Sea coast (including Thurston Island) is a more important source for offshore IRD than PIG and Thwaites Glacier because it is topographically more elevated compared to the downstream sections of PIG and Thwaites Glacier. This coastline also has more outcrops (Burton-Johnson et al., 2016), so that glaciers draining this area are likely to carry more englacial and supraglacial detritus. In addition, the glaciers draining the eastern Amundsen Sea coastline are either tidewater glaciers without ice shelves or feed into thin ice shelves, such as the Abbot Ice Shelf and the Cosgrove Ice Shelf. Icebergs calved from tide water glaciers carry more basal debris than icebergs calved from ice shelves (e.g. Powell et al., 1984), while the Abbot and Cosgrove ice shelves are too thin to be affected by melting caused by upwelling Circumpolar Deep Water (e.g. Pritchard et al., 2012; Shepherd et al., 2018). The latter will also apply to icebergs released by these ice shelves into the Amundsen Sea, which is in agreement with the observation that small sized icebergs are common along this coastline (Mazur et al., 2016), and that these icebergs are more easily transported westward by the Antarctic Coastal Current, i.e. also across Bear Ridge. Thus, icebergs calved from the eastern Amundsen Sea coastline probably still retain some basal debris in addition to supra- and englacial debris. In contrast, deep-keeled and IRD-poor icebergs calved from the central Pine Island Glacier Ice Shelf, Thwaites Ice Tongue and the Eastern Thwaites Ice Shelf can drift westwards only until they run aground on Bear Ridge (Stammerjohn et al. 2015; Mazur et al., 2016) or shallows north of Thwaites Glacier, where large icebergs repeatedly ground (Ferrigno et al., 1993; St-Laurent et al., 2017). Only after their draft has decreased sufficiently by further oceanic melting at their bases, which will lead to melt out of most remaining basal debris, they will be able to drift further westwards. Further investigations on the age distribution on IRD deposited on the Amundsen Sea shelf will provide more insights into the importance of the

topography of the glacier catchment and the configuration of the ice margin for controlling the offshore IRD supply.

3.5.4. Summary of provenance of detritus supplied by Pine Island Glacier and Thwaites Glacier

Our data clearly show that glaciogenic detritus delivered by Pine Island Glacier and Thwaites Glacier can be distinguished based on the isotopic, geochemical, clay and bulk mineralogical and rock magnetic signatures of surface sediments deposited proximal to the ice front or below the ice shelf (Figure 3.8). The PIG signature in particular can be assigned with a high degree of confidence since we analysed sediments recovered below its ice shelf. Glaciomarine sediments shed by PIG have low ε_{Nd} values (~-9), high $^{87}Sr/^{86}Sr$ ratios (~0.728) as well as low smectite (~5%) and low kaolinite (~18%) contents when compared to detritus delivered by Thwaites Glacier. PIG further supplies less fine grained (SD) magnetite (ARM ~160 mA/m) compared to Thwaites Glacier, and delivers less pyroxene and feldspar offshore. Furthermore, the $^{40}Ar/^{39}Ar$ ages of ice-rafted hornblende and biotite grains sourced from PIG fall within the 170-270 Ma age interval, with the most striking characteristic being the absence of mid-Cretaceous ages. The subglacial bed below PIG is likely composed of evolved granites and/or Jurassic to Early Palaeozoic granites, as well as infills of sedimentary strata originating from erosion of these bedrock sources.

The provenance fingerprint of Thwaites Glacier shows a signal rather different from that of PIG. It supplies detritus that has higher ε_{Nd} values (~-4) and lower $^{87}Sr/^{86}Sr$ ratios (0.714). The substrate under its ice drainage basin is a major source for both smectite (~20%) and kaolinite (~37%), more fine grained (SD) magnetite (ARM ~326 mA/m) and goethite and/or hematite (HIRM >700 mA/m), and has generally a mafic signature (high pyroxene). Ice-rafted hornblende and biotite grains are characterized by a major $^{40}Ar/^{39}Ar$ age peak at ~115 Ma and a minor peak at ~35 Ma, as well as a broad age spectrum spanning from 110 to 330 Ma. Kaolinite indicates presence of pre-Oligocene sedimentary strata, possibly located in the Bentley Subglacial Trench and/or Byrd Subglacial Basin (Hillenbrand et al., 2003; Ehrmann et al., 2011). Relatively high contents of smectite as well as fine-grained (SD) magnetite support the presence of mafic rocks, while the IRD signal indicates hornblende and biotite bearing granitoids (e.g. granites, granodiorites, tonalites) of Cretaceous to Palaeozoic ages. Onshore and offshore data show presence of gabbros of ~35 Ma (i.e. Dorrel Rock type),

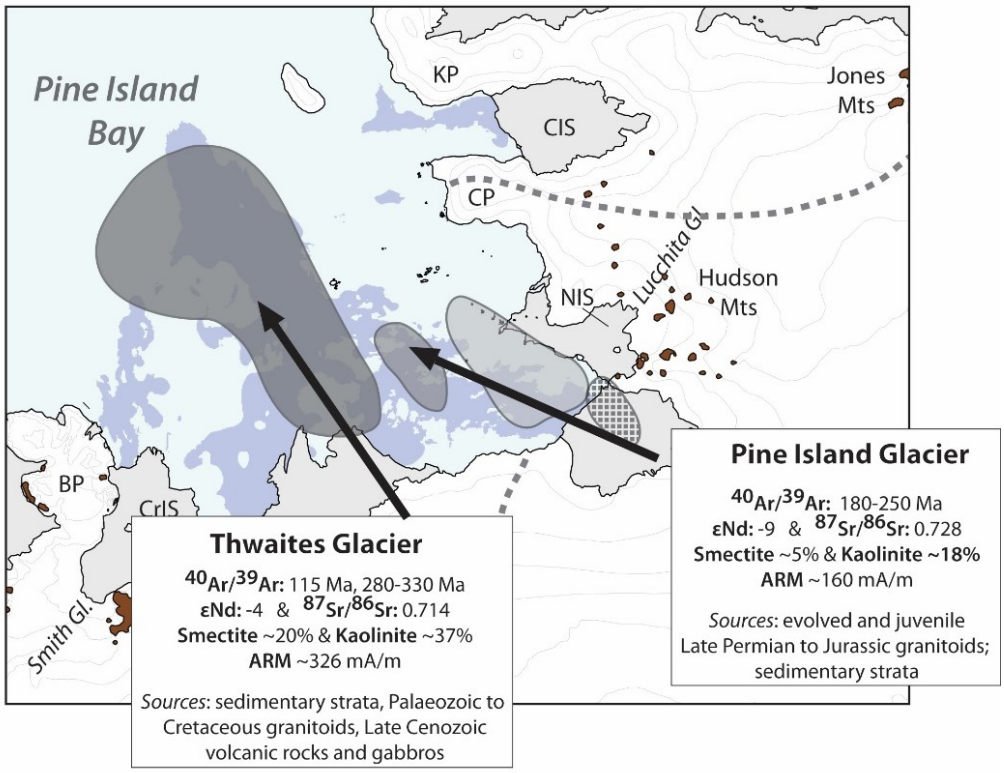

Summary of offshore distinctive provenance fingerprints:

	eastern PIB	central PIB	western PIB	sub-ice shelf PIG
$^{40}Ar/^{39}Ar$ (Ma)	~35, 110 to 330	90 to 270	170 to 270	*no data*
εNd	-5.0 to -2.3	-6.3 to -5.9	-8.2 to -6.9	-9.1 to -8.3
$^{87}Sr/^{86}Sr$	0.712 to 0.717	0.717 to 0.719	0.718 to 0.724	0.726 to 0.730
Smectite (%)	9 to 20 %	10 to 16 %	2 to 10 %	4 to 8 %
Kaolinite (%)	19 to 37 %	17 %	14 to 26 %	14 to 18 %
ARM (mA/m)	200 to 330	180 to 190	120 to 190	*no data*

Figure 3.8. Summary figure of main provenance characteristics, showing major 40Ar/39Ar age peaks of combined ice-rafted hornblende and biotite grains, Sr and Nd isotopic compositions of the fine fraction, selected clay mineral assemblages and anhysteretic remanent magnetization (ARM) of detrital seafloor surface sediments from the Central Pine Island Glacier (PIB) Ice Shelf and eastern, central and western Pine Island Bay (PIB). The different fields in grey show the various geographical group as discussed in text. Also shown are major terrestrial sources for the detrital sediments (see text for further details).

---

although we further suggest that younger gabbros form the basement based on previously observed aeromagnetic anomalies (Bingham et al., 2012; Golynsky et al., 2018), as well as a mineralogical bias towards hornblende grains with young ages, which largely absent in the biotite record. Our conclusion of the presence of both bedrock and sedimentary substrate at the

bed of the Thwaites drainage basin is in agreement with the interpretation of airborne radar data (Schroeder et al., 2014).

Overall, the signature of sediments in central PIB fall between the PIG and Thwaites Glacier signatures in western PIB, as observed, for instance, in the Sr and Nd isotope ratios (Figure 3.2). This indicates that a mixture of glaciomarine sediments delivered from both sources is deposited there. Whether all sediment samples in western PIB represent a pure Thwaites Glacier source, depends on the end-member assignment for Thwaites Glacier detritus. For instance, core sites PS75/166-3 and PS75/167-1 are both located proximal to the Thwaites Glacier front, but record ε_{Nd} values of -3.4 and -4.5 respectively. The average ε_{Nd} signature of sediments from western PIB is ~-4.2. Both sites, however, are located in different bathymetric settings: While site PS75/166-3 is located in a narrow, deep basin just in front of the eastern tip of Thwaites Ice Tongue that may extend southwards under the ice tongue, site PS75/167-1 is located on a bedrock high (Figure 3.1; for a detailed bathymetry map see Figure 6 in Larter et al. 2014, and Figure 1 in Kuhn et al., 2017). The basin, from which core PS75/166-3 was recovered, is considered as part of a drainage network for subglacial meltwater which was active during the last glacial period (Kuhn et al., 2017). Given that a similar subglacial network probably exists under Thwaites Glacier today (Schroeder et al., 2013; Smith et al., 2017), we speculate that the basin may be influenced by the deposition meltwater plumites originating from subglacial meltwater spilled out at the Thwaites Glacier grounding line. Such meltwater carries with it an average signature of all eroded substrate below the ice catchment (Licht and Hemming, 2017). Hence, we believe that the provenance of the sediments at site PS75/166-3 is more representative of glaciogenic detritus supplied by Thwaites Glacier than sediments at site PS75/168-1. Implication for this is that the provenance signal of Pine Island Glacier can still be traced in fine-grained sediments from western PIB.

3.6. Provenance of subglacial and deglacial-transitional sediments in Pine Island Bay: Implications for higher erosion rates by minor ice streams?

Subglacial and deglacial sediments at site PS104/012-2 near the Northern Ice Shelf in eastern PIB show significant contributions from younger mafic rocks, with the most proximal source being the Hudson Mountains (i.e. elevated ε_{Nd}, smectite contents, MgO and V/Hf, and lower $^{87}Sr/^{86}Sr$)(Figure 3.9). During the LGM, the ice sheet in this region was >150 m thicker

than today (Johnson et al., 2014), and on the inner shelf of the eastern Amundsen Sea Embayment Pine Island Glacier merged with Thwaites Glacier, Haynes Glacier, Pope Glacier and Smith Glacier, forming a huge palaeo-ice stream that advanced through Pine Island Trough seawards to the shelf break (e.g. Larter et al., 2014, and references therein). Our provenance data for the subglacial and deglacial sediments at site PS104/012-2 indicate that during the time of their deposition glaciers draining through the Hudson Mountains fed into the Pine Island Glacier tributary and were not blocked by an extended grounded Pine Island Glacier or an extended Central PIG Ice Shelf. Our finding is consistent with the recent reconstruction of palaeo-ice flow directions in the vicinity of site PS104/012-2 based on seafloor geomorphology (Figure 2a in Arndt et al., 2018). The LGM ice-sheet thickening in the region (Johnson et al., 2014) implied more ice coverage of the outcropping volcanic edifices on the Hudson Mountains, but would have only marginally increased the area of subglacially eroded volcanic rocks, making it an unlikely cause for the change in provenance recorded in core PS104/012-2. Additionally, ice sheet models render it unlikely that the positions of ice divides around the Hudson Mountains changed considerably between the LGM and today (e.g. Pollard and DeConto, 2009, 2012; Golledge et al., 2013; Pollard et al., 2016). We here suggest that changes in the subglacial erosive regime below Lucchitta Glacier and other glaciers draining the Hudson Mountains since the LGM, possibly after the last major retreat of the local grounding line, are the most likely reason for the observed provenance changes. Modern ice flow through the Hudson Mountain is relatively slow (Rignot et al., 2011, 2014), and probably cold-based with low basal melting rates in the upstream sections of the glaciers (Joughin et al., 2009; Pattyn, 2010). During the LGM and the last deglaciation, however, basal temperatures of the entire WAIS may have been close to or at the pressure-melting point (Golledge et al., 2013), possibly enhancing erosion of volcanic rocks located to the east of today's Northern Ice Shelf.

The prominent downcore provenance change in core PS104/012-2 contrast with minor or absent downcore provenance changes in both the cores from below the Central PIG Ice Shelf and the marine cores PS104/009-1, PS69/295-1 and NBP99-02 PC51 (Figure 3.9). The absence of significant changes in their provenance indicates similar sourced detritus has been carried to these sites since the LGM or since the onset of glacial retreat. Based on geomorphological features (i.e. mega-scale glacial lineation, meltwater channels), detrital material transport to these sites at the LGM was sourced from PIG (Nitsche et al., 2013; Larter et al., 2014; Graham et al., 2016; Kuhn et al., 2017). Most of the modern PIG is warm-based (Pattyn, 2010), hence erosion is likely to occur over its entire ice drainage basin (Licht and Hemming, 2017) now and possibly during the LGM (Golledge et al., 2013). A slightly higher smectite supply to

central and western PIB, when ice was grounded at or located proximal to these sites, suggests that more glaciogenic detritus sourced from an extended Thwaites Glacier was deposited here together with material supplied by PIG.

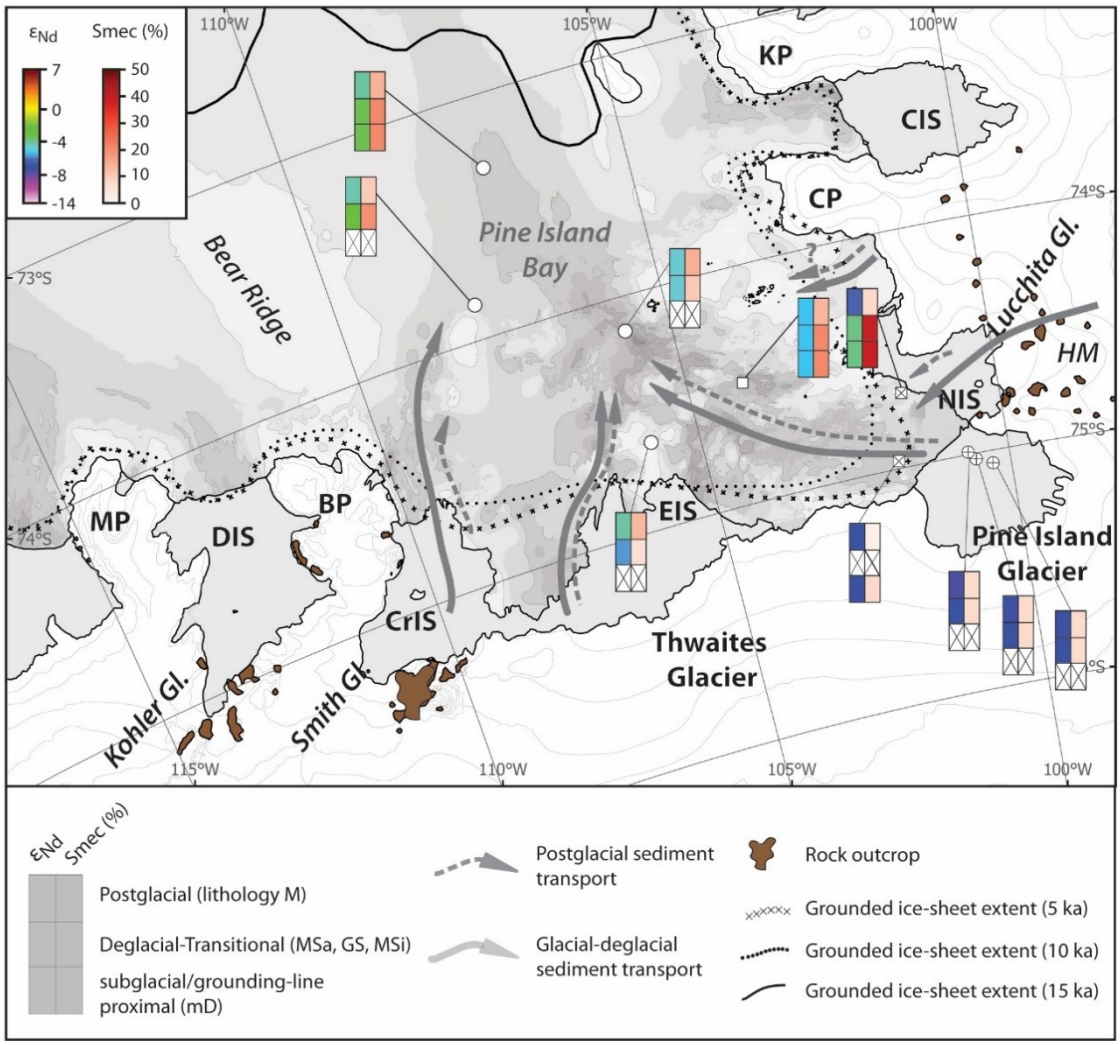

Figure 3.9. Summary map of neodymium isotopic composition of fine-fraction (<63μm) and smectite contents of the clay fraction of sedimentary sequences deposited on Pine Island Bay (PIB). Depositional environment is taken from Figure 3.3. Stippled arrows show major delivery route of postglacial (Late Holocene to modern) sediments to the PIB, while filled arrow indicate major delivery for glacial-deglacial (Last Glacial Maximum to pre-Late Holocene) sediments to the PIB. Size of the arrows are only indicative to represent a change in the delivery flux between glacial/deglacial and postglacial sediments. Grounded ice-sheet extent is from The RAISED Consortium et al. (2014). Bathymetry is shown in greyscale after Figure 3.1.

Provenance of fine-grained detritus in deglacial sediments of cores PS75/167-1 and PS173-1 from the eastern and southeastern part of the PIB group indicates higher input from PIG. This was either caused by an advanced grounding line position of this ice stream, which is evident from palaeo-ice flow directions archived in the geomorphological record of the seabed (Nitsche et al., 2013; Larter et al., 2014; Graham et al., 2016), or, less likely, a more westward position of the ice divide between PIG and Thwaites Glacier during the last deglaciation. This observation contrasts with the provenance in the subglacial and deglacial sediments from sites PS104/021-1 and PS75/177-1 from the northern and northwestern part of the western PIB group. There, higher smectite contents are not paired with higher ferromagnesian compositions, as observed in core PS104/012-2. Given the higher ε_{Nd} and lower $^{87}Sr/^{86}Sr$ values in these sediments, supply of glacial detritus by Thwaites Glacier and/or Haynes Glacier and/or glaciers draining into the Crosson Ice Shelf (i.e. Smith and Pope Glaciers) may have been more important during the LGM than today. Similar to ice draining through the Hudson Mountains, the basal thermal state of these glaciers may have played a role in changing the erosion rate at the ice base (Hallet et al., 1996; Staiger et al., 2006). Cosmogenic exposure ages obtained from the vicinity of Pope Glacier have shown that the LGM ice sheet there was up to >330 m thicker than today (Johnson et al., 2008).

In summary, we observe significant past changes in the sediment supply by minor ice drainage systems (i.e. glaciers draining into the Northern Ice Shelf and the Crosson Ice Shelf) that suggest changes in their basal thermal state from warm-based (thicker ice) to cold-based (thin ice) since the LGM. However, isotopic compositions of sedimentary sequences deposited in the flowline of the Pine Island and Thwaites Glaciers since the LGM remain very similar. This finding shows that the provenance of glaciogenic detritus delivered by these two ice drainage basins did not vary over an entire glacial to interglacial cycle (at least since the LGM) and hence further endorses the use of their (modern) detrital fingerprint to trace the sediment supply by these two glaciers in the past. On the contrary, absence of the (modern) detrital signature of the Pine Island and/or Thwaites Glacier in downcore sediments can be indicative of either a shift the thermal state, or related to a reduction of sediment supply from their ice drainage basins (i.e. significant grounding line retreat, “ungrounding” of their base). Although our results are limited by the lack of precise chronological constrains, comparing changes in the provenance fingerprint between subglacial, transitional and post-glacial sediments provides a first insight into temporal changes in the source areas during glacial and deglacial times and allows for reconstructing related changes in ice sheet flow and basal ice conditions.

3.7. Conclusions

This chapter provided the first multi-proxy provenance study on seafloor surface sediments from Pine Island Bay in order to detect the fingerprints of Pine Island Glacier and Thwaites Glacier. We further investigated subglacial and deglacial-transitional sediments in order to characterize past changes in provenance related to changes in WAIS dynamics. Our results allow to draw the following conclusions:

1) Glaciogenic detritus supplied by Pine Island Glacier is characterized by low ε_{Nd} values (~-9), high $^{87}Sr/^{86}Sr$ ratios (~0.728), low smectite contents (<10%) and coarse hornblende and biotite grains derived from Late Permian to Jurassic (170-270 Ma) intrusive rocks. Sediments shed by this glacier can be clearly distinguished from sediments shed by other glaciers draining the Amundsen Sea sector of the WAIS.

2) Glaciogenic detritus delivered by Thwaites Glacier has a rather different provenance signature, with high ε_{Nd} values (~3.4), low $^{87}Sr/^{86}Sr$ ratios (0.714), high smectite (20%) and kaolinite contents (37%), coarse biotite and hornblende grains with $^{40}Ar/^{39}Ar$ cooling ages of <40 Ma and 110 to 330 Ma (peak at 115 Ma) and high contents of fine-grained magnetite and goethite. Overall, we infer a much more varied geology under Thwaites Glacier than under Pine Island Glacier, with a bed consisting of sedimentarystrata, Cretaceous-Carboniferous granitoids and Cenozoic volcanic rocks and gabbros.

3) Our data show that at present IRD sourced from Pine Island Glacier is not transported over long distances across the continental shelf of the Amundsen Sea Embayment. The IRD signal is relatively muted in sediments from central and western PIB, while the IRD signal of Thwaites Glacier becomes muted at core sites located further offshore. Smaller, debris-laden icebergs sourced from the eastern coast of the Amundsen Sea Embayment may overprint the IRD signal of Pine Island Glacier and Thwaites Glacier.

4) Most of the subglacial and deglacial-transitional sediments analysed in this study do not show a provenance signature significantly different from that of modern sediments at the same site. The largest provenance change, however, occurred in cores offshore from the Northern Ice Shelf and the Crosson Ice Shelf. We suggest that the glaciers supplying detritus to these core sites changed from warm-based (thicker ice) to cold-based (thinner ice)since the LGM, which caused a decrease in erosion of volcanic rocks in the catchments of the corresponding glaciers.

Statement of Contribution

The work presented here was part of a collaborative effort to which the author, Tina van de Flierdt (Imperial College, UK), Claus-Dieter Hillenbrand (BAS, UK) and Thomas Frederichs (University of Bremen, Germany) contributed to the initial idea. Claus-Dieter Hillenbrand, James Smith (BAS, UK) and Gerhard Kuhn (AWI, Germany) supplied the sample material. Thomas Frederichs conducted all rock magnetic investigation on the samples. Gerhard Kuhn and Werner Ehrmann (University of Leipzig, Germany) provided support in the bulk and clay mineral investigation on the samples. Sidney R. Hemming (L-DEO, Columbia University, US) conducted the $^{40}Ar/^{39}Ar$ measurements on hornblende and biotite minerals. Sam J. Hammond (Open University, UK) provided support with the major and trace element analysis. Stefanie Brachfeld (Montclair State University, US) and Cathleen Doherty (Rutgers University, US) provided some of the $^{40}Ar/^{39}Ar$ hornblende and biotite, and neodymium isotope data.

Chapter 4

The provenance fingerprint of Late Pleistocene sediments in the Amundsen Sea, West Antarctica: Implications for eccentricity-paced sediment supply and West Antarctic Ice Sheet stability

Chapter Summary

This chapter presents the results and discussion of the first geochemical downcore study of detrital sediment provenance undertaken on the West Antarctic margin in the Amundsen Sea for the late Pleistocene. Strontium (Sr) and neodymium (Nd) isotopic fingerprints of fine-grained (<63μm) detrital sediments and $^{40}Ar/^{39}Ar$ ages of iceberg-rafted hornblende and biotite grains were obtained for two continuous sediment cores (i.e. PS58/254 and PC493). I here focus on the records obtained between 1.1 Ma and 0.2 Ma, while Chapter 5 addresses the results and discussion of the remaining section (0.2 Ma to 0.0 Ma).

Records of sea-level highstands and ice-sheet model results suggest that the West Antarctic Ice Sheet (WAIS) significantly retreated from its present ice margin during previous Pleistocene interglacials, but direct marine geological evidence for such a retreat has remained elusive to this date. Our working hypothesis is that a significant destabilization of this ice sheet would have caused erosion in and sediment supply from distinct geological source regions to our sites by shifting the location of subglacial erosion further inland, which ultimately should be recorded in offshore marine records proximal to the ice sheet.

The Sr and Nd isotope-derived provenance of fine-grained (<63μm) detrital sediments at sites PS58/254 sand PC493 overlaps with the fingerprint of modern sediments deposited on the eastern and western Amundsen Sea shelf, respectively, revealing proximal sources for the sediments transported offshore from the shelf to the continental slope and rise. The sedimentary record from Site PS58/254 shows pronounced Sr isotopic variations between glacials and interglacials that largely reflect eccentricity oscillations over the last 1.1 Ma. Eccentricity-forcing is also observed, although less pronounced, in the Nd isotope record. In contrast, Sr and Nd isotope data from core PC493 do not show clear glacial-interglacial variability, possibly reflecting uniform geological units eroded in the direct hinterland of this site.

$^{40}Ar/^{39}Ar$ ages of iceberg-rafted grains show that a source from the eastern Amundsen Sea coast prevailed at both sites during glacial and interglacial stages, documented by abundant hornblende and biotite ages from 80 to ~300 Ma. Younger (<80 Ma) grains are predominantly found in interglacial samples from site PS58/254, recording an additional source supplied by icebergs calved from the Wrigley Gulf-Hobbs Coast and/or Sulzberger Bay, and transported to our site by the Antarctic Circumpolar Current. No glacial-interglacial variability in ice-rafted sediment provenance was recorded at site PC493.

Overall, our new fine-grained and ice-rafted sediment late Pleistocene provenance data do lack evidence for significant retreat of the WAIS. While uniform sediment provenance

fingerprints could be interpreted to reflect an invariant hinterland geology, we here suggest that Pine Island and Thwaites Glacier signatures are distinct enough to leave a geochemical fingerprint, should they retreat. Our data hence is in support for a stable WAIS during the Late Pleistocene, with ice retreating no further towards the interior of the continent compared to the modern ice margin.

4.1. Introduction

The WAIS contains enough ice to raise sea level by up to 4.3 meters, if completely melted (Fretwell et al., 2013). This "marine-based" ice sheet is inherent unstable because large parts of its base are grounded well below sea-level on bedrock that deepens towards the interior of the continent, so that any initial ice retreat may result in a positive feedback that leads to further thinning and retreat (Weertman et al., 1974; Mercer, 1978; Hughes, 1981; Schoof, 2007). Modern mass gain of the WAIS by accumulation of snow and ice is mainly balanced by iceberg calving and melting at the base of floating ice shelves and ice tongues fringing the ice sheet, with the latter process being controlled today by inflow of warm Circumpolar Deep Water (CDW) onto the continental shelf and into sub-ice shelf cavities (Thoma et al., 2008; Jenkins et al., 2010, 2016; Wåhlin et al., 2010, 2012, 2013; Jacobs et al., 2011; Dutrieux et al., 2014; The IMBIE Team, 2018). An observational study from the western Ross Sea as well as modelling studies have indicated a highly dynamic behaviour of the WAIS over the last few millions of years, with oscillations in synchrony with orbital forcing that may have resulted in its collapse at different times (Naish et al., 2009; DeConto et al., 2012; Pollard and DeConto, 2009, 2012; Pollard et al. 2015; DeConto and Pollard, 2016).

The Pleistocene epoch (2.5 Ma to 12 ka), was characterised by a number of 'super-interglacials' as well as a gradual shift in the Earth's climate between 1.2 and 0.6 Ma, the Mid Pleistocene transition (MPT; e.g. Rutherford and D'Hondt, 2000; Clark et al., 2006). While the latter may have been initiated by an abrupt increase in Antarctic ice volume (Rutherford and D'Hondt, 2000; Elderfield et al., 2012), full-scale ice collapse of the WAIS has been suggested for a number of interglacials. One of the most prominent super-interglacials is Marine Isotope Stage (MIS) 31 (1081-1062 kyr; MIS boundaries from Lisiecki and Raymo, 2005). MIS 31 period was subject to the highest high-latitude insolation values of the last 5 Ma (Laskar et al.,

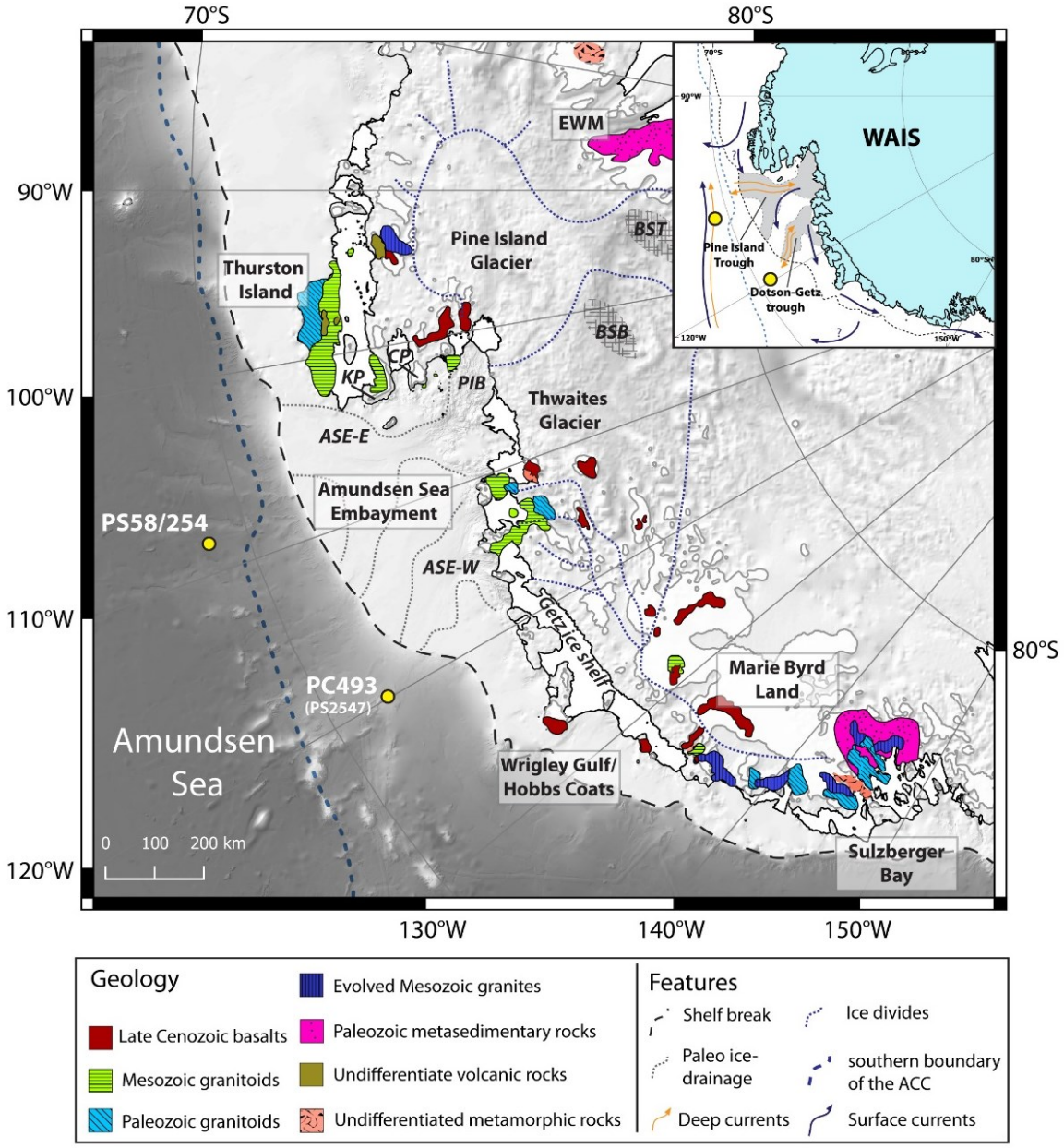

Figure 4.1. Simplified geological map of the study area, illustrating major geological units discussed in text (based on Simões Pereira et al., 2018; see Chapter 2 for further details). Also shown in map is the regional bathymetry and subglacial topography (Arndt et al., 2013). Onshore, blue dotted lines represent major ice divides of the West Antarctic Ice Sheet. Offshore, black dotted lines outline major bathymetric troughs which incise the continental shelf. Black dashed line represents the continent shelf break, while blue dashed line is the southern boundary of the Antarctic Circumpolar Current (ACC) (Orsi et al., 1995). Core sites studied in this chapter are marked as yellow circles. Inlet: Blue arrows represent major surface

(caption continues on next page)

Figure 4.1. (*continued*) currents (Gladstone et al., 2001; Assmann et al., 2005), while yellow/orange arrows denote deep (down to ~1000m water depth) currents (Holland et al., 2010; Assmann et al., 2013; Ha et al., 2014). Grey shading represent the two bathymetric troughs discussed in this chapter. Abbreviations: ASE-E: eastern Amundsen Sea Embayment, ASE-W: western Amundsen Sea Embayment, BSB: Byrd Subglacial Basin, BST: Bentley Subglacial Trench, CP: Canisteo Peninsula, EWM: Ellsworth-Whitmore Mountain, KP: King Peninsula, WAIS: West Antarctic Ice Sheet. PIB = Pine Island Bay.

2004), caused by a combination of high obliquity, eccentricity and precession that led to an exceptionally warm and long interglacial stage. A drill core retrieved during the Cape Roberts Project (CRP-1) in the western Ross Sea revealed 2-5°C elevated Antarctic sea surface temperatures during MIS 31 and changes in water mass stratification, in pace with orbital precession forcing, and significant reduction of Antarctic ice volume (Scherer et al., 2008).

Sedimentology, physical properties and clay mineral assemblages from marine sediment core PS58/254 from the Amundsen Sea (also investigated for this study) show a notable anomaly that occurred between MIS 15 (621-563 ka) and MIS 13 (533-478 ka), which may indicate a prolonged warm period that could have triggered substantial WAIS retreat or even collapse (Hillenbrand et al., 2009a). Evidence for a "warm" glacial MIS 14 is confirmed by the EPICA Dome C ice core in East Antarctica, which shows more elevated CO_2 levels and slightly warmer (+1°C) temperatures when compared to any other glacial period of the last 800 kyr (Siegenthaler et al., 2005; Jouzel et al., 2007). Further observations possibly supporting a significant WAIS retreat around MIS 15 to 13 come from sub-ice shelf drill core AND-1B (ANDRILL project) from the Ross Sea Embayment, where a high-sheared diatom-bearing mudstone layer marks a brief period of reduced ice-shelf extent or an open-marine setting (McKay et al., 2012). The age of this event is however not conclusive in the AND-1B core.

Another study that suggested a late Quaternary collapse of the WAIS was published by Scherer et al. (1998) based on <0.75 Myr old sediment samples recovered from beneath the interior of the WAIS (i.e. ice stream B discharging from the Siple Dome coast into the Ross Sea). Several subglacial sediment samples contained Quaternary marine diatoms with high levels of cosmogenic beryllium-10 (^{10}Be), interpreted to evidence an open-marine environment at this location. However, Burckle et al. (1997) showed that the reworked marine diatom frustules could have been deposited on top of the WAIS by wind, transferred down to the ice-

sheet base by internal ice flow in combination with basal melting, and finally incorporated in the subglacial sediment bed (cf. Kellogg and Kellogg, 1996). Hillenbrand et al. (2002, 2009a) subsequently argued that this mechanism may also explain the elevated 10Be concentrations of the sediments, as ^{10}Be is preferentially adhering to diatom frustules in the water column. Furthermore, a recently published study on the Ross Sea sector of the West Antarctic ice sheet by Kingslake et al. (2018) indicated that the WAIS grounding line may have retreated close to the sites studied by Scherer et al. (1998) at the beginning of the Holocene, implying only minor reduction in WAIS volume and size.

Moving closer towards present day, MIS 11 (374-424 ka) was a particularly long interglacial (see review in Past Interglacials Working Group of PAGES, 2016). Pronounced sea-level highstands in the Bermudas and Bahamas during the middle Pleistocene, as reconstructed from elevated deposits of marine sediments dated between 570 and 390 ka (uranium-series, amino-acid racemisation), were attributed to ~20 m of global sea-level rise that must have originated from collapses of the WAIS and Greenland Ice Sheet, and partial retreat of the East Antarctic Ice Sheet (EAIS) (Hearty et al., 1999; Kindler and Hearty, 2000). Since then, the exact highstand of these deposits has been corrected for glacio-isostasy (now ~10 m; Raymo and Mitrovica, 2012) and its origin from a mega-highstand of global sea level or a mega-tsunami was fiercely debated (McMurtry et al., 2007, 2008; Hearty and Olson, 2008). Moreover, Kindler et al. (2011) presented evidence that the Bahamas were tectonically not as stable as previously thought, with the last tilting event occurring at some time between 1.0 and 0.5 Ma. In the Southern Ocean, sedimentological and diatom investigations of marine sedimentary records lack evidence for a Pleistocene WAIS collapse during MIS 11 (Kunz-Pirrung et al., 2002; Hillenbrand et al., 2002).

In summary, various interglacials have been put forward as potential periods for a major WAIS collapse, but no conclusive evidence from the marine geological record exists so far. Recently published transient, three-dimensional climate simulations used to drive the Antarctic ice sheet model of DeConto and Pollard (2016) over the last eight glacial cycles also failed to reproduce a total WAIS collapse during this time span (Tigchelaar et al., 2018) questioning the role of large West Antarctic sea level contributions during the late Pleistocene. The case of "super-interglacial" MIS 5e will be further developed in the following chapter (Chapter 6).

We here take a different approach to search for a late Pleistocene collapse of the West Antarctic ice sheet using radiogenic isotope fingerprinting of detrital glacio-marine sediments to derive their provenance (see reviews in Hemming 2004; Licht and Hemming, 2017). In detail, we study two continuous Pleistocene marine sediment cores, collected from the

continental rise and slope site off the Amundsen Sea (Figure 4.1), in order to investigate Pleistocene WAIS dynamics. Glaciers along the Amundsen Sea coast drain ~20% of the WAIS, and currently show extensive ice thinning, negative mass balance and grounding line retreat (Pritchard et al., 2009; Shephard et al., 2012; Mouginot et al., 2014; Rignot et al., 2008, 2014; Gardner et al., 2018; The IMBIE Team 2018). The Amundsen Sea sector is further considered as the main "exit gateway" for icebergs during a potential WAIS collapse (e.g. MacAyeal et al., 1992), and offers a strategic location to investigate past WAIS dynamics. Strontium (Sr) and neodymium (Nd) isotope fingerprints of the <63μm fraction of detrital sediments, as well as $^{40}Ar/^{39}Ar$ dating on individual coarse-grained (>150μm) hornblende and biotite grains are used to reveal where the sediments, deposited over the past ~1.2 Ma, were eroded from. This information in turn is interpreted in the context of late Pleistocene WAIS dynamics. Although the full record is presented in this chapter, the last 200 kyrs (including MIS 5e; ~130 kyr) will be discussed in Chapter 5 only.

4.2. Study sites and sediment provenance background

Site PS58/254 is located on the western flank of a sediment drift on the continental rise in the eastern Amundsen Sea (69°19°S, 108°27°W, water depth 4014 m, Figure 4.1). The sediment record at this site is the composite of two cores recovered from the same site, piston core PS58/254-1 (recovery 18.31 m) and multi-core PS58/254-2 (recovery 0.42 m), which were both collected during RV Polarstern cruise ANT-XVIII/5a in 2001. In the following, core depths for this site are given as centimetre composite depth (cmcd). Sedimentological data (i.e. lithology, physical properties, proxies for biological productivity, grain size distribution, clay mineral provenance and palaeomagnetic properties) from this site were previously described and interpreted by Hillenbrand et al. (2009a). The lithology of the recovered sediments comprises diatom-bearing muds alternating with lithogenic muds (Appendix Figure 4.1). The age model for core PS58/254 was published in Hillenbrand et al. (2009a) (see Appendix Table 4.1). The boundary between the Brunhes and Matuyama chron (780 ka; based on Berggren et al., 1995) was identified at 1437-1447 cmcd, while the Jaramillo subchron (990-1070 ka) is located between 1717 and 1777 cmcd. Absence of calcareous foraminiferal tests in the most of the sediments prohibited the application of $\delta^{18}O$ stratigraphy. Sedimentary opal content and the barium (Ba)/aluminium (Al) ratio, which is an indicator for the content of biogenic Ba, can

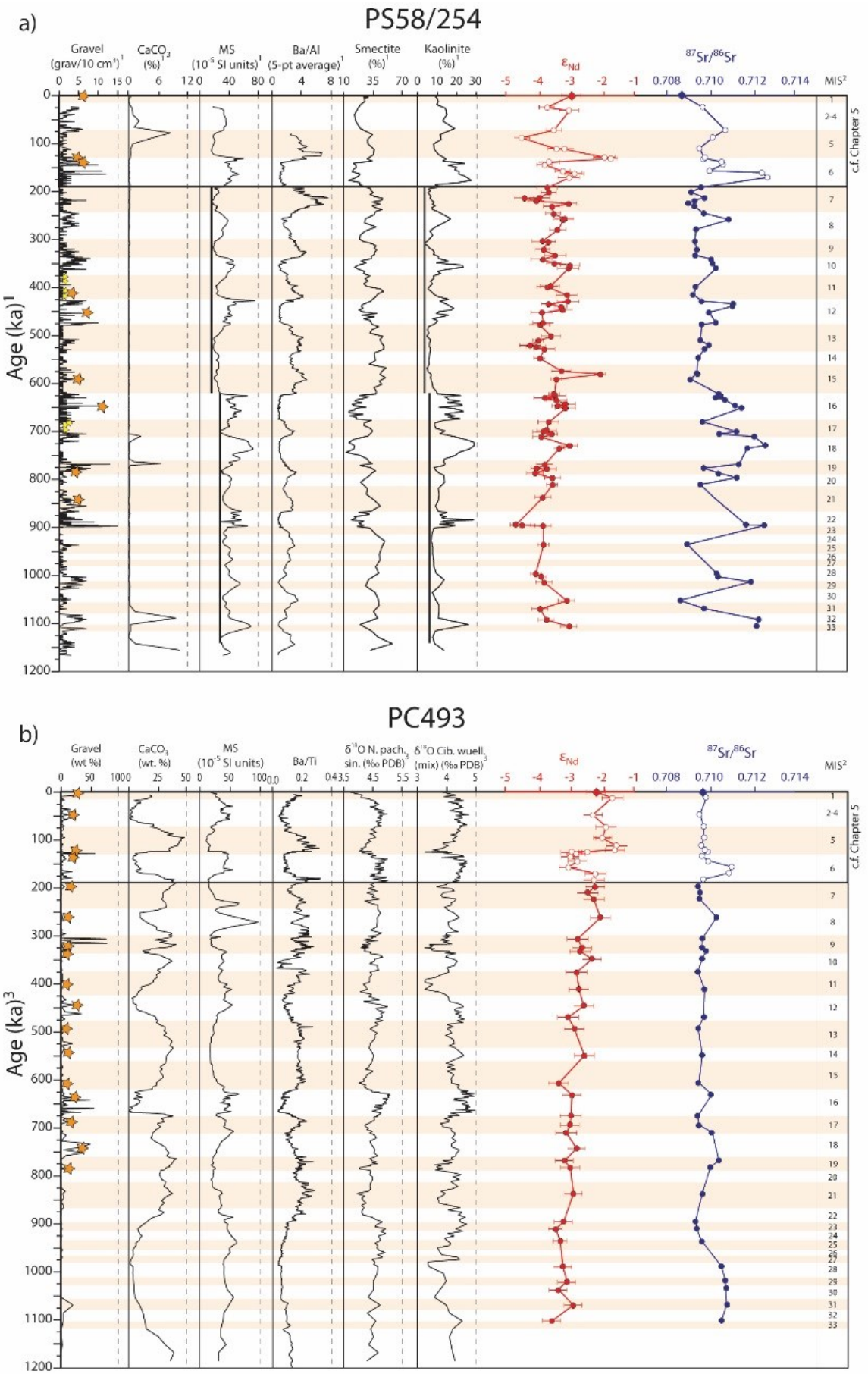

(caption on next page)

Figure 4.2. Downcore summary of Late Pleistocene sediments from a) core site PS58/254 and b) PC493. Detrital neodymium isotopic composition (ε_{Nd}; filled red circles) and detrital Sr isotopic composition ($^{87}Sr/^{86}Sr$: filled blue circles) are from this study. Open symbols denote MIS 5 to moden results, which will be discussed in Chapter 5. Blue and red diamond symbols represent Sr and Nd isotopic composition of detrital <63μm surface sediments at site PS58/254 and PC493 respectively. Age model, gravel content, $CaCO_3$, magnetic susceptibility (MS), barium(Ba)/ aluminium(Al), smectite and kaolinite data for core PS58/254 are taken from [1]Hillenbrand et al. (2009a). Marine Isotope Stage (MIS) boundaries are from [2]Lisiecki and Raymo (2005); Age model and $\delta^{18}O$ record of the epibenthic foraminifer Cibicidoides cf. wuellerstorfi and the planktic foraminifer Neogloboquadrina pachyderma sinistral is from [3]Williams et al. (submitted). Orange (large) stars indicate depths of samples analysed for ice-rafted (>150μm) hornblende and biotite $^{40}Ar/^{39}Ar$ age populations (including surface samples investigated by Simões Pereira et al., 2018). Yellow (small) stars indicate depth of samples investigated for ice-rafted biotite $^{40}Ar/^{39}Ar$ age population of sediments from site PS58/254, and which were subsequently grouped together for their respective interglacial stage.

---

both be interpreted in terms of palaeoproductivity. South of the polar front, palaeoproductivity in the Southern Ocean in turn is typically enhanced during interglacials (e.g. Nürnberg et al., 1997; Bonn et al., 1998; Hillenbrand and Cortese, 2006; Pudsey and Camerlenghi, 1998; Jaccard et al., 2013), allowing correlation of peaks in opal and Ba/Al with peak interglacials in the global benthic foraminifera $\delta^{18}O$ stack (LR04 stack; Lisiecki and Raymo, 2005). Such correlation was performed down to MIS 22 (900-866 ka, ~1650 cmcd). The older sediments were assigned ages by extending the linear sedimentation rate back to the top of the Jaramillo subchron. The presence of the Jaramillo subchron allows to precisely identify MIS 31 (1062-1080 ka). The age model established by Hillenbrand et al. (2009a) was subsequently backed up by diatom biostratigraphy published by Konfirst et al. (2012).

Site PC493 is located on top of a seamount on the continental slope in the western Amundsen Sea (71°08°S, 119°55°W, water depth 2077 m; Figure 4.1) and was recovered during RV James Clark Ross cruise JR179 in 2008. This site was cored before in 1994 on expedition ANT-XI/3 with RV Polarstern (site PS2547, see Hillenbrand et al., 2002). The sediments of PC493 are mainly composed of foraminiferal ooze and sandy mud (Appendix Figure 4.2). Throughout the last 800 ka, site PC493 was located above the Calcite

Compensation Depth (CCD) which allowed for the deposition and preservation of calcareous foraminifera. Oxygen-isotope ratios of the epibenthic foraminifer Cibicidoides cf. wuellerstorfi and the planktic foraminifer Neogloboquadrina pachyderma sinistral reflect changes in temperature and global ice volume and were correlated with the LR04 stack (Williams et al. submitted; Appendix Table 4.2). At site PC493, the Brunhes-Matuyama boundary and the Jaramillo subchron were identified at ~283 cm and from ~324 cm (top) to 328 cm (bottom), respectively (Williams et al., submitted).

Both sites are bathed by CDW, which is upwelling onto the Amundsen Sea shelf, with site PS58/254 being located in the path of the clockwise flowing Antarctic Circumpolar Current (ACC) and site PC493 being located south of the southern boundary of the ACC, where the westward flowing Antarctic coastal current prevails (Orsi et al., 1995; Sokolov and Rintoul, 2009; Figure 4.1 inlet). Sites PS58/254 and PC493 are located off two cross-shelf bathymetric troughs that incise the Amundsen Sea shelf and mark the pathways of two major palaeo-ice streams, i.e. the Pine Island Trough and the Dotson-Getz Trough, respectively (Figure 4.1 inlet). Sediment drifts, such as the drift from which core PS58/254 was recovered, are created by the interaction of downslope turbidity currents, originating from the continental slope, with along-slope bottom currents (Rebesco et al., 1996; Nitsche et al., 2000; Lucchi et al., 2002; Dowdeswell et al., 2006). Sediment supply to the upper continental slope is suggested to mainly take place during glacial times (Rebesco et al., 1996). Then, grounded ice streams advanced through the troughs to (near) the shelf break and slope instability increased due to high supply of unsorted glaciogenic debris and incision of the shelf break by sediment-laden meltwater. As a result, gravitational downslope processes transported the material down to the continental rise, where it was redeposited by bottom currents (Pudsey and Camerlenghi, 1998; Hillenbrand and Ehrmann, 2002; Lucchi et al., 2002; Amblas et al., 2006). Interglacial terrigenous sediment supply to the continental margin is generally low. Meltwater plumes are mainly limited to the inner shelf, and supply of small volumes of terrigenous sediment by tidal and wind driven currents and iceberg transport takes place together with pelagic settling of biogenic particles produced during the short open-marine season (e.g. Grobe and Mackensen, 1992; Pudsey and Camerlenghi, 1998). This supply of biogenic material allows for bioturbation of interglacial sediments by benthic organisms, which causes homogenization of these sediments. On the contrary, site PC493 is located on a seamount which stand ~400 m above the surrounding seafloor. The high bathymetric position of this site impedes (or at least reduces) lateral sediment transport by the CDW or deposition by gravitational downslope processes (e.g.

Hernández-Molina et al., 2004, 2006). Sediment deposition mainly occurs as sediment-laden tidal and wind-driven current and ice-rafting.

The two study sites are suitable locations for recording past WAIS dynamics because they are located offshore from the Amundsen Sea Embayment, i.e. the "weak underbelly" of the WAIS (e.g. Hughes, 1981; Joughin and Alley, 2011), which is supposed to act as an exit gate for icebergs during collapse (e.g. MacAyeal, 1992). During periods when the WAIS had retreated or collapsed, iceberg-rafted detritus (IRD) should have originated from the bedrock sources still covered by grounded ice, especially those areas below the modern WAIS that would have been situated above sea level in its absence (e.g. Figure 1 in Jamieson et al. 2014), and should have been transported to our sites via icebergs. Subglacial erosion depends on bedrock erodibility, basal ice velocity, ice thickness and the basal thermal regime (e.g. Jamieson et al., 2010), with the latter three factors favouring subglacial erosion in the downstream sections of modern ice streams around the fringes of the WAIS, where flow velocity (e.g. Rignot et al., 2011) and basal melting (e.g. Pattyn 2010) are highest whilst the ice is relatively thin (e.g. Fretwell et al., 2013). This is consistent with the observation that the IRD and fine-grained detrital sediment provenance in contemporary and Late Holocene marine sediments along the Pacific margin of Antarctica matches that of near-coastal bedrock sources in the West Antarctic hinterland (Simões Pereira et al., 2018). If bedrock sources in ice drainage areas that persisted during times of a "contracted" or collapsed WAIS were geologically distinct from modern sources, then we would expect to see a corresponding signal in our downcore IRD of fine-grained detrital sediment records (i.e. Cook et al., 2013; Williams et al., 2010). Furthermore, a complete WAIS collapse could result in the opening of seaway corridors between the Amundsen Sea, the Weddell Sea and possibly the Ross Sea (Vaughan et al., 2011) that could allow for the passage of icebergs from East Antarctica to our sites. Thus, a prominent East Antarctic provenance signal in the IRD records at our sites would provide conclusive evidence for such a seaway opening in response to a WAIS collapse.

4.3. Sample selection and methods

In total 125 samples from core sites PS58/254 (n=82) and PC493 (n=45) were selected for fine-grained detrital Sr and Nd isotope analysis (Figure 4.2, Table 4.1). Samples were selected based on the variation in the magnetic susceptibility, which, in the first instance, is a

proxy for input of terrigenous detritus but can also be a proxy for provenance changes (e.g. Diekmann et al., 2000; Hillenbrand et al., 2009a), and the Ba/Al (PS58/254) or Ba/Ti (PC493) ratios, which are proxies for biological productivity. This selection allows identifying sediment provenance changes that occurred over glacial-interglacial cycles. Data for seafloor surface sediment samples from both sites are from Simões Pereira et al. (2018; see Chapter 2).

The record for core site PS58/254 comprises of 40 interglacial samples extending back to MIS 31 and 33; glacial samples go back to MIS 32. 25 interglacial samples and 20 glacial samples were selected from core site PC493. In order to better resolve changes in the sediment provenance during the last 200 kyrs (including the MIS 6/5 transition), 14 (PS58/254) and 13 (PC493) samples were selected to provide a higher temporal resolution for this time interval, which will be further discussed in Chapter 5.

Bulk sediment samples were wet sieved into <63μm, 63-150μm and >150μm fractions. Splits (~500 mg) of homogenised fine-grained (<63μm) sediment were sequentially leached to remove biogenic carbonate and authigenic ferromanganese coatings. Calcium carbonate was removed by leaching of dried sediments with buffered acetic acid (Biscaye, 1965). Extraction of ferromanganese oxides and oxyhydroxides was performed by leaching the dried sediments with a reductive hydroxylamine hydrochloride (NH_2OH) solution for 2 hrs and again for ~12 hrs, following Rutberg et al. (2000). No removal of biogenic opal was undertaken. Sediments at site PC493 contain only traces of siliceous microfossils (site PS2547; cf. Hillenbrand et al., 2002), whereas biogenic opal content in core PS58/254 reaches up to ~30 wt.% (Hillenbrand et al., 2009a), However, the concentrations of Sr and Nd in opal are known to be very low (~5 ppm and ~3 ppm, respectively; Grousset et al., 1998), and therefore our provenance results analysed are unlikely to be affected by opal-bound Sr and Nd (cf. Bayon et al., 2002). An aliquot of ~50mg of leached (i.e. detrital) sample was weighted into a Teflon beaker and dissolved using a mixture of 2ml of HF (27M), 1ml of HNO_3 (16M) and 0.8ml of $HClO_4$ (20M) for 3-4 days on a hotplate. Precipitates of fluorides were dissolved by fluxing samples in 6M HCl. Strontium and Nd were separated from the sample matrix by ion chromatography using a three separate columns. Firstly, the entire sample was loaded onto a column with cation-exchange resin AG50W X-8 (200-400 mesh) to separate Sr and the rare-earth elements (including Nd) from the sample matrix. Strontium was purified by loading the Sr cut from the cation-exchange column onto a Sr Spec column (Sr-Spec resin: 100-200 mesh size, after Pin and Bassin, 1992). Neodymium was separated from the other rare-earth elements using Ln-spec resin (50-100μm mesh; after Pin and Zalduegui, 1997).

Table 4.1. Strontium and neodymium isotopic compositions of late Pleistocene (~0.2 to 1.1 Ma) detrital <63μm sediments deposited at site PS58/254

Sediment core	Core depth (cmbsf)	Core depth (cmcd)	Depositional age (ka)	MIS[b]	$^{143}Nd/^{144}Nd$	± 2 S.E.	ε_{Nd}	± 2 S.D.	$^{87}Sr/^{86}Sr$	± 2 S.E.
PS58/254-2	00-02 [a]	0	0	1	0.512486	0.000006	-2.96	0.30	0.708704	0.000004
PS58/254-1	227-228	245.5	192	7	0.512448	0.000009	-3.71	0.32	0.709603	0.000007
PS58/254-1	253-253	271.5	202	7	0.512450	0.000010	-3.66	0.24	0.709139	0.000005
PS58/254-1	282-283	300.5	213	7	0.512436	0.000009	-3.95	0.32	0.709327	0.000010
PS58/254-1	283[c]	301	214	7	0.512411	0.000008	-4.43	0.30		
	duplicate sample[d]				0.512441	0.000011	-3.84	0.32	0.709280	0.000008
PS58/254-1	297-298	315.5	219	7	0.512432	0.000007	-4.01	0.20	0.709321	0.000010
PS58/254-1	311.5-313	330.5	225	7	0.512484	0.000008	-3.01	0.23	0.709003	0.000005
PS58/254-1	327-328	345.5	231	7	0.512453	0.000009	-3.61	0.25	0.709289	0.000008
PS58/254-1	360-361	378.5	246	8	0.512457	0.000007	-3.52	0.23	0.709718	0.000005
PS58/254-1	373[c]	391	257	8	0.512475	0.000006	-3.17	0.30		
PS58/254-1	376-377	394.5	259	8	0.512474	0.000010	-3.20	0.33	0.710921	0.000008
PS58/254-1	400-401	418.5	280	8	0.512463	0.000009	-3.42	0.25	0.709369	0.000005
PS58/254-1	433 [c]	451	304	9	0.512439	0.000005	-3.88	0.30		
PS58/254-1	434-435	452.5	304	9	0.512450	0.000006	-3.67	0.23	0.709323	0.000006
PS58/254-1	471-472	489.5	321	9	0.512441	0.000007	-3.85	0.23	0.709391	0.000005
PS58/254-1	498-499	516.5	333	9	0.512461	0.000009	-3.45	0.33	0.709321	0.000010
PS58/254-1	517-518	535.5	341	10	0.512439	0.000012	-3.88	0.33	0.710083	0.000007
PS58/254-1	534-535	552.5	349	10	0.512459	0.000006	-3.49	0.23	0.710139	0.000005
PS58/254-1	543 [c]	561	353	10	0.512485	0.000005	-2.98	0.30		
PS58/254-1	559-560	577.5	360	10	0.512482	0.000009	-3.04	0.33	0.710329	0.000007
	duplicate				0.512493	0.000009	-2.82	0.32	0.710377	0.000007
PS58/254-1	633 [c]	651	397	11	0.512453	0.000006	-3.61	0.30		
PS58/254-1	636-637	654.5	399	11	0.512448	0.000007	-3.70	0.33	0.709383	0.000012
PS58/254-1	667-668	685.5	416	11	0.512480	0.000010	-3.09	0.33	0.709261	0.000007
PS58/254-1	696-697	714.5	429	12	0.512482	0.000008	-3.04	0.33	0.709665	0.000009
PS58/254-1	710-711	728.5	434	12	0.512449	0.000009	-3.70	0.20	0.711102	0.000006
PS58/254-1	724-725	742.5	440	12	0.512470	0.000008	-3.28	0.20	0.711072	0.000005
PS58/254-1	743 [c]	761	447	12	0.512474	0.000007	-3.20	0.30		
PS58/254-1	759-760	777.5	452	12	0.512439	0.000008	-3.87	0.33	0.709992	0.000008
PS58/254-1	817-818	835.5	474	12	0.512442	0.000009	-3.83	0.32	0.710297	0.000008
PS58/254-1	827-828	845.5	478	12	0.512436	0.000009	-3.95	0.32	0.709637	0.000008
PS58/254-1	863 [c]	881	502	13	0.512454	0.000005	-3.58	0.30		
PS58/254-1	876-877	894.5	511	13	0.512434	0.000013	-3.98	0.17	0.709565	0.000007
PS58/254-1	891-892	909.5	521	13	0.512421	0.000007	-4.24	0.32	0.709969	0.000007
PS58/254-1	913 [c]	913	523		0.512430	0.000006	-4.07	0.30		
PS58/254-1	902-903	920.5	528	13	0.512444	0.000008	-3.79	0.32	0.709776	0.000009
PS58/254-1	927-928	945.5	547	14	0.512436	0.000007	-3.95	0.17	0.709468	0.000007
PS58/254-1	963 [c]	981	574	15	0.512471	0.000005	-3.26	0.30		
PS58/254-1	972-973	990.5	580	15	0.512521	0.000007	-2.27	0.32	0.709422	0.000010
	duplicate				0.512534	0.000014	-2.03	0.17	0.709394	0.000006
	duplicate				0.512520	0.000013	-2.30	0.28	0.709337	0.000006
PS58/254-1	988-989	1006.5	591	15	0.512463	0.000011	-3.42	0.17	0.709108	0.000007
PS58/254-1	1036-1037	1054.5	623	16	0.512459	0.000008	-3.49	0.17	0.710429	0.000007
PS58/254-1	1046-1047	1064.5	626	16	0.512461	0.000008	-3.45	0.32	0.710536	0.000009
PS58/254-1	1061-1062	1079.5	630	16	0.512444	0.000009	-3.79	0.32	0.710283	0.000008
PS58/254-1	1077-1078	1095.5	635	16	0.512464	0.000006	-3.40	0.32	0.710721	0.000008
PS58/254-1	1103 [c]	1121	643	16	0.512478	0.000009	-3.12	0.30		
PS58/254-1	1116-1117	1134.5	647	16	0.512464	0.000011	-3.39	0.17	0.711188	0.000007
PS58/254-1	1132-1133	1150.5	652	16	0.512477	0.000009	-3.13	0.32	0.711497	0.000008
PS58/254-1	1220-1221	1238.5	680	17	0.512450	0.000008	-3.66	0.32	0.709678	0.000009
PS58/254-1	1253 [c]	1271	699	17	0.512447	0.000006	-3.72	0.30		
PS58/254-1	1257-1258	1275.5	701	17	0.512442	0.000008	-3.83	0.32	0.711262	0.000008

(table continues on next page)

PS58/254-1	1266-1267	1284.5	706	17	0.512456	0.000010	-3.56	0.17	0.710448	0.000006
PS58/254-1	1276-1277	1294.5	711	17	0.512438	0.000007	-3.89	0.26	0.712083	0.000009
PS58/254-1	1303 [c]	1321	730	18	0.512458	0.000006	-3.52	0.30		
	duplicate				0.512484	0.000008	-3.01	0.26	0.712598	0.000007
PS58/254-1	1312-1313	1330.5	736	18	0.512467	0.000008	-3.34	0.17	0.711759	0.000007
PS58/254-1	1368-1369	1386.5	769	19	0.512441	0.000010	-3.84	0.25	0.711376	0.000007
PS58/254-1	1389-1390	1407.5	777	19	0.512431	0.000007	-4.04	0.17	0.709720	0.000006
PS58/254-1	1393 [c]	1411	778	19	0.512447	0.000006	-3.72	0.30		
PS58/254-1	1415-1416	1433.5	787	19	0.512429	0.000007	-4.08	0.26	0.710408	0.000008
PS58/254-1	1427-1428	1445.5	797	20	0.512459	0.000009	-3.49	0.20	0.711270	0.000008
PS58/254-1	1437-1438	1455.5	811	20	0.512456	0.000008	-3.55	0.17	0.709568	0.000006
PS58/254-1	1458-1459	1476.5	837	21	0.512439	0.000008	-3.88	0.25	0.710168	0.000008
PS58/254-1	1610-1611	1628.5	895	22	0.512398	0.000010	-4.69	0.17	0.711701	0.000007
	duplicate				0.512411	0.000008	-4.43	0.21	0.711660	0.000008
PS58/254-1	1617-1618	1635.5	897	22	0.512447	0.000012	-3.72	0.17	0.712553	0.000007
PS58/254-1	1659-1660	1677.5	936	25	0.512442	0.000011	-3.83	0.17	0.708973	0.000007
PS58/254-1	1704-1705	1722.5	997	28	0.512430	0.000009	-4.07	0.17	0.710334	0.000007
	duplicate				0.512423	0.000009	-4.20	0.26		
PS58/254-1	1709-1710	1727.5	1003	28	0.512438	0.000009	-3.91	0.17	0.710393	0.000008
PS58/254-1	1717-1717	1735.5	1014	28	0.512445	0.000008	-3.76	0.20	0.711927	0.000008
PS58/254-1	1746-1747	1764.5	1053	30	0.512482	0.000010	-3.05	0.20	0.708605	0.000009
	repeat				0.512473	0.000013	-3.22	0.25		
PS58/254-1	1759-1760	1777.5	1070	31	0.512439	0.000006	-3.88	0.20	0.709764	0.000008
PS58/254-1	1776-1777	1794.5	1093	32	0.512449	0.000008	-3.68	0.20	0.712289	0.000007
PS58/254-1	1786-1787	1804.5	1106	33	0.512481	0.000007	-3.07	0.25	0.712190	0.000007
	repeat				0.512474	0.000011	-3.19	0.17		

a) Taken from Simões Pereira et al., 2018 (see Chapter 2)

b) Marine Isotope Stages (MIS) based on Lisiecki and Raymo, 2005

c) Pilot data analysed by Carys Cook using same methodology

d) Duplicate sample values represent full procedural replicates of sample powders (i.e. from leaching to digestion to column chemistry). Duplicate values represent procedural replicates of leached (detrital) sample powders (i.e. from digestion to column chemistry). Repeat values represent measurement replicates of the same sample after column chemistry.

Neodymium cuts were dried and taken up in 1% HNO_3 in preparation for isotopic measurements on a Nu Instruments multi-collector inductively plasma mass spectrometer (MC-ICP-MS) in the MAGIC laboratories at Imperial College. Measurements were performed in static mode, and instrument mass bias was corrected for using a $^{146}Nd/^{144}Nd$ ratio of 0.7219 and applying an exponential law. 144Sm contribution to the 144Nd signal was monitored and was always well below the correctable threshold of 0.1%. In total 14 analytical sessions over a period of 30 months gave the following $^{143}Nd/^{144}Nd$ JNdi standard ratios: 0.512144 ±0.000012 (n =13), 0.512157 ±0.000010 (n =13), 0.512116 ±0.000012 (n =17), 0.512095 ±0.000017 (n =25), 0.512081 ±0.000017 (n =17), 0.512121 ±0.000013 (n =10), 0.512116 ±0.000010 (n =16), 0.512113 ±0.000013 (n =27), 0.512121 ±0.000013 (n =23), 0.512102 ±0.000009 (n =22), 0.512137 ±0.000011 (n =20), 0.512119 ±0.000015 (n =28), 0.512117 ±0.000013 (n =17), 0.512124 ±0.000016 (n =21). Measured $^{143}Nd/^{144}Nd$ ratios for all samples were corrected for using the offset of the average JNdi $^{143}Nd/^{144}Nd$ ratio of the session relative to the accepted value of 0.512115 (Tanaka et al., 2000). Full procedural repeats of USGS BCR-2 standard during the course of this study yielded a $^{143}Nd/^{144}Nd$ ratio of 0.512639 ±0.000014 (2.S.D., n=58), in excellent agreement with the recommended value of 0.512638 ±0.000015. Neodymium blanks were generally below 50 pg (n=8), except for three batches which yielded 150, 210 and 440 pg of total Nd (<0.15 % of the total Nd amount in samples and hence negligible).

Strontium was loaded in 1µl of HCl (6M) onto degassed tungsten filaments, and covered by 1 µl of tantalum chloride activator solution, before analysis on a Thermo Scientific thermal ionisation mass spectrometer (TIMS) in the MAGIC laboratories at Imperial College. Radiogenic $^{87}Sr/^{86}Sr$ ratios were normalized to a stable $^{88}Sr/^{86}Sr$ ratio of 8.375 to correct for instrumental mass bias using an exponential law. ^{87}Rb interferences were always kept below 0.02% of the total 87Sr signal by burning of Rb prior to analysis (‘flash heating’). Strontium isotope measurements were carried out over a period of 27 months, which included replacement of the graphite inlets of all Faraday cups of the TIMS in February 2017. Hence, reported $^{87}Sr/^{86}Sr$ values (Tables 4.1, 4.2) were corrected for two different long term average SRM987 standard values of 0.710263 ±0.000015 2.S.D. (n =50) and 0.710250 ±0.000010 (n =39), for before and after February 2017 respectively, relative to the accepted ratio of 0.710252 ±0.000013 (Weis et al., 2006). Procedural standard reference material BCR-2, analysed throughout the course of sample analysis, gave an $^{87}Sr/^{86}Sr$ ratio of 0.705012 ±0.000016 2.S.D (n =17), in excellent agreement with the accepted value of 0.705013 ±0.000010 2.S.D. (n =13) (Weis et al., 2006). Procedural blanks were consistently below 120pg (n =10).

Table 4.2. Strontium and neodymium isotopic compositions of late Pleistocene (~0.2 to 1.1 Ma) detrital <63μm sediments deposited at site PC493

Sediment core	Depth (cmbsf)	Deposition age (ka)	MIS[b]	$^{143}Nd/^{144}Nd$	± 2 S.E.	ε_{Nd}	± 2 S.D.	$^{87}Sr/^{86}Sr$	± 2 S.E.
PC493[a]	00-01	0	1	0.512526	0.000007	-2.18	0.29	0.709711	0.000005
PC493	100-101	197	7	0.512525	0.000005	-2.21	0.29	0.709480	0.000006
PC493	103-104	210	7	0.512513	0.000009	-2.44	0.32	0.709577	0.000007
PC493	106-107	223	7	0.512523	0.000009	-2.25	0.32	0.709544	0.000007
PC493	113-114	262	8	0.512533	0.000006	-2.04	0.30	0.710349	0.000007
PC493	125-127	306	9	0.512490	0.000009	-2.89	0.28	0.709685	0.000006
	repeat[d]			0.512497	0.000010	-2.75	0.32		
PC493	139-140[c]	325	9	0.512504	0.000006	-2.61	0.29		
	duplicate sample							0.709672	0.000007
PC493	145-146	333	9	0.512501	0.000010	-2.66	0.32	0.709857	0.000006
PC493	150-151[c]	348	10	0.512520	0.000006	-2.31	0.29		
	duplicate sample			0.512512	0.000008	-2.46	0.25	0.709674	0.000008
PC493	156-157	375	11	0.512496	0.000010	-2.78	0.32	0.709475	0.000007
PC493	163-164[c]	411	11	0.512499	0.000007	-2.71	0.30		
	duplicate			0.512496	0.000008	-2.76	0.25	0.709787	0.000008
PC493	172-173[c]	447	12	0.512507	0.000008	-2.56	0.30		
PC493	178-179	469	12	0.512482	0.000013	-3.04	0.32	0.709744	0.000006
PC493	184-184[c]	493	13	0.512492	0.000006	-2.85	0.30		
	duplicate			0.512510	0.000008	-2.50	0.25	0.709493	0.000007
PC493	194-195[c]	549	14	0.512508	0.000005	-2.54	0.30		
	duplicate			0.512509	0.000007	-2.51	0.25	0.709675	0.000007
PC493	205-206[c]	606	15	0.512467	0.000009	-3.34	0.30		
	duplicate			0.512484	0.000008	-3.01	0.25	0.709527	0.000008
PC493	216-217[c]	631	16	0.512488	0.000006	-2.93	0.29		
	duplicate			0.512498	0.000009	-2.72	0.25	0.710115	0.000008
PC493	249-250	675	16	0.512486	0.000009	-2.96	0.32	0.709485	0.000006
PC493	255-256[c]	694	17	0.512485	0.000007	-2.99	0.29		
	duplicate							0.709514	0.000008
PC493	260-261	710	17	0.512479	0.000011	-3.10	0.32	0.710150	0.000006
PC493	266-267[c]	746	18	0.512495	0.000015	-2.78	0.27		
PC493	272-273	768	19	0.512475	0.000009	-3.17	0.28	0.710456	0.000006
PC493	279-280[c]	783	20	0.512485	0.000006	-2.98	0.29		
	duplicate			0.512494	0.000007	-2.82	0.25	0.710058	0.000008
PC493	292-293	837	21	0.512490	0.000010	-2.90	0.28	0.709681	0.000007
PC493	304-305	896	22	0.512474	0.000010	-3.20	0.28	0.709364	0.000006
PC493	307-308	910	23	0.512462	0.000010	-3.43	0.21	0.709423	0.000007
PC493	312-313	935	24	0.512469	0.000009	-3.29	0.21	0.709628	0.000006
PC493	323-324	989	28	0.512473	0.000010	-3.22	0.28	0.710575	0.000007
PC493	325-326	1020	29	0.512479	0.000010	-3.10	0.28	0.710769	0.000006
PC493	326-327	1036	30	0.512465	0.000010	-3.37	0.28	0.710780	0.000006
PC493	328-329	1069	31	0.512489	0.000009	-2.90	0.28	0.710815	0.000007
PC493	330-331	1102	32	0.512455	0.000012	-3.56	0.28	0.710584	0.000007

a) Taken from Simões Pereira et al., 2018 (see Chapter 2)

b) Marine Isotope Stages (MIS) based on Lisiecki and Raymo, 2005

c) Pilot data analysed by Carys Cook using same methodology

d) Duplicate values represent procedural replicates of leached (detrital) sample powders (i.e. from digestion to column chemistry). Repeat values represent measurement replicates of the same sample after column chemistry.

Hornblende and biotite grains were hand-picked from the coarse sediment fraction (>150μm) after sieving. At both sites this size fraction comprises exclusively IRD. No gravitational downslope processes is deemed capable of transporting and depositing grains of this size to site PC493 due to its elevation (Hillenbrand et al., 2002). The drift sediments at site PS58/254, on the other hand, consist predominantly of mud (i.e. silt and clay), so that even terrigenous sand ≥63μm is considered as IRD (Hillenbrand et al., 2009a). Five interglacial samples (MIS 5, 11, 15, 17, 19 and 21) and three glacial samples (MIS 6, 12, 16) were analysed from core PS58/254 (Figure 4.3, Appendix Table 4.3), and one sample from each interglacial

and glacial stage starting with MIS 19 was analysed from core PC493 (Figure 4.4, Table 4.3). Core PS58/254 was picked for both hornblende and biotite grains (n =195), but exclusively biotite grains were analysed from samples representing MIS 11 (611, 621, 681, 691 cmcd), MIS 17 (1241, 1251, 1271 and 1281 cmcd) and MIS 21 (1481 and 1491 cmcd) due to loss of hornblende grains during shipment. Similarly, only biotite grains were analysed from core PC493 (n=333; hornblende grains were lost during shipment). On average, 20 grains were picked for each sample, although grain numbers per sample range from 9 to 37. Hornblende and biotite grains alongside monitor standard grains were irradiated at the USGS reactor in Denver, Colorado. $^{40}Ar/^{39}Ar$ measurements were carried out at the Argon Geochronology for the Earth Sciences (AGES) laboratory at the Lamont-Doherty Earth Observatory using single-step CO_2 laser fusion. J-values were calculated based on the normalization of co-irradiated Fish Canyon sanidine ages of 28.201±0.046 Ma (Kuiper et al., 2008). Measured argon isotope ratios were corrected for nuclear interferences (Dalrymple et al., 1981), atmospheric argon ($^{40}Ar/^{36}Ar$ =298.6, Lee et al., 2006), procedural blanks, and mass discrimination from repeated measurements of blanks and air pipettes.

4.4. Results

4.4.1. Strontium and neodymium isotope composition of fine-grained detritus

In the following we describe the Sr and Nd isotope results in both cores, PS58/254 and PC493, prior to MIS 6 (older than 191 ka, i.e. >244 cmcd in core PS58/254 and >99 cm in core PC493, respectively). Neodymium isotope compositions are reported as epsilon values (ε_{Nd}), which describe the deviations of the measured $^{143}Nd/^{144}Nd$ ratio from the chondritic ratio of 0.512638 in part per 10,000 (Jacobsen and Wasserburg, 1980).

Neodymium isotope values in PS58/254 and PC493 show a small range between MIS 7 and MIS 32, with ε_{Nd} values from -4.7 to -2.8 (omitting one PS58/254 sample at 990-991 cmcd; ε_{Nd} =-2.3) and ε_{Nd} = -3.5 to -2.0, respectively. The ε_{Nd} record of PS58/254 lacks a clear display of glacial-interglacial changes compared to the Sr isotope record. In general, we observe however increase in Nd isotopic compositions going from glacial to interglacial stages, with glacial samples usually displaying ε_{Nd} values of ~-4 and interglacial samples showing ε_{Nd} values of ~-3 (Figure 4.5). In detail, the observe trends in Nd isotopic composition does not always occur at the transition between glacial and interglacial stages, but can occurs slightly after or before the transition.

Strontium isotope ratios show variability in the third digit in PS58/254 ($^{87}Sr/^{86}Sr$: 0.7086 to 0.7126) and P493 ($^{87}Sr/^{86}Sr$: 0.7094 to 0.7108) between MIS 7 and MIS 32 (Figure 4.2, 4.5). The $^{87}Sr/^{86}Sr$ record in core PS58/254 is characterized by clear glacial-interglacial cyclicity, with higher ratios during or just slightly before glacial stages, with the exception of MIS 14 (Figure 4.2). A pronounced change in the amplitude of the Sr isotope signal is furthermore observed before and after ~675 ka (~1270 cmcd).

Overall, Sr and Nd isotopic compositions show different patterns between the two cores (Figure 4.2). While PS58/254 sediments display glacial/interglacial cycles in sediment compositions, Nd and Sr isotope records in core PC493 are smoother. A general trend is however detectable towards higher Nd isotope values over the entire sediment record towards the present day (ε_{Nd} = ~-3.2 during MIS 32 and ε_{Nd} ~ -2.2 during MIS 7) towards the present day. In general, increase in $^{87}Sr/^{86}Sr$ ratios obtained for detrital sediments in core PC493 generally correlate with an increase in the $^{87}Sr/^{86}Sr$ ratio at site PS58/254 over the same time period (Figure 4.2) compared to interglacials, omitting the interval below ~800 ka (i.e. >292 cmcd) where $^{87}Sr/^{86}Sr$ ratios show longer wavelength fluctuations.

4.4.2. $^{40}Ar/^{39}Ar$ ages on hornblende and biotite grains

In total, 78 hornblende and 89 biotite grains were analysed in core PS58/254 (prior to MIS 6). The $^{40}Ar/^{39}Ar$ ages range from modern (~1 Ma) to 356 Ma (Figure 4.3; Appendix Table 4.3). No systematic shift can be observed between the hornblende and biotite age populations. Glacial samples (12, 16) display well-defined age population peaks at ~260 Ma and ~100 Ma. Interglacial samples, in contrast, show more scattered age distributions. A notable feature of interglacial samples is the high numbers of grains with ages <80 Ma and 30-180 Ma (~140 Ma age peak) compared to glacial samples (Figs. 4.3, 4.6). In contrast, age peaks at ~100 Ma, and ~240 Ma can be observed in glacial and in interglacial samples. Only biotite grains were analysed in core PC493 (n = 255) (Figure 4.3). Ages vary between modern (~1 Ma) and 490 Ma, with most of the grains covering ages from ~80 Ma to 260 Ma. Individual samples show a relatively high age scatter, with no notable differences between glacial and interglacial samples (Figure 4.6). Stacked $^{40}Ar/^{39}Ar$ age populations for all glacial and interglacial samples, however, show a pronounced age peak at ~100 Ma and a minor age peaks around 170 Ma and ~235 Ma in both glacial and interglacial samples (Figure 4.6). In contrast to PS58/254, we do not observe a significant number of grains <80 Ma old.

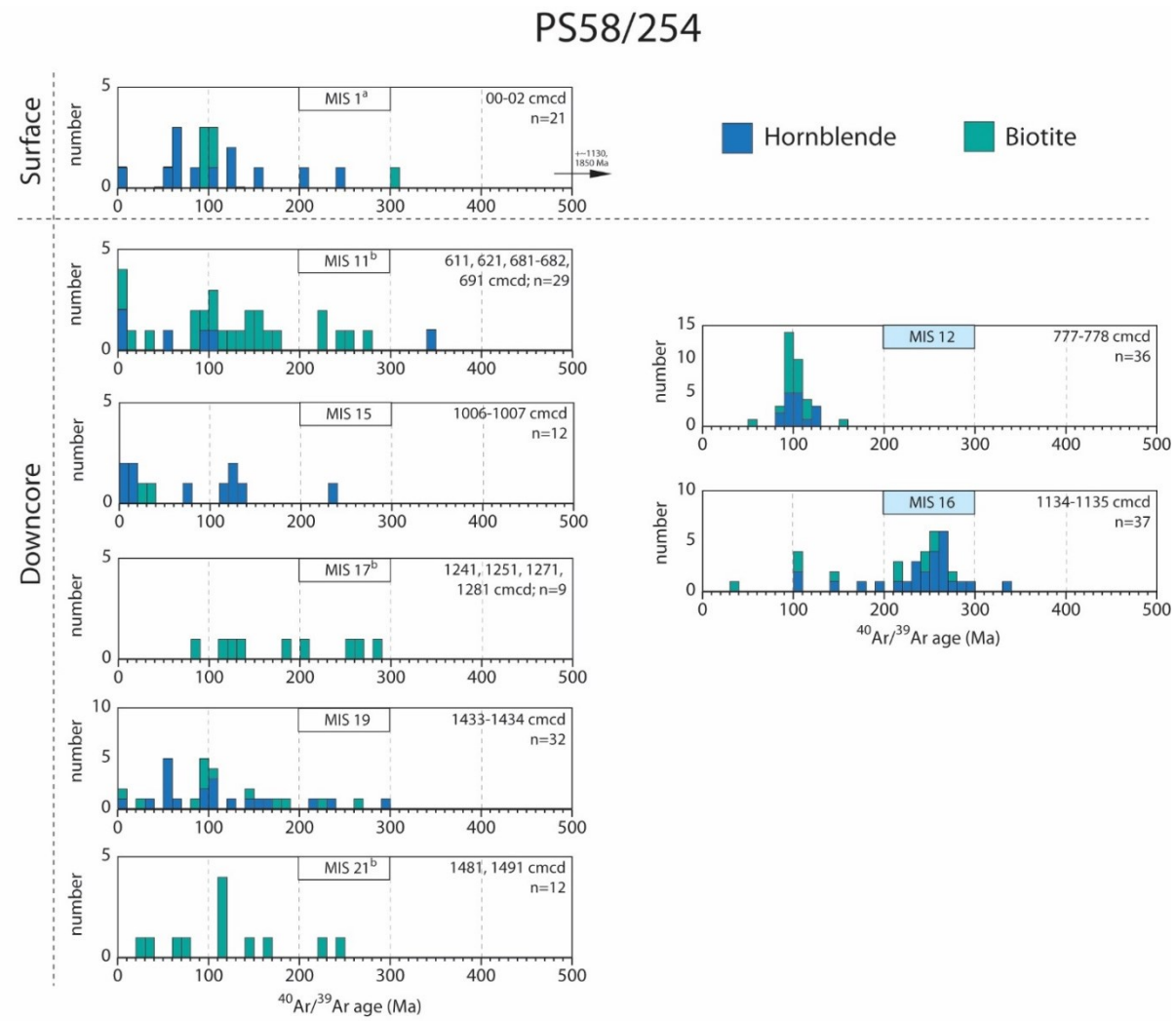

Figure 4.3. Stacked $^{40}Ar/^{39}Ar$ age histograms (10 Ma age bin intervals) of hornblende (blue) and biotite (green) from ice-rafted (>150µm) sediments from site PS58/254, showing the distribution of grains varying between 0 and ~ 350 Ma. Surface (MIS 1) data is from [a]Simões Pereira et al., 2018. [b]MIS 11 (omitting sample at depth 681-682 cmcd), MIS 12 and MIS 16 samples were exclusively picked and analysed for biotite.

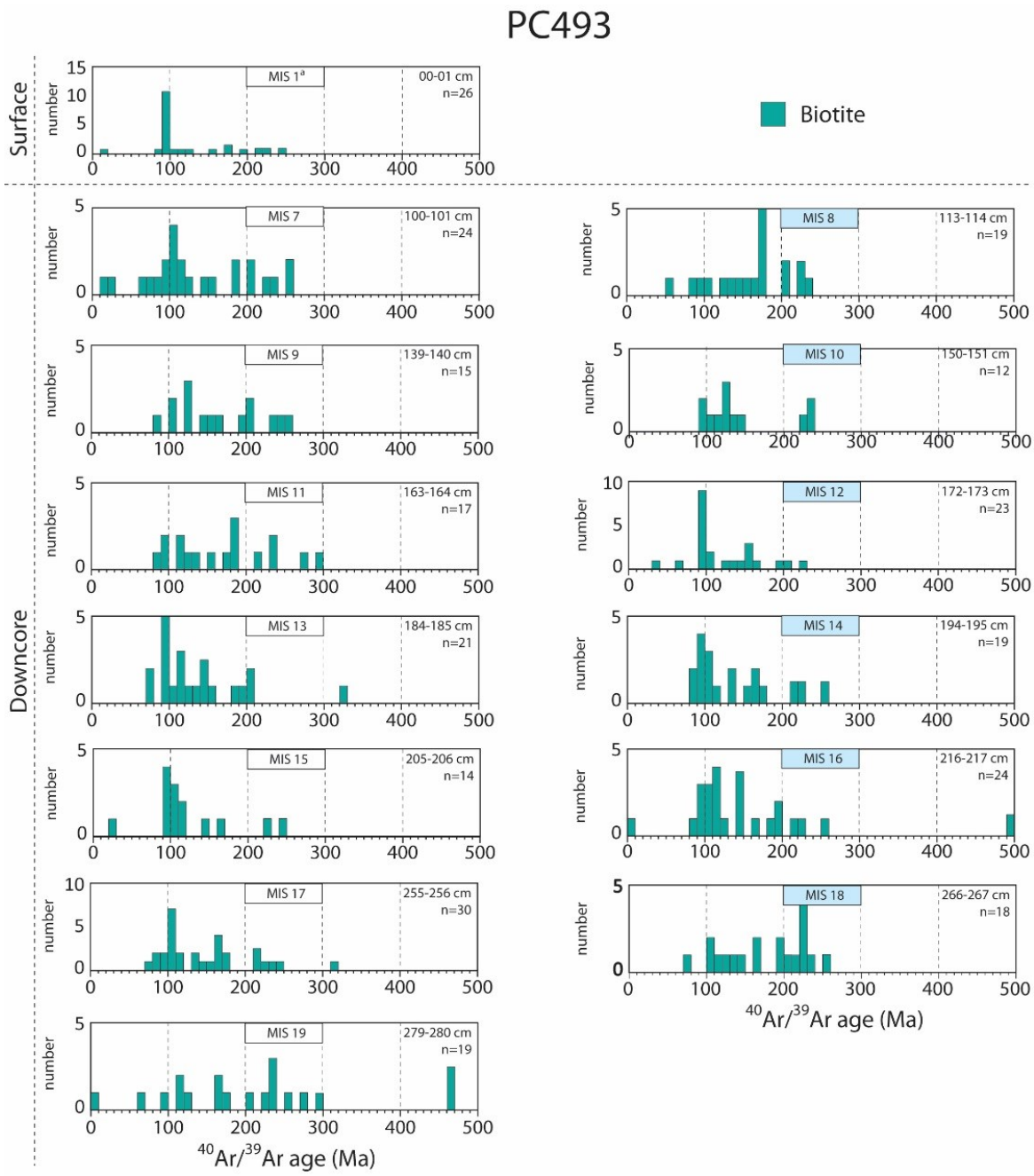

Figure 4.4. $^{40}Ar/^{39}Ar$ age histograms (10 Ma age bin intervals) of biotite (green) from ice-rafted (>150μm) sediments from site P493, showing the distribution of grains varying between 0 and ~ 350 Ma, as well as two grains at ~460 Ma and ~500 Ma. Surface (MIS 1) data is from [a]Simões Pereira et al., 2018. Note that we see no particular distinction in the age distribution between glacial and interglacial samples.

4.5. Discussion: Provenance at sites PS58/254 and PC493

4.5.1. Sources for fine-grained sediments over glacial-interglacial cycles

The Nd and Sr isotopic composition of late Pleistocene (~1.2 Ma – 0.2 Ma) detrital sediments from core PS58/254 (ε_{Nd}: -4.7 to -2.8; $^{87}Sr/^{86}Sr$: 0.7086 to 0.7126) and core PC493 (ε_{Nd}: -3.5 to -2.0; $^{87}Sr/^{86}Sr$: 0.7094 to 0.7108) overlap almost entirely with the isotopic signatures of modern and Late Holocene detrital sediments deposited on the Amundsen Sea Embayment (ASE) continental shelf (Figure 4.5; see Chapter 2 for a detailed description on the sediment provenance and transport on the Amundsen Sea Embayment). In detail, fine-grained interglacial detritus from site PS58/254 matches the provenance fingerprint of modern and Late Holocene sediments from (eastern) Pine Island Trough in the eastern ASE. This observation suggests direct northward sediment transport from the continental shelf to the rise. The isotopic fingerprint of shelf sediments in the eastern ASE was described in Chapter 2 and Chapter 3. During interglacials, tidal and wind driven currents carry fine-grained detritus originating from sediment-laden meltwater plumes that are released at the grounding line of Pine Island Glacier (with low ε_{Nd} values of ~-9 and high $^{87}Sr/^{86}Sr$ ratios of ~0.729 due to glacial erosion of evolved Jurassic granites; Figs. 4.1, 4.5) and Thwaites Glacier (Nakayama et al. 2013) seaward towards the shelf break. Along their northward transport pathway, sediments become progressively mixed with detritus shed from the eastern ASE coast, i.e. Canisteo Peninsula, King Peninsula and Thurston Island, where extensive Palaeozoic to Cretaceous granitoids crop out (Figs. 4.1, 4.5; Pankhurst et al., 1993; 1998; Mukasa and Dalziel, 2000).

Interglacial deposition at site PS58/254 is dominated by pelagic settling of these particles, but also affected by lateral bottom current transport because the site is located on the flank of a sediment drift (e.g. Nitsche et al., 2000; Uenzelmann-Neben and Gohl, 2012). A distal and lateral sediment transport to site PS58/254 is observed by high smectite contents (~35%) in interglacial sediments (Figure 4.2; Hillenbrand et al., 2009a). Seafloor surface (i.e. Late Holocene) sediments on the Amundsen Sea shelf have lower smectite contents (<29%) (Ehrmann et al., 2011), indicating a distal smectite source at least for the interglacial sediments deposited at site PS58/254, implying either westward supply from the volcanic Peter I Island (Figure 4.1 inlet), eastward current transport from the Ross Sea or southward delivery of smectite-enriched detritus from the South Pacific basin with upwelling CDW (Hillenbrand et al., 2003; Ehrmann et al., 2011). The platy nature of smectite minerals makes them more susceptible to be carried over long distances. Smectite and ε_{Nd} value do not co-vary in core

PS58/254 (Figure 4.2), indicating that smectite contents have little impact on the overall Nd isotopic compositions. Neodymium isotopic compositions of the mud fraction (combined clay and silt fractions) indicate a proximal source, meaning that the overall mud is not as far-travelled as the smectite minerals.

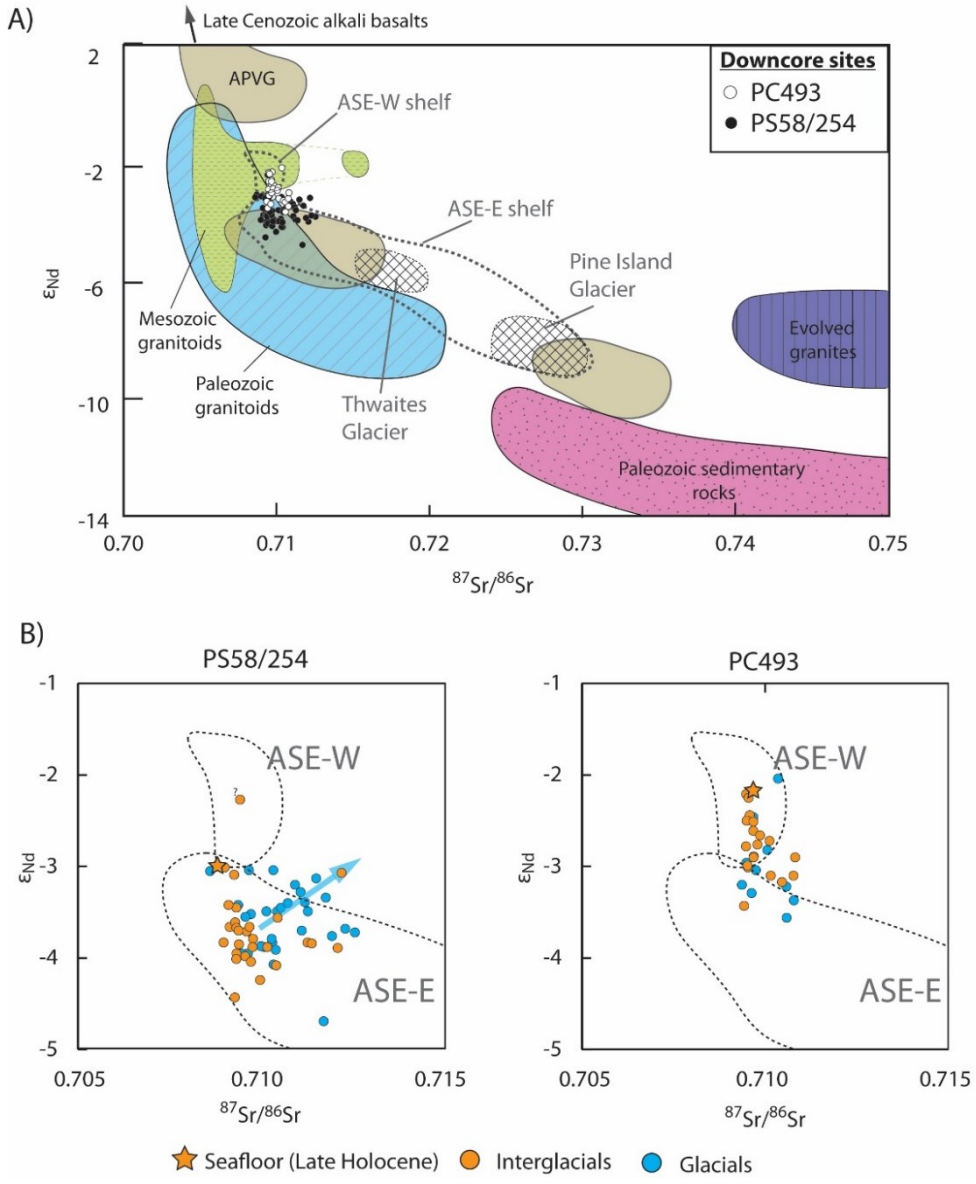

Figure 4.5. (a) Strontium and neodymium isotopic compositions of detrital fine-grained (<63µm) sediments from site PS58/254 (black circles) and PC493 (white circles). The Sr and Nd isotopic composition of major bedrock outcrops is based on Simões Pereira et al., 2018 and references therein (cf. Pankhurst et al. 1993, Riley et al., 2003, 2010, 2017, Korhonen et al., 2010), and colour is matched with geological units in Figure 4.1. Thick dotted lines outline the

(caption continues on next page)

Figure 4.5. (*continued*) composition represent the overall fine-grained detrital sediments from the eastern Amundsen Sea Embayment (ASE-E) and the western Amundsen Sea Embayment (taken from Chapter 2; i.e. Simões Pereira et al., 2018). Hashed fields represent the Sr and Nd provenance signature of detrital <63μm shelf surface sediments proximal to Pine Island Glacier (cf. inner Pine Island Bay; Chapter 3) and Thwaites Glacier (cf. outer Pine Island Bay); (b) Glacial (blue) and interglacial (orange) Sr and Nd isotope fingerprint of fine-grained detrital sediments from core site PS58/254 (left) and PC493 (right). Blue arrow denotes a trend for sediments deposited during glacial stages to plot outside the modern shelf sediment fingerprint at site PS58/254.

During glacial period, subglacial debris is transported to the shelf break at the base of grounded ice streams advancing through Pine Island Trough and Dotson-Getz Trough (e.g. Larter et al., 2014; Dowdeswell et al., 2006). As in other parts of the Antarctic continental margin (e.g. Grobe and Mackensen 1992; Pudsey and Camerlenghi, 1998; Hillenbrand et al., 2002), the high accumulation of this unsorted debris at the shelf break triggered gravitational downslope transport processes, such as turbidity currents. Similar to drift sediments on the western Antarctic Peninsula continental rise (e.g. Rebesco et al., 1996; Pudsey 2000; Lucchi et al., 2002; Hillenbrand and Ehrmann, 2002), the fine-grained suspended load of the turbidity currents would have been captured, transported eastwards and deposited on the drifts by a bottom current (Nitsche et al., 2000; Dowdeswell et al., 2006; Uenzelmann-Neben and Gohl, 2012). Together with meltwater plumites that might have reached the rise drifts directly, bottom current deposition would have controlled sedimentation at site PS58/254, explaining the silty-clayey composition of its glacial sediments (Hillenbrand et al., 2009a). The Sr and Nd isotope signatures of glacial samples in core PS58/254 do, however, not all plot within the field of the observed surface sample signatures from the ASE shelf. Notably, the range in ε_{Nd} values is similar to interglacial samples, but $^{87}Sr/^{86}Sr$ ratios are elevated (Figure 4.5). $^{87}Sr/^{86}Sr$ ratios in turn co-vary with kaolinite content (r^2=0.6), but show no covariation with clay contents (Appendix Figure 4.3). These correlations suggest that the Sr isotope ratio is controlled by provenance (e.g. Eisenhauer et al., 1999; Tütken et al., 2002) or weathering (e.g. Blum and Erel, 1995) rather than by a grain-size effect. Hillenbrand et al. (2009a) argued that kaolinite is primarily supplied by glacial erosion of sedimentary strata in the upstream parts of the drainage basins of Pine Island and Thwaites Glaciers (i.e. Bentley Subglacial Trench and/or Byrd Subglacial Basin, Figure 4.1) during both, glacials and interglacials. During glacial times

when the WAIS grounding line advanced closer to the shelf break, thereby eroding the underlying shelf sediments, the kaolinite supply to the rise increased (Hillenbrand et al., 2009a) and was accompanied by sediments carrying a higher $^{87}Sr/^{86}Sr$ ratio. Dipping sedimentary strata on the ASE shelf below the Last Glacial Maximum to Late Holocene sediment cover were detected by shipborne geophysical observations (Wellner et al., 2001; Lowe and Anderson, 2002, 2003; Graham et al., 2009; Gohl et al., 2013) and recovered by shallow drilling on the shelf (Gohl et al., 2017). Similar to dipping strata on the Bellingshausen Sea shelf (Hillenbrand et al., 2009b), these older strata may well have a provenance signature different from the modern sources to the subglacial detritus. Mega-scale glacial lineations indicate that fast ice flow occurred on the middle and outer shelf sections of Pine Island-Thwaites Trough above the sedimentary strata (e.g. Wellner et al., 2001; Graham et al., 2010; Jakobsson et al, 2011), indicating fast flowing warm-based ice with higher rates of subglacial erosion. Future studies on the sediment drill cores collected during RV Polarstern cruise PS104 in 2017, which were not yet studied for their clay mineral content and isotopic fingerprint, may provide further support for a shelf-derived provenance of glacial sediments at site PS58/254.

While interglacial sediment transport processes to site PC493 would have been similar to those affecting site PS58/254, glacial-time turbidity currents are likely to have by-passed this slope site due to its position on a seamount (Hillenbrand et al., 2002; Lu et al, 2016). Thus pelagic settling probably dominated both interglacial and glacial deposition at site PC493, possibly with some meltwater plumite deposition during glacials. Site PC493 is located offshore from the Dotson-Getz Trough in the western ASE. As for PS58/254, the majority of detrital Sr and Nd signatures match the provenance of shelf sediments, but in this case the modern and Late Holocene sediments on the western ASE shelf (Figure 4.5). This match can be interpreted as indicating direct detritus supply from the Dotson-Getz Coast to the seamount, during glacial and interglacial stages. Modern sediments in the Dotson-Getz Trough are characterized by relatively uniform Sr-Nd isotope values (Figure 4.5), which overall indicates erosion of relatively similar source rocks composed of Cretaceous to Palaeozoic granitoids (Figure 4.1). The gradual increase in the Nd isotopic composition of detrital sediments at site PC493 over time may either be due to a slight change in the area of subglacial erosion in the WAIS hinterland (e.g. increasing subglacial volcanism or gradual erosion of a non-volcanic province so that its surface decreased), or by a decrease in deposition of fine-grained sediments supplied from the eastern ASE by icebergs drifting westward with the Antarctic coastal current.

4.5.2. Sources for iceberg-rafted sediments over glacial-interglacial cycles

Hornblende and biotite grains picked from the same sample in core PS58/254 record similar age patterns (Figure 4.3). Although small differences in age peaks between hornblende and biotite $^{40}Ar/^{39}Ar$ age populations have been observed for the modern/Late Holocene sediments from the ASE shelf (up to ~10 Ma; see Chapter 2), overall grain numbers in the samples of core PS58/254 are too low to resolve these differences. Furthermore, magmatic intrusions of igneous rocks into the continental crust occurred over a time span of <10 Ma during the Cretaceous (Riley et al., 2018) and Triassic (Pankhurst et al., 1993), which is significantly lower than the overall age range of our samples.

The coastal hinterland of the Amundsen Sea is composed of large calc-alkaline granite, granodiorite and syenogranite intrusive bodies that were intruded as part of the active margin of Gondwana from the Permian to Cretaceous times (~80-150 Ma and 220-290 Ma; U-Pb zircon, K-Ar and $^{40}Ar/^{39}Ar$ hornblende, biotite, muscovite, whole rock ages; Pankhurst et al., 1993, 1998; Mukasa and Dalziel, 2000; Kipf et al., 2012; Craddock et al., 2017), as well as Late Oligocene to Pleistocene, mainly alkali basaltic volcanoes that bulge out of the ice surface (e.g. LeMasurier, 1990; LeMasurier and Rex, 1991; Hart et al., 1997; Rocchi et al., 2006). The majority of hornblende and biotite grains in cores PS58/254 and PC493 have $^{40}Ar/^{39}Ar$ cooling ages that match the geology of the nearby coastal regions (Figure 4.6, 4.7), documenting the igneous history of West Antarctica in the Amundsen Sea sector. In general, geochronological investigation from the onshore outcrops display a notorious gap in 150-200 Ma ages using various dating methods. The offshore record from the shelf and continental rise and slope clearly contains hornblende and biotite grains of such ages, hence attesting that rocks with such cooling ages exist in the hinterland, particularly in the eastern Amundsen Sea coast (Figure 4.6). This in turn suggests a general sample bias in the onshore record (i.e. such rocks have not been sampled and dated yet) or presence of such outcrops solely below the ice margin.

Interestingly, interglacial sediments at site PS58/254 contain a significant amount of grains younger <80 Ma when compared to glacial samples from the same site and glacial and interglacial samples in the PC493 record. Extensive Late Cenozoic alkali basalts crop out in the Amundsen Sea sector (LeMasurier, 1990; LeMasurier and Rex, 1991; Hart et al., 1997), while early Cenozoic igneous rocks (~50 Ma U-Pb zircon; Mukasa and Dalziel, 2000) were identified in Pine Island Bay (Figure 4.8). At a first glance, IRD transport from these sources to site PS58/254 seems unlikely because most of the rocks described from the former locations

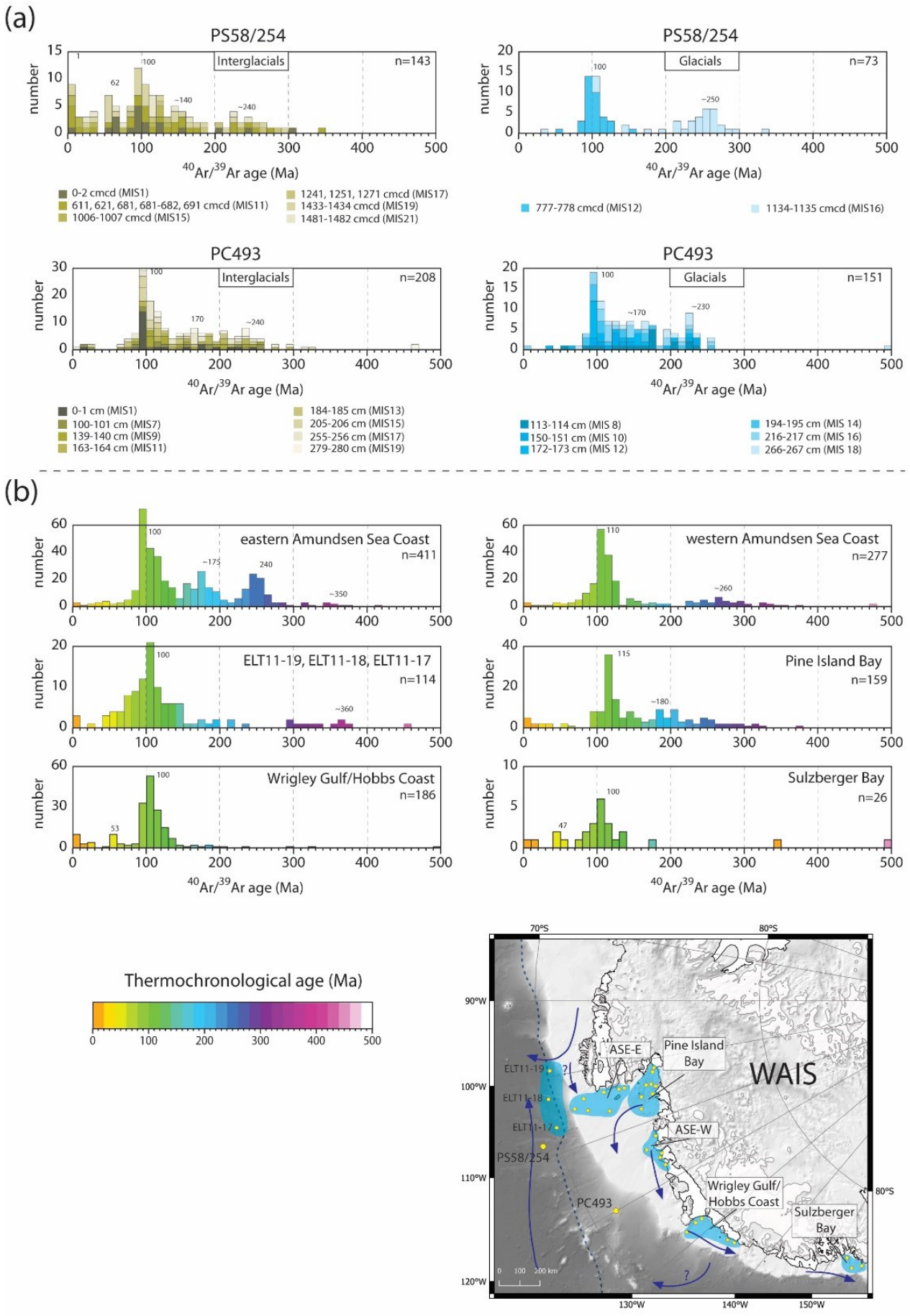

(caption on next page)

Figure 4.6. (*continued*) (a) Stacked histograms of $^{40}Ar/^{39}Ar$ hornblende and biotite (combined) age populations of interglacial (left) and glacial (right) samples of PS58/254 (upper row) and PC493 (lower row), including previously measured surface samples (Simões Pereira et al., 2018). Note that a higher number of <80 Ma grains occurs in interglacial samples of core PS58/254 and that glacial stages are better defined in their age peaks than interglacials; (b) histograms of ice-rafted (>150µm) $^{40}Ar/^{39}Ar$ hornblende and biotite (combined) ages populations from surface samples on various offshore sectors (blue field in map) off West Antarctica (cf. Chapter 2 and Chapter 3; includes data from Roy et al., 2007). Blue arrow denotes major surface currents as in Figure 4.1 inlet. Colour of histograms is to match with colour bar in Figure 4.8.

---

are mafic volcanic rocks and thus usually do not contain large amounts of hornblende or biotite minerals. Grains <80 Ma are rare in the ASE shelf sediments proximal to the latter source (Figure 4.6). However, up to 10% of the Late Cenozoic volcanic rocks consist of felsic rocks (LeMasurier et al., 2011), including rhyolites and rhyodacites (Rocchi et al., 2006), which could have supplied biotite grains <80 Ma. Age populations of IRD in surface samples from shelf sediments in Wrigley Gulf, along the Hobbs Coast and in Sulzberger Bay, showed a secondary peak <50 Ma (Figure 4.6; Simões Pereira et al., 2018), which could indicate supply of biotite and hornblende grains from an unknown granitic-dioritic source inland of the Getz Ice Shelf (Spiegel et al., 2016) or from such felsic volcanic rocks. Core-top sediments at other continental rise drift sites proximal to site PS58/254 (ELT11-17, ELT11-18, ELT11-19, Figure 4.6) also contain a significant amount of grains <80 Ma old (~15 %), in addition to a major hornblende and biotite age peak at 100 Ma and a minor age peak at ~360 Ma. The latter age peak is mostly observed at site ELT11-19, which is situated at the southern boundary of the ACC (Figure 4.6). Hence, the potential source for these ~360 Ma grains originate from the eastern Thurston Island (Mount Feury gabbro, K-Ar hornblende age of ~330 Ma; Pankhurst et al., 1993), which then are carried to site ELT11-19 by westward flowing icebergs. The remaining two Eltanin core sites and site PS58/254 lie within the ACC. Most of the icebergs calved along the Amundsen Sea coast drift westwards with the coastal current but are then injected into the eastward flowing ACC in the westernmost Amundsen Sea and the eastern Ross Sea (Gladstone et al., 2001; Tournadre et al., 2016). Thus, site PS58/254 and the Eltanin core sites are likely to be affected by deposition of IRD sourced from the Amundsen Sea coast, and from the Wrigley Gulf-Hobbs Coast and/or Sulzberger Bay.

Grains from glacial and interglacial samples at site PC493 originate from the eastern ASE coast, as we observe significant amounts of grains with ages from 180-220 Ma in glacial and interglacial samples that match the age population of IRD in shelf sediments from the eastern ASE (Figs. 4.6, 4.7), indicating supply of icebergs sourced there via the Antarctic coastal current. In contrast, ice proximal samples in the western ASE, as well as from the Wrigley Gulf-Hobbs Coast and Sulzberger Bay, lack this peak in their age population. During glacial times, grounded ice advanced periodically to the shelf break. Ice streams originating from the western Amundsen Sea coast flowed along the Dotson-Getz Trough (Graham et al., 2009; Smith et al., 2011; Larter et al., 2014), carrying glacially eroded detritus from the hinterland of the Dotson Ice Shelf and the eastern parts of the Getz Ice shelf to near the shelf break. We would therefore expect fewer (or a negligible number of) hornblende and biotite grains with ages from ~180-220 Ma and more grains with ages of ~110 Ma in glacial samples of core PC493. The glacial IRD record at site PC493, however, does not support this hypothesis. Overall, the stacked glacial age population of core PC493 shows similarities with that of Late Holocene IRD on the eastern ASE shelf. There, the Pine Island-Thwaites and the Cosgrove-Abbot palaeo-ice streams advanced to the outer shelf during past glacial periods (Gohl et al., 2013; Hochmuth and Gohl, 2013; Larter et al., 2014; Klages et al. 2015), transporting subglacial detritus to the ice stream front, from where calved icebergs drifting in the coastal current transported this IRD to site PC493 (Figure 4.8). The fact that the glacial IRD signature at site PC493 is dominated by an eastern ASE provenance rather than a western ASE provenance shows that during past glacial periods the Pine Island-Thwaites palaeo-ice stream was a more important outlet for the WAIS than the Dotson-Getz palaeo ice stream. This is in agreement with LGM models (e.g. Golledge et al., 2012) that also predict a much higher glacial sediment supply in the eastern than in the western ASE (Golledge et al., 2013).

4.6. Paleoenvironmental significance of the detrital provenance signature

4.6.1. Eccentricity modulated ice sheet changes during the Late Pleistocene

The Nd and especially the Sr isotope record from site PS58/254 shows low-frequency oscillations that broadly relate to eccentricity-paced orbital changes (Figure 4.7). Furthermore, we observe that high-frequency fluctuations in magnetic susceptibility in this core are in pace with precession, while higher amplitude and low-frequency changes are aligned with eccentricity. Magnetic susceptibility of marine sediments is dependent on the concentration

and grain-size of ferrimagnetic minerals (mostly fine-grained magnetite; Frederichs et al., 1999; Liu et al., 2012), which, in turn, is a function of terrigenous source composition and dilution by biogenic material (e.g. Pudsey and Howe, 1998). Data for core PS58/254 showed not only that high magnetic susceptibility values during glacials coincide with coarser magnetic grain size, whilst interglacials are characterised by low magnetic susceptibility and low magnetic grain size, but also that the concentration of magnetic minerals in this core reflects sediment provenance (Hillenbrand et al., 2009a). Sediments from site PC493 show a more muted signal, as observed in the ε_{Nd} values, but the $^{87}Sr/^{86}Sr$ signal of this core correlates with the $^{87}Sr/^{86}Sr$ record of PS58/254 at least for the last 800 ka. Given that site PC493 is located on a seamount and that provenance is not influence by deep oceanic current, correlation between the $^{87}Sr/^{86}Sr$ records at both sites indicates that provenance relates to shelf processes and hence mirrors changes in the terrigenous sediment supply in relation to the waxing and waning of the WAIS.

Recent numerical simulation with transient climate forcing show that those drivers fluctuated with period of about 100,000 yrs over the last 800,000 yrs (Tigchelaar et al., 2018). However, precession-paced changes in local insolation further forced additional mass loss (i.e. ice retreat) during periods of high sea level and CO_2. This precessional-phasing could derive from a weak precessional component in atmospheric CO_2, which is the major driver of Antarctic temperatures (Timmerman et al., 2014). Northern Hemisphere summer insolation forcing to the northern ice sheets further contributes to the precessional component in the global sea level forcing. In the marine realm, obliquity generally dominated the global benthic $\delta^{18}O$ record (Raymo and Nisancioglu, 2003; Lisiecki and Raymo, 2005; Elderfield et al., 2012). Raymo et al. (2006) proposed that the anti-phased hemispheric influence of the precession cycle on glacial melt is cancelled out in globally averaged marine records (i.e. ocean $\delta^{18}O$, sea-level), leaving behind the signal of the in-phase obliquity. On East Antarctica, Late Pliocene (i.e. 3.5 to 2.5 Ma) sediments at site U1361, offshore of the marine-based portion of the East Antarctic ice sheet that is located above the Wilkes Subglacial Basin, show that the rate of accumulation of iceberg-rafted debris vary with eccentricity and precession (Patterson et al., 2014). The authors suggested that the duration of the melt season and the development of extensive sea-ice fields after ~3.5 Ma, which caused northward migration of westerly winds and ocean fronts, was modulated by precession-paced austral summer insolation maximal. Larger sea-ice cover limited the influence of upwelling CDW at the East Antarctic ice margin, hence reducing its grounding line instability.

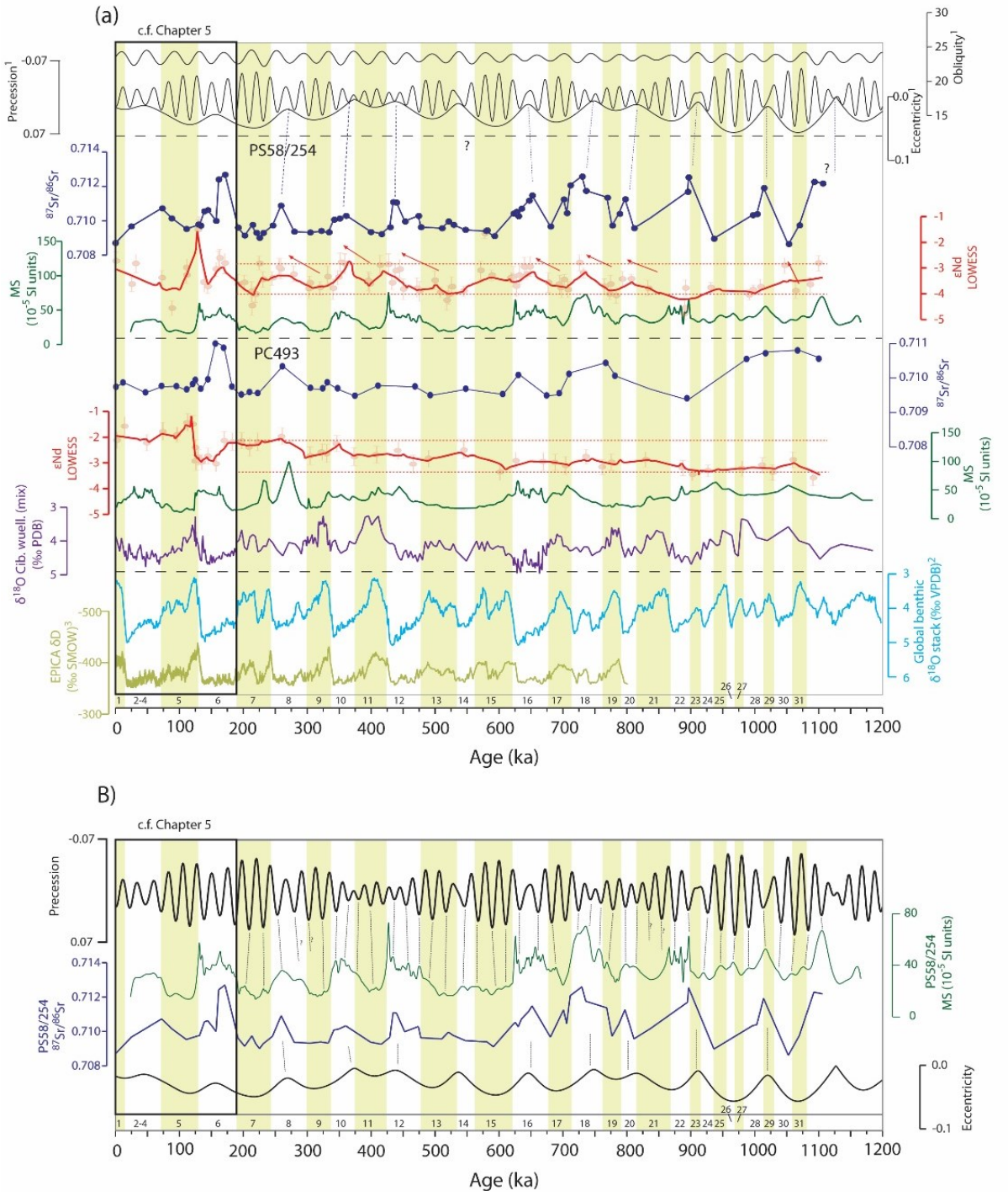

Figure 4.7. (a) Downcore record of sediments from PS58/254 and PC493 (taken from Figure 4.2). The neodymium isotope record is displayed using a LOWESS (locally weighted regression and smoothing scatter plots) smoothing function, with the actual values shown in background. Orbital parameters are from [1]Laskar et al., 2004. Global benthic $\delta^{18}O$ stack is from [2]Lisiecki and Raymo (2005), and EPICA dome deuterium (δD) profile is from [3]Jouzel et al. (2007); (b) eccentricity-paced fluctuation of the $^{87}Sr/^{86}Sr$ detrital <63µm record of core PS58/254, as well as precession-paced fluctuations of magnetic susceptibility records (circled numbers represent Marine Isotope Stages).

Overall, our data supports that the WAIS evolved with eccentricity and precession-paced changes in the orbital forcing during the Late Pleistocene and provides further support for previous numerical models and geological observation off East Antarctica (Tigchelaar et al., 2018; Patterson et al., 2014), although the latter record is for the Late Pliocene. It is possible the Antarctic ice sheets may have evolved altogether with a period of ~100'000 yrs and 23'000 yrs since the Late Pliocene (i.e. our data and Patterson et al., 2014). Prior to this date, marine geological evidence from the Ross Sea suggests that obliquity was the major forcing for WAIS oscillations during the Pliocene (Naish et al., 2009), which is consistent with numerical models that shows 41 ky-paced cyclic WAIS fluctuations (Pollard and DeConto, 2009, 2012; DeConto and Pollard, 2016).

4.6.2. Implication for West Antarctic Ice Sheet stability during the Late Pleistocene

Throughout the Late Pleistocene (0.2 Ma to 1.1 Ma), we do not observe any prominent provenance anomaly at sites PS58/254 and PC493 that could indicate a major drawdown of the WAIS. The IRD record at site PC493 does not display any significant change in the provenance over the past ~800'000 yrs, with glacial and interglacial samples showing similar $^{40}Ar/^{39}Ar$ age population. This IRD record at site PS58/254 shows a similar $^{40}Ar/^{39}Ar$ age pattern as for site PC493 for grains older than 80 Ma. Both indicate that IRD originate from the eastern Amundsen Sea coast, with iceberg originating from this sector being carried by the westward coast current to site PC493, before being injected into the ACC and further transported to site PS58/254. The younger <80 Ma grains have their source in the Wrigley Gulf-Hobbs Coast and/or Sulzberger Bay sector. A major disintegration of the West Antarctic Ice Sheet is believed to result in higher iceberg calving (i.e. IRD supply) (e.g. MacAyeal 1992). Under warming conditions and pronounced ice sheet retreat, ice sheets are capable of releasing "armadas" of debris-laden icebergs that can travel up to 2000 km and deliver IRD from specific source areas to the marine realm (e.g. Hemming, 2004; Williams et al., 2010; Cook et al., 2014). Such icebergs should eventually pass through site PC493 before being injected into the ACC to then be subsequently carried through site PS58/254. The sites studied by us have relatively low sedimentation rates (~2 and 0.3 cm/ka), yet do not document high (accumulation rates of) gravel and lithogenic material (Figure 4.2). Furthermore, we would expect IRD from destabilizing ice drainages to overwhelm, or at least alter, the background IRD signature of glacial-interglacial periods during times of rapid retreat. Our downcore data here does not

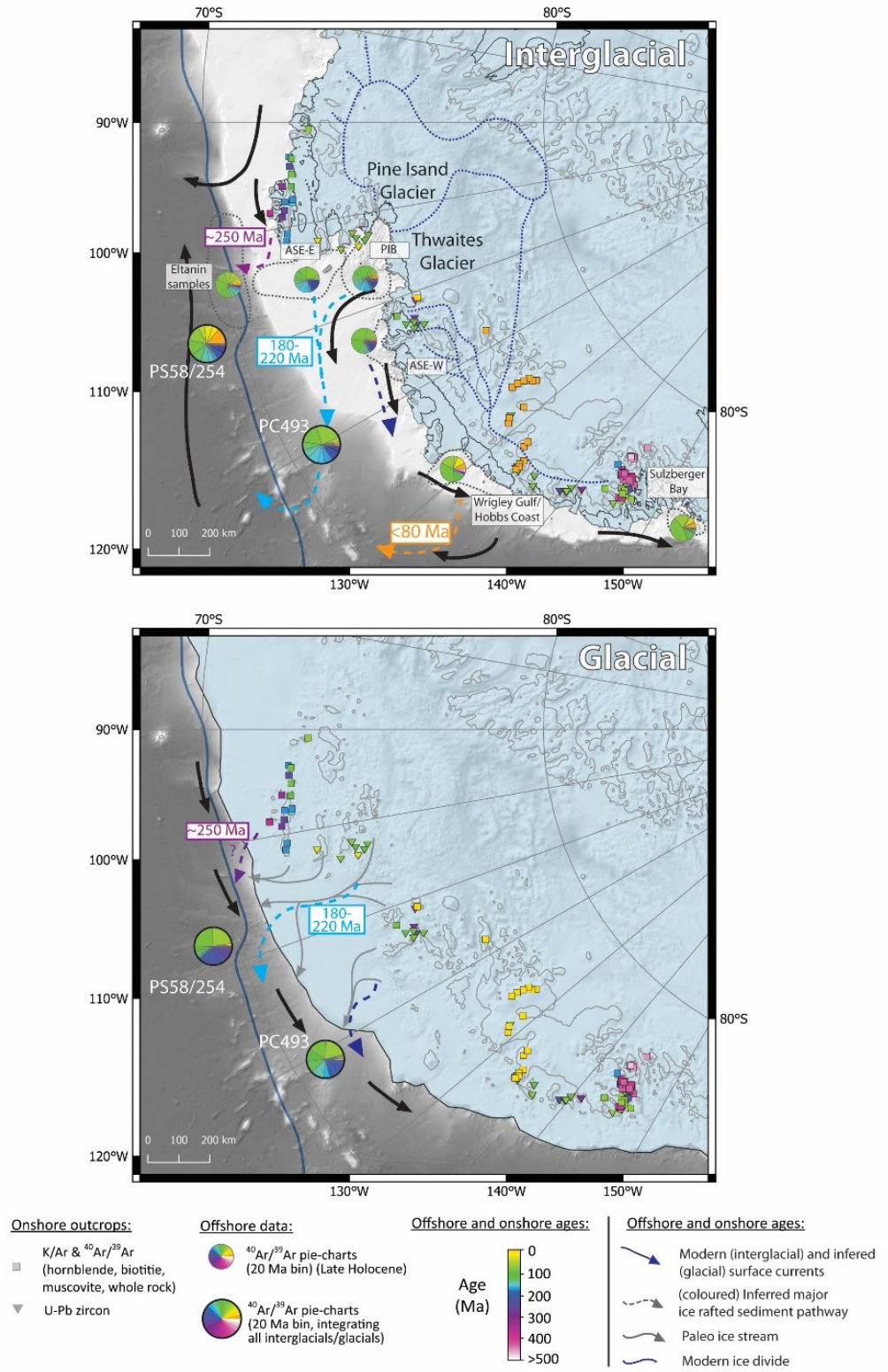

Figure 4.8. Distribution of thermochronological ages in offshore sediments and terrestrial outcrops of West Antarctica (cf. taken from Chapter 2; cf. Appendix Table 2.2; Simões Pereira et al., 2018). $^{40}Ar/^{39}Ar$ ages of ice-rafted hornblende and biotite grains are presented as pie charts in 20 Ma increments. Small pie charts correspond to the age distribution of hornblende and biotite picked from ice-rafted surface sediments on various sectors around West

(caption on next page)

Figure 4.8. (*continued*) West Antarctica (cf. Figure 4.6). Larger pie charts (with black contour) indicate the age distribution of stacked interglacial (upper map) and glacial (lower map) samples of cores PS58/254 and PC493. Outcrop ages are displayed with different symbols depending on the type of mineral and the method applied. Blue shading represent modern ice extent and ice extent and ice extent during the Last Glacial Maximum (Larter et al., 2014). Blue line in the offshore represent the southern boundary of the Antarctic Circumpolar Current. Coloured dashed arrows denote major ice-rafted debris transport pathways. Black arrows denote major modern (cf. Figure 4.1 inlet) and glacial (cf. see text) surface currents. Abbreviation - ASE-E: eastern Amundsen Sea Embayment; ASE-W: western Amundsen Sea Embayment; PIB: Pine Island Bay.

---

suggest any large perturbation in the IRD signal from a prominent source from the Pine Island and Thwaites Glaciers, i.e. absence of <115 Ma (except ~35 Ma), significant ages of ~115 Ma and large population of 180-260 Ma (Figure 4.6; cf. Chapter 3). Further investigation on a larger number of mineral grains for individual glacial-interglacial stages would, however, be advantageous to provide a stronger support for the previous statement.

Even in the case where IRD does not represent an unequivocal proxy for collapse (Hillenbrand et al., 2009a), we would still expect a pronounced shift in the provenance signature of fine-grained sediments. Previous studies have shown that major retreat of marine-based portions of the Laurentide and East Antarctic ice sheets were readily detected by a distinct provenance fingerprint in fine-grained detrital sediments (and IRD) deposited offshore (Hemming, 2004; Cook et al., 2013). In Chapter 3, we have shown that the geochemical fingerprint of the Thwaites Glacier (ε_{Nd} ~-4; $^{87}Sr/^{86}Sr$ ~0.714), and particularly of the Pine Island Glacier (ε_{Nd} ~-9; $^{87}Sr/^{86}Sr$ ~0.728), is significantly different from the surrounding sectors along the Amundsen Sea coast (e.g. Figure 4.5, 4.6; see Chapter 3). Hence, if a similar destabilization process has occurred for the WAIS as for the East Antarctic Ice Sheet (Cook et al., 2013), we should expect a prominent shift in the provenance in our sediment records caused by (even minor) sediment supply from the destabilizing Pine Island Glacier and/or Thwaites Glacier. In addition, ice retreats are characterized by large meltwater pulses (e.g. Weaver et al., 2003; Golledge et al., 2014) such that sediment delivery is further supplied over larger distances. Even in the case where subglacial geology below the modern Pine Island and Thwaites Glaciers remains (geochemically) uniform, ice retreat over these basins and increase in meltwater supply over these sectors is expected to deliver sediments from destabilizing

sectors with (at least) a "modern" signature to the offshore. We would hence expect a provenance anomaly in our sediment records characterized by (much) lower ε_{Nd} values and (much) higher $^{87}Sr/^{86}Sr$ ratios. Although unpinning of the WAIS inhibits the erosive capacity over the over the Pine Island and Thwaites Glaciers basins, grounding line retreat and subsequent increase in meltwater, and hence that should cause should cause a change in the isotopic composition. Unpinning from bedrock would only create a shift in provenance towards proximal sources. Although our Sr isotope record at both sites show cyclic fluctuations consistent with orbital forcing and global climatic oscillations, we do not observe any specific age interval in the two cores with an exceptional or distinct Sr and Nd isotopic provenance and/or $^{40}Ar/^{39}Ar$ age signature from 1.1 Ma to 0.2 Ma that would indicate a major provenance change.

Our data indicates, however, that a particular warm period extended the entire interval from MIS 15 to MIS 13, confirming the previous finding of Hillenbrand et al. (2009a). The $^{87}Sr/^{86}Sr$ signal at both sites, but particularly at site PS58/254, is characterized by the absence of an $^{87}Sr/^{86}Sr$ glacial (i.e. MIS 14) peak. In addition, other proxies, such as magnetic susceptibility, biological productivity proxy and clay mineral provenance data all indicate that glacial MIS 14 was more similar to an interglacial than a glacial. During MIS 14, Antarctic air temperature were ~1°C warmer than today and CO_2 slightly higher than at any other glacial stage of the last 800 kyr (Siegenthaler et al., 2005; Jouzel et al., 2007), making it one of the warmest glacial periods of the Late Pleistocene. Unequivocal evidence for a large retreat or collapse during this period is, however, not supported by our data.

The hypothesis that the WAIS remained relatively stable over the past 800'000 years was already formulated by Hillenbrand et al. (2002) based on the sedimentary record at site PS2547. More recently, the numerical simulation using a transient climate model by Tigchelaar et al (2018) did not reproduce a partial or collapse of the WAIS for the past ~800'000 years, except when applying unrealistically large (+4°C) subsurface ocean warming. These results oppose previous findings of several models and data-based investigation, which suggest that the WAIS collapsed at least once during the last 800'000 years and should have produced an armada of icebergs (MacAyeal, 1992; Scherer et al., 1998; Pollard and DeConto, 2009). Several scenarios could explain the absence of a significant IRD and/or fine-grained layer with a predominant provenance signal matching that of the Pine Island and Thwaites Glaciers in PC493 and PS58/254, or a provenance signal indicating higher supply from an East Antarctic source. An explanation for the lack of higher amounts of East Antarctic IRD is that the Trans-

Antarctic seaways that opened up in response to a total WAIS collapse (Vaughan et al., 2011) remained covered by ice shelves as it is suggested by the model results of MacAyeal (1992). This would have prevented icebergs calved from the EAIS to drift into the Amundsen Sea. An explanation for the lack of IRD evidence for a significant WAIS retreat is that higher sea-surface temperature in the Amundsen Sea during a warm interglacial could cause melting of most debris-laden icebergs over the shelf and before reaching site PC493 (cf. Hillenbrand et al., 2009a). This scenario is, however, unlikely, as even under a sea-surface warming of 8°C, icebergs were apparently able to transport IRD over a distance of several 100s of kilometres from their sources (Cook et al., 2014). Overall, our data provide support for a stable WAIS from 1.1 Ma to 0.2 Ma, adding to the findings of previous model and data-driven studies on the WAIS (Hillenbrand et al., 2002; Tigchelaar et al., 2018). This conclusion however implies that mass loss from the WAIS did not significantly contribute to global sea-level rise over this time period. A fundamental question that remains unanswered is which areas contributed to late Pleistocene sea-level highstands, as observed for example in Western Australia with 5-9 m of eustatic sea-level during MIS 11 (O'Leary et al., 2013). A recent study by Wilson et al. (2018) showed that the East Antarctic Ice Sheet may have been more vulnerable and susceptible to significant ice loss during the late Pleistocene than previously thought. Sedimentary provenance analysis in a sediment core proximal to the marine-based Wilkes Land Basin using Sr and Nd isotope fingerprints showed that the ice margin retreated towards the interior of the continent, causing up to 4 m sea-level equivalent. This study highlights the possibility that sectors of the Antarctic Ice Sheet other than the WAIS may have played a significant role in sea-level fluctuations during the late Pleistocene.

4.7. Conclusions

The Sr and Nd isotopic fingerprint of fine-grained sediments of Pleistocene sequences (1.1 to 0.2 Ma) at sites PS58/254 and PC493 reveals sediment supply that agrees with the signature of modern sediments on the Amundsen Sea shelf. Both cores record a narrow range of ε_{Nd} values and $^{87}Sr/^{86}Sr$ ratios that can be readily correlated to bedrock sources in the nearby Amundsen Sea sector. Similarly, the $^{40}Ar/^{39}Ar$ dates on iceberg-rafted hornblende and biotite grains in glacial and interglacial samples are characterized by distinct ages of ~160-220 Ma that allow to identify their source as the eastern ASE coast. We observe a distinct IRD

provenance in interglacial samples from core PS58/254, where grains recording young (<80 Ma) cooling ages that are probably sourced from an unknown granitic-dioritic source under the Getz Ice Shelf and/or felsic volcanic rocks in the hinterland of Wrigley Gulf-Hobbs Coast and Sulzberger Bay.

The $^{87}Sr/^{86}Sr$ record in core PS58/254 shows cyclic variations that broadly correlate with eccentricity over the last 1.1 Ma. Changes in the magnetic susceptibility, which is considered a proxy for provenance, show minor precession-paced fluctuations together with a dominant eccentricity-influence. These results may open up the possibility to study the impact of orbital forcing on WAIS dynamics (i.e. advance and retreat) in more detail, which is a prerequisite for improving the reliability of ice sheet models.

Overall, relatively uniform Sr and Nd isotope values in the fine-grained sediments of the studied cores, as well as similar glacial-interglacial $^{40}Ar/^{39}Ar$ age populations of the iceberg-rafted hornblende and biotite grains indicate that no major changes in the sediment supply occurred between 1.1 and 0.2 Ma. If Thwaites and Pine Island glacier indeed carry a characteristic fingerprint that deviates from modern shelf sediments, the new record has to be interpreted as a lack of evidence of major destabilization of the Pine Island and Thwaites Glaciers. Our data hence provide a strong case for a stable WAIS during the Late Pleistocene.

Statement of Contribution

The work presented here was part of a collaborative effort to which the author, Tina van de Flierdt (Imperial College, UK) and Claus-Dieter Hillenbrand (BAS, UK) contributed to the initial idea. Carys P. Cook and Tina van de Flierdt provided some of the neodymium isotope data. Claus-Dieter Hillenbrand provided some of the data for PC493 (i.e. gravel counts, $CaCO_3$, magnetic susceptibility, Ba/Ti, stable isotope data). Clay content of PS58/254 were measured by Gerhard Kuhn. Sidney R. Hemming (L-DEO, Columbia University, US) conducted the $^{40}Ar/^{39}Ar$ measurements on hornblende and biotite minerals. Tom Williams (University of Cambridge, UK) provided the age model for core PC493.

Chapter 5

West Antarctic Ice Sheet retreat during Termination II revealed by isotopic provenance analysis of marine detrital sediments from the Amundsen Sea

Chapter Summary

Analysis of the isotopic provenance of fine-grained detrital (<63μm) sediments and iceberg-rafted debris (IRD, >150μm) can provide valuable information about past deglaciations on Antarctica. Marine Isotope Stage (MIS) 5e, which represents the last interglacial period (~130-116 ka), when global temperatures were between 0°C and 2°C warmer than today (Hoffman et al., 2017), in particular is suggested to have experienced major retreat of the West Antarctic Ice Sheet (WAIS) margin or even total WAIS collapse, leading to elevated global sea-level.

In this chapter, I investigate the provenance of sediments deposited at sites PS58/254 and PC493 in the Amundsen Sea since the penultimate glaciation during MIS 6 (~191-130 ka). Comparison of $^{40}Ar/^{39}Ar$ ages of iceberg-rafted hornblende and biotite grains deposited at the two core sites with onshore thermochronology and ages of IRD grains in Late Holocene to modern seafloor sediments deposited proximal to the Amundsen Sea coast allows to interpret our results in terms of glacial-interglacial fluctuations of the position of the westerlies, which caused a directional change in surface currents above the sites. During the penultimate glaciation, surface currents carried icebergs with an IRD load with an easterly provenance (i.e. eastern Thurston Island) to site PS58/254, while during the last and present Interglacial and surface currents carried detritus-laden icebergs with a westerly source (i.e. Wrigley Gulf-Hobbs Coast) to this site. In contrast, Site PC493 was continuously situated beneath westward-flowing surface currents since at least ~191 ka.

Both cores share many similarities in the strontium (Sr) and neodymium (Nd) isotope fingerprint of fine-grained sediments. Overall, our data show a strong decoupling between the strontium and neodymium isotope records of fine-grained detritus, with maxima in $^{87}Sr/^{86}Sr$ ratios during the penultimate glaciation (~ 165 ka), and pronounced shifts towards higher $^{143}Nd/^{144}Nd$ ratios around Termination II (~130-125 ka). Strontium isotope peaks are interpreted to represent erosion of sedimentary strata on the Amundsen Sea shelf during glacial advance, which is suggested to carry a much more distinctive (higher) Sr isotope ratio than for Nd in comparison with the signature of local source rocks. Abrupt excursions in Nd isotopic compositions are interpreted to represent a decrease (or even cessation) in sediment supply from the Pine Island Glacier and Thwaites Glacier basins, resulting in a loss of the characteristic fingerprints in the offshore sediments, arguing hence for large grounding line retreat towards the interior of, or even "ungrounding" of the base of the WAIS from these ice drainage basins.

Comparison with downcore data for the past 800 kyrs at both core sites supports that the last interglacial is the period to have experienced the largest reduction in WAIS extent of the entire late Pleistocene. Although the exact magnitude of WAIS retreat remains unresolved, our data here provide evidence for the largest retreat of the grounding line in the Amundsen Sea sector of the late Pleistocene having occurred during MIS 5e.

5.1. Introduction

The low-lying largely marine-based WAIS is sensitive to oceanographic and atmospheric warming, and is assumed to have undergone partial or total collapse in the past (e.g. Pollard and DeConto, 2009, 2012; Joughin and Alley, 2011; Dutton et al., 2015; Pollard et al., 2015; DeConto and Pollard, 2016). Numerous lines of indirect evidence suggest that major deglaciation of the WAIS occurred during the late Pleistocene (cf. Chapter 4), particularly during Marine Isotope Stage (MIS) 5e (~130-116 ka; i.e. the Last Interglacial (LIG), which corresponds to the Eemian in Europe or Sangamonian in North America; e.g. Lisiecki and Raymo, 2005). A probabilistic assessment of the MIS 5e sea-level highstand found, with 95% of confidence, that global sea-level was at least 6.6 m higher than today and that the ice sheets at both poles contributed at least 2.5 m of equivalent sea-level rise (ESL), although timing of melting between both polar ice sheets may differ (Kopp et al., 2009; cf. Dutton et al., 2015). Ice core data and simulation suggests that melting of the Greenland ice sheet led to ~2 meters of ESL (NEEM community members, 2013), implying that Antarctic Ice Sheets must have contributed significantly to MIS 5e sea-level rise, but this number has recently been challenge to be higher (~5 meters; Yau et al., 2016). The exact contribution and locations of Antarctic ice sheet melting are uncertain, but several authors inferred a contribution of ~3.3 m of ESL from the marine-based portions of the WAIS (e.g. Bamber et al. 2009). Compilation of age-elevation data reconstructed from uranium-series (U-Th) dated fossil corals yielded an estimated sea-level highstand of 5.5 to 9 meters during the LIG, with the upper limit requiring partial or even total melting of the Greenland Ice Sheet and the WAIS, with additional contribution from the East Antarctic Ice Sheet because thermal ocean expansion and melting of mountain glaciers worldwide could only have contributed up to ca. 1 m (Kopp et al., 2009; Dutton and Lambeck, 2012; Dutton et al., 2015; Wilson et al., 2018). Sea-level rise of up to 9 meters is consistent with mapping and U-Th ages of fossil coral reefs in Western

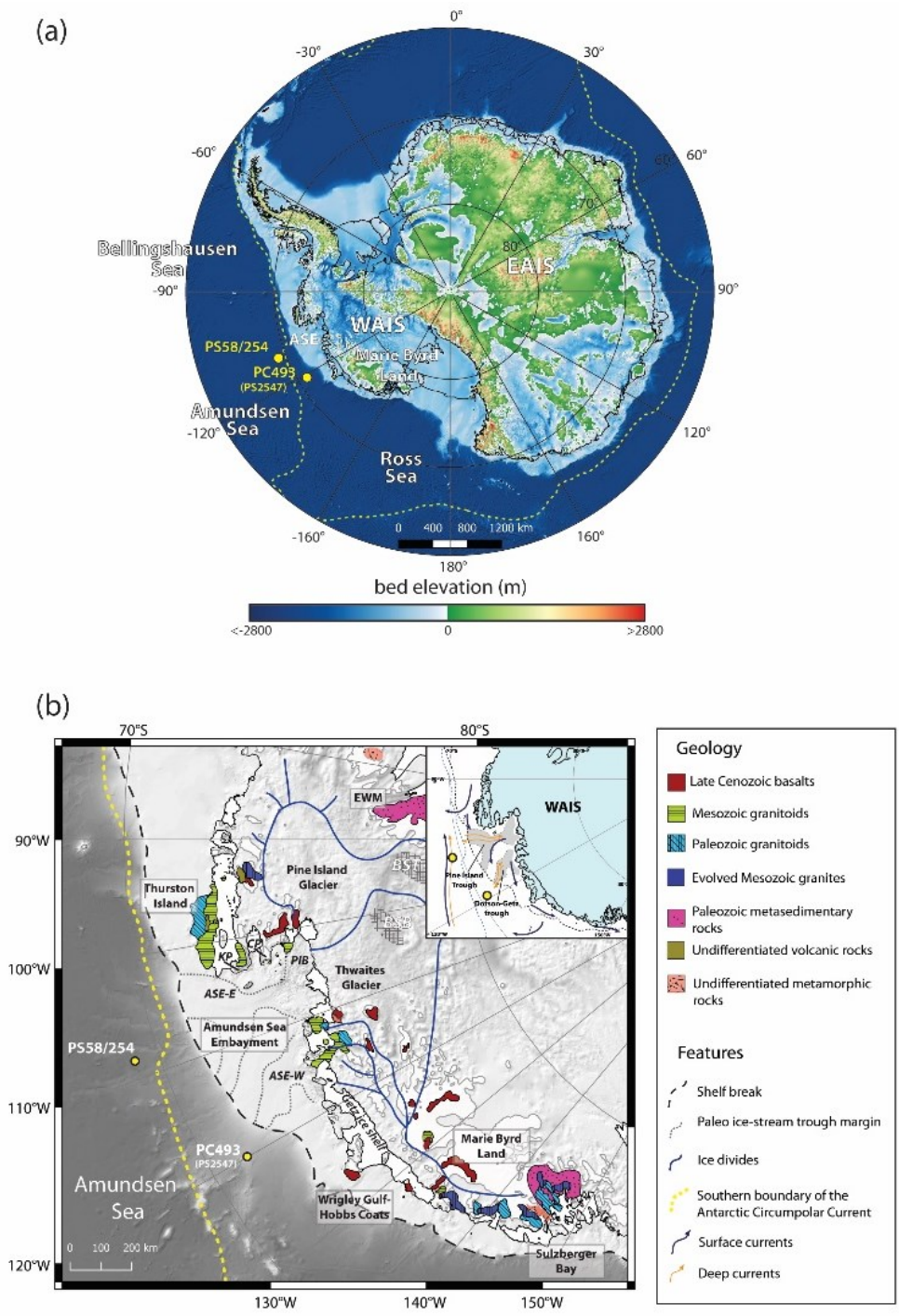

Figure 5.1. (a) Overview map of Antarctica with bed topography from BEDMAP 2 (Fretwell et al., 2013) and bathymetry from IBCSO (Arndt et al., 2013) and sites of the studied marine sediment cores. Thick white dashed lines designate approximate boundaries of the marine-based portions of the West Antarctic Ice Sheet (WAIS). Thin white dashed line marks the location of the southern boundary of the Antarctic Circumpolar Current (SBACC; Orsi et al., 1995). Note that site PS58/254 is located north of the SBACC and site PC493 is located south of the SBACC. (b) Simplified geological map of the study area, illustrating major geological units discussed in text (based on Simões Pereira et al., 2018; see Chapter 2 for further details).

(caption on next page)

Figure 5.1. (*continued*) Onshore, blue dotted lines represent major ice divides of the West Antarctic Ice Sheet. Two major bathymetric troughs, which incise the continental shelf and mark the pathways of the Pine Island-Thwaites and the Dotson-Getz palaeo-ice streams, are grey shaded and outlined as black dotted lines. Core sites are marked by yellowdots. The location of the SBACC is now marked by a yellow dotted line. Inlet: Blue arrows represent major surface currents (Gladstone et al., 2001; Assmann et al., 2005), while yellow/orange arrows denote deep (down to ~1000m water depth) currents (Holland et al., 2010; Assmann et al., 2013; Ha et al., 2014). Abbreviations: ASE-E: eastern Amundsen Sea Embayment, ASE-W: western Amundsen Sea Embayment, BSB: Byrd Subglacial Basin, BST: Bentley Subglacial Trench , CP: Canisteo Peninsula, EWM: Ellsworth-Whitmore Mountain, KP: King Peninsula, PIB: Pine Island Bay.

Australia, after correcting for glacial isostatic adjustment and regional tectonics (O'Leary et al., 2013).

Regional evidence for important environmental changes affecting the polar ice sheets is provided by proxy investigations on ice cores. For instance, data from the NEEM ice core drilled in NW Greenland indicate that the Greenland Ice Sheet contributed only ca. 2 m to the MIS 5e sea-level highstand, although cosmogenic exposure ages obtained from basal debris in Greenland Ice Core GISP2 are consistent with a scenario that Greenland was nearly ice-free during that time (Schaefer et al., 2016). Data from the EPICA Dome C ice core from East Antarctica show that during recent interglacial stages, and particularly during the LIG, local atmospheric temperatures were up to ~4 °C (Jouzel et al., 2007) and possibly even up to 7 °C (Sime et al., 2009) warmer than today. Although southern hemisphere warming is expected during interglacials due to deglaciation-induced slowdown of the Atlantic Meridional Overturning Circulation, the relative magnitude of warming is best explained by significant WAIS retreat, which acts as a local amplifier through changes in ice sheet topography and meltwater-thermohaline circulation interplay (Masson-Delmotte et al., 2010; Holden et al., 2011). On the other hand, the spatial pattern of $\delta^{18}O$ anomalies during MIS 5e recorded in several East Antarctic ice cores including EPICA Dome C is consistent with a major reduction in sea-ice extent rather than WAIS volume during the LIG (Holloway et al., 2016). Also ice sheet simulations focusing on the state of the WAIS during MIS 5e show contrasting results. While an Antarctic ice sheet model using improved ice physics, i.e. hydrofracturing and ice cliff failure, reconstructed complete WAIS collapse during MIS 5e (Pollard et al., 2015; cf.

DeConto and Pollard, 2016), a recently published transient, three-dimensional climate simulation used to drive the Antarctic ice sheet model of DeConto and Pollard (2016) over the last eight glacial cycles failed to reproduce a total WAIS collapse during this time span (Tigchelaar et al., 2018). Although both models demonstrate WAIS sensitivity to orbital forcing, the contribution of the WAIS to global sea-level during the LIG remains elusive.

The aim of this study is to test whether a distinct isotopic fingerprint in glaciomarine sediments from the Amundsen Sea can be detected and related to changes in the location of subglacial erosion (i.e. source of the terrigenous detritus) towards the interior of the continent indicating partial or even full collapse of the WAIS during the LIG. The isotope systems utilised are Sr and Nd isotopic compositions of fine-grained (<63μm) detrital sediments, which are expressed as $^{87}Sr/^{86}Sr$ ratios and ε_{Nd} values (which denotes the deviation of the measured $^{143}Nd/^{144}Nd$ from the Chondritic Uniform Reservoir in parts per 10,000) respectively, as well as $^{40}Ar/^{39}Ar$ cooling ages of iceberg-rafted (IRD, >150μm) hornblende and biotite grains. The Sr and Nd isotopic composition of bedrock is largely determined by the age and lithology of the rock formation (Taylor and McLennan, 1995), which allows differentiation of material originating from lithologically distinct source areas. In glaciomarine environments, detrital (<63μm) Sr and Nd isotopic composition have been shown to record the integrated fingerprints of bedrock and sediment sources eroded under the ice (Hemming et al., 1998; Farmer et al., 2003, 2006; Colville et al., 2011; Pierce et al., 2011, 2017; Cook et al., 2013, 2017; Farmer and Licht, 2016; Simões Pereira et al., 2018). While samarium(Sm)/Nd ratios tend to behave conservatively in nature, meaning that they are not fractionated by comminution, sorting or weathering, the rubidium(Rb)/Sr ratio is less conservative and hence more readily affected by these low-temperature processes (e.g. Eisenhauer et al., 1999; Goldstein and Hemming, 2003). The $^{40}Ar/^{39}Ar$ age of iceberg-rafted hornblende and biotite grains furthermore allows to directly identify the cooling age of source rocks. Hornblende and biotite have different closure temperatures of ~550 °C and 300 °C, respectively (Harrison, 1982; Harrison et al., 1985), meaning that their geochronological clock "starts" only when the source rock cooled down below its respective closure temperature. In Antarctica, these attributes have been exploited to infer source and transport pathways of iceberg-rafted grains deposited at proximal and distal sites to the ice margin (Roy et al. 2007; Williams et al. 2010; Pierce et al. 2011, 2014, 2017; Cook et al., 2014, 2017; Simões Pereira et al., 2018).

In this chapter, I focus on two sediment cores, PS58/254 and PC493, retrieved from the West Antarctic continental margin in the Amundsen Sea (Pacific sector of the Southern Ocean),

and investigate the provenance fingerprint of Late Pleistocene sediments deposited since the penultimate glaciation (i.e. MIS 6, ~191-130 ka). Of particular interest is the transition from the penultimate glaciation towards the LIG, i.e. Termination II, which started at ~130 ka. Glacial-interglacial changes in the sediment supply since MIS 6 are compared to regional and global climate and oceanographic records, provenance changes in Pleistocene sediments deposited at the same sites between 0.2 to 1.1 Ma (see Chapter 4), and provenance signatures of Late Holocene to modern surface sediments deposited in the Amundsen Sea sector (Simões Pereira et al., 2018; see Chapter 2 and 3).

5.2. Core material and study site

Core PS58/254 was recovered from the distal western flank of a sediment drift on the continental rise in the eastern Amundsen Sea (69°19°S, 108°27°W, water depth 4014 m, Figure 5.1) during RV Polarstern cruise ANT-XVIII/5a in 2001. Loss of the upper 18 cm of core top sediment in piston core PS58/254-1 was compensated with sediments from multiple core PS58/254-2 collected from the same site (Hillenbrand et al., 2009). Core depths are hence given as centimetre composite depth (cmcd). The sediment record is composed of alternation of diatom-bearing muds with lithogenic muds and was previously investigated for its sedimentological properties (lithology, physical properties, grain size distribution, proxies for biological productivity, clay mineralogy and palaeomagnetic properties) (Hillenbrand et al., 2009). The authors reconstructed the age model of this core on the basis of palaeomagnetic investigations and correlation of cyclic fluctuations in opal content, which is an indicator for palaeoproductivity, and barium(Ba)/aluminium(Al)ratios, a proxy for biogenic Ba, to the global benthic foraminiferal $\delta^{18}O$ stack (LR04 stack; Lisiecki and Raymo, 2005). The age model was subsequently supported by diatom biostratigraphy (Konfirst et al. 2012). Core PC493 was collected from the top of a seamount on the continental slope of the western Amundsen Sea (71°08°S, 119°55°W, water depth 2077 m; Figure 5.1) during cruise JR179 with RRS James Clark Ross in 2008 and is located at the same site as earlier studied core PS2547 (Hillenbrand et al., 2002). The sediments of core PC493 are composed of foraminifera-bearing sandy muds alternating with foraminiferal muds and foraminiferal oozes, indicating that the site was located above the Calcite Compensation Depth over the last 1.1 Ma (i.e. deposition and preservation of calcareous foraminifera). The age model of this core is based

on palaeomagnetic age constraints and oxygen isotope stratigraphy. The latter was constructed by correlating oxygen-isotope ratios of the epibenthic foraminifer Cibicidoides cf. wuellerstorfi and the planktic foraminifer Neogloboquadrina pachyderma sinistral to the LR04 stack (Williams et al., submitted; cf. age model for core PS2547 in Hillenbrand et al., 2002).

Both sites PS58/254 and PC493 are bathed by upwelling Circumpolar Deep Water (CDW), with site PS58/254 being situated within the eastward-flowing Antarctic Circumpolar Current (ACC) and site PC493 being situated south of the southern boundary of the ACC, where westward-flowing surface currents prevail (Orsi et al., 1995; Sokolov and Rintoul, 2009). Both cores are located off two major bathymetric troughs which incise the continental shelf in the eastern and western Amundsen Sea Embayment (ASE) (Figure 5.1). The Pine Island and Dotson-Getz troughs, respectively, were eroded by the repeated advances of major palaeo-ice streams towards the shelf break during past glacial times (Lowe and Anderson, 2002; Graham et al., 2009; Jakobsson et al., 2012; Gohl et al., 2013; Nitsche et al., 2013; Larter et al., 2014). Sediment supply to the continental rise occured primarily via gravitational downslope processes, such as turbidity currents originating from the continental slope, with suspended fine-grained particles captured by an eastward flowing along-slope bottom current before being deposited on the drifts, including site PS58/254 (Nitsche et al., 2000; Dowdeswell et al., 2006; Konfirst et al., 2012). Additional terrigenous sediment was delivered to this site by tidal and wind driven currents and through iceberg-rafting. Site PC493, on the contrary, sits on top of a seamount, which largely prevents lateral sediment supply to this site by bottom current or gravitational downslope transport (Hillenbrand et al., 2002; Lu et al., 2016). The unique location of site PC493 indicates that sediments were mainly supplied by tidal and wind driven currents and/or iceberg-rafting.

5.3. Sample selection and analytical methods

In total, 16 sediment samples from core PS58/254 and core PC493, respectively, spanning the last ~200 kyrs were selected for Sr and Nd isotope analysis on the detrital (<63μm) fraction (Tables 5.1 and 5.2). Samples were primary selected based on changes in magnetic susceptibility, which is often used as a proxy for provenance changes (e.g. Diekmann et al., 2000; Hillenbrand et al., 2009), and in the Ba/Al ratio (for PS58/254) and Ba/titanium(Ti) ratio

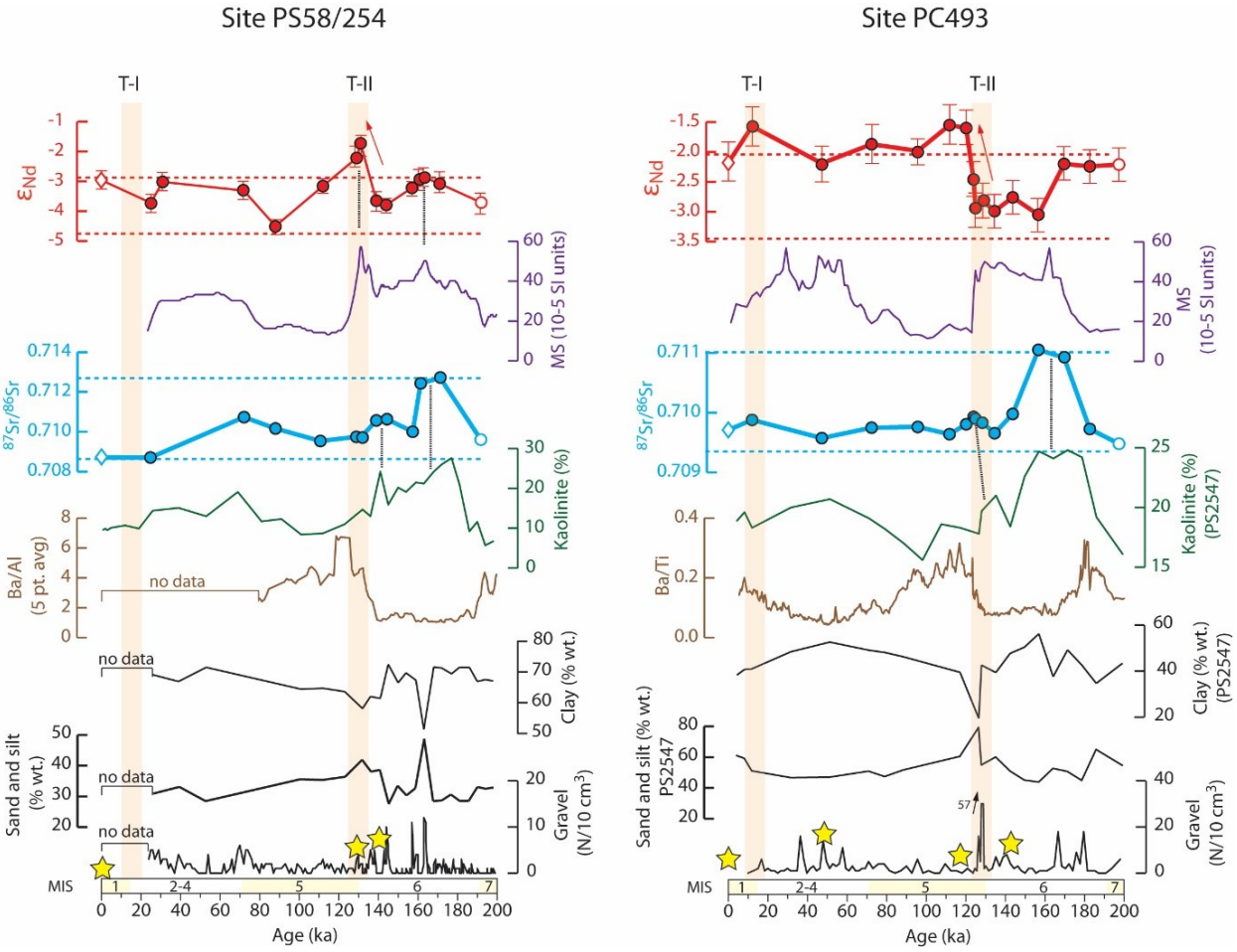

Figure 5.2. Late Pleistocene sediment records from sites PS58/254 and PC493. Neodymium and Sr isotopic compositions from this study are given as filled red and blue circles, respectively. The isotopic compositions of Late Holocene to modern seafloor sediments from the same core sites are given as diamond symbols (cf. Simões Pereira et al., 2018; see Chapter 2), while the isotopic compositions of sediments deposited prior to the penultimate glaciation (i.e. Marine Isotope Stage (MIS) 7) are given as filled white circles (data from Chapter 4). The overall range of downcore Sr and Nd isotopic compositions at both sites from 191 ka to 1.1 Ma are indicated by the dotted red and blue horizontal lines (cf. Chapter 4). Stars indicate the depths of samples analysed for hornblende and biotite $^{40}Ar/^{39}Ar$ age populations. Magnetic susceptibility (MS), kaolinite contents, barium(Ba)/aluminium(Al) and Ba/titanium(Ti) ratios, respectively, mud , sand and IRD (= gravel [>2mm] per cm core depth in number of grains for PS58/254 and in wt.% for PC493) contents and age models are from Hillenbrand et al. (2009) for core PS58/254 and from Williams et al. (submitted) for core PC493. Kaolinite content for site PC493 is taken from core PS2547 (Hillenbrand et al., 2002), which was collected from the same site. T-I: Termination I; T-II: Termination II. Red shadings indicate Terminations I and II.

Table 5.1. Strontium and neodymium isotopic compositions of late Pleistocene (0.0 to 0.2 Ma) detrital <63μm sediments deposited at site PS58/254

Sediment core	Core depth (cmbsf)	Core depth (cmcd)	Deposition age (ka)	MIS[b]	$^{143}Nd/^{144}Nd$	± 2 S.E.	ε_{Nd}	± 2 S.D.	$^{87}Sr/^{86}Sr$	± 2 S.E.
PS58/254-2[a]	00-02	0	0	1	0.512486	0.000006	-2.96	0.30	0.708704	0.000004
PS58/254-1	02-03	20	25	2-4	0.512447	0.000011	-3.72	0.24	0.709673	0.000006
PS58/254-2	25[c]	25	31	2-4	0.512483	0.000005	-3.02	0.30		
PS58/254-1	38-39	56	72	5	0.512468	0.000010	-3.31	0.20	0.710733	0.000005
	repeat[d]				*0.512459*	*0.000015*	*-3.50*	*0.24*		
PS58/254-1	52-53	70	88	5	0.512407	0.000011	-4.50	0.24	0.710161	0.000004
PS58/254-1	73[c]	91	112	5	0.512476	0.000007	-3.16	0.29		
	duplicate sample			5	*0.512462*	*0.000010*	*-3.44*	*0.24*	*0.709533*	*0.000005*
PS58/254-1	88-89	106	129	5	0.512524	0.000008	-2.22	0.32	0.709743	0.000008
	repeat				*0.512515*	*0.000010*	*-2.41*	*0.51*		
PS58/254-1	92-93	110	131	6	0.512549	0.000009	-1.73	0.23	0.709748	0.000006
PS58/254-1	109-110	127	139	6	0.512451	0.000008	-3.65	0.32	0.710566	0.000008
PS58/254-1	121-122	139	144	6	0.512444	0.000009	-3.79	0.23	0.710630	0.000005
	repeat				*0.512441*	*0.000009*	*-3.83*	*0.33*		
PS58/254-1	150-151	168	157	6	0.512473	0.000008	-3.22	0.23	0.710000	0.000004
PS58/254-1	159-160	177	161	6	0.512487	0.000008	-2.94	0.32	0.712431	0.000009
PS58/254-1	163[c]	181	163	6	0.512491	0.000006	-2.86	0.30		
PS58/254-1	181-182	199	171	6	0.512480	0.000009	-3.08	0.20	0.712707	0.000005
	repeat				*0.512483*	*0.000011*	*-3.03*	*0.33*		

a) Taken from Simões Pereira et al., 2018 (see Chapter 2)

b) Marine Isotope Stages (MIS) based on Lisiecki and Raymo, 2005

c) Pilot data analysed by Carys Cook using same methodology

d) Duplicate values represent procedural replicates of leached (detrital) sample powders (i.e. from digestion to column chemistry). Repeat values represent measurement replicates of the same sample after column chemistry.

(for PC493), both used here as a proxy for palaeoproductivity. In addition, we investigated 28 iceberg-rafted (>150μm) hornblende and biotite grains from two intervals in core PS58/254 spanning the penultimate glaciation (~139 ka) and Termination II (~128 ka), respectively, and 52 iceberg-rafted hornblende grains from three intervals in core PC493 spanning the penultimate glaciation (~ 143 ka), LIG (~120 ka) and MIS 3 (~47 ka) (Appendix Tables 4.3 and 4.4). Only biotite grains could be analysed from core PC493 because hornblende grains were lost during shipping.

In the following, we summarize the methodology for detrital (<63μm) Sr and Nd isotope analysis and ice-rafted hornblende and biotite $^{40}Ar/^{39}Ar$ dating, which was previously described in Chapter 4. Bulk sediment samples were wet sieved at <63μm, 63-150μm and >150μm. Splits (~50 mg) of homogenized <63μm fraction were sequentially leached to remove biogenic carbonate using buffered acetic acid (Biscaye, 1965) and authigenic (i.e. ferromanganese) coatings using hydroxylamine hydrochloride (NH_2OH) (following Rutberg et al., 2000). Approximately 50 mg of the residual (i.e. detrital) fraction was subsequently dissolved in pre-cleaned Teflon beakers using an acid mixing solution of HF (27M, 2ml), HNO_3 (16M, 1ml) and $HClO_4$ (20M, 0.8) for 3-4 days. A three-stage ion chromatography was

Table 5.2. Strontium and neodymium isotopic compositions of late Pleistocene (0.0 to 0.2 Ma) detrital <63μm sediments deposited at site PS58/254

Sediment Core	Depth (cmbsf)	Deposition age (ka)	MIS[b]	$^{143}Nd/^{144}Nd$	± 2 S.E.	ε_{Nd}	± 2 S.D.	$^{87}Sr/^{86}Sr$	± 2 S.E.
PC493[a]	00-01	0	1	0.512526	0.000007	-2.18	0.29	0.709711	0.000005
PC493	04-05	12	1	0.512557	0.000013	-1.57	0.28	0.709879	0.000007
	repeat[d]			0.512552	0.000008	-1.67	0.32		
PC493	25-26[c]	47	2-4	0.512521	0.000006	-2.28	0.29		
	duplicate sample			0.512526	0.000009	-2.19	0.25	0.709574	0.000008
PC493	40-41	72	5	0.512542	0.000008	-1.87	0.32	0.709749	0.000007
PC493	48-49	95	5	0.512536	0.000011	-2.00	0.28		
	duplicate sample			0.512537	0.000009	-1.98	0.21	0.709764	0.000007
	repeat							0.709695	0.000006
PC493	54-55	112	5	0.512559	0.000009	-1.55	0.32	0.709640	0.000006
PC493	57-58[c]	120	5	0.512556	0.000008	-1.60	0.29		
	duplicate sample							0.709806	0.000007
PC493	59-60	124	5	0.512512	0.000013	-2.46	0.28	0.709930	0.000008
PC493	60-61	125	5	0.512487	0.000008	-2.94	0.32	0.709899	0.000007
PC493	64-65	129		0.512494	0.000010	-2.82	0.28	0.709828	0.000007
PC493	68-69	135	6	0.512485	0.000011	-2.99	0.28	0.709656	0.000008
PC493	73-74[c]	144	6	0.512497	0.000005	-2.76	0.29		
	duplicate sample							0.709979	0.000008
PC493	80-81	157	6	0.512481	0.000009	-3.05	0.28	0.711052	0.000008
PC493	87-88	170	6	0.512525	0.000009	-2.20	0.32	0.710923	0.000009
PC493	94-95	183	6	0.512523	0.000010	-2.24	0.32	0.709727	0.000007

a) Taken from Simões Pereira et al., 2018 (see Chapter 2)

b) Marine Isotope Stages (MIS) based on Lisiecki and Raymo, 2005

c) Pilot data analysed by Carys Cook using same methodology

d) Duplicate values represent procedural replicates of leached (detrital) sample powders (i.e. from digestion to column chemistry). Repeat values represent measurement replicates of the same sample after column chemistry.

applied to extract Sr and Nd from the matrix. Samples were loaded onto a column with cation-exchange resin (AG50W X-8, 200-400 mesh). The Sr cut from this column was subsequently loaded onto a Sr spec column (Sr-Spec resin: 100-200 mesh size, after Pin and Bassin, 1992) to purify Sr, while a purified Nd cut was obtained by further separation from other rare-earth elements using Ln-spec resin (50-100μm mesh; after Pin and Zalduegui, 1997). All Nd and Sr isotopic compositions were measured on a Nu Instruments multi-collector inductively coupled plasma spectrometer (MC-ICP-MS) and a Thermo Scientific thermal ionization mass spectrometer (TIMS), respectively, at the MAGIC laboratories at Imperial College. Samples from this study were analysed together with samples in Chapter 4. Detailed description on instrumental mass bias correction, JNdi ($^{143}Nd/^{144}Nd$) and SRM987 ($^{87}Sr/^{86}Sr$) standard session ratios, and quality controls (USGS BCR-2 standard, blanks) are provided in Chapter 4. In summary, repeated USGS BCR-2 standard ratios measured over the course of this study yielded a $^{143}Nd/^{144}Nd$ ratio of 0.512639 ±0.000014 (2.S.D., n=58) and $^{87}Sr/^{86}Sr$ ratio of 0.710263 ±0.000015 (2.S.D., n =50) and 0.710250 ±0.000010 (2.S.D., n =39), which are identical within error with the recommended values of 0.512638 ± 0.000015 and 0.710252±0.000013, respectively (Weis et al., 2006). Contribution of Nd blank was constantly below 0.15% of the total sample Nd amount, while Sr blanks were consistently below 120 pg.

Hornblende and biotite grains were hand-picked from the terrigenous coarse (>150µm) sediment fraction and sent together with monitor standard grains to the USGS reactor in Denver, CO, for irradiation. $^{40}Ar/^{39}Ar$ ages were acquired using single-step CO_2 laser fusion at the Argon Geochronology for the Earth Sciences (AGES) laboratories at the Lamont-Doherty Earth Observatory, NY. J-values were obtained by normalizing co-irradiated Fish Canyon sanidine ages to 28.201±0.046 Ma (Kuiper et al., 2008), and measured $^{40}Ar/^{39}Ar$ ratios were corrected for nuclear interferences (Dalrymple et al., 1981), atmospheric argon ($^{40}Ar/^{36}Ar$ =298.6, Lee et al., 2006), procedural blanks, and mass discrimination from repeated measurements of blanks and air pipettes.

5.4. Results

5.4.1. Strontium and Neodymium isotopic composition of detrital fine-grained (<63µm) sediments

In the following, results and discussion on Sr and Nd isotopic composition of fine-grained sediments from site PS58/254 and PC493 include data on their seafloor surface sediments (Simões Pereira et al., 2018; cf. Chapter 2) and one sample from MIS 7 (cf. Chapter 4). Fine-grained detritus of marine sediments deposited at site PS58/254 over the last ~191 ka yields ε_{Nd} values between -4.5 and -1.7 and $^{87}Sr/^{86}Sr$ ratios between 0.7095 and 0.7127. Site PC493 displays a narrower range of isotopic compositions, with ε_{Nd} ranging between -3.1 and -1.5 and $^{87}Sr/^{86}Sr$ ratios between 0.7095 and 0.7111 (Table 5.2). Both sediment records show a prominent shift in the Nd isotopic compositions around/after Termination II. In detail, the ε_{Nd} values at site PS58/254 shift from a value of ~-3.8 at ~140 ka to a value of -1.7 at 131 ka, and back to -4.5 at 90 ka. At site PC493, the relatively uniform ε_{Nd} values around -3.1 to -2.8 from 125 to 157 ka during the penultimate glacial show a shift to values > -2.3 maintained afterwards, with peak values of ~-1.6 slightly after Termination II (~120 ka). These shifts represent the largest Nd isotope variations in both cores over the last 1.1 Ma (Figure 5.2, cf. Chapter 4) and correlate with shifts in magnetic susceptibility and Ba/Al and Ba/Ti ratios, respectively, at both sites (Figure 5.2). Following the change in the Nd isotopic fingerprint during Termination II, ε_{Nd} values in core PS58/254 become progressively lower (~-4.5 at 88 ka) before shifting toward the signature of modern surface sediments (ε_{Nd} ~-3), while values

in core PC493 remain relatively uniform with Nd isotope values approaching the Nd isotope signature of the surface sediment from the same core site (ε_{Nd} ~-2).

Sediments deposited at both sites during the penultimate glaciation at around 165 ka are characterized by a large increase in Sr isotopic ratios. At site PS58/254, $^{87}Sr/^{86}Sr$ ratios increase from a value of 0.7096 at 192 ka (cf. Chapter 4) to 0.7127 at 171 ka. At site PC493, $^{87}Sr/^{86}Sr$ ratios increase from a value of 0.7097 at 183 (cf. Chapter 4) to 0.7111 at 157 ka. Both Sr isotope records show a $^{87}Sr/^{86}Sr$ decrease to pre-peak values of ~0.7125 and 0.7110 around 150-160 ka, and a "bulge" at ~142 ka (0.7106) and ~125 ka (0.7099), respectively. The major and minor excursions in $^{87}Sr/^{86}Sr$ ratios at both sites correlate with an increase in the kaolinite content of the clay fraction (<2 μm) recorded both at site PS58/254 (Hillenbrand et al., 2009) and site PS2547 (same site as PC493; Hillenbrand et al., 2002) (Figure 5.1, 5.2).

Overall, a strong decoupling between the Sr and Nd isotope signatures of detrital sediments is observed for both sites. Increases in $^{87}Sr/^{86}Sr$ ratios are observed during the penultimate glaciation, while ε_{Nd} increases occur during/after Termination II.

5.4.2. $^{40}Ar/^{39}Ar$ ages of iceberg-rafted hornblende and biotite grains

$^{40}Ar/^{39}Ar$ age populations of iceberg-rafted hornblende and biotite grains deposited at sites PS58/254 and PC493 between ~40 ka and 140 ka are displayed in Figure 5.3. Cooling ages for the penultimate glaciation (MIS 6) at site PS58/254 range from 70 to 360 Ma, with three well-defined age peaks at ~100 Ma, ~180 Ma and 345 Ma (n= 19). The latter two age peaks are not well developed in the interglacial samples. For instance, both interglacial samples from MIS 5e (n= 9) and MIS 1 (n=21) show many similarities, recording a significant number of hornblende and biotite grains with $^{40}Ar/^{39}Ar$ ages of <10 Ma and ~50 Ma, as well as ages around between 80 and 150 Ma. The latter age range is mostly visible in sample from MIS 1, which further contains several grains dated at 200-310 Ma (n= 3) and 1100-1900 Ma (n= 2).

In contrast to the distinct glacial vs interglacial IRD ages observed at site PS58/254, samples at site PC493 show less variability in biotite $^{40}Ar/^{39}Ar$ ages. The IRD deposited at site PC493 during the penultimate glaciation (MIS 6) and LIG (MIS 5) shows predominantly $^{40}Ar/^{39}Ar$ biotite ages between 80 and 240 Ma, with two large age populations at ~100-110 Ma and ~215 Ma. Furthermore, sporadic biotite ages of 6 Ma, ~50 Ma and ~261 Ma occur. One additional sample was taken from MIS 3 (~47 ka), which shows a similar $^{40}Ar/^{39}Ar$ age distribution as for IRD deposited during the penultimate glaciation and the LIG, with a (minor) age peak around ~110 Ma and a high number of grains with ages between 200 and 290 Ma, in

addition to two grains with younger ages of 13 Ma and 52 Ma. Most of the downcore $^{40}Ar/^{39}Ar$ ages, as well as a predominant ~100 Ma age peak can be found in the MIS 1 sample from site PC493 (Simões Pereira et al., 2018; Chapter 2).

5.5. Discussion

5.5.1. Controls on detrital strontium and neodymium isotopic compositions in Amundsen Sea sediments and their association with glacial advance and retreat events

Strontium and Nd isotope results for late Pleistocene fine-grained sediments deposited on the Amundsen Sea continental slope and rise over the last ~191 kyrs largely agree with the Sr and Nd isotope fingerprint of Late Holocene to modern seafloor sediments deposited in the ASE (Figure 5.4). Glacial and interglacial provenance signatures of sediments from core PC493 generally overlap with the signature of seafloor samples deposited along the Dotson-Getz Trough in the western ASE, which indicates direct northward sediment delivery from the shelf to our site (Figure 5.1b inlet). The isotope fingerprint of core PS58/254 is more varied than in core PC493, but generally agrees with Sr and Nd isotopic compositions of seafloor sediments deposited along the Pine Island Trough in the eastern ASE, implying a similar northward sediment supply from the shelf to the site of deposition. Two samples from the penultimate glaciation (~157-170 ka) plot outside the isotopic range of the ASE, while two samples deposited during Termination II (~112-120 ka) record a similar isotopic fingerprint to the western ASE. We will discuss the unique isotope fingerprints of these samples in the following sections.

Except for these outliers, fine-grained detritus of sediments deposited at site PS58/254 and PC493 over the last ~191 kyrs most likely originated from Palaeozoic to Mesozoic granitoids that extensively crop out along the Amundsen Sea coast (Figure 5.4). These magmatic bodies were formed as part of the long-lived subduction of the proto-Pacific plate below the active margin of West Antarctica (Pankhurst et al., 1993, 1998; Mukasa and Dalziel, 2000). The geology of the Amundsen Sea coast is further characterized by extensive outcrops ofLate Cenozoic volcanic rocks (e.g. LeMasurier, 1990 LeMasurier and Rex, 1989), but significant input from these sources to our sites is unlikely due to the absence of their radiogenic neodymium isotope and unradiogenic Sr isotope fingerprint (Figures 5.2, 5.3; see Chapter 2).

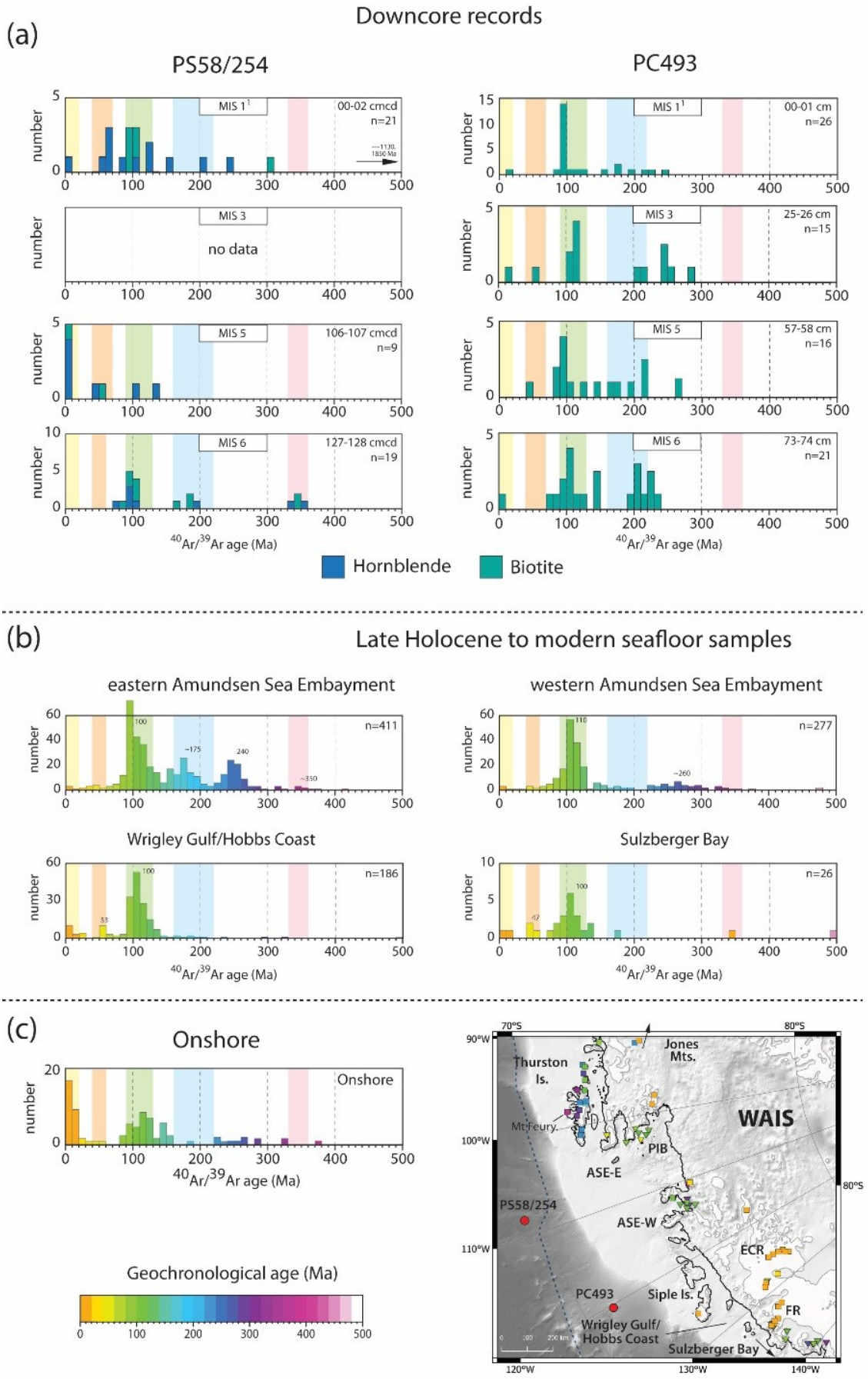

(caption on next page)

Figure 5.3. (a) Histograms (10 Myrs bins) showing $^{40}Ar/^{39}Ar$ ages of iceberg-rafted hornblende and biotite grains from sediments deposited at sites PS58/254 and PC493 during the penultimate glaciation (i.e. MIS 6; 143 and 139 ka), Last Interglacial (MIS 5, 128 and 120 ka) and MIS 3 (47 ka) . Data for MIS 1 are taken from Simões Pereira et al. (2018; cf. Chapter 2). Specific age intervals relevant for this study are shown in yellow (<20 Ma), orange (40-60 Ma), green (90-130 Ma), blue (160-220 Ma) and purple (330-360 Ma). b) $^{40}Ar/^{39}Ar$ ages of iceberg-rafted hornblende and biotite grains in Late Holocene to modern seafloor sediments from the Amundsen Sea shelf and in the Sulzberger Bay (Simões Pereira et al., 2018; cf. Chapter 2). c) Compilation of onshore K-Ar and $^{40}Ar/^{39}Ar$ whole rock, hornblende and biotite (squares) and U-Pb zircon (reversed triangle) ages (LeMasurier and Rex, 1989; Pankhurst et al., 1993, 1998; Hart et al, 1997; Mukasa and Dalziel, 2000; Rocchi et al., 2006; Kipf et al., 2012). Spatial distribution of onshore data is shown in the map. ASE-E: eastern Amundsen Sea Embayment; ASE-W: western Amundsen Sea Embayment; ECR: Executive Committee Range; FR: Flood Ranges; WAIS: West Antarctic Ice Sheet.

Although the overall range of isotopic composition for sediments in cores PS58/254 and PC493 points towards proximal sources, both Sr and Nd isotope records do not co-vary (Figs. 5.2, 5.5) as would be expected based on global correlations where sediment provenance is the sole governing factor. Current sorting of detrital particles, i.e. grain-size effects, generally exerts a major influence on the Sr isotopic composition of marine sediments. Preferential breakdown of Rb-rich minerals (i.e. K-feldspars, biotite) over Sr-rich minerals (i.e. plagioclase, pyroxene) into clay minerals produces a disproportionate enrichment of Rb over Sr contents in the clay and fine-grained fraction of marine sediments, resulting in more radiogenic $^{87}Sr/^{86}Sr$ ratios (Biscaye and Dasch, 1971; Eisenhauer et al. 1999; Tütken et al., 2002; Goldstein and Hemming, 2003; Blum and Erel, 2003). In contrast, different minerals tend to have similar Sm/Nd ratios (e.g. Bayon et al., 2009; Garçon et al., 2013; Rickli et al., 2014) and hence largely reflect the bulk rock/sediment composition. If preferential deposition of clay and fine-grained material at our sites influenced the Sr isotopic composition, we would expect to see $^{87}Sr/^{86}Sr$ ratios to co-vary with clay content in sediments. However, we do not observe any correlation between $^{87}Sr/^{86}Sr$ ratios and clay contents at site PS58/254 (Figure 5.3; Appendix Figure 4.3). Similarly, the Sr isotopic composition at site PC493 does not reveal a significant relationship with clay content (Figure 5.2). The distinct increase in $^{87}Sr/^{86}Sr$ ratios occurred simultaneously (~165 ka) at both core sites despite their different depositional settings. Coinciding changes in

the $^{87}Sr/^{86}Sr$ ratios in both cores are hence more likely to indicate a regional rather and a site specific control. In the absence of clear indication of grain size control on the Sr isotopic composition of fine-grained detritus at both core sites, changes in the sediment supply related to WAIS dynamics are the most likely explanation for the observed changes in $^{87}Sr/^{86}Sr$ ratios.

Glacial advance and retreat can cause erosion of sources with distinct isotopic compositions. In East Antarctica, decoupling between Sr and Nd isotopic compositions in sediments deposited between 3.38 and 4.99 Ma at ODP Site 1165 on the continental rise offshore from Prydz Bay (Cook, 2013) is suggested to be related to the large range of $^{87}Sr/^{86}Sr$

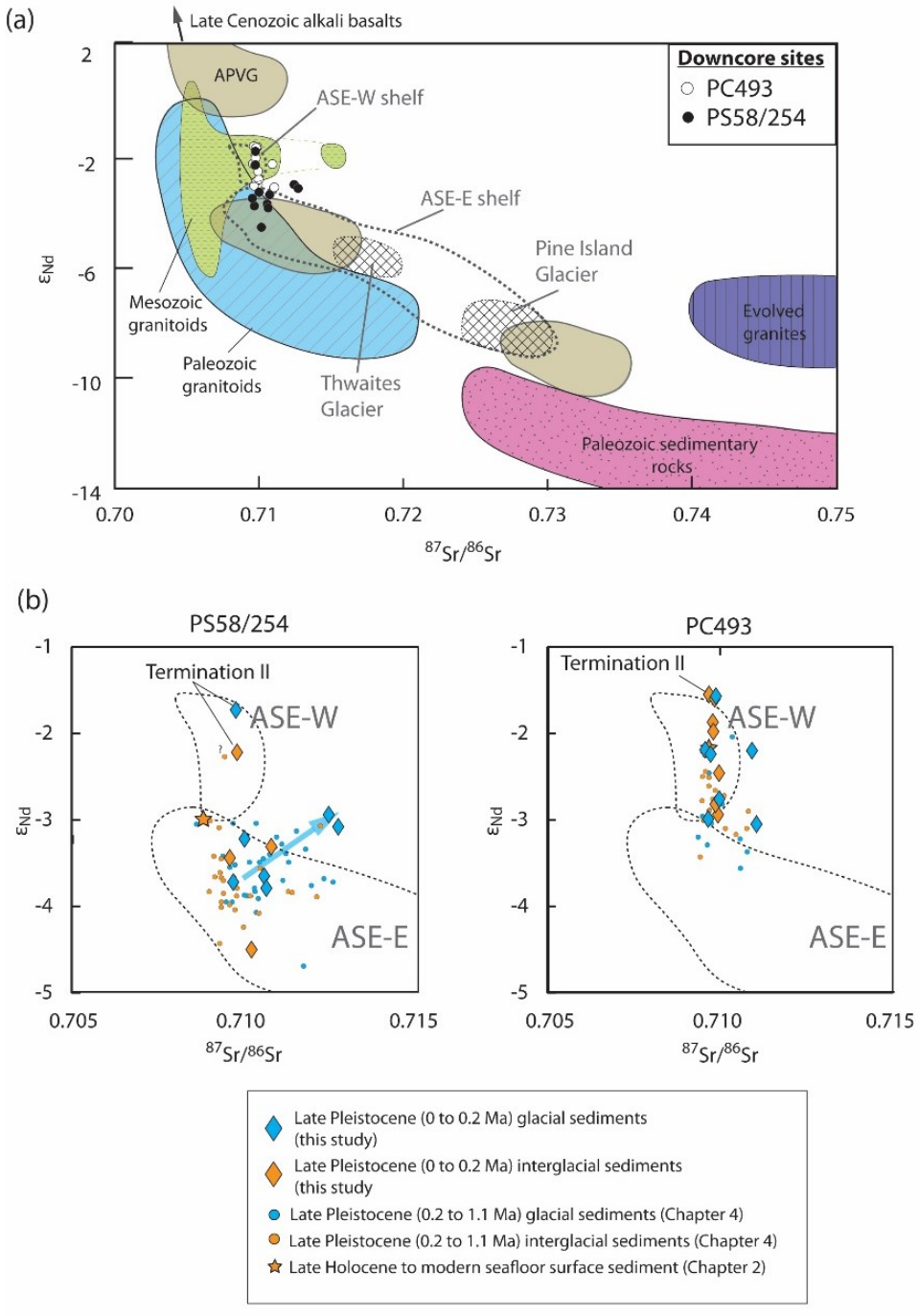

(caption on next page)

Figure 5.4. (a) Strontium and neodymium isotopic compositions of detrital fine (<63μm) sediments from sites PS58/254 (black circles) and PC493 (white circles) deposited over the last ~191 kyrs. The Sr and Nd isotopic composition of major bedrock outcrops is based on Simões Pereira et al., 2018 and references therein (cf. Pankhurst et al. 1993, Riley et al., 2001, 2010, 2016, Korhonen et al., 2010), and colour is matched with geological units in Figure 5.1b. Thick dotted lines outline the composition of Late Holocene to modern fine-grained detrital seafloor sediments from the eastern Amundsen Sea Embayment (ASE-E) and the western Amundsen Sea Embayment (ASE-W) (taken from Chapter 2; i.e. Simões Pereira et al., 2018). Hatched fields represent the Sr and Nd provenance signatures of seafloor surface sediments proximal to Pine Island Glacier (cf. inner Pine Island Bay; Chapter 3) and Thwaites Glacier (cf. western Pine Island Bay); APVG: Antarctic Peninsula Volcanic Group; (b) Glacial (blue) and interglacial (orange) Sr and Nd isotope fingerprints of sediments from cores PS58/254 (left) and PC493 (right). Diamond symbols represent data presented in this chapter, while small circles indicate data of downcore sediments from the same sites deposited between 0.2 and 1.1 Ma and presented in Chapter 4. Asterisks indicate the isotopic signature of seafloor sediments from the same sites (Simões Pereira et al., 2018; see Chapter 2). Blue arrow highlights sediments deposited at site PS58/254 during MIS 6, which plot outside the provenance fingerprint of Late Holocene to modern shelf sediments.

isotopic signatures in onshore outcrops around Prydz Bay, which was caused by disturbance of the Rb-Sr systems of the source rocks during magmatic intrusion or metamorphism. In the Amundsen Sea sector, Palaeozoic to Cretaceous rocks show a relatively large range of Sr and Nd isotopic compositions (ε_{Nd}: -5 to 0; $^{87}Sr/^{86}Sr$: 0.704 to 0.715) that exceeds the observed variability of our downcore data (Figure 5.4). Moreover, Jurassic granites from the Jones Mountains in the north-eastern hinterland of the ASE (see Chapter 3) show more evolved isotopic signatures (ε_{Nd}: -9 to -6; $^{87}Sr/^{86}Sr$: 0.743 to 0.762), while volcanic rocks elsewhere in the hinterland of the Amundsen Sea are much more radiogenic in their isotopic composition (ε_{Nd} >5; $^{87}Sr/^{86}Sr$ <0.704). However, (slight) changes in the relative contribution of these sources rocks to our sediments is likely to produce changes in the isotopic composition for both tracers rather than in the $^{87}Sr/^{86}Sr$ ratio alone. Erosion and sediment supply from an additional source is therefore suggested to produce the decoupling between Sr and Nd isotopic compositions observed in the aforementioned outlier samples. Both $^{87}Sr/^{86}Sr$ records show

correlation with kaolinite contents, with more radiogenic Sr isotopes being associated with higher kaolinite contents. This observation suggests sediment contribution from sedimentary rocks located in the interior of West Antarctica or occurring as dipping sedimentary strata on the Amundsen Sea shelf (Hillenbrand et al., 2002, 2009; Ehrmann et al., 2011; see Chapter 4). During RV Polarstern cruise PS104 in 2017, Oligocene to Miocene (?) sedimentary strata containing abundant mudstones were collected from site PIT-4 on the eastern ASE shelf using the MeBo seabed drilling device (Gohl et al., 2017; S. Bohaty and C.-D. Hillenbrand, pers. comm. 08/2018). Clay contents of these mudstones are mostly between 38 and 56 wt.% (G. Kuhn, pers. comm. 08/2018), thus the modestly high (pelagic) clay fraction in these rocks probably causes an increase in the Rb/Sr ratio of these rocks, and hence in the $^{87}Sr/^{86}Sr$ ratio. The Rb/Sr of pelagic clays is much larger (~6.1) compared to average sediments (~0.8), while Sm/Nd ratios are relatively similar (6.1 vs 5.4, respectively) (Taylor and McLennan, 2001). Contribution of detritus from these mudstones to our deposition sites might therefore explain the large increase in $^{87}Sr/^{86}Sr$ ratios with no associated change in ε_{Nd} values. Late Cretaceous to early Cainozoic sedimentary strata drilled during expedition PS104 at site PIT-3 contain up to ca. 75% kaolinite (W. Ehrmann, C.-D. Hillenbrand and U. Salzmann, pers. comm. 08/2018) and are therefore the most likely source for kaolinite.

Decoupling between Sr and Nd isotopic compositions during Termination II is more difficult to explain but could be related to sediment supply from multiple sources. For instance, additional input from Late Cenozoic volcanic sources, which crop out extensively along the Amundsen Sea coast (Figure 5.1, 5.4), could easily result in an increase in ε_{Nd} values, as observed in our sediment records. Increased contribution from these volcanic rock would, however, also cause a significant decrease in the $^{87}Sr/^{86}Sr$ ratios which is not observed. We hence suggest that supply of detritus from Late Cretaceous and Early Cainozoic sedimentary strata cropping out on the shelf, which leads to an increase in the $^{87}Sr/^{86}Sr$ ratio, compensates for the decrease in Sr isotopic compositions. This hypothesis is supported by a minor bulge in $^{87}Sr/^{86}Sr$ ratios (i.e. erosion of sedimentary rocks) which coincides with the increase in ε_{Nd} values (Figure 5.2).

In summary, decoupling of Sr and Nd isotopic compositions in cores PS58/254 and PC493 can be related to changes in the sediment source rather than grain-size effects, although the exact nature of the source rocks remains to be tested by Sr and Nd isotope analyses on the recently recovered MeBo drill cores. In general, $^{87}Sr/^{86}Sr$ ratios in our two downcore records can be used as a tracer of erosion of sedimentary rocks located on the ASE shelf during glacial

advance. Neodymium isotopic compositions of the studied detrital sediments, however, record an increase in supply from volcanic sources during Termination II. The suggested source location of radiogenic Nd from the eastern coastline of the Amundsen Sea, adjacent to Pine Island Glacier, calls for increased erosion from this local highland during interglacials. But how can this signal be reconciled with the predictions made in Chapter 3 for Pine Island and Thwaites glacier retreats?

5.5.2. Do fine-grained detrital sediments provide a retreat signal of the West Antarctic ice sheet?

Both cores show a significant excursion in the Nd isotopic compositions of fine-grained sediments towards higher ε_{Nd} values of ~-1.7 deposited at, or shortly after, Termination II, indicating a significant change in the source during this time period. As mentioned earlier, we rule out weathering or mineral sorting to be the cause for the observed shifts. Hence, I suggest that the (almost) concomitant change in the Nd provenance data at both sites is related to a retreat of the erosive ice towards the interior of the continent.

In Chapter 3, I have described the modern isotopic fingerprint of glaciogenic sediments delivered by the Pine Island and Thwaites Glaciers. Detritus delivered by these two glaciers are characterized by lower Nd isotopic composition of ε_{Nd} ~ -9 and -4, respectively (and high $^{87}Sr/^{86}Sr$ ratios of 0.728 and 0.714, respectively) compared to the overall neodymium isotope compositions of the downcore sediments at our sites, as well as from the surrounding sectors along the Amundsen Sea coast (Figure 5.4; cf. Chapter 3 for a detailed description). These two glaciers are most likely the supplier for detrital sediments to the Amundsen Sea (Embayment) during the Last Glacial Maximum (~ca. 19-25 ka) and Late Holocene (e.g. Golledge et al., 2013; Witus et al., 2014). A shift towards more radiogenic (higher) neodymium isotopic compositions at our sites during Termination II is related to a decrease or end in sediment supply from the two glaciers to our sites over this time period, which is caused by significant grounding line retreat towards or even 'ungrounding' of the WAIS base from the interior of the ice drainage basins. Shrinking of the overall size of the ice drainage basins may have reduced the cumulative sediment flux to the offshore (e.g. Golledge et al., 2013), while an ungrounding would impede erosion of the subglacial substrate of the Pine Island and Thwaites Galciers basins. In other sectors, for instance in the hinterland of the eastern Amundsen Sea coast, ice caps have remained present even during the strongest modelled interglacials of the

late Pleistocene (e.g. DeConto and Pollard, 2016). Continuous sediment supply from this sector, which is characterized by extensively outcropping Cenozoic volcanic rocks (ε_{Nd} > 5; e.g. Futa and LeMasurier, 1983) and Mesozoic granitoids (ε_{Nd} of -6 to 0, with an average of ~-2; Pankhurst et al., 1993)(Figure 5.4), can explain for the observed increase in Nd isotopic compositions in our sediments in the case of diminished supply from the Pine Island and Thwaites Glaciers. Our data here does however not allow to estimate the exact extent of grounding line retreat during, or shortly after Termination II. Further investigation on the decoupling between Sr and Nd isotopic compositions during this time interval are needed to provide a full picture. I suggest that detrital material deposited on the continental shelf or slope, which has been eroded from sedimentary rocks on the shelf during the precedent glacial advance and which is characterized by distinctively high $^{87}Sr/^{86}Sr$ ratios (Section 5.5.1), is supplied to our sites via gravitational currents, further diluting the consequent decrease in $^{87}Sr/^{86}Sr$ ratio in the case of significant grounding line retreat.

5.5.3. Glacial-interglacial changes in the provenance of iceberg-rafted debris

Sites PS58/254 and PC493 reveal $^{40}Ar/^{39}Ar$ hornblende and biotite ages between ~90 and 360 Ma over the past 191 kyrs, which is in agreement with published K-Ar hornblende and biotite and U-Pb zircon ages from onshore outcrops around the ASE (Pankhurst et al., 1993, 1998; Mukasa and Dalziel, 2000; Kipf et al., 2012; Figure 5.3). In addition, hornblende and biotite grains collected from Late Holocene to modern seafloor sediments from the ASE are characterized by age populations similar to those of the IRD in the two cores (Simões Pereira et al., 2018; Figure5.3), which further indicates proximal IRD sources for core sites PS58/254 and PC493.

In detail, the IRD samples at sites PS58/254 and PC493 deposited during the penultimate glaciation show relatively well-defined age peaks compared to the LIG (Figure 5.3). During past glaciations, ice streams extended from the interior of the Amundsen Sea sector of the WAIS towards the shelf break, carrying glacial detritus from their source areas to the ice margin (Jakobsson et al., 2012; Gohl et al., 2013; Larter et al. 2014; Golledge et al., 2012, 2013). The well-defined age peaks could hence represent material from specific source areas, which were carried along specific flowlines towards the ice margin. For instance, IRD of the MIS 6 sample in core PS58/254 shows a discrete age peak around ~355 Ma, indicating that its likely source is on eastern Thurston Island (i.e. Mount Feury gabbro, hornblende K-Ar

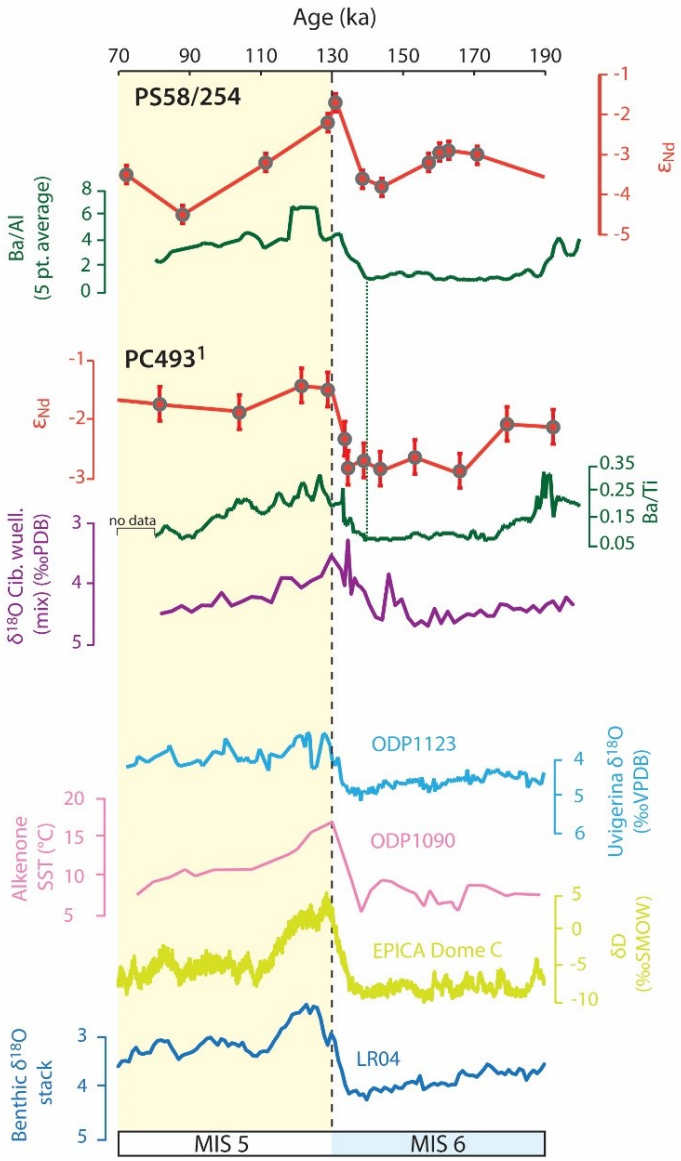

Figure 5.5. Comparison of Nd isotopic records at sites PS58/254 and PC493 with proxies for paleoproductivity at both sites and the benthic $\delta^{18}O$ record from core PC493 (from Hillenbrand et al., 2009, and Williams et al. submitted) for the time period between 70 and 191 kyrs. Also shown are oceanographic and climatic records from Antarctica and the Southern Ocean, such as the benthic $\delta^{18}O$ record from ODP Site 1123 east of New Zealand (Elderfield et al., 2012), alkenone sea-surface temperatures (SST) at ODP Site 1090 in the sub-Antarctic sector of the Atlantic Ocean (Martínez-Garia et al., 2009), deuterium record of the EPICA Dome C ice core in East Antarctica (Jouzel et al., 2007) and the global benthic $\delta^{18}O$ stack (Lisiecki and Raymo, 2005). [1]Age model of PC493 has been shifted by ~10 ka to fit the excursion in paleoproductivity proxies at both sites (green dotted line).

326 ±35 Ma; Pankhurst et al., 1993; Figure 5.3). Given that during glacial advances ice streams draining this area terminated at the shelf break several hundreds of kilometres east of site PS58/254, additional transport by the coastal current is required to carry sediment-laden icebergs westwards towards site PS58/254. Ice-rafted biotite grains deposited at sitePC493 during MIS 6 show well-defined $^{40}Ar/^{39}Ar$ age peaks around ~100 Ma and 190-230 Ma. Argon age populations of proximal hornblende and biotite grains from Late Holocene to modern seafloor sediments from the ASE shelf show that mineral grains with $^{40}Ar/^{39}Ar$ ages of 160-220 Ma are mainly sourced from the eastern Amundsen Sea coast and/or Pine Island Bay (Figure 5.3; cf. Chapter 2 and 3). The relatively high proportion of 160-220 Ma old grains (~25%) in MIS 6 - and to a lesser extent MIS 3 - samples from core PC493 hence indicates an IRD source from the eastern ASE coast. Ice streams extended from today's coast toward the shelf break in the eastern ASE during past glacials (e.g. Jakobsson et al., 2012; Gohl et al., 2013; Larter et al. 2014; Golledge et al., 2013), allowing ransport of icebergs by the westward-flowing coastal current to site PC493. The Dotson-Getz Ice Stream also advanced to the shelf break (e.g. Larter et al., 2009; Graham et al., 2009; Smith et al., 2011; Larter et al., 2014), which is located proximal to site PC493 (Figure 5.1). However, palaeo-drainage basins in the eastern ASE (especially that of Pine Island-Thwaites) were much larger than that of the Dotson-Getz (Golledge et al., 2013), possibly overshadowing any IRD signal from the western ASE at site PC493.

IRD grains deposited at site PS58/254 during MIS 5 show a significant $^{40}Ar/^{39}Ar$ age population <10 Ma and include two grains with an age of ~50 Ma. This observation requires a source outside the ASE hinterland. Late Pleistocene interglacial samples at site PS58/254 deposited prior to MIS 5 contain hornblende and biotite grains with similarly young $^{40}Ar/^{39}Ar$ ages of <80 Ma. The source for these young grains (see Chapter 4) is the Wrigley Gulf-Hobbs Coast sector in the westernmost Amundsen Sea (Figure 5.3; cf. Chapter 4). Extensive outcropping Late Cenozoic volcanoes in Marie Byrd Land (LeMasurier and Rex, 1989; Hole and LeMasurier, 1994) could hence be the source of IRD grains during MIS 15, 11 (Chapter 4) and 5 (this chapter). Presence of ~50 Ma grains in Late Holocene to modern shelf sediments proximal to the Wrigley Gulf-Hobbs Coast sector has also been linked to an exotic granitic-dioritic source below the ice inland of the Getz Ice Shelf (Spiegel et al., 2016). Icebergs from this sector drift westwards with the coastal current before being injected northwards into the eastward flowing ACC at the boundary between the Amundsen and Ross seas (Gladstone et al., 2001; Tournadre et al., 2016). In contrast, biotite grains deposited during MIS 5 at site PC493 contain a large number of hornblende and biotite grains of 160-220 Ma that have their

source on the eastern ASE coast and/or Pine Island Bay, which indicate westward iceberg transport by the coastal current to our site during MIS 5.

As mentioned earlier, even in the most extreme (i.e. retreated) WAIS model simulations for MIS 5e using modified ice physics, ice caps remain present in topographic highlands of Marie Byrd Land and in the hinterland of the eastern Amundsen Sea coast (DeConto and Pollard, 2016; Figure 5.1). The Marie Byrd Land sector is characterized by numerous volcanic edifices (e.g. LeMasurier, 1990), which form most of the outcrops there, particularly in the Executive Committee and Flood ranges and in coastal areas, such on Siple Island (Figure 5.3). A possible explanation for increased IRD supply from the Wrigley Gulf-Hobbs Coast sector during the LIG could be a decrease in detritus-laden iceberg supply from other sectors along the Amundsen Sea coast due to large retreat or even 'ungrounding' of the ice sheet.. Floating of ice in the Pine Island Glacier and Thwaites Glacier drainage basins would result in the formation of large ice shelves (MacAyeal, 1992; Feldmann and Levermann, 2014), which would contain only minor quantities of glacial debris as detritus generally melts out at or near the grounding line (e.g. Orheim and Elverøi, 1981; Domack and Harris, 1998). More detailed IRD investigations are needed to resolve the exact timing, sources and causes of the observed glacial-interglacial variations in the IRD signal.

5.5.4. Paleoenvironmental context and implications of the sedimentary provenance analysis: Indication for the Late Pleistocene WAIS retreat occurring during Termination II ?

The Nd isotope excursion during Termination II is the largest observed excursion in Nd isotopic compositions of detrital sediments in both sediment cores occurring over the entire Late Pleistocene (Figure 5.2; cf. Figure 4.2 in Chapter 4). Our data therefore indicates that the LIG is the most likely time period to have experienced the largest WAIS deglaciation event over the entire Late Pleistocene, with noticeably different erosional patterns compared to those observed from the modern WAIS. Warm water incursions onto the continental shelf are suggested as the main driver for ice retreat (e.g. Pollard and DeConto, 2009). Hillenbrand et al. (2017) presented multi-proxy data on sediment cores and foraminifer shells showing the influence of Circumpolar Deep Water inflow on driving recent and past WAIS retreat. The driving force for CDW upwelling is linked to buoyancy changes and regional climatic variability related to latitudinal shifts in the Southern Hemisphere westerly winds (Thoma et al., 2008; Wåhlin et al., 2013; Dutrieux et al., 2014). On glacial-interglacial time scales, a

general poleward shift in the westerlies was concluded for times of atmospheric warming (Toggweiler et al., 2006). The shift in the westerlies during glacial and interglacial times of the last ~191 kyrs is confirmed by our IRD data of PS58/254, with hornblende and biotite grains indicating a western provenance in interglacial samples (i.e. ACC influence), and grains an eastern provenance in glacial samples (i.e. northern shift of the fronts, coastal current influence). Site PC493 is always located southward of the southern boundary of the ACC and hence under the influence of the coastal current.

Our new records of changes in the erosional regime of the WAIS, potentially linked to WAIS retreat during the LIG can be compared to regional and global climatic records. For instance, the timing of the deuterium change in the EDC ice core from East Antarctica coincides with our Nd isotope provenance shift in PS58/254 (Jouzel et al., 2007). At its LIG peak, the deuterium record indicates regional temperature that were at least 4.5 °C (Jouzel et al., 2007) and potentially up to 6 °C warmer (Sime et al., 2009) than today. Parallel changes during the LIG can also be observed in distal benthic $\delta^{18}O$ records, such as those from ODP Site 1123 on the Chatham Rise east of New Zealand (Elderfield et al., 2012) and the global LR04 stack, which has been related to melting of the Greenland and/or Antarctic ice sheets (Figure 5.5). Oceanographic changes during MIS 5e are furthermore documented by increased (alkenone) sea-surface temperature at ODP Site 1090 in the sub-Antarctica sector of the Atlantic Ocean (Martínez-Garcia et al., 2009), as well as deep-ocean temperatures at ODP Site 1123 derived from the Mg/Ca ratios of benthic foraminifera shells (Elderfield et al., 2012) (Figure 5.5). The relationship between these records and potential WAIS retreat is unclear, but the idea has been put forward that significant WAIS retreat could have had an amplifying effect on oceanographic changes through deglaciation-forced slowdown of the thermohaline circulation by injecting large meltwater quantities to the ocean (Masson-Delmotte et al., 2010; Holden et al., 2011). Although our new data cannot provide insights into the exact extent of the WAIS during the LIG, our data suggest that the most significant change in erosional patterns around the Amundsen Sea, possible coupled to WAIS retreat, occurred during MIS 5e, some 130 ka.

5.6. Conclusions

Analysis of the Sr and Nd isotopic composition of fine-grained detrital sediments and $^{40}Ar/^{39}Ar$ ages of hornblende and biotite grains in two cores off the Amundsen Sea embayment reveals significant changes in the sediment delivery over the past 191 kyrs. Ice-rafted debris deposited at site PS58/254 is characterized by an easterly source originating from the eastern Thurston Island during glacial MIS 6, and a westerly source in the Wrigley Gulf-Hobbs Coast area during interglacial MIS 5 and MIS 1. The change in the IRD provenance can be interpreted by a southward migration of the westerlies during interglacial times, changing the direction of the surface current above site PS58/254. The other site, PC493, was continuously located underneath prevailing westward flowing coastal currents irrespective of the climatic regime.

Decoupling of Sr and Nd isotope records indicates erosion of composite sources. The hypothesis put forward in this chapter is that the glacial (~160 ka) peak in $^{87}Sr/^{86}Sr$ ratios in both cores, which correlates with kaolinite maxima, indicates erosion of Late Cretaceous and Cainozoic sedimentary strata on the shelf. The Nd isotope records reveal the largest shifts during Termination II, which can potentially be linked with WAIS retreat due to the restriction of erosion to basaltic sources in Marie Byrd Land and around the Hudson Mountains coupled with the disappearance of the characteristic modern isotope fingerprint of the detritus supplied from the Pine Island Glacier drainage basin, indicating ungrounding of the WAIS in this area (i.e. formation of a huge floating ice shelf). Furthermore, the timing of the observed provenance changes coincides with global and regional records of atmospheric and oceanic temperatures. Although our data does not allow the exact determination of WAIS extent/retreat during MIS 5e, it nevertheless suggest MIS 5e as the main candidate for WAIS collapse during the entire Late Pleistocene.

Statement of Contribution

The work presented here was part of a collaborative effort to which the author, Tina van de Flierdt (Imperial College, UK) and Claus-Dieter Hillenbrand (BAS, UK) contributed to the initial idea. Carys P. Cook and Tina van de Flierdt provided some of the neodymium isotope data. Claus-Dieter Hillenbrand provided some of the data for PC493 (i.e. gravel counts, $CaCO_3$, magnetic susceptibility, Ba/Ti, stable isotope data). Clay content of PS58/254 were measured by Gerhard Kuhn. Sidney R. Hemming (L-DEO, Columbia University, US) conducted the $^{40}Ar/^{39}Ar$ measurements on hornblende and biotite minerals. Tom Williams (University of Cambridge, UK) provided the age model for core PC493.

Chapter 6

Summary and Future Perspectives

6.1. New insights into the past behaviour of the West Antarctic Ice Sheet during the late Pleistocene

The overarching aim of this thesis was to advance our understanding on the behaviour of the West Antarctic Ice Sheet (WAIS) during the late Pleistocene (i.e. past 1.1 million years). In this thesis I have presented (isotope) geochemical data on seafloor surface sediments and downcore sediments deposited around West Antarctica, with a particular focus on the Amundsen Sea. This data has been used to infer sediment provenance and thereby reveal new insights into the glacial history of the WAIS. Below, I summarize how this aim was achieved by outlining major findings of my research, presented in the framework of the four main objectives presented in Chapter 1.3.

Objective 1: Examine the overall geochemical (i.e. isotopic) variability of modern seafloor surface sediments around West Antarctica

I have shown in Chapter 2 that detrital glaciomarine sediments, deposited off West Antarctica, reveal large variability in their isotopic and geochemical composition, allowing to differentiate between various ice drainage sectors on the West Antarctic continent. The results furthermore provide insights on ice-covered geology and sediment transport pathways in the Pacific sector of the Southern Ocean. The new results present a baseline map, essential for any downcore provenance study in the marine realm off West Antarctica, paving the way to investigate WAIS dynamics back in time (Chapters 4 and 5; cf. Chapter 6.2).

Objective 2: Characterize the fingerprint of glaciogenic sediments delivered by the Pine Island and Thwaites Glaciers

Pine Island and Thwaites Glaciers are the two currently most closely monitored glacial systems in West Antarctica due to their accelerating mass loss. By applying a large multi-proxy provenance toolbox (i.e. isotopic, geochemical, bulk and clay mineralogy, rock magnetic properties) to marine sediments from the Pine Island Bay, Amundsen Sea, I found characteristic fingerprints associated with these two glaciers (Chapter 3). Glaciogenic detritus delivered by the Pine Island Glacier and the Thwaites Glacier is (isotopically) distinct enough to open up the possibility to trace the respective absence or presence of these two ice drainage systems

back in time. In a first step towards this direction, I have shown that the provenance of sedimentary sequences deposited in the flowline of the two glaciers since the Last Glacial Maximum remained largely unvaried.

Objective 3: Reconstruct the detrital provenance of the two sediment cores from the Amundsen Sea spanning the past 1.1 Myrs to constrain the evolution of late Pleistocene WAIS in the Amundsen Sea sector

In Chapter 4, I presented a first geochemical downcore provenance study of detrital sediments deposited in the Pacific sector of the West Antarctic margin for the late Pleistocene. The data presented in this chapter show evidence for eccentricity-paced fluctuations in the supply of fine-grained sediment from the WAIS, related to minor (?) changes in the position of the ice margin between 1.1 and 0.2 million years. In addition, the provenance of ice-rafted debris reveals a southward shift in the location of the southern boundary of the Antarctic Costal Current, and hence the position of the westerlies, during interglacials. Overall, our data does not provide any evidence for significant WAIS retreat between 1.1 and 0.2 Ma, and supports a relatively stable late Pleistocene WAIS.

Objective 4: Investigate whether a major disintegration or collapse of the WAIS occurred during the peak of the last interglacial period, Marine Isotope Stage 5e

In contrast, a remarkable excursion in the fine-grained (neodymium) isotopic composition is observed at, or shortly after, Termination II (~130 ka). This provenance shift is the largest signal recorded in both sediment cores, highlighting the potential for substantial change in the source of the detrital sediments delivered to the Amundsen Sea during the last interglacial. I interpreted these results in terms of significant grounding line retreat of the ice sheet, with reduced or even ceased sediment supply from the Pine Island Glacier and Thwaites Glacier basins. These findings are important, as they suggest a large change in WAIS dynamics during the last interglacial period, and mark the first data-based corroboration of model-based predictions for the state of the WAIS during the late Pleistocene.

6.2. Remarks on the limitation of this study

An inherent limitation in applying provenance studies in the marine realm off Antarctica is that much of the continental geology is unknown. Rock exposure on Antarctica accounts only for up to 2% of the surface, with much of it located in the Antarctic Peninsula and Transantarctic Mountains. The geology of West Antarctica remains to a large extent unmapped. In my thesis, I provided a summary on the exisiting literature on the geology as well as airborne and satellite investigations on West Antarctica (c.f. Chapter 2) in order to constrain the bedrock under the ice.

Additional insights can be derived using sedimentary provenance, as long as lithological, mineralogical or grain-size biases are considered, which is why I opted for a multi-provenance tracer approach to reduce any inherent bias in using one tracer along. This approach allowed identification of multiple source rocks to our sediments, such as contribution of glacial detritus from young volcanic rocks and Cretaceous granitoids to the offshore load in the Wrigley Gulf/Hobbs Coast (c.f. Chapter 2). In areas where the subglacial geology is totally unknown, such as below the Pine Island and Thwaites Glaciers, my datasets would benefit from rigorous statistical processing, for instance using multivariate analysis (e.g. principal component analysis), to disentangle the signature of multiple source rocks below the ice.

Finally, the two main sediment cores utilised for reconstructing the late Pleistocene in the Amundsen Sea (PS58/254 and PC493) are the only ones available the area. Although the sedimentology of these records has been formerly described and published, an exact understanding on how these sediments relate to ice-sheet changes through time remains poorly constrained. To this end, future studies on proximal or well-characterized distal sediment cores could provide further support to our interpretation.

6.3. Concluding remarks and future research directions

My work has provided novel and significant insights into the traceability and evolution of the WAIS over the last 1.1 million years based on isotopic and geochemical provenance data on detrital sediments deposited off the West Antarctic margin. My finding of a relatively stable WAIS throughout most of the late Pleistocene, despite large cyclic fluctuation in global mean temperatures and atmospheric pCO_2 and hence climate, comes probably as a surprise to some. Less of a surprise is that the exception to this statement comes from data on the last interglacial. Although the exact extent of WAIS ice retreat remains unresolved, I have shown that the largest reduction in WAIS extent of the entire late Pleistocene occurred most likely during MIS 5e.

There is ample scope for ample future provenance work in the Amundsen Sea using radiogenic isotope analysis of marine sediments. Currently, an unprecedented effort to study the Amundsen Sea and past and future stability of the West Antarctic ice sheet is underway. RV Polarstern expedition PS104 to the Amundsen Sea shelf in February 2017, retrieved the first shallow (<36m) drill cores of consolidated Cenozoic sedimentary strata from the Amundsen Sea shelf using the sea floor drill rig MeBo (Gohl et al., 2013). Future provenance studies on this invaluable core material will provide detailed insights on the paleo-glaciological behaviour of the WAIS and the environment in the Amundsen Sea embayment during the Cretaceous and Cenozoic. IODP expedition 374 to the Ross Sea sailed in January to February 2018 and recovered a Neogene sequence of sediments from a shelf to rise transect in the Ross Sea, allowing insights into WAIS dynamics from a different location (McKay et al., 2018). Planned IODP Expedition 379 to the Amundsen Sea (January-March 2019) has the goal to drill a transect from the inner shelf to the outer shelf in the Amundsen Sea in order to provide a detailed Cenozoic record of the WAIS from an Amundsen Sea perspective. Conducting provenance studies on the recovered material has been an integral part in the planning for both IODP expeditions. Lastly, NSF and NERC jointly funded in 2018 the five year £20 million Thwaites programme, a focussed effort to constrain the future of Thwaites glacier and its contribution to sea level rise. Part of the programme is also the collection of new sedimentary records adjacent to the Thwaites glacier.

The geochemical data presented in this thesis provide an invaluable baseline for all of these programmes and projects. Although this thesis was limited to the use of strontium and neodymium isotopic compositions of fine detritus, and $^{40}Ar/^{39}Ar$ dating of ice-rafted hornblende and biotite grains, as provenance tracers of detrital sediments, there is a vast array

of other isotope systems that could be exploited. Examples include, but are not limited to hafnium (Hf) and lead (Pb) isotopic compositions of fine detritus, potassium-argon (K-Ar) dating of fine detritus, and uranium-lead (U-Pb) zircon dating as well as apatite fission track and U-Th-He ages. Expanding the provenance toolbox to other systems can help with a more detailed identification of source areas of detrital sediments, and hence provide further insights onto the ice-covered West Antarctic geology and past WAIS dynamics. To summarize, collection of new core material from the Amundsen Sea shelf, and the possibility of expanding the provenance approach presented in this thesis to other isotope systems, open the possibility of providing higher spatial and temporal resolution records of the state of the WAIS during the Cenozoic than could be investigated in this thesis. I made a start, and more work has to follow now.

Bibliography

Adams, C. J., 1986. Geochronological studies of the Swanson Formation of Marie Byrd Land, West Antarctica, and correlation with northern Victoria Land, East Antarctica, and South Island, New Zealand. New *Zealand Journal of Geology and Geophysics* 29 (3), 345-358.

Adams, C. J., 1987. Geochronology of granite terranes in the Ford Ranges, Marie Byrd Land, West Antarctica. *New Zealand Journal of Geology and Geophysics* 30, 51-57.

Adams, C. J., Pankhurst, R. J., Maas, R., Millar, I. L., 2005. Nd and Sr isotopic signatures of metasedimentary rocks around the South Pacific margin and implications for their provenance. In: Vaughan A. P. M., Leat P. T. and Pankhurst R. J. (eds). Terrane Processes at the Margins of Gondwana. Geological Society, London, Special Publications 246, 113-141.

Adams, C. J., Seward, D., Weaver, S. D., 1995. Geochronology of Cretaceous granites and metasedimentary basement on Edward VII Peninsula, Marie Byrd Land, West Antarctica. *Antarctic Science* 7 (3), 265-277.

Aitken, A. E., and Bell, T. J., 1998. Holocene glacimarine sedimentation and macrofossil palaecology in the Canadian High Arctic: environmental controls. *Marine Geology* 145, 151–171.

Aitken, A. R. A., Young, D. A., Ferraccioli, F., Betts, P. G., Greenbaum, J. S., Richter, T. G., Roberts, J. L., Blankenship, D. D., Siegert, M. J., 2014. The subglacial geology of Wilkes Land, East Antarctica. *Geophysical Research Letters* 41, 2390-2400.

Amblas, D., Urgeles, R., Canals, M., Calafat, A. M., Rebesco, M., Camerlenghi, A., Estrada, F., De Batist, M., Hughes-Clarke, J. E., 2006. Relationship between continental rise development and palaeo-ice sheet dynamics, Northern Antarctic Peninsula Pacific margin. *Quaternary Science Reviews* 25 (9-10), 933-944.

Anandakrishnan, S., Blankenship, D. D., Alley, R. B., and Stoffa, P. L., 1998. Influence of subglacial geology on the position of a West Antarctic ice stream from seismic observations. *Nature* 394 (6688), 62.

Arndt, J. E., Larter, R. D., Friedl, P., Gohl, K., Höppner, K., the Science Team of Expedition PS104, 2018. Bathymetric controls on calving processes at Pine Island Glacier. The *Cryosphere* 12, 2039–2050.

Arndt, J. E., Schenke, H. W., Jakobsson, M., Nitsche, F. O., Buys, G., Goleby, B., Rebesco, M., Bohoyo, F., Hong, J., Black, J., Greku, R., Udintsev, G., Barrios, F., Reynoso-Peralta, W., Taisei, M., Wigley, R., 2013. The International Bathymetric Chart of the Southern Ocean (IBCSO) Version 1.0—A new bathymetric compilation covering circum-Antarctic waters. *Geophysical Research Letters* 40 (12), 3111-3117.

Arneborg, L., Wåhlin, A. K., Björk, G, Liljebladh, B., Orsi, A. H., 2012. Persistent inflow of warm water onto the central Amundsen shelf. Nature *Geoscience* 5, 876-880, doi:10.1038/ngeo1644.

Assmann, K. M., Hellmer, H. H., Jacobs, S. S., 2005. Amundsen Sea ice production and transport. *Journal of Geophysical Research* 110, C12013.

Assmann, K., Jenkins, A., Shoosmith, D., Walker, D., Jacobs, S. S., Nicholls, K., 2013. Variability of circumpolar deep water transport onto the Amundsen Sea continental shelf through a shelf break trough. *Journal of Geophysical Research* 118, 6603–6620.

Bamber, J. L., Riva, R. E. M., Vermeersen, B. L. A., LeBrocq, A. M., 2009. Reassessment of the potential sea-level rise from a collapse of the West Antarctic Ice Sheet. *Science* 324, 901–903.

Basak, C., and Martin, E. E., 2013. Antarctic weathering and carbonate compensation at the Eocene–Oligocene transition. *Nature Geoscience* 6 (2), 121.

Bayon, G., Burton, K. W., Soulet, G., Vigier, N., Dennielou, B., Etoubleau, J., Ponzevera, E., German, C. R., Nesbitt, R. W., 2009. Hf and Nd isotopes in marine sediments: constraints on global silicate weathering. *Earth and Planetary Science Letters* 277, 318–326.

Bayon, G., German, C. R., Boella, R. M., Milton, J. A., Taylor, R. N., Nesbitt, R. W., 2002. An improved method for extracting marine sediment fractions and its application to Sr and Nd isotopic analysis. *Chemical Geology* 187 (3-4), 179-199.

Behrendt, J. C., 2013. The aeromagnetic method as a tool to identify Cenozoic magmatism in the West Antarctic Rift System beneath the West Antarctic Ice Sheet—A review; Thiel subglacial volcano as possible source of the ash layer in the WAISCORE. *Tectonophysics* 585, 124-136.

Bell, R. E., Blankenship, D. D., Finn, C. A., Morse, D. L., Scambos, T. A., Brozena, J. M., and Hodge, S. M., 1998. Influence of subglacial geology on the onset of a West Antarctic ice stream from aerogeophysical observations. *Nature* 394 (6688), 58.

Benn, D., and Evans, D. J., 2014. *Glaciers and glaciation,* 2nd Edition. Routledge, 816 pp.

Bennett, M. M., and Glasser, N. F., 2011. *Glacial geology: ice sheets and landforms*. John Wiley & Sons, 385 pp.

Berggren, W. A., Kent, D. V., Swisher, C. C., Aubry, M. P., 1995. A revised Cenozoic geochronology and chronostratigraphy. In: Berggren, W.A., Kent, D.V., Aubry, M.P., Hardenbohl, J. (Eds.), Geochronology, Time Scales and Stratigraphic Correlation: Framework for an Historical Geology, vol. 54. Soc. Sediment. Geol., Spec. Publ. Soc. Econ. Paleontol. Mineral., 129–212.

Bertram, R. A., Wilson, D. J., van de Flierdt, T., McKay, R. M., Patterson, M. O., Jimenez-Espejo, F. J., Escutia, C., Duke, G. C., Taylor-Silva, B. I., Riesselman, C. R., 2018. Pliocene deglacial event timelines and the biogeochemical response offshore Wilkes Subglacial Basin, East Antarctica. *Earth and Planetary Science Letters* 494, 109-116.

Bhatia, M. R., and Crook, K. A., 1986. Trace element characteristics of graywackes and tectonic setting discrimination of sedimentary basins. *Contributions to Mineralogy and Petrology* 92 (2), 181-193.

Bingham, R. G., Ferraccioli, F., King, E. C., Larter, R. D., Pritchard, H. D., Smith, A. M., Vaughan, D. G., 2012. Inland thinning of West Antarctic Ice Sheet steered along subglacial rifts. *Nature* 487, 468-471.

Biscaye, P. E., 1965. Mineralogy and sedimentation of recent deep-sea clay in the Atlantic Ocean and adjacent seas and oceans. *GSA Bulletin* 76 (7), 803-832.

Biscaye, P. E., and Dasch, E. J., 1971. Rubidium, Strontium, Strontium-Isotope System in Deep-Sea Sediments - Argentine Basin. Journal of Geophysical Research 76 (21), 5087.

Bloemendal, J., King, J. W., Hall, F. R., Doh, S. J., 1992. Rock magnetism of Late Neogene and Pleistocene deep-sea sediments: Relationship to sediment source, diagenetic processes, and sediment lithology. *Journal of Geophysical Research: Solid Earth* 97 (B4), 4361-4375.

Blum, J. D., and Erel, Y. Radiogenic isotopes in weathering and hydrology. Surface and Ground Water, Weathering, Erosion and Soils, In: Treatise on Geochemistry, (Elsevier, 2003), p. 365-392.

Blum, J. D., and Erel, Y., 1995. A silicate weathering mechanism linking increases in marine 87Sr/86Sr with global glaciation. *Nature* 373 (6513), 415.

Blum, J. D., and Erel, Y., 1997. Rb-Sr isotope systematics of a granitic soil chronosequence: The importance of biotite weathering. *Geochimica et Cosmochimica Acta* 61 (15), 3193-3204.

Boger, S. D., 2011. Antarctica — Before and after Gondwana. *Gondwana Research* 19, 335-371.

Bonn, W. J., Gingele, F. X., Grobe, H., Mackensen, A., Fütterer, D. K., 1998. Palaeoproductivity at the Antarctic continental margin: opal and barium records for the last 400 ka. *Palaeogeography, Palaeoclimatology, Palaeoecology* 139 (3), 195-211.

Brachfeld, S., Domack, E., Kissel, C., Laj, C., Leventer, A., Ishman, S., Gilbert, R., Camerlenghi, A., Eglinton, L. B., 2003. Holocene history of the Larsen-A Ice Shelf constrained by geomagnetic paleointensity dating. *Geology* 31, 749-752.

Bradschaw, J. D., Pankhurst, R. J., Weaver, S. D., Storey, B. C., Muir, R. J., Ireland, T. R., 1997. New Zealand Superterranes recognized in Marie Byrd Land and Thurston Island. In: Ricci C. A. (eds), The Antarctic Region: Geological Evolution and Processes, 429-436.

Burckle, L. H., Kellogg, D. A., Kellogg, T. B., Fastook, J. L., 1997. A mechanism for emplacement and concentrations of diatoms in glacigenic deposits. *Boreas* 26, 55–60.

Burn, R. W. 1984. The geology of the LeMay Group, Alexander Island. Scientific Report British Antarctic Survey 109.

Burton-Johnson, A., and Riley, T. R., 2015. Autochthonous v. accreted terrane development of continental margins: a revised in situ tectonic history of the Antarctic Peninsula. *Journal of the Geological Society* 172, 822-835.

Care, B. W., 1983. The petrology of the Rouen Mountains, northern Alexander Island. British Antarctic Survey Bulletin 52, 63–86.

Carter, A., Riley, T. R., Hillenbrand, C. D., Rittner, M., 2017. Widespread Antarctic glaciation during the late Eocene. *Earth and Planetary Science Letters* 458, 49-57.

Carvajal, G. K., Wåhlin, A. K., Eriksson, L. E. B., Ulander, L. M. H., 2013. Correlation between synthetic aperture radar surface winds and deep water velocity in the Amundsen Sea, Antarctica. *Remote Sensing* 5, 4088–4106, doi:10.3390/rs5084088.

Cawood, P. A., 2005. Terra Australis Orogen: Rodinia breakup and development of the Pacific and Iapetus margins of Gondwana during the Neoproterozoic and Paleozoic. *Earth-Science Reviews* 69, 249-279.

Chester, R., and Hughes, M. J., 1967. A chemical technique for the separation of ferro-manganese minerals, carbonate minerals and adsorbed trace elements from pelagic sediments. *Chemical Geology* 2, 249-262.

Clark, P. U., Archer, D., Pollard, D., Blum, J. D., Rial, J. A., Brovkin, V., Mix, A. C., Pisias, N. G., Roy, M., 2006. The middle Pleistocene transition: characteristics, mechanisms, and implications for long-term changes in atmospheric pCO2. *Quaternary Science Reviews* 25 (23-24), 3150-3184.

Collier, R., and Edmond, J., 1984. The trace element geochemistry of marine biogenic particulate matter. *Progress in Oceanography* 13 (2), 113-199.

Colville,E. J., Carlson, A. E., Beard, B. L., Hatfield, R. G., Stoner, J. S., Reyes, A. V., Ullman, D. J., 2011. Sr-Nd-Pb Isotope Evidence for Ice-Sheet Presence on Southern Greenland during the Last Interglacial. *Science* 333 (6042), 620-623.

Cook, C. P., 2013. Insights into the behaviour of the Pliocene East Antarctic Ice Sheet from provenance studies of marine sediments using radiogenic isotopes (PhD Thesis: Imperial College London).

Cook, C. P., Hemming, S. R., van de Flierdt, T., Pierce Davis, E. L., Williams, T., Galindo, A. L., Jimenez-Espejo, F. J., Escutia, C., 2017. Glacial erosion of East Antarctica in the Pliocene: a comparative study of multiple marine sediment provenance tracers. *Chemical Geology* 466, 199-218.

Cook, C. P., Hill, D. J., van de Flierdt, T., Williams, T., Hemming, S. R., Dolan, A. M., Pierce, E. L., Escutia, C., Harwood, D., Cortese, G., Gonzales, J. J., 2014. Sea surface temperature control on the distribution of far-traveled Southern Ocean ice-rafted detritus during the Pliocene. *Paleoceanography* 29, doi:10.1002/2014PA002625.

Cook, C. P., van de Flierdt, T., Williams, T., Hemming, S. R., Iwai, M., Kobayashi, M., Jimenez-Espejo F. J., Escutia, C., González, J. J., Khim, B.-K., McKay, R. M., Passchier, S., Bohaty, S., Riesselman, C. R., Tauxe, L., Sugisaki, S., Galindo, A. L., Patterson, M. O., Sangiorgi, F., Pierce,

E. L., Brinkhuis, H., IODP Expedition 318 Scientists, 2013. Dynamic behaviour of the East Antarctic ice sheet during Pliocene warmth. *Nature Geoscience* 6, 765-769.

Corr, H. F. J., and Vaughan, D. G., 2008. A recent volcanic eruption beneath the West Antarctic ice sheet. *Nature Geoscience* 1, 122-125.

Coxall, H. K., Wilson, P. A., Palike, H., Lear, C. H., Backman, J., 2005. Rapid stepwise onset of Antarctic glaciation and deeper calcite compensation in the Pacific Ocean, *Nature* 433, 53-57.

Craddock, J. P., Schmitz, M. D., Crowley, J. L., Larocque, J., Pankhurst, R. J., Juda, N., Konstantinou, A., Storey, B., 2017. Precise U-Pb zircon ages and geochemistry of Jurassic granites, Ellsworth-Whitmore terrane, central Antarctica. *GSA Bulletin* 129(1-2), 118-136.

Cunningham, A. P., Larter, R. D., Barker, P. F., Gohl, K., Nitsche F. O., 2002. Tectonic evolution of the Pacific margin of Antarctica 2. Structure of Late Cretaceous–early Tertiary plate boundaries in the Bellingshausen Sea from seismic reflection and gravity data. Journal of Geophysical Research: Solid Earth 107 (B12), EPM 6-1 – EPM 6-20, doi: 10.1029/2002JB001897.

Curtis, M. L, Leat, P. T., Riley, T. R., Storey, B. C., Millar, I. L., Randall, D. E., 1999. Middle Cambrian rift-related volcanism in the Ellsworth Mountains, Antarctica: tectonic implications for the palaeo-Pacific margin of Gondwana. Tectophysics 304, 275-299.

Dalrymple, G. B., Alexander, E. C. Jr., Lanphere, M. A., Kraker, G. P., 1981. Irradiation of samples for 40Ar/39Ar dating using the Geological Survey TRIGA reactor. U.S. Geological Survey Professional Paper 1176.

Dalziel, I. W. D. and Elliot, D. H., 1982. West Antarctica: Problem child of Gondwanaland. *Tectonics* 1 (1), 3-19.

Dasch, E. J., 1969. Strontium isotopes in weathering profiles, deep-sea sediments, and sedimentary rocks. *Geochimica et Cosmochimica Acta* 33 (12), 1521.

DeConto, R. M., and Pollard, D., 2016. Contribution of Antarctica to past and future sea-level rise. *Nature* 531, 591-597. doi: 10.1038/nature17145.

DeConto, R. M., Galeotti, S., Pagani, M., Tracy, D., Schaefer, K., Zhang, T., Pollard, D., Beerling, D. J., 2012. Past extreme warming events linked to massive carbon release from thawing permafrost. *Nature* 484 (7392), 87.

Diekmann, B., and Kuhn, G., 1999. Provenance and dispersal of glacial–marine surface sediments in the Weddell Sea and adjoining areas, Antarctica: ice-rafting versus current transport. *Marine Geology* 158, 209-231.

Diekmann, B., and Kuhn, G., 2002. Sedimentary record of the mid-Pleistocene climate transition in the southeastern South Atlantic (ODP Site 1090). Palaeogeography, Palaeoclimatology, *Palaeoecology*, 182 (3), 241-258.

Diekmann, B., Kuhn, G., Rachold, V., Abelmann, A., Brathauer, U., Fütterer, D. K., Gersonde, R., Grobe, H., 2000. Terrigenous sediment supply in the Scotia Sea (Southern Ocean): response to Late Quaternary ice dynamics in Patagonia and on the Antarctic Peninsula. *Palaeogeography, Palaeoclimatology, Palaeoecology* 162 (3), 357-387.

Doubleday, P. A., Macdonald, D. I. M., Nell, P. A. R., 1993. Sedimentology and structure of the trench-slope to forearc basin transition in the Mesozoic of Alexander Island, Antarctica. *Geological Magazine* 130 (6), 737-754.

Dowdeswell, J. A., Evans, J., Ó Cofaigh, C., Anderson, J. B., 2006. Morphology and sedimentary processes on the continental slope off Pine Island Bay, Amundsen Sea, West Antarctica. *GSA Bulletin* 118 (5-6), 606-619.

Downing, G. E., Hemming, S. R., Jost, A., Roy, M., 2013. 40Ar/39Ar hornblende provenance clues about Heinrich event 3 (H3). In: Jourdan, F., Mark, D.F. and Verati C. (eds): Advances in

40Ar/39Ar Dating: from Archaeology to Planetary Sciences, Geological Society, London, Special Publications 378, 245-263.

Ducklow, H. W., Wilson, S. E., Post, A. F., Stammerjohn, S. E., Erickson, M., Lee, S.H., Lowry, K. E., Sherrell, R. M., Yager, P. L., 2015. Particle flux on the continental shelf in the Amundsen Sea Polynya and western Antarctic Peninsula. *Elem Sci Anth* 3, 000046. doi:10.12952/journal.elementa.000046.

Dutrieux, P., De Rydt, J., Jenkins, A., Holland, P. R., Ha, H. K., Lee, S. H., Steig, E. J., Ding, Q., Abrahamsen, E. P., Schröder, M., 2014. Strong sensitivity of Pine Island ice-shelf melting to climatic variability. *Science* 343 (6167), 174-178.

Dutton, A., and Lambeck, K., 2012. Ice volume and sea level during the last interglacial. *Science* 337 (6091), 216-219.

Dutton, A., Carlson, A. E., Long, A. J., Milne, G. A., Clark, P. U., DeConto, R., Horton, B. P., Rahmstorf, S., Raymo, M. E., 2015. Sea-level rise due to polar ice-sheet mass loss during past warm periods. *Science*, 349 (6244), aaa4019.

Ehrmann, W. U., and Mackensen, A., 1992. Sedimentological evidence for the formation of an East Antarctic ice-sheet in Eocene Oligocene time. *Palaeogeography, Palaeoclimatology, Palaeoecology* 93 (1-2), 85-112.

Ehrmann, W. U., Hillenbrand, C.-D., Smith, J. A., Graham, A. G. C. Kuhn, G., Larter, R. D., 2011. Provenance changes between recent and glacial-time sediments in the Amundsen Sea embayment, West Antarctica: clay mineral assemblage evidence. *Antarctic Science* 23 (5), 471-486.

Ehrmann, W. U., Melles, M., Kuhn, G., Grobe, H., 1992. Significance of clay mineral assemblages in the Antarctic Ocean. *Marine Geology* 107, 249–273.

Eisenhauer, A., Meyer, H., Rachold, V., Tütken, T., Wiegand, B., Hansen, B. T., Spielhagen, R. F., Lindemann, F., Kassens, H., 1999. Grain size separation and sediment mixing in Arctic Ocean sediments: evidence from the strontium isotope systematic. *Chemical Geology* 158, 173-188.

Elderfield, H., Ferretti, P., Greaves, M., Crowhurst, S., McCave, I. N., Hodell, D. A., Piotrowski, A. M., 2012. Evolution of ocean temperature and ice volume through the mid-Pleistocene climate transition. *Science* 337 (6095), 704-709.

Enderlein, P., and Larter, R. D., 2008. Cruise Report JR 179-RRS James Clark Ross-February to April 2008-Marine biological and marine geological and geophysical studies in the Amundsen and Bellingshausen Seas. British Antarctic Survey.

Farmer, G. L., and Licht, K., 2016. Generation and fate of glacial sediments in the central Transantarctic Mountains based on radiogenic isotopes and implications for reconstructing past ice dynamics. *Quaternary Science Reviews* 150, 98–109.

Farmer, G. L., Barber, D., Andrews, J., 2003. Provenance of Late Quaternary ice-proximal sediments in the North Atlantic: Nd, Sr and Pb isotopic evidence. *Earth and Planetary Science Letters* 209, 227-243.

Farmer, G. L., Licht, K., Swope, R. J., Andrews, J., 2006. Isotopic constraints on the provenance of fine-grained sediment in LGM tills from the Ross Embayment, Antarctica. *Earth and Planetary Science Letters* 249, 90-107.

Feldmann, J., and Levermann, A., 2015. Collapse of the West Antarctic Ice Sheet after local destabilization of the Amundsen Basin. Proceedings of the National Academy of Sciences 112 (46), 14191-14196.

Feldmann, J., and Levermann, A., 2015. Collapse of the West Antarctic Ice Sheet after local destabilization of the Amundsen Basin. Proceedings of the National Academy of Sciences 112 (46), 14191-14196.

Ferraccioli, F., Armadillo, E., Jordan, T., Bozzo, E., Corr, H., 2009. Aeromagnetic exploration over the East Antarctic Ice Sheet: A new view of the Wilkes Subglacial Basin. *Tectonophysics* 478 (1-2), 62-77.

Ferraccioli, F., Bozzo, E., Damaske, D., 2002. Aeromagnetic signatures over western Marie Byrd Land provide insight into magmatic arc basement, mafic magmatism and structure of the Eastern Ross Sea Rift flank. *Tectonophysics* 347, 139-165.

Ferraccioli, F., Jones, P. C., Vaughan, A. P. M., Leat, P. T., 2006. New aerogeophysical view of the Antarctic Peninsula: More pieces, less puzzle. *Geophysical Research Letters* 33, L05310.

Ferrando, R., Roperch, P., Morata, D., Arriagada, C., Ruffet, G., Córdova, M. L., 2014. A paleomagnetic and magnetic fabric study of the Illapel Plutonic Complex, Coastal Range, central Chile: Implications for emplacement mechanism and regional tectonic evolution during the mid-Cretaceous. *Journal of South American Earth Science* 50, 12-26.

Flowerdew, M. J., Millar, I. L., Vaughan, A. P. M., Pankhurst, R. J., 2005. Age and tectonic significance of the Lassiter Coast Intrusive Suite, eastern Ellsworth Land, Antarctic Peninsula. *Antarctic Science* 17, 443–452, doi:10.1017/S0954102005002877.

Flowerdew, M. J., Tyrrell, S., Riley, T. R., Whitehouse, M. J., Mulvaney, R., Leat, P. T., Marschall, H. R., 2012. Distinguishing East and West Antarctic sediment sources using the Pb isotope composition of detrital K-feldspar. *Chemical Geology* 292–293, 88–102, doi:10.1016/j.chemgeo.2011.11.006.

Frederichs, T., Bleil, U., Däumler, K., von Dobeneck, T., Schmidt, A., 1999. The magnetic view on the marine paleoenvironment: parameters, techniques and potentials of rock magnetic studies as a key to paleoclimatic and paleoceanographic changes. In: Fischer, G., Wefer, G. (Eds.), Use of Proxies in Paleoceanography: Examples from the South Atlantic. Springer, Berlin Heidelberg, 575–599.

Fretwell, P. et al., 2013. Bedmap2: improved ice bed, surface and thickness datasets for Antarctica. *The Cryosphere* 7, 375-393.

Futa, K., and LeMasurier, W. E., 1983. Nd and Sr isotopic studies on Cenozoic mafic lavas from West Antarctica - another source for continental alkali basalts. *Contributions to Mineralogy and Petrology* 83 (1-2), 38-44.

Gale, A., Dalton, C. A., Langmuir, C. H., Su, Y., Schilling, J. G., 2013. The mean composition of ocean ridge basalts. *Geochemistry, Geophysics, Geosystems* 14 (3), 489–518.

Galeotti, S., DeConto, R., Naish, T., Stocchi, P., Florindo, F., Pagani, M., Barrett, P., Bohaty, S. M., Lanci, L., Pollard, D., Sandroni, S., Talarico, F. M., Zachos, J. C., 2016. Antarctic Ice Sheet variability across the Eocene-Oligocene boundary climate transition. *Science*, doi:10.1126/science.aab0669.

Garçon, M., Chauvel, C., France-Lanord, C., Huyghe, P., Lavé, J., 2013. Continental sedimentary processes decouple Nd and Hf isotopes, *Geochimica et Cosmochimica* Acta 121, 177-195. doi:10.1016/j.gca.2013.07.027.

Gardner, A. S., Moholdt, G., Scambos, T., Fahnstock, M., Ligtenberg, S., van den Broeke, M., Nilsson, J., 2018. Increased West Antarctic and unchanged East Antarctic ice discharge over the last 7 years. *The Cryosphere* 12(2), 521-547.

Garzanti, E., Andò, S., Vezzoli, G., 2008. Settling-equivalence of detrital minerals and grain-size dependence of sediment composition. *Earth and Planetary Science Letters* 273, 138–151.

Garzanti, E., Andò, S., Vezzoli, G., 2009. Grain-size dependence of sediment composition and environmental bias in provenance studies. Eart*h and Planetary Science Letters* 277 (3-4), 422-432.

Gladstone, R. M., Bigg, G. R., Nicholls, K. W., 2001. Iceberg trajectory modelling and meltwater injection in the Southern Ocean. *Journal of Geophysical Research* 106, 19903-19915.

Gohl, K., 2006. The Expedition ANTARKTIS-XXIII/4 of the Research Vessel "Polarstern" in 2006. Berichte zur Polar- und Meeresforschung, 557, 166pp.

Gohl, K., 2010. The Expedition of the Research Vessel "Polarstern" to the Amundsen Sea, Antarctica, in 2010 (ANT-XXVI/3), Berichte zur Polar- und Meeresforschung, Alfred Wegener Institute for Polar and Marine Research, Bremerhaven, Germany, 168 pp.

Gohl, K., 2017. The Expedition PS104 of the Research Vessel POLARSTERN to the Amundsen Sea in 2017, BReports on Polar and Marine Research, Alfred Wegener Institute for Polar and Marine Research, Bremerhaven, Germany, 168 pp.

Gohl, K., Freudenthal, T., Hillenbrand, C.-D., Klages, J., Larter, R., Bickert, T., Bohaty, S., Ehrmann, W., Esper, O., Frederichs, T., Gebhardt, C., Küssner, K., Kuhn, G., Pälike, H., Ronge, T., Simões Pereira, P., Smith, J., Uenzelmann-Neben, G., van de Flierdt, T., the Science Team of Expedition PS104, 2017. MeBo70 seabed drilling on a polar continental shelf: Operational report and lessons from drilling in the Amundsen Sea Embayment of West Antarctica. *Geochemistry, Geophysics, Geosystems* 18 (11), 4235-4250.

Gohl, K., Uenzelmann-Neben, G., Larter, R. D., Hillenbrand, C.-D., Hochmuth, K., Kalberg, T., Weigelt, E., Davy, B., Kuhn, G., Nitsche, F. O., 2013. Seismic stratigraphic record of the Amundsen Sea Embayment shelf from pre-glacial to recent times: Evidence for a dynamic West Antarctic ice sheet. *Marine Geology* 344, 115-131.

Goldstein, S. L., and Hemming, S. R., 2003. Long-lived isotopic tracers in oceanography, paleoceanography, and ice-sheet dynamics. Treatise on Geochemistry (Oxford, Elsevier, 2003).

Golledge, N. R., Fogwill, C. J., Mackintosh, A. N., Buckley, K. M., 2012. Dynamics of the last glacial maximum Antarctic ice-sheet and its response to ocean forcing. *Proceedings of the National Academy of Sciences* 109 (40), 16052-16056.

Golledge, N. R., Levy, R. H., McKay, R. M., Fogwill, C. J., White, D. A., Graham, A. G., Smith, J., Hillenbrand, C.-D., Licht, K. J., Denton, G. H., Ackert Jr, R. P., Maas, S. M., Hall, B. L., 2013. Glaciology and geological signature of the Last Glacial Maximum Antarctic ice sheet. *Quaternary Science Reviews* 78, 225-247.

Golledge, N. R., Menviel, L., Carter, L., Fogwill, C. J., England, M. H., Cortese, G., Levy, R. H., 2014. Antarctic contribution to meltwater pulse 1A from reduced Southern Ocean overturning. *Nature Communications* 5, 5107.

Golledge, N. R., Thomas, Z. A., Levy, R. H., Gasson, E. G. W., Naish, T. R., McKay, R. M., Kowalewski, D. E., Fogwill, C. J., 2017. Antarctic climate and ice-sheet configuration during the early Pliocene interglacial at 4.23 Ma. *Climate of the Past* 13 (7), 959–975.

Golynsky, A. V., et al., 2018. New Magnetic Anomaly Map of the Antarctic. *Geophysical Research Letters* 45 (13), 6437-6449.

Graham, A. G., Larter, R. D., Gohl, K., Dowdeswell, J. A., Hillenbrand, C.-D., Smith, J. A., Evans, J., Kuhn, G., Deen, T., 2010. Flow and retreat of the Late Quaternary Pine Island-Thwaites palaeo-ice stream, West Antarctica. *Journal of Geophysical Research: Earth Surface* 115(F3).

Graham, A. G., Larter, R. D., Gohl, K., Hillenbrand, C.-D., Smith, J. A., Kuhn, G., 2009. Bedform signature of a West Antarctic palaeo-ice stream reveals a multi-temporal record of flow and substrate control. *Quaternary Science Reviews* 28 (25-26), 2774-2793.

Graham, A. G., Nitsche, F. O., Larter, R. D., and Gohl, K., 2016. Submarine landform assemblage produced beneath the Dotson–Getz palaeo-ice stream, West Antarctica. Geological Society, London, Memoirs 46 (1), 345-348.

Grobe, H., and Mackensen, A., 1992. Late Quaternary climatic cycles as recorded in sediments from the Antarctic continental margin. The Antarctic paleoenvironment: A perspective on Global Change; Antarctic Research Series 56, 349-376.

Grousset, F. E., Labeyrie, L., Sinko, J. A., Cremer, M., Bond, G., Duprat, J., Cortijo, E., Huon, S., 1993. Patterns of ice-rafted detritus in the glacial north-Atlantic. *Paleoceanography* 8 (2), 175-192.

Grousset, F. E., Parra, M., Bory, A., Martinez, P., Bertrand, P., Shimmield, G., Ellam, R. M., 1998. Saharan wind regimes traced by the Sr–Nd isotopic composition of subtropical Atlantic sediments: last glacial maximum vs today. *Quaternary Science Reviews* 17 (4-5), 395-409.

Gwiazda, R. H., Hemming, S. R., Broecker, W. S., 1996. Provenance of icebergs during Heinrich event 3 and the contrast to their sources during other Heinrich episodes. *Paleoceanography* 11 (4), 371-378.

Ha, H. K., Wåhlin, A. K., Kim, T. W., Lee, S.H., Lee, J. H., Lee, H. J., Hong, C. S., Arneborg, L., Björk, G., Kalén, O., 2014. Circulation and Modification of warm deep water on the Central Amundsen Shelf. *Journal of Physical Oceanography* 44 (5), 1493–1501.

Hallet, B., Hunter, L., Bogen, J., 1996. Rates of erosion and sediment evacuation by glaciers: A review of field data and their implications. *Global and Planetary Change* 12 (1-4), 213-235.

Harrison, T. M., 1982. Diffusion of 40Ar in hornblende. *Contributions to Mineralogy and Petrology* 78 (3), 324-331.

Harrison, T. M., Duncan, I., Dougall, I., 1985. Diffusion of 40Ar in biotite: Temperature, pressure and compositional effects. *Geochimica et Cosmochimica Acta* 49 (11), 2461-2468.

Hart, S. R., Blusztajn, J., LeMasurier, W. E., Rex, D. C., 1997. Hobbs Coast Cenozoic volcanism: Implications for the West Antarctic rift system. *Chemical Geology* 139 (1-4), 223-248.

Hathway, B., 2001. Sims Island: first data from a Pliocene alkaline volcanic centre in eastern Ellsworth Land. *Antarctic Science* 13 (1), 87-88.

Hearty, P. J., and Olson, S. L., 2008. Mega-highstand or megatsunami? Discussion of McMurtry, et al. (Elevated marine deposits in Bermuda record a late Quaternary megatsunami: Sed. Geol. 200 (2007) 155–165). *Sedimentary G*eology 203, 307–312.

Hearty, P. J., Kindler, P., Cheng, H., Edwards, R. L., 1999. A +20 m middle Pleistocene sea-level highstand (Bermuda and the Bahamas) due to partial collapse of Antarctic ice. *Geology* 27, 375–378.

Heinrich, H., 1988. Origin and consequences of cyclic ice rafting in the northeast Atlantic Ocean during the past 130,000 years. *Quaternary Research* 29 (2), 142-152.

Hemming, S. R., 2004. Heinrich events: massive late Pleistocene detritus layers of the North Atlantic and their global climate imprint. *Reviews of Geophysics* 42, RG1005.

Hemming, S. R., and Hajdas, I., 2003. Ice-rafted detritus evidence from Ar-40/Ar-39 ages of individual hornblende grains for evolution of the eastern margin of the Laurentide ice sheet since 43 C-14 ky. *Quaternary International* 99, 29-43.

Hemming, S. R., Bond, G. C., Broecker, W. S., Sharp, W. D., Klas-Mendelson, M., 2000. Evidence from Ar-40/Ar-39 ages of individual hornblende grains for varying Laurentide sources of iceberg discharges 22,000 to 10,500 yr BP. *Quaternary Research* 54 (3), 372-383.

Hemming, S. R., Broecker, W. S., Sharp, W. D., Bond, G. C., Gwiazda, R. H., McManus, J. F., Klas, M., Hajdas, I., 1998. Provenance of Heinrich layers in core V28-82, northeastern Atlantic: Ar-40/Ar-39 ages of ice-rafted hornblende, Pb isotopes in feldspar grains, and Nd-Sr-Pb isotopes in the fine sediment fraction. *Earth and Planetary Science Letters* 164 (1-2), 317-333.

Hemming, S. R., van de Flierdt, T., Goldstein, S. L., Franzese, A. M., Roy, M., Gastineau, G., Landrot, G., 2007. Strontium isotope tracing of terrigenous sediment dispersal in the Antarctic Circumpolar Current: Implications for constraining frontal positions. *Geochemistry, Geophysics, Geosystems* 8 (6), Q06N13.

Hernández-Molina, F. J., Larter, R. D., Rebesco, M., Maldonado, A., 2004. Miocene changes in bottom current regime recorded in continental rise sediments on the Pacific margin of the Antarctic Peninsula. *Geophysical Research Letters* 31(22).

Hernández-Molina, F. J., Larter, R. D., Rebesco, M., Maldonado, A., 2006. Miocene reversal of bottom water flow along the Pacific Margin of the Antarctic Peninsula: stratigraphic evidence from a contourite sedimentary tail. *Marine Geology* 228(1-4), 93-116.

Hillenbrand, C.-D., and Cortese, G., 2006. Polar stratification: a critical view from the Southern Ocean. *Palaeogeography, Palaeoclimatology, Palaeoecology* 242 (3-4), 240-252.

Hillenbrand, C.-D., and Ehrmann, W., 2002. Distribution of clay minerals in drift sediments on the continental rise west of the Antarctic Peninsula, ODP Leg 178, Sites 1095 and 1096. In: Barker, P. F., Camerlenghi, A., Acton, G. D., Ramsay, A. T. S. (Eds.), Proc. ODP Sci. Results 178, pp. 1 – 29. (CD-ROM). Available from: Ocean Drilling Program, Texas A&M University, College Station, TX 77845-9547, U.S.A.

Hillenbrand, C.-D., Ehrmann, W., Larter, R. D., Benetti, S., Dowdeswell, J. A., Ó Cofaigh, C., Graham, A. G. C., Grobe, H., 2009b. Clay mineral provenance of sediments in the southern Bellingshausen Sea reveals drainage changes of the West Antarctic Ice Sheet during the Late Quaternary. *Marine Geology* 265 (1-2), 1-18.

Hillenbrand, C.-D., Fütterer, D. K., Grobe, H., Frederichs, T., 2002. No evidence for a Pleistocene collapse of the West Antarctic Ice Sheet from continental margin sediments recovered in the Amundsen Sea. *Geo-Marine Letters* 22, 51–59.

Hillenbrand, C.-D., Grobe, H., Diekmann, B., Kuhn, G., Fütterer, D. K., 2003. Distribution of clay minerals and proxies for productivity in surface sediments of the Bellingshausen and Amundsen seas (West Antarctica) - Relation to modern environmental conditions. *Marine Geology* 193, 253-271.

Hillenbrand, C.-D., Kuhn, G., Frederichs, T., 2009a. Record of a Mid-Pleistocene depositional anomaly in West Antarctic continental margin sediments: an indicator for ice-sheet collapse? *Quaternary Science Reviews* 28, 1147-1159.

Hillenbrand, C.-D., Kuhn, G., Smith, J. A., Gohl, K., Graham, A. G. C., Larter, R. D., Klages, J. P., Downey, R., Moreton, S. G., Forwick, M., Vaughan, D. G., 2013. Grounding-line retreat of the West Antarctic Ice Sheet from inner Pine Island Bay. *Geology* 41 (1), 35-38, doi: 10.1130/G33469.1.

Hillenbrand, C.-D., Larter, R. D., Dowdeswell, J. A., Ehrmann, W., Ó Cofaigh, C., Benetti, S., Graham, A.G.C., Grobe, H., 2010a. The sedimentary legacy of a palaeo-ice stream on the shelf of the southern Bellingshausen Sea: Clues to West Antarctic glacial history during the Late Quaternary. *Quaternary Science Reviews* 29 (19-20), 2741-2763.

Hillenbrand, C.-D., Smith, J. A., Hodell, D. A., Greaves, M., Poole, C. R., Kender, S., Williams, M., Andersen, T. J., Jernas, P. E., Elderfield, H., Klages, J. P., Roberts, S. J., Gohl, K., Larter, R. D., Kuhn, G., 2017. West Antarctic Ice Sheet retreat driven by Holocene warm water intrusions. *Nature* 547, 43-48.

Hillenbrand, C.-D., Smith, J.A., Kuhn, G., Esper, O., Gersonde, R., Larter, R. D., Maher, B., Moreton, S. G., Shimmield, T. M., Korte, M., 2010b. Age assignment of a diatomaceous ooze deposited in the western Amundsen Sea Embayment after the Last Glacial Maximum. *Journal of Quaternary Science* 25, 280-295.

Hochmuth, K., and Gohl, K., 2013. Glaciomarine sedimentation dynamics of the Abbot glacial trough of the Amundsen Sea Embayment shelf, West Antarctica. Geological Society, London, Special Publications, 381, SP381-21.

Hodges, K. V. Geochronology and thermochronology in orogenic systems. *Treatise on Geochemistry* (Oxford, Eselvier, 2003)

Hofmann, E. E., Klinck, J. M., Lascara, C. M., and Smith, D. A., 1996. Water Mass Distribution and Circulation West of the Antarctic Peninsula and Including Bransfield Strait, in: Ross, R. M.,

Hofmann, E. E., and Quetin, L. B. (eds.), Foundations for Ecological Research West of the Antarctic Peninsula, Antarctic Research Series, American Geophysical Union, Washington, D.C., 61–81.

Holden, P. B., Edwards, N. R., Wolff, E. W., Valdes, P. J., Singarayer, J. S., 2011. The Mid-Brunhes Event and West Antarctic ice sheet stability. *Journal of Quaternary Science* 26 (5), 474-477.

Holden, P. B., Edwards, N. R., Wolff, E. W., Valdes, P. J., Singarayer, J. S., 2011. The Mid-Brunhes Event and West Antarctic ice sheet stability. *Journal of Quaternary Science* 26 (5), 474-477.

Hole, M. J., and LeMasurier, W. E., 1994. Tectonic controls on the geochemical compositions of Cenozoic mafic alkaline volcanic rocks from West Antarctica. *Contributions to Mineralogy and Petrology* 117 (2), 187-202.

Holland, P. R., Jenkins, A., Holland, D. M., 2010. Ice and ocean processes in the Bellingshausen Sea, Antarctica, *Journal of Geophysical Research* 115, C05020. doi:10.1029/2008JC005219, 2010.

Holloway, M. D., Sime, L. C., Singarayer, J. S., Tindall, J. C., Bunch, P., Valdes, P. J., 2016. Antarctic last interglacial isotope peak in response to sea ice retreat not ice-sheet collapse. *Nature Communications* 7, 12293.

Holt, J. W., Blankenship, D. D., Morse, D. L., Young, D. A., Peters, M. E., Kempf, S. D., Richter, T. G., Vaughan, D. G., Corr, H. F., 2006. New boundary conditions for the West Antarctic Ice Sheet: Subglacial topography of the Thwaites and Smith glacier catchments. *Geophysical Research Letters* 33 (9), doi: 10.1029/2005GL025588.

Houben, A. J., Bijl, P. K., Pross, J., Bohaty, S. M., Passchier, S., Stickley, C. E., Röhl, U., Sugisaki, S., Tauxe, L., van de Flierdt, T., Olney, M., Sangiorgi, F., Sluijs, A., Escutia, C., Expedition 318 Scientists, 2013. Reorganization of Southern Ocean plankton ecosystem at the onset of Antarctic glaciation. *Science* 340 (6130), 341-344.

Hughes, T. J., 1981. The weak underbelly of the West Antarctic ice sheet. *Journal of Glaciology* 27(97), 518-525.

Imbrie, J., Hays, J. D., Martinson, D. G., McIntyre, A., Mix, A. C., Morley, J. J., Pisias, N. G., Prell, W. L., Shackleton, N. J., 1984. The orbital theory of Pleistocene climate: support from a revised chronology, of the marine d18O record. In: Berger, A. (Ed.) Milankovitch and Climate, Part 1. Springer, New York, pp. 269–305.

Jaccard, S. L., Hayes, C. T., Martínez-García, A., Hodell, D. A., Anderson, R. F., Sigman, D. M., Haug, G. H., 2013. Two modes of change in Southern Ocean productivity over the past million years. *Science* 339 (6126), 1419-1423.

Jacobs, S. S., Jenkins, A., Giulivi, C. F., Dutrieux, P., 2011. Stronger ocean circulation and increased melting under Pine Island Glacier ice shelf. *Nature Geoscience* 4, 519-523.

Jacobs, S., Giulivi, C., Dutrieux, P., Rignot, E., Nitsche, F., Mouginot, J., 2013. Getz ice shelf melting response to changes in ocean forcing. *Journal of Geophysical Research* 118, 4152–4168, doi:10.1002/jgrc.20298.

Jacobsen, S. B., and Wasserburg, G. J., 1980. Sm–Nd isotopic evolution of chondrites. *Earth and Planetary Science Letters* 50, 139-155.

Jakobsson, M., Anderson, J. B., Nitsche, F. O., Dowdeswell, J. A., Gyllencreutz, R., Kirchner, N, Mohammad, R., O'Regan, M., Alley, R. B., Anandakrishnan, S., Eriksson, B., Kirshner, A., Fernandez, R., Stolldorf, T., Minzoni, R., Majewski, W., 2011. Geological record of ice shelf break-up and grounding line retreat, Pine Island Bay, West Antarctica. *Geology* 39 (7), 691-694.

Jakobsson, M., Anderson, J. B., Nitsche, F. O., Gyllencreutz, R., Kirshner, A. E., Kirchner, N., O'Regan, M., Mohammad, R., Eriksson, B. (2012). Ice sheet retreat dynamics inferred from glacial morphology of the central Pine Island Bay Trough, West Antarctica. *Quaternary Science Reviews*, 38, 1-10.

Jamieson, S. S., Stokes, C. R., Ross, N., Rippin, D. M., Bingham, R. G., Wilson, D. S., Margold, M., Bentley, M. J., 2014. The glacial geomorphology of the Antarctic ice sheet bed. *Antarctic Science* 26 (6), 724-741.

Jamieson, S. S., Sugden, D. E., and Hulton, N. R., 2010. The evolution of the subglacial landscape of Antarctica. *Earth and Planetary Science Letters* 293 (1-2), 1-27.

Jenkins, A., Dutrieux, P., Jacobs, S. S., McPhail, S. D., Perrett, J. R., Webb, A. T., White, D., 2010. Observations beneath Pine Island Glacier in West Antarctica and implications for its retreat. *Nature Geoscience* 3 (7), 468-472.

Jenkins, A., Dutrieux, P., Jacobs, S. S., Steig, E. J., Gudmundsson, G. H., Smith, J. A., Heywood, E. J., 2016. Decadal ocean forcing and Antarctic ice sheet response: Lessons from the Amundsen Sea. *Oceanography* 29 (4), 106-117.

Jeong, S., Howat, I. M., Bassis, J. N., 2016. Accelerated ice shelf rifting and retreat at Pine Island Glacier, West Antarctica. Geophysical Research Letters, 43 (22).

Johnson, J. S., Bentley, M. J., Gohl, K., 2008. First exposure ages from the Amundsen Sea embayment, West Antarctica: The late Quaternary context for recent thinning of Pine Island, Smith, and Pope Glaciers. *Geology* 36 (3), 223-226.

Johnson, J. S., Bentley, M. J., Smith, J. A., Finkel, R. C., Rood, D. H., Gohl, K., Balco, G., Larter, R. D., Schaefer, J. M., 2014. Rapid thinning of Pine Island Glacier in the early Holocene. *Science* 343, 999-1001.

Jordan, T. A., Ferraccioli, F., Armadillo E., Bozzo, E., 2013a. Crustal architecture of the Wilkes Subglacial Basin in East Antarctica, as revealed from airborne gravity data. *Tectonophysics* 585, 196-206.

Jordan, T. A., Ferraccioli, F., Vaughan, D. G., Holt, J. W., Corr, H., Blankenship, D. D., Diehl, T. M., 2010. Aerogravity evidence for major crustal thinning under the Pine Island Glacier region (West Antarctica). *GSA Bulletin* 122 (5-6), 714-726.

Jordan, T. J., Ferraccioli, F., Ross, N., Corr, H. F. J., Leat, P. T., Bingham, R. G., Rippin, D. M., le Brocq, A., Siegert, M. J., 2013b. Inland extent of the Weddell Sea Rift imaged by new aerogeophysical data. *Tectonophysics* 585, 137-160.

Joughin, I., and Alley, R., 2011. Stability of the West Antarctic ice sheet in a warming world. *Nature Geoscience* 4, 506-513.

Joughin, I., Smith, B. E., Holland, D. M., 2010. Sensitivity of 21st Century sea level to ocean-induced thinning of Pine Island Glacier, Antarctica. *Geophysical Research Letters* 37 (20).

Joughin, I., Smith, B. E., Medley, B., 2014. Marine Ice Sheet Collapse Potentially Under Way for the Thwaites Glacier Basin, West Antarctica. *Science* 344, 735.

Joughin, I., Tulaczyk, S., Bamber, J. L., Blankenship, D., Holt, J. W., Scambos, T., Vaughan, D. G., 2009. Basal conditions for Pine Island and Thwaites Glaciers, West Antarctica, determined using satellite and airborne data. *Journal of Glaciology* 55 (190), 245-257.

Jouzel, J., et al., 2007. Orbital and millennial Antarctic climate variability over the past 800,000 years. *Science* 317 (5839), 793-796.

Kalén, O., 2017. Ocean Circulation in the Amundsen Sea, West Antarctica. (PhD Thesis, Summary: University of Gothenburg. http://hdl.handle.net/2077/52056, accessed on 31/08/2018).

Katz, R. F., and Worster, M. G., 2010. Stability of ice-sheet grounding lines. *Proceedings of the Royal Society A-Mathematical Physical and Engineering Sciences* 466 (2118), 1597-1620.

Kellogg, D.E., and Kellogg, T.B., 1996. Diatoms in South Pole ice: implications for eolian contamination of Sirius Group deposits. *Geology* 24, 115–118.

Kellogg, T. B., and Kellogg, D. E., 1987. Recent glacial history and rapid ice stream retreat in the Amundsen Sea. *Journal of Geophysical Research: Solid Earth* 92 (B9), 8859-8864.

Kennedy, D. S., and Anderson, J. B., 1989. Glacial-marine sedimentation and Quaternary glacial history of Marguerite Bay, Antarctic Peninsula. *Quaternary Research* 31 (2), 255-276.

Kennett, J. P., 1977. Cenozoic Evolution of Antarctic Glaciation, the Circum-Antarctic Ocean, and Their Impact on Global Paleoceanography, *Journal of Geophysical Research* 82, 3843-3859.

Kennett, J. P., and Shackleton, N. J., 1976. Oxygen Isotopic Evidence for the development of the psychrosphere 38 Myr ago, *Nature* 260, 515-515.

Kim, C.-S., Kim, T.-W., Cho, K.-H., Ha, H. K., Lee, SH., Kim, H.-C., Lee, J.-H., 2016a. Variability of the Antarctic Coastal Current in the Amundsen Sea. Estuarine, Coastal and Shelf *Science* 181, 123-133, http://dx.doi.org/10.1016/j.ecss.2016.08.004.

Kim, I., Hahm, D., Rhe, T. S., Kim, T. W., Kim, C.-S., Lee, S. H., 2016b. The distribution of glacial meltwater in the Amundsen Sea, Antarctica, revealed by dissolved helium and neon. *Journal of Geophysical Research: Oceans* 121, 1654-1666.

Kim, M., Hwang, J., Kim, H., Kim, D., Yang, E., Ducklow, H. W., La, H. S., Lee, S. H., Park, J., Lee, SH., 2015. Sinking particle flux in the sea ice zone of the Amundsen Shelf, Antarctica. *Deep-Sea Research Part I* 101, 110-117, https://doi.org/10.1016/j.dsr.2015.04.002.

Kimura, S., Jenkins, A., Regan, H., Holland, P. R., Assmann, K. M., Whitt, D. B., van Wessem, M., van de Berg, W., Reijmer, C. H., Dutrieux, P., 2017. Oceanographic Controls on the Variability of Ice-Shelf Basal Melting and Circulation of Glacial Meltwater in the Amundsen Sea Embayment, Antarctica. *Journal of Geophysical Research: Oceans* 122 (12), 10131-10155.

Kindler, P., and Hearty, P.J., 2000. Elevated marine terraces from Eleuthera (Bahamas) and Bermuda: sedimentological, petrographic, and geochronological evidence for important deglaciation events during the middle Pleistocene. *Global and Planetary Change* 24, 41–58.

Kingslake, J., Scherer, R. P., Albrecht, T., Coenen, J., Powell, R. D., Reese, R., Stansell, N. D., Tulaczyk, S., Waering, M. G., Whitehouse, P. L., 2018. Extensive retreat and re-advance of the West Antarctic Ice Sheet during the Holocene. *Nature* 558, 430-434.

Kipf, A., Mortimer, N., Werner, R., Gohl, K., van de Bogaard, P., Hauff, F., Hoernle, K., 2012. Granitoids and dykes of the Pine Island Bay region, West Antarctica. *Antarctic Science* 24 (5), 473-484, doi:10.1017/S0954102012000259.

Kipf, A., Mortimer, N., Werner, R., Gohl, K., van de Bogaard, P., Hauff, F., Hoernle, K., 2012. Granitoids and dykes of the Pine Island Bay region, West Antarctica. Antarctic *Science* 24 (5), 473-484.

Kirshner, A. E., Anderson, J. B., Jakobsson, M., O'Regan, M., Majewski, W., Nitsche, F. O., 2012. Post-LGM deglaciation in Pine island Bay, west Antarctica. *Quaternary Science Reviews* 38, 11-26.

Klages, J. P., Kuhn, G., Graham, A. G., Hillenbrand, C.-D., Smith, J. A., Nitsche, F. O., Larter, R. D., Gohl, K., 2015. Palaeo-ice stream pathways and retreat style in the easternmost Amundsen Sea Embayment, West Antarctica, revealed by combined multibeam bathymetric and seismic data. *Geomorphology* 245, 207-222.

Kleman, J., Applegate, P. J., 2014. Durations and propagation patterns of ice sheet instability events. *Quaternary Science Reviews* 92, 32-39.

Komar, P. D., Baba, J., Cui, B., 1984. Grain-size analyses of mica within sediments and the hydraulic equivalence of mica and quartz. *Journal of Sedimentary Petrology* 54, 1379–1391.

Konfirst, M. A., Scherer, R. P., Hillenbrand, C.-D., Kuhn, G., 2012. A marine diatom record from the Amundsen Sea—Insights into oceanographic and climatic response to the Mid-Pleistocene Transition in the West Antarctic sector of the Southern Ocean. *Marine Micropaleontology* 92, 40-51.

Kopp, R. E., Simons, F. J., Mitrovica, J. X., Maloof, A. C., Oppenheimer, M., 2009. Probabilistic assessment of sea level during the last interglacial stage. *Nature* 462 (7275), 863.

Korhonen, F. J., Saito, S., Brown, M., Siddoway, C. S., Day, J. M. D., 2010. Multiple Generations of Granite in the Fosdick Mountains, Marie Byrd Land, West Antarctica: Implications for Polyphase Intracrustal Differentiation in a Continental Margin Setting. *Journal of Petrology* 51 (3), 627-670.

Kuhn, G., Hillenbrand, C. D., Kasten, S., Smith, J. A., Nitsche, F. O., Frederichs, T., Wiers, S., Ehrmann, W., Klages, J. P., Mogollón, J. M., 2017. Evidence for a palaeo-subglacial lake on the Antarctic continental shelf. *Nature Communications* 8, doi:10.1038/ncomms15591.

Kuiper, K. F., Deino, A., Hilgen, F. J., Krijgsman, W., Renne, P. R., Wijbrans, J. R., 2008. Synchronizing Rock Clocks of Earth History. *Science* 320 (5875), 500-504.

Kunz-Pirrung, M., Gersonde, R., Hodell, D. A., 2002. Mid-Brunhes century-scale diatom sea surface temperature and sea ice records from the Atlantic sector of the Southern Ocean (ODP Leg 177, Sites 1093, 1094 and core PS2089-2). *Palaeogeography, Palaeoclimatology, Palaeoecology* 182, 305–328.

Lamy, F., Gersonde, R., Winckler, G., Esper, O., Jaeschke, A., Kuhn, G., Ullermann, J., Martinez-Garcia, A., Lambert, F., Kilian, R., 2014. Increased Dust Deposition in the Pacific Southern Ocean During Glacial Periods. *Science* 343, 403-407.

Larter, R. D., and Barker, P. F., 1991. Effects of ridge crest-trench interaction on Antarctic-Phoenix Spreading: Forces on a young subducting plate. Journal of Geophysical Research: Solid Earth 96 (B12), 19’583-19’607.

Larter, R. D., Cunningham, A. P., Barker, P. F., Gohl, K., Nitsche F. O., 2002. Tectonic evolution of the Pacific margin of Antarctica 1. Late Cretaceous tectonic reconstructions. *Journal of Geophysical Research: Solid Earth* 107 (B12), EPM 5-1 – EPM 5-19, doi:10.1029/2000JB000052.

Larter, R. D., et al., 2014. Reconstruction of changes in the Amundsen Sea and Bellingshausen Sea sector of the West Antarctic Ice Sheet since the Last Glacial Maximum. *Quaternary Science Reviews* 100, 55-86.

Laskar, J., Robutel, P., Joutel, F., Gastineau, M., Correia, A. C. M., Levrard, B., 2004. A long-term numerical solution for the insolation quantities of the Earth. *Astronomy & Astrophysics* 428 (1), 261-285.

Lear, C. H., Bailey, T. R., Pearson, P. N., Coxall, H. K., Rosenthal, Y., 2008. Cooling and ice growth across the Eocene-Oligocene transition. *Geology* 36 (3), 251-254.

Lear, C. H., Rosenthal, Y., Coxall, H. K., Wilson, P. A., 2004. Late Eocene to early Miocene ice sheet dynamics and the global carbon cycle. *Paleoceanography* 19(4).

Leat, P. T., Scarrow, J. H., Millar, I. L., 1995. On the Antarctic Peninsula batholith. *Geological Magazine* 32 (4), 3990412.

Lee, J.-Y., Marti, K., Severinghaus, J. P., Kawamura, K., Yoo H.-S., Lee, J. B., Kim J. S., 2006. A redetermination of the isotopic abundances of atmospheric Ar. *Geochimica et Cosmochimica Acta* 70 (17), 4507-4512.

LeMasurier, W. E., 1990. Late Cenozoic volcanism on the Antarctic plate: An overview. In: W.E. LeMasurier and J. W. Thomson (Editors), Volcanoes of the Antarctic Plate and Southern Oceans. Antarctic Research Series 48, American Geophysical Union, Washington, D.C., 1-17.

LeMasurier, W. E., and Rex, D. C., 1989. Evolution of linear ranges in Marie Byrd Land, West Antarctica. *Journal of Geophysical Research* 94 (86), 7223-7236.

LeMasurier, W. E., and Rex, D. C., 1991, The Marie Byrd Land volcanic province and its relation to the Cainozoic West Antarctic rift system. In: Tingey, R. J., ed., *The geology of Antarctica:* New York, Oxford University Press, p. 249–284.

LeMasurier, W. E., Choi, S. H., Kawachi, Y., Mukasa, S. B., Rogers, N. W., 2011. Evolution of pantellerite-trachyte-phonolite volcanoes by fractional crystallization of basanite magma in a continental rift setting, Marie Byrd Land, Antarctica. *Contributions to Mineralogy and Petrology* 162 (6), 1175-1199.

Levy, R., et al., 2016. Antarctic ice sheet sensitivity to atmospheric CO2 variations in the early to mid-Miocene. *Proceedings of the National Academy of Sciences*, 113 (13), 3453-3458.

Licht, K. J., and Hemming, S. R., 2017. Analysis of Antarctic glacigenic sediment provenance through geochemical and petrologic applications. *Quaternary Science Reviews* 164, 1-24.

Licht, K. J., and Palmer, E. F., 2013. Erosion and transport by Byrd Glacier, Antarctica during the Last Glacial Maximum. *Quaternary Science Reviews* 62, 32-48.

Licht, K. J., Hennessy, A. J., Welke, B. M., 2014. The U-Pb detrital zircon signature of West Antarctic ice stream tills in the Ross embayment, with implications for Last Glacial Maximum ice flow reconstructions. *Antarctic Science* 26 (6), 687-697.

Lindow, J., Kamp, P. J. J., Mukasa, S. B., Kleber, M., Lisker, F., Gohl, K., Kuhn, G., Spiegel, C., 2016. Exhumation history along the eastern Amundsen Sea coast, West Antarctica, revealed by low-temperature thermochronology. *Tectonophysics* 35, 2239-2257.

Lisiecki, L. E., and Raymo, M. E., 2005. Plio–Pleistocene climate evolution: trends and transitions in glacial cycle dynamics. *Quaternary Science Reviews* 26, 56–69.

Liu, Q., Roberts, A. P., Larrasoana, J. C., Banerjee, S. K., Guyodo, Y., Tauxe, L., Oldfield, F., 2012. Environmental magnetism: principles and applications. *Reviews of Geophysics* 50 (4), RG4002.

Lowe, A. L., and Anderson, J. B., 2002. Late Quaternary retreat of the West Antarctic Ice Sheet in Pine Island Bay, Antarctica. *Quaternary Science Reviews* 21, 1879–1897.

Lowe, A. L., and Anderson, J. B., 2003. Evidence for abundant subglacial meltwater beneath the paleo-ice sheet in Pine Island Bay, Antarctica. *Journal of Glaciology* 49 (164), 125-138.

Lu, Z., Hoogakker, B. A., Hillenbrand, C.-D., Zhou, X., Thomas, E., Gutchess, K. M., Lu, W., Jones, L., Rickaby, R. E., 2016. Oxygen depletion recorded in upper waters of the glacial Southern Ocean. *Nature Communications* 7, 11146.

Lucchi, R. G., Rebesco, M., Camerlenghi, A., Busetti, M., Tomadin, L., Villa, G., Perisco, D., Morigi, C., Bonci, M. C., Giorgetti, G., 2002. Mid-late Pleistocene glacimarine sedimentary processes of a high-latitude, deep-sea sediment drift (Antarctic Peninsula Pacific margin). *Marine Geology* 189 (3), 343-370.

Ludwig, K. R., 2003. Isoplot 3.00: A Geochronological Toolkit for Microsoft Excel , Berkeley Geochronology Center, Berkeley, CA.

Lüthi, D., Le Floch, M., Bereiter, B., Blunier, T., Barnola, J. M., Siegenthaler, U., Raynaud, D., Jouzel, J., Fischer, H., Kawamura, K., Stocker, T. F., 2008. High-resolution carbon dioxide concentration record 650,000–800,000 years before present. *Nature* 453 (7193), 379.

Luyendyk, B., Cisowski, S., Smith, C., Richard, S., Kimbrough, D., 1996. Paleomagnetic study of the northern Ford Ranges, western Marie Byrd Land, West Antarctica: Motion between West and East Antarctica. *Tectonics* 15 (1), 122-141.

MacAyeal, D. R., 1992. Irregular oscillations of the West Antarctic ice sheet. *Nature* 359 (6390), 29-32.

Martínez-Garcia, A., Rosell-Melé, A., Geibert, W., Gersonde, R., Masqué, P., Gaspari, V.,Barbante, C., 2009. Links between iron supply, marine productivity, sea surface temperature, and CO2 over the last 1.1 Ma. *Paleoceanography* 24 (1), PA1207.

Maslanyj, M. P., and Storey, B. C., 1990. Regional Aeromagnetic Anomalies in Ellsworth Land: Crustal structure and Mesozoic microplate boundaries within West Antarctica. *Tectonics* 9 (6), 1515-1532.

Masson-Delmotte, V., Stenni, B., Pol, K., Braconnot, P., Cattani, O., Falourd, S., Kageyama, M., Jouzel, J., Landais, A., Minster, B., Barnola, J. M., Chappellaz J., Krinner, G., Johnsen, S., Röthlisberger, R., Hansen, J., Mikolajewics, U., Otto-Bliesner, B., 2010. EPICA Dome C record of glacial and interglacial intensities. *Quaternary Science Reviews* 29 (1-2), 113-128.

Mazur, A. K., Wåhlin, A. K., Krężel, A., 2017. An object-based SAR image iceberg detection algorithm applied to the Amundsen Sea. *Remote Sensing of Environment* 189, 67-83.

Mazur, A. K., WÅhlin, A. K., Krężel, A., 2017. An object-based SAR image iceberg detection algorithm applied to the Amundsen Sea. *Remote Sensing of Environment* 189, 67-83.

McCarron, J. J., and Smellie, J. L., 1998. Tectonic implications of fore-arc magmatism and generation of high-magnesian andesites: Alexander Island, Antarctica. *Journal of the Geological Society*, London 155, 269-280.

McCave, I. N., Thornalley, D. J. R., Hall, I. R., 2017. Relation of sortable silt grain-size to deep-sea current speeds: Calibration of the 'Mud Current Meter'. *Deep-Sea Research I* 127, 1-12.

McKay, R., Naish, T., Powell, R., Barrett, P., Scherer, R., Talarico, F., Kyle, P., Monien, D., Kuhn, G., Jackolski, C., Williams, T., 2012. Pleistocene variability of Antarctic ice sheet extent in the Ross embayment. *Quaternary Science Reviews* 34, 93-112.

McKay, R.M., De Santis, L., Kulhanek, D.K., and the Expedition 374 Scientists, 2018. Expedition 374 Preliminary Report: Ross Sea West Antarctic Ice Sheet History. International Ocean Discovery Program, 374, https://doi.org/10.14379/iodp.pr.374.2018

McLennan, S. M., Hemming, S. R., McDaniel, D. K., Hanson, G. N., 1993. Geochemical approaches to sedimentation, provenance and tectonics. In: Johnsson M. J., and Basu A. (eds), Processes Controlling the Composition of Clastic Sediments. Geological Society of America Special Paper 284.

McLennan, S.M., 2001. Relationships between the trace element composition of sedimentary rocks and upper continental crust. *Geochemistry, Geophysics, Geosystems* 2 (4), doi:10.1029/2000GC000109.

McMurtry, G. M., Tappin, D. R., Sedwick, P. N., Wilkinson, I., Fietzke, J., Sellwood, B., 2007. Elevated marine deposits in Bermuda record a late Quaternary megatsunami. *Sedimentary Geology* 200, 155–165.

McMurtry, G. M., Tappin, D. R., Sedwick, P. N., Wilkinson, I., Fietzke, J., Sellwood, B., 2008. Reply to ''Mega-highstand or megatsunami? Discussion of McMurtry, et al. ''Elevated marine deposits in Bermuda record a late Quaternary megatsunami'': Sedimentary Geology 200 (2007) 155–165'' by Paul J. Hearty and Storrs L. Olson. *Sedimentary Geology* 203, 313–319. doi:10.1016/j.sedgeo.2007.11.008.

Mercer, J. H., 1978. West Antarctic ice sheet and CO2 greenhouse effect: a threat of disaster. Nature 271 (5643), 321.

Merino, N., Le Sommer, J., Durand, G., Jourdain, N. C., Madec, G., Mathiot, P., Tournadre, J., 2016. Antarctic icebergs melt over the Southern Ocean: Climatology and impact on sea ice. *Ocean Modelling* 104, 99-110.

Miles, T., Lee, S. H., Wåhlin, A., Ha H. K., Kim T. W., Assmann K. M., Schofield O., 2016. Glider observations of the Dotson Ice Shelf outflow. *Deep-Sea Research II* 123, 16-29.

Millar, I. L., and Pankhurst, R. J., 1987. Rb-Sr geochronology of the region between the Antarctic Peninsula and the Transantarctic Mountains: Haag Nunataks and Mesozoic granitoids. *Geophysical Monograph Series* 40, 151-160.

Millar, I. L., Pankhurst, R. J., Fanning, C. M., 2002. Basement chronology of the Antarctic Peninsula: recurrent magmatism and anatexis in the Palaeozoic Gondwana Margin. *Journal of the Geological Society*, London 159, 145-157.

Miller, K. G., Wright, J. D., Browning, J. V., 2005. Visions of ice sheets in a greenhouse world: Marine *Geology* 217 (3-4), 215-231.

Mortimer, N., Gans, P., Calvert, A., Walker, N., 1999. Geology and thermochronometry of the east edge of the Median Batholith (Median Tectonic Zone): a new perspective on Permian to Cretaceous crustal growth of New Zealand. *The Island Arc* 8, 404-425.

Mouginot, J., Rignot, E., Scheuchl, B., 2014. Sustained increase in ice discharge from the Amundsen Sea Embayment, West Antarctica, from 1973 to 2013. *Geophysical Research Letters* 41, 1576–1584.

Mukasa, S. B., and Dalziel, I. W. D., 2000. Marie Byrd Land, West Antarctica: Evolution of Gondwana's Pacific margin constrained by zircon U-Pb geochronology and feldspar common-Pb isotopic compositions. *GSA Bulletin* 112 (4), 611-627.

Murphy, E. J., Hofmann, E. E., Watkins, J. L., Johnston, N. M., Piñones, A., Ballerini, T., Hill, S. L., Trathan, P. N., Tarling, G. A., Cavanagh, R. A., Young, E. F., Thorpe, S.E., Fretwell, P., 2013. Comparison of the structure and function of Southern Ocean regional ecosystems: the Antarctic Peninsula and South Georgia. *Journal of Marine Systems* 109, 22–42.

Muto, A., Peters, L. E., Gohl, K., Sasgen, I., Alley, R. B., Anandakrishnan, S., Riverman, K. L., 2016. Subglacial bathymetry and sediment distribution beneath Pine Island Glacier ice shelf modeled using aerogravity and in situ geophysical data: New results. *Earth and Planetary Science Letters* 433, 63-75.

Naish, T., et al., 2009. Obliquity-paced Pliocene West Antarctic Ice Sheet oscillations. *Nature* 458, 322-328.

Nakayama, Y., Schröder, M., Hellmer, H. H., 2013. From circumpolar deep water to the glacial meltwater plume on the eastern Amundsen Shelf. *Deep Sea Research Part I: Oceanographic Research Papers* 77, 50-62.

Naveira-Garabato, A. C., Forryan, A., Dutrieux, P., Brannigan, L., Biddle, L. C., Heywood, K. J., Jenkins, A., Firing, Y. L., Kimura, S., 2017. Vigorous lateral export of the meltwater outflow from beneath an Antarctic ice shelf. *Nature* 542 (7640), 219.

Neumann, M., and Ehrmann, W., 2000. Mineralogy of sediments from CRP-2/2A, Victoria Land Basin, Antarctica as revealed by x-ray diffraction. *Terra Antartica* 7 (4), 575-580.

Neumann, M., and Ehrmann, W., 2001. Mineralogy of sediments from CRP-3, Victoria Land Basin, Antarctica, as revealed by X-ray diffraction. *Terra Antartica* 8 (4), 523-532.

Nitsche, F. O., Cunningham, A. P., Larter, R. D., Gohl, K., 2000. Geometry and development of glacial continental margin depositional systems in the Bellingshausen Sea. *Marine Geology* 162 (2-4), 277-302.

Nitsche, F. O., Gohl, K., Larter, R. D., Hillenbrand, C. D., Kuhn, G., Smith, J. A., Jacobs, S., Anderson, J. B., Jakobsson, M., 2013. Paleo ice flow and subglacial meltwater dynamics in Pine Island Bay, West Antarctica. *The Cryosphere* 7 (1), 249-262.

Nürnberg, C. C., Bohrmann, G., Schlüter, M., Frank, M., 1997. Barium accumulation in the Atlantic sector of the Southern Ocean: Results from 190,000-year records. *Paleoceanography and Paleoclimatology* 12 (4), 594-603.

O'Leary, M. J., Hearty, P. J., Thompson, W. G., Raymo, M. E., Mitrovica, J. X., Webster, J. M., 2013. Ice sheet collapse following a prolonged period of stable sea level during the last interglacial. *Nature Geoscience* 6 (9), 796.

Oppenheimer, M., 1998. Global warming and the stability of the West Antarctic Ice Sheet. *Nature* 393, 325-332.

Orsi, A. H., Whitworth, T., Nowlin, W. D., 1995. On the meridional extent and fronts of the Antarctic Circumpolar Current. *Deep-Sea Research* Part I-Oceanographic Research Papers 42 (5), 641-673.

Pagani, M., Huber, M., Liu, Z., Bohaty, S. M., Henderiks, J., Sijp, W., Krishnan, S., DeConto, R. M., 2011. The role of carbon dioxide during the onset of Antarctic glaciation. *Science* 334 (6060), 1261-1264.

Pankhurst, R. J., and Rowley, P. D., 1991. Rb-Sr study of Cretaceous plutons from southern Antarctic Peninsula and eastern Ellsworth Land, Antarctica. In: Thomson, M. R. A., Crame, J. A. and Thomson, J. W. (eds), *Geological Evolution of Antarctica*. Cambridge University Press, 1991.

Pankhurst, R. J., Hole, M. J., Brook, M., 1988. Isotope evidence for the origin of Andean granites. *Royal Society of Edinburgh Transactions: Earth Sciences* 79, 123-133.

Pankhurst, R. J., Millar, I. L., Grunow, A. M., Storey, B. C., 1993. The Pre-Cenozoic Magmatic History of the Thurston Island Crustal Block, West Antarctica. *Journal of Geophysical Research* 98 (B7), 11835-11849.

Pankhurst, R. J., Riley, T. R., Fanning, C. M., Kelley, S. P., 2000. Episodic Silicic Volcanism in Patagonia and the Antarctic Peninsula: Chronology of Magmatism Associated with the Break-up of Gondwana. *Journal of Petrology* 41 (5), 605-625.

Pankhurst, R. J., Weaver, S. D., Bradshaw, J. D., Storey, B. C., Ireland, T. R., 1998. Geochronology and geochemistry of pre-Jurassic superterranes in Marie Byrd Land, Antarctica. *Journal of Geophysical Research: Solid Earth* 103 (B2), 2529-2547.

Parada, M. A., Féraud, G., Fuentes, F., Aguirre, L., Morata, D., Larrondo, P., 2005. Ages and cooling history of the Early Cretaceous Caleu pluton: testimony of a switch from a rifted to a compressional continental margin in central Chile, *Journal of the Geological Society of London* 162, 273-287.

Past Interglacials Working Group of PAGES., 2016. Interglacials of the last 800,000 years. *Reviews of Geophysics* 54 (1), 162-219.

Patterson, M. O., McKay, R., Naish, T., Escutia, C., Jimenez-Espejo, F. J., Raymo, M. E., Meyers, S. R., Tauxe, L., Brinkhuis, H., IODP Expedition 318 Scientists, 2014. Orbital forcing of the East Antarctic ice sheet during the Pliocene and Early Pleistocene. *Nature Geoscience* 7 (11), 841.

Pattyn, F., Matsuoka, K., Berte, J., 2010. Glacio-meteorological conditions in the vicinity of the Belgian Princess Elisabeth Station, Antarctica. *Antarctic Science* 22 (1), 79-85.

Payne, A. J., Vieli, A., Shepherd A. P., Wingham D. J., Rignot E., 2004. Recent dramatic thinning of largest West Antarctic ice stream triggered by oceans, *Geophysical Research Letters* 31, L23401, doi:10.1029/2004GL021284.

Peck, V. L., Hall, I. R., Zahn, R., Grousset, F., Hemming, S. R., Scourse, J. D., 2007. The relationship of Heinrich events and their European precursors over the past 60 ka BP: a multi-proxy ice-rafted debris provenance study in the North East Atlantic. *Quaternary Science Reviews* 26 (7-8), 862-875.

Pierce, E. L., Hemming, S. R., Williams, T., van de Flierdt, T., Thomson, S. N., Reiners, P. W., Gehrels G. E., Brachfeld, S. A., Goldstein, S. L., 2014. A comparison of detrital U–Pb zircon, 40Ar/39Ar hornblende, 40Ar/39Ar biotite ages in marine sediments off East Antarctica: Implications for the geology of subglacial terrains and provenance studies. *Earth-Science Reviews* 138, 156-178.

Pierce, E. L., van de Flierdt, T., Williams, T., Hemming, S. R., Cook, C. P., Passchier, S., 2017. Evidence for a dynamic East Antarctic ice sheet during the mid-Miocene climate transition. *Earth and Planetary Science Letters* 478, 1-13. https://doi.org/10.1016/j.epsl.2017.08.011.

Pierce, E. L., Williams, T., van de Flierdt, T., Hemming, S. R., Goldstein, S. L., Brachfeld, S. A., 2011. Characterizing the sediment provenance of East Antarctica's weak underbelly: The Aurora and Wilkes sub-glacial basins. *Paleoceanography* 26, PA4217, doi:10.1029/2011PA002127.

Pin, C., and Bassin, C., 1992. Evaluation of a strontium-specific extraction chromatographic method for isotopic analysis in geological-materials. *Analytica Chimica Acta* 269 (2), 249-255.

Pin, C., and Zalduegui, J. F. S., 1997. Sequential separation of light rare-earth elements, thorium and uranium by miniaturized extraction chromatography: Application to isotopic analyses of silicate rocks. *Analytica Chimica Acta* 339 (1-2), 79-89.

Planquette, H., Sherrell, R. M., Stammerjohn, S., Field, M. P., 2013. Particulate iron delivery to the water column of the Amundsen Sea, Antarctica. *Marine Chemistry* 153, 15-30.

Pollard, D., and DeConto, R. M., 2009. Modelling West Antarctic Ice Sheet growth and collapse through the past five million years. *Nature* 458, 329-332.

Pollard, D., and DeConto, R. M., 2012. Description of a hybrid ice sheet-shelf model, and application to Antarctica. *Geoscientific Model Development* 5 (5), 1273.

Pollard, D., DeConto, R. M., Alley, R. B., 2015. Potential Antarctic Ice Sheet retreat driven by hydrofracturing and ice cliff failure. *Earth and Planetary Science Letters* 412, 112-121.

Pritchard, H. D., Arthern, R. J., Vaughan, D. G., Edwards, L. A., 2009. Extensive dynamic thinning on the margins of the Greenland and Antarctic ice sheets. *Nature* 461, 971-975.

Pritchard, H., Ligtenberg S., Fricker H., Vaughan D., van den Broeke M. R., Padman L., 2012. Antarctic ice-sheet loss driven by basal melting of ice shelves. *Nature* 484 (7395), 502–505.

Pudsey, C. J., 2000. Sedimentation on the continental rise west of the Antarctic Peninsula over the last three glacial cycles. *Marine Geology* 167 (3), 313-338.

Pudsey, C. J., and Camerlenghi, A., 1998. Glacial–interglacial deposition on a sediment drift on the Pacific margin of the Antarctic Peninsula. *Antarctic Science* 10 (3), 286-308.

Pudsey, C. J., and Howe, J. A., 1998. Quaternary history of the Antarctic Circumpolar Current: evidence from the Scotia Sea. *Marine Geology* 148(1-2), 83-112.

Randall-Goodwin, E., Meredith, M. P., Jenkins, A., Yager, P. L., Sherrell, R. M., Abrahamsen, E. P., Guerrero, R., Yuan, X., Mortlock, R. A., Gavahan, K., Alderkamp, A.-C., Ducklow, H., Robertson, R., Stammerjohn, S.E., 2015. Freshwater distributions and water mass structure in the Amundsen Sea Polynya region, Antarctica, *Elem Sci Anth* 3 (1), 000065. doi: 10.12952/journal.elementa.000065.

Raymo, M. E., and Mitrovica, J. X., 2012. Collapse of polar ice sheets during the stage 11 interglacial. *Nature* 483 (7390), 453.

Raymo, M. E., and Nisancioglu, K. H., 2003. The 41 kyr world: Milankovitch's other unsolved mystery. *Paleoceanography* 18 (1).

Raymo, M. E., Lisiecki, L. E., Nisancioglu, K. H., 2006. Plio-Pleistocene ice volume, Antarctic climate, and the global δ18O record. *Science* 313 (5786), 492-495.

Rebesco, M., Larter, R. D., Camerlenghi, A., Barker, P. F., 1996. Giant sediment drifts on the continental rise west of the Antarctic Peninsula. *Geo-Marine Letters* 16 (2), 65-75.

Reyes, A.V., Carlson, A. E., Beard, B. L., Hatfield, R. G., Stoner, J. S., Winsor, K., Welke, B., Ullman, D.J., 2014. South Greenland ice-sheet collapse during Marine Isotope Stage 11. *Nature* 510, 525-528.

Richard, S. M., Smith, C. H., Kimbrough, D. L., Fitzgerald, P. G., Luyendyk, B. P., McWilliams, M. O., 1994. Cooling History of the Northern Ford Ranges, Marie Byrd Land, West Antarctica. *Tectonics* 13 (4), 837-857.

Rickli, J., Gutjahr, M., Vance, D., Fischer Gödde, M., Hillenbrand, C.-D., Kuhn, G., 2014. Neodymium and hafnium boundary contributions to seawater along the West Antarctic continental margin. Earth and Planetary Science Letters 394, 99-110.

Rignot, E., 2002. Mass balance of East Antarctic glaciers and ice shelves from satellite data. *Annals of Glaciology* 34, 217-227.

Rignot, E., and Jacobs, S. S., 2002. Rapid bottom melting widespread near Antarctic ice sheet grounding lines. *Science* 296 (5575), 2020-2023.

Rignot, E., Bamber, J. L., van den Broeke, M. R., Davis, C., Li, Y., van de Berg, W. J., van Meijgaard, E., 2008. Recent Antarctic ice mass loss from radar interferometry and regional climate modelling. *Nature Geoscience* 1, 106-110.

Rignot, E., Mouginot, J., Morlighem, M., Seroussi, H., Scheuchl, B., 2014. Widespread, rapid grounding line retreat of Pine Island, Thwaites, Smith, and Kohler glaciers, West Antarctica, from 1992 to 2011. *Geophysical Research Letters* 41, 3502-3509.

Rignot, E., Velicogna, I., van den Broeke, M. R., Monaghan, A., Lenaerts, J. T., 2011. Acceleration of the contribution of the Greenland and Antarctic ice sheets to sea level rise. *Geophysical Research Letters* 38 (5), L05503.

Riley, T. R., Burton-Johnson, A., Flowerdew, M. J., Whitehouse, M. J., 2018. Episodicity within a mid-Cretaceous magmatic flare-up in West Antarctica: U-Pb ages of the Lassiter Coast intrusive suite, Antarctic Peninsula, and correlations along the Gondwana margin. *GSA Bulletin* 130 (7-8), 1177-1196.

Riley, T. R., Flowerdew, M. J., Pankhurst, R. J., Leat, P. T., Millar, I. L., Fanning, C. M., Whitehouse, M. J., 2017. A revised geochronology of Thurston Island, West Antarctica, and correlations along the proto-Pacific margin of Gondwana. *Antarctic Science* 29 (1), 47-60.

Riley, T. R., Leat, P. T., Kelley, S. P., Millar, I. L., Thirlwall, M. F., 2003. Thinning of the Antarctic Peninsula lithosphere through the Mesozoic: evidence from Middle Jurassic basaltic lavas. *Lithos* 67 (3-4), 163-179.

Riley, T. R., Leat, P. T., Pankhurst, R. J., Harris, C., 2001. Origins of Large Volume Rhyolitic Volcanism in the Antarctic Peninsula and Patagonia by Crustal Melting. *Journal of Petrology* 42 (6), 1043-1065.

Rocchi, S., LeMasurier, W.E., Di Vincenzo, G., 2006. Oligocene to Holocene erosion and glacial history in Marie Byrd Land, West Antarctica, inferred from exhumation of the Dorrel Rock intrusive complex and from volcano morphologies. *GSA Bulletin* 118, 991–1005, doi:10.1130/B25675.1.

Roy, M., van de Flierdt, T., Hemming, S. R., Goldstein, S. L., 2007. (40)Ar/(39)Ar ages of hornblende grains and bulk Sm/Nd isotopes of circum-Antarctic glacio-marine sediments: Implications for sediment provenance in the Southern Ocean. *Chemical Geology* 244 (3-4), 507-519.

Rutberg, R. L., Hemming, S. R., Goldstein, S. L., 2000. Reduced North Atlantic Deep Water flux to the glacial Southern Ocean inferred from neodymium isotope ratios. *Nature* 405, 935-938.

Rutford, R. H., Craddock, C., Bastien, T. W., 1968. Late Tertiary glaciation and sea-level changes in Antarctica. *Palaeogeography, Palaeoclimatology, Palaeoecology* 5 (1), 15-39.

Rutherford, S., and D'Hondt, S., 2000. Early onset and tropical forcing of 100,000-year Pleistocene glacial cycles. *Nature* 408 (6808), 72-75.

Ryan, C. J., 2005. Mesozoic to Cenozoic igneous rocks from Northwestern Graham Land: constraints on the tectonomagmatic evolution of the Antarctic Peninsula. PhD thesis, University of Brighton.

Scambos, T. A., et al., 2017. How much, how fast?: A science review and outlook for research on the instability of Antarctica's Thwaites Glacier in the 21st century. *Global and Planetary Change* 153, 16-34.

Scarrow, J. H., Leat, P. T., Wareham, C. D., Millar, I. L., 1998. Geochemistry of mafic dykes in the Antarctic Peninsula continental-margin batholith: a record of arc evolution. *Contribution to Mineralogy and Petrology* 131, 289-305.

Schaefer, J. M., Finkel, R. C., Balco, G., Alley, R. B., Caffee, M. W., Briner, J. P., Young, N. E., Gow, A. J., Schwartz, R., 2016. Greenland was nearly ice-free for extended periods during the Pleistocene. *Nature* 540 (7632), 252.

Scher, H. D., and Martin, E. E., 2006. Timing and climatic consequences of the opening of Drake Passage. *Science* 312 (5772), 428-430.

Scher, H. D., Bohaty, S. M., Zachos, J. C., Delaney, M. L., 2011. Two-stepping into the icehouse: East Antarctic weathering during progressive ice-sheet expansion at the Eocene–Oligocene transition. *Geology* 39 (4), 383-386.

Scherer, R. P., Aldahan, A., Tulaczyk, S., Possnert, G., Engelhardt, H., Kamb, B., 1998. Pleistocene Collapse of the West Antarctic Ice Sheet. *Science* 281 (5373), 82-85.

Scherer, R. P., Bohaty, S. M., Dunbar, R. B., Esper, O., Flores, J. A., Gersonde, R., Harwood, D. M., Roberts, A. P., Taviani, M., 2008. Antarctic records of precession-paced insolation-driven warming during early Pleistocene Marine Isotope Stage 31. *Geophysical Research Letters* 35 (3), L03505.

Scheuchl, B., Mouginot, J., Rignot, E., Morlighem, M., Khazendar, A., 2016. Grounding line retreat of Pope, Smith, and Kohler Glaciers, West Antarctica, measured with Sentinel-1a radar interferometry data. *Geophysical Research Letters* 43 (16), 8572-8579.

Schoof, C., 2007. Ice sheet grounding line dynamics: Steady states, stability, and hysteresis. *Journal of Geophysical Research* 112, 133-138.

Schroeder, D. M., Blankenship, D. D., Young, D. A. (2013). Evidence for a water system transition beneath Thwaites Glacier, West Antarctica. *Proceedings of the National Academy of Sciences* 110 (30), 12225-12228.

Schroeder, D. M., Blankenship, D. D., Young, D. A., Quartini, E., 2014. Evidence for elevated and spatially variable geothermal flux beneath the West Antarctic Ice Sheet. *Proceedings of the National Academy of Sciences* 111 (25), 9070-9072.

Schwartz, J. J., Klepeis, K. A., Sadorski, J. F., Stowell, H. H., Tulloch, A. J., Coble, M. A., 2017. The tempo of continental arc construction in the Mesozoic Median Batholith, Fiordland, New Zealand. Lithosphere 9 (3), 343-365.

Shepherd, A., et al., 2012. A reconciled estimate of ice-sheet mass balance. *Science* 338, 1183–1189.

Siegenthaler, et al., 2005. Stable carbon cycle-climate relationship during the Late Pleistocene. *Science* 310, 1313–1317.

Sime, L. C., Wolff, E. W., Oliver, K. I. C., Tindall, J. C., 2009. Evidence for warmer interglacials in East Antarctic ice cores. *Nature* 462 (7271), 342.

Simões Pereira, P., van de Flierdt, T., Hemming, S.R., Hammond, S.J., Kuhn, G., Brachfeld, S., Doherty, C., Hillenbrand, C.-D., 2018. Geochemical fingerprints of glacially eroded bedrock from West Antarctica: detrital thermochronology, radiogenic isotope systematics and trace element geochemistry in Late Holocene glacial-marine sediments. *Earth-Science Reviews* 182, 204-232.

Smellie, J. L., 1999. Lithostratigraphy of Miocene-Recent, alkaline volcanic fields in the Antarctic Peninsula and eastern Ellsworth Land. *Antarctic Science* 11 (3), 362-378.

Smith, A. M., Jordan, T. A., Ferraccili, F., Bingham, R. G., 2013. Influence of subglacial conditions on ice stream dynamics: Seismic and potential field data from Pine Island Glacier, West Antarctica. *Journal of Geophysical Research: Solid Earth* 118, 1471-1482.

Smith, A. M., Vaughan, D. G., Doake, C. S. M., Johnson, A. C., 1999. Surface Lowering of the Ice Ramp at Rothera Point, Antarctic Peninsula, in Response to Regional Climate Change, *Annals of Glaciology* 27, 113–118.

Smith, J. A., Andersen, T. J., Shortt, M., Gaffney, A. M., Truffer, M., Stanton, T. P., Bindschadler, R., Dutrieux, P., Jenkins, A., 2017. Sub-ice-shelf sediments record history of twentieth-century retreat of Pine Island Glacier. *Nature* 541, 77-80.

Smith, J. A., Hillenbrand, C.-D., Kuhn, G., Klages, J. P., Graham A. G. C., 2014. New constraints on the timing of West Antarctic Ice Sheet retreat in the eastern Amundsen Sea since the Last Glacial Maximum. *Global and Planetary Change* 122, 224-237.

Smith, J. A., Hillenbrand, C.-D., Kuhn, G., Larter, R. D., Graham, A. G. C., Ehrmann, W., Moreton, S. G., Forwick, M., 2011. Deglacial history of the West Antarctic Ice Sheet in the western Amundsen Sea Embayment. *Quaternary Science Reviews* 30, 488-505.

Sokolov, S., and Rintoul, S. R., 2009. Circumpolar structure and distribution of the Antarctic Circumpolar Current fronts: 1. Mean circumpolar paths. *Journal of Geophysical Research* 114, C11018, doi: 10.1029/2008JC005108.

Spiegel, C., Lindow, J., Kamp, P. J. J., Meisel, O., Mukasa, S. B., Lisker, F., Kuhn, G., Gohl, K., 2016. Tectonomorphic evolution of Marie Byrd Land – Implications for Cenozoic rifting activity and onset of West Antarctic glaciation. *Global and Planetary Change* 145, 98-115.

Staiger, J. W., Gosse, J., Little, E. C., Utting, D. J., Finkel, R., Johnson, J. V., Fastook, J., 2006. Glacial erosion and sediment dispersion from detrital cosmogenic nuclide analyses of till. *Quaternary Geochronology* 1 (1), 29-42.

Stammerjohn, S. E., Maksym, T., Massom, R.A A., Lowry, K. E., Arrigo, K. R., Yuan, X., Raphael, M., Randall-Goodwin, E., Sherrell, R. M., Yager, P. L., 2015. Seasonal sea ice changes in the Amundsen Sea, Antarctica, over the period of 1979–2014. *Elem Sci Anth* 3, doi:10.12952/journal.elementa.000055.

Steig, E. J., Ding, Q., Battisti, D. S., and Jenkins, A., 2012. Tropical forcing of Circumpolar Deep Water inflow and outlet glacier thinning in the Amundsen Sea Embayment, West Antarctica. *Annals of Glaciology* 53 (60), 19-28.

St-Laurent, P., Klinck, J. M., Dinniman, M. S., 2015. Impact of local winter cooling on the melt of Pine Island Glacier, Antarctica. *Journal of Geophysical Research: Oceans*, 120 (10), 6718-6732.

Storey, B. C., and Alabaster, T., 1991. Tectonomagmatic controls on Gondwana break-up models: evidence from the proto-pacific margin of Antarctica. *Tectonics* 10 (6), 1274-1288.

Storey, B. C., Dalziel, I. W., D., Garrett, S. W., Grunow, A. M, Pankhurst, R. J., Vennum, W. R., 1988. West Antarctica in Gondwanaland: Crustal blocks, reconstruction and breakup processes. *Tectonophysics* 155, 381-390.

Storey, B. C., Pankhurst, R. J., Johnson, A. C., 1994. The Grenville Province within Antarctica: a test of the SWEAT hypothesis. *Journal of the Geological Society* 151, 1-4.

Storey, B. C., Vaughan, A. P. M., Millar, I. L., 1996. Geodynamic evolution of the Antarctic Peninsula during Mesozoic times and its bearing on Weddell Sea history. Geological Society, London, Special Publications 108, 87-103.

Struve, T., van de Flierdt T., Burke, A., Robinson, L. F., Hammond, S. J., Crocket, K. C., Bradtmiller, L. I., Auro, M. E., Mohamed, K. J., White, N. J., 2016. Neodymium isotopes and concentrations in aragonitic scleractinian cold-water coral skeletons - Modern calibration and evaluation of palaeo-applications. *Chemical Geology* 453, 146-168.

Tanaka, T., Togashi, S., Kamioka, H., Amakawa, H., Kagami, H., Hamamoto, T., Yuhara, M., Orihashi, Y., Yoneda, S., Shimizu, H., Kunimaru, T., Takahashi, K., Yanagi, T., Nakano, T., Fujimaki, H., Shinjo, R., Asahara, Y., Tanimizu, M., Dragusanu, C., 2000. JNdi-1: a neodymium isotopic reference in consistency with LaJolla neodymium. *Chemical Geology* 168 (3-4), 279-281.

Taylor, S. R. and McLennan, S. M., 2001. Chemical composition and element distribution in the Earth's crust. In: *Encyclopedia of Physical Science and Technology*, New York: Academic Press.

Taylor, S. R., and McLennan, S. M., 1995. The geochemical evolution of the continental crust. *Reviews of Geophysics* 33 (2), 241-265.

The IMBIE Team, 2018. Mass balance of the Antarctic Ice Sheet from 1992 to 2017. *Nature* 558, 219-222.

The RAISED Consortium, 2014. A community-based geological reconstruction of Antarctic Ice Sheet deglaciation since the Last Glacial Maximum. *Quaternary Science Reviews* 100, 1-9.

Thoma, M., Jenkins, A., Holland, D., Jacobs, S., 2008. Modelling Circumpolar Deep Water intrusions on the Amundsen Sea continental shelf, Antarctica, *Geophysical Research Letters* 35, L18602. doi:10.1029/2008GL034939.

Thomas, R. H., Sanderson, T. J., Rose, K. E., 1979. Effect of climatic warming on the West Antarctic ice sheet. *Nature* 277 (5695), 355.

Tigchelaar, M., Timmermann, A., Pollard, D., Friedrich, T., Heinemann, M., 2018. Local insolation changes enhance Antarctic interglacials: Insights from an 800,000-year ice sheet simulation with transient climate forcing. *Earth and Planetary Science Letters* 495, 69-78.

Timmermann, A., Friedrich, T., Timm, O. E., Chikamoto, M. O., Abe-Ouchi, A., Ganopol-ski, A., 2014. Modeling obliquity and CO2 effects on Southern Hemisphere climate during the past 408ka. *Journal of Climate* 27, 1863–1875.

Tinto, K. J., and Bell, R. E., 2011. Progressive unpinning of Thwaites Glacier from newly identified offshore ridge: Constraints from aerogravity. *Geophysical Research Letters* 38 (20).

Tochilin, C. J., Reiners, P. W., Thomson, S. N., Gehrels, G. E., Hemming, S. R., Pierce, E. L., 2012. Erosional history of the Prydz Bay sector of East Antarctica from detrital apatite and zircon geo- and thermochronology multidating. *Geochemistry, Geophysics, Geosystems* 13.

Toggweiler, J. R., Russell, J. L., Carson, S. R., 2006. Midlatitude westerlies, atmospheric CO2, and climate change during the ice ages. *Paleoceanography* 21 (2), PA2005.

Tournadre, J., Bouhier, N., Girard-Ardhuin, F., Rémy, F., 2016. Antarctic icebergs distribution 1992–2014. *Journal Geophysical Research* 121 (1), 327-349.

Tucholke, B. E., Hollister, C. D., Weaver, F. M., Vennum, W. R., 1976. Continental rise and abyssal plain sedimentation in the Southeast Pacific Basin — leg 35 Deep Sea Drilling Project. In: Hollister, C. D., Craddock, C., et al. (eds.), Initial Reports of the Deep Sea Drilling Project 35, 291-300.

Tulaczyk, S., Kamb, B., Scherer, R. P., Engelhardt, H. F., 1998. Sedimentary processes at the base of a West Antarctic ice stream; constraints from textural and compositional properties of subglacial debris. *Journal of Sedimentary Research* 68 (3), 487-496.

Turner J., Orr A., Gudmundsson G. H., Jenkins A., Bingham R. G., Hillenbrand C.-D., Bracegirdle T. J., 2017. Atmosphere-ocean-ice interactions in the Amundsen Sea Embayment, West Antarctica. *Reviews of Geophysics* 55, doi:10.1002/2016RG000532.

Tütken, T., Eisenhauer, A., Wiegand, B., Hansen, B. T., 2002. Glacial–interglacial cycles in Sr and Nd isotopic composition of Arctic marine sediments triggered by the Svalbard/Barents Sea ice sheet. *Marine Geology* 182 (3), 351-372.

Uenzelmann-Neben, G., and Gohl, K., 2012. Amundsen Sea sediment drifts: archives of modifications in oceanographic and climatic conditions. *Marine Geology* 299, 51-62.

Underwood, M. B., and Pickering, K. T., 1996. Clay-mineral provenance, sediment dispersal patterns, and mudrock diagenesis in the Nankai accretionary prism, southwest Japan. *Clays and Clay Minerals* 44 (3), 339-356.

van de Flierdt, T., Goldstein, S. L., Hemming, S. R., Roy, M., Frank, M., Halliday, A. N., 2007. Global neodymium-hafnium isotope systematics – revisited. *Earth and Planetary Science Letters* 259 (3-4), 432-441.

van Wyk de Vries, M. , Bingham, R. G., Hein, A. S., 2017. A new volcanic province: an inventory of subglacial volcanoes in West Antarctica. Geological Society, London, Special Publications, 461, SP461-7.

Vaughan, A. P. M., and Storey, B. C., 2000. The eastern Palmer Land shear zone: a new terrane accretion model for the Mesozoic development of the Antarctic Peninsula. *Journal of the Geological Society,* London 157, 1243-1256.

Vaughan, A. P. M., Eagles, G., Flowerdew, M. J., 2012a. Evidence for a two-phase Palmer Land event from crosscutting structural relationships and emplacement timing of the Lassiter Coast Intrusive Suite, Antarctic Peninsula: Implications for mid-Cretaceous Southern Ocean plate configuration. *Tectonics* 31, TC1010.

Vaughan, A. P. M., Kelley, S., Storey, B., 2002. Mid-Cretaceous ductile deformation on the Eastern Palmer Land Shear Zone, Antarctica, and implications for timing of Mesozoic terrane collision. Geol. Mag. 139 (4), 465-471.

Vaughan, A. P. M., Storey, B. C., Kelley, S. P., Barry, T. L., Curtis, M. L., 2012b. Synkinematic emplacement of Lassiter Coast Intrusive Suite plutons during the Palmer Land Event: evidence for mid-Cretaceous sinistral transpression at the Beaumont Glacier in eastern Palmer Land. *Journal of the Geological Society*, London, 169, 759-771.

Vaughan, A. P. M., Wareham, C. D., Johnson, A. C., Kelley, S. P., 1998. A Lower Cretaceous, syn-extensional magmatic source for a linear belt of positive magnetic anomalies: the Pacific Margin Anomaly (PMA), western Palmer Land, Antarctica. Earth and Planetary Science Letters 158, 143-155.

Vaughan, D. G., Barnes, D. K. A., Fretwell, P. T., Bingham, R. G., 2011. Potential seaways across West Antarctica. Geochemistry, Geophysics, Geosystems 12 (10), Q10004, doi:10.1029/2011GC003688.

Vaughan, D. G., Corr, H. F., Ferraccioli, F., Frearson, N., O'Hare, A., Mach, D., Holt, J. W., Blankenship, D. D., Morse, D. L., Young, D. A., 2006. New boundary conditions for the West Antarctic ice sheet: Subglacial topography beneath Pine Island Glacier. *Geophysical Research Letters* 33 (9), L09501.

Veevers, J. J., and Saeed, A., 2013. Age and composition of Antarctic sub-glacial bedrock reflected by detrital zircons, erratics, and recycled microfossils in the Ellsworth Land–Antarctic Peninsula–Weddell Sea–Dronning Maud Land sector (240°E–0°–015°E). *Gondwana Research* 23, 296-332.

Wåhlin, A. K., Kalén, O., Arneborg, L., Björk, G., Carvajal, G. K., Ha, H. K., Kim, T. W., Lee, S.H., Stranne, C., 2013. Variability of warm deep water inflow in a submarine trough on the Amundsen Sea shelf, *Journal of Physical Oceanography* 43, 2054–2070.

Wåhlin, A. K., Kalén, O., Assmann, K., Darelius, E., Ha, H. K., Lee, S.H., 2016. Sub-inertial oscillations on the central Amundsen Shelf, *Journal of Physical Oceanography* 46 (9), 2573-2582, https://doi.org/10.1175/JPO-D-14-0257.1

Wåhlin, A. K., Muench, R. D., Arneborg, L., Björk, G., Ha, H. K., Lee, S. H., Alsén, H., 2012. Some implications of Ekman layer dynamics for cross-shelf exchange in the Amundsen Sea. *Journal of Physical Oceanography* 42 (9), 1461-1474.

Wåhlin, A. K., Yuan, X., Björk, G., Nohr, C., 2010. Inflow of warm Circumpolar Deep Water in the Central Amundsen Shelf, *Journal of Physical Oceanography* 40 (6), 1427–1434.

Walker, D. P., Brandon, M. A., Jenkins, A., Allen, J. T., Dowdeswell, J. A., Evans, J., 2007. Oceanic heat transport onto the Amundsen Sea shelf through a submarine glacial trough. *Geophysical Research Letters* 34, L02602.

Walker, D. P., Jenkins, A., Assmann, K. M., Shoosmith, D. R., Brandon, M. A., 2013. Oceanographic observations at the shelf break of the Amundsen Sea, Antarctica. *Journal of Geophysical Research: Oceans* 118, 2906-2918.

Walter, H. J., Hegner, E., Diekmann, B., Kuhn, G., Rutgers van der Loeff, M. M., 2000. Provenance and transport of terrigenous sediment in the South Atlantic Ocean and their relations to glacial and interglacial cycles: Nd and Sr isotopic evidence. *Geochimica et Cosmochimica Acta* 64 (22), 3814-3827.

Weaver, A. J., Saenko, O. A., Clark, P. U., Mitrovica, J. X., 2003. Meltwater pulse 1A from Antarctica as a trigger of the Bølling-Allerød warm interval. *Science* 299 (5613), 1709-1713.

Weaver, S. D., Adams, C. J., Pankhurst, R. J., Gibson, I. L., 1992. Granites of Edward VII Peninsula, Marie Byrd Land: anorogenic magmatism related to Antarctic-New Zealand rifting. *Transactions of the Royal Society of Edinburgh: Earth Sciences* 83 (1-2), 281-290.

Weertman, J., 1974. Stability of the junction of an ice sheet and an ice shelf. Journal of Glaciology 13 (67), 3-11.

Weis, D., Kieffer, B., Maerschalk, C., Barling, J., de Jong, J., Williams, G. A., Hanano, D., Pretorius, W., Mattielli, N., Scoates, J. S., Goolaerts, A., Friedman, R. M., Mahoney, J. B., 2006. High-precision isotopic characterization of USGS reference materials by TIMS and MC-ICP-MS. *Geochemistry, Geophysics, Geosystems* 7 (8). doi:10.1029/2006GC001283.

Welke, B., Licht, K., Hennessy, A., Hemming, S.R., Pierce Davis, E. L., Kassab, C., 2016. Applications of detrital geochronology and thermochronology from glacial deposits to the Paleozoic and Mesozoic thermal history of the Ross Embayment, Antarctica. *Geochemistry, Geophysics, Geosystems* 17, 2762-2780.

Wellner, J. S., Lowe, A. L., Shipp, S. S., and Anderson, J. B., 2001. Distribution of glacial geomorphic features on the Antarctic continental shelf and correlation with substrate: implications for ice behavior. *Journal of Glaciology*, 47 (158), 397-411.

Wendt, A. S., Vaughan, A. P. M., Tate, A., 2008. Metamorphic rocks in the Antarctic Peninsula region. *Geological Magazine* 145 (5), 1-22.

Wever, H. E., and Storey, B. C., 1992. Bimodal magmatism in northeast Palmer Land, Antarctic Peninsula: geochemical evidence for a Jurassic ensialic back-arc basin. *Tectonophysics* 205, 239-259.

Wever, H. E., Millar, I. L., Pankhurst, R. J., 1994. Geochronology and radiogenic isotope geology of Mesozoic rocks from eastern Palmer Land, Antarctic Peninsula: crustal anatexis in arc-related granitoid genesis. *Journal of South American Earth Sciences* 7 (1), 69-83.

Wilch, T. I., and McIntosh, W. C., 2000. Eocene and Oligocene volcanism at Mount Petras, Marie Byrd Land: implications for middle Cenozoic ice sheet reconstructions in West Antarctica. *Antarctic Science* 12 (4), 477-491.

Williams, T. J., Hillenbrand, C.-D., Piotrowski, A. M., Allen, C. S., Frederichs, T., Smith, J. A., Ehrmann, W., Hodell, D. A. Palaeocirculation and ventilation history of Southern Ocean sourced deep water masses during the last 800,000 years. Paleoceanography and Paleoclimatology (submitted).

Williams, T., van de Flierdt, T., Hemming, S. R., Chung, E., Roy, M., Goldstein, S. L., 2010. Evidence for iceberg armadas from East Antarctica in the Southern Ocean during the late Miocene and early Pliocene. *Earth and Planetary Science Letters* 290 (3-4), 351-361.

Wilson, D. J., Bertram, R. A., Needham, E. F., van de Flierdt, T., Welsh, K. J., McKay, R. M., Mazumder, A., Riesselman, C. R., Jimenez-Espejo, F. J., Escutia, C. Ice loss from the East Antarctic Ice Sheet during late Pleistocene interglacials. *Nature* (in press)

Wise, M. G., Dowdeswell, J. A., Jakobsson, M., Larter, R. D., 2017. Evidence of marine ice-cliff instability in Pine Island Bay from iceberg-keel plough marks. *Nature* 550, 506, doi: 10.1038/nature24458.

Witus, A. E., Branecky, C. M., Anderson, J. B., Szczuciński, W., Schroeder, D. M., Blankenship, D. D., Jakobsson, M., 2014. Meltwater intensive glacial retreat in polar environments and investigation of associated sediments: example from Pine Island Bay, West Antarctica. *Quaternary Science Reviews* 85, 99-118.

Yau, A. M., Bender, M. L., Robinson, A., and Brook, E. J., 2016. Reconstructing the last interglacial at Summit, Greenland: Insights from GISP2. *Proceedings of the National Academy of Sciences* 113 (35), 9710-9715.

Zachos, J. C., Breza, J. R., Wise, S. W., 1992. Early Oligocene ice-sheet expansion on Antarctica; stable isotope and sedimentological evidence from Kerguelen Plateau, southern Indian Ocean, *Geology* 20, 569-673.

Zachos, J., Pagani, M., Sloan, L., Thomas, E., Billups, K., 2001. Trends, rhythms, and aberrations in global climate 65 Ma to present. *Science* 292 (5517), 686-693.

Zhang, Y. G., Pagani, M., Liu, Z., Bohaty, S. M., DeConto, R., 2013. A 40-million-year history of atmospheric CO2. Philosophical Transactions of the Royal Society A 371:20130096.

Zwally, H. J., M. B. Giovinetto, M. A. Beckley, J. L. Saba, 2012. Antarctic and Greenland drainage systems, GSFC Cryospheric Sciences Laboratory.

Appendices

Appendix 1

Published Manuscript

Earth-Science Reviews 182 (2018) 204–232

Contents lists available at ScienceDirect

Earth-Science Reviews

journal homepage: www.elsevier.com/locate/earscirev

Geochemical fingerprints of glacially eroded bedrock from West Antarctica: Detrital thermochronology, radiogenic isotope systematics and trace element geochemistry in Late Holocene glacial-marine sediments

Patric Simões Pereira[a,b,*], Tina van de Flierdt[b], Sidney R. Hemming[c,d], Samantha J. Hammond[e], Gerhard Kuhn[f], Stefanie Brachfeld[g], Cathleen Doherty[h], Claus-Dieter Hillenbrand[i]

[a] Grantham Institute for Climate Change and the Environment, Imperial College London, South Kensington Campus, London SW7 2AZ, UK
[b] Department of Earth Science and Engineering, Imperial College London, South Kensington Campus, London SW7 2AZ, UK
[c] Department of Earth and Environmental Sciences, Columbia University, Lamont-Doherty Earth Observatory, Palisades, NY 10964, USA
[d] Department of Earth and Environmental Sciences, Columbia University, New York, NY 10027, USA
[e] Department of Environment, Earth and Ecosystems, The Open University, Walton Hall, Milton Keynes MK7 6AA, UK
[f] Alfred-Wegener-Institut, Helmholtz-Zentrum für Polar- und Meeresforschung, Marine Geosciences, Bremerhaven 27568, Germany
[g] Department of Earth and Environmental Studies, Montclair State University, Montclair, NJ 07043, USA
[h] Environmental and Occupational Health Sciences Institute, Rutgers University, Piscataway, NJ 08854, USA
[i] British Antarctic Survey, High Cross, Madingley Road, Cambridge CB3 0ET, UK

ARTICLE INFO

Keywords:
Geochemical provenance
West Antarctic Ice Sheet
Subglacial geology
Sediment transport pathways

ABSTRACT

Geochemical provenance studies of glacial-marine sediments provide a powerful approach to describe subglacial geology, sediment transport pathways, and past ice sheet dynamics. The marine-based West Antarctic Ice Sheet (WAIS) is considered highly vulnerable to ocean warming and sea level rise that is likely to cause its rapid and irreversible retreat. Studies of its past response to climate change are hence essential for projecting its future behaviour. The application of radiogenic and trace element provenance studies for past ice sheet reconstructions requires surveying the geographic variability of geochemical compositions of glaciomarine sediments. In this study, we characterize the provenance of the detrital fraction of 67 Late Holocene marine sediment samples collected off the Pacific margin of West Antarctica (60°W to 160°W), including $^{40}Ar/^{39}Ar$ ages of individual hornblende and biotite grains (> 150 μm), as well as Sr and Nd isotope and trace element composition of the fine-grained (< 63 μm) sediment fraction. Overall, this approach allows differentiating West Antarctica into five source regions: the Antarctic Peninsula, Bellingshausen Sea, Amundsen Sea, Wrigley Gulf-Hobbs Coast and Sulzberger Bay. Minor geochemical variability is found within each individual sector due to local variability in onland geology. $^{40}Ar/^{39}Ar$ ages of iceberg-rafted hornblende and biotite grains record primarily Carboniferous to Lates Quaternary ages (~0 to 380 Ma), with a notable age peak of ~100 Ma, associated with plutonic intrusions or deformation events during the mid-Cretaceous. Permian-Jurassic $^{40}Ar/^{39}Ar$ ages are widespread in the Amundsen Sea sector, marking episodes of large-volume magmatism along the long-lived continental margin. Metasedimentary rocks and Late Cenozoic alkali basalts in West Antarctica cannot be detected using detrital hornblende and biotite $^{40}Ar/^{39}Ar$ ages due to the absence or small grain-size (i.e. < 150 μm) of these minerals in such rocks. These sources can however be readily recognized by their fine-grained geochemical composition. In addition, geographic trends in the provenance from proximal to distal sites provide insights into major sediment transport pathways. While the transport of fine-grained detritus follows bathymetric cross-shelf troughs, the distribution of iceberg-rafted grains shows influence by transport in the Antarctic Coastal Current. Our study provides the first systematic geochemical characterisation of sediment provenance off West Antarctica, and highlights the importance of combining multiple provenance approaches in different size fractions of glacial-marine sediments, and paves the way to investigate past WAIS dynamics.

* Corresponding author at: Grantham Institute for Climate Change and the Environment, Imperial College London, South Kensington Campus, London SW7 2AZ, UK.
E-mail address: p.simoes-pereira14@imperial.ac.uk (P. Simões Pereira).

https://doi.org/10.1016/j.earscirev.2018.04.011
Received 17 November 2017; Received in revised form 20 April 2018; Accepted 30 April 2018
Available online 04 May 2018
0012-8252/

1. Introduction

The West Antarctic Ice Sheet (WAIS) holds enough ice to raise global sea-level by 4.3 m if completely melted (Fretwell et al., 2013). Its base rests largely on surfaces of bedrock and sedimentary strata that are well below sea level with an inland-deepening slope, making the WAIS vulnerable to changing environmental conditions (e.g. Oppenheimer, 1998), particularly to ocean warming and sea-level rise via the marine ice sheet instability hypothesis (e.g. Rignot and Jacobs, 2002; Schoof, 2007; Katz and Worster, 2010; Jacobs et al., 2011; Joughin and Alley, 2011; Pritchard et al., 2012) and/or marine ice cliff instability (DeConto and Pollard, 2016; Wise et al., 2017). This vulnerability is confirmed by modern observational data, which show thinning of ice shelves, acceleration of ice stream flow, and overall mass loss in the Pacific sector of the WAIS (Payne et al., 2004; Rignot et al., 2008; Pritchard et al., 2009, 2012; Shepherd et al., 2012; Mouginot et al., 2014). Most of the current retreat occurs in the Amundsen Sea sector, which drains approximately ~35% of the WAIS. High rates of mass loss originate from the Pine Island and Thwaites glaciers, with potential collapse being hypothesised to occur in as little as ~400 years (Oppenheimer, 1998 and references therein; Vaughan et al., 2011; Joughin et al., 2014). The proposed mechanism for collapse is an irreversible retreat of the grounding line (Schoof, 2007; Katz and Worster, 2010), facilitated by the landward dipping bed under the WAIS. Thereby, the bathymetric setting of the continental shelf may trigger initial retreat by allowing relatively warm Circumpolar Deep Water that is upwelling onto the shelf to enter sub-ice shelf cavities through cross-shelf troughs carved by past ice stream advances (e.g. Walker et al., 2007, 2013; Jenkins et al., 2010, 2016).

While modern and historical processes leading to ice-sheet loss are increasingly well studied and understood (e.g. Hillenbrand et al., 2017; Smith et al., 2017; Turner et al., 2017), reconstructions of the past stability of the WAIS are still sparse (e.g. Scherer et al., 1998; Hillenbrand et al., 2002, 2009a; Pollard and DeConto, 2009; Naish et al., 2009; Vaughan et al., 2011). One promising tool to learn about past ice stability has been to study the provenance of marine detrital sediments. Radiogenic isotope fingerprinting and dating has been successfully applied to reconstruct ice sheet history in the Northern Hemisphere (e.g. Gwiazda et al., 1996; Hemming et al., 1998; Hemming and Hajdas, 2003; Peck et al., 2007; Downing et al., 2013; Reyes et al., 2014) and around East Antarctica (e.g. Williams et al., 2010; Pierce et al., 2011, 2014, 2017; Cook et al., 2013, 2014, 2017). Geochemical (i.e. radiogenic isotope composition) studies of glacially derived sediments with a West Antarctic provenance have so far been restricted to the Ross Sea (Farmer et al., 2006; Licht and Palmer, 2013; Licht et al., 2014), glacial till samples from distinct ice streams (Farmer and Licht, 2016; Licht et al., 2014; Welke et al., 2016), and only a few marine sediment core top analyses along the West Antarctic margin (Walter et al., 2000; Roy et al., 2007; van de Flierdt et al., 2007; Hemming et al., 2007).

In this study, we close this gap and describe the detailed geochemical provenance of glacially derived Late Holocene sediments along the Pacific margin of West Antarctica. Our primary motivation is to identify isotopic and geochemical fingerprints for individual WAIS sectors, and to characterize its subglacial geology building on the pioneering work of Roy et al. (2007), van de Flierdt et al. (2007) and Hemming et al. (2007). Paramount to such studies is the knowledge of the geological history of the exposed and subglacial bedrock (Figs. 1, 2) and its overall geochemical variability. Outcrop studies, integrated with airborne and field geophysical campaigns have significantly increased our knowledge of the hidden bedrock below the Antarctic Ice Sheet (e.g. Ferraccioli et al., 2009; Smith et al., 2013; Jordan et al., 2013a, 2013b; Aitken et al., 2014). Investigations of sediments that are shed from Antarctica can also contribute to understanding subglacial geology as well as providing the groundwork for using this approach to document the past history of the ice sheets. Here we present results on the geochemical signature of 67 surface sediment samples using $^{40}Ar/^{39}Ar$ ages of individual hornblende and biotite grains (> 150 μm or > 63 μm), and strontium (Sr) and neodymium (Nd) isotope ratios and trace element compositions of the fine-grained fraction (< 63 μm). We present these results in the context of published studies of the geology and geochemistry of West Antarctica from field observations and geophysical investigations. By combining different provenance tools, we characterize source sectors of glacigenic detritus, a vital precondition for unravelling the history of the WAIS by tracing down-core provenance changes in marine sediment records. We place a particular emphasis on the Amundsen Sea sector, and relate our new sediment provenance results to specific ice drainage signatures, as well as pathways and transport mechanisms that may deliver sediments to their sites of deposition.

2. Regional Framework of West Antarctica

2.1. Tectonic history

The Antarctic continent preserves a geological record from ~3.5 Ga to present. Most known Precambrian rocks are found in East Antarctica (see Boger, 2011 for a recent review), while West Antarctica generally has a younger, largely Phanerozoic, geological history. West Antarctica consists of four micro-continental blocks: the Antarctic Peninsula, Ellsworth-Whitmore Mountains, Thurston Island and Marie Byrd Land (Dalziel and Elliot, 1982) (Figs. 1, 2).

The 'birth' of West Antarctica is largely associated with the onset of the accretionary Terra Australis (Ross) Orogeny (~510 Ma). The Terra Australis Orogeny took place after suturing of West Gondwana (South American and South African shields) and the Australo-Antarctic plates (Kuunga Orogen), which shifted the locus of active subduction from between the pre-collision complexes of Gondwana towards the Proto-Pacific margin (Cawood, 2005). This orogenic event resulted in deformation of passive margin sediments, formation of back-arc basins with quiescent sedimentation (Ellsworth-Whitmore Mountains, Fig. 1), and led to arc-type plutonism and subsequent crustal accretion onto the Gondwana margin (Cawood, 2005; Boger, 2011).

Convergence along the Pacific margin of Gondwana led to deposition and subsequent accretion of Cambrian-Ordovician turbiditic sequences, and intrusion of Devonian-Carboniferous (~375–345 Ma) granitoids. Relicts of these Early Palaeozoic rocks are found in the Ross province of Marie Byrd Land (Pankhurst et al., 1998; Mukasa and Dalziel, 2000), on Thurston Island (Pankhurst et al., 1993; Riley et al., 2017) and in the Eastern Domain of the Antarctic Peninsula (Millar et al., 2002), considered as the innermost and oldest arc-terranes in West Antarctica (Vaughan and Storey, 2000) (Figs. 1, 2).

During the late Carboniferous, collision of Gondwana with Laurentia terminated the Terra Australis Orogeny, which was followed by the Gondwanide Orogeny (Fig. 1). This transition marked the initiation of a series of magmatic arc terranes, largely calc-alkaline granodiorite, diorite, and monzogranite intrusions in the Central Domain (Amundsen Province) of Marie Byrd Land and in the Central Domain of the Antarctic Peninsula during the Late Palaeozoic-Mesozoic. Notable episodes of magmatism occurred during the late Triassic-early Jurassic (236–199 Ma), mid-Jurassic (~180–160 Ma) and Early to Late Cretaceous (~140–80) (Leat et al., 1995; Storey et al., 1996). Though initially disconnected from Antarctica, these terranes became accreted to the continent by the end of the Cretaceous.

The outermost terrane belt in West Antarctica, the Western Domain of the Antarctic Peninsula (Vaughan and Storey, 2000) is composed of Carboniferous to Late Cretaceous accretionary sedimentary rocks such as those found on Alexander Island (Fig. 2). This terrane accreted to the West Antarctic margin by 103–107 Ma, leading to back-arc plutonism and metamorphism of the Western and Central Domain in the mid-Cretaceous (Wendt et al., 2008; Vaughan et al., 2012a).

Gondwana break-up led to extensive extrusion of Jurassic volcanic

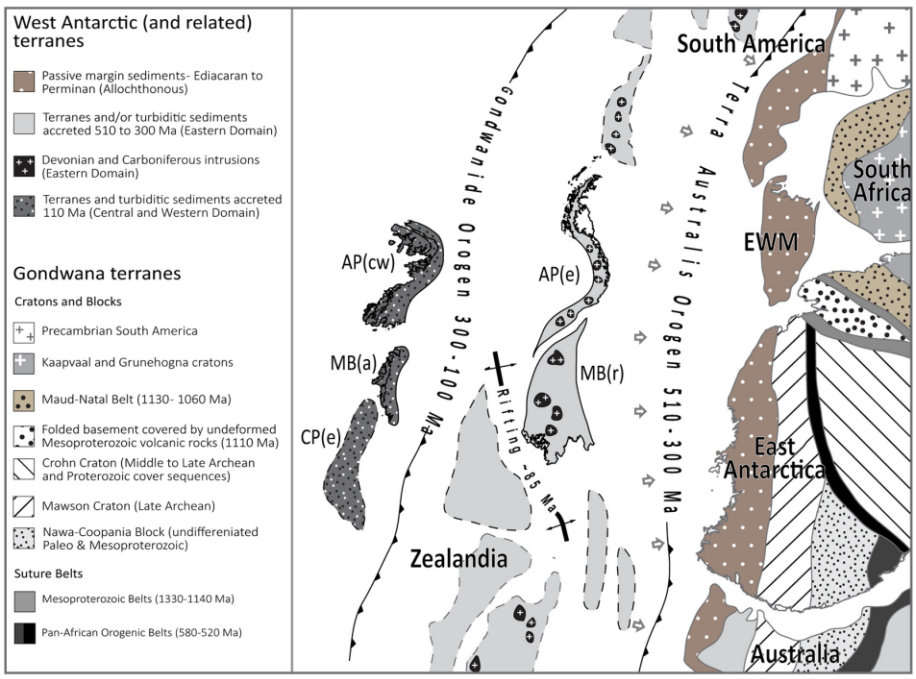

Fig. 1. Tectonic reconstruction of West Antarctica during the Early Palaeozoic to Cretaceous (modified from Boger, 2011). AP – Antarctic Peninsula, MB(a) – Amundsen Province of Marie Byrd Land, related to the Central Domain, MB(r) – Ross Province of Marie Byrd Land, related to the Eastern Domain, CP – Campbell Plateau. Indices: e – Eastern Domain, c – Central Domain, w – Western Domain.

rocks documented by outcrops in the Antarctic Peninsula, and resulted in rifting away of Zealandia in the Cretaceous (Weaver et al., 1992; Pankhurst et al., 2000; Korhonen et al., 2010). Plutonism on West Antarctica continued until the Cenozoic with a diachronous eastward cessation of subduction (Larter and Barker, 1991; Leat et al., 1995; Larter et al., 2002; Cunningham et al., 2002; Mukasa and Dalziel, 2000). This was followed and accompanied by the extrusion of the widespread Late Cenozoic alkali basalts (e.g. Futa and LeMasurier, 1983; Hole and LeMasurier, 1994), which crop out extensively in central West Antarctica, especially the Marie Byrd Land volcanic province (e.g. LeMasurier and Rex, 1991).

2.2. Oceanography

The dominant oceanographic feature off (West) Antarctica is the eastward flowing Antarctic Circumpolar Current (ACC), which is driven by the West Wind Drift, creating a clockwise flow around the Antarctic continent (Orsi et al., 1995; Sokolov and Rintoul, 2009). In the eastern Pacific sector of West Antarctica the Southern Boundary of the ACC (SBACC) follows approximately the shelf break (Sokolov and Rintoul, 2009), but the SBACC runs slightly north of it in the eastern Amundsen Sea and deviates further away from the continent towards the Ross Sea (Orsi et al., 1995; Walker et al., 2013) (Fig. 2). Wind stress and buoyancy forcing drive the westward flowing Antarctic Coastal Current, which spans the area between the SBACC and the coast (e.g. Stammerjohn et al., 2015; Kim et al., 2016a), creating a westward flowing surface current (Fig. 2). This general circulation pattern is complicated by local winds and large cyclonic gyres, such as in the Bellingshausen Sea (Fig. 2) and the Ross Sea. On the shelf of the Bellingshausen Sea, for instance, significant quantities of icebergs initially drift westwards with the coastal current but are then directed northwards near Thurston Island eventually joining the eastward flowing ACC (Gladstone et al., 2001; Sokolov and Rintoul, 2009). In the Pacific sector of the Southern Ocean, deep warm water upwells onto the continental shelf (Fig. 2 inset), locally protrudes towards the coast via bathymetric cross-shelf troughs, which were eroded by WAIS advances during past ice ages, and causes the bases of floating ice shelves to melt (e.g. Walker et al., 2007; Thoma et al., 2008; Jenkins et al., 2010; Arneborg et al., 2012; Randall-Goodwin et al., 2015). In the Amundsen Sea Embayment (ASE) the resulting glacial meltwater is detected in the mid-layer of the water column at about 400–500 m and flows northward along incised troughs towards the shelf break (e.g. Kim et al., 2016b).

The velocities of ocean currents measured and/or modelled in the surface and deep waters of our study area are on average ca. ≤5 cm/s, with a maximum of 22 cm/s (Assmann et al., 2005; Wåhlin et al., 2010, 2012, 2013, 2016; Jacobs et al., 2011, 2013; Arneborg et al., 2012; Carvajal et al., 2013; Walker et al., 2013; Ducklow et al., 2015; Kim et al., 2015; Randall-Goodwin et al., 2015). Exceptions to this are the westward flowing Antarctic Coastal Current in front of the Dotson Ice Shelf, and a local current within the Amundsen Polyna. The former current reaches a speed up to 40 cm/s in a narrow layer at 70 m water depth (Kim et al., 2016a), but this speed decreases to below 22 cm/s when integrated over the entire water column (Randall-Goodwin et al., 2015). The latter Amundsen Polynya current is characterized by a flow speed ≤27 cm/s detected at 430 m water depth north of the Dotson and westernmost Getz ice shelves (Kim et al., 2016a). These velocities will become important when discussing transport pathways of detrital mineral grains later on.

3. Approach and samples

3.1. Approach to provenance fingerprinting

Analysis of the provenance of marine detrital sediments requires the consideration of a variety of glaciological and geological factors (see

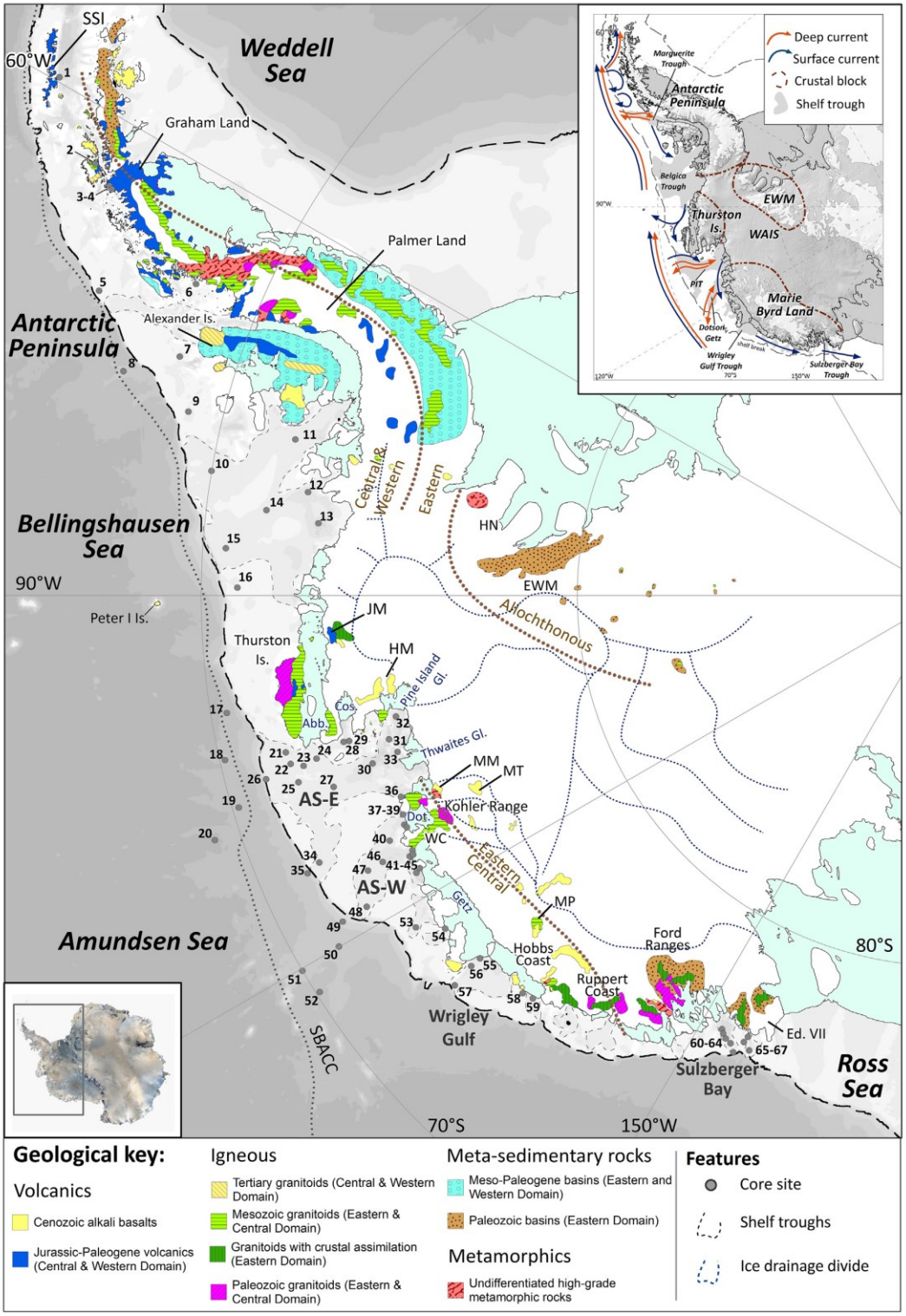

(caption on next page)

Fig. 2. Simplified geological map of West Antarctica, including major geological units discussed in the text (Futa and LeMasurier, 1983; Storey et al., 1988; Pankhurst et al., 1993; McCarron and Smellie, 1998; Mukasa and Dalziel, 2000; Ferraccioli et al., 2002; Korhonen et al., 2010; Burton-Johnson and Riley, 2015). Thin blue dotted lines on the continent represent divides between major ice drainage basins, and brown dotted lines mark approximate boundaries between tectonic domains (Pankhurst et al., 1998; Vaughan and Storey, 2000). Grey dashed line on the continental shelf outlines bathymetric troughs, dashed black lines indicate the approximate location of the shelf break, and dotted line offshore marks position of the Southern Boundary of the Antarctic Circumpolar Current (SBACC; Orsi et al., 1995). Sites of surface sediments analysed in this study are shown as grey circles and numbers refer to their position in Table 1. Abbreviations: Abb – Abbot Ice Shelf; AS: Amundsen Sea; Cos – Cosgrove Ice Shelf; Dot – Dotson Ice Shelf; Ed. VII – Edward VII Peninsula: EWM – Ellsworth-Whitmore Mountains; FR – Ford Ranges; JM – Jones Mts; HN – Haag Nunataks; HM – Hudson Mts; MM – Mt Murphy; MP – Mount Petras; MT – Mt Takahe; SSI – South Shetland Islands.; TI – Thurston Island; WAIS – West Antarctic Ice Sheet; WC – Walgreen Coast. Inset: Digital elevation model of Antarctica (Bamber et al., 2009) with major crustal blocks of West Antarctica (Dalziel and Elliot, 1982). White contours denote bedrock above modern sea-level (Fretwell et al., 2013). Blue arrows denote main surface ocean currents (Gladstone et al., 2001; Assmann et al., 2005; Murphy et al., 2013) and orange arrows denote deep (i.e. down to ca. 1000 m water depth) currents (Holland et al., 2010; Assmann et al., 2013; Murphy et al., 2013; Ha et al., 2014). Palaeo-ice streams are shown in grey.

review by Licht and Hemming, 2017). Glacial influence on provenance records is exerted by preferential subglacial erosion of specific substrates. Glacial-marine transport and depositional processes in the ocean can furthermore introduce sorting and hence affect mineral assemblages in sediments. Geologically, onland bedrock needs to provide sufficient geochemical heterogeneity in order to produce distinct isotopic fingerprints. In addition, different rock types and mineral components are prone to be disproportionately represented in different grain-size fractions. Plutonic and high-grade metamorphic rocks, for instance, are rich in coarse-grained minerals, and are therefore likely to be over-represented in the coarse fraction of marine sediments. In contrast, sedimentary rocks consist of recycled continental material, and typically show a finer texture as well as depletion in minerals that are less resistant to chemical and physical weathering, such as hornblende and biotite (e.g. Pierce et al., 2014). Erosion of sedimentary rocks would lead to enrichment of these minerals in the fine fraction of glacial-marine sediments.

To limit the risk of neglecting or over-representing a particular rock type, we apply different geochemical tracers and analyse two different size-fractions of the same sediment sample. We investigate $^{40}Ar/^{39}Ar$ ages of ice-rafted (> 150 μm) hornblende and biotite grains, as well as Sr and Nd isotope and trace element compositions of fine-grained (< 63 μm) detritus. Dating of individual grains from marine sediments has been shown to provide powerful insights into the thermo-metamorphic history of the parent rocks. In the Southern Ocean, detailed studies on the provenance of East Antarctic glacial-marine sediments have shed light on previously documented as well as undiscovered geological provinces below the ice (e.g. Roy et al., 2007; Cook et al., 2014, 2017; Pierce et al., 2014, 2017). Even though most studies so far have focused on $^{40}Ar/^{39}Ar$ analysis of hornblende grains, recent work has elegantly demonstrated how biotite can provide complementary information on source rock metamorphism (Pierce et al., 2011, 2014). Both minerals are major rock-forming constituents and are present in a variety of lithologies. The advantage of using the dual dating approach relies on the fact that different lithologies might contain different amounts of hornblende and biotite grains. Additionally, hornblende and biotite minerals have different closure temperatures for argon of ~550°C and ~300°C, respectively (Harrison, 1982; Harrison et al., 1985) and hence reflect different points on the cooling path following a major extrusive or tectono-metamorphic event. The distinct attributes between both chronometers can be exploited to extract information on the source rock, only if both minerals originate from the same source. In the marine environment, however, selective transport pathways may compromise such coupling. Critical factors to consider are ocean current speeds, which determine the grain sizes and types of detrital mineral grains being eroded, transported, or deposited and hydraulic equivalence (i.e settling behaviour) of the different mineral types, which determines preferential transport and deposition of one mineral grain type over another.

In order to overcome the potential bias created by using mineral tracers, which rely on the existence of rocks containing these minerals, we also chose to investigate Sr and Nd isotopic compositions and trace element geochemistry of fine-grained (< 63 μm) detritus. Fine-grained material can be eroded from any type of geology, and its radiogenic isotope composition depends on the age and lithology of the source formation (Taylor and McLennan, 1995). Hence, fine-grained Sr and Nd isotopic compositions have the potential to record an integrated signature of bedrock eroded under an ice stream or ice margin (Hemming et al., 1998; Farmer et al., 2003, 2006; Colville et al., 2011; Pierce et al., 2011; Cook et al., 2013, 2017; Farmer and Licht, 2016). Samarium (Sm) and Nd are not fractionated during continental erosion due to their nearly equal incorporation in most rock forming minerals. Neodymium model ages, based on the long-lived ^{147}Sm to ^{143}Nd decay system, are thus effective at reconstructing the mantle extraction age of precursor material of sediments (Goldstein and Hemming, 2003). Different minerals tend to have very similar Sm/Nd ratios (e.g. Bayon et al., 2009; Garçon et al., 2013; Rickli et al., 2014), making it unlikely that Nd isotopic compositions in sediments are majorly influenced by sedimentary sorting and/or weathering. In contrast, comminution of minerals with variable Rb/Sr ratios can produce grain-size effects in the $^{87}Sr/^{86}Sr$ ratio, particularly due to the enrichment of clay minerals and biotite in the fine-grained fraction (e.g. Eisenhauer et al., 1999; Goldstein and Hemming, 2003). Additionally, $^{87}Sr/^{86}Sr$ ratios can be fractionated during continental weathering due to the different solubility of the parent isotope ^{87}Rb compared to the daughter isotope ^{87}Sr (e.g. Blum and Erel, 1997).

3.2. Samples and site selection

For this study, we selected 67 proximal to distal seafloor surface sediment samples from the Pacific margin of West Antarctica. In total, 59 samples were provided from core repositories of the British Antarctic Survey (Cambridge), the Alfred-Wegener Institute for Polar and Marine Research (Bremerhaven), and the Antarctic Marine Geology Research Facility at the Florida State University (formerly at Tallahassee, FL). We additionally complemented our sample selection by eight samples previously studied by Roy et al. (2007), which we picked for $^{40}Ar/^{39}Ar$ age analysis of biotite grains, not carried out in the original study. Table 1 provides a full description of the site locations and water depths, coring devices, and sample depths. Sites proximal to individual major ice streams were selected to identify the geochemical fingerprint of each ice drainage basin and therefore to constrain subglacial geology (Fig. 2). Distal sites were selected to test whether provenance signatures from the terminus of an active ice stream can be traced offshore, with the future goal to reconstruct ice history through time by analysing down-core records. Most sampling sites are located in the ASE, the modern-day locus of major ice stream retreat (e.g. Rignot et al., 2008, 2014), and proposed site of substantial WAIS retreat in the past (e.g. Vaughan et al., 2011).

Most sediment samples used in this study are seafloor surface samples collected with box and multiple corers, and thus are of modern or at least Late Holocene age, which has been confirmed by AMS ^{14}C dating and/or ^{210}Pb analyses for several of these samples (Hillenbrand et al., 2010a, 2010b, 2013; Smith et al., 2011, 2014). Other samples were chosen solely due to their geographical position. Even though no chronological constraints were available for some of those samples, e.g.

Table 1
$^{39}Ar/^{40}Ar$ ages analysed in ice-rafted (> 150 μm or > 63 μm) hornblende and biotite grains from surface sediments off West Antarctica.

Core Site	Site location	Core depth (cm)	Sector[a]	Size fraction	Gear	Latitude	Longitude	Water depth (m)	Hornblende grains	Biotite grains	Reference[b]
1	DF86–48	28–34	AP		piston corer	-62.68	-59.74	1234			
2	DF85–53	39–44	AP	> 150 μm	piston corer	-64.56	-63.16	201	55		this study
3	PD88–111 Grab37	Surface	AP		surface grab	-65.14	-63.97	240			
4	PD88–111 Grab41	Surface	AP		surface grab	-65.23	-64.09	200			
5	ELT05–22	4–6	AP	> 150 μm	piston corer	-65.95	-70.25	373	91	7	Roy et al., 2007; this study
6	DF85–82	28–33	AP	> 150 μm	piston corer	-68.24	-67.50	275	39		this study
7	PS2524–1	0–1	AP		box corer	-68.49	-72.72	458			
8	ELT05–20	2–4	AP	> 150 μm	trigger core	-67.18	-74.78	2926	37	7	Roy et al., 2007; this study
9	BC470	0–2	BS		box corer	-69.09	-76.39	670			
10	ELT42–09	0–2	BS	> 150 μm	piston corer	-69.99	-80.39	567	30	19	Roy et al., 2007; this study
11	BC361	0–1	BS	> 150 μm	box corer	-71.99	-76.55	633	38	38	this study
12	GC362	0–1	BS		box corer	-72.60	-80.83	846			
13	BC364	0–1	BS	63 μm-2 mm	box corer	-72.98	-83.44	1010		20	this study
14	BC369	0–2	BS	150 μm-2 mm	box corer	-71.58	-82.86	587	47	44	this study
15	BC459	0–1	BS	> 150 μm	box corer	-70.61	-86.25	676	61	46	this study
16	PS2543–3	0–1	BS		multi-corer	-70.95	-89.36	537			
17	ELT11–19	0–2	AS-E	> 150 μm	trigger corer	-70.42	-99.25	3808	63	16	Roy et al., 2007; this study
18	ELT11–18	2–4	AS-E	> 150 μm	piston corer	-70.14	-102.82	3786	24	5	Roy et al., 2007; this study
19	ELT11–17	2–4	AS-E	> 150 μm	trigger corer	-70.17	-106.64	3456	6	5	Roy et al., 2007; this study
20	PS58/254–2	0–2	AS-E	> 150 μm	multi-corer	-69.31	-108.45	4016	14	7	this study
21	PS75/192–2	0–1	AS-E		giant box corer	-71.74	-103.33	793			
22	PS69/255–3	0–1	AS-E	150 μm-2 mm	giant box corer	-71.80	-104.36	654	31		this study
23	PS69/251–1	0–1	AS-E		giant box corer	-72.11	-104.81	573			
24	DF85–109	11–17	AS-E	> 150 μm	piston corer	-72.49	-104.48	567	30		this study
25	BC451	0–1	AS-E	150 μm-2 mm	box corer	-71.87	-106.04	568	49	51	this study
26	BC455	0–1	AS-E	> 150 μm	box corer	-71.07	-105.08	807	54	44	this study
27	BC485	0–3	AS-E	150 μm-2 mm	box corer	-72.73	-107.29	692	15	26	this study
28	DF85 96–1	83–88	AS-E	> 150 μm	piston corer	-73.30	-103.62	786	30		this study
29	PS69/299–1	0–1	AS-E	150 μm-2 mm	giant box corer	-73.44	-103.65	718	24	57	this study
30	BC482	0–2	AS-E		box corer	-73.89	-106.27	1113			
31	BC476	0–2	AS-E		box corer	-74.48	-104.42	1120			
32	PS75/159–1	0–1	AS-E	63 μm-2 mm	gravity corer	-74.80	-102.36	1046	1		this study
33	PS75/168–1	0–1	AS-E	63 μm-2 mm	gravity corer	-74.61	-105.87	652	9		this study
34	BC442	0–1	AS-E	150 μm-2 mm	box corer	-71.68	-113.01	608	47	53	this study
35	BC443	0–1	AS-E	150 μm-2 mm	box corer	-71.28	-113.46	1789	55	39	this study
36	PS69/281–3	0–1	AS-W		giant box corer	-74.33	-110.21	213			
37	NBP07–02 SMG6	Surface	AS-W		surface grab	-74.21	-111.90	343			
38	BC420	0–2	AS-W	> 150 μm	box corer	-74.14	-112.86	806	24	15	this study
39	NBP00–01 KC24	13–19	AS-W		kasten corer	-74.17	-113.18	301			
40	BC421	0–1	AS-W	> 150 μm	box corer	-73.62	-113.71	833	32	21	this study
41	BC412	0–1	AS-W	63 μm-2 mm	box corer	-73.92	-115.86	1128	19	33	this study
42	NBP00–01 PC22	5–10	AS-W		piston corer	-74.06	-115.46	1171			
43	NBP00–01 KC21	5–10	AS-W	> 150 μm	kasten corer	-74.03	-115.84	1049	35		this study
44	NBP07–02 SMG5	Surface	AS-W		surface grab	-74.02	-117.30	350			
45	PS69/275–2	0–1	AS-W	> 150 μm	giant box corer	-73.89	-117.55	1517	11	37	this study
46	BC407	0–2	AS-W	> 150 μm	box corer	-73.21	-115.24	815	6	18	this study
47	PS69/283–5	0–1	AS-W	150 μm-2 mm	giant box corer	-72.76	-115.38	612	52	44	this study
48	BC431	0–1	AS-W	> 150 μm	box corer	-72.30	-118.16	512	45	42	this study
49	BC433	0–1	AS-W	150 μm-2 mm	box corer	-71.56	-118.31	1722	43	41	this study
50	BC492	0–1	AS-W	> 150 μm	box corer	-71.15	-119.96	2073		26	this study
51	ELT33–12	2–6	AS-W	> 150 μm	piston corer	-70.00	-120.17	2615	27	18	Roy et al., 2007; this study
52	ELT33–11	0–2	AS-W	> 63 μm	piston corer	-70.10	-122.26	3639	10		Roy et al., 2007
53	PS2545–1	0–1	AS-W		giant box corer	-73.16	-121.95	636			
54	NBP00–01 KC17	7–13	AS-W		kasten corer	-73.79	-123.53	891			

(*continued on next page*)

Table 1 (*continued*)

Core Site	Site location	Core depth (cm)	Sector[a]	Size fraction	Gear	Latitude	Longitude	Water depth (m)	Hornblende grains	Biotite grains	Reference[b]
55	NBP99–02 PC21	8–13	WH	> 150 μm	piston corer	-74.08	-127.79	702	9	5	this study
56	NBP99–02 TC23	0–3	WH		trigger weight corer	-73.78	-127.86	726			
57	NBP00–01 PC14	1–3	WH	> 150 μm	piston corer	-73.11	-128.32	591	51		this study
58	PS75/133–1	0–1	WH	> 150 μm	giant box corer	-74.34	-133.08	474	19	40	this study
59	PS75/130–2	0–1	WH	> 150 μm	giant box corer	-74.45	-134.15	793	22	40	this study
60	DF83-III BC28	2–4	SB	> 63 μm	box corer	-76.83	-152.48	1024	18		this study
61	NBP96–01 PC12	0–3	SB		(giant) piston corer	-76.74	-152.85	881			
62	NBP96–01 TC13	0–3	SB		trigger weight corer	-76.65	-153.36	739			
63	NBP99–02 Grab20	Surface	SB		surface grab	-76.41	-154.82	458			this study
64	DF83 PC31	0–3	SB	> 63 μm	piston corer	-76.60	-154.10	713	5		this study
65	DF83-III BC26A	1–3	SB	> 63 μm	box corer	-76.95	-155.62	1353	3		
66	NBP96–01 JTC11	0–3	SB		trigger weight corer	-76.78	-155.44	392			
67	DF83-III BC33	3.5–5.5	SB		box corer	-76.63	-156.40	770			

[a] AP: Antarctic Peninsula sector, BS: Bellingshausen Sea, AS-E: eastern Amundsen Sea, AS-W: western Amundsen Sea, WH: Wrigley Gulf-Hobbs Coast, SB: Sulzberger Bay.

[b] See Appendix S1 for complete dataset.

shelf samples from Sulzberger Bay, the stratigraphic position of these samples near the seafloor surface assures that they are most likely not older than Late Holocene, which is evident from AMS ^{14}C ages of such samples in the Bellingshausen, Amundsen and Ross Seas and on the western Antarctic Peninsula margin (The RAISED Consortium, 2014). We followed this approach to avoid the potential influence of past changes in erosion or sediment transport/deposition on the provenance of the studied sediments.

As detailed in Section 2, current speeds in the study area are typically ≤22 cm/s. This flow velocity is too low to move sand particles (≥63 μm), which would require current speeds exceeding 26–29 cm/s (e.g. McCave et al., 2017). Large sheeted (flaky) biotite grains have a hydraulic equivalence to smaller (bulky) hornblende grains according to Komar et al. (1984) and Garzanti et al. (2008, 2009). These studies concluded that coarse grained (> 150 μm) biotite grains are hydraulically equivalent to quartz grains with a size exceeding ~75 μm. Such grains would not be moved by the ocean currents typical for the West Antarctic margin, allowing interpretation of biotite grains > 150 μm as subglacial debris, which was released by grounded ice directly at the coast or transported by icebergs further offshore, alongside hornblende grains > 150 μm. Several samples, however, have been picked for hornblende and biotite grains from the 63–150 μm fraction due to a low amount of grains in these samples. Due to the weak ocean currents in the study area, bulky hornblende grains from the 63–150 μm fraction are likely unaffected by hydrodynamic sorting and provide the same lithologic information as the coarser > 150 μm size fraction. Sediment samples from sites 13 and 41 (Table 1, Fig. 2) were, however, picked for biotite grains from the 63–150 μm fraction only. These results will hence be discussed separately (i.e. potential for selective mineral transport by ocean currents).

4. Analytical procedures

Sediment samples were freeze-dried, weighed, and wet sieved through a 63-micron sieve. The sand fraction (> 63 μm) was subsequently dry sieved at 150 μm to obtain the > 150 μm fraction (Table 1). The fine-grained (< 63 μm) fraction was separated by gravitational settling, after which the clear supernatant was discarded, and sediment was dried in an oven at 60°C. Approximately 1g of < 63 μm sediment was leached with buffered acetic acid to remove calcium carbonate, followed by 0.02 M hydroxylamine hydrochloride solution to extract Fe-Mn oxyhydroxide coatings (Rutberg et al., 2000). Finally, the dried residue from leaching was thoroughly homogenised using an agate mortar.

Hornblende and biotite grains were hand-picked from the coarse (> 150 μm) fraction for ^{40}Ar/^{39}Ar age analysis on 43 of the 67 samples. Picking was extended to include the > 63 μm fraction only if too few grains were available in the > 150 μm fraction. Eight samples were exclusively picked from the 63–150 μm fraction, of which seven were picked for hornblende grains and two for biotite grains (Table 1; Appendix S1). Fresh (i.e. glassy or black) grains were hand-picked from the coarse fraction with weathering being relatively minor or negligible (see also Licht and Hemming, 2017). Single grains and monitor standards (Fish Canyon sanidine) were irradiated at the USGS reactor in Denver, CO. Calibration for the neutron flux was based on J-values calculated to normalize Fish Canyon sanidine ages to 28.201 +/- 0.046 Ma (Kuiper et al., 2008). ^{40}Ar/^{39}Ar ages were calculated from measurements of gas released using a single-step CO_2 laser fusion at the Argon Geochronology for the Earth Sciences (AGES) laboratory at Lamont-Doherty Earth Observatory. Argon isotope ratios were corrected for atmospheric argon (^{40}Ar/^{36}Ar = 298.6, Lee et al., 2006), procedural blanks and mass discrimination from frequent measurements of blanks and air pipettes. Nuclear interference corrections were made based on the values reported by Dalrymple et al. (1981).

Radiogenic isotope (Sr, Nd) and trace element analyses were carried out on two separate aliquots (~50 mg) from the residual and leached

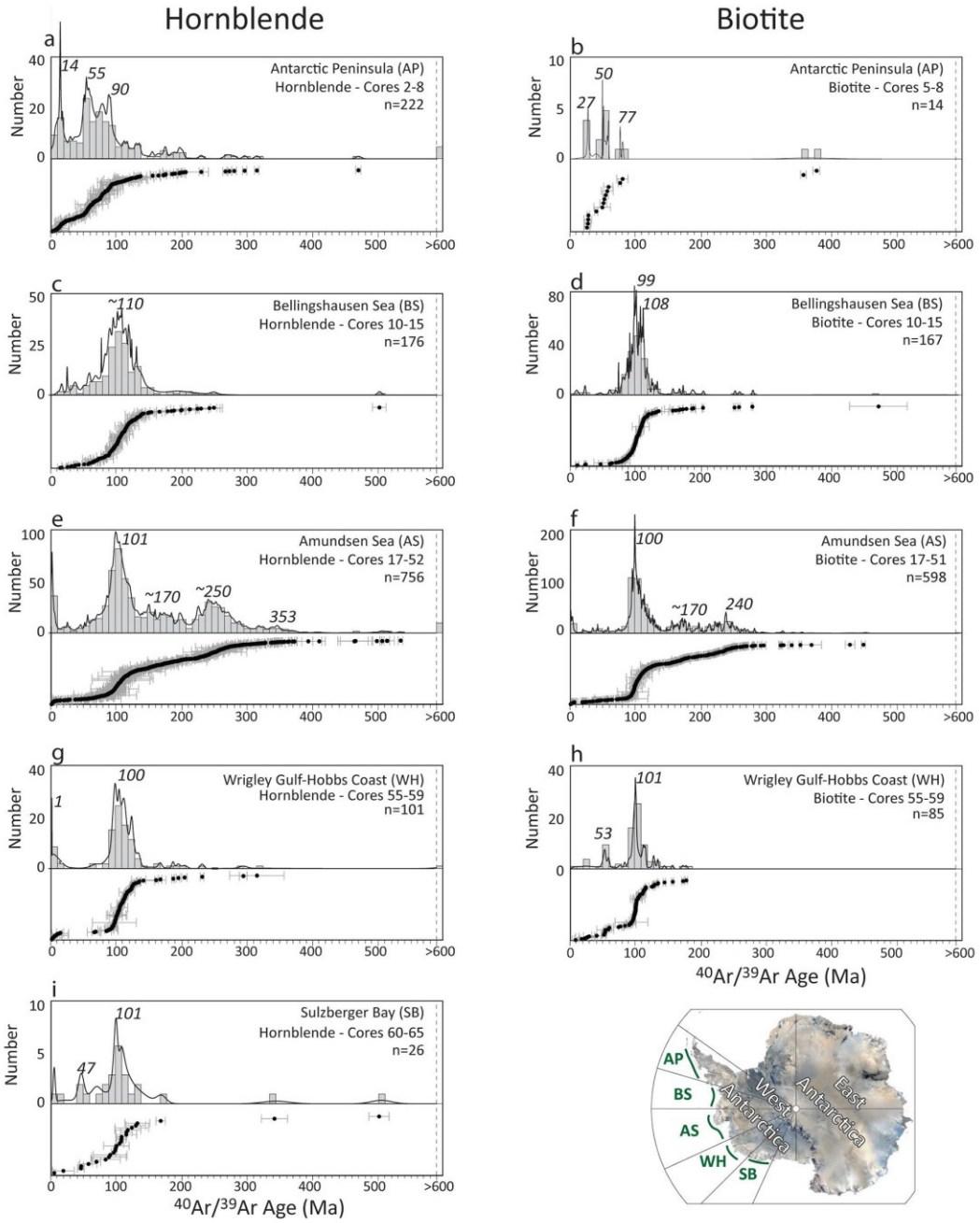

Fig. 3. $^{40}Ar/^{39}Ar$ ages of hornblende and biotite grains from five sectors off the Pacific margin of West Antarctica. Histograms are produced using 10 Ma as bin intervals. Probability density plots (ISOPLOT4.15; Ludwig, 2003) are superimposed, and individual ages are shown with uncertainties in the lower panel. Results include previously analysed $^{40}Ar/^{39}Ar$ ages of hornblende grains from Roy et al. (2007) (see Table 1).

(i.e. detrital) < 63 μm sediment fraction. Aliquots were weighed into pre-cleaned Savillex vials and dissolved in a mixture of HF (2 ml), HNO_3 (1 ml) and $HClO_4$ (0.8 ml) for three to four days on a hotplate until no visible particles remained. After digestion, one set of aliquots were dried and taken up in acid for the three-stage ion exchange chromatography in preparation for Sr and Nd isotope analysis. The Sr fraction was extracted from the sample matrix using Eichrom's Sr Spec resin in HNO_3 medium (similar to Hemming et al., 2007, modified from Pin and Bassin, 1992). The sample matrix was collected from this step and rare earth elements (REEs) were subsequently separated from the sample matrix using a cation exchange resin (AG50W-X8) in HCl medium (following the specific method of Struve et al., 2016). The Nd fraction was subsequently separated from the other REEs using Ln-Spec resin in HCl medium (modified after Pin and Zalduegui, 1997).

Dried Sr cuts were re-dissolved in 6 M HCl, loaded as 1µl aliquots on degassed tungsten filaments, and covered by 1µl of $TaCl_5$ activator solution. Strontium isotopes were measured using a Trition Thermal Ionisation Mass Spectrometer (TIMS) in the Mass Spectrometry and Isotope Geochemistry laboratories at Imperial College London (MAGIC). Measured $^{87}Sr/^{86}Sr$ ratios were corrected for mass bias using an exponential law and assuming a $^{88}Sr/^{86}Sr$ ratio of 8.375. Repeated SRM987 standard measurements over the duration of three months yielded an $^{87}Sr/^{86}Sr$ ratio of 0.710261 ± 13 (2 S.D., n = 31), in agreement with the published value for SRM987 of 0.710252 ± 13 (2 S.D., n = 88; Weis et al., 2006). Strontium blanks were typically below 200 pg (n = 5), except for one batch that yielded a blank of 460 pg Sr.

Neodymium isotope ratios were analysed on a Nu Plasma HR MC-ICP-MS in the MAGIC laboratories. Neodymium isotope ratios were corrected for instrumental mass bias using a $^{146}Nd/^{144}Nd$ ratio of 0.7219 and an exponential law. Measured $^{143}Nd/^{144}Nd$ ratios for all samples are reported after correcting for the average JNdi $^{143}Nd/^{144}Nd$ ratio of the session to the accepted value of 0.512115 (Tanaka et al., 2000). Blanks for the Nd procedure were typically below 10 pg (n = 3) but always below 40 pg (n = 1). Repeat measurements of the USGS BCR-2 standard over multiple runs during the course of this study yielded $^{143}Nd/^{144}Nd$ ratios of 0.512637 ± 14 (2 S.D., n = 43) and $^{87}Sr/^{86}Sr$ ratios of 0.705011 ± 13 (2 S.D., n = 12), in agreement with published values of by Weis et al. (2006).

Aliquots for trace element analysis were dried and transported to the Open University in Milton Keynes, and made up to a 1000-fold dilution of the original sample weight with MQ H_2O, such that the final solutions were in a 0.45 M HNO_3 matrix. Trace element analyses were conducted at the Open University, using an Agilent 8800 ICP-QQQ. The ICP-QQQ has a collision / reaction (ORS) cell, which allows for targeted removal of interference ions. Most elements reported here are measured using no gas (if interferences are not an issue) or He gas in the collision reaction cell, with the exception of the REE, which were measured in mass shift mode, using O_2 in the cell. Analyses were calibrated against five USGS reference materials (BIR-1, W-2, DNC-1, BHVO-2, AGV-1) at the start of each measurement session. An internal standard was added on line to monitor and correct for instrument drift. In addition, a monitor block, consisting of the reference material BCR-2, a repeated unknown, and a nitric solution, was run every five to seven unknowns, to assess the drift correction and monitor the precision and accuracy of analyses. Oxide formation (measured as CeO^+ / Ce^+) was kept low at < 1.0% in no gas, or < 0.6% in He gas mode, and doubly charged species (Ce^{++} / Ce^+) at < 1.5% and < 1.0%, respectively. Detection limits of trace elements were typically 2–50ppt in solution for light elements and ≤2ppt for mid to heavy elements (Rb–U). Overall, precision on repeated BCR-2 standard measurements (n = 12) was usually below 5%, while accuracy checks were below 10% (except for Ti at 18%).

5. Results

5.1. $^{40}Ar/^{39}Ar$ ages of individual hornblende and biotite grains

$^{40}Ar/^{39}Ar$ ages for 1281 hornblende and 864 biotite grains are reported in Table 1 and Appendix S1 and illustrated in Fig. 3 for each geographical sector. From east to west, the sectors are: Antarctic Peninsula (AP sector, 60–75°W), Bellingshausen Sea (BS sector, 75–90°W), Amundsen Sea (AS sector, 90–125°W), Wrigley Gulf-Hobbs Coast (WH sector, 125–150°W) and Sulzberger Bay (SB sector, 150–160°W). Our results include 178 hornblende $^{40}Ar/^{39}Ar$ ages previously reported by Roy et al. (2007).

5.1.1. Antarctic Peninsula (AP, 60–75°W, core sites 1–8)

In the AP sector we find a continuous hornblende $^{40}Ar/^{39}Ar$ age spectrum from 0 to ~320 Ma with three major peaks at 14 Ma, 55 Ma and ~90 Ma, and some scattered older grains of ~480–1000 Ma and ~1600–2000 Ma (n = 222; Fig. 3a). Significantly fewer biotite grains (n = 14) were analysed for $^{40}Ar/^{39}Ar$ ages (Table 1). Three minor age clusters occur in the 23–83 Ma age interval, with three peak ages of ~27 Ma, ~50 Ma and ~77 Ma (Fig. 3b). Two single grains record ages of 360–380 Ma.

5.1.2. Bellingshausen Sea (BS, 75–90°W, core sites 9–16)

In the BS sector a continuous hornblende $^{40}Ar/^{39}Ar$ age spectrum spans from 0–260 Ma, but with a dominant cluster between ~75 and 140 Ma, a peak of ~110 Ma, and one older grain at 510 Ma (n = 176; Fig. 3c). Biotite $^{40}Ar/^{39}Ar$ ages (n = 167) yield a similar age range, predominantly from 0 to ~280 Ma, with the majority of grain ages in the interval between 75 and 135 Ma, and with peaks at ~99 Ma and ~108 Ma. One older grain dates back to 480 Ma (Fig. 3d). The finer sand size-fraction (63 − 150 µm) of site 13 was picked for biotite grains, and hence the $^{40}Ar/^{39}Ar$ ages for this sample could be influenced by ocean current transport because biotite grains of this size can be affected by relatively weak ocean currents with flow speeds as observed in the Bellingshausen Sea. However, age distribution observed at site 13 shows no pattern deviating from that of other core samples in the BS sector, with the majority of the ages ranging from 94–120 Ma (Appendix S1).

5.1.3. Amundsen Sea (AS, 90–125°W, core sites 17–54)

The AS sector is the main focus of this study and a total of 756 hornblende grains and 598 biotite grain ages are reported for this sector. A continuous hornblende $^{40}Ar/^{39}Ar$ age spectrum from 0 to ~380 Ma shows two noticeable peaks at ~101 Ma and ~250 Ma. A significant number of grains with ages ranging from 140 to ~210 Ma are found, which are notably absent from the other sectors. A minor age peak is observed at ~353 Ma. Though significantly smaller in number, older hornblende grains also appear in these sediments (n = 20), with age clusters of 400–550 Ma, 640–800 Ma, 1120–1360 Ma, 1700–1850 Ma and 2600–2800 Ma (Fig. 3e, Appendix S1). Biotite $^{40}Ar/^{39}Ar$ ages (n = 598) spread from 0 to ~300 Ma, with a prominent peak at ~100 Ma, and secondary peaks at ~170 and 240 Ma. Nine older grains yield ages of ~330–375 Ma, ~450 and 890 Ma (Fig. 3f). The apparent modern (~0 Ma) age peaks observed in both minerals in the AS sector seem suspicious as the corresponding grains were primarily picked from core 49 situated on the upper continental slope, and are not detected in other sectors (Fig. 2). Biotite grains from site 41 were picked from a smaller size-fraction (Table 2) and hence could potentially be influenced by ocean current transport due to fast flow speeds detected off the Dotson Ice Shelf (Kim et al., 2016a). However, $^{40}Ar/^{39}Ar$ ages from this sample do not reveal any pattern deviating from that of $^{40}Ar/^{39}Ar$ ages in nearby core samples (Appendix S1). We hence consider differential sorting of biotite and hornblende mineral grains of the same size fraction to be negligible in our study area.

5.1.4. Wrigley Gulf-Hobbs Coast (WH, 125–150°W, core sites 55–59)

A total of 101 hornblende ages obtained from the WH sector record well defined $^{40}Ar/^{39}Ar$ ages with populations around 0–20 Ma and 65–140 Ma, and age probability peaks at ~0 Ma and ~100 Ma as well as three scattered ages of ~210 Ma, 300 Ma and 610 Ma (Fig. 3g). Biotite $^{40}Ar/^{39}Ar$ ages (n = 85) cover a similar age range from 0 to ~150 Ma, with some scattered ages of ~180 Ma, but the dominant age probability peak at 101 Ma is slightly older than the one defined by the hornblende grains. A second minor age peak is detected around ~53 Ma, which is absent in the hornblende age spectrum (Fig. 3h).

5.1.5. Sulzberger Bay (SB, 150–160°W, cores 60–67)

Most hornblende $^{40}Ar/^{39}Ar$ ages (n = 26) from the SB sector range from 0 to ~135 Ma, and show a well-defined age probability peak at ~100 Ma. Minor age peaks occur at ~48 Ma and ~5 Ma and three individual grains yield ages of ~170 Ma, 350 Ma and 510 Ma (Fig. 3i). No biotite grains were picked/analysed from this sector.

Table 2
Sr and Nd isotope compositions of the detrital fraction (< 63 μm) and clay mineral assemblages (< 2 μm) of surface sediments off West Antarctica.

Core Site	Site location	Sector[a]	$^{87}Rb/^{86}Sr$[b]	$^{87}Sr/^{86}Sr$ (± 2 S.E.)	$^{147}Sm/^{144}Nd$[b]	$^{143}Nd/^{144}Nd$ (± 2 S.E.)	ε_{Nd}	± 2 S.D.[c]	T_{DM} (Ma)[d]	Ref.[e]	Ill(%)	Sme (%)	Kln(%)	Chl(%)	Ref.[e]
1	DF86–48*	AP				0.512751 ± 8	2.20	0.36							
2	DF85–53	AP													
3	PD88–111 Grab37*	AP				0.512725 ± 9	1.69	0.36							
4	PD88–111 Grab41*	AP				0.512719 ± 9	1.57	0.36							
5	ELT05–22	AP		0.705281 ± 5	0.1366	0.512685 ± 10	0.92		920	2,3					
6	DF85–82	AP													
7	ELT05–20	AP		0.708198 ± 7	0.1341	0.512469 ± 18	-3.30		1304	2,3					
8	PS2524–1	AP	1.423	0.708926 ± 5	0.1179	0.512453 ± 8	-3.61	0.21	1109	1	58	8	0	34	4
9	BC470	BS	1.628	0.710100 ± 4	0.1179	0.512405 ± 8	-4.55	0.28	1185	1					
10	ELT42–09	BS			0.1255	0.512420 ± 9	-4.25		1261	2					
11	BC361	BS	1.706	0.709714 ± 5	0.1160	0.512392 ± 16	-4.80	0.32	1183	1	44	20	5	31	5
12	GC362	BS	1.920	0.711165 ± 5	0.1173	0.512349 ± 6	-5.64	0.29	1267	1	52	19	6	23	5
13	BC364	BS	1.846	0.713189 ± 5	0.1142	0.512267 ± 6	-7.24	0.30	1353	1	66	7	2	25	5
14	BC369	BS	1.547	0.710320 ± 4	0.1152	0.512359 ± 9	-5.44	0.24	1224	1	46	20	3	30	5
15	BC459	BS	1.399	0.710539 ± 4	0.1136	0.512321 ± 10	-6.18	0.28	1262	1	52	16	6	26	6 (GC372)
16	PS2543–3	BS	1.889	0.712397 ± 5	0.1123	0.512285 ± 7	-6.89	0.21	1301	1	59	14	4	23	4
17	ELT11–19	AS-E		0.707928 ± 6	0.1271	0.512470 ± 10	-3.28		1197	2,3					
18	ELT11–18	AS-E		0.709790 ± 5	0.1213	0.512399 ± 5	-4.66		1239	2,3					
19	ELT11–17	AS-E		0.710616 ± 8	0.1257	0.512400 ± 16	-4.64		1299	2,3					
20	PS58/254–2	AS-E	1.658	0.708704 ± 4	0.1185	0.512486 ± 6	-2.96	0.30	1064	1	33	38	12	17	7
21	PS75/192–2	AS-E	1.726	0.710162 ± 5	0.1127	0.512408 ± 8	-4.49	0.21	1121	1					
22	PS69/255–3	AS-E	1.541	0.709971 ± 5	0.1135	0.512402 ± 8	-4.61	0.24	1139	1	41	27	14	18	7
23	PS69/251–1	AS-E	2.041	0.711226 ± 6	0.1123	0.512396 ± 8	-4.71	0.21	1133	1	41	25	16	18	7
24	DF85–109	AS-E													
25	BC451	AS-E	2.255	0.711652 ± 5	0.1131	0.512429 ± 10	-4.07	0.28	1092	1	46	23	16	14	7
26	BC455	AS-E	1.703	0.710384 ± 5	0.1117	0.512415 ± 9	-4.34	0.28	1099	1	45	24	16	15	7
	repeat[f]			*0.710365 ± 5*		*0.512415 ± 7*	*-4.35*	*0.16*							
27	BC485	AS-E	2.789	0.713436 ± 4	0.1141	0.512425 ± 9	-4.16	0.28	1110	1	46	19	19	15	7
28	DF85 96–1	AS-E													
29	PS69/299–1	AS-E	1.193	0.707947 ± 5	0.1118	0.512470 ± 8	-3.28	0.24	1018	1	41	26	7	25	7
30	BC482	AS-E	3.303	0.715235 ± 4	0.1118	0.512399 ± 9	-4.67	0.28	1125	1	44	19	23	15	7
31	BC476	AS-E	3.903	0.718795 ± 6	0.1116	0.512329 ± 10	-6.03	0.28	1226	1	52	16	17	16	7
32	PS75/159–1	AS-E	4.659	0.723959 ± 5	0.1100	0.512267 ± 8	-7.24	0.21	1299	1					
33	PS75/168–1	AS-E	3.557	0.716904 ± 6	0.1096	0.512406 ± 8	-4.52	0.21	1090	1	50	13	21	16	7 (PS69/292–3)
34	BC442	AS-E	1.946	0.710417 ± 4	0.1131	0.512465 ± 9	-3.37	0.28	1039	1	47	18	19	16	7
35	BC443	AS-E	1.712	0.710181 ± 5	0.1135	0.512454 ± 8	-3.58	0.28	1059	1	47	20	18	16	7
36	PS69/281–3	AS-W	2.058	0.709504 ± 6	0.1116	0.512542 ± 8	-1.87	0.28	909	1	42	14	29	15	7
37	NBP07–02*	AS-W				0.512512 ± 8	-2.46	0.32							
38	BC420	AS-W	2.084	0.710125 ± 5	0.1167	0.512519 ± 6	-2.32	0.29	992	1	47	13	18	22	7
39	NBP00–01 KC24*	AS-W				0.512660 ± 9	0.43	0.37							
40	BC421	AS-W	2.205	0.710011 ± 5	0.1124	0.512499 ± 8	-2.71	0.28	981	1	43	22	19	16	7
41	BC412	AS-W	2.109	0.709682 ± 5	0.1148	0.512496 ± 9	-2.76	0.28	1008	1	40	21	20	19	7
42	NBP00–01 PC22*	AS-W				0.512517 ± 10	-2.35	0.29							
43	NBP00–01 KC21*	AS-W				0.512495 ± 8	-2.79	0.29							
44	NBP07–02*	AS-W				0.512486 ± 8	-2.97	0.32							
45	PS69/275–2	AS-W	2.446	0.710115 ± 5	0.1144	0.512517 ± 8	-2.35	0.29	973	1	43	20	20	16	7
46	BC407	AS-W	2.275	0.709903 ± 4	0.1134	0.512509 ± 7	-2.52	0.24	975	1	43	18	22	18	7
	repeat			*0.710041 ± 5*		*0.512504 ± 9*	*-2.62*	*0.21*							
47	PS69/283–5	AS-W	2.180	0.709881 ± 4	0.1133	0.512492 ± 7	-2.86	0.20	1000	1	43	20	19	18	7
48	BC431	AS-W	1.746	0.708959 ± 4	0.1136	0.512488 ± 8	-2.92	0.28	1008	1	46	17	19	18	7
49	BC433	AS-W	1.848	0.709845 ± 4	0.1128	0.512505 ± 7	-2.59	0.28	976	1	43	17	21	18	7
50	BC492	AS-W	1.697	0.709711 ± 5	0.114	0.512526 ± 7	-2.18	0.29	954	1					
51	ELT33–12	AS-W		0.712846 ± 6	0.1188	0.512358 ± 8	-5.46		1272	2,3					
52	ELT33–11	AS-W		0.709086 ± 6	0.1187	0.512502 ± 10	-2.65		1040	2,3					

(*continued on next page*)

Table 2 (*continued*)

Core Site	Site location	Sector[a]	$^{87}Rb/^{86}Sr$[b]	$^{87}Sr/^{86}Sr$ (± 2 S.E.)	$^{147}Sm/^{144}Nd$[b]	$^{143}Nd/^{144}Nd$ (± 2 S.E.)	ε_{Nd}	± 2 S.D.[c]	T_{DM} (Ma)[d]	Ref.[e]	Ill(%)	Sme (%)	Kln(%)	Chl(%)	Ref.[e]
53	PS2545–1	AS-W	1.809	0.708276 ± 7	0.1144	0.512553 ± 8	-1.66	0.21	918	1	39	28	23	10	4
54	NBP00–01 KC17*	WH				0.512653 ± 8	0.29	0.32							
55	NBP99–02 PC21*	WH				0.512610 ± 7	-0.54	0.32							
56	NBP99–02 TC23	WH	1.012	0.705656 ± 5	0.1156	0.512667 ± 10	0.57	0.24	752	1	37	27	20	17	1
57	NBP00–01 PC14	WH	1.045	0.705917 ± 4	0.1155	0.512654 ± 9	0.32	0.24	770	1	37	25	20	18	1
58	PS75/133–1	WH	1.081	0.706122 ± 4	0.1151	0.512703 ± 8	1.26	0.30	693	1	36	28	14	21	1
59	PS75/130–2	WH	0.891	0.705889 ± 4	0.1158	0.512697 ± 5	1.14	0.29	707	1					
60	DF83-III BC28	SB	7.142	0.741188 ± 4	0.1133	0.512085 ± 8	-10.79	0.24	1616	1					
61	NBP96–01 PC12	SB	7.492	0.743425 ± 4	0.1131	0.512077 ± 9	-10.95	0.24	1623	1					
62	NBP96–01 TC13	SB	8.265	0.747045 ± 5	0.1127	0.512063 ± 8	-11.22	0.24	1639	1					
63	NBP99–02 Grab20	SB				0.512058 ± 7	-11.31	0.32							
64	DF83 PC31	SB	8.324	0.747928 ± 5	0.1129	0.512030 ± 8	-11.86	0.24	1691	1					
65	DF83-III BC26A	SB	8.010	0.742576 ± 4	0.1119	0.512096 ± 9	-10.58	0.24	1576	1					
66	NBP96–01 JTC11	SB	8.224	0.749275 ± 4	0.1118	0.512050 ± 10	-11.47	0.24	1643	1					
	repeat			*0.749534 ± 6*		*0.512633 ± 8*	*-11.52*	*0.16*							
67	DF83-III BC33	SB	7.976	0.741931 ± 4	0.1128	0.512080 ± 8	-10.89	0.24	1616	1					

[a] See Table 1.

[b] Calculated from elemental compostion of the same sample (Table 3).

[c] Standard deviation based on the reproducibility of the $^{143}Nd/^{144}Nd$ ratio of the JNdi standard during each run: 0.512224 ± 14 (n = 24), 0.512116 ± 12 (n = 17), 0.512144 ± 12 (n = 13), 0.512157 ± 10 (n = 12), 0.512106 ± 12 (n = 32), 0.512149 ± 11 (n = 27) and 0.512142 ± (n = 16).

[d] Nd model ages relative to present depleted mantle (DM) using a one-stage evolution model: $^{147}Sm/^{144}Nd$ = 0.2136; $^{143}Nd/^{144}Nd$ = 0.51315.

[e] (1) this study; (2) Roy et al., 2007; (3) Hemming et al., 2007; (4) Hillenbrand et al., 2002; (5) Hillenbrand et al., 2009; (6) Hillenbrand et al., 2010; (7) Ehrmann et al., 2011.

[f] Repeat values represent full procedural replicats of sample powders (i.e. from digestion, through ion exchange chromatography, to mass spectrometry).

* Samples denoted with a star were analysed at L-DEO for their Nd isotopic composition using similar methodologies to those described in the main text, but run on a AXIOM MC-ICP-MS (see van de Flierdt et al., 2008, for more details on methodology).

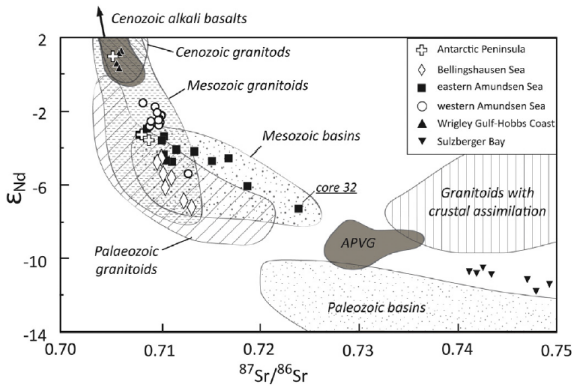

Fig. 4. Neodymium and strontium isotopic compositions of detrital surface sediments along the Pacific margin of West Antarctica. Marine sediment data are displayed as symbols according to geographical sectors defined in Table 1 (only samples where both Nd and Sr isotope ratios were measured are shown). Isotopic compositions of major bedrock outcrops on land are compiled from the literature (see Appendix S2) and correspond to the units displayed in Fig. 2 (Note: For simplicity data from high-grade metamorphic rocks are not displayed). APVG = Antarctic Peninsula Volcanic Group.

5.2. Neodymium and strontium isotope composition of fine-grained detrital sediments

In total, 66 and 54 samples were analysed for their detrital Nd and Sr isotopic composition respectively. The Nd isotope results are expressed as epsilon values (ε_{Nd}), which denotes the deviation from a chondritic value of 0.512638 in parts per 10,000 (Jacobsen and Wasserburg, 1980). Neodymium and Sr isotope results from the study of Roy et al. (2007) on eight additional distal samples are included in the following results and subsequent discussion (Table 2).

Overall, detrital continental margin sediments off West Antarctica have Nd isotopic compositions ranging from −12 to +2 and $^{87}Sr/^{86}Sr$ ratios from 0.7493 to 0.7057 (Fig. 4, Table 2). The values are anti-correlated as expected from global trends, and are distinct for individual sectors. The highest Nd isotope values and the lowest Sr isotope ratios are found in the WH sector (ε_{Nd} = −0.5 to 1.3, $^{87}Sr/^{86}Sr$ = 0.7056 to 0.7061), in the westernmost sample from the AS sector (site 54; ε_{Nd} = 0.3) and in the easternmost samples from the AP sector (site 1 and 3–5: ε_{Nd} = 0.9 to 2.2; $^{87}Sr/^{86}Sr$ ~0.7053). The other end of the data range is defined by samples from SB, i.e. offshore from western Marie Byrd Land (Fig. 2), with Nd isotopic compositions of −11.9 to −10.6 and $^{87}Sr/^{86}Sr$ = 0.7411 to 0.7493. Detrital shelf sediments from the AS sector reveal intermediate values, but with distinctly different values in the eastern and western AS. In the eastern AS, lower Nd and higher radiogenic Sr values (ε_{Nd} ~-7.3, $^{87}Sr/^{86}Sr$ ~ 0.7240) are found in a sample taken in front of Pine Island Glacier (site 32, Table 2, Fig. 2). Along the eastern flank of the AS sector the isotopic fingerprints of the samples change systematically northwards across the shelf to higher Nd and lower Sr isotopic compositions (site 20: ε_{Nd} ~-3.3, $^{87}Sr/^{86}Sr$ ~ 0.7079). A uniform signature is observed in the western AS sector, where shelf sediments yield Nd and Sr isotopic compositions of ε_{Nd} ~-2.9 to −1.7 and $^{87}Sr/^{86}Sr$ ~0.7082 to 0.7101 (n = 17), except sample from site 39 proximal to Dotson Ice Shelf (ε_{Nd} = 0.4; $^{87}Sr/^{86}Sr$ was not measured) and site 51 on the lower continental slope (ε_{Nd} ~-5.5; $^{87}Sr/^{86}Sr$ = 0.7128). Detrital surface sediments from the BS extend from the values recorded in the western AS and on the eastern AS shelf towards lower Nd and higher Sr values, along a steeper slope (ε_{Nd} = −7.3 to −4.2, $^{87}Sr/^{86}Sr$ = 0.7097 to 0.7132, n = 8; Fig. 4). General anti-correlation of Nd and Sr isotopes in fine-grained detrital sediments off West Antarctica, in addition to the extremely uniform values observed in the western AS from ice proximal to ice distal (ocean) locations, indicate that both isotope systematics are predominantly governed by provenance and not by sedimentary sorting or weathering.

5.3. Trace element composition of fine-grained detrital sediments

Trace element compositions, including full REE patterns, were analysed on the < 63 μm fraction of 44 detrital seafloor sediment samples. The data are reported in Table 3 and are illustrated in mid-ocean ridge basalt (MORB)-normalized spider diagrams (Fig. 5). Overall, detrital sediments show compositions comparable to Post-Archean Average Shale (PAAS) (McLennan, 2001). Some elements, however, deviate from PAAS. Zirconium (Zr) concentrations show considerable scatter (Fig. 5), while the elemental ratio of the two high-field strength elements Zr and yttrium (Y) are high in sediments from the WH sector (Zr/Y ~10.5) and low in sediments from the SB sector (Zr/Y ~4) as well as in sediments proximal to Pine Island and Thwaites glaciers (Zr/Y ~5). Similarly, high Sr over thorium (Th) ratios of 25–30 are observed in WH, at site 29 on the AS (Sr/Th ~25) and in the AP sector (site 8, Sr/Th ~27), with the latter sector being mostly characterized by very low thorium (Table 3). The ratio of Th over scandium (Sc), which generally describes the relative contribution of basic and felsic rocks (Taylor and McLennan, 1995), is elevated in the samples from sites 32 and 33 proximal to Pine Island and Thwaites glaciers (1.5–2.0), but low in WH (~0.8–1), sites 8 to 11 from the AP and BS sectors (0.6–0.8) and in one distal sample from site 20 in the AS sector (0.6). Europium anomalies are moderately negative (Eu/Eu^* = 0.5–0.9) in most samples, and correlate well with Th/Sc (R^2 = 0.67; Fig. 6) and Sr/Th ratios (R^2 = 0.87) (Table 3).

6. Provenance of glacial-marine sediments

In this section we evaluate the provenance signature of coarse and fine-grained detrital sediment from the seafloor in conjunction with onshore geochemical (Sr and Nd isotope values) and geochronological data (K-Ar and $^{40}Ar/^{39}Ar$ ages on hornblende, biotite, mica grains and whole rock samples, U/Pb zircon ages, and Rb-Sr whole rock ages) compiled from the literature (Appendix S2). Knowledge of the regional tectonic history of West Antarctica is a prerequisite in order to relate offshore $^{40}Ar/^{39}Ar$ mineral ages to bedrock sources, particularly in areas where $^{40}Ar/^{39}Ar$ cooling ages are scarce and comparison with other geochronological data is required. Overall, offshore $^{40}Ar/^{39}Ar$ ages match those reported for outcrops onland, recording largely the erosion of syn-tectonic Palaeozoic to Cenozoic plutons emplaced onto the former magmatic arc along the Gondwana margin, with distinctive thermal age peaks at ~245 Ma, ~170 Ma, ~100 Ma and 50–90 Ma. Onshore U-Pb ages on zircons on crystalline bedrock are sparse, but fall in the range of our offshore $^{40}Ar/^{39}Ar$ data, reflecting West Antarctica's active margin settings. In addition to the thermochronological ages, fine-grained Sr and Nd isotope and trace element fingerprints from the < 63 μm sediment fraction record an integrated signal of the erosion of major outcropping lithologies. The observed fingerprint in marine sediments allows to distinguish between glaciomarine sediments supplied by five major source sectors on West Antarctica. The integrated signal allows furthermore to identify erosion of volcanic and sedimentary rocks, which are inherently difficult to detect using hornblende and biotite $^{40}Ar/^{39}Ar$ ages (i.e. 'mineralogical or grain-size bias').

6.1. Antarctic Peninsula (AP)

6.1.1. Provenance of ice-rafted detritus

Outcrops of young Late Cretaceous (< 90 Ma) to Cenozoic igneous rocks have been documented on the Antarctic Peninsula, especially along the western coasts of Graham and Palmer Land and on Alexander

Table 3
Trace element composition of detrital < 63 μm surface sediments off West Antarctica (in ppm).

Core Site	Site location	Sector (a)	Li	Sc	Ti	V	Cr	Mn	Co	Ni	Cu	Zn	Rb	Sr	Y	Zr	Cs	Ba	La	Ce	Pr
1	DF86–48	AP																			
2	DF85–53	AP																			
3	PD88–111 Grab37*	AP																			
4	PD88–111 Grab41*	AP																			
5	ELT05–22	AP																			
6	DF85–82	AP																			
7	ELT05–20	AP																			
8	PS2524–1	AP	54	15	4123	108	50	661	12	21	34	137	122	247	21	84	5	634	22.8	50.6	5.4
9	BC470	BSE	47	14	3954	90	44	542	9	17	16	144	120	213	23	96	6	966	26.8	57.7	6.1
10	ELT42–09	BSE																			
11	BC361	BSE	40	15	4115	94	43	612	11	18	23	131	129	218	22	98	6	883	27.5	59.7	6.0
12	GC362	BSE	40	14	4151	90	42	634	11	22	22	128	146	220	25	101	6	1131	31.0	65.0	6.7
13	BC364	BSE	19	8	2675	51	31	418	6	16	21	72	108	169	19	65	3	566	24.3	50.1	5.3
14	BC369	BSE	41	14	4329	85	40	596	10	19	23	125	133	249	24	108	6	1568	30.7	66.0	6.8
15	BC459	BSE	32	13	4300	74	37	523	8	13	19	95	118	245	25	116	5	1312	34.3	70.7	7.7
16	PS2543–3	BSE	33	11	3511	70	36	559	10	27	19	101	148	226	23	96	5	748	32.0	69.7	7.0
17	ELT11–19	ASE-E																			
18	ELT11–18	ASE-E																			
19	ELT11–17	ASE-E																			
20	PS58/254–2	ASE-E	36	19	4528	90	51	546	11	25	105	125	109	190	19	146	5	646	23.0	52.8	5.2
21	PS75/192–2	ASE-E	38	12	4677	80	41	468	9	15	20	103	137	231	25	146	6	1025	35.5	76.3	7.8
22	PS69/255–3	ASE-E	38	13	4781	79	45	470	9	17	22	96	140	263	26	152	6	1343	34.9	76.8	8.1
23	PS69/251–1	ASE-E	39	12	4759	79	41	479	9	16	20	103	148	209	28	163	7	727	38.4	82.3	8.4
24	DF85–109	ASE-E																			
25	BC451	ASE-E	42	14	4884	86	49	521	10	19	24	113	165	211	29	181	9	1032	41.2	90.4	9.3
26	BC455	ASE-E	36	13	4755	81	48	480	9	16	24	101	144	245	27	178	7	1540	40.1	84.6	8.8
	repeat		*37*	*12*	*4569*	*81*	*45*	*483*	*9*	*15*	*24*	*100*	*142*	*250*	*28*	*195*	*6*	*1514*	*40.3*	*85.7*	*8.8*
27	BC485	ASE-E	47	14	4924	89	49	544	11	21	27	124	180	187	32	194	11	979	46.0	98.5	10.1
28	DF85 96–1	ASE-E																			
29	PS69/299–1	ASE-E	31	13	4393	88	50	564	10	16	18	107	127	308	21	111	5	662	31.1	65.8	6.9
30	BC482	ASE-E	43	11	4284	74	41	509	9	20	23	102	159	139	26	144	10	676	38.7	80.3	8.4
31	BC476	ASE-E	50	14	4745	84	54	521	11	23	24	112	203	150	30	137	12	732	47.0	96.7	10.3
32	PS75/159–1	ASE-E	58	13	4624	81	53	474	10	24	18	101	213	133	30	134	12	711	44.5	91.9	9.8
33	PS75/168–1	ASE-E	58	13	5404	83	47	506	10	19	15	109	210	171	36	210	12	615	55.0	113.1	12.0
34	BC442	ASE-E	42	13	5684	90	52	489	11	21	24	117	151	224	29	219	8	1101	42.7	92.6	9.5
35	BC443	ASE-E	41	14	5319	86	51	507	11	21	35	113	146	247	29	197	8	2080	40.6	88.7	8.9
36	PS69/281–3	ASE-W	48	13	5832	94	46	574	14	23	19	128	163	230	34	263	11	598	50.9	104.5	11.1
37	NBP07–02	ASE-W																			
38	BC420	ASE-W	47	17	6113	119	62	762	16	28	25	134	152	211	31	200	9	664	41.7	88.7	9.3
39	NBP00–01 KC24	ASE-W																			
40	BC421	ASE-W	48	16	5613	106	57	608	13	24	28	140	152	200	28	202	9	641	41.6	87.8	9.1
41	BC412	ASE-W	49	14	5395	111	50	722	14	25	33	141	146	201	28	179	9	658	40.4	85.6	9.2
42	NBP00–01 KC22	ASE-W																			
43	NBP00–01 KC21	ASE-W																			
44	NBP07–02	ASE-W																			
45	PS69/275–2	ASE-W	57	15	5561	120	53	542	13	26	37	179	165	195	29	214	11	747	43.5	95.1	9.6
46	BC407	ASE-W	58	15	5815	116	53	687	14	26	27	175	155	198	28	192	10	622	41.1	90.8	9.4
	repeat		*61*	*15*	*5709*	*116*	*53*	*659*	*14*	*26*	*26*	*170*	*159*	*187*	*28*	*194*	*9*	*597*	*41.8*	*90.2*	*9.1*

(*continued on next page*)

Table 3 (*continued*)

Core Site	Site location	Sector (a)	Li	Sc	Ti	V	Cr	Mn	Co	Ni	Cu	Zn	Rb	Sr	Y	Zr	Cs	Ba	La	Ce	Pr
47	PS69/283–5	ASE-W	50	14	5819	101	52	608	13	26	28	149	152	202	27	211	9	595	40.2	90.2	9.0
48	BC431	ASE-W	43	15	5726	103	53	610	14	24	27	130	146	241	26	194	8	799	40.1	88.7	8.9
49	BC433	ASE-W	46	15	5503	98	44	592	12	22	41	139	152	238	29	252	9	2212	42.3	98.4	9.2
50	BC492	ASE-W	43	15	5259	93	47	581	12	22	48	129	141	240	26	235	8	2972	36.7	88.1	8.1
51	ELT33–12	ASE-W																			
52	ELT33–11	ASE-W																			
53	PS2545–1	ASE-W	54	14	5868	98	47	667	14	27	37	160	146	233	25	174	8	546	36.5	80.2	8.1
54	NBP00–01 KC17	ASE-W																			
55	NBP99–02 PC21	WG																			
56	NBP99–02 TC23	WG	25	13	8695	94	64	593	16	25	23	125	98	281	22	243	4	479	32.3	71.0	7.4
57	NBP00–01 PC14	WG	31	13	7712	91	59	629	14	24	27	126	103	284	24	237	4	513	34.3	77.1	7.5
58	PS75/133–1	WG	31	11	6716	76	45	600	10	18	16	114	107	287	26	308	4	653	37.9	82.9	8.5
59	PS75/130–2	WG	32	12	6736	94	52	674	15	24	19	113	106	344	22	227	4	618	35.3	75.2	7.8
60	DF83-III BC28	SBE	76	15	4522	98	78	380	13	34	22	115	219	89	26	119	17	588	42.5	88.6	9.6
61	NBP96–01 PC12	SBE	71	15	4516	98	81	378	13	35	21	129	223	87	26	117	17	617	42.9	90.7	9.8
62	NBP96–01 TC13	SBE	71	15	4302	102	83	365	13	35	22	115	219	77	23	110	16	593	43.0	89.4	9.7
63	NBP99–02 Grab20	SBE																			
64	DF83 PC31	SBE	66	14	4100	98	81	329	12	32	22	108	212	74	23	111	15	568	42.2	88.9	9.6
65	DF83-III BC26A	SBE	81	16	4343	104	81	392	13	32	23	119	257	93	22	96	20	674	40.3	84.7	9.1
66	NBP96–01 JTC11	SBE	81	16	4474	101	79	374	13	31	22	109	258	91	25	94	19	620	45.5	95.7	10.7
	repeat		*97*	*15*	*4212*	*101*	*74*	*391*	*12*	*31*	*23*	*113*	*262*	*85*	*29*	*108*	*19*	*592*	*48.2*	*100.8*	*10.8*
67	DF83-III BC33	SBE	78	16	4518	101	80	385	13	33	21	119	254	92	23	106	20	669	44.3	92.2	10.1

Core Site	Nd	Sm	Eu	Gd	Tb	Dy	Ho	Er	Yb	Lu	Hf	Pb	Th	U	Sr/Th	Sr/Zr	Zr/Y	Th/Sc	Ce/Ce* (b)	Eu/ Eu*(b)
1																				
2																				
3																				
4																				
5																				
6																				
7																				
8	20.9	4.1	0.9	3.5	0.6	3.3	0.7	2.1	1.9	0.3	2.2	11.4	9.0	1.7	27.35	2.95	3.98	0.60	1.05	0.77
9	23.6	4.6	1.0	3.9	0.6	3.6	0.8	2.2	2.2	0.3	2.6	11.9	11.0	1.9	19.42	2.21	4.26	0.78	1.04	0.71
10																				
11	23.3	4.5	1.0	3.8	0.6	3.5	0.7	2.1	2.2	0.3	2.8	18.0	11.7	1.8	18.61	2.22	4.45	0.80	1.06	0.73
12	25.8	5.0	1.1	4.2	0.7	3.9	0.8	2.3	2.4	0.4	2.7	20.3	13.3	1.9	16.52	2.19	4.01	0.92	1.03	0.70
13	20.1	3.8	0.8	3.2	0.5	3.0	0.6	1.8	1.9	0.3	1.8	15.1	10.1	1.3	16.73	2.59	3.48	1.20	1.02	0.70
14	26.1	5.0	1.1	4.2	0.7	3.8	0.8	2.3	2.2	0.3	3.0	17.0	11.7	1.9	21.23	2.31	4.56	0.84	1.05	0.73
15	29.0	5.5	1.1	4.5	0.7	4.0	0.8	2.4	2.5	0.4	3.2	17.1	12.0	2.0	20.40	2.11	4.64	0.93	1.00	0.69
16	26.8	5.0	1.1	4.1	0.6	3.8	0.8	2.3	2.1	0.3	2.6	24.8	10.2	1.6	22.14	2.36	4.18	0.91	1.07	0.75

(*continued on next page*)

Table 3 (*continued*)

Core	Site	Nd	Sm	Eu	Gd	Tb	Dy	Ho	Er	Yb	Lu	Hf	Pb	Th	U	Sr/Th	Sr/Zr	Zr/Y	Th/Sc	Ce/Ce* (b)	Eu/ Eu*(b)
17																					
18																					
19																					
20		19.8	3.9	0.8	3.2	0.5	3.0	0.6	1.8	1.9	0.3	3.4	20.1	10.5	1.5	18.03	1.30	7.71	0.56	1.11	0.72
21		29.4	5.5	1.1	4.5	0.7	4.0	0.8	2.4	2.4	0.4	3.7	18.1	13.5	2.2	17.13	1.58	5.83	1.11	1.06	0.69
22		30.7	5.8	1.1	4.7	0.7	4.2	0.9	2.6	2.5	0.4	4.2	19.4	14.1	2.4	18.63	1.72	5.90	1.12	1.05	0.67
23		31.8	5.9	1.1	4.8	0.8	4.4	0.9	2.7	2.5	0.4	4.2	21.0	15.6	2.5	13.45	1.29	5.85	1.30	1.06	0.64
24																					
25		34.8	6.5	1.1	5.2	0.8	4.7	1.0	2.8	2.9	0.4	4.6	26.0	19.7	2.8	10.73	1.17	6.29	1.45	1.06	0.60
26		33.1	6.1	1.1	4.9	0.8	4.4	0.9	2.6	2.6	0.4	4.7	21.0	18.4	2.6	13.35	1.38	6.57	1.42	1.03	0.61
		33.4	*6.2*	*1.2*	*5.1*	*0.8*	*4.6*	*0.9*	*2.7*	*2.7*	*0.4*	*4.9*	*21.8*	*15.0*	*2.5*						
27		37.5	7.1	1.2	5.7	0.9	5.2	1.1	3.1	3.1	0.5	4.8	28.0	22.8	3.5	8.21	0.96	6.08	1.62	1.05	0.57
28																					
29		26.8	4.9	1.1	4.0	0.6	3.6	0.7	2.1	2.1	0.3	3.0	18.8	12.5	2.0	24.56	2.79	5.15	0.96	1.03	0.76
30		31.6	5.8	1.0	4.6	0.7	4.1	0.9	2.4	2.5	0.4	3.8	24.2	19.5	2.8	7.14	0.97	5.63	1.70	1.02	0.57
31		38.6	7.1	1.2	5.7	0.9	5.0	1.0	3.0	3.0	0.4	3.9	27.6	23.9	3.5	6.30	1.10	4.50	1.67	1.01	0.59
32		36.8	6.7	1.2	5.5	0.9	5.0	1.0	3.0	2.8	0.4	3.6	27.1	19.6	3.1	6.79	0.99	4.46	1.50	1.01	0.60
33		44.5	8.1	1.3	6.6	1.0	6.0	1.2	3.5	3.3	0.5	5.1	30.6	24.8	3.6	6.90	0.81	5.84	1.98	1.01	0.54
34		35.6	6.7	1.2	5.3	0.8	4.8	1.0	2.8	2.9	0.4	5.5	24.2	17.2	2.6	13.07	1.02	7.50	1.28	1.06	0.63
35		33.7	6.3	1.2	5.2	0.8	4.6	1.0	2.7	2.8	0.4	5.0	22.1	15.7	2.5	15.75	1.26	6.87	1.14	1.07	0.63
36		41.9	7.7	1.3	6.2	1.0	5.7	1.1	3.2	3.0	0.5	6.4	33.0	19.9	3.1	11.55	0.88	7.68	1.52	1.01	0.58
37																					
38		35.3	6.8	1.2	5.5	0.9	5.1	1.1	3.0	3.0	0.4	4.8	28.0	18.7	2.7	11.25	1.05	6.46	1.09	1.03	0.62
39																					
40		34.6	6.4	1.2	5.3	0.8	4.6	0.9	2.7	2.7	0.4	5.0	28.3	19.5	2.8	10.23	0.99	7.09	1.25	1.04	0.61
41		35.2	6.7	1.2	5.4	0.8	4.6	1.0	2.6	2.6	0.4	4.7	32.9	18.5	2.6	10.85	1.12	6.39	1.28	1.02	0.61
42																					
43																					
44																					
45		36.1	6.8	1.2	5.4	0.8	4.8	1.0	2.8	2.7	0.4	5.2	28.8	20.5	3.9	9.52	0.91	7.26	1.33	1.07	0.58
46		36.0	6.7	1.2	5.5	0.9	4.8	1.0	2.8	2.6	0.4	4.7	33.8	17.9	3.1	11.04	1.03	6.74	1.20	1.06	0.60
		34.7	*6.5*	*1.2*	5.3	0.8	*4.7*	*0.9*	*2.7*	*2.6*	*0.4*	*4.6*	*32.9*	*17.1*	2.9						
47		33.9	6.4	1.2	5.1	0.8	4.6	0.9	2.7	2.5	0.4	5.1	30.8	16.8	2.5	12.05	0.96	7.94	1.18	1.09	0.62
48		33.9	6.4	1.2	5.1	0.8	4.4	0.9	2.5	2.6	0.4	4.9	29.4	17.8	2.4	13.59	1.25	7.33	1.17	1.08	0.64
49		34.6	6.5	1.2	5.2	0.8	4.8	1.0	2.8	2.8	0.4	6.0	24.7	16.9	2.4	14.03	0.94	8.64	1.15	1.15	0.63
50		30.2	5.7	1.1	4.6	0.7	4.2	0.9	2.5	2.5	0.4	5.7	20.6	14.0	2.1	17.15	1.02	9.18	0.91	1.18	0.65
51																					
52																					
53		30.7	5.8	1.1	4.7	0.7	4.1	0.8	2.4	2.3	0.3	4.2	27.4	15.1	2.2	15.40	1.34	6.98	1.04	1.07	0.63
54																					
55																					
56		28.3	5.4	1.3	4.6	0.7	4.1	0.8	2.3	2.1	0.3	5.6	20.7	9.9	1.6	28.42	1.16	10.88	0.77	1.06	0.82
57		29.0	5.5	1.3	4.7	0.7	4.2	0.8	2.4	2.2	0.3	5.4	24.5	11.3	1.7	25.07	1.20	9.76	0.88	1.10	0.77
58		32.8	6.2	1.5	5.0	0.8	4.3	0.9	2.4	2.3	0.3	6.9	18.6	11.2	1.8	25.63	0.93	11.82	1.05	1.06	0.82
59		30.2	5.8	1.3	4.6	0.7	3.9	0.8	2.2	2.1	0.3	4.9	20.0	11.2	1.6	30.79	1.52	10.31	0.92	1.04	0.77
60		36.9	6.9	1.2	5.4	0.8	4.5	0.9	2.6	2.5	0.4	3.2	17.7	17.7	2.2	5.03	0.75	4.61	1.20	1.01	0.60
61		37.5	7.0	1.2	5.4	0.8	4.5	0.9	2.6	2.5	0.4	3.2	22.7	18.1	2.3	4.78	0.74	4.49	1.19	1.02	0.60
62		37.2	6.9	1.2	5.2	0.7	4.0	0.8	2.3	2.2	0.3	3.0	18.1	18.3	2.3	4.20	0.70	4.77	1.19	1.01	0.59
63																					
64		36.7	6.9	1.2	5.2	0.8	4.1	0.8	2.3	2.4	0.3	3.1	19.3	17.5	2.2	4.24	0.67	4.76	1.25	1.02	0.61
65		34.8	6.4	1.1	4.9	0.7	3.9	0.8	2.2	2.1	0.3	2.7	19.5	21.4	2.4	4.35	0.97	4.40	1.35	1.01	0.58
66		40.5	7.5	1.1	5.6	0.8	4.5	0.9	2.5	2.3	0.3	2.7	20.5	21.7	3.6	4.21	0.97	3.75	1.36	1.00	0.54
		41.1	*7.6*	*1.2*	*6.0*	*0.9*	*4.8*	*1.0*	*2.7*	*2.5*	*0.4*	*2.9*	*23.2*	*20.6*	*2.3*						
67		38.2	7.1	1.1	5.3	0.8	4.3	0.9	2.4	2.3	0.4	3.0	17.9	22.4	2.6	4.12	0.88	4.50	1.43	1.00	0.56

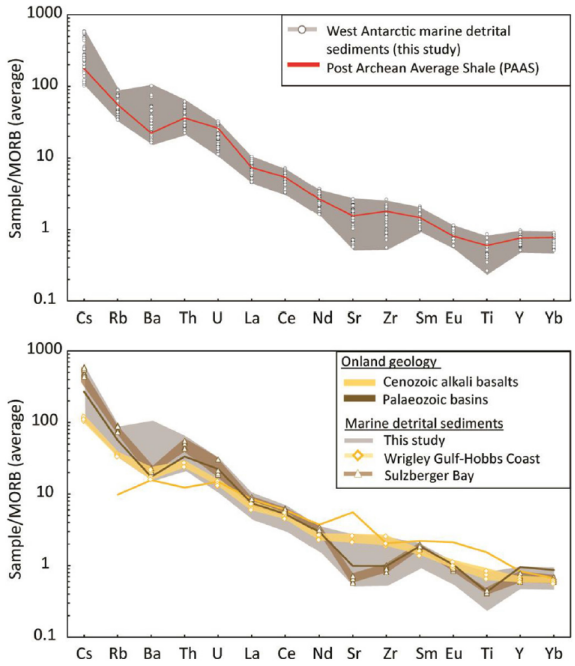

Fig. 5. a) Trace element compositions of fine-grained (< 63 μm) detrital surface sediments along the Pacific margin of West Antarctica, normalized to average mid-ocean ridge basalts and arranged in order of incompatibility (Gale et al., 2013). Individual sample results are indicated by white circles in the upper graphs, while the red line denotes the composition of the Post-Archean Average Shale (PAAS, McLennan, 2001). The grey field denotes marine sediment samples from this study. b) Sediments from the Wrigley Gulf-Hobbs Coast sector are now shown as diamonds connected by a yellow line, and sediments from Sulzberger Bay are shown as triangles connected by a brown line. The grey field denotes samples from the Antarctic Peninsula (AP), Bellingshausen Sea (BS) and Amundsen Sea (AS) sectors. The patterns for these two groups are similar to onland results obtained for Late Cenozoic alkali basalts (yellow line; Futa and LeMasurier, 1983; Hart et al., 1997) and Palaeozoic meta-sedimentary rocks (brown line; Korhonen et al., 2010), respectively.

Island (Leat et al., 1995; McCarron and Smellie, 1998; Ryan, 2005; Fig. 2, Appendix S2), recording the latest stage of the eastward-propagating cessation of ocean crust subduction under the Antarctic plate. Of particular interest are igneous rocks of ~12–14 Ma (particularly of hornblende-bearing mafic dykes), 20–21, 47–68 Ma and ~85 Ma, which crop out along the coast of Marguerite Bay on the west side of the Antarctic Peninsula, and at the northern tip of Alexander Island (Fig. 2 e.g. Ryan, 2007; Appendix S2), and which could explain the majority of the mineral grain ages observed in the shelf sediments. The extensively outcropping metasedimentary rocks of Carboniferous to Cretaceous age on Alexander Island are depleted in amphiboles and micas (Pierce et al., 2014) and hence not captured in the offshore $^{40}Ar/^{39}Ar$ age record. The signature of these sedimentary rocks is however observed by qualitative petrographic analysis and fine-grained Sr and Nd isotope fingerprints. In particular, site 8 sediments contain quarzitic clasts (quartz, feldspars), fine-grained dark lithic clasts (mudstone?), and lithic clasts with a fine-grained pink matrix. This is consistent with erosion of the metasedimentary formation on Alexander Island, which is largely composed of feldspathic sandstone, siltstone and black mudstones (Burn, 1984), as well as igneous rocks (lava, tuffs) similar to the Tertiary volcanics present on the island (Care, 1983).

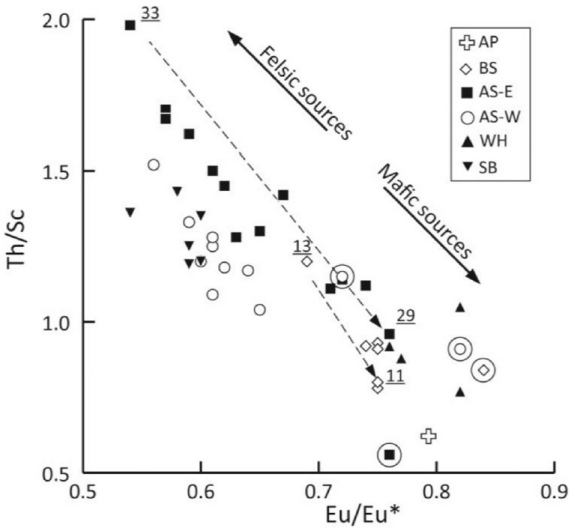

Fig. 6. Diagram of Th/Sc vs Eu/Eu* compositions of surface sediments along the Pacific margin of West Antarctica. Circled samples denote sediments with positive cerium anomalies (Ce/Ce* > 1.1), indicating minor redox processes affecting the sediments or their sources. Numbers indicate core sites of samples, which are discussed in more detail in the main text. Abbreviations: AP – Antarctic Peninsula, BS – Bellingshausen Sea, AS-E – eastern Amundsen Sea, AS-W – western Amundsen Sea, WH – Wrigley Gulf – Hobbs Coast, SB – Sulzberger Bay.

6.1.2. *Provenance of fine-grained detritus*

Outcrops of Cretaceous to Cenozoic plutonic and volcanic (< 97 Ma) rocks are characterised by radiogenic Nd and Sr isotopic compositions (ε_{Nd} ~-2 to 5; $^{87}Sr/^{86}Sr$ ~0.703–0.708; Pankhurst et al., 1988; McCarron and Smellie, 1998; Riley et al., 2001, 2003; Ryan, 2005, Fig. 4, Appendix S2), which are distinct from Jurassic to Cretaceous granitoids in the Antarctic Peninsula and the Amundsen Sea region (ε_{Nd}: −8 to 0; $^{87}Sr/^{86}Sr$ ~0.703–0.715) (Fig. 4; Appendix S2). The Antarctic Peninsula Volcanic Group and/or nearby granitoids hence seem to be the likely source for the fine-grained detritus with relatively radiogenic values observed at site 1–4, most proximal to the Graham Land coast (Fig. 2; Table 2). Sites 7 and 8 are located near to the Alexander Island, where extensive occurrences of arkosic sedimentary rocks (Fig. 2, Doubleday et al., 1993) are characterized by less radiogenic Nd isotope values (ε_{Nd}: −8 to −3; Fig. 3; Adams et al., 2005). The agreement between onshore data and our new offshore data indicate a local source for the marine sediments in the AP sector. We note, however, that a mixture between the granitic and volcanic rocks, which crop out on Alexander Island, could yield a similar isotopic fingerprint.

6.2. *Bellingshausen Sea (BS)*

6.2.1. *Provenance of ice-rafted detritus*

Bedrock exposures along the BS coast are extremely rare (Fig. 2) and limited to outcrops of some Cretaceous igneous rocks (Rb-Sr whole rock ages of 113 to 128 Ma; Pankhurst and Rowley, 1991) and Miocene-Quaternary volcanic rocks (Smellie, 1999; Hathway, 2001). Aeromagnetic investigations detected the 'Pacific Margin Anomaly' in the coastal region flanking the BS, notably in its eastern sector (Ferraccioli et al., 2006), which has been linked to mafic and intermediate basement rocks $^{40}Ar/^{39}Ar$ dated at 129–141 Ma by (Maslanyj and Storey, 1990; Vaughan et al., 1998). Hornblende and biotite $^{40}Ar/^{39}Ar$ ages, extracted from our marine sediment samples, record a dominant age

interval of 74 to ~140 Ma with well-defined age peaks of ~110 Ma and ~99–108 Ma, respectively. Onland source rock candidates for such ages are mid-Cretaceous felsic plutons intruding metasedimentary rocks in eastern Palmer Land (Fig. 2; $^{40}Ar/^{39}Ar$ dated to 95–119 Ma; Vaughan et al., 2012b), and/or older terranes which have been affected by the amphibolite-grade thermo-metamorphic Palmer Land event at 103–107 Ma (Wendt et al., 2008; Vaughan et al., 2012a). We suggest that this Palmer Land thermal event potentially affected large parts of the coast around the Bellingshausen Sea. Supporting evidence for this idea comes from the absence of mafic intrusion ages (i.e. Pacific Margin Anomaly; 129–141 Ma) in the sedimentary record of the eastern BS sector. Furthermore, distinctively different geologies along the eastern and western coasts of the Bellingshausen Sea seem not to be reflected in the iceberg-rafted component of the offshore sediments, which show a narrow range of $^{40}Ar/^{39}Ar$ age populations in both hornblende and biotite grains between sites 11 and 13 indicating regional thermal resetting (Appendix S2; Fig. 2).

6.2.2. Provenance of fine-grained detritus

Surface sediments in the BS are characterized by lower Nd isotopic composition for a given $^{87}Sr/^{86}Sr$ value compared to the other sectors (ε_{Nd} = −7.3 to −4.2, $^{87}Sr/^{86}Sr$ = 0.7097 to 0.7132; Fig. 4). Volcanic rocks of the Antarctic Peninsula Volcanic Group, situated inland of the BS coast (Figs. 2, 4), could provide the less radiogenic Nd isotopic compositions, but are Jurassic in age (~160–190 Ma) and have high $^{87}Sr/^{86}Sr$ values (Riley et al., 2001). The Cenozoic alkali basalts have very high Nd and low Sr isotope values and thus are unlikely to explain the observed signature in the shelf sediments (Fig. 4). Furthermore, clay mineral data from shelf sediments in the BS sector (Table 2) make it unlikely that volcanic source rock from along the BS coast contribute significantly to the observed provenance of the glacial-marine sediments, because enhanced smectite contents (indicative of supply of volcanic detritus) are restricted to samples from the easternmost BS sector along the west coast of Alexander Island (Hillenbrand et al., 2009b). More negative ε_{Nd} values, as well as felsic trace element patterns (high Th/Sc, Eu/Eu* and low Sr/Zr and Zr/Y), are consistent indicators of a more evolved source (e.g. McLennan et al., 1993), notably in the western BS sector. This observation is in agreement with the clay mineral composition of marine sediments along the southern coast of the BS (Hillenbrand et al., 2009b), which is characterised by high illite and low smectite contents (sites 11 to 12), indicating a granitic or gneissic source (Fig. 5). Felsic bedrock in the southern hinterland of the BS has indeed been inferred from aeromagnetic observations, with ilmenite-rich intrusions in the west contrasting with magnetite-rich counterparts to the east responsible for the Pacific Margin Anomaly (Ferraccioli et al., 2006).

6.3. Amundsen Sea

6.3.1. Provenance of ice-rafted detritus

Ice-rafted hornblende and biotite grains in sediments from the AS are distinct from other sectors on the Pacific margin of West Antarctica because of the significant presence of $^{40}Ar/^{39}Ar$ ages > 140 Ma (Fig. 3e, f). Predominant hornblende age peaks are ~100–110 Ma, ~140–210 Ma, ~250 Ma and ~350 Ma, and ~100–110 Ma, ~170 and ~240 Ma for biotite grains (Fig. 7). Similar age populations have been detected in coastal outcrops of mainly calc-alkaline igneous and metaigneous granitoid rocks around the ASE by using a variety of dating methods (Pankhurst et al., 1993, 1998; Mukasa and Dalziel, 2000; Kipf et al., 2012; Riley et al., 2017; Appendix S2).

In detail, sites proximal to the coast reveal a different provenance between the Walgreen Coast in the western AS, and the coast extending from Thurston Island towards Pine Island Bay in the eastern AS (Fig. 2). Sites 22 and 24–29 along the eastern AS coast are characterized by a large number of grains with ages from 140–210 Ma, while grains from sites proximal to the Walgreen Coast (sites 38, 40–41 and 45) lack such ages (Fig. 7). Ice-rafted debris (IRD) supplied by icebergs calved from of the Abbot and Cosgrove Ice Shelves (Fig. 2), as well as from Pine Island and/or Thwaites glaciers (sites 32–33) are likely sources for the observed $^{40}Ar/^{39}Ar$ ages of 140–210 Ma. The unique geological signature of the Thurston Island block, with its characteristic Jurassic ages, was already specified by Pankhurst et al. (1993), based on biotite and hornblende K-Ar ages (~150 Ma) and is also present in our offshore record.

Peak Cretaceous ages for both hornblende and biotite grains are slightly but distinctively (~10 Ma) different between the eastern and western ASE (Fig. 7). Hornblende and biotite grains supplied from the Walgreen Coast (western ASE) record ages of 108–110 Ma, while erosion along the eastern ASE coast sheds grains with a pronounced ~100 Ma age peak (Fig. 7). This difference in mineral age population between the western and eastern Amundsen Sea sectors can be related to the diachronous eastward cessation of subduction, and therefore a progression of calc-alkaline magmatism from Marie Byrd Land towards Thurston Island (Mukasa and Dalziel, 2000). Finally, a minor ~353 Ma age peak is visible in ice-rafted hornblende grains, particularly at sites 18, 22 and 25–27 proximal to Thurston Island, but not in biotite grains (Fig. 2, 7; Appendix S1). Matching ages can be identified onland from a granodioritic orthogneiss formation cropping out on the eastern side of Thurston Island, which has been dated by zircon U-Pb to ~349 Ma (Riley et al., 2017). Material from these outcrops could either be carried by icebergs into the eastern AS sector via the Antarctic Coastal Current, or similar outcrops could be located below ice streams feeding the Abbot Ice Shelf, which eventually calves into the eastern ASE.

Rocks cropping out along the Walgreen Coast have Cretaceous (~100–130 Ma, zircon U-Pb and $^{40}Ar/^{39}Ar$ plateau) and Late Palaeozoic ages (~250 Ma and ~350–500 Ma, zircon U-Pb) (Pankhurst et al., 1998; Mukasa and Dalziel, 2000; Kipf et al., 2012). These ages are mostly found in the grains of the proximal offshore sediments, except for the 350–500 Ma age interval, which may be absent due to the limited onshore occurrence of rocks of that age and the limited amount of grains analysed in the marine sediments.

One striking observation when comparing the geological map (Fig. 2) with the marine detrital mineral grain ages (Fig. 3) is the notable absence of ages that can be related to outcropping Late Cenozoic alkali basalt volcanoes (e.g. Hudson Mountains, Mount Murphy and Mount Takahe, Fig. 2), with the exception of site 49 from the continental slope. Explanations for this observation could either involve the limited extent of such lithologies below the erosive ice drainage compared to the igneous batholith, or the fact that hornblende and biotite grains are not present or are too fine-grained to be detected in the coarse (i.e. > 150 μm) fraction of marine samples, and hence not reflected in the $^{40}Ar/^{39}Ar$ age spectrum.

6.3.2. Provenance of fine-grained detritus

Similar to the $^{40}Ar/^{39}Ar$ ages of the ice-rafted grains, the Sr and Nd isotopic composition of the fine-grained sediments in the AS can be separated into an eastern and western sub-sector, broadly delimited by the extent of the Pine Island and Cosgrove-Abbot troughs in the East and the Dotson-Getz Trough in the West, which are incised into the continental shelf (Larter et al., 2014; Figs. 2, 4). Sediments in the western AS are characterized by a very homogeneous Sr and Nd isotope signature (ε_{Nd} ~-2.9 to −1.8 and $^{87}Sr/^{86}Sr$ ~0.7082 to 0.7101), which correlates with the isotopic signature of Mesozoic granites and granodiorites observed in coastal outcrops (Fig. 4, 9). We note that sites 36 to 45 are located proximal to the Dotson Ice Shelf and various parts of the Getz Ice Shelf along the Walgreen Coast. The glaciers feeding into these ice shelves drain distinct, separate basins, but nevertheless the offshore sediment samples record very similar Sr and Nd isotope fingerprints. Site 39 marks an exception to this general pattern (Fig. 2, 9), because it is characterized by distinctively higher ε_{Nd} values, potentially due to a much localised source. Supply of material eroded from Palaeozoic granites seems to be a minor contributor to the fine-grained detritus,

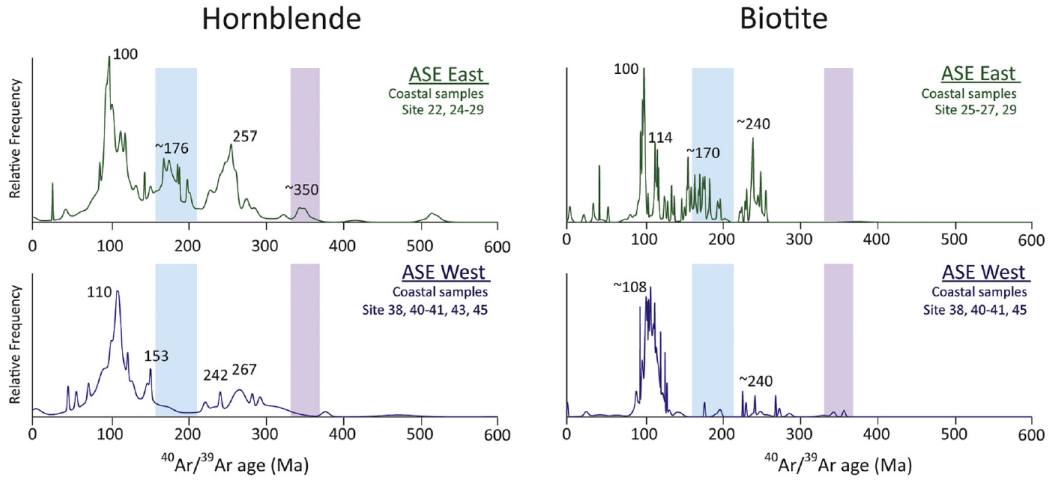

Fig. 7. Relative frequency of $^{40}Ar/^{39}Ar$ ages on hornblende and biotite grains from proximal locations in the Amundsen Sea Embayment (ASE). Upper panel displays results for the eastern ASE (sites 22 and 24–29) and lower panel displays results for the western ASE (sites 38, 40–41 and 45). Note the presence of a significant population of hornblende grains with ages of ~140–210 Ma (blue shading) and ~350 Ma (purple shading) in the eastern ASE and their absence from the western ASE.

similar to what was observed for the IRD fraction from sites in this area.

In the eastern AS, sediment recovered just in front of Pine Island Glacier (site 32) shows a different and distinct radiogenic isotope fingerprint (ε_{Nd} = −7.2; $^{87}Sr/^{86}Sr$ = 0.7240; Table 2). This unradiogenic signature is unlikely to be related to proximal outcropping young volcanic rocks, which have more radiogenic (higher) ε_{Nd} and lower Sr isotope ratios (ε_{Nd} ~5; $^{87}Sr/^{86}Sr$ ~0.703; Hart et al., 1997). Seismic reflection and airborne potential field data provide evidence for a mixed bed below Pine Island Glacier, consisting of unconsolidated and consolidated sedimentary strata, basement rocks and igneous intrusives (Smith et al., 2013). Rocks similar to the Palaeozoic sedimentary outcrops on western Marie Byrd Land could be one candidate to contribute to the observed signature (Fig. 4). Petrographic studies on coarse-grained clasts (> 2 mm) in seafloor surface sediments in a nearby core (PS75/215–1), however, found a largely granitic source for this IRD (Lindow et al., 2016). It is unclear whether the IRD originated from below Pine Island Glacier or from granitic islands cropping out in Pine Island Bay. Overall, given the presence of igneous basement and granitic IRD in shelf sediments proximal to Pine Island Glacier, we suggest that the distinctively low ε_{Nd} values and high $^{87}Sr/^{86}Sr$ ratios in fine-grained detrital sediments at site 32 represent a significant input from evolved granites, which experienced significant crustal assimilation during mantle extraction (Fig. 4), or sedimentary infill eroded from this source. Such granites crop out further inland in the Jones Mountains and in the Ellsworth-Whitmore Mountains (Fig. 2, Pankhurst et al., 1993; Millar and Pankhurst, 1987). This interpretation is further supported by trace metal compositions showing low Th/Sc and Eu/Eu* (Fig. 6), and high Th/Zr ratios (see Table 3 for values). Such ratios are indicative of felsic rocks such as evolved granites or granites that encountered more crustal assimilation (e.g. McLennan et al., 1993; Taylor and McLennan, 1995).

Along the eastern flank of the AS sector, ε_{Nd} values become consistently lower with increasing distance from inner Pine Island Bay, while $^{87}Sr/^{86}Sr$ values become higher, and eventually overlap with the composition of the local Mesozoic granites (Figs. 4, 9). A logical interpretation of this pattern is increasing input of material from the eastern coast of the ASE (between Thurston Island and Pine Island Glacier), where extensive Mesozoic granites are exposed (Figs. 4 and 9).

6.4. Wrigley Gulf-Hobbs Coast

6.4.1. Provenance of ice-rafted detritus

The Hobbs Coast is characterized by granitoid outcrops with zircon U-Pb ages of ~115 Ma at Mt. Petras (Figs. 2, 8), and similar ages elsewhere along the Ruppert Coast in migmatitic, anorogenic, and I-type granitoids (Mukasa and Dalziel, 2000). This age is well reflected in the $^{40}Ar/^{39}Ar$ ages of coarse hornblende and biotite grains in marine sediments from the WH sector with a dominance of ages between 90 and 130 Ma, and slightly younger peak ages of ~100 Ma and ~101 Ma, respectively (Fig. 3g,h). Older Palaeozoic granitoids crop out along the Ruppert Coast and in the Ford Ranges. It is however, unlikely that such rocks are present below the drainage basin of the western Getz Ice Shelf, as they are rich in hornblende and biotite grains recording undisturbed K-Ar mineral ages of 324–375 Ma (Adams, 1987), which we do not find in the age population of our grains. A secondary biotite $^{40}Ar/^{39}Ar$ age peak of ~53 Ma detected at site 58 is more difficult to explain, as rocks of suitable ages are unknown from the local geology. Previous studies on IRD from sites 58 and 59 have focused on apatite fission track (AFT) thermochronology (Spiegel et al., 2016) and found widespread AFT ages of 60 to 80 Ma. AFT thermochronology is based on the analysis of lattice damage caused by the spontaneous fission of radiogenic ^{238}U. This method has a lower closure temperature of ~120°C, and Spiegel et al. (2016) correlated AFT ages of 60 to 80 Ma with Cretaceous granitoids, which makes them an unlikely source for ~53 Ma old biotite grains. Basement rocks with (post-) Miocene AFT cooling ages (~20 Ma) on the other hand were interpreted by Spiegel et al. (2016) to reflect an unknown source under the Getz Ice Shelf drainage basin. This source is not found in proximal outcrops, but is likely to be composed of granitic and/or diorite material given the petrographic data on IRD (> 2 mm) from the same site. These rocks could account for our observed ~53 Ma $^{40}Ar/^{39}Ar$ age in the biotite population.

A small number of young hornblende ages (< 10 Ma, n = 9) are found in the detrital sediments, tracing the erosion of young alkali basalts. Erosion of these volcanic rocks is further confirmed by petrographic IRD analysis carried out by Spiegel et al. (2016), revealing the contribution of ~40% from volcanogenic clasts that can be associated with the local alkali basalts. Given the extent of outcropping Cenozoic volcanic rocks in the hinterland of the WH sector (Fig. 2), the relative absence of a significant young age peak in our data signifies that these

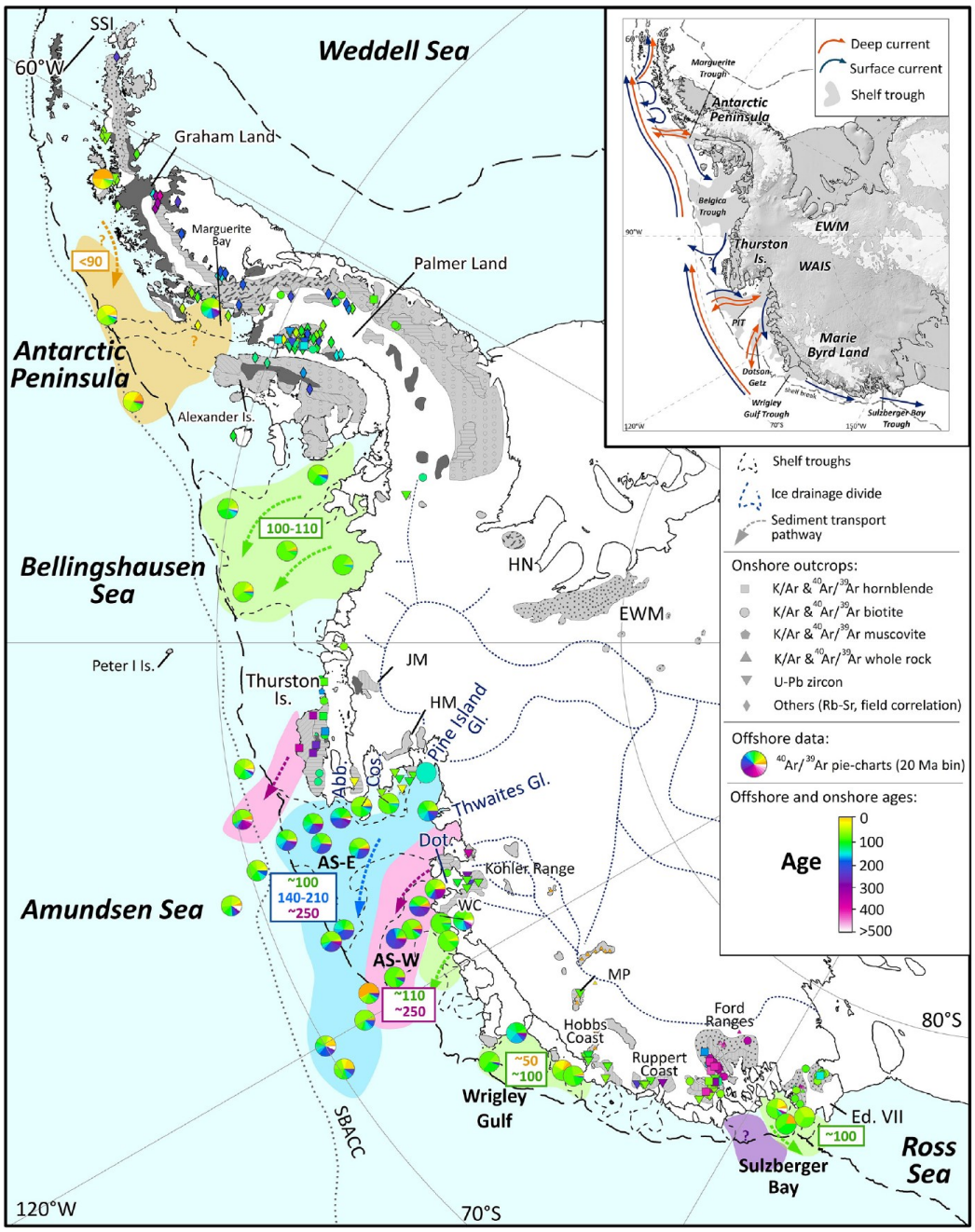

Fig. 8. Distribution of thermochronological ages in offshore sediments and terrestrial outcrops of West Antarctica. $^{40}Ar/^{39}Ar$ ages of ice-rafted hornblende and biotite grains are presented as pie charts in 20 Ma increments. Outcrop ages are displayed with different symbols depending on the type of mineral and the method applied (see Appendix S2). Simplified geology is shown in grey-scale after Fig. 2. Thick dashed black lines indicate the approximate location of the shelf break. Coloured dashed arrows and underlying colour field denote major ice-rafted debris transport pathways. Abbreviations and inlet figure are the same as for Fig. 2.

volcanic rocks are likely to contain hornblende and biotite grains that are too small to be detected in coarse marine samples (i.e picked from > 150 μm fraction).

6.4.2. Provenance of fine-grained detritus

The fine-grained detritus of the WH sector (and site 54 in the western AS, Fig. 2) has high ε_{Nd} values and low $^{87}Sr/^{86}Sr$ ratios (Fig. 4), which can be explained by the two major lithologies cropping out along the Hobbs and Ruppert Coasts, the Late Cenozoic alkali basalts and

Cretaceous calc-alkaline granites (Fig. 2). Mixing calculations between these two end-members suggests a ~30% contribution from alkali basalts and ~70% contribution from Cretaceous granites to the sediments (average Mesozoic granitoids vs. average Late Cenozoic alkali basalts, Appendix S2). This assessment is in agreement with the petrographic IRD analysis by Spiegel et al. (2016) and further supported by trace element compositions of our detrital sediment samples, which indicate a mixture between a Mesozoic granitic end-member and Cenozoic alkali basalts (Fig. 4b). In detail, high Sr/Th (~28) and Zr/Y ratios (~10.5; Table 3) and slightly elevated Eu/Eu* ratios relative to the other studied sectors (~0.8) are all consistent with a significant contribution from mafic alkali basalts to the detrital composition of the seafloor sediments.

6.5. Sulzberger Bay

6.5.1. Provenance of ice-rafted debris

During the mid-Cretaceous, rifting of Zealandia from western Marie Byrd Land led to the intrusion of extensive anorogenic granitoids with K-Ar ages of ~98–105 Ma (Richard et al., 1994; Adams et al., 1995). These rocks are predominantly exposed in the Ford Ranges and on Edward VII Peninsula, where they crop out alongside Palaeozoic granodiorites (i.e. Ford Granodiorite Suite) and Cambrian-Ordovician metasedimentary rocks (i.e. Swanson Formation) (Weaver et al., 1992; Adams et al., 1995, Fig. 2). The Ford Granodiorite Suite contains coarse hornblende and biotite grains with zircon U-Pb and K-Ar hornblende and biotite ages of 320–370 Ma (Adams, 1987; Pankhurst et al., 1998). Predominant hornblende $^{40}Ar/^{39}Ar$ ages of 90 to 130 Ma (peak age: ~100 Ma; n = 26) in marine sediments in SB indicate limited erosion from the Ford Granodiorite Suite, with the exception of two grains with ages of 347 Ma and 510 Ma (Appendix S1). A more likely source for the IRD in the SB sector is hence Edward VII Peninsula (Fig. 2). This conclusion seems in contrast to aeromagnetic investigations of the area, which inferred a larger extent for the Ford Granodiorite Suite on Edward VII Peninsula (Ferraccioli et al., 2002). Overall, however, our age distribution is in agreement with the ages of local A-type granites, the thermal overprinting ages and the absence of hornblende grains in the sedimentary Swanson Formation (Adams et al., 1995, see Pierce et al., 2014, for a discussion on durability of hornblende grains in the sedimentary cycle), which crops out extensively on Edward VII Peninsula.

6.5.2. Provenance of fine-grained sediments

In contrast to the IRD signature, low Nd (ε_{Nd}: −11.9 to −10.5) and high Sr isotope values ($^{87}Sr/^{86}Sr$: 0.7411 to 0.7493) in the fine-grained detritus in the SB sector show a strong affinity to the metasedimentary Swanson Formation (ε_{Nd}: −13.4 to −10.5 and $^{87}Sr/^{86}Sr$: 0.7264 to 0.7618) (Pankhurst et al., 1998; Korhonen et al., 2010; Fig. 3). In detail, Nd isotopic compositions are slightly higher and Nd model ages are slightly younger (~1600 Ma, Table 2) than documented for the Swanson Formation on land (1650–1800 Ma; Appendix S2). An additional source is therefore needed to explain the observed signatures, which is readily found in the local A-type granites intruding the Swanson Formation on Edward VII Peninsula (Weaver et al., 1992). A mixture between Palaeozoic sediments from the Swanson Formation and Cretaceous anorogenic granitoids in the marine detrital sediments from the SB sector is further suggested by low Sr/Th ratios (4–5) and characteristic low Eu anomalies (Eu/Eu* ~ 0.6), and is consistent with coarse and fine-grained geochemical signatures in marine sediments from the area.

7. Comparison of different provenance proxies

7.1. $^{40}Ar/^{39}Ar$ ages in hornblende vs biotite grains

Combined analyses of $^{40}Ar/^{39}Ar$ ages from hornblende and biotite grains in detrital sediments allows for more detailed provenance analysis due to the different closure temperatures of both minerals (~550°C and 300°C, respectively). In the case of East Antarctica, partial or total resetting of lower temperature thermochronometers has been observed in several sectors. For example, in detrital sediments from the Wilkes Land sector (90°E to 135°E), a characteristic ~1494 Ma peak age is found in hornblende grains, but is absent from the biotite grains. This observation has been linked to partial resetting of biotite grain ages during the Grenville orogeny (Pierce et al., 2014).

In West Antarctica, coastal geology is dominated by Andean-style plutonism of Permian or younger age, resulting in large diorite, granodiorite, monzogranite and syenite intrusions, which in many cases are not overprinted by any major younger tectono-metamorphic events (except for the regional Palmer Land Event at 103–107 Ma). If marine sediment sites are proximal enough to the continental source areas, which carry both large hornblende and biotite grains, as is the case for many of the West Antarctic plutonites, and if the erosional pathway from source to sink does not separate the two mineral phases by differential current sorting, combined biotite-hornblende $^{40}Ar/^{39}Ar$ data sets may be used to broadly support provenance interpretations by inferred cooling rates. We think that a case can be made as large parts of our data set meet these criteria. Overall, probability peaks of hornblende grain ages are similar to or slightly older than those of biotite grains around West Antarctica (Fig. 3). Both minerals record a dominant Cretaceous age peak (100–110 Ma) in all sectors, apart from the AP sector (Fig. 3). This age interval is particularly well defined in most of the sectors and peak ages between both mineral systems vary by as little as ~2 Ma in the detrital marine sediments (e.g. AS sector; Fig. 7). Because magmatic activity has been largely episodic (e.g. Pankhurst et al., 1993; Leat et al., 1995), we suggest that these ages point towards regional sources from the same lithological unit (i.e. batholith). Derived cooling rates for the Cretaceous source rocks would be extremely fast (~ > 100°C per million years between 550 and 350°C). To our knowledge, there are no detailed investigations on the cooling rates of Cretaceous I-type granitoids from West Antarctica. Concordant ages between zircon U-Pb ages, and reliable $^{40}Ar/^{39}Ar$, K-Ar and Rb-Sr data have nonetheless been observed for intrusive I-type granites on Palmer Land (Pankhurst and Rowley, 1991; Flowerdew et al., 2005; Vaughan et al., 2012b). Thermochronological investigations on Cretaceous A-type granites in the Ford Ranges ('Byrd Coast Granites'; Fig. 2) have revealed cooling rates of > 100°C/Ma, associated with granitic intrusion into the shallow crust (Richard et al., 1994). In South America, the emplacement of large Cretaceous plutonic rocks was coeval with the build-up of the Cretaceous batholith on West Antarctica. The mid-Cretaceous plutonic complex in the Coastal Range of central Chile show similar rapid cooling of gabbro to granodiorite suites (93 to 95 Ma based on coupled $^{40}Ar/^{39}Ar$ hornblende, biotite and plagioclase ages), and similar crystallization ages of the same batholith (95–97 Ma; zircon U-Pb ages; (Parada et al., 2005; Ferrando et al., 2014). Another comparison can be made for the eastern AS, where detrital hornblende grains yield well-defined ages of ~257 Ma and biotite grains record a younger age of 240 Ma (Fig. 7). This age difference would imply an approximate cooling rate of ~15°C per million years for the Permian-Triassic source rocks. This result is consistent with cooling rates of similarly aged dioritic to granodioritic rocks from Thurston Island (~12.5°C/Ma based on K/Ar and $^{40}Ar/^{39}Ar$ on hornblende and biotite; Pankhurst et al., 1993) and calc-alkaline diorites of the Median Batholith in New Zealand (~20°C per million years, Mortimer et al., 1999), which formed the continuation of the Amundsen Sea province prior to the onset of rifting (Bradshaw et al., 1997; Vaughan and Storey, 2000).

Offshore from the Walgreen Coast, pre-Cretaceous (> 140 Ma) biotite grains are relatively rare compared to hornblende grains (Fig. 7). This observation is explained either by the presence of intermediate to mafic sources which carry more hornblende than biotite (i.e. granodiorite and diorite; Pierce et al., 2014), or by thermal resetting of biotite ages during the Cretaceous. Permian diorite and granodiorite outcrops of ~243 Ma and ~283 Ma (zircon U-Pb, Mukasa and Dalziel, 2000)

have been identified in the Kohler Range, which is fed by ice streams flowing towards the Walgreen Coast, and could hence indicate a (minor) mineralogical bias towards biotite in the area.

In several locations, a marked distinction between the two chronometers is observed in the offshore record. In addition to the previously mentioned exotic biotite ages of ~53 Ma in the WH sector, hornblende ages of ~350 Ma, which are absent in the biotite record, were found in the eastern AS sector (Fig. 7). Comparison with the proximal geology relate these ages to the emplacement of a granodioritic-orthogneiss on Thurston Island (Rb-Sr whole rock: ~309 Ma, Pankhurst et al., 1993; zircon U-Pb: ~349 Ma, Riley et al., 2017). These gneisses show evidence for realignment and recrystallization of biotite crystals, indicating that a thermal event is likely to have affected the cooling ages of these crystals, possibly during later intrusions of the widespread Permian-Triassic plutonic rocks (~240 Ma).

7.2. Fine-grained sediment provenance derived from radiogenic isotopes and trace elements versus clay mineralogy

Along the Pacific margin of West Antarctica, most of the previous provenance work has focussed on the analysis of mineral assemblages in the clay fraction (< 2 μm), which was published by Hillenbrand and Ehrmann (2002), Hillenbrand et al. (2003, 2009b) and Ehrmann et al. (2011). In this study, we expanded the existing clay mineral data set by analysing additional samples from the Wrigley Gulf-Hobbs Coast sector (Table 2). We here show that the combined study of clay mineralogy and fine-grained sediment fingerprints provides complimentary information on their onshore source.

In the AP and BS sectors, high illite content in shelf sediments (45–70 %) has been found offshore from the eastern tip of Alexander Island, as well as in the western part of the BS sector (Table 2; Hillenbrand and Ehrmann, 2002; Hillenbrand et al., 2003). The high abundance of illite in these areas was suggested to originate from granitic and gneissic sources. Assumption of a granitic-gneissic source on Alexander Island is based on the presence of plutonic rocks in the eastern part of the island (i.e. the Rouen Mountains; Care, 1983) and the dominance of quartz-mica schistose/gneissic pebbles believed to be derived from the Rouen Mts. in subglacial tills recovered in cores from the nearby shelf (Kennedy and Anderson, 1989). However, erosion of these Tertiary rocks would produce a more radiogenic isotopic fingerprint in the fine-grained material of site 6 than what is observed ($\varepsilon_{Nd} \sim 2$ and $^{87}Sr/^{86}Sr \sim 0.705$; McCarron and Smellie, 1998) (Fig. 4). We suggest that the extensively outcropping accretionary sedimentary rocks on Alexander Island (LeMay Formation), which was shown to have high illite content (e.g. Underwood and Pickering, 1996) and Nd isotope values of ~ −8 to −3 (Fig. 4), are the more likely source rocks for the fine-grained fraction.

The trace element fingerprint (e.g. Th/Sc, Eu/Eu*) of shelf sediments in the BS reveals a mafic eastern sector and a felsic western sector (Fig. 6). This finding is confirmed by the clay mineral composition of the sediments that contain up to 66% illite and only 7% smectite in the western part of this sector, while in the eastern part of the sector 44% illite and 20% smectite are found (Hillenbrand et al., 2009b). In addition, these observations agree with geophysical surveys, which suggested a felsic composition of the hinterland of the western BS (i.e. Central Domain Eastern Zone; Ferraccioli et al., 2006). Shelf sediments further offshore record a mixed signature between these end-members (Hillenbrand et al., 2009b), which is consistent with our new data. For example, site 15 ($\varepsilon_{Nd} = -6.2$, Th/Sc = 0.93 and illite = 52%) shows detrital contribution from both end-members (Tables 2 and 3). Based on the clay mineral assemblage in the BS, Hillenbrand et al. (2003) proposed sediment material being carried northward by wind- and tide-driven currents without significant influence of the westward-driven coastal current. This fits with our observations, implying a similar sediment transport for the fine-grained sediment (< 63 μm).

In the AS sector, high kaolinite content in shelf sediments (up to 30 %) has been suggested to originate from pre-Oligocene sedimentary rocks beneath the Pine Island and Thwaites glaciers (Hillenbrand et al., 2003; Ehrmann et al., 2011), probably sourced from the Byrd Subglacial Basin (Fig 2). Such sedimentary rocks do not crop out in the hinterland of the AS (Fig. 2), making their geochemical signature elusive. The comparison between clay mineralogy and the fine-grained geochemistry yields clear correlations between kaolinite content and trace elements (not shown in figures). For example, hafnium (Hf), zirconium (Zr), and Nd exhibit a positive correlation with kaolinite content (R^2 = 0.67, 0.62 and 0.62, respectively), while a negative correlation can be observed between kaolinite content and Sr/Zr ratios (R^2 = 0.83). In general, kaolinite is associated with chemical weathering of bedrock under warm and humid conditions (Biscaye, 1965), and if it is found in Antarctica today, it is assumed to be derived from pre-Oligocene sedimentary strata as it cannot form under glacial conditions (e.g. Ehrmann et al., 1992). High Field Strength Elements (HFSEs) such as Zr or Hf, on the other hand, tend to be immobile during chemical weathering and remain in the residues of weathering while lithophile elements (i.e. Sr) are preferentially leached away. Hence, it is tempting to suggest that correlation between kaolinite and Sr/Zr is related to the presence of weathered outcrops in the hinterland. However, we do not observe a relationship between kaolinite and $^{87}Sr/^{86}Sr$ ratios, making glacial weathering a less likely candidate, and instead favour a provenance change as an explanation for Sr concentrations and isotopic compositions.

8. Geochemical signature of ice drainage basins and influence of marine sediment transport

Detailed geochemical characterization of the sediment provenance offshore from individual ice drainage basins gives valuable information on the integrated signature of subglacial geology and dispersal of glacially eroded detritus onto the shelf and further into the deep sea. It also provides the necessary modern day understanding how to use provenance analyses for palaeo-ice sheet reconstructions from marine downcore records (e.g. for East Antarctica; Cook et al., 2013, 2017; Pierce et al., 2017). The relatively young geological history of West Antarctica means that individual ice drainage basins will show less pronounced geochemical differences when compared to East Antarctica (e.g. Pierce et al., 2011, 2014) or the North Atlantic (e.g. Hemming, 2004). For instance, Pb analyses of K-feldspars grains have been shown to be a valuable tool for distinguishing erosional inputs from West and East Antarctic source terranes (Flowerdew et al., 2012). However, Pb isotopic values are remarkably uniform on West Antarctica due to the exclusively mantle-derived sources for the exposed crystalline bedrock (Mukasa and Dalziel, 2000; Flowerdew et al., 2012). Our multi-proxy approach nevertheless allows us to distinguish distinct ice drainage basins within West Antarctica as well as sediment transport pathways.

8.1. Coarse-grained detrital sediment signature and potential transport pathways

The modern IRD in the Southern Ocean is supplied by melting of calved icebergs. Ice-rafting has been described as the main mechanism for the transport of coarse detritus from the Antarctic continent to the pelagic realm as ocean currents can only transport finer sediments (e.g. Diekmann and Kuhn, 1999). The westward flowing Antarctic Coastal Current is of particular relevance, as it dominates the transport of icebergs in proximity to the coast (e.g. Stammerjohn et al., 2015; Kim et al., 2016a; Fig. 8). We find a strong contrast in IRD provenance patterns between the AP and the BS sectors (Figs. 3, 8). Relatively young ages observed in the AP sector are sourced from the west coast of the Antarctic Peninsula, where outcrops of magmatic rocks of Late Cretaceous to Cenozoic ages produced by the eastward migration of the active subduction of the (proto-) Pacific plate under West Antarctica during that time are widespread (Leat et al., 1995). This can be

explained by the fact that most icebergs from the Antarctic Peninsula are deflected northwards into the ACC by cyclonic gyres on the shelf before reaching the BS sector (e.g. Hofmann et al., 1996; Smith et al., 1999; cf. Hillenbrand et al., 2003) (Fig. 8).

In the BS sector, the $^{40}Ar/^{39}Ar$ hornblende and biotite ages are relatively uniform in proximal and distal sediments and record sources with a strong mid-Cretaceous thermo-metamorphic event related to suturing between the western/central domains with the eastern domain of the Antarctic Peninsula (Fig. 1). These ages are not found in the AP sector. A large cyclonic gyre in the southern Bellingshausen Sea deflects the coastal current along the eastern flank of Thurston Island (~95°W) (Gladstone et al., 2001; Assmann et al., 2005; cf. Hillenbrand et al., 2003), injecting most of the icebergs into the ACC. Some westward IRD transport may also occur within the Antarctic Coastal Current, but this is difficult to trace due to the ubiquitous nature of mid-Cretaceous thermochronological ages around West Antarctica (Fig. 8, Appendix S1).

Most of the outcrops in the AS sector are located around Thurston Island and along the Walgreen Coast, where ice streams are feeding into the Abbott and Cosgrove and the Dotson and Getz ice shelves, respectively (Fig. 2). Proximal ice-rafted grains in these two areas show similar mid-Cretaceous and Permian-Triassic ages (~100 Ma and ~250 Ma), but are distinct from the other sectors by the presence of grains with Jurassic ages (140–210 Ma), which mainly occur offshore from the Abbott and Cosgrove ice shelves (Fig. 7, 8). Although the numbers of grains analysed in samples just offshore from Pine Island Glacier (n = 1) and Thwaites Glacier (n = 9) are low, they also include grains of Jurassic ages (Appendix S1). This shows that the main source for Jurassic hornblende and biotite grains to the AS sector (and off West Antarctica) originates from the Cosgrove and Abbott ice shelves and from the Pine Island and Thwaites glaciers. In addition, surface currents in the ASE are influenced by the Antarctic Coastal Current. This current is overall weak (~1.0 cm s^{-1}) within the embayment, but appears strongest near the coastline (Assmann et al., 2005; Stammerjohn et al., 2015; Kim et al., 2016a). We observe Jurassic grains at sites on the continental slope and rise offshore from Dotson-Getz Trough (sites 50–52). We suggest that icebergs that drift generally westwards within the ASE (e.g. Mazur et al., 2017) transport the Jurassic grains from the eastern ASE to these locations, which are all situated south of the southern boundary of the ACC (Figs. 2, 8).

In general, IRD in samples from the continental slope and rise in the Amundsen Sea shows a larger age population (~30–80 Ma) than IRD on the continental shelf (Fig. 8). This feature is particularly pronounced around 70°S latitude. Source areas for grains of this age range could be either the western AP or the Hobbs Coast (sites 58–59) (Figs. 3, 8), both of which would require iceberg drift in opposing directions. Support for an AP provenance comes from petrographic observations on Plio-Pleistocene ice-rafted cobbles at DSDP Leg 35 Site 324 (located offshore from site 17) that show a provenance from Alexander Island (Tucholke et al., 1976; Veevers and Saeed, 2013). An argument against a far-travelled signal from the AP, however, is the lack of significant numbers of hornblende and biotite grains of this age range in the BS, as well as the existence of the large gyre in the BS, which carries most of the icebergs north-east towards the ACC (e.g. Assmann et al., 2005) (Fig. 8). Oceanographic observations indicate that sites at around 70°S in the Amundsen Sea are located within the eastward flow of the ACC (Orsi et al., 1995; Stammerjohn et al., 2015). This suggests that the source of the ~30–80 Ma old grains at the corresponding sites lies to the west. Indeed, our samples from the Hobbs Coast shelf show a well-defined ~50 Ma age peak, which indicates this area as the potential source for these young detrital grains (Fig 3h). The corresponding sites are located proximal to the westernmost Getz Ice Shelf. While the ~54 Ma age is unknown from onshore outcrops, it could represent a hidden source under the ice (cf. Spiegel et al., 2016). At present, icebergs calving from the westernmost Getz Ice Shelf drift westwards with the Antarctic Coastal Current towards the Ross Sea and are injected into the ACC offshore from Sulzberger Bay (Merino et al., 2016; Tournadre et al., 2016).

8.2. Fine-grained detrital sediment signature and potential transport pathways

In the modern Southern Ocean, coarse grained terrigenous debris is typically transported by icebergs, which follow wind-driven surface currents. Fine-grained sediments are also transported by these icebergs, but suspended particulates can additionally be transported by meltwater plumes, tidal, thermohaline, and geostrophic currents, as well as gravitational downslope processes such as turbidity currents (e.g. Aitken and Bell, 1998; Pudsey and Camerlenghi, 1998; Diekmann and Kuhn, 1999). Similar to the sand provenance signature, the geochemical fingerprint of the studied proximal fine-grained glacial-marine sediments off West Antarctica matches the nearby coastal geology very well, excluding a significant contribution of dust, which plays a more important role for the deposition of fine-grained detritus in the Sub-Antarctic Pacific sector of the Southern Ocean (e.g. Lamy et al., 2014). The fingerprint of sediments can be traced offshore, revealing the transport pathway of fine grains across the continental shelves.

In the AP sector, similarities in the radiogenic isotope fingerprint of site 7 on the shelf and site 8 located on the continental rise suggest seaward transport of detrital particles originating from the metasedimentary rocks on Alexander Island (Table 2, Fig. 9). Such a transport pathway across the western Antarctic Peninsula continental shelf has been described before for fine-grained terrigenous detritus (Hillenbrand and Ehrmann, 2002). In the BS, proximal sites denote felsic and mafic sources in both its western and eastern parts, consistent with aeromagnetic observations in the area (Ferraccioli et al., 2006; Bingham et al., 2002). Following the Belgica palaeo-ice stream Trough northwards, sediments record a mixing signature between these two areas, which has previously been attributed by wind- and tidal-driven currents (Hillenbrand et al., 2003, 2009).

A good example of bathymetrically constrained dispersal of fine-grained detritus is observed in the AS sector. Provenance of sediments proximal to the Pine Island and Thwaites glaciers is distinct, pointing to a felsic source or igneous rock with a geochemical signature of enhanced crustal assimilation underneath these two major ice drainage basins. Progressive northward change in sediment provenance along the eastern AS requires that sediment with this distinct fingerprint is transported northwards, and diluted along the way with Palaeozoic-Mesozoic source rocks along the eastern flank of the ASE (Fig. 9). The fact that samples from Dotson-Getz Trough show a uniform fine-grained fingerprint indicates that no significant cross shelf transport of fine-grained particles from further east or west occurred, as this would be recognizable in the radiogenic isotope signature of the samples. A candidate for the observed undiluted northward sediment transport is the northward return flow of upwelled Circumpolar Deep Water, after interacting with the base of the ice shelves, as Antarctic Surface Water (Jenkins et al., 2016). Observation from autonomous underwater vehicles found melt-laden outflow from ice shelves in the ASE to carry suspended sediment, which is sourced from the sediment-laden base of the ice shelves (Jenkins et al., 2016; Miles et al., 2016). This sediment-laden meltwater reaches the mid-depths of the water column and is transported northwards along the bathymetric troughs (e.g. Kim et al., 2016b). Release of this suspended particulate matter occurs notably along its main transport pathway, explaining the consistent provenance signatures of fine-grained sediment along the cross-shelf troughs in the ASE.

8.3. The geochemical fingerprint of West Antarctic provenance regions in the Pacific sector of the Southern Ocean

An integrated provenance approach allows for a characterization of subglacial sources from individual ice drainage basins along the Pacific

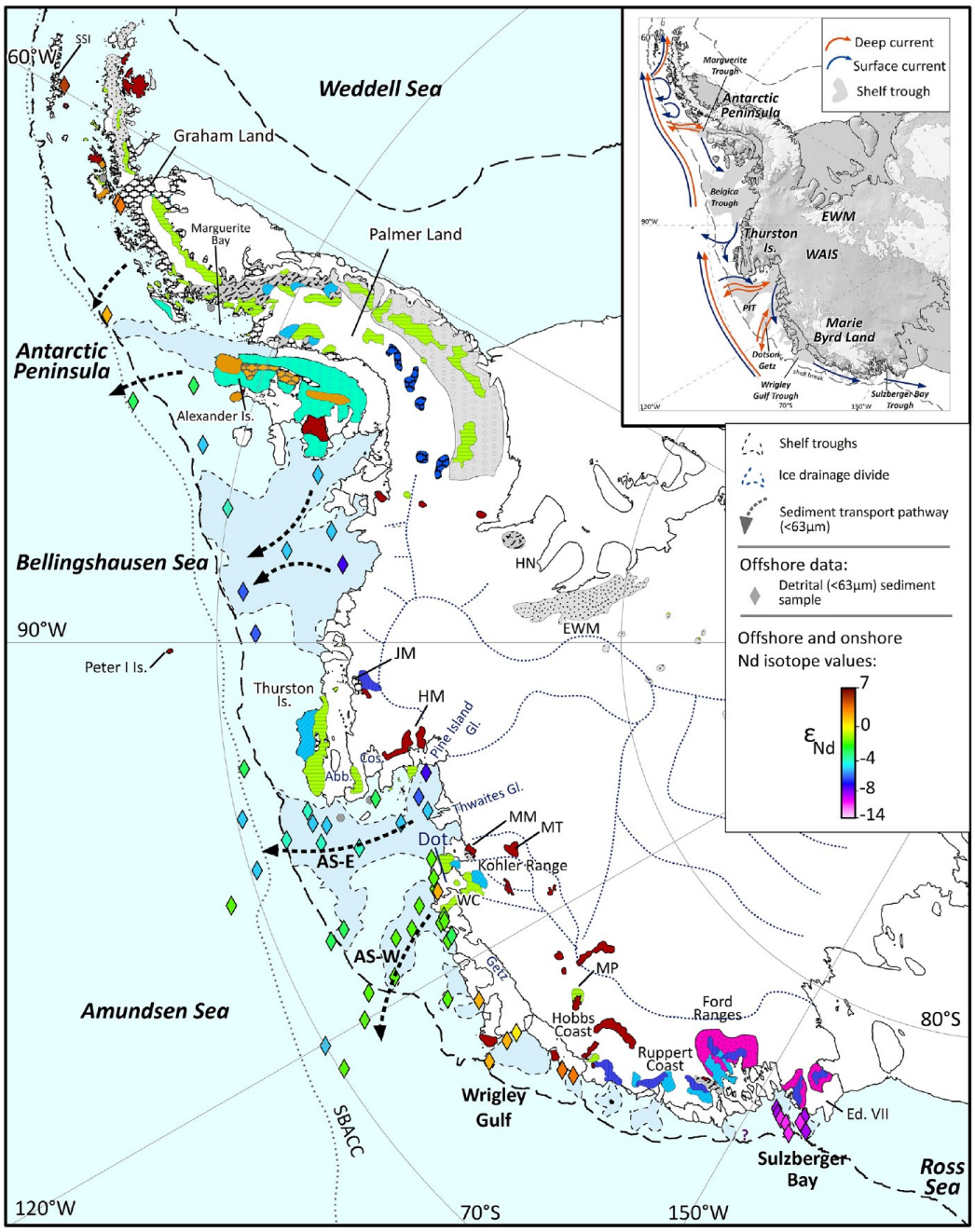

Fig. 9. Distribution of Nd isotope composition (ε_{Nd}) in marine sediments and terrestrial rocks. The geology is based on Fig. 2. Note: Colour scheme for outcrops is based on the average Nd isotopic composition of the lithology (see Appendix S2 for data assimilated from the literature). Geological units which could not be assigned a Nd isotope fingerprint are shown in grey. Two different colours were assigned to the Antarctic Peninsula Volcanic Group depending on the regional geochemical variation of these rocks (e.g. Riley et al., 2001, see Appendix S2 and text). Dashed black lines delineate the approximate location of the shelf break. Black dashed arrows denote major fine-grained (< 63um) transport pathways. Abbreviations and inlet figure same as for Fig. 2.

margin of West Antarctica. Figure 10 presents provenance characteristics compiled from our new data set and previously published studies for five different West Antarctic sectors. An erosional source from the Antarctic Peninsula is best identified by a predominance of $^{40}Ar/^{39}Ar$ ages spanning 30–90 Ma in coarse-grained IRD and a very radiogenic fingerprint of fine-grained detrital sediments (ε_{Nd} up to +0.9 and $^{87}Sr/^{86}Sr$ ratios down to 0.705). The only other West Antarctic area that exhibits similar characteristics is the Hobbs Coast, where most biotite

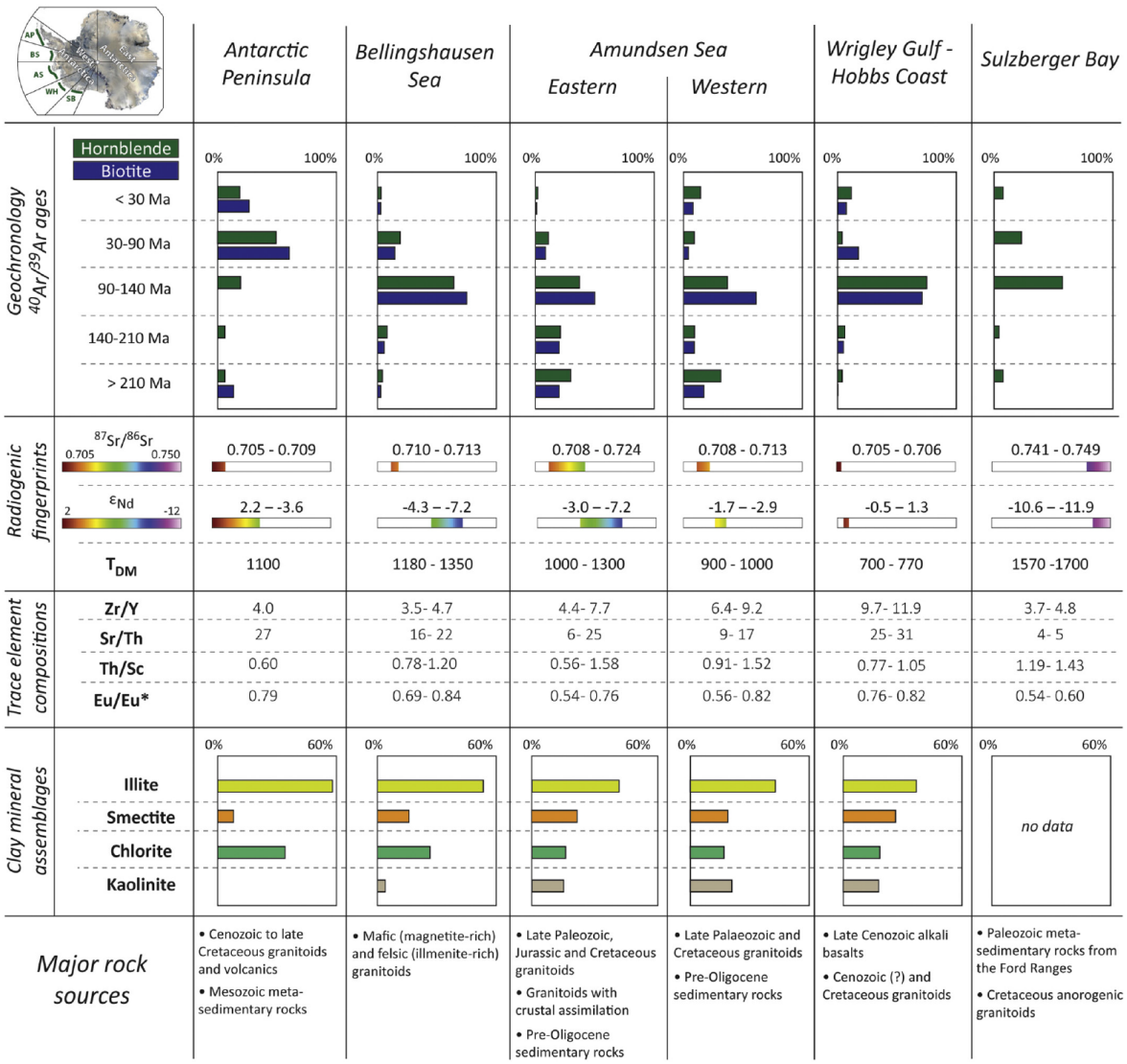

Fig. 10. Summary figure of geochemical and clay mineralogical provenance characteristics of different sectors along the Pacific margin of West Antarctica as derived from analyses of detrital marine sediments. Clay mineral assemblages are taken from Hillenbrand and Ehrmann (2002), Hillenbrand et al. (2003, 2009b) and Ehrmann et al. (2011), and major terrestrial rock sources are compiled from the literature (see text for further details).

and hornblende $^{40}Ar/^{39}Ar$ ages are, however, older (90–140 Ma) and Nd model ages are younger (700 to 770 Ma). Both areas are also relatively far apart from each other, which should not impede their respective identification in down-core studies on marine sediment cores collected proximal to these source regions. The Bellingshausen Sea sector shows a predominance of IRD $^{40}Ar/^{39}Ar$ ages around ~110 Ma, which are similar to those from the Wrigley Gulf-Hobbs Coast sector (~100 Ma), but the fine-grained detritus in the former sector has lower Nd values and higher $^{87}Sr/^{86}Sr$ ratios ($\varepsilon_{Nd} = -4.3$ to -7.2; $^{87}Sr/^{86}Sr = 0.710–0.713$), as well as significantly older Nd model ages (1180–1350 Ma). The oldest protolith ages in West Antarctica are indicated by Nd model ages of 1570 to 1700 Ma in Sulzberger Bay, which also stands out by the unradiogenic isotope fingerprint of fine-grained detrital sediments ($\varepsilon_{Nd} < -10.6$; $^{87}Sr/^{86}Sr > 0.741$).

Finally, a more detailed picture starts emerging for the Amundsen Sea sector, the locus of major glacial ice loss in Antarctica today. While both the eastern and western AS sub-sectors are characterized by hornblende and biotite ages of ~110 Ma and 240–260 Ma, ages of 140 to 210 Ma are more prevalent in the eastern ASE. Furthermore, source rocks to the eastern ASE seem to extend to older Nd model ages (up to 1300 Ma, $\varepsilon_{Nd} = -7.2$) than in the western ASE (900–1000 Ma, $\varepsilon_{Nd} = -1.7$ to -2.9). Further studies are required to reveal whether this observation points to a distinct bedrock source under Pine Island Glacier, a result with major implications for tracing past WAIS retreat and collapse.

9. Conclusions

We here report for the first time a detailed geochemical approach to unraveling different provenance sectors along the Pacific margin of

West Antarctica. By investigating the fingerprints of fine-grained terrigenous detritus and coarse-grained ice-rafted debris in ice-sheet proximal to distal marine sediments of Late Holocene age, we draw the following conclusions:

(1) Thermochronological $^{40}Ar/^{39}Ar$ dating on individual mineral grains highlights the Phanerozoic history of West Antarctica. Hornblende and biotite ages can be readily associated with extensively outcropping granites and granodiorites and allow us to distinguish the following sectors: Antarctic Peninsula (~52 and ~74 Ma), Bellingshausen Sea, Wrigley Gulf-Hobbs Coast and Sulzberger Bay sectors (~100–110 Ma) and Amundsen Sea sector (~100–110 Ma and ~140 to 360 Ma). $^{40}Ar/^{39}Ar$ dating of hornblende and biotite grains is less suitable for detecting Late Cenozoic alkali basalts and metasedimentary units around West Antarctica (i.e. mineralogical or grain-size bias).
(2) Strontium (Sr) and neodymium (Nd) isotopic compositions in fine-grained detrital sediments match the coastal geology, and observed geochemical variability can be readily related to genetic and lithological differences in source rocks. Data range from radiogenic values around the (young) Antarctic Peninsula ($\varepsilon_{Nd} = -3.6$ to $+0.9$; $^{87}Sr/^{86}Sr = 0.705–0.709$) to less radiogenic values around the Sulzberger Bay, where mantle extraction ages point to a much older protolith (up to 1700 Ma). An exciting finding is a potentially distinct geological source (i.e. Cretaceous granites that experienced extensive crustal assimilation) beneath Pine Island Glacier, which was identified in the radiogenic isotope composition of fine-grained sediments near its calving front. While major Palaeozoic to Mesozoic geological units in West Antarctica are identified in the provenance of the marine sediments, the fine fraction analyses prove particularly useful in detecting Late Cenozoic alkali basalts and metasedimentary rocks, as well as distinguishing A-type granites and granites with pronounced crustal assimilation signatures.
(3) Despite an overall small variation of trace element compositions in marine detrital sediments off West Antarctica, they nevertheless complement isotopic provenance analyses and are broadly indicative of mafic and felsic source rocks. Significant variability within individual ice drainage basins may prove useful for provenance studies on the local to regional scale, as indicated by contrasting hinterland geology between the eastern and western Bellingshausen Sea, the eastern and western Amundsen Sea embayment, Wrigley Gulf-Hobbs Coast and Sulzberger Bay.
(4) Combined provenance studies on different size fractions of detrital sediments enable monitoring of modern sediment transport pathways. For example, the occurrence of ~140–210 Ma old ice-rafted grains in the western Amundsen Sea sector, which originate from the eastern coast of the Amundsen Sea Embayment, highlights the modern pathway of wind-driven iceberg trajectories within the area. On the other hand, fine-grained sediments can additionally be transported by currents, as exemplified by an evolving radiogenic isotope signature from Pine Island Bay towards the shelf break.

Our study highlights the importance of integrated studies for identifying the geochemical fingerprints of individual ice drainage basins around West Antarctica. Such modern-day studies do not only provide the basis for any attempts to reconstruct ice drainage patterns and ice sheet extent in West Antarctica during the past, but also allow valuable insights into the geology under the ice. Towards this end it would be beneficial to conduct future work on building a large and comprehensive onshore and offshore data base of U-Pb zircon ages.

Acknowledgments

P. Simões Pereira acknowledges the Kristian Gerhard Jebsen Foundation for supporting his PhD scholarship. S. Brachfeld and C. Doherty acknowledge support from National Science Foundation grant 0348274. We thank B. Coles and K. Kreissig for their assistance in the lab, W. Ehrmann for analysing the clay mineral assemblages on several samples and T. Riley for constructive discussions. We also thank the shipboard scientific parties, captains, officers and crews of the various expeditions. The careful and constructive comments of the two anonymous reviewers are gratefully acknowledged. This research used samples provided by the Antarctic Marine Geology Research Facility (AMGRF) formerly at Florida State University.

Appendix A. Supplementary data

Supplementary data to this article can be found online at https://doi.org/10.1016/j.earscirev.2018.04.011.

References

Adams, C.J., 1987. Geochronology of granite terranes in the Ford Ranges, Marie Byrd Land, West Antarctica. N. Z. J. Geol. Geophys. 30, 51–57.
Adams, C.J., Seward, D., Weaver, S.D., 1995. Geochronology of Cretaceous granites and metasedimentary basement on Edward VII Peninsula, Marie Byrd Land, West Antarctica. Antarct. Sci. 7 (3), 265–277.
Adams, C.J., Pankhurst, R.J., Maas, R., Millar, I.L., 2005. Nd and Sr isotopic signatures of metasedimentary rocks around the South Pacific margin and implications for their provenance. In: Vaughan, A.P.M., Leat, P.T., Pankhurst, R.J. (Eds.), Terrane Processes at the Margins of Gondwana. vol. 246. Geological Society, London, Special Publications, pp. 113–141.
Aitken, A.E., Bell, T.J., 1998. Holocene glacimarine sedimentation and macrofossil palaecology in the Canadian High Arctic: environmental controls. Mar. Geol. 145, 151–171.
Aitken, A.R.A., Young, D.A., Ferraccioli, F., Betts, P.G., Greenbaum, J.S., Richter, T.G., Roberts, J.L., Blankenship, D.D., Siegert, M.J., 2014. The subglacial geology of Wilkes Land, East Antarctica. Geophys. Res. Lett. 41, 2390–2400.
Arneborg, L., Wåhlin, A.K., Björk, G., Liljebladh, B., Orsi, A.H., 2012. Persistent inflow of warm water onto the central Amundsen shelf. Nat. Geosci. 5, 876–880. http://dx.doi.org/10.1038/ngeo1644.
Assmann, K.M., Hellmer, H.H., Jacobs, S.S., 2005. Amundsen Sea ice production and transport. J. Geophys. Res. 110, C12013.
Assmann, K., Jenkins, A., Shoosmith, D., Walker, D., Jacobs, S.S., Nicholls, K., 2013. Variability of circumpolar deep water transport onto the Amundsen Sea continental shelf through a shelf break trough. J. Geophys. Res. 118, 6603–6620.
Bamber, J.L., Riva, R.E.M., Vermeersen, B.L.A., LeBrocq, A.M., 2009. Reassessment of the potential sea-level rise from a collapse of the West Antarctic Ice Sheet. Science 324, 901–903.
Bayon, G., Burton, K.W., Soulet, G., Vigier, N., Dennielou, B., Etoubleau, J., Ponzevera, E., German, C.R., Nesbitt, R.W., 2009. Hf and Nd isotopes in marine sediments: constraints on global silicate weathering. Earth Planet. Sci. Lett. 277, 318–326.
Bingham, R.G., Ferraccioli, F., King, E.C., Larter, R.D., Pritchard, H.D., Smith, A.M., Vaughan, D.G., 2002. Inland thinning of West Antarctic Ice Sheet steered along subglacial rifts. Nature 487, 468–471.
Biscaye, P.E., 1965. Mineralogy and sedimentation of recent deep-sea clay in Atlantic Ocean and adjacent seas and oceans. GSA Bull. 76, 803–832.
Blum, J., Erel, Y., 1997. Rb-Sr isotope systematics of a granitic soil chronosequence: the importance of biotite weathering. Geochim. Cosmochim. Acta 61 (15), 3193–3204.
Boger, S.D., 2011. Antarctica — Before and after Gondwana. Gondwana Res. 19, 335–371.
Bradshaw, J.D., Pankhurst, R.J., Weaver, S.D., Storey, B.C., Muir, R.J., Ireland, T.R., 1997. New Zealand Superterranes recognized in Marie Byrd Land and Thurston Island. In: Ricci, C.A. (Ed.), The Antarctic Region: Geological Evolution and Processes, pp. 429–436.
Burn, R.W., 1984. The geology of the LeMay Group, Alexander Island. Sci. Rep. Br. Antarct. Surv. 109.
Burton-Johnson, A., Riley, T.R., 2015. Autochthonous v. accreted terrane development of continental margins: a revised in situ tectonic history of the Antarctic Peninsula. J. Geol. Soc. 172, 822–835.
Care, B.W., 1983. The petrology of the Rouen Mountains, northern Alexander Island. Br. Antarct. Surv. Bull. 52, 63–86.
Carvajal, G.K., Wåhlin, A.K., Eriksson, L.E.B., Ulander, L.M.H., 2013. Correlation between synthetic aperture radar surface winds and deep water velocity in the Amundsen Sea, Antarctica. Remote Sens. 5, 4088–4106. http://dx.doi.org/10.3390/rs5084088.
Cawood, P.A., 2005. Terra Australis Orogen: Rodinia breakup and development of the Pacific and Iapetus margins of Gondwana during the Neoproterozoic and Paleozoic. Earth Sci. Rev. 69, 249–279.
Colville, E.J., Carlson, A.E., Beard, B.L., Hatfield, R.G., Stoner, J.S., Reyes, A.V., Ullman, D.J., 2011. Sr-Nd-Pb isotope evidence for ice-sheet presence on Southern Greenland during the last interglacial. Science 333 (6042), 620–623.
Cook, C.P., van de Flierdt, T., Williams, T., Hemming, S.R., Iwai, M., Kobayashi, M., Jimenez-Espejo, F.J., Escutia, C., González, J.J., Khim, B.-K., McKay, R.M., Passchier, S., Bohaty, S., Riesselman, C.R., Tauxe, L., Sugisaki, S., Galindo, A.L., Patterson, M.O., Sangiorgi, F., Pierce, E.L., Brinkhuis, H., Expedition 318 Scientists, I.O.D.P., 2013. Dynamic behaviour of the East Antarctic ice sheet during Pliocene warmth. Nat. Geosci. 6, 765–769.

Cook, C.P., Hill, D.J., van de Flierdt, T., Williams, T., Hemming, S.R., Dolan, A.M., Pierce, E.L., Escutia, C., Harwood, D., Cortese, G., Gonzales, J.J., 2014. Sea surface temperature control on the distribution of far-travelled Southern Ocean ice-rafted detritus during the Pliocene. Paleoceanography 29. http://dx.doi.org/10.1002/2014PA002625.

Cook, C.P., Hemming, S.R., van de Flierdt, T., Pierce Davis, E.L., Williams, T., Galindo, A.L., Jimenez-Espejo, F.J., Escutia, C., 2017. Glacial erosion of East Antarctica in the Pliocene: a comparative study of multiple marine sediment provenance tracers. Chem. Geol. 466, 199–218.

Cunningham, A.P., Larter, R.D., Barker, P.F., Gohl, K., Nitsche, F.O., 2002. Tectonic evolution of the Pacific margin of Antarctica 2. Structure of Late Cretaceous–early Tertiary plate boundaries in the Bellingshausen Sea from seismic reflection and gravity data. J. Geophys. Res. Solid Earth 107 (B12) (EPM 6-1 EPM 6-20). https://doi.org/10.1029/2002JB001897.

Dalrymple, G.B., Alexander Jr., E.C., Lanphere, M.A., Kraker, G.P., 1981. Irradiation of samples for 40Ar/39Ar dating using the Geological Survey TRIGA reactor. In: U.S. Geological Survey Professional Paper 1176.

Dalziel, I.W.D., Elliot, D.H., 1982. West Antarctica: problem child of Gondwanaland. Tectonics 1 (1), 3–19.

DeConto, R.M., Pollard, D., 2016. Contribution of Antarctica to past and future sea-level rise. Nature 531, 591–597. http://dx.doi.org/10.1038/nature17145.

Diekmann, B., Kuhn, G., 1999. Provenance and dispersal of glacial–marine surface sediments in the Weddell Sea and adjoining areas, Antarctica: ice-rafting versus current transport. Mar. Geol. 158, 209–231.

Doubleday, P.A., Macdonald, D.I.M., Nell, P.A.R., 1993. Sedimentology and structure of the trench-slope to forearc basin transition in the Mesozoic of Alexander Island, Antarctica. Geol. Mag. 130 (6), 737–754.

Downing, G.E., Hemming, S.R., Jost, A., Roy, M., 2013. 40Ar/39Ar hornblende provenance clues about Heinrich event 3 (H3). In: Jourdan, F., Mark, D.F., Verati, C. (Eds.), Advances in 40Ar/39Ar Dating: From Archaeology to Planetary Sciences. 378. Geol. Soc. Lond., Spec. Publ., pp. 245–263.

Ducklow, H.W., Wilson, S.E., Post, A.F., Stammerjohn, S.E., Erickson, M., Lee, S.H., Lowry, K.E., Sherrell, R.M., Yager, P.L., 2015. Particle flux on the continental shelf in the Amundsen Sea Polynya and western Antarctic Peninsula. Elem. Sci. Anth. 3, 000046. http://dx.doi.org/10.12952/journal.elementa.000046.

Ehrmann, W.U., Melles, M., Kuhn, G., Grobe, H., 1992. Significance of clay mineral assemblages in the Antarctic Ocean. Mar. Geol. 107, 249–273.

Ehrmann, W.U., Hillenbrand, C.-D., Smith, J.A., Graham, A.G.C., Kuhn, G., Larter, R.D., 2011. Provenance changes between recent and glacial-time sediments in the Amundsen Sea embayment, West Antarctica: clay mineral assemblage evidence. Antarct. Sci. 23 (5), 471–486.

Eisenhauer, A., Meyer, H., Rachold, V., Tütken, T., Wiegand, B., Hansen, B.T., Spielhagen, R.F., Lindemann, F., Kassens, H., 1999. Grain size separation and sediment mixing in Arctic Ocean sediments: evidence from the strontium isotope systematic. Chem. Geol. 158, 173–188.

Farmer, G.L., Licht, K., 2016. Generation and fate of glacial sediments in the central Transantarctic Mountains based on radiogenic isotopes and implications for reconstructing past ice dynamics. Quat. Sci. Rev. 150, 98–109.

Farmer, G.L., Barber, D., Andrews, J., 2003. Provenance of Late Quaternary ice-proximal sediments in the North Atlantic: Nd, Sr and Pb isotopic evidence. Earth Planet. Sci. Lett. 209, 227–243.

Farmer, G.L., Licht, K., Swope, R.J., Andrews, J., 2006. Isotopic constraints on the provenance of fine-grained sediment in LGM tills from the Ross Embayment, Antarctica. Earth Planet. Sci. Lett. 249, 90–107.

Ferraccioli, F., Bozzo, E., Damaske, D., 2002. Aeromagnetic signatures over western Marie Byrd Land provide insight into magmatic arc basement, mafic magmatism and structure of the Eastern Ross Sea Rift flank. Tectonophysics 347, 139–165.

Ferraccioli, F., Jones, P.C., Vaughan, A.P.M., Leat, P.T., 2006. New aerogeophysical view of the Antarctic Peninsula: more pieces, less puzzle. Geophys. Res. Lett. 33, L05310.

Ferraccioli, F., Armadillo, E., Jordan, T., Bozzo, E., Corr, H., 2009. Aeromagnetic exploration over the East Antarctic Ice Sheet: a new view of the Wilkes Subglacial Basin. Tectonophysics 478 (1–2), 62–77.

Ferrando, R., Roperch, P., Morata, D., Arriagada, C., Ruffet, G., Córdova, M.L., 2014. A paleomagnetic and magnetic fabric study of the Illapel Plutonic Complex, Coastal Range, central Chile: implications for emplacement mechanism and regional tectonic evolution during the mid-Cretaceous. J. S. Am. Earth Sci. 50, 12–26.

Flowerdew, M.J., Millar, I.L., Vaughan, A.P.M., Pankhurst, R.J., 2005. Age and tectonic significance of the Lassiter Coast Intrusive Suite, eastern Ellsworth Land, Antarctic Peninsula. Antarct. Sci. 17, 443–452. http://dx.doi.org/10.1017/S0954102005002877.

Flowerdew, M.J., Tyrrell, S., Riley, T.R., Whitehouse, M.J., Mulvaney, R., Leat, P.T., Marschall, H.R., 2012. Distinguishing East and West Antarctic sediment sources using the Pb isotope composition of detrital K-feldspar. Chem. Geol. 292–293, 88–102. http://dx.doi.org/10.1016/j.chemgeo.2011.11.006.

Fretwell, P., et al., 2013. Bedmap2: improved ice bed, surface and thickness datasets for Antarctica. Cryosphere 7, 375–393.

Futa, K., LeMasurier, W.E., 1983. Nd and Sr isotopic studies on Cenozoic mafic lavas from West Antarctica - another source for continental alkali basalts. Contrib. Mineral. Petrol. 83 (1-2), 38–44.

Gale, A., Dalton, C.A., Langmuir, C.H., Su, Y., Schilling, J.G., 2013. The mean composition of ocean ridge basalts. Geochem. Geophys. Geosyst. 14 (3), 489–518.

Garçon, M., Chauvel, C., France-Lanord, C., Huyghe, P., Lavé, J., 2013. Continental sedimentary processes decouple Nd and Hf isotopes. Geochim. Cosmochim. Acta 121, 177–195. http://dx.doi.org/10.1016/j.gca.2013.07.027.

Garzanti, E., Andò, S., Vezzoli, G., 2008. Settling-equivalence of detrital minerals and grain-size dependence of sediment composition. Earth Planet. Sci. Lett. 273, 138–151.

Garzanti, E., Andò, S., Vezzoli, G., 2009. Grain-size dependence of sediment composition and environmental bias in provenance studies. Earth Planet. Sci. Lett. 277 (3-4), 422–432.

Gladstone, R.M., Bigg, G.R., Nicholls, K.W., 2001. Iceberg trajectory modelling and meltwater injection in the Southern Ocean. J. Geophys. Res. 106, 19903–19915.

Goldstein, S.L., Hemming, S.R., 2003. Long-lived isotopic tracers in oceanography, paleoceanography, and ice-sheet dynamics. In: Treatise on Geochemistry. Elsevier, Oxford.

Gwiazda, R.H., Hemming, S.R., Broecker, W.S., 1996. Provenance of icebergs during Heinrich event 3 and the contrast to their sources during other Heinrich episodes. Paleoceanography 11 (4), 371–378.

Ha, H.K., Wåhlin, A.K., Kim, T.W., Lee, S.H., Lee, J.H., Lee, H.J., Hong, C.S., Arneborg, L., Björk, G., Kalén, O., 2014. Circulation and Modification of warm deep water on the Central Amundsen Shelf. J. Phys. Oceanogr. 44 (5), 1493–1501. https://doi.org/10.1175/JPO-D-13-0240.1.

Harrison, T.M., 1982. Diffusion of 40Ar in hornblende. Contrib. Mineral. Petrol. 78 (3), 324–331.

Harrison, T.M., Duncan, I., Dougall, I., 1985. Diffusion of 40Ar in biotite: temperature, pressure and compositional effects. Geochim. Cosmochim. 49 (11), 2461–2468.

Hart, S.R., Blusztajn, J., LeMasurier, W.E., Rex, D.C., 1997. Hobbs Coast Cenozoic volcanism: implications for the West Antarctic rift system. Chem. Geol. 139 (1-4), 223–248.

Hathway, B., 2001. Sims Island: first data from a Pliocene alkaline volcanic centre in eastern Ellsworth Land. Antarct. Sci. 13 (1), 87–88.

Hemming, S.R., 2004. Heinrich events: massive late Pleistocene detritus layers of the North Atlantic and their global climate imprint. Rev. Geophys. 42, RG1005. http://dx.doi.org/10.1029/2003RG000128.

Hemming, S.R., Hajdas, I., 2003. Ice-rafted detritus evidence from Ar-40/Ar-39 ages of individual hornblende grains for evolution of the eastern margin of the Laurentide ice sheet since 43 C-14 ky. Quat. Int. 99, 29–43.

Hemming, S.R., Broecker, W.S., Sharp, W.D., Bond, G.C., Gwiazda, R.H., McManus, J.F., Klas, M., Hajdas, I., 1998. Provenance of Heinrich layers in core V28-82, northeastern Atlantic: Ar-40/Ar-39 ages of ice-rafted hornblende, Pb isotopes in feldspar grains, and Nd-Sr-Pb isotopes in the fine sediment fraction. Earth Planet. Sci. Lett. 164 (1-2), 317–333.

Hemming, S.R., van de Flierdt, T., Goldstein, S.L., Franzese, A.M., Roy, M., Gastineau, G., Landrot, G., 2007. Strontium isotope tracing of terrigenous sediment dispersal in the Antarctic Circumpolar Current: Implications for constraining frontal positions. Geochem. Geophys. Geosyst. 8 (6).

Hillenbrand, C.-D., Ehrmann, W., 2002. Distribution of clay minerals in drift sediments on the continental rise west of the Antarctic Peninsula, ODP Leg 178, Sites 1095 and 1096. In: Barker, P.F., Camerlenghi, A., Acton, G.D., Ramsay, A.T.S. (Eds.), Proc. ODP Sci. Results. 178. Ocean Drilling Program, Texas A&M University, College Station, TX, U.S.A, pp. 1–29 Available from.

Hillenbrand, C.-D., Fütterer, D.K., Grobe, H., Frederichs, T., 2002. No evidence for a Pleistocene collapse of the West Antarctic Ice Sheet from continental margin sediments recovered in the Amundsen Sea. Geo-Mar. Lett. 22, 51–59.

Hillenbrand, C.-D., Grobe, H., Diekmann, B., Kuhn, G., Fütterer, D.K., 2003. Distribution of clay minerals and proxies for productivity in surface sediments of the Bellingshausen and Amundsen seas (West Antarctica) - Relation to modern environmental conditions. Mar. Geol. 193, 253–271.

Hillenbrand, C.-D., Kuhn, G., Frederichs, T., 2009a. Record of a Mid-Pleistocene depositional anomaly in West Antarctic continental margin sediments: an indicator for ice-sheet collapse? Quat. Sci. Rev. 28, 1147–1159.

Hillenbrand, C.-D., Ehrmann, W., Larter, R.D., Benetti, S., Dowdeswell, J.A., Ó Cofaigh, C., Graham, A.G.C., Grobe, H., 2009b. Clay mineral provenance of sediments in the southern Bellingshausen Sea reveals drainage changes of the West Antarctic Ice Sheet during the Late Quaternary. Mar. Geol. 265 (1–2), 1–18.

Hillenbrand, C.-D., Larter, R.D., Dowdeswell, J.A., Ehrmann, W., Ó Cofaigh, C., Benetti, S., Graham, A.G.C., Grobe, H., 2010a. The sedimentary legacy of a palaeo-ice stream on the shelf of the southern Bellingshausen Sea: clues to West Antarctic glacial history during the Late Quaternary. Quat. Sci. Rev. 29 (19-20), 2741–2763.

Hillenbrand, C.-D., Smith, J.A., Kuhn, G., Esper, O., Gersonde, R., Larter, R.D., Maher, B., Moreton, S.G., Shimmield, T.M., Korte, M., 2010b. Age assignment of a diatomaceous ooze deposited in the western Amundsen Sea Embayment after the Last Glacial Maximum. J. Quat. Sci. 25, 280–295.

Hillenbrand, C.-D., Kuhn, G., Smith, J.A., Gohl, K., Graham, A.G.C., Larter, R.D., Klages, J.P., Downey, R., Moreton, S.G., Forwick, M., Vaughan, D.G., 2013. Grounding-line retreat of the West Antarctic Ice Sheet from inner Pine Island Bay. Geology 41 (1), 35–38. http://dx.doi.org/10.1130/G33469.1.

Hillenbrand, C.-D., Smith, J.A., Hodell, D.A., Greaves, M., Poole, C.R., Kender, S., Williams, M., Andersen, T.J., Jernas, P.E., Elderfield, H., Klages, J.P., Roberts, S.J., Gohl, K., Larter, R.D., Kuhn, G., 2017. West Antarctic Ice Sheet retreat drive by Holocene warm water intrusions. Nature 547, 43–48.

Hofmann, E.E., Klinck, J.M., Lascara, C.M., Smith, D.A., 1996. Water mass distribution and circulation west of the Antarctic Peninsula and including bransfield strait. In: Ross, R.M., Hofmann, E.E., Quetin, L.B. (Eds.), Foundations for Ecological Research West of the Antarctic Peninsula. Antarctic Research Series American Geophysical Union, Washington, D.C., pp. 61–81.

Hole, M.J., LeMasurier, W.E., 1994. Tectonic controls on the geochemical compositions of Cenozoic mafic alkaline volcanic rocks from West Antarctica. Contrib. Mineral. Petrol. 117 (2), 187–202.

Holland, P.R., Jenkins, A., Holland, D.M., 2010. Ice and ocean processes in the Bellingshausen Sea, Antarctica. J. Geophys. Res. 115, C05020. http://dx.doi.org/10.1029/2008JC005219.

Jacobs, S.S., Jenkins, A., Giulivi, C.F., Dutrieux, P., 2011. Stronger ocean circulation and increased melting under Pine Island Glacier ice shelf. Nat. Geosci. 4, 519–523.
Jacobs, S.S., Giulivi, C., Dutrieux, P., Rignot, E., Nitsche, F., Mouginot, J., 2013. Getz ice shelf melting response to changes in ocean forcing. J. Geophys. Res. 118, 4152–4168. http://dx.doi.org/10.1002/jgrc.20298.
Jacobsen, S.B., Wasserburg, G.J., 1980. Sm–Nd isotopic evolution of chondrites. Earth Planet. Sci. Lett. 50, 139–155.
Jenkins, A., Dutrieux, P., Jacobs, S.S., McPhail, S.D., Perrett, J.R., Webb, A.T., White, D., 2010. Observations beneath Pine Island Glacier in West Antarctica and implications for its retreat. Nat. Geosci. 3 (7), 468–472.
Jenkins, A., Dutrieux, P., Jacobs, S.S., Steig, E.J., Gudmundsson, G.H., Smith, J.A., Heywood, E.J., 2016. Decadal ocean forcing and Antarctic ice sheet response: Lessons from the Amundsen Sea. Oceanography 29 (4), 106–117.
Jordan, T.A., Ferraccioli, F., Armadillo, E., Bozzo, E., 2013a. Crustal architecture of the Wilkes Subglacial Basin in East Antarctica, as revealed from airborne gravity data. Tectonophysics 585, 196–206.
Jordan, T.A., Ferraccioli, F., Ross, N., Corr, H.F.J., Leat, P.T., Bingham, R.G., Rippin, D.M., le Brocq, A., Siegert, M.J., 2013b. Inland extent of the Weddell Sea Rift imaged by new aerogeophysical data. Tectonophysics 585, 137–160.
Joughin, I., Alley, R., 2011. Stability of the West Antarctic ice sheet in a warming world. Nat. Geosci. 4, 506–513.
Joughin, I., Smith, B.E., Medley, B., 2014. Marine Ice Sheet Collapse Potentially Under Way for the Thwaites Glacier Basin, West Antarctica. Science 344, 735.
Katz, R.F., Worster, M.G., 2010. Stability of ice-sheet grounding lines. Proc. R. Soc. A 466 (2118), 1597–1620.
Kennedy, D.S., Anderson, J.B., 1989. Glacial-marine sedimentation and quaternary glacial history of Marguerite Bay, Antarctic Peninsula. Quat. Res. 31 (2), 255–276.
Kim, M., Hwang, J., Kim, H., Kim, D., Yang, E., Ducklow, H.W., La, H.S., Lee, S.H., Park, J., Lee, S.H., 2015. Sinking particle flux in the sea ice zone of the Amundsen Shelf, Antarctica. Deep-Sea Res. 101, 110–117. http://dx.doi.org/10.1016/j.dsr.2015.04.002.
Kim, C.-S., Kim, T.-W., Cho, K.-H., Ha, H.K., Lee, S.H., Kim, H.-C., Lee, J.-H., 2016a. Variability of the Antarctic Coastal current in the Amundsen Sea. Estuar. Coast. Shelf Sci. 181, 123–133. http://dx.doi.org/10.1016/j.ecss.2016.08.004.
Kim, I., Hahm, D., Rhe, T.S., Kim, T.W., Kim, C.-S., Lee, S.H., 2016b. The distribution of glacial meltwater in the Amundsen Sea, Antarctica, revealed by dissolved helium and neon. Journal of Geophysical Research: Oceans 121, 1654–1666.
Kipf, A., Mortimer, N., Werner, R., Gohl, K., van de Bogaard, P., Hauff, F., Hoernle, K., 2012. Granitoids and dykes of the Pine Island Bay region, West Antarctica. Antarct. Sci. 24 (5), 473–484. http://dx.doi.org/10.1017/S0954102012000259.
Komar, P.D., Baba, J., Cui, B., 1984. Grain-size analyses of mica within sediments and the hydraulic equivalence of mica and quartz. J. Sediment. Petrol. 54, 1379–1391.
Korhonen, F.J., Saito, S., Brown, M., Siddoway, C.S., Day, J.M.D., 2010. Multiple generations of granite in the Fosdick mountains, Marie byrd land, West Antarctica: Implications for polyphase intracrustal differentiation in a continental margin setting. J. Petrol. 51 (3), 627–670.
Kuiper, K.F., Deino, A., Hilgen, F.J., Krijgsman, W., Renne, P.R., Wijbrans, J.R., 2008. Synchronizing rock clocks of earth history. Science 320 (5875), 500–504.
Lamy, F., Gersonde, R., Winckler, G., Esper, O., Jaeschke, A., Kuhn, G., Ullermann, J., Martinez-Garcia, A., Lambert, F., Kilian, R., 2014. Increased dust deposition in the pacific Southern ocean during glacial periods. Science 343, 403–407.
Larter, R.D., Barker, P.F., 1991. Effects of ridge crest-trench interaction on Antarctic-Phoenix Spreading: Forces on a young subducting plate. J. Geophys. Res. Solid Earth 96 (B12), 19'583–19'607.
Larter, R.D., Cunningham, A.P., Barker, P.F., Gohl, K., Nitsche, F.O., 2002. Tectonic evolution of the Pacific margin of Antarctica 1. Late Cretaceous tectonic reconstructions. J. Geophys. Res. Solid Earth 107 (B12) (EPM 5-1–EPM 5-19). https://doi.org/10.1029/2000JB000052.
Larter, R.D., et al., 2014. Reconstruction of changes in the Amundsen Sea and Bellingshausen Sea sector of the West Antarctic Ice Sheet since the Last Glacial Maximum. Quat. Sci. Rev. 100, 55–86.
Leat, P.T., Scarrow, J.H., Millar, I.L., 1995. On the Antarctic Peninsula batholith. Geol. Mag. 32 (4), 3990412.
Lee, J.-Y., Marti, K., Severinghaus, J.P., Kawamura, K., Yoo, H.-S., Lee, J.B., Kim, J.S., 2006. A redetermination of the isotopic abundances of atmospheric Ar. Geochim. Cosmochim. Acta 70 (17), 4507–4512.
LeMasurier, W.E., Rex, D.C., 1991. The Marie Byrd Land volcanic province and its relation to the Cainozoic West Antarctic rift system. In: Tingey, R.J. (Ed.), The Geology of Antarctica. Oxford University Press, New York, pp. 249–284.
Licht, K.J., Hemming, S.R., 2017. Analysis of Antarctic glacigenic sediment provenance through geochemical and petrologic applications. Quat. Sci. Rev. 164, 1–24.
Licht, K.J., Palmer, E.F., 2013. Erosion and transport by Byrd Glacier, Antarctica during the Last Glacial Maximum. Quat. Sci. Rev. 62, 32–48.
Licht, K.J., Hennessy, A.J., Welke, B.M., 2014. The U-Pb detrital zircon signature of West Antarctic ice stream tills in the Ross embayment, with implications for Last Glacial Maximum ice flow reconstructions. Antarct. Sci. 26 (6), 687–697.
Lindow, J., Kamp, P.J.J., Mukasa, S.B., Kleber, M., Lisker, F., Gohl, K., Kuhn, G., Spiegel, C., 2016. Exhumation history along the eastern Amundsen Sea coast, West Antarctica, revealed by low-temperature thermochronology. Tectonophysics 35, 2239–2257.
Ludwig, K.R., 2003. Isoplot 3.00: A Geochronological Toolkit for Microsoft Excel. Berkeley Geochronology Center, Berkeley, CA.
Maslanyj, M.P., Storey, B.C., 1990. Regional aeromagnetic anomalies in Ellsworth land: Crustal structure and Mesozoic microplate boundaries within West Antarctica. Tectonics 9 (6), 1515–1532.
Mazur, A.K., Wåhlin, A.K., Krężel, A., 2017. An object-based SAR image iceberg detection algorithm applied to the Amundsen Sea. Remote Sens. Environ. 189, 67–83.
McCarron, J.J., Smellie, J.L., 1998. Tectonic implications of fore-arc magmatism and generation of high-magnesian andesites: Alexander Island, Antarctica. J. Geol. Soc. Lond. 155, 269–280.
McCave, I.N., Thornalley, D.J.R., Hall, I.R., 2017. Relation of sortable silt grain-size to deep-sea current speeds: Calibration of the 'Mud Current Meter. Deep-Sea Res. 127, 1–12.
McLennan, S.M., 2001. Relationships between the trace element composition of sedimentary rocks and upper continental crust. Geochem. Geophys. Geosyst. 2 (4). http://dx.doi.org/10.1029/2000GC000109.
McLennan, S.M., Hemming, S.R., McDaniel, D.K., Hanson, G.N., 1993. Geochemical approaches to sedimentation, provenance and tectonics. In: Johnsson, M.J., Basu, A. (Eds.), Processes Controlling the Composition of Clastic Sediments. Geological Society of America Special Paper 284.
Merino, N., Le Sommer, J., Durand, G., Jourdain, N.C., Madec, G., Mathiot, P., Tournadre, J., 2016. Antarctic icebergs melt over the Southern Ocean: Climatology and impact on sea ice. Ocean Model. 104, 99–110.
Miles, T., Lee, S.H., Wåhlin, A., Ha, H.K., Kim, T.W., Assmann, K.M., Schofield, O., 2016. Glider observations of the Dotson Ice Shelf outflow. Deep-Sea Res. 123, 16–29.
Millar, I.L., Pankhurst, R.J., 1987. Rb-Sr geochronology of the region between the Antarctic Peninsula and the Transantarctic Mountains: Haag Nunataks and Mesozoic granitoids. Geophys. Monogr. Ser. 40, 151–160.
Millar, I.L., Pankhurst, R.J., Fanning, C.M., 2002. Basement chronology of the Antarctic Peninsula: recurrent magmatism and anatexis in the Palaeozoic Gondwana Margin. J. Geol. Soc. Lond. 159, 145–157.
Mortimer, N., Gans, P., Calvert, A., Walker, N., 1999. Geology and thermochronometry of the east edge of the Median Batholith (Median Tectonic Zone): a new perspective on Permian to Cretaceous crustal growth of New Zealand. Island Arc 8, 404–425.
Mouginot, J., Rignot, E., Scheuchl, B., 2014. Sustained increase in ice discharge from the Amundsen Sea Embayment, West Antarctica, from 1973 to 2013. Geophys. Res. Lett. 41, 1576–1584.
Mukasa, S.B., Dalziel, I.W.D., 2000. Marie Byrd Land,West Antarctica: Evolution of Gondwana's Pacific margin constrained by zircon U-Pb geochronology and feldspar common-Pb isotopic compositions. GSA Bull. 112 (4), 611–627.
Murphy, E.J., Hofmann, E.E., Watkins, J.L., Johnston, N.M., Piñones, A., Ballerini, T., Hill, S.L., Trathan, P.N., Tarling, G.A., Cavanagh, R.A., Young, E.F., Thorpe, S.E., Fretwell, P., 2013. Comparison of the structure and function of Southern Ocean regional ecosystems: the Antarctic Peninsula and South Georgia. J. Mar. Syst. 109, 22–42.
Naish, T., et al., 2009. Obliquity-paced Pliocene West Antarctic Ice Sheet oscillations. Nature 458, 322–328.
Oppenheimer, M., 1998. Global warming and the stability of the West Antarctic Ice Sheet. Nature 393, 325–332.
Orsi, A.H., Whitworth, T., Nowlin, W.D., 1995. On the meridional extent and fronts of the Antarctic Circumpolar Current. Deep-Sea Research Part I-Oceanographic Research Papers 42 (5), 641–673.
Pankhurst, R.J., Rowley, P.D., 1991. Rb-Sr study of Cretaceous plutons from southern Antarctic Peninsula and eastern Ellsworth Land, Antarctica. In: Thomson, M.R.A., Crame, J.A., Thomson, J.W. (Eds.), Geological Evolution of Antarctica. Cambridge University Press, pp. 1991.
Pankhurst, R.J., Hole, M.J., Brook, M., 1988. Isotope evidence for the origin of Andean granites. R. Soc. Edinburgh Trans. 79, 123–133.
Pankhurst, R.J., Millar, I.L., Grunow, A.M., Storey, B.C., 1993. The Pre-Cenozoic Magmatic History of the Thurston Island Crustal Block, West Antarctica. J. Geophys. Res. 98 (B7), 11'835–11'849.
Pankhurst, R.J., Weaver, S.D., Bradshaw, J.D., Storey, B.C., Ireland, T.R., 1998. Geochronology and geochemistry of pre-Jurassic superterranes in Marie Byrd Land, Antarctica. J. Geophys. Res. Solid Earth 103 (B2), 2529–2547.
Pankhurst, R.J., Riley, T.R., Fanning, C.M., Kelley, S.P., 2000. Episodic Silicic Volcanism in Patagonia and the Antarctic Peninsula: Chronology of Magmatism Associated with the Break-up of Gondwana. J. Petrol. 41 (5), 605–625.
Parada, M.A., Féraud, G., Fuentes, F., Aguirre, L., Morata, D., Larrondo, P., 2005. Ages and cooling history of the Early Cretaceous Caleu pluton: testimony of a switch from a rifted to a compressional continental margin in central Chile. J. Geol. Soc. Lond. 162, 273–287.
Payne, A.J., Vieli, A., Shepherd, A.P., Wingham, D.J., Rignot, E., 2004. Recent dramatic thinning of largest West Antarctic ice stream triggered by oceans. Geophys. Res. Lett. 31, L23401. http://dx.doi.org/10.1029/2004GL021284.
Peck, V.L., Hall, I.R., Zahn, R., Grousset, F., Hemming, S.R., Scourse, J.D., 2007. The relationship of Heinrich events and their European precursors over the past 60 ka BP: a multi-proxy ice-rafted debris provenance study in the North East Atlantic. Quat. Sci. Rev. 26 (7-8), 862–875.
Pierce, E.L., Williams, T., van de Flierdt, T., Hemming, S.R., Goldstein, S.L., Brachfeld, S.A., 2011. Characterizing the sediment provenance of East Antarctica's weak underbelly: The Aurora and Wilkes sub-glacial basins. Paleoceanography 26. http://dx.doi.org/10.1029/2011PA002127.
Pierce, E.L., Hemming, S.R., Williams, T., van de Flierdt, T., Thomson, S.N., Reiners, P.W., Gehrels, G.E., Brachfeld, S.A., Goldstein, S.L., 2014. A comparison of detrital U–Pb zircon, 40Ar/39Ar hornblende, 40Ar/39Ar biotite ages in marine sediments off East Antarctica: Implications for the geology of subglacial terrains and provenance studies. Earth Sci. Rev. 138, 156–178.
Pierce, E.L., van de Flierdt, T., Williams, T., Hemming, S.R., Cook, C.P., Passchier, S., 2017. Evidence for a dynamic East Antarctic ice sheet during the mid-Miocene climate transition. Earth Planet. Sci. Lett. 478, 1–13. http://dx.doi.org/10.1016/j.epsl.2017.08.011.
Pin, C., Bassin, C., 1992. Evaluation of a strontium-specific extraction chromatographic method for isotopic analysis in geological-materials. Anal. Chim. Acta 269 (2),

249–255.
Pin, C., Zalduegui, J.F.S., 1997. Sequential separation of light rare-earth elements, thorium and uranium by miniaturized extraction chromatography: Application to isotopic analyses of silicate rocks. Anal. Chim. Acta 339 (1-2), 79–89.
Pollard, D., DeConto, R.M., 2009. Modelling West Antarctic Ice Sheet growth and collapse through the past five million years. Nature 458, 329–332.
Pritchard, H.D., Arthern, R.J., Vaughan, D.G., Edwards, L.A., 2009. Extensive dynamic thinning on the margins of the Greenland and Antarctic ice sheets. Nature 461, 971–975.
Pritchard, H.D., Ligtenberg, S., Fricker, H., Vaughan, D., van den Broeke, M.R., Padman, L., 2012. Antarctic ice-sheet loss driven by basal melting of ice shelves. Nature 484 (7395), 502–505.
Pudsey, C.J., Camerlenghi, A., 1998. Glacial–interglacial deposition on a sediment drift on the Pacific margin of the Antarctic Peninsula. Antarct. Sci. 10 (3), 286–308.
Randall-Goodwin, E., Meredith, M.P., Jenkins, A., Yager, P.L., Sherrell, R.M., Abrahamsen, E.P., Guerrero, R., Yuan, X., Mortlock, R.A., Gavahan, K., Alderkamp, A.-C., Ducklow, H., Robertson, R., Stammerjohn, S.E., 2015. Freshwater distributions and water mass structure in the Amundsen Sea Polynya region, Antarctica. Elem Sci Anth 3 (1), 000065. http://dx.doi.org/10.12952/journal.elementa.000065.
Reyes, A.V., Carlson, A.E., Beard, B.L., Hatfield, R.G., Stoner, J.S., Winsor, K., Welke, B., Ullman, D.J., 2014. South Greenland ice-sheet collapse during Marine Isotope Stage 11. Nature 510, 525–528.
Richard, S.M., Smith, C.H., Kimbrough, D.L., Fitzgerald, P.G., Luyendyk, B.P., McWilliams, M.O., 1994. Cooling History of the Northern Ford Ranges, Marie Byrd Land, West Antarctica. Tectonics 13 (4), 837–857.
Rickli, J., Gutjahr, M., Vance, D., Fischer Gödde, M., Hillenbrand, C.-D., Kuhn, G., 2014. Neodymium and hafnium boundary contributions to seawater along the West Antarctic continental margin. Earth Planet. Sci. Lett. 394, 99–110.
Rignot, E., Jacobs, S.S., 2002. Rapid Bottom Melting Widespread near Antarctic Ice Sheet Grounding Lines. Science 296, 2020–2023.
Rignot, E., Bamber, J.L., van den Broeke, M.R., Davis, C., Li, Y., van de Berg, W.J., van Meijgaard, E., 2008. Recent Antarctic ice mass loss from radar interferometry and regional climate modelling. Nat. Geosci. 1, 106–110.
Rignot, E., Mouginot, J., Morlighem, M., Seroussi, H., Scheuchl, B., 2014. Widespread, rapid grounding line retreat of Pine Island, Thwaites, Smith, and Kohler glaciers, West Antarctica, from 1992 to 2011. Geophys. Res. Lett. 41, 3'502–3'509.
Riley, T.R., Leat, P.T., Pankhurst, R.J., Harris, C., 2001. Origins of Large Volume Rhyolitic Volcanism in the Antarctic Peninsula and Patagonia by Crustal Melting. J. Petrol. 42 (6), 1043–1065.
Riley, T.R., Leat, P.T., Kelley, S.P., Millar, I.L., Thirlwall, M.F., 2003. Thinning of the Antarctic Peninsula lithosphere through the Mesozoic: evidence from Middle Jurassic basaltic lavas. Lithos 67 (3-4), 163–179.
Riley, T.R., Flowerdew, M.J., Pankhurst, R.J., Leat, P.T., Millar, I.L., Fanning, C.M., Whitehouse, M.J., 2017. A revised geochronology of Thurston Island, West Antarctica, and correlations along the proto-Pacific margin of Gondwana. Antarct. Sci. 29 (1), 47–60.
Roy, M., van de Flierdt, T., Hemming, S.R., Goldstein, S.L., 2007. (40)Ar/(39)Ar ages of hornblende grains and bulk Sm/Nd isotopes of circum-Antarctic glacio-marine sediments: Implications for sediment provenance in the Southern Ocean. Chem. Geol. 244 (3-4), 507–519.
Rutberg, R.L., Hemming, S.R., Goldstein, S.L., 2000. Reduced North Atlantic Deep Water flux to the glacial Southern Ocean inferred from neodymium isotope ratios. Nature 405, 935–938.
Ryan, C.J., 2005. Mesozoic to Cenozoic Igneous Rocks from Northwestern Graham Land: Constraints on the Tectonomagmatic Evolution of the Antarctic Peninsula (PhD thesis). University of Brighton.
Scherer, R.P., Aldahan, A., Tulaczyk, S., Possnert, G., Engelhardt, H., Kamb, B., 1998. Pleistocene collapse of the West Antarctic ice sheet. Science 281 (5373), 82–85.
Schoof, C., 2007. Ice sheet grounding line dynamics: Steady states, stability, and hysteresis. J. Geophys. Res. 112, 133–138.
Shepherd, A., et al., 2012. A reconciled estimate of ice-sheet mass balance. Science 338, 1183–1189.
Smellie, J.L., 1999. Lithostratigraphy of Miocene-Recent, alkaline volcanic fields in the Antarctic Peninsula and eastern Ellsworth Land. Antarct. Sci. 11 (3), 362–378.
Smith, A.M., Vaughan, D.G., Doake, C.S.M., Johnson, A.C., 1999. Surface Lowering of the Ice Ramp at Rothera Point, Antarctic Peninsula, in Response to Regional Climate Change. Ann. Glaciol. 27, 113–118.
Smith, J.A., Hillenbrand, C.-D., Kuhn, G., Larter, R.D., Graham, A.G.C., Ehrmann, W., Moreton, S.G., Forwick, M., 2011. Deglacial history of the West Antarctic Ice Sheet in the western Amundsen Sea Embayment. Quat. Sci. Rev. 30, 488–505.
Smith, A.M., Jordan, T.A., Ferraccili, F., Bingham, R.G., 2013. Influence of subglacial conditions on ice stream dynamics: Seismic and potential field data from Pine Island Glacier, West Antarctica. J. Geophys. Res. Solid Earth 118, 1471–1482.
Smith, J.A., Hillenbrand, C.-D., Kuhn, G., Klages, J.P., Graham, A.G.C., 2014. New constraints on the timing of West Antarctic Ice Sheet retreat in the eastern Amundsen Sea since the Last Glacial Maximum. Glob. Planet. Chang. 122, 224–237.
Smith, J.A., Andersen, T.J., Shortt, M., Gaffney, A.M., Truffer, M., Stanton, T.P., Bindschadler, R., Dutrieux, P., Jenkins, A., 2017. Sub-ice-shelf sediments record history of twentieth-century retreat of Pine Island Glacier. Nature 541, 77–80.
Sokolov, S., Rintoul, S.R., 2009. Circumpolar structure and distribution of the Antarctic Circumpolar Current fronts: 1. Mean circumpolar paths. J. Geophys. Res. 114, C11018. http://dx.doi.org/10.1029/2008JC005108.
Spiegel, C., Lindow, J., Kamp, P.J.J., Meisel, O., Mukasa, S.B., Lisker, F., Kuhn, G., Gohl, K., 2016. Tectonomorphic evolution of Marie Byrd Land – Implications for Cenozoic rifting activity and onset of West Antarctic glaciation. Glob. Planet. Chang. 145, 98–115.
Stammerjohn, S.E., Maksym, T., Massom, R.A.A., Lowry, K.E., Arrigo, K.R., Yuan, X., Raphael, M., Randall-Goodwin, E., Sherrell, R.M., Yager, P.L., 2015. Seasonal sea ice changes in the Amundsen Sea, Antarctica, over the period of 1979–2014. Elem Sci Anth 3. http://dx.doi.org/10.12952/journal.elementa.000055.
Storey, B.C., Dalziel, I.W.D., Garrett, S.W., Grunow, A.M., Pankhurst, R.J., Vennum, W.R., 1988. West Antarctica in Gondwanaland: Crustal blocks, reconstruction and breakup processes. Tectonophysics 155, 381–390.
Storey, B.C., Vaughan, A.P.M., Millar, I.L., 1996. Geodynamic evolution of the Antarctic Peninsula during Mesozoic times and its bearing on Weddell Sea history. Geol. Soc. Lond., Spec. Publ. 108, 87–103.
Struve, T., van de Flierdt, T., Burke, A., Robinson, L.F., Hammond, S.J., Crocket, K.C., Bradtmiller, L.I., Auro, M.E., Mohamed, K.J., White, N.J., 2016. Neodymium isotopes and concentrations in aragonitic scleractinian cold-water coral skeletons - Modern calibration and evaluation of palaeo-applications. Chem. Geol. 453, 146–168.
Tanaka, T., Togashi, S., Kamioka, H., Amakawa, H., Kagami, H., Hamamoto, T., Yuhara, M., Orihashi, Y., Yoneda, S., Shimizu, H., Kunimaru, T., Takahashi, K., Yanagi, T., Nakano, T., Fujimaki, H., Shinjo, R., Asahara, Y., Tanimizu, M., Dragusanu, C., 2000. JNdi-1: a neodymium isotopic reference in consistency with LaJolla neodymium. Chem. Geol. 168 (3-4), 279–281.
Taylor, S.R., McLennan, S.M., 1995. The geochemical evolution of the continental crust. Rev. Geophys. 33 (2), 241–265.
The RAISED Consortium, 2014. A community-based geological reconstruction of Antarctic Ice Sheet deglaciation since the Last Glacial Maximum. Quat. Sci. Rev. 100, 1–9.
Thoma, M., Jenkins, A., Holland, D., Jacobs, S., 2008. Modelling Circumpolar Deep Water intrusions on the Amundsen Sea continental shelf, Antarctica. Geophys. Res. Lett. 35, L18602. http://dx.doi.org/10.1029/2008GL034939.
Tournadre, J., Bouhier, N., Girard-Ardhuin, F., Rémy, F., 2016. Antarctic icebergs distribution 1992–2014. J. Geophys. Res. 121 (1), 327–349.
Tucholke, B.E., Hollister, C.D., Weaver, F.M., Vennum, W.R., 1976. Continental rise and abyssal plain sedimentation in the Southeast Pacific Basin — leg 35 Deep Sea Drilling Project. In: Hollister, C.D., Craddock, C. (Eds.), Initial Rep. Deep Sea Drill. Proj. vol. 35. pp. 291–300.
Turner, J., Orr, A., Gudmundsson, G.H., Jenkins, A., Bingham, R.G., Hillenbrand, C.-D., Bracegirdle, T.J., 2017. Atmosphere-ocean-ice interactions in the Amundsen Sea Embayment, West Antarctica. Rev. Geophys. 55. http://dx.doi.org/10.1002/2016RG000532.
Underwood, M.B., Pickering, K.T., 1996. Clay-mineral provenance, sediment dispersal patterns, and mudrock diagenesis in the Nankai accretionary prism, southwest Japan. Clay Clay Miner. 44 (3), 339–356.
van de Flierdt, T., Goldstein, S.L., Hemming, S.R., Roy, M., Frank, M., Halliday, A.N., 2007. Global neodymium-hafnium isotope systematics – revisited. Earth Planet. Sci. Lett. 259 (3-4), 432–441.
van de Flierdt, T., Hemming, S.R., Goldstein, S.L., Gehrels, G., Cox, S.E., 2008. Evidence against a young volcanic origin of the Gamburtsev Subglacial Mountains, Antarctica. Geophys. Res. Lett. 35 (21), L21303. http://dx.doi.org/10.1029/2008GL035564.
Vaughan, A.P.M., Storey, B.C., 2000. The eastern Palmer Land shear zone: a new terrane accretion model for the Mesozoic development of the Antarctic Peninsula. J. Geol. Soc. 157, 1243–1256.
Vaughan, A.P.M., Wareham, C.D., Johnson, A.C., Kelley, S.P., 1998. A Lower Cretaceous, syn-extensional magmatic source for a linear belt of positive magnetic anomalies: the Pacific Margin Anomaly (PMA), western Palmer Land, Antarctica. Earth Planet. Sci. Lett. 158, 143–155.
Vaughan, D.G., Barnes, D.K.A., Fretwell, P.T., Bingham, R.G., 2011. Potential seaways across West Antarctica. Geochem. Geophys. Geosyst. 12 (10), Q10004. http://dx.doi.org/10.1029/2011GC003688.
Vaughan, A.P.M., Eagles, G., Flowerdew, M.J., 2012a. Evidence for a two-phase Palmer Land event from crosscutting structural relationships and emplacement timing of the Lassiter Coast Intrusive Suite, Antarctic Peninsula: Implications for mid-Cretaceous Southern Ocean plate configuration. Tectonics 31, TC1010.
Vaughan, A.P.M., Storey, B.C., Kelley, S.P., Barry, T.L., Curtis, M.L., 2012b. Synkinematic emplacement of Lassiter Coast Intrusive Suite plutons during the Palmer Land Event: evidence for mid-Cretaceous sinistral transpression at the Beaumont Glacier in eastern Palmer Land. J. Geol. Soc. 169, 759–771.
Veevers, J.J., Saeed, A., 2013. Age and composition of Antarctic sub-glacial bedrock reflected by detrital zircons, erratics, and recycled microfossils in the Ellsworth Land–Antarctic Peninsula–Weddell Sea–Dronning Maud Land sector (240°E–0°–015°E). Gondwana Res. 23, 296–332.
Wåhlin, A.K., Yuan, X., Björk, G., Nohr, C., 2010. Inflow of warm Circumpolar Deep Water in the Central Amundsen Shelf. J. Phys. Oceanogr. 40 (6), 1427–1434.
Wåhlin, A.K., Muench, R.D., Arneborg, L., Björk, G., Ha, H.K., Lee, S.H., Alsén, H., 2012. Some implications of Ekman layer dynamics for cross-shelf exchange in the Amundsen Sea. J. Phys. Oceanogr. 42 (9), 1461–1474.
Wåhlin, A.K., Kalén, O., Arneborg, L., Björk, G., Carvajal, G.K., Ha, H.K., Kim, T.W., Lee, S.H., Stranne, C., 2013. Variability of warm deep water inflow in a submarine trough on the Amundsen Sea shelf. J. Phys. Oceanogr. 43, 2054–2070.
Wåhlin, A.K., Kalén, O., Assmann, K., Darelius, E., Ha, H.K., Lee, S.H., 2016. Sub-inertial oscillations on the central Amundsen Shelf. J. Phys. Oceanogr. 46 (9), 2573–2582. http://dx.doi.org/10.1175/JPO-D-14-0257.1.
Walker, D.P., Brandon, M.A., Jenkins, A., Allen, J.T., Dowdeswell, J.A., Evans, J., 2007. Oceanic heat transport onto the Amundsen Sea shelf through a submarine glacial trough. Geophys. Res. Lett. 34, L02602.
Walker, D.P., Jenkins, A., Assmann, K., Shoosmith, D.R., Brandon, M.A., 2013. Oceanographic observations at the shelf break of the Amundsen Sea, Antarctica. Journal of Geophysical Research: Oceans 118, 2906–2918.
Walter, H.J., Hegner, E., Diekmann, B., Kuhn, G., Rutgers van der Loeff, M.M., 2000.

Provenance and transport of terrigenous sediment in the South Atlantic Ocean and their relations to glacial and interglacial cycles: Nd and Sr isotopic evidence. Geochim. Cosmochim. Acta 64 (22), 3814–3827.
Weaver, S.D., Adams, C.J., Pankhurst, R.J., Gibson, I.L., 1992. Granites of Edward VII Peninsula, Marie Byrd Land: anorogenic magmatism related to Antarctic-New Zealand rifting. Trans. R. Soc. Edinb. Earth Sci. 83 (1-2), 281–290.
Weis, D., Kieffer, B., Maerschalk, C., Barling, J., de Jong, J., Williams, G.A., Hanano, D., Pretorius, W., Mattielli, N., Scoates, J.S., Goolaerts, A., Friedman, R.M., Mahoney, J.B., 2006. High-precision isotopic characterization of USGS reference materials by TIMS and MC-ICP-MS. Geochem. Geophys. Geosyst. 7 (8). http://dx.doi.org/10.1029/2006GC001283.
Welke, B., Licht, K., Hennessy, A., Hemming, S.R., Pierce Davis, E.L., Kassab, C., 2016. Applications of detrital geochronology and thermochronology from glacial deposits to the Paleozoic and Mesozoic thermal history of the Ross Embayment, Antarctica. Geochem. Geophys. Geosyst. 17, 2762–2780.
Wendt, A.S., Vaughan, A.P.M., Tate, A., 2008. Metamorphic rocks in the Antarctic Peninsula region. Geol. Mag. 145 (5), 1–22.
Williams, T., van de Flierdt, T., Hemming, S.R., Chung, E., Roy, M., Goldstein, S.L., 2010. Evidence for iceberg armadas from East Antarctica in the Southern Ocean during the late Miocene and early Pliocene. Earth Planet. Sci. Lett. 290 (3-4), 351–361.
Wise, M.G., Dowdeswell, J.A., Jakobsson, M., Larter, R.D., 2017. Evidence of marine ice-cliff instability in Pine Island Bay from iceberg-keel plough marks. Nature 550, 506. http://dx.doi.org/10.1038/nature24458.

Appendix Figure 2.1. Leaching tests on five seafloor surface sediments on the Pacific sector of West Antarctica and one downcore sediment from core site PS58/254-1 (see Appendix Table 2.3 for full dataset and leaching procedures).

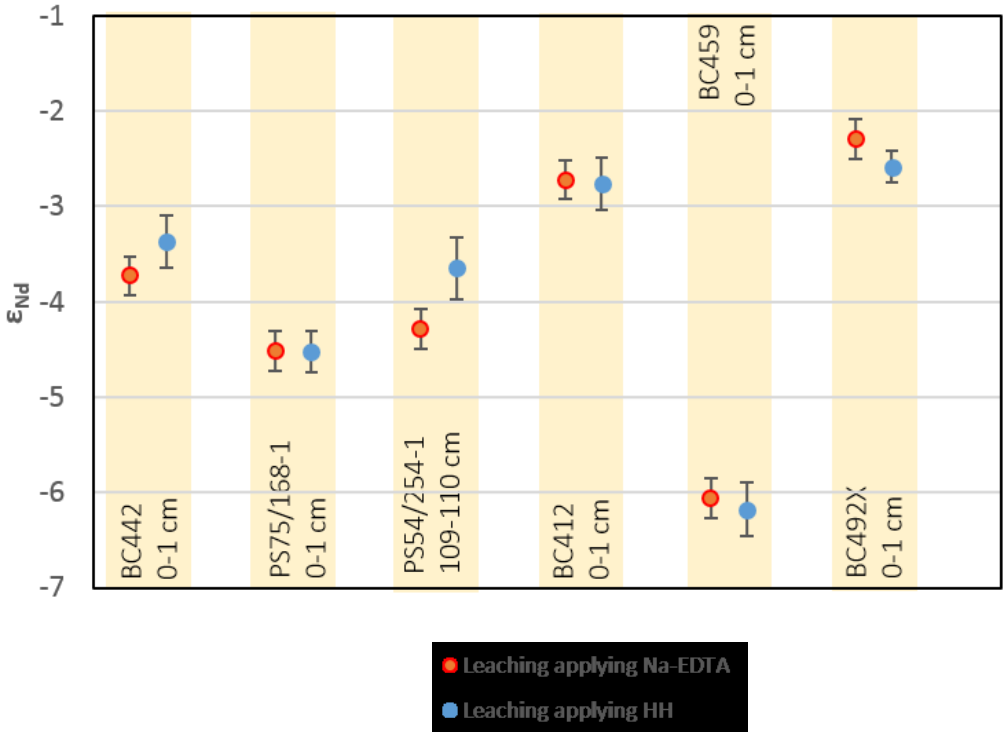

Appendix Figure 3.1 Lithology of core sites PS104/009-1, PS104/012-2, PS104/021-1, PS75/173 and PS75/177 (PI: Claus-Dieter Hillenbrand)

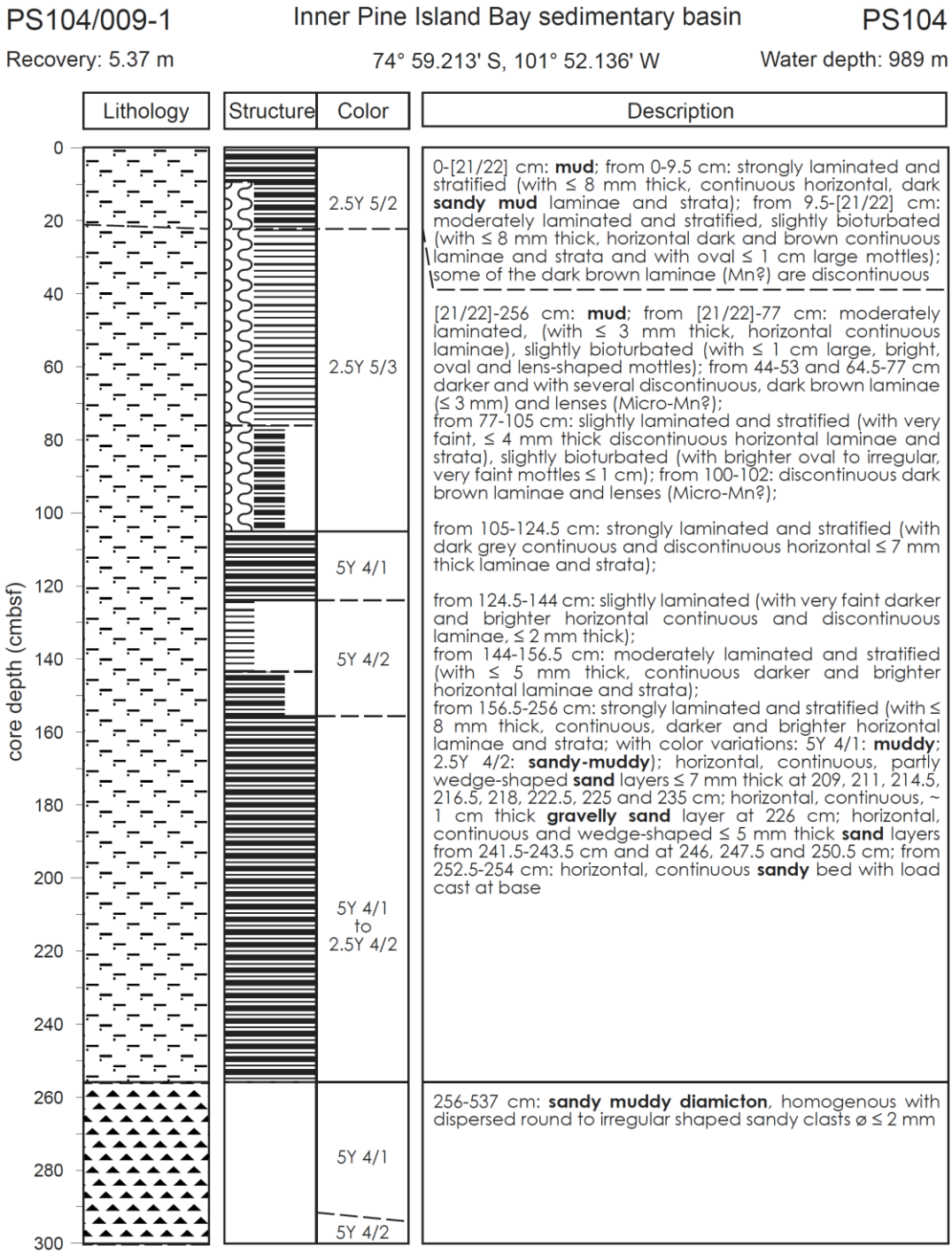

(continues on next page)

PS104/009-1 Inner Pine Island Bay sedimentary basin PS104

Recovery: 5.37 m 74° 59.213' S, 101° 52.136' W Water depth: 989 m

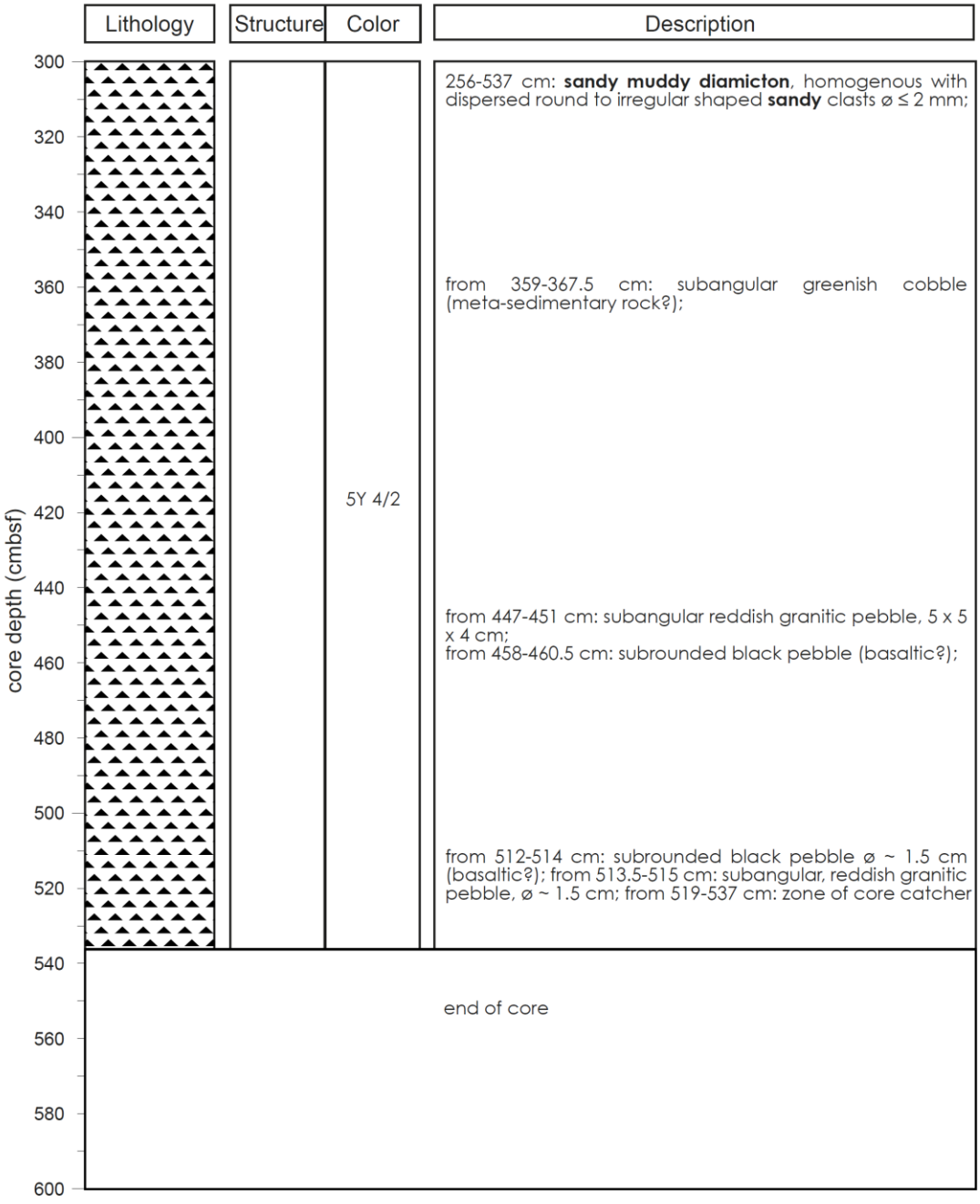

(continues on next page)

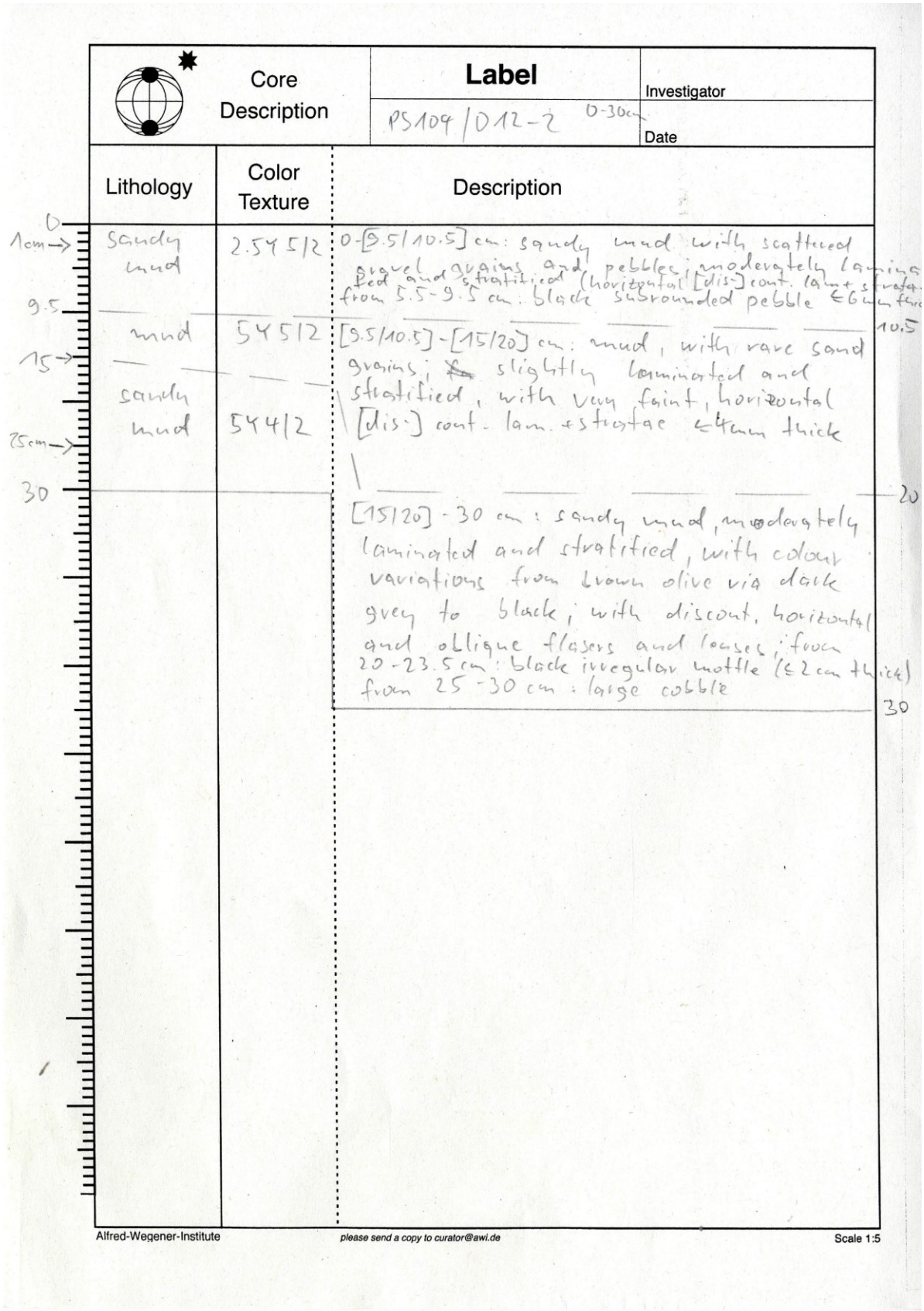

Core Description

Label

PS109/012-2 0-30cm

Investigator

Date

Lithology	Color Texture	Description
sandy mud	2.5Y 5/2	0-[9.5/10.5] cm: sandy mud with scattered gravel grains and pebbles; moderately laminated and stratified (horizontal [dis.] cont. lam. + strata from 5.5-9.5 cm: black subrounded pebble ∈6cm fro
mud	5Y 5/2	[9.5/10.5]-[15/20] cm: mud, with rare sand grains; ~~&~~ slightly laminated and stratified, with very faint, horizontal [dis.] cont. lam. + strata ∈4mm thick
sandy mud	5Y 4/2	[15/20]-30 cm: sandy mud, moderately laminated and stratified, with colour variations from brown olive via dark grey to black; with discont. horizontal and oblique flasers and lenses; from 20-23.5 cm: black irregular mottle (∈2 cm thick) from 25-30 cm: large cobble

Alfred-Wegener-Institute please send a copy to curator@awi.de Scale 1:5

(continues on next page)

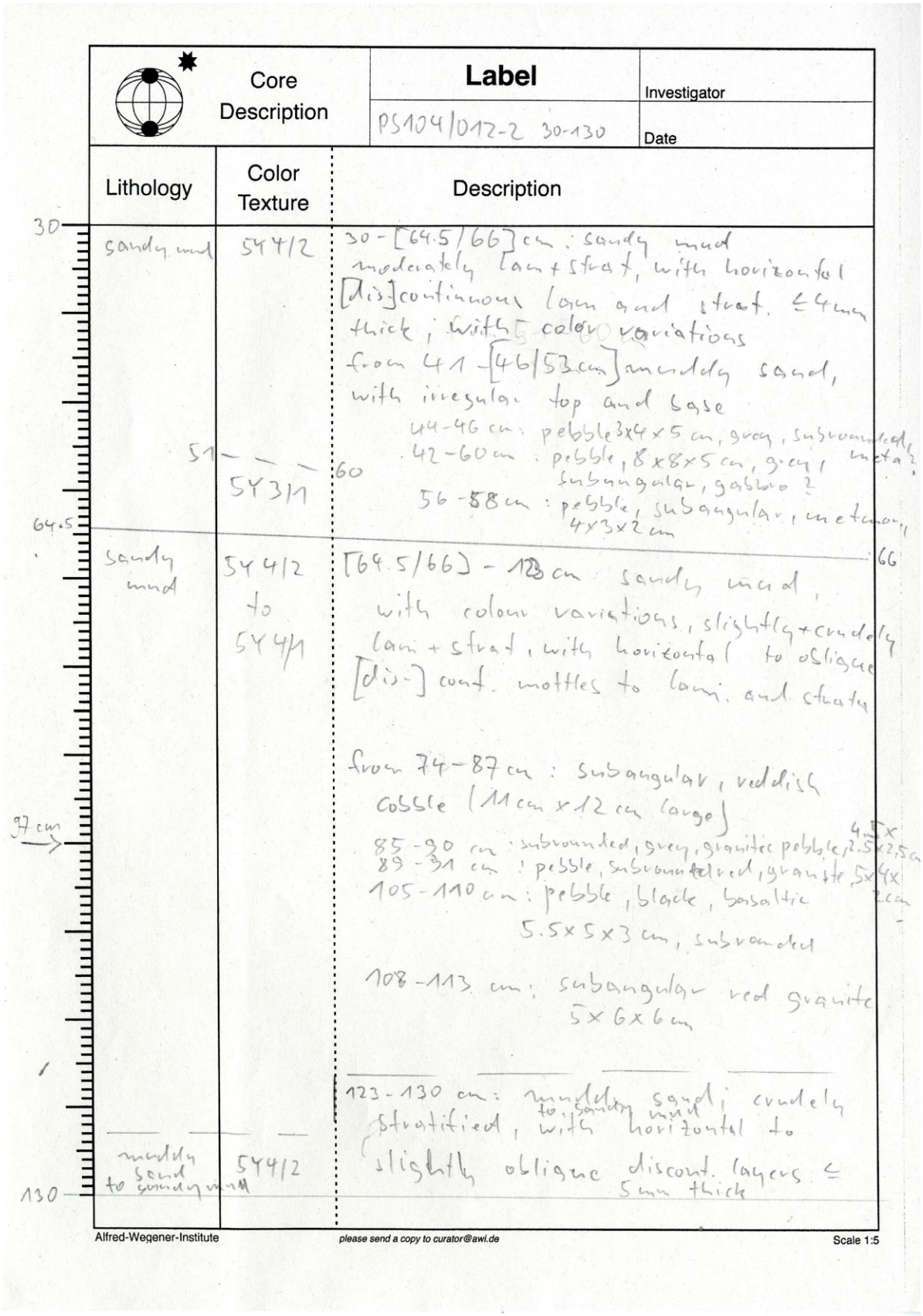

Core Description

Label

PS104/012-2 30-130

Investigator

Date

Lithology	Color Texture	Description
sandy mud	5Y4/2	30 - [64.5/66] cm: sandy mud moderately lam + strat, with horizontal [dis]continuous lam and strat. ≤ 4 mm thick; with 5 color variations from 41 - [46/53 cm] muddy sand, with irregular top and base 44-46 cm: pebble 3x4x5 cm, grey, subrounded, meta ? 42-60 cm: pebble, 8x8x5 cm, grey, subangular, gabbro ? 56-58 cm: pebble, subangular, metam., 4x3x2 cm
51 — — — 60	5Y3/1	
64.5		
sandy mud	5Y4/2 to 5Y4/1	[64.5/66] - 123 cm: sandy mud, with colour variations, slightly + crudely lam + strat, with horizontal to oblique [dis-] cont. mottles to lam. and strata from 74-87 cm: subangular, reddish cobble (11 cm x 12 cm large) 85-90 cm: subrounded, grey, granitic pebble, 4.5x 2.5x2,5 cm 89-91 cm: pebble, subrounded red, granite, 5x4x 2 cm 105-110 cm: pebble, black, basaltic 5.5x5x3 cm, subrounded 108-113 cm: subangular red granite 5x6x6 cm
66		
97 cm →		
muddy sand to sandy mud	5Y4/2	123-130 cm: muddy sand to sandy mud; crudely stratified, with horizontal to slightly oblique discont. layers ≤ 5 mm thick
130		

Alfred-Wegener-Institute

please send a copy to curator@awi.de

Scale 1:5

(continues on next page)

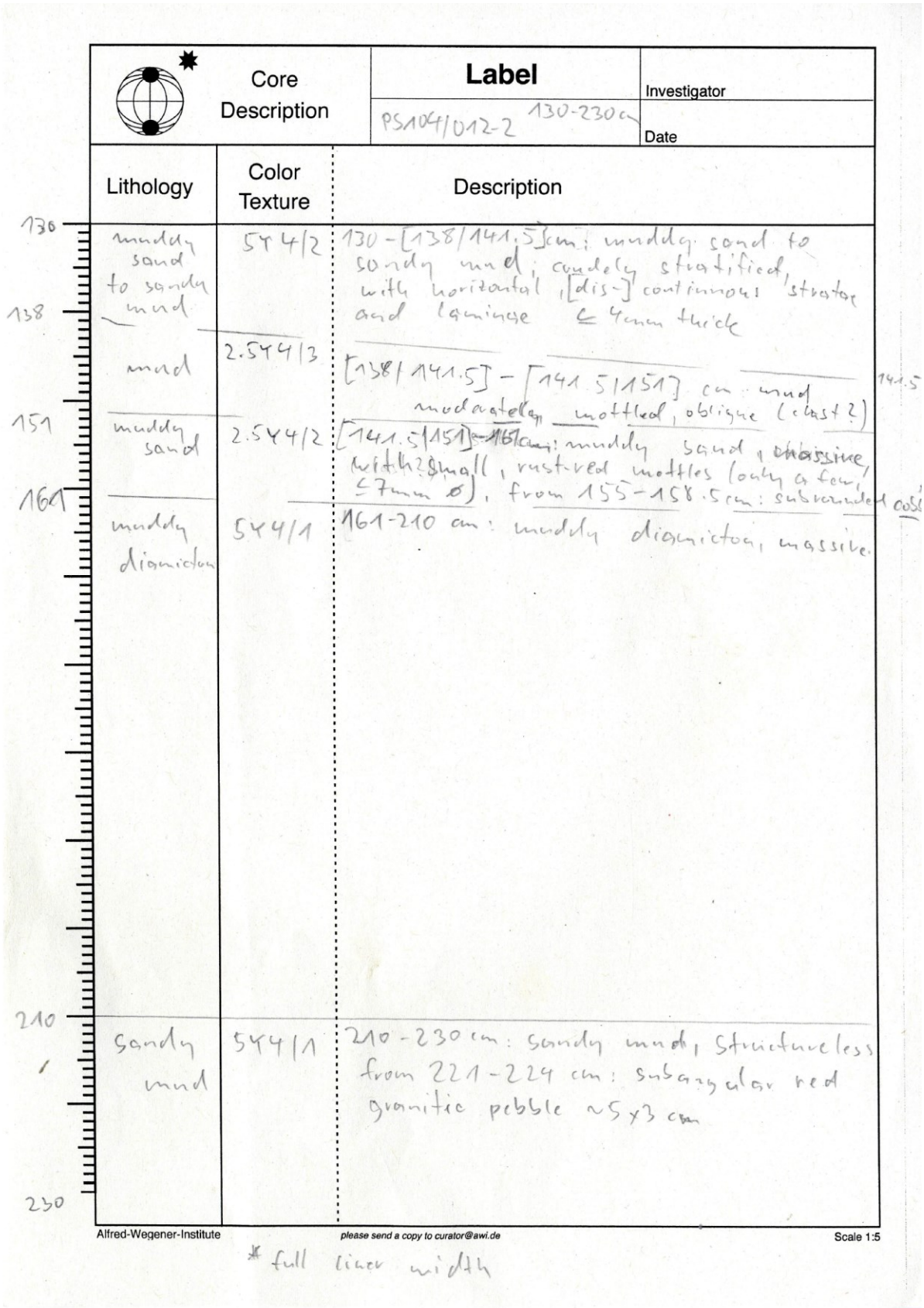

Core Description

Label

PS104/012-2 130-230cm

Investigator

Date

Lithology	Color Texture	Description
muddy sand to sandy mud	5Y 4/2	130 - [138/141.5] cm: muddy sand to sandy mud; crudely stratified, with horizontal, [dis-] continuous strata and laminae ≤ 4mm thick
mud	2.5Y 4/3	[138/141.5] - [141.5/151] cm: mud moderately mottled, oblique (cast?)
muddy sand	2.5Y 4/2	[141.5/151] - 161 cm: muddy sand, massive, with ?small, rust-red mottles (only a few, ≤ 7mm ⌀), from 155 - 158.5 cm: subrounded
muddy diamicton	5Y 4/1	161-210 cm: muddy diamicton, massive.
sandy mud	5Y 4/1	210 - 230 cm: sandy mud, structureless from 221 - 224 cm: subangular red granitic pebble ~5 x 3 cm

130 138 151 161 210 230

141.5

Alfred-Wegener-Institute please send a copy to curator@awi.de Scale 1:5

* full liner width

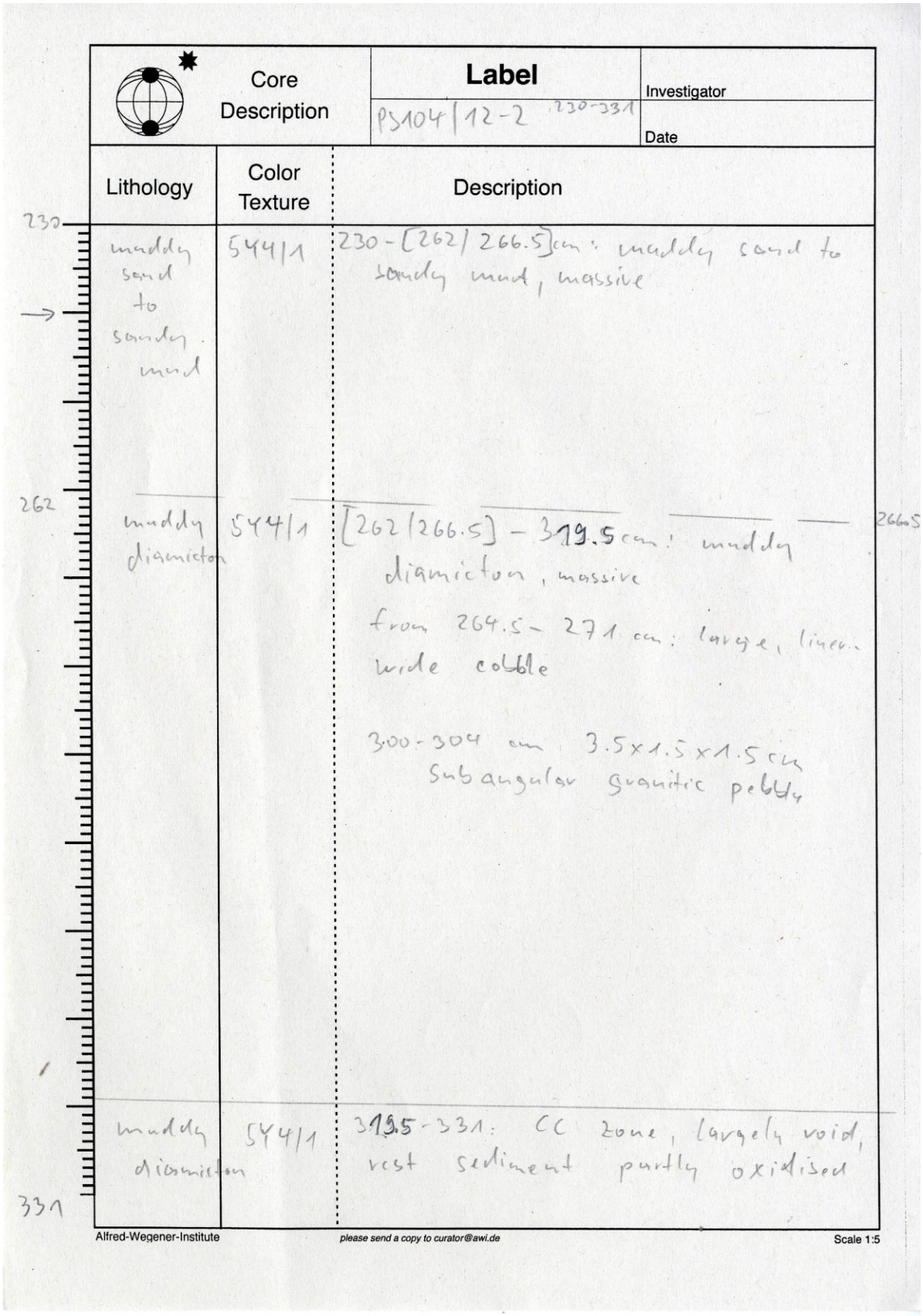

Core Description

Label

PS104/12-2 230-331

Investigator

Date

Lithology	Color Texture	Description
muddy sand to sandy mud	5Y4/1	230-[262/266.5]cm: muddy sand to sandy mud, massive
muddy diamicton	5Y4/1	[262/266.5] - 319.5 cm: muddy diamicton, massive from 264.5 - 271 cm: large, linear wide cobble 300-304 cm 3.5x1.5x1.5 cm Subangular granitic pebble
muddy diamicton	5Y4/1	319.5-331: CC zone, largely void, rest sediment partly oxidised

230 262 266.5 331

Alfred-Wegener-Institute please send a copy to curator@awi.de Scale 1:5

(continues on next page)

PS104/021-1 Pine Island Trough PS104

Recovery: 1.09 m 73° 18.290' S, 107° 06.570' W Water depth: 882 m

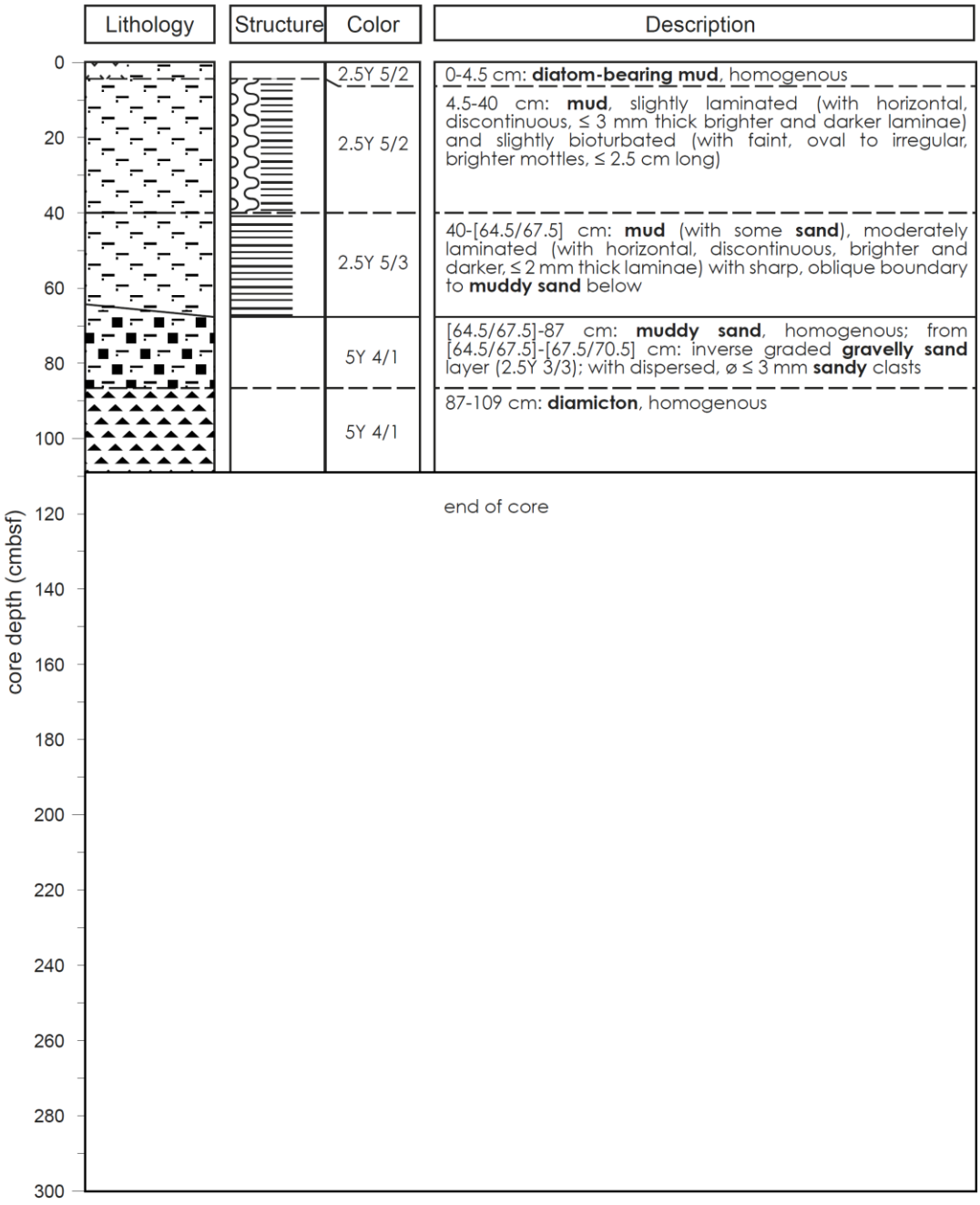

(continues on next page)

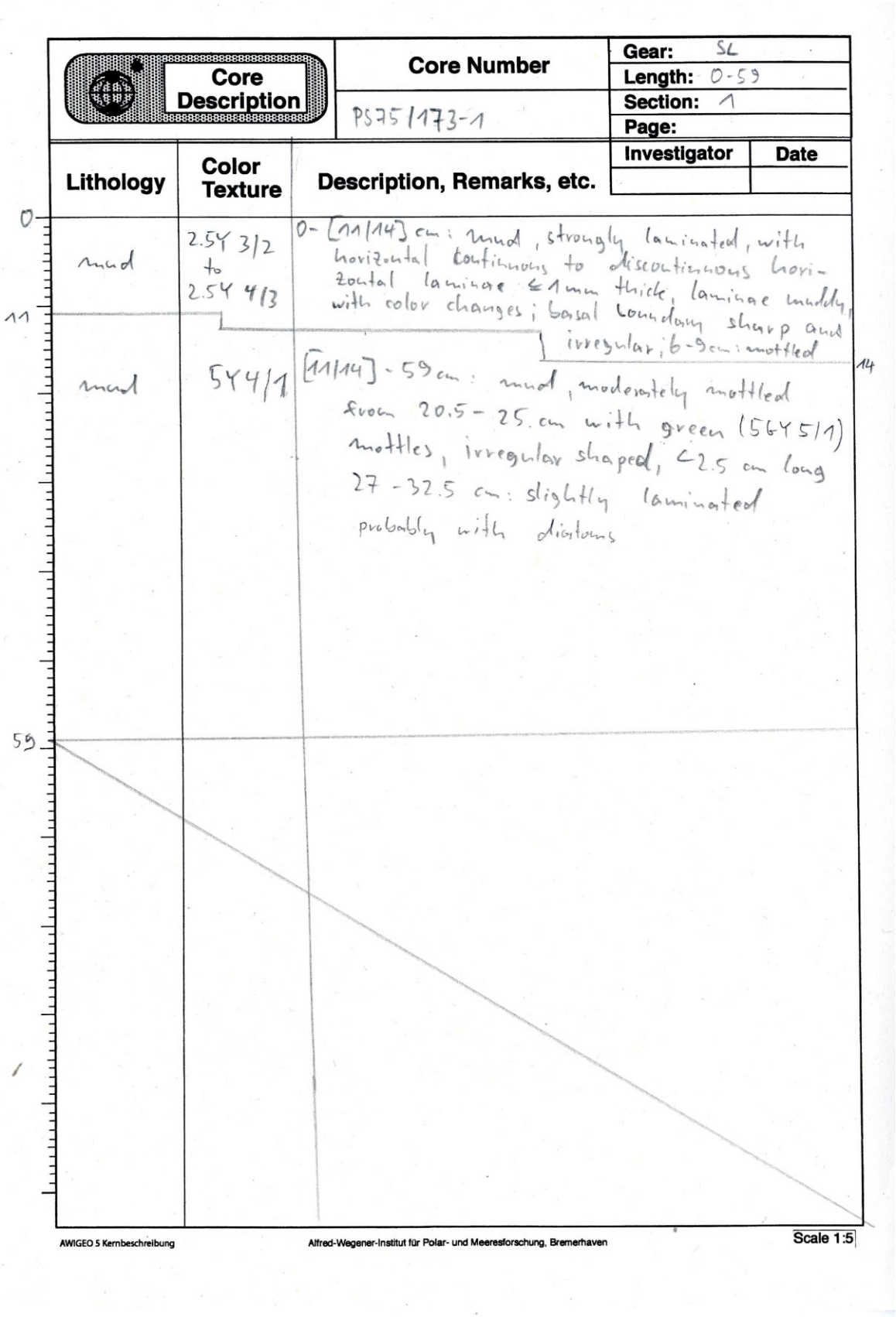

Core Description

Core Number	Gear: SL
PS75/173-1	Length: 0-59
	Section: 1
	Page:
	Investigator / Date

Lithology	Color Texture	Description, Remarks, etc.
0		
mud	2.5Y 3/2 to 2.5Y 4/3	0-[11/14] cm: mud, strongly laminated, with horizontal continuous to discontinuous horizontal laminae ≤1 mm thick, laminae muddy, with color changes; basal boundary sharp and irregular, 6-9 cm: mottled
11		
mud	5Y 4/1	[11/14]-59 cm: mud, moderately mottled from 20.5-25 cm with green (5GY 5/1) mottles, irregular shaped, <2.5 cm long 27-32.5 cm: slightly laminated probably with diatoms
14		
59		

AWIGEO 5 Kernbeschreibung — Alfred-Wegener-Institut für Polar- und Meeresforschung, Bremerhaven — Scale 1:5

(continues on next page)

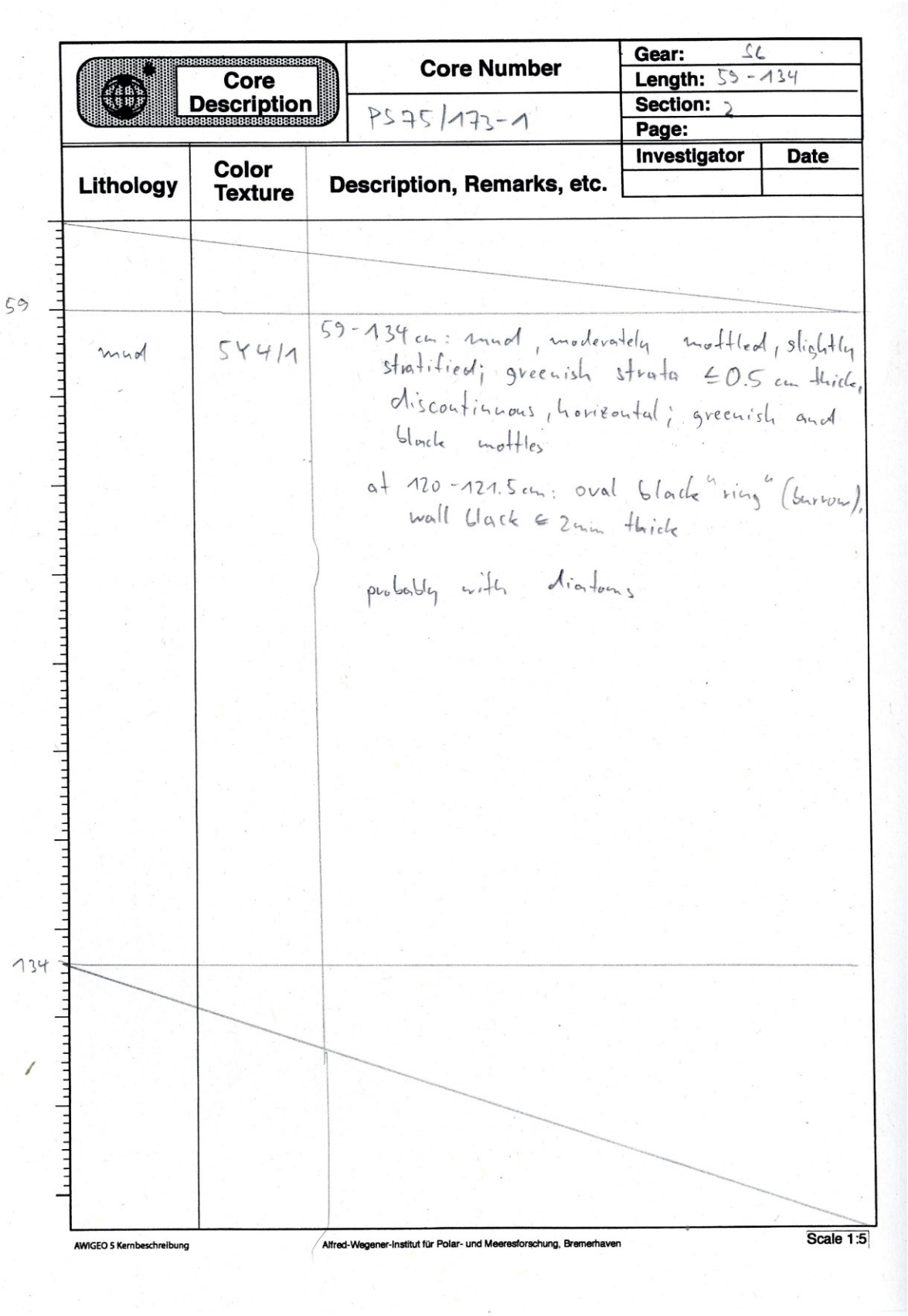

Core Description

Core Number	Gear: SL
PS75/173-1	Length: 59 - 134
	Section: 2
	Page:
	Investigator: Date:

Lithology	Color Texture	Description, Remarks, etc.
59		
mud	5Y4/1	59 - 134 cm: mud, moderately mottled, slightly stratified; greenish strata ≤ 0.5 cm thick, discontinuous, horizontal; greenish and black mottles at 120 - 121.5 cm: oval black "ring" (burrow), wall black ≤ 2 mm thick probably with diatoms
134		

AWIGEO 5 Kernbeschreibung — Alfred-Wegener-Institut für Polar- und Meeresforschung, Bremerhaven — Scale 1:5

(continues on next page)

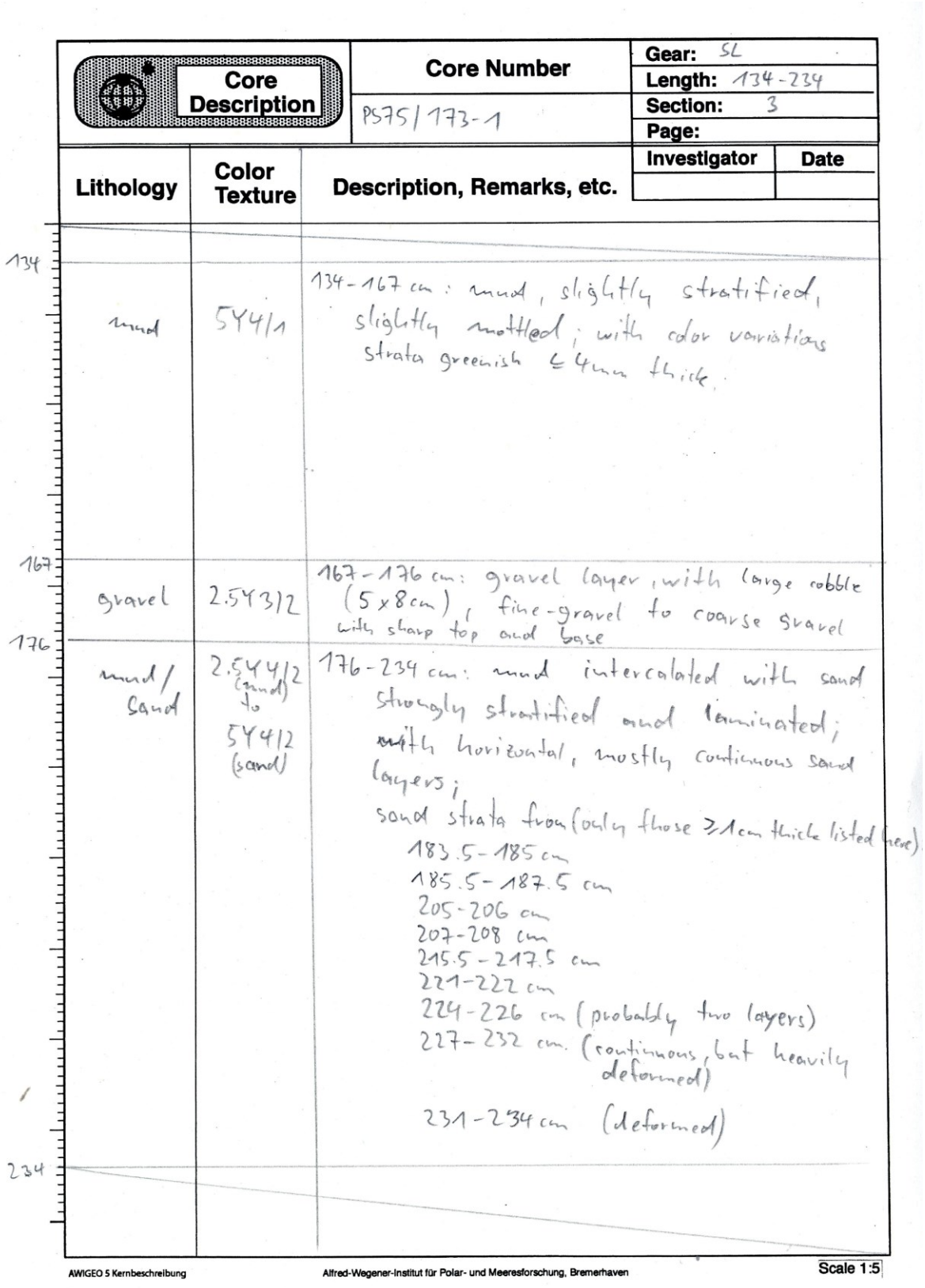

Core Description

Core Number	Gear: SL
PS75/173-1	Length: 134-234
	Section: 3
	Page:
	Investigator / Date

Lithology	Color Texture	Description, Remarks, etc.
134		
mud	5Y4/1	134-167 cm: mud, slightly stratified, slightly mottled; with color variations strata greenish ≤ 4mm thick.
167		
gravel	2.5Y3/2	167-176 cm: gravel layer, with large cobble (5x8cm), fine-gravel to coarse gravel with sharp top and base
176		
mud/ sand	2.5Y4/2 (mud) to 5Y4/2 (sand)	176-234 cm: mud intercalated with sand strongly stratified and laminated; with horizontal, mostly continuous sand layers; sand strata from (only those ≥1cm thick listed here): 183.5-185 cm; 185.5-187.5 cm; 205-206 cm; 207-208 cm; 215.5-217.5 cm; 221-222 cm; 224-226 cm (probably two layers); 227-232 cm (continuous, but heavily deformed); 231-234 cm (deformed)
234		

AWIGEO 5 Kernbeschreibung — Alfred-Wegener-Institut für Polar- und Meeresforschung, Bremerhaven — Scale 1:5

(continues on next page)

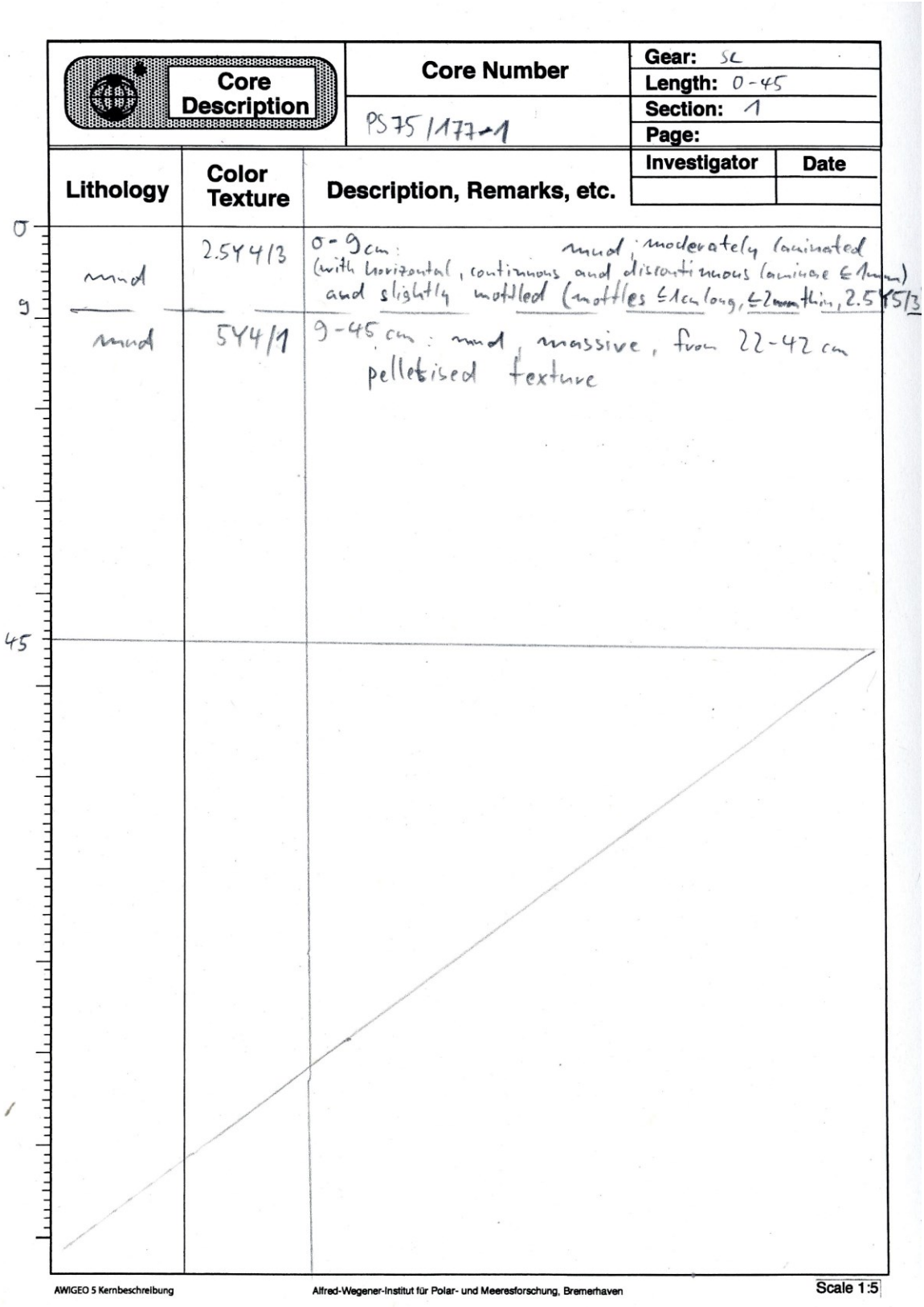

Core Description

Core Number	Gear: SL
PS75/177-1	Length: 0-45
	Section: 1
	Page:
	Investigator / Date

Lithology	Color Texture	Description, Remarks, etc.
0		
mud	2.5Y4/3	0-9 cm: mud, moderately laminated (with horizontal, continuous and discontinuous laminae ≤1mm) and slightly mottled (mottles ≤1cm long, ≤2mm thin, 2.5Y5/3
9		
mud	5Y4/1	9-45 cm: mud, massive, from 22-42 cm pelletised texture
45		

AWIGEO 5 Kernbeschreibung — Alfred-Wegener-Institut für Polar- und Meeresforschung, Bremerhaven — Scale 1:5

(continues on next page)

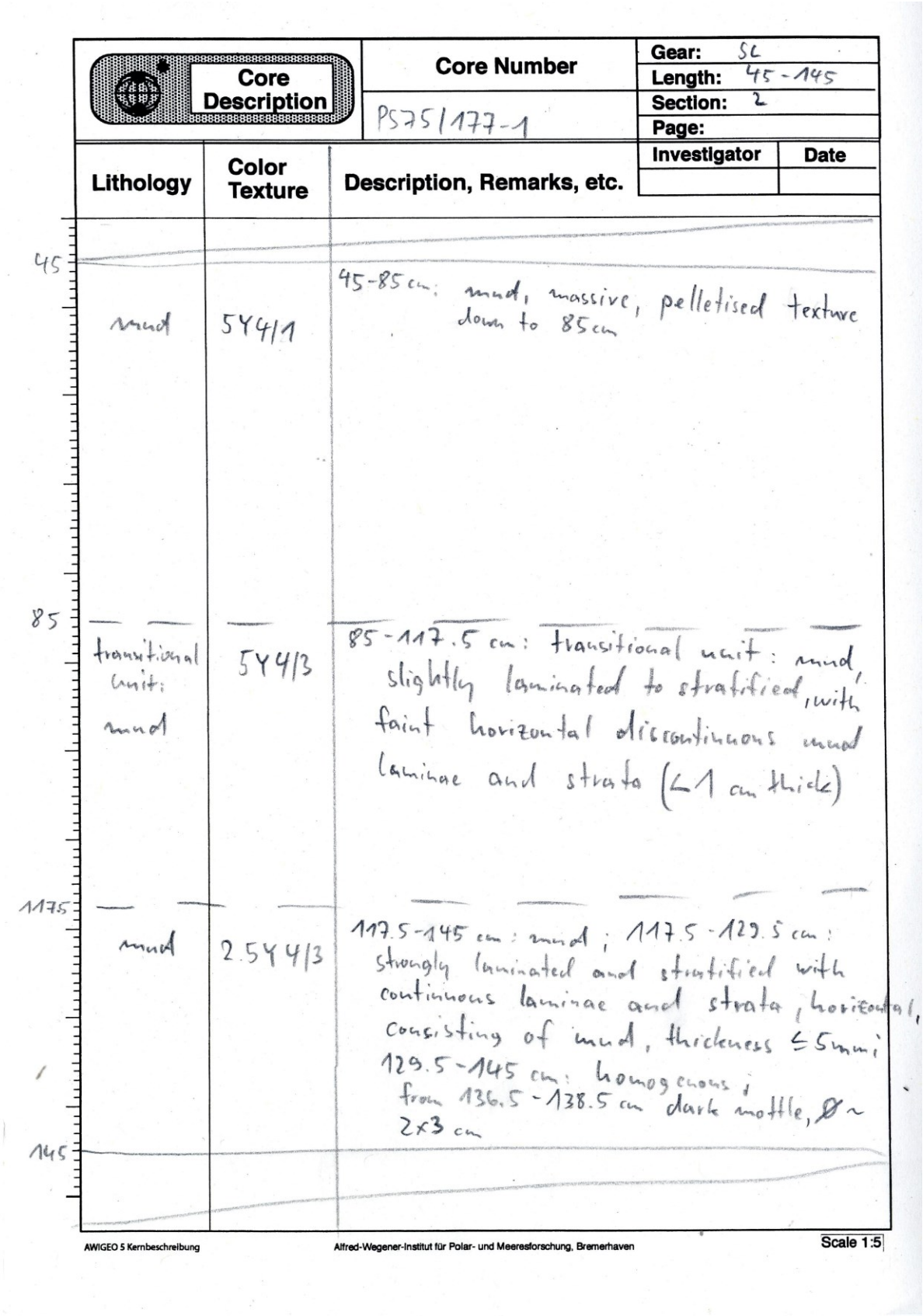

Core Description

Core Number	Gear: SL
PS75/177-1	Length: 45 - 145
	Section: 2
	Page:
	Investigator / Date:

Lithology	Color Texture	Description, Remarks, etc.
45		
mud	5Y4/1	45-85 cm: mud, massive, pelletised texture down to 85 cm
85		
transitional unit: mud	5Y4/3	85-117.5 cm: transitional unit: mud, slightly laminated to stratified, with faint horizontal discontinuous mud laminae and strata (<1 cm thick)
117.5		
mud	2.5Y4/3	117.5-145 cm: mud; 117.5-129.5 cm: strongly laminated and stratified with continuous laminae and strata, horizontal, consisting of mud, thickness ≤5 mm; 129.5-145 cm: homogenous; from 136.5-138.5 cm dark mottle, Ø ~ 2x3 cm
145		

AWIGEO 5 Kernbeschreibung — Alfred-Wegener-Institut für Polar- und Meeresforschung, Bremerhaven — Scale 1:5

(continues on next page)

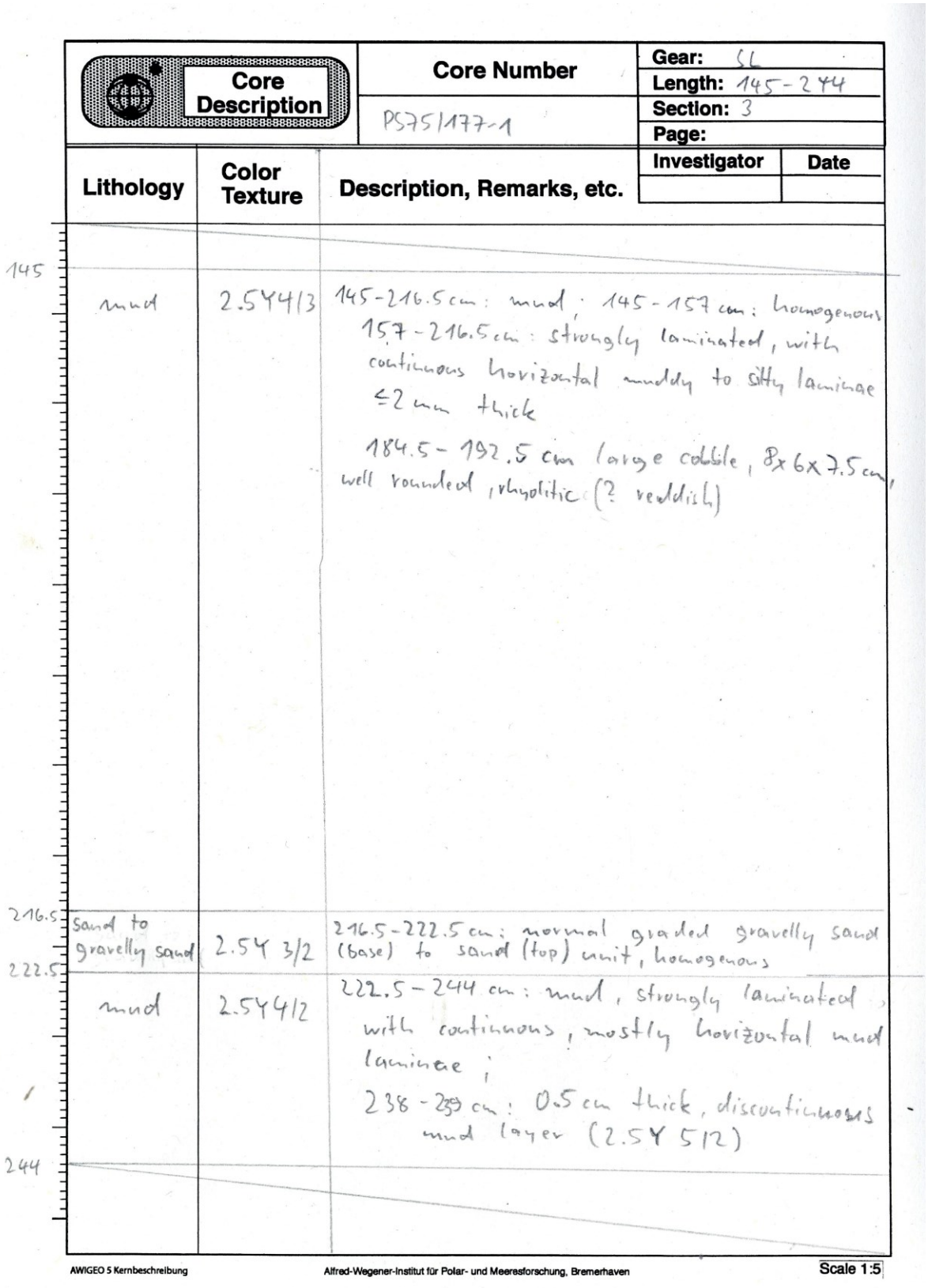

Core Description

Core Number	Gear: SL
PS75/177-1	Length: 145 - 244
	Section: 3
	Page:
	Investigator / Date:

Lithology	Color Texture	Description, Remarks, etc.
145		
mud	2.5Y4/3	145-216.5 cm: mud; 145-157 cm: homogenous 157-216.5 cm: strongly laminated, with continuous horizontal muddy to silty laminae ≤2 mm thick 184.5 - 192.5 cm large cobble, 8x6x7.5 cm, well rounded, rhyolitic (? reddish)
216.5		
sand to gravelly sand	2.5Y 3/2	216.5-222.5 cm: normal graded gravelly sand (base) to sand (top) unit, homogenous
222.5		
mud	2.5Y4/2	222.5 - 244 cm: mud, strongly laminated, with continuous, mostly horizontal mud laminae; 238 - 239 cm: 0.5 cm thick, discontinuous mud layer (2.5Y 5/2)
244		

AWIGEO 5 Kernbeschreibung — Alfred-Wegener-Institut für Polar- und Meeresforschung, Bremerhaven — Scale 1:5

(continues on next page)

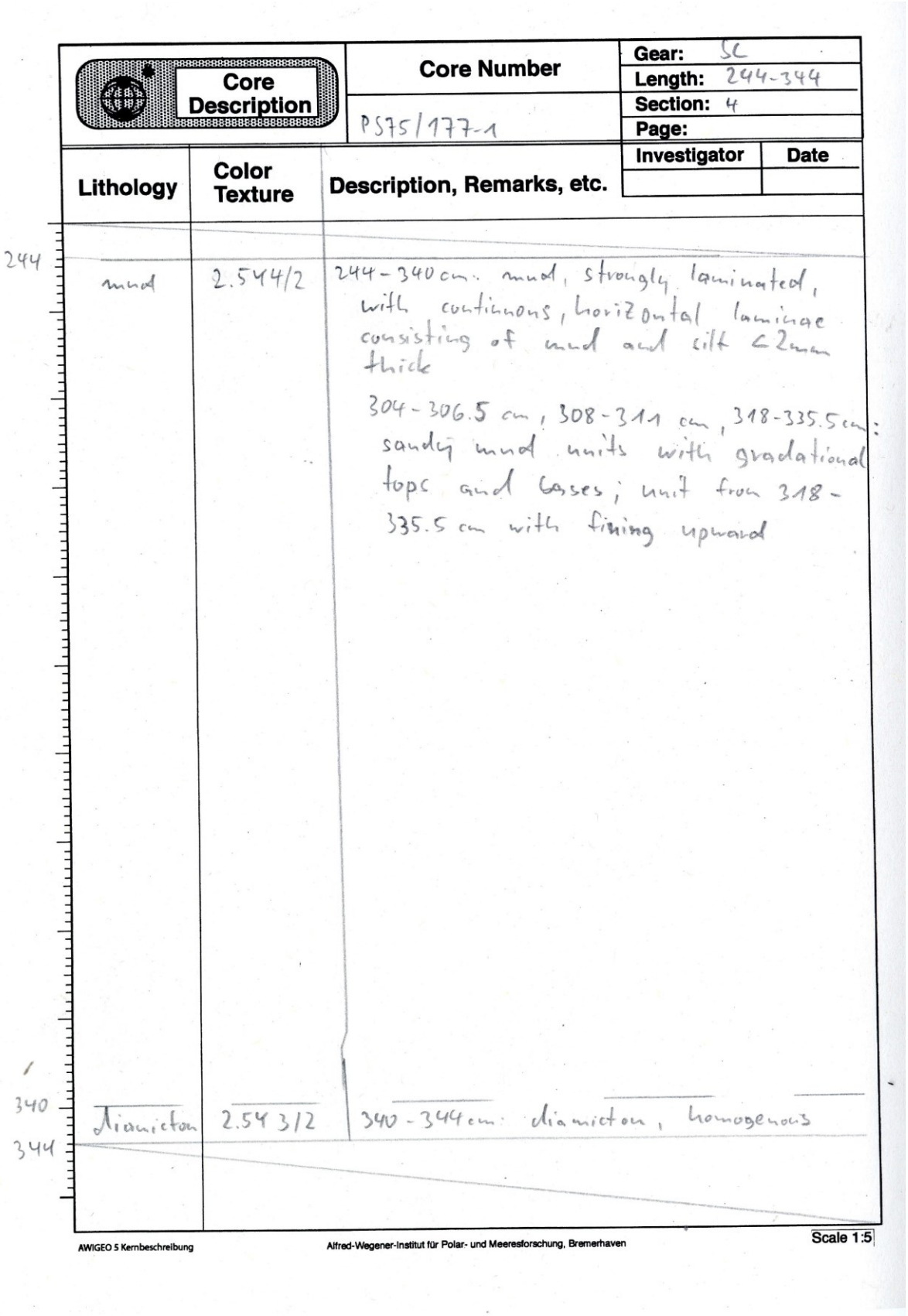

Core Description

Core Number	Gear: SC
PS75/177-1	Length: 244-344
	Section: 4
	Page:
	Investigator / Date

Lithology	Color Texture	Description, Remarks, etc.
244 mud	2.5Y4/2	244-340 cm: mud, strongly laminated, with continuous, horizontal laminae consisting of mud and silt <2mm thick 304-306.5 cm, 308-311 cm, 318-335.5 cm: sandy mud units with gradational tops and bases; unit from 318-335.5 cm with fining upward
340 Diamicton	2.5Y 3/2	340-344 cm: diamicton, homogenous
344		

AWIGEO 5 Kernbeschreibung — Alfred-Wegener-Institut für Polar- und Meeresforschung, Bremerhaven — Scale 1:5

(continues on next page)

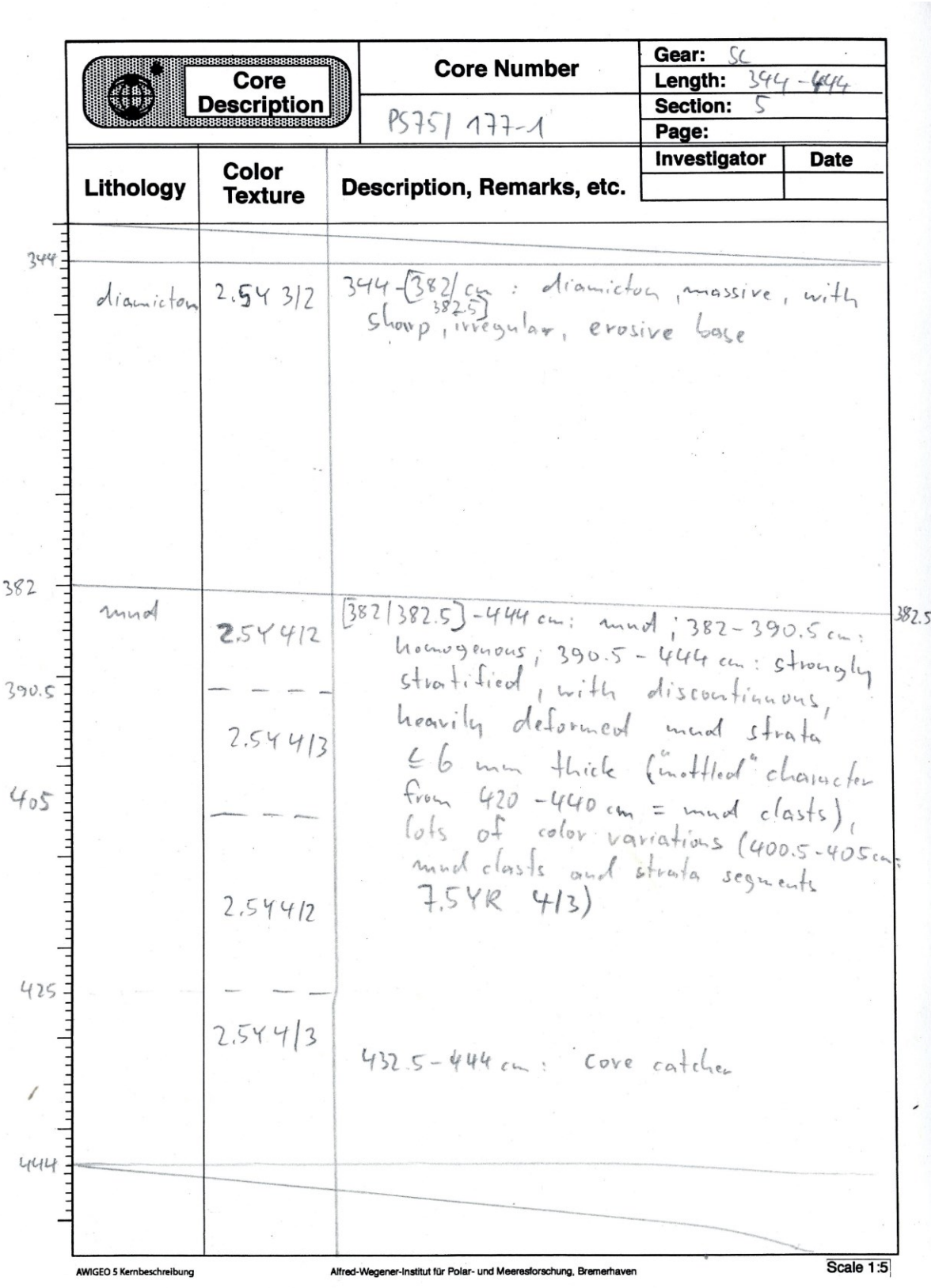

Core Description

Core Number	Gear: SC
PS75/177-1	Length: 344 - 444
	Section: 5
	Page:
	Investigator / Date

Lithology	Color Texture	Description, Remarks, etc.
344		
diamicton	2.5Y 3/2	344 - [382/382.5] cm: diamicton, massive, with sharp, irregular, erosive base
382		
mud	2.5Y 4/2	[382/382.5] - 444 cm: mud; 382 - 390.5 cm: homogenous; 390.5 - 444 cm: strongly stratified, with discontinuous, heavily deformed mud strata ≤ 6 mm thick ("mottled" character from 420 - 440 cm = mud clasts), lots of color variations (400.5 - 405 cm: mud clasts and strata segments 7.5YR 4/3)
390.5		
	2.5Y 4/3	
405		
	2.5Y 4/2	
425		
	2.5Y 4/3	432.5 - 444 cm: Core catcher
444		

382.5

AWIGEO 5 Kernbeschreibung — Alfred-Wegener-Institut für Polar- und Meeresforschung, Bremerhaven — Scale 1:5

(continues on next page)

Appendix Figure 3.2. $^{40}Ar/^{39}Ar$ ages on ice-rafted hornblende and biotite grains from the Pine Island Bay

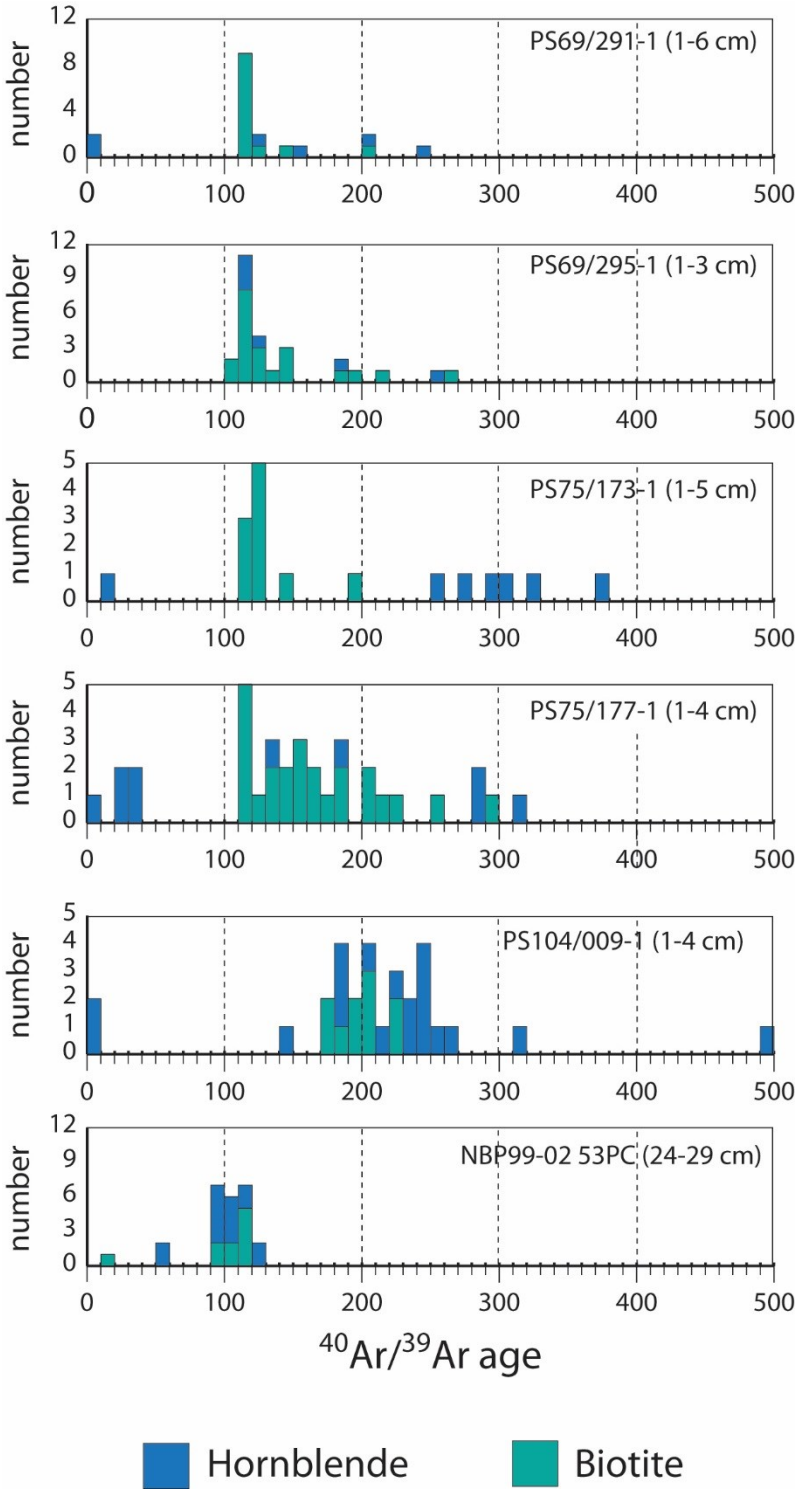

Appendix Figure 3.3. Aeromagnetic map of the Amundsen Sea sector of the West Antarctic Ice Sheet from Bingham et al. (2012). Yellow circles denote potenital subglacial young (Late Cenozoic) volcanic edifices (from van Wyk de Vries et al., 2017). Blue overlying line show main hydrological pathways below the Pine Island and Thwaites Glaciers (from Wright et al., 2008). Arrow show the location of the two major aeromagnetic anomalies below the Thwaites Glaciers discussed in the main text. Note that these anomalies are not overlain by volcanic edifices.

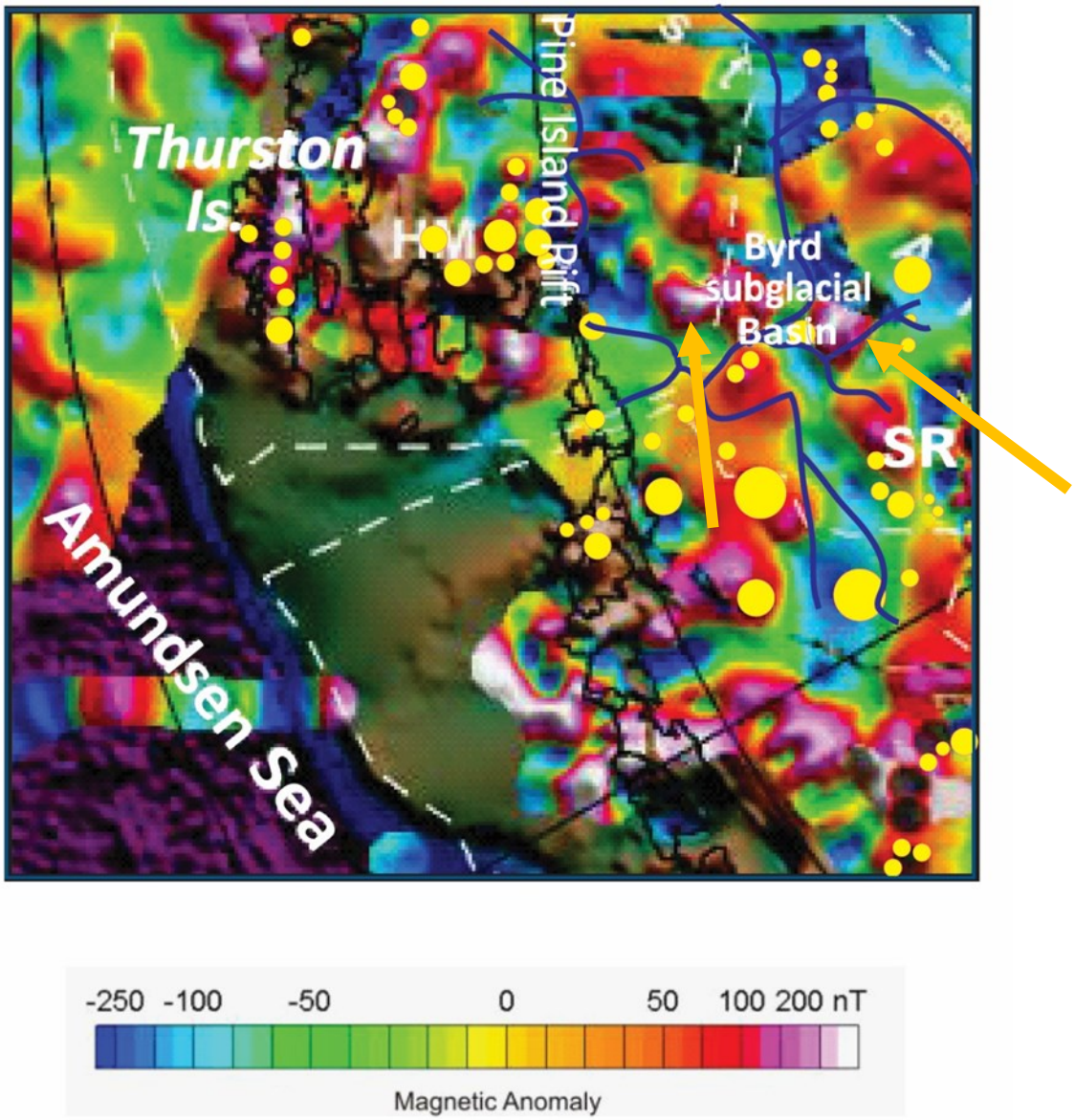

Appendix Figure 4.1. Lithology of core site PS58/254

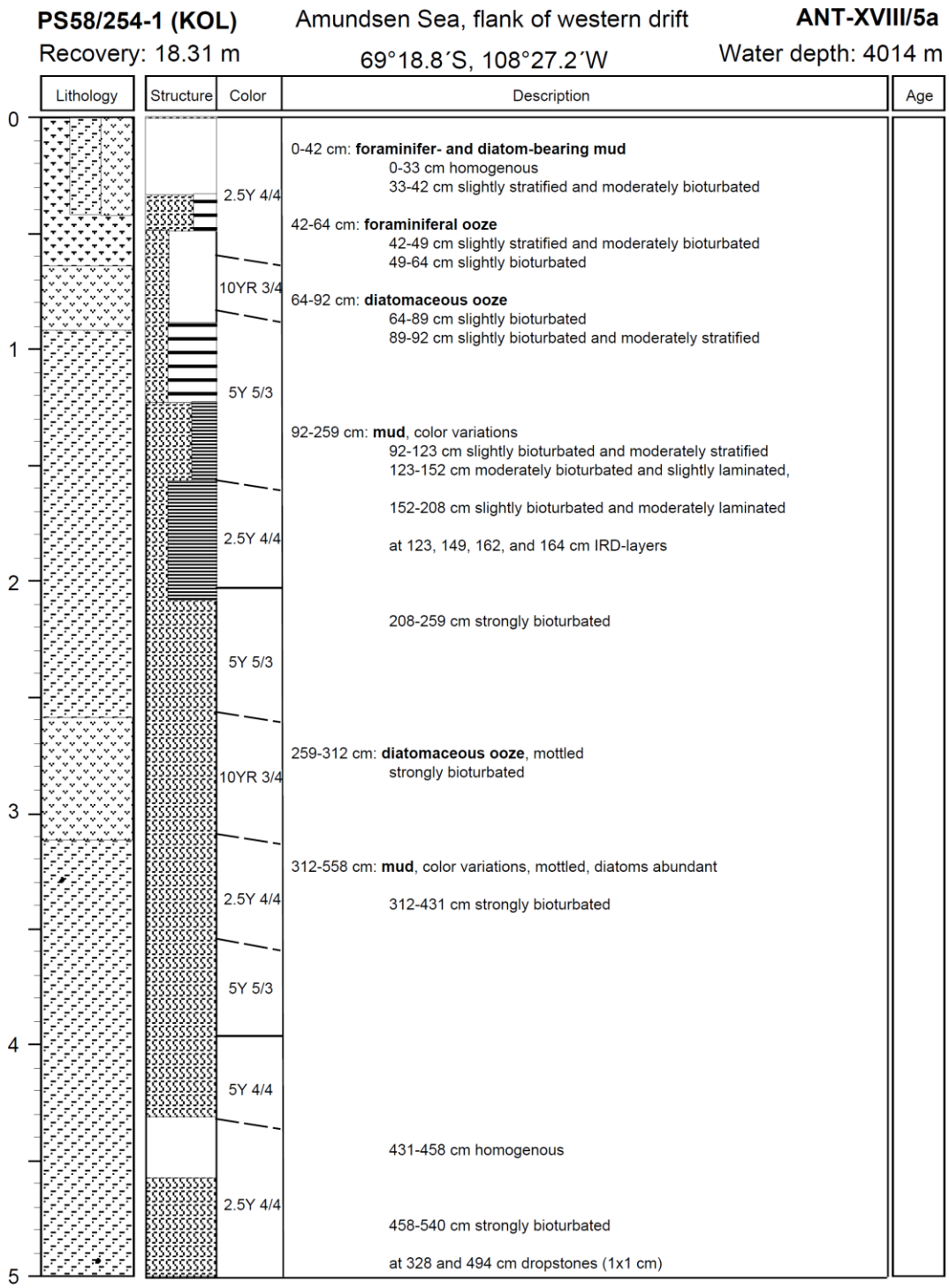

(continues on next page)

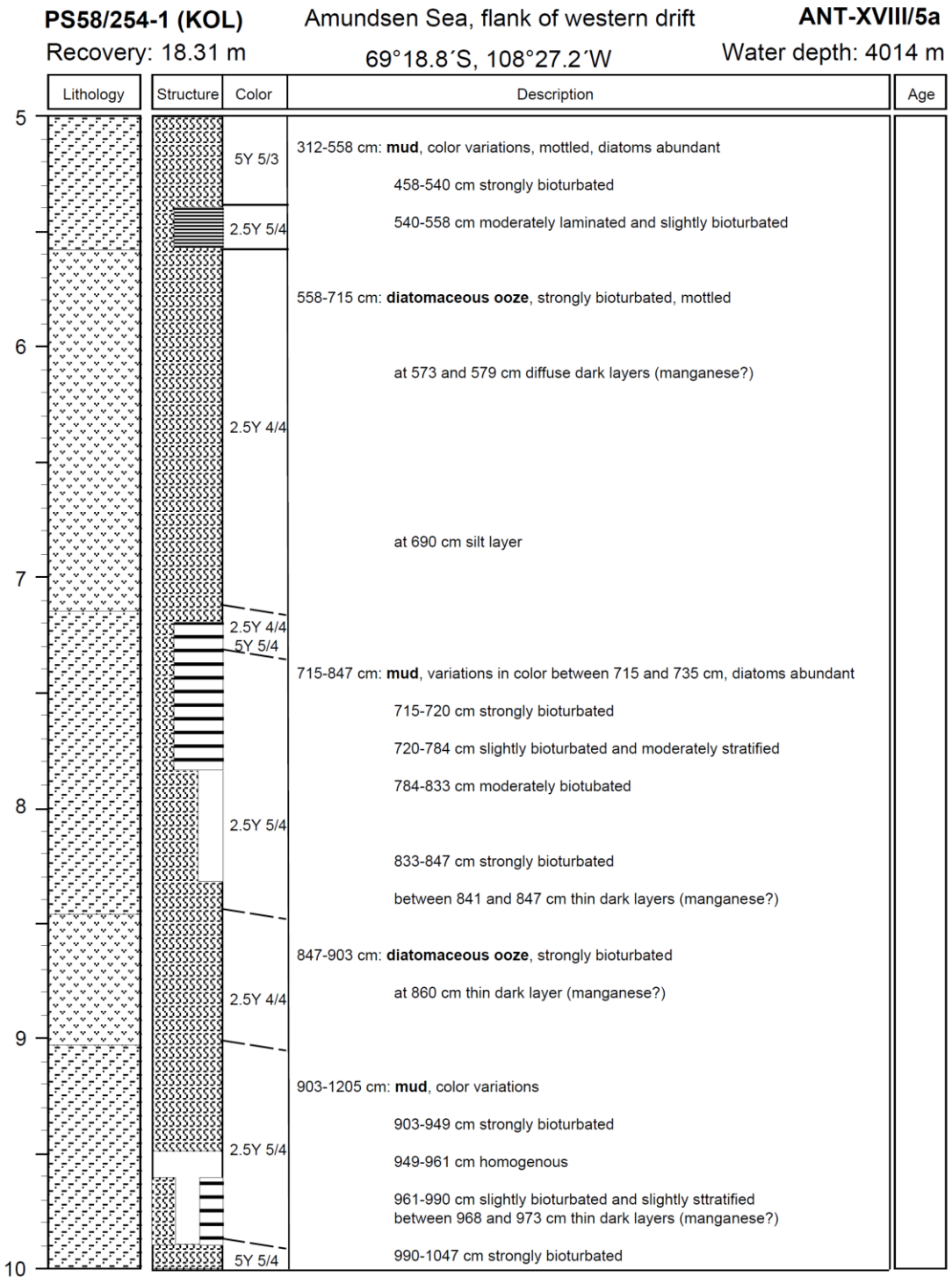

(continues on next page)

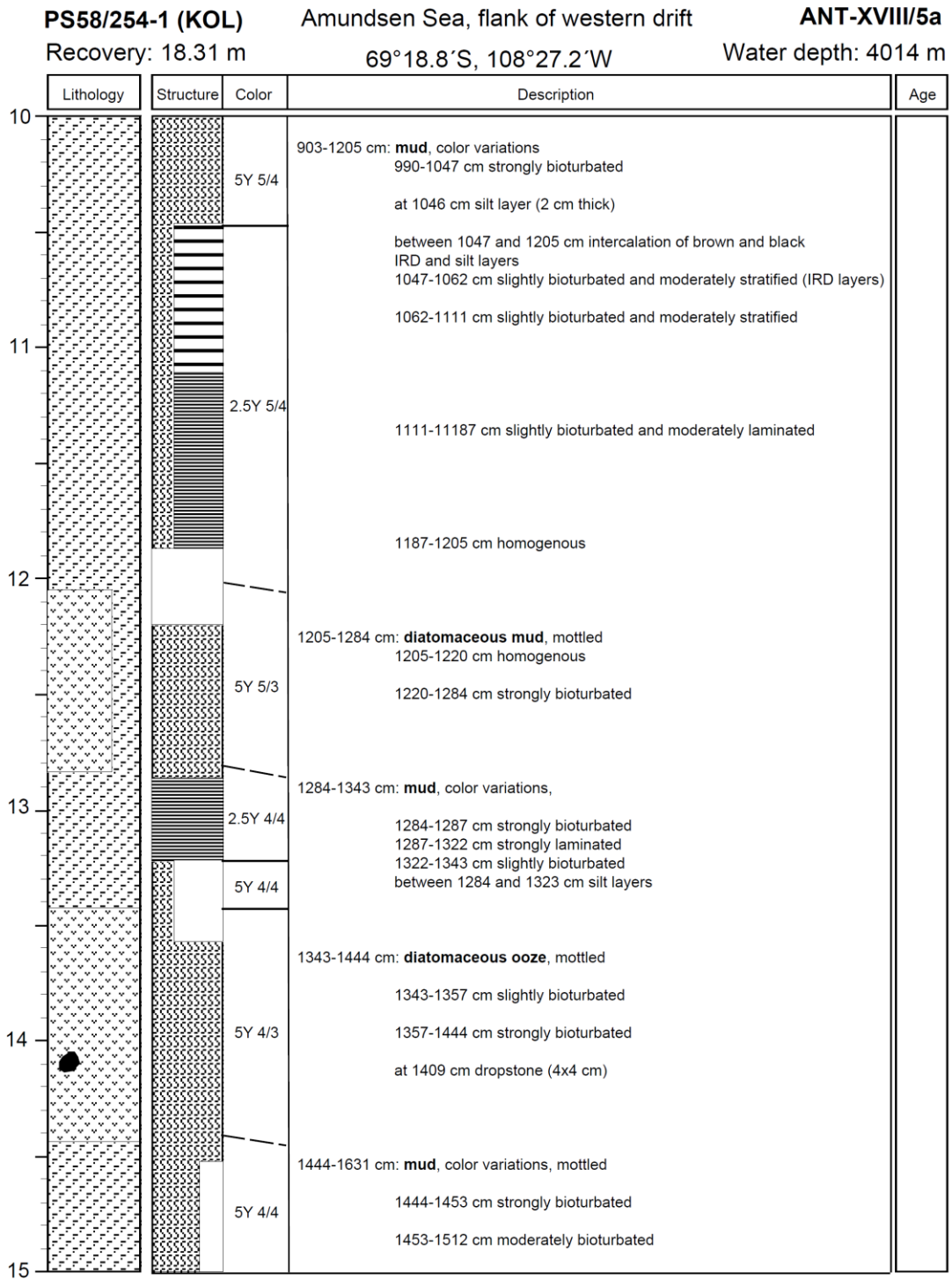
PS58/254-1 (KOL)
Amundsen Sea, flank of western drift
ANT-XVIII/5a
Recovery: 18.31 m
69°18.8´S, 108°27.2´W
Water depth: 4014 m
Lithology
Structure
Color
Description
Age
10
11
12
13
14
15
5Y 5/4
2.5Y 5/4
5Y 5/3
2.5Y 4/4
5Y 4/4
5Y 4/3
5Y 4/4
903-1205 cm: mud, color variations
990-1047 cm strongly bioturbated
at 1046 cm silt layer (2 cm thick)
between 1047 and 1205 cm intercalation of brown and black IRD and silt layers
1047-1062 cm slightly bioturbated and moderately stratified (IRD layers)
1062-1111 cm slightly bioturbated and moderately stratified
1111-11187 cm slightly bioturbated and moderately laminated
1187-1205 cm homogenous
1205-1284 cm: diatomaceous mud, mottled
1205-1220 cm homogenous
1220-1284 cm strongly bioturbated
1284-1343 cm: mud, color variations,
1284-1287 cm strongly bioturbated
1287-1322 cm strongly laminated
1322-1343 cm slightly bioturbated
between 1284 and 1323 cm silt layers
1343-1444 cm: diatomaceous ooze, mottled
1343-1357 cm slightly bioturbated
1357-1444 cm strongly bioturbated
at 1409 cm dropstone (4x4 cm)
1444-1631 cm: mud, color variations, mottled
1444-1453 cm strongly bioturbated
1453-1512 cm moderately bioturbated

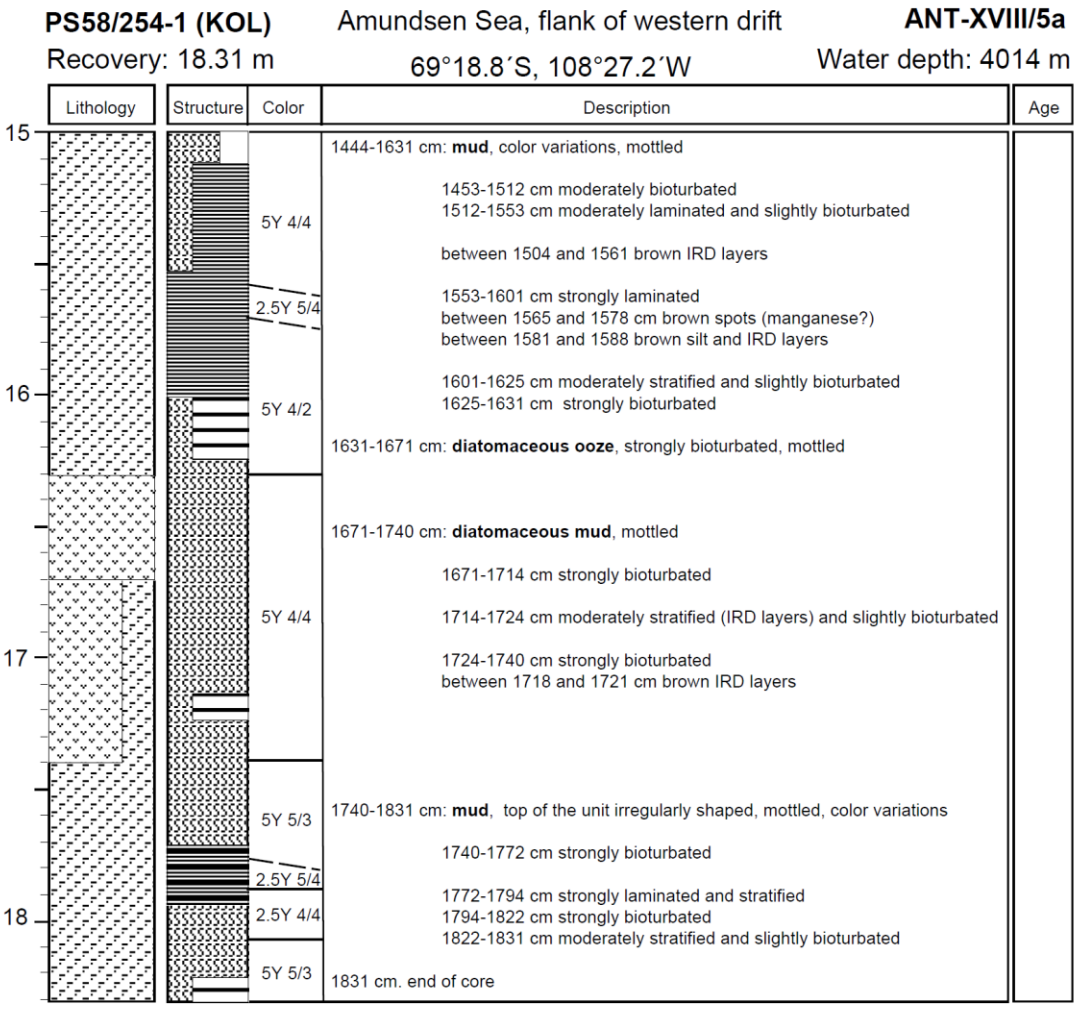
PS58/254-1 (KOL)
Amundsen Sea, flank of western drift
ANT-XVIII/5a
Recovery: 18.31 m
69°18.8´S, 108°27.2´W
Water depth: 4014 m
Lithology
Structure
Color
Description
Age
15
16
17
18
5Y 4/4
2.5Y 5/4
5Y 4/2
5Y 4/4
5Y 5/3
2.5Y 5/4
2.5Y 4/4
5Y 5/3
1444-1631 cm: mud, color variations, mottled
1453-1512 cm moderately bioturbated
1512-1553 cm moderately laminated and slightly bioturbated
between 1504 and 1561 brown IRD layers
1553-1601 cm strongly laminated
between 1565 and 1578 cm brown spots (manganese?)
between 1581 and 1588 brown silt and IRD layers
1601-1625 cm moderately stratified and slightly bioturbated
1625-1631 cm strongly bioturbated
1631-1671 cm: diatomaceous ooze, strongly bioturbated, mottled
1671-1740 cm: diatomaceous mud, mottled
1671-1714 cm strongly bioturbated
1714-1724 cm moderately stratified (IRD layers) and slightly bioturbated
1724-1740 cm strongly bioturbated
between 1718 and 1721 cm brown IRD layers
1740-1831 cm: mud, top of the unit irregularly shaped, mottled, color variations
1740-1772 cm strongly bioturbated
1772-1794 cm strongly laminated and stratified
1794-1822 cm strongly bioturbated
1822-1831 cm moderately stratified and slightly bioturbated
1831 cm. end of core

Appendix Figure 4.2. Lithology of core site PC493

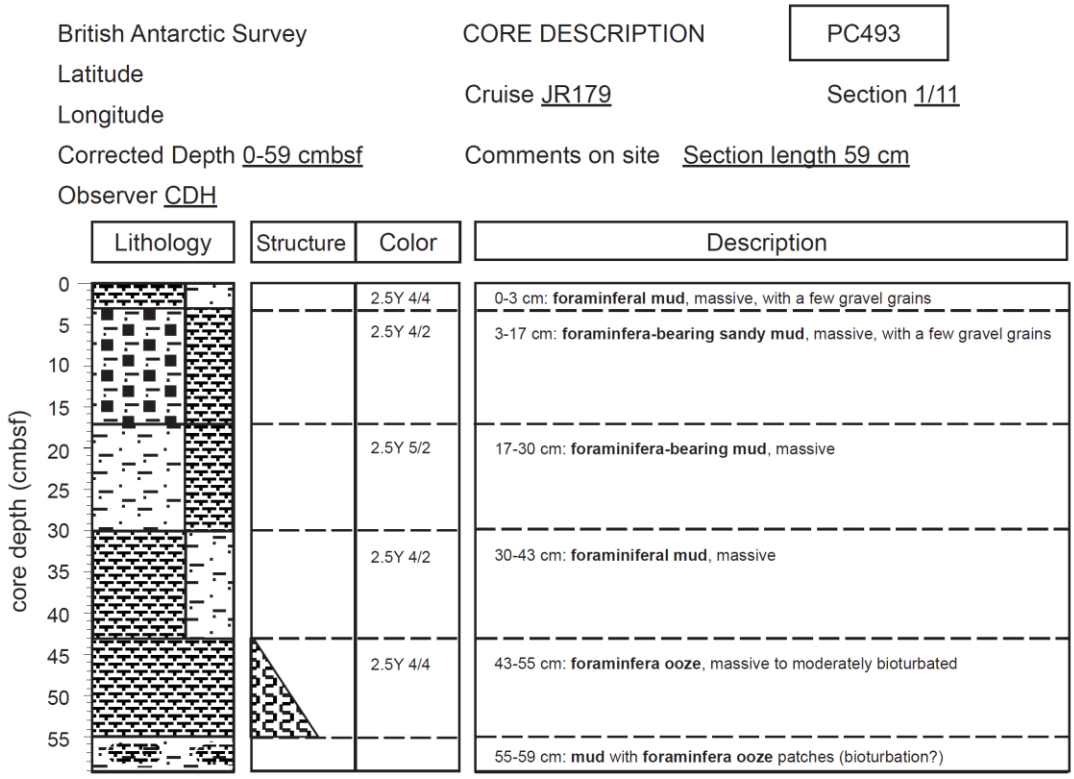

(continues on next page)

British Antarctic Survey | CORE DESCRIPTION | PC493

Latitude

Longitude | Cruise JR179 | Section 2/11

Corrected Depth 59-155 cmbsf | Comments on site Section length 96 cm

Observer CDH

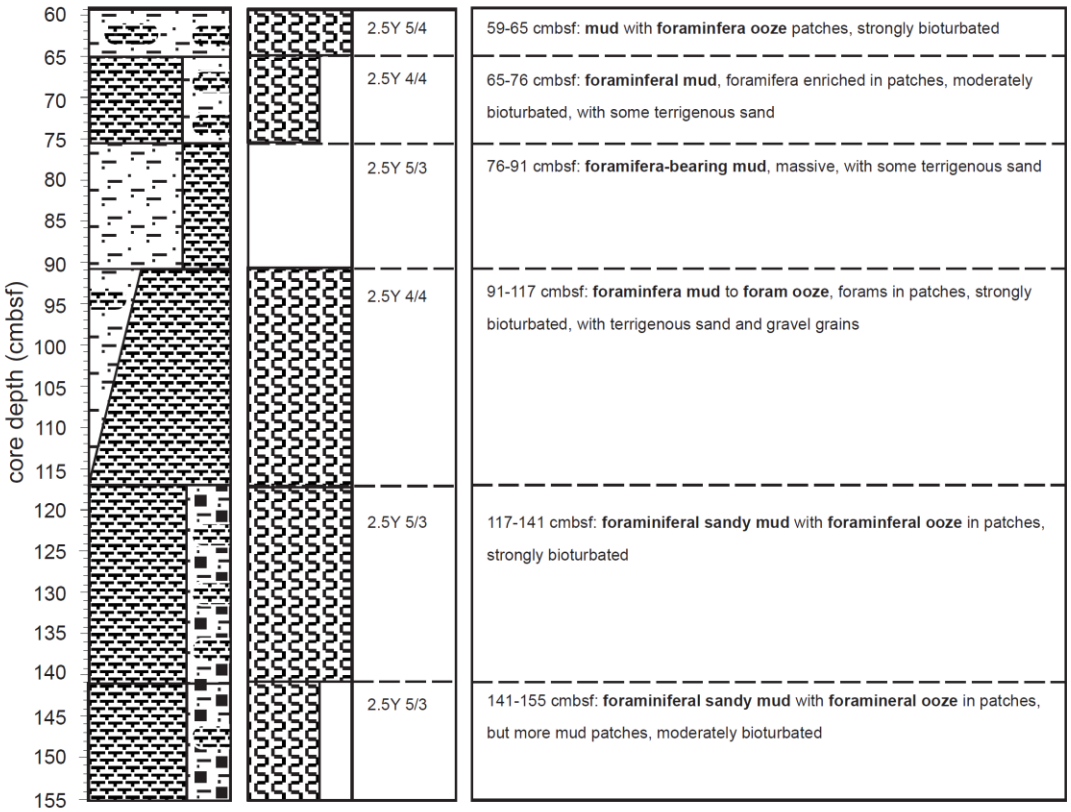

(continues on next page)

British Antarctic Survey | CORE DESCRIPTION | PC493

Latitude

Longitude | Cruise JR179 | Section 3/11

Corrected Depth 155-257 cmbsf | Comments on site Section length 102cm

Observer CDH

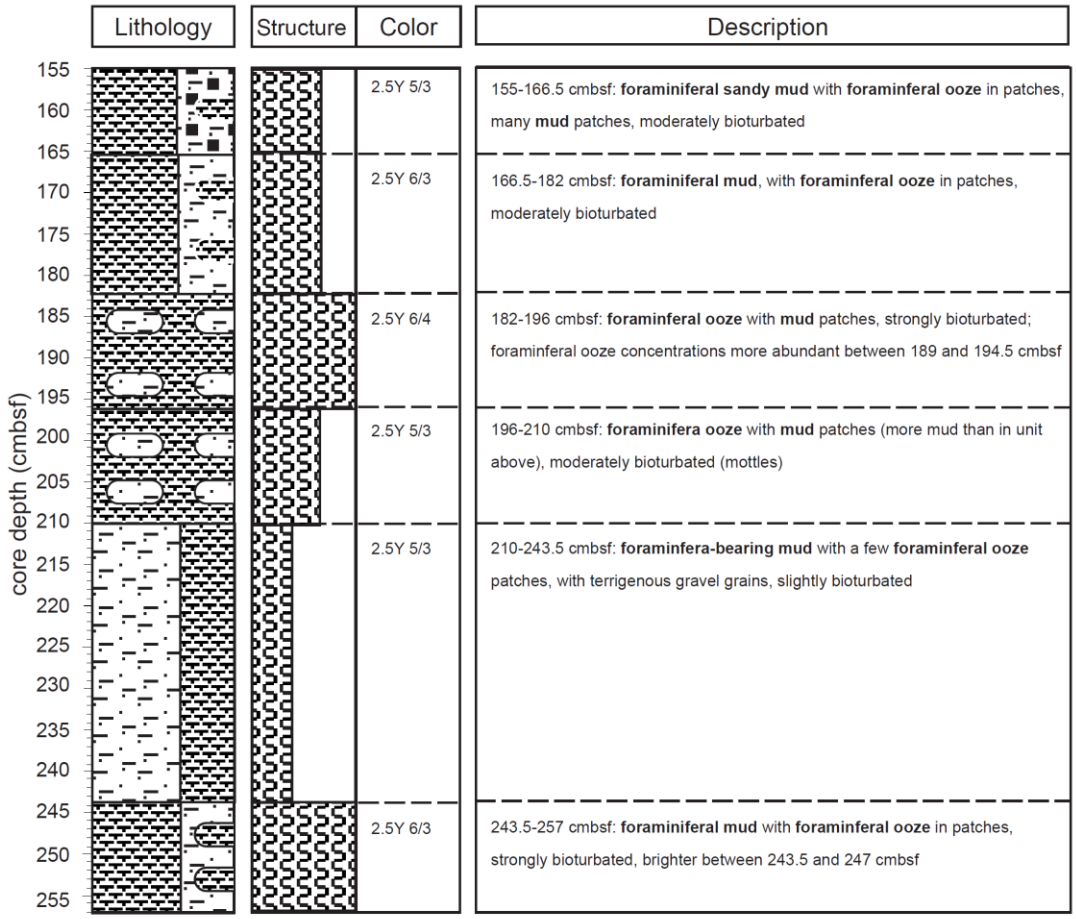

Appendix Figure 4.3. Clay content (%) vs strontium isotopic compositions of fine (<63µm) detrital sediments from sediment core PS54/254-1.

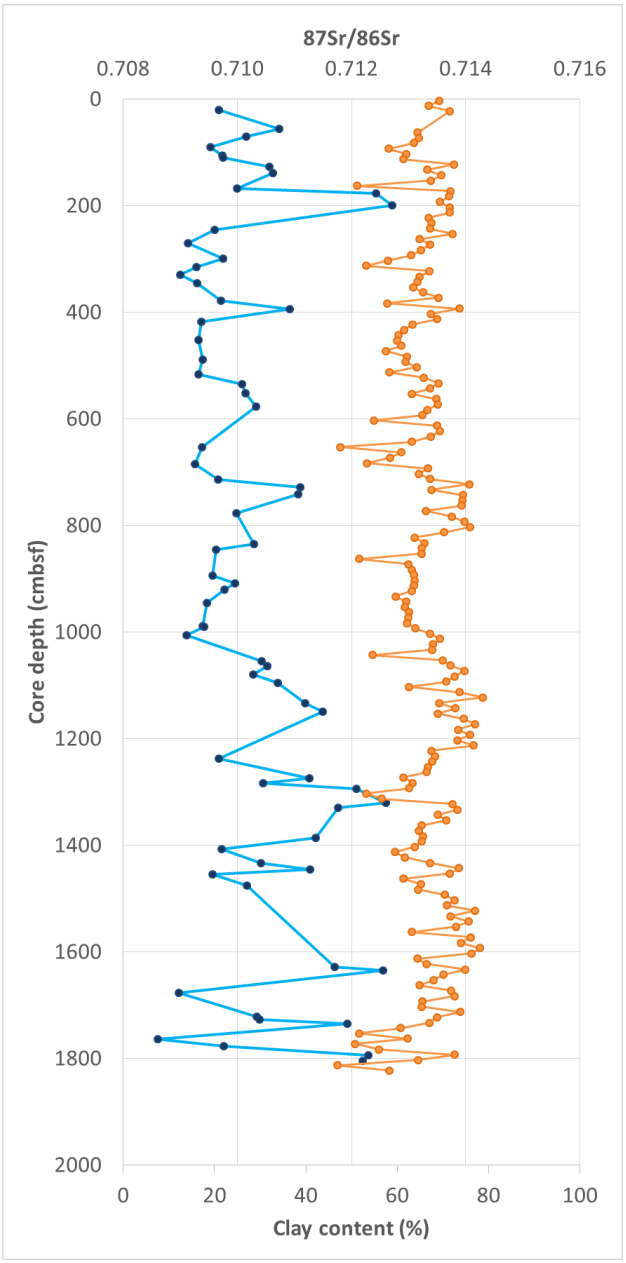

Appendix Table 2.1. Complete results of $^{40}Ar/^{39}Ar$ dating of hornblende grains from the ice-rafted (>150μm or >63μm) fraction of glacial-marine surface sediments off the Pacific sector of West Antarctica

Appendix Table 2.1.1. $^{40}Ar/^{39}Ar$ hornblende data

Site[a]	Sector[a]	Lab. No.	Core name	Ca/K	Cl/K	Mol ^{39}Ar	$\%^{40}Ar$*	Age (Ma)	±	Ref[b]
2	AP	12653-43	DF85-53 (39-44)	6.5	-0.06	0.011	13	1.0	9.3	
2	AP	12653-30	DF85-53 (39-44)	25.1	0.05	0.013	9	3.7	7.7	
2	AP	12653-49	DF85-53 (39-44)	9.4	0.06	0.013	6	5.1	7.6	
2	AP	12653-48	DF85-53 (39-44)	28.8	0.31	0.004	8	5.2	22.9	
2	AP	12535-11	DF85-53 (39-44)	14.0	0.06	0.157	3	6.4	1.3	
2	AP	12653-08	DF85-53 (39-44)	11.3	0.12	0.048	31	8.3	2.2	
2	AP	12653-17	DF85-53 (39-44)	14.2	0.07	0.026	11	8.6	4.1	
2	AP	12653-40	DF85-53 (39-44)	6.4	0.10	0.005	34	9.7	17.2	
2	AP	12653-04	DF85-53 (39-44)	14.5	0.07	0.038	11	10.9	3.0	
2	AP	12535-02	DF85-53 (39-44)	47.6	0.07	0.060	1	10.9	5.0	
2	AP	12653-02	DF85-53 (39-44)	14.2	0.07	0.057	23	11.7	1.9	
2	AP	12669-16	DF85-53 (39-44)	6.7	0.02	0.032	6	11.8	3.7	
2	AP	12653-10	DF85-53 (39-44)	15.0	0.10	0.033	42	12.6	2.7	
2	AP	12669-18	DF85-53 (39-44)	6.7	0.04	0.028	58	12.9	3.6	
2	AP	12535-01	DF85-53 (39-44)	36.4	0.05	0.184	11	13.6	0.8	
2	AP	12535-05	DF85-53 (39-44)	15.0	0.05	0.055	16	13.9	1.1	
2	AP	12535-04	DF85-53 (39-44)	11.6	0.07	0.127	35	13.9	0.5	
2	AP	12535-03	DF85-53 (39-44)	10.8	0.13	0.193	43	14.3	0.3	
2	AP	12653-01	DF85-53 (39-44)	8.8	0.04	0.157	65	14.4	0.6	
2	AP	12535-06	DF85-53 (39-44)	8.4	0.12	0.092	48	14.6	0.5	
2	AP	12669-22	DF85-53 (39-44)	2.8	0.01	0.099	57	14.7	1.1	
2	AP	12669-17	DF85-53 (39-44)	1.3	0.01	0.154	82	15.2	0.7	
2	AP	12669-13	DF85-53 (39-44)	2.8	0.01	0.144	94	17.6	0.8	
2	AP	12535-09	DF85-53 (39-44)	19.6	0.04	0.024	8	17.7	2.6	
2	AP	12669-19	DF85-53 (39-44)	1.4	0.01	0.113	70	17.8	1.0	
2	AP	12669-14	DF85-53 (39-44)	2.0	0.01	0.060	106	18.5	1.9	
2	AP	12653-09	DF85-53 (39-44)	18.6	0.13	0.027	59	18.8	3.5	
2	AP	12653-25	DF85-53 (39-44)	43.4	0.08	0.008	46	20.4	11.5	
2	AP	12669-15	DF85-53 (39-44)	1.6	0.02	0.051	81	21.3	2.2	
2	AP	12653-35	DF85-53 (39-44)	82.9	0.13	0.010	81	21.8	10.1	
2	AP	12653-16	DF85-53 (39-44)	19.9	0.00	0.009	50	22.0	10.6	
2	AP	12653-20	DF85-53 (39-44)	16.0	0.08	0.026	20	24.6	3.9	
2	AP	12653-19	DF85-53 (39-44)	18.1	-0.02	0.009	14	26.8	11.5	
2	AP	12653-31	DF85-53 (39-44)	18.0	0.05	0.019	37	29.1	5.6	
2	AP	12653-47	DF85-53 (39-44)	17.4	0.22	0.005	58	33.4	19.1	
2	AP	12653-13	DF85-53 (39-44)	31.0	0.13	0.014	4	37.0	10.1	
2	AP	12653-38	DF85-53 (39-44)	15.9	-0.02	0.010	58	37.9	9.6	
2	AP	12669-02	DF85-53 (39-44)	27.5	0.09	0.024	12	42.3	7.6	
2	AP	12653-45	DF85-53 (39-44)	15.5	0.10	0.012	78	46.5	7.9	
2	AP	12653-46	DF85-53 (39-44)	14.6	0.12	0.009	92	50.4	10.0	
2	AP	12535-07	DF85-53 (39-44)	17.1	0.12	0.019	41	51.3	2.5	
2	AP	12653-21	DF85-53 (39-44)	29.3	0.14	0.010	22	54.3	10.3	
2	AP	12653-56	DF85-53 (39-44)	70.0	0.09	0.008	17	55.8	11.9	
2	AP	12653-03	DF85-53 (39-44)	34.0	0.12	0.025	25	58.9	4.4	
2	AP	12669-24	DF85-53 (39-44)	41.4	0.03	0.006	11	60.6	19.5	
2	AP	12535-10	DF85-53 (39-44)	17.4	0.13	0.021	23	65.9	2.8	
2	AP	12653-22	DF85-53 (39-44)	31.2	0.15	0.005	65	72.8	15.8	
2	AP	12653-24	DF85-53 (39-44)	22.9	0.10	0.007	267	76.4	13.0	
2	AP	12653-23	DF85-53 (39-44)	10.6	0.07	0.004	50	88.6	23.5	
2	AP	12653-44	DF85-53 (39-44)	15.3	0.06	0.006	70	92.5	15.2	

2	AP	12653-32	DF85-53 (39-44)	78.1	0.17	0.003	11	103.7	31.5	
2	AP	12653-51	DF85-53 (39-44)	19.5	-0.08	0.003	57	108.5	29.4	
2	AP	12653-33	DF85-53 (39-44)	23.9	0.12	0.006	243	113.4	16.7	
2	AP	12653-26	DF85-53 (39-44)	13.5	0.16	0.004	81	189.0	20.5	
2	AP	12653-06	DF85-53 (39-44)	25.4	0.00	0.128	96	2035.7	3.7	
5	AP	11054-12	ELT05-22 (4-6)	22.1			34	26.9	5.1	Roy et al., 2007
5	AP	11054-35	ELT05-22 (4-6)	12.2			30	30.0	1.5	Roy et al., 2007
5	AP	17592-38A	ELT05-22 (4-6)	36.4	0.15	0.006	19	35.8	7.0	
5	AP	11054-42	ELT05-22 (4-6)	17.2			36	37.7	8.8	Roy et al., 2007
5	AP	11054-39	ELT05-22 (4-6)	24.1			58	39.4	4.3	Roy et al., 2007
5	AP	11054-34	ELT05-22 (4-6)	9.9			44	42.6	5.4	Roy et al., 2007
5	AP	11054-20	ELT05-22 (4-6)	27.4			38	45.0	4.6	Roy et al., 2007
5	AP	17592-34A	ELT05-22 (4-6)	16.9	0.17	0.005	16	46.7	7.9	
5	AP	11054-04	ELT05-22 (4-6)	17.3			67	49.4	1.8	Roy et al., 2007
5	AP	11054-14	ELT05-22 (4-6)	28.3			50	49.7	3.0	Roy et al., 2007
5	AP	17592-43A	ELT05-22 (4-6)	10.8	0.10	0.004	12	50.6	10.0	
5	AP	17592-52A	ELT05-22 (4-6)	5.9	0.01	0.056	61	51.4	0.7	
5	AP	11054-13	ELT05-22 (4-6)	25.9			37	52.3	5.6	Roy et al., 2007
5	AP	11054-41	ELT05-22 (4-6)	20.7			35	53.0	6.0	Roy et al., 2007
5	AP	11054-10	ELT05-22 (4-6)	18.2			70	54.0	2.0	Roy et al., 2007
5	AP	11054-57	ELT05-22 (4-6)	18.9			41	54.4	16.0	Roy et al., 2007
5	AP	11054-09	ELT05-22 (4-6)	28.0			58	54.4	2.9	Roy et al., 2007
5	AP	17592-03A	ELT05-22 (4-6)	36.2	0.06	0.169	40	54.5	0.6	
5	AP	11054-46	ELT05-22 (4-6)	17.5			32	55.1	3.4	Roy et al., 2007
5	AP	17592-20A	ELT05-22 (4-6)	16.9	0.08	0.011	49	55.9	3.9	
5	AP	17592-37A	ELT05-22 (4-6)	18.1	0.09	0.013	17	56.1	3.6	
5	AP	11054-03	ELT05-22 (4-6)	26.7			67	56.2	3.9	Roy et al., 2007
5	AP	17592-33A	ELT05-22 (4-6)	15.2	0.14	0.007	61	56.9	5.5	
5	AP	17592-36A	ELT05-22 (4-6)	39.4	0.09	0.014	32	57.0	3.0	
5	AP	11054-27	ELT05-22 (4-6)	22.7			15	57.1	11.1	Roy et al., 2007
5	AP	11054-19	ELT05-22 (4-6)	13.6			84	57.8	1.3	Roy et al., 2007
5	AP	11054-44	ELT05-22 (4-6)	17.0			83	58.0	2.6	Roy et al., 2007
5	AP	11054-48	ELT05-22 (4-6)	13.4			87	59.7	3.5	Roy et al., 2007
5	AP	17592-23A	ELT05-22 (4-6)	12.5	0.12	0.010	42	60.7	4.4	
5	AP	11054-15	ELT05-22 (4-6)	14.7			73	61.0	1.6	Roy et al., 2007
5	AP	17592-12A	ELT05-22 (4-6)	25.8	0.07	0.010	40	62.8	4.5	
5	AP	17592-28A	ELT05-22 (4-6)	38.0	0.14	0.002	7	62.9	25.5	
5	AP	11054-50	ELT05-22 (4-6)	27.9			45	64.7	9.0	Roy et al., 2007
5	AP	11054-51	ELT05-22 (4-6)	13.7			84	64.8	4.9	Roy et al., 2007
5	AP	11054-29	ELT05-22 (4-6)	27.3			34	65.3	8.8	Roy et al., 2007
5	AP	17592-18A	ELT05-22 (4-6)	18.3	0.09	0.007	60	67.7	6.7	
5	AP	17592-32A	ELT05-22 (4-6)	13.4	0.11	0.009	61	68.4	4.6	
5	AP	17592-06A	ELT05-22 (4-6)	51.3	0.07	0.011	16	69.5	5.1	
5	AP	11054-21	ELT05-22 (4-6)	20.6			27	71.2	3.7	Roy et al., 2007
5	AP	17592-35A	ELT05-22 (4-6)	26.2	0.14	0.004	8	74.0	11.5	
5	AP	11054-43	ELT05-22 (4-6)	28.1			34	74.2	12.1	Roy et al., 2007
5	AP	17592-40A	ELT05-22 (4-6)	13.8	0.16	0.002	71	75.9	16.0	
5	AP	11054-16	ELT05-22 (4-6)	28.4			62	76.0	5.3	Roy et al., 2007
5	AP	11054-36	ELT05-22 (4-6)	40.6			56	77.0	2.8	Roy et al., 2007
5	AP	11054-01	ELT05-22 (4-6)	41.4			57	77.9	3.5	Roy et al., 2007
5	AP	11054-32	ELT05-22 (4-6)	15.9			99	78.1	4.3	Roy et al., 2007
5	AP	17592-27A	ELT05-22 (4-6)	24.6	0.14	0.003	52	78.3	12.5	
5	AP	11054-47	ELT05-22 (4-6)	26.0			24	78.4	13.0	Roy et al., 2007
5	AP	11054-24	ELT05-22 (4-6)	12.5			56	78.7	2.7	Roy et al., 2007
5	AP	17592-45A	ELT05-22 (4-6)	2.2	0.03	0.002	36	79.0	19.2	
5	AP	11054-54	ELT05-22 (4-6)	28.9			36	79.2	10.2	Roy et al., 2007
5	AP	17592-41A	ELT05-22 (4-6)	34.5	0.02	0.002	40	79.7	22.8	
5	AP	11054-11	ELT05-22 (4-6)	16.3			66	80.4	2.2	Roy et al., 2007
5	AP	17592-14A	ELT05-22 (4-6)	54.8	0.35	0.005	13	80.6	10.5	
5	AP	11054-28	ELT05-22 (4-6)	15.9			36	83.2	6.7	Roy et al., 2007

5	AP	11054-08	ELT05-22 (4-6)	23.3			70	83.5	1.9 Roy et al., 2007
5	AP	11054-25	ELT05-22 (4-6)	15.4			71	83.8	5.9 Roy et al., 2007
5	AP	11054-33	ELT05-22 (4-6)	25.7			21	84.7	23.3 Roy et al., 2007
5	AP	11054-45	ELT05-22 (4-6)	16.9			42	87.5	9.7 Roy et al., 2007
5	AP	17592-11A	ELT05-22 (4-6)	22.0	0.07	0.017	72	88.0	2.7
5	AP	11054-52	ELT05-22 (4-6)	15.8			67	89.1	8.1 Roy et al., 2007
5	AP	11054-23	ELT05-22 (4-6)	14.0			78	90.2	3.0 Roy et al., 2007
5	AP	11054-02	ELT05-22 (4-6)	21.2			57	90.4	2.0 Roy et al., 2007
5	AP	17592-02A	ELT05-22 (4-6)	25.1	0.09	0.023	11	90.6	4.6
5	AP	11054-07	ELT05-22 (4-6)	40.2			52	90.9	5.8 Roy et al., 2007
5	AP	17592-22A	ELT05-22 (4-6)	22.3	0.05	0.011	24	91.7	4.9
5	AP	17592-16A	ELT05-22 (4-6)	31.6	0.10	0.004	12	92.1	12.1
5	AP	17592-13A	ELT05-22 (4-6)	18.6	0.11	0.014	22	92.1	3.9
5	AP	11054-22	ELT05-22 (4-6)	22.5			65	92.2	6.5 Roy et al., 2007
5	AP	17592-17A	ELT05-22 (4-6)	36.2	0.10	0.002	47	93.8	17.8
5	AP	17592-39A	ELT05-22 (4-6)	20.6	0.08	0.002	27	94.8	17.1
5	AP	17592-01A	ELT05-22 (4-6)	19.6	0.04	0.038	9	97.4	4.9
5	AP	17592-31A	ELT05-22 (4-6)	50.3	0.12	0.005	11	100.5	9.9
5	AP	17592-07A	ELT05-22 (4-6)	29.5	0.09	0.009	37	101.1	5.9
5	AP	17592-29A	ELT05-22 (4-6)	21.7	0.13	0.002	32	105.1	16.6
5	AP	17592-10A	ELT05-22 (4-6)	22.0	0.08	0.005	52	110.1	10.1
5	AP	17592-04A	ELT05-22 (4-6)	272.3	0.16	0.005	2	116.0	34.3
5	AP	17592-30A	ELT05-22 (4-6)	27.3	0.10	0.002	62	120.1	20.3
5	AP	11054-49	ELT05-22 (4-6)	35.9			37	123.2	18.5 Roy et al., 2007
5	AP	17592-42A	ELT05-22 (4-6)	32.9	0.01	0.001	28	130.7	29.2
5	AP	17592-05A	ELT05-22 (4-6)	29.6	0.14	0.045	39	133.6	1.7
5	AP	17592-21A	ELT05-22 (4-6)	58.0	0.11	0.001	50	134.5	35.9
5	AP	17592-19A	ELT05-22 (4-6)	22.6	0.07	0.004	50	138.7	9.8
5	AP	11054-06	ELT05-22 (4-6)	32.9			86	166.6	3.3 Roy et al., 2007
5	AP	11054-56	ELT05-22 (4-6)	24.3			20	175.3	21.4 Roy et al., 2007
5	AP	11054-37	ELT05-22 (4-6)	17.4			75	205.3	2.0 Roy et al., 2007
5	AP	17592-15A	ELT05-22 (4-6)	79.9	0.30	0.001	13	209.2	35.7
5	AP	11054-30	ELT05-22 (4-6)	21.5			93	478.4	4.1 Roy et al., 2007
5	AP	17592-26A	ELT05-22 (4-6)	34.7	0.00	0.003	85	920.8	26.3
5	AP	11054-40	ELT05-22 (4-6)	8.5			97	1594.4	4.4 Roy et al., 2007
5	AP	11054-31	ELT05-22 (4-6)	13.0			99	1775.5	8.2 Roy et al., 2007
6	AP	12661-16	DF85-82 (28-33)	29.8	0.06	0.008	6	21.6	15.0
6	AP	12661-28	DF85-82 (28-33)	16.9	0.06	0.020	24	45.5	5.5
6	AP	12661-19	DF85-82 (28-33)	26.5	0.07	0.021	27	64.7	5.1
6	AP	12661-12	DF85-82 (28-33)	40.8	0.04	0.022	40	64.7	4.9
6	AP	12661-09	DF85-82 (28-33)	14.3	0.03	0.020	39	77.2	5.1
6	AP	12661-11	DF85-82 (28-33)	13.8	0.02	0.029	40	77.4	3.9
6	AP	12661-14	DF85-82 (28-33)	12.7	0.04	0.023	60	79.2	4.8
6	AP	12661-08	DF85-82 (28-33)	19.3	0.02	0.014	33	86.9	7.5
6	AP	12661-10	DF85-82 (28-33)	9.4	0.03	0.098	50	88.5	1.6
6	AP	12527-15	DF85-82 (28-33)	23.2	0.03	0.057	44	89.0	1.6
6	AP	12527-07	DF85-82 (28-33)	16.6	0.02	0.236	72	89.8	1.0
6	AP	12527-08	DF85-82 (28-33)	10.6	0.01	0.187	53	92.2	1.2
6	AP	12527-02	DF85-82 (28-33)	6.6	0.00	0.645	62	92.7	1.0
6	AP	12527-17	DF85-82 (28-33)	13.9	0.02	0.070	41	93.2	1.7
6	AP	12661-13	DF85-82 (28-33)	21.6	0.00	0.012	35	98.5	7.9
6	AP	12661-17	DF85-82 (28-33)	10.6	0.10	0.013	19	115.4	8.4
6	AP	12527-13	DF85-82 (28-33)	6.5	0.07	0.157	73	118.3	1.3
6	AP	12661-15	DF85-82 (28-33)	18.6	0.06	0.013	50	119.4	7.9
6	AP	12661-05	DF85-82 (28-33)	14.4	-0.01	0.035	70	125.9	3.7
6	AP	12527-14	DF85-82 (28-33)	6.6	0.01	0.286	42	131.4	1.8
6	AP	12661-01	DF85-82 (28-33)	21.0	0.02	0.196	61	137.2	1.6
6	AP	12661-27	DF85-82 (28-33)	11.3	0.02	0.082	71	138.0	2.0
6	AP	12661-02	DF85-82 (28-33)	18.5	0.03	0.144	63	157.5	1.9
6	AP	12661-07	DF85-82 (28-33)	17.5	0.02	0.022	66	174.3	4.9

6	AP	12527-09	DF85-82 (28-33)	12.3	0.01	0.264	66	177.7	2.0	
6	AP	12661-03	DF85-82 (28-33)	9.8	0.02	0.095	88	177.9	2.3	
6	AP	12527-11	DF85-82 (28-33)	20.9	0.02	0.091	50	187.7	2.5	
6	AP	12527-10	DF85-82 (28-33)	12.1	0.01	0.095	83	192.7	2.2	
6	AP	12527-18	DF85-82 (28-33)	15.1	0.03	0.094	84	199.2	2.2	
6	AP	12527-05	DF85-82 (28-33)	30.8	0.03	0.076	36	199.6	3.3	
6	AP	12527-06	DF85-82 (28-33)	28.2	0.02	0.146	50	201.5	2.5	
6	AP	12661-06	DF85-82 (28-33)	14.2	0.02	0.052	89	233.6	3.1	
6	AP	12527-12	DF85-82 (28-33)	50.6	0.04	0.027	55	271.3	4.0	
6	AP	12527-16	DF85-82 (28-33)	18.9	0.01	0.052	57	277.2	3.5	
6	AP	12527-03	DF85-82 (28-33)	28.5	0.03	0.077	51	284.8	3.7	
6	AP	12661-04	DF85-82 (28-33)	9.8	0.02	0.113	98	301.2	3.3	
6	AP	12527-01	DF85-82 (28-33)	65.5	0.02	0.236	72	320.0	3.5	
6	AP	12527-04	DF85-82 (28-33)	13.1	0.03	0.260	87	789.3	8.2	
6	AP	12661-18	DF85-82 (28-33)	11.7	0.01	0.013	12	1076.3	33.8	
8	AP	17594-08A	ELT 05-20 (2-4)	8.5	0.03	0.008	3	1.7	4.5	
8	AP	17594-05A	ELT 05-20 (2-4)	7.4	0.02	0.008	19	6.0	4.8	
8	AP	17594-15A	ELT 05-20 (2-4)	11.3	0.02	0.006	31	8.4	6.1	
8	AP	17594-26A	ELT 05-20 (2-4)	3.9	0.00	0.008	43	9.1	2.0	
8	AP	17594-24A	ELT 05-20 (2-4)	4.7	0.00	0.007	31	11.7	2.3	
8	AP	17594-35A	ELT 05-20 (2-4)	8.6	0.07	0.001	20	17.9	12.7	
8	AP	17594-29A	ELT 05-20 (2-4)	4.5	0.03	0.002	87	33.6	9.1	
8	AP	17594-32A	ELT 05-20 (2-4)	4.0	0.02	0.015	13	36.0	2.6	
8	AP	17594-02A	ELT 05-20 (2-4)	9.9	0.00	0.022	61	50.7	1.8	
8	AP	17594-37A	ELT 05-20 (2-4)	12.3	0.02	0.009	28	52.7	3.2	
8	AP	17594-19A	ELT 05-20 (2-4)	2.0	0.01	0.026	78	55.4	0.8	
8	AP	17594-10A	ELT 05-20 (2-4)	27.8	0.11	0.014	57	56.5	2.5	
8	AP	17594-01A	ELT 05-20 (2-4)	12.0	0.06	0.006	48	58.7	5.7	
8	AP	17594-21A	ELT 05-20 (2-4)	20.3	0.13	0.003	53	59.2	5.7	
8	AP	17594-12A	ELT 05-20 (2-4)	8.9	0.04	0.032	59	59.3	1.2	
8	AP	17594-11A	ELT 05-20 (2-4)	18.7	0.12	0.007	48	59.7	5.3	
8	AP	17594-18A	ELT 05-20 (2-4)	10.7	0.03	0.040	39	62.7	1.2	
8	AP	11009-25	ELT 05-20 (2-4)	15.1			84	63.9	4.9	Roy et al., 2007
8	AP	17594-06A	ELT 05-20 (2-4)	27.8	0.09	0.024	20	64.2	2.4	
8	AP	17594-04A	ELT 05-20 (2-4)	17.0	0.08	0.010	38	67.6	3.8	
8	AP	17594-28A	ELT 05-20 (2-4)	22.6	0.05	0.002	58	69.7	8.3	
8	AP	17594-27A	ELT 05-20 (2-4)	16.8	0.14	0.002	45	72.0	7.1	
8	AP	17594-34A	ELT 05-20 (2-4)	32.8	0.14	0.001	16	75.4	14.7	
8	AP	17594-25A	ELT 05-20 (2-4)	13.3	0.09	0.004	38	75.8	4.4	
8	AP	17594-03A	ELT 05-20 (2-4)	38.7	0.07	0.005	32	75.9	7.8	
8	AP	11009-54	ELT 05-20 (2-4)	17.2			89	76.6	6.7	Roy et al., 2007
8	AP	11009-03	ELT 05-20 (2-4)	16.9			77	82.0	2.6	Roy et al., 2007
8	AP	17594-20A	ELT 05-20 (2-4)	13.4	0.03	0.016	18	82.3	3.7	
8	AP	17594-07A	ELT 05-20 (2-4)	34.7	0.07	0.005	16	82.6	7.4	
8	AP	11009-59	ELT 05-20 (2-4)	22.3			100	85.2	18.9	Roy et al., 2007
8	AP	11009-56	ELT 05-20 (2-4)	19.2			94	87.8	15.4	Roy et al., 2007
8	AP	17594-17A	ELT 05-20 (2-4)	13.4	0.05	0.004	73	94.0	7.8	
8	AP	11009-41	ELT 05-20 (2-4)	24.8			75	103.0	24.5	Roy et al., 2007
8	AP	17594-31A	ELT 05-20 (2-4)	28.8	0.02	0.003	27	112.7	11.8	
8	AP	11009-01	ELT 05-20 (2-4)	17.2			93	113.9	1.5	Roy et al., 2007
8	AP	17594-13A	ELT 05-20 (2-4)	29.0	0.04	0.001	20	122.6	25.4	
8	AP	11009-65	ELT 05-20 (2-4)	25.0			135	125.6	22.5	Roy et al., 2007
10	BS	17598-29A	ELT 42-09 (0-2)	5.8	0.03	0.007	6	36.7	5.9	
10	BS	11006-35	ELT 42-09 (0-2)	23.3			78	70.0	12.7	Roy et al., 2007
10	BS	17598-27A	ELT 42-09 (0-2)	2.4	-0.05	0.001	9	73.2	24.0	
10	BS	11006-25	ELT 42-09 (0-2)	9.9			90	91.0	1.8	Roy et al., 2007
10	BS	11006-21	ELT 42-09 (0-2)	18.1			76	100.8	9.1	Roy et al., 2007
10	BS	11006-22	ELT 42-09 (0-2)	8.5			94	101.4	2.6	Roy et al., 2007
10	BS	11006-30	ELT 42-09 (0-2)	19.3			79	102.7	6.8	Roy et al., 2007

10	BS	11006-29	ELT 42-09 (0-2)	15.4			90	103.0	3.5	Roy et al., 2007
10	BS	11006-13	ELT 42-09 (0-2)	15.2			83	104.9	4.4	Roy et al., 2007
10	BS	11006-02	ELT 42-09 (0-2)	11.3			90	108.6	1.9	Roy et al., 2007
10	BS	11006-14	ELT 42-09 (0-2)	16.3			93	111.8	3.2	Roy et al., 2007
10	BS	11006-34	ELT 42-09 (0-2)	7.0			89	114.4	3.2	Roy et al., 2007
10	BS	11006-28	ELT 42-09 (0-2)	7.6			77	114.5	1.5	Roy et al., 2007
10	BS	11006-07	ELT 42-09 (0-2)	7.9			94	116.9	1.0	Roy et al., 2007
10	BS	11006-17	ELT 42-09 (0-2)	12.7			87	117.5	3.5	Roy et al., 2007
10	BS	11006-37	ELT 42-09 (0-2)	12.5			75	119.1	3.9	Roy et al., 2007
10	BS	17598-07A	ELT 42-09 (0-2)	2.1	0.00	0.008	66	120.4	5.2	
10	BS	11006-01	ELT 42-09 (0-2)	10.3			84	121.2	1.1	Roy et al., 2007
10	BS	11006-05	ELT 42-09 (0-2)	15.9			77	125.2	5.6	Roy et al., 2007
10	BS	11006-38	ELT 42-09 (0-2)	7.4			100	125.2	1.9	Roy et al., 2007
10	BS	17598-16A	ELT 42-09 (0-2)	12.4	0.06	0.004	20	126.8	7.7	
10	BS	17598-19A	ELT 42-09 (0-2)	10.8	0.03	0.006	31	130.4	5.6	
10	BS	11006-03	ELT 42-09 (0-2)	10.9			80	131.0	1.2	Roy et al., 2007
10	BS	11006-33	ELT 42-09 (0-2)	32.1			92	133.7	8.1	Roy et al., 2007
10	BS	17598-17A	ELT 42-09 (0-2)	15.5	0.03	0.028	52	133.9	2.0	
10	BS	11006-09	ELT 42-09 (0-2)	8.9			90	138.9	4.0	Roy et al., 2007
10	BS	11006-24	ELT 42-09 (0-2)	19.5			98	141.2	7.3	Roy et al., 2007
10	BS	11006-39	ELT 42-09 (0-2)	20.4			135	191.5	11.0	Roy et al., 2007
10	BS	17598-24A	ELT 42-09 (0-2)	14.9	0.08	0.002	17	215.7	14.1	
10	BS	17598-31A	ELT 42-09 (0-2)	4.8	0.00	0.016	96	511.2	3.0	
11	BS	18577-11A	BC 361 Y (Surf)	6.0	-0.02	0.003	22	59.3	10.3	
11	BS	18576-11A	BC 361 Y (Surf)	23.3	0.01	0.001	53	64.6	11.1	
11	BS	18576-23A	BC 361 Y (Surf)	14.4	0.08	0.002	52	67.2	14.2	
11	BS	18577-09A	BC 361 Y (Surf)	4.8	-0.03	0.003	14	71.8	10.0	
11	BS	18576-12A	BC 361 Y (Surf)	31.5	0.07	0.001	43	73.3	12.0	
11	BS	18576-14A	BC 361 Y (Surf)	31.5	0.02	0.001	38	73.9	12.8	
11	BS	18576-02A	BC 361 Y (Surf)	5.2	0.01	0.101	67	78.3	0.3	
11	BS	18576-16A	BC 361 Y (Surf)	16.8	0.04	0.005	78	81.5	2.7	
11	BS	18576-25A	BC 361 Y (Surf)	16.9	0.05	0.002	103	84.0	13.1	
11	BS	18577-08A	BC 361 Y (Surf)	1.2	0.03	0.002	46	89.9	12.1	
11	BS	18576-37A	BC 361 Y (Surf)	3.1	0.00	0.016	72	90.9	1.9	
11	BS	18576-38A	BC 361 Y (Surf)	11.0	0.03	0.007	84	93.1	4.1	
11	BS	18576-36A	BC 361 Y (Surf)	12.9	0.03	0.003	65	97.1	11.1	
11	BS	18576-27A	BC 361 Y (Surf)	11.2	0.02	0.003	69	100.3	9.4	
11	BS	18576-05A	BC 361 Y (Surf)	2.1	0.00	0.027	68	103.4	0.8	
11	BS	18576-19A	BC 361 Y (Surf)	19.0	0.08	0.002	82	104.4	14.2	
11	BS	18576-06A	BC 361 Y (Surf)	18.6	0.02	0.010	78	105.6	1.9	
11	BS	18576-26A	BC 361 Y (Surf)	8.9	0.04	0.002	89	109.8	18.1	
11	BS	18576-15A	BC 361 Y (Surf)	11.1	0.01	0.006	83	110.9	2.3	
11	BS	18576-08A	BC 361 Y (Surf)	8.4	0.03	0.003	92	111.7	4.2	
11	BS	18577-10A	BC 361 Y (Surf)	11.5	0.00	0.005	56	115.0	5.2	
11	BS	18576-33A	BC 361 Y (Surf)	8.7	0.00	0.007	101	115.3	3.9	
11	BS	18576-13A	BC 361 Y (Surf)	22.6	0.03	0.002	83	116.6	5.1	
11	BS	18576-30A	BC 361 Y (Surf)	28.5	0.02	0.001	68	118.1	18.4	
11	BS	18576-28A	BC 361 Y (Surf)	8.8	0.03	0.007	84	118.9	4.0	
11	BS	18576-07A	BC 361 Y (Surf)	9.4	0.02	0.031	93	122.4	0.6	
11	BS	18576-09A	BC 361 Y (Surf)	11.6	0.01	0.002	83	122.5	5.9	
11	BS	18576-24A	BC 361 Y (Surf)	7.9	0.01	0.007	91	123.7	4.1	
11	BS	18576-01A	BC 361 Y (Surf)	6.0	0.02	0.174	82	125.4	0.5	
11	BS	18576-20A	BC 361 Y (Surf)	24.9	-0.03	0.002	70	131.7	13.2	
11	BS	18576-04A	BC 361 Y (Surf)	1.6	0.01	0.044	88	133.1	0.5	
11	BS	18576-39A	BC 361 Y (Surf)	12.1	0.04	0.003	97	136.9	10.2	
11	BS	18576-35A	BC 361 Y (Surf)	23.8	0.02	0.002	95	137.8	15.6	
11	BS	18576-21A	BC 361 Y (Surf)	12.8	0.00	0.003	91	139.7	11.8	
11	BS	18576-22A	BC 361 Y (Surf)	19.5	0.04	0.001	40	139.8	24.2	
11	BS	18576-17A	BC 361 Y (Surf)	23.6	0.06	0.003	90	150.6	9.9	
11	BS	18576-32A	BC 361 Y (Surf)	24.2	-0.02	0.003	78	152.9	10.7	

11	BS	18576-18A	BC 361 Y (Surf)	40.8	-0.11	0.001	102	216.1	29.8
14	BS	18170-44A	BC369 (0-2)	2.5	0.00	0.032	12	16.6	1.5
14	BS	18172-26A	BC369 (0-2)	12.5	0.08	0.012	22	25.7	1.6
14	BS	18172-04A	BC369 (0-2)	28.8	0.05	0.003	80	30.7	14.1
14	BS	18172-14A	BC369 (0-2)	38.7	0.09	0.008	20	38.0	2.6
14	BS	18172-29A	BC369 (0-2)	16.1	0.04	0.005	76	81.2	3.7
14	BS	18170-28A	BC369 (0-2)	2.4	-0.02	0.006	44	81.5	4.5
14	BS	18172-16A	BC369 (0-2)	17.2	0.03	0.007	69	84.8	2.5
14	BS	18172-27A	BC369 (0-2)	14.5	0.04	0.005	74	90.4	3.5
14	BS	18172-41A	BC369 (0-2)	10.8	0.03	0.005	41	94.6	9.5
14	BS	18172-03A	BC369 (0-2)	11.4	0.02	0.016	64	94.8	2.3
14	BS	18172-35A	BC369 (0-2)	14.5	-0.03	0.004	53	95.2	10.7
14	BS	18172-15A	BC369 (0-2)	15.9	0.03	0.017	59	96.6	1.2
14	BS	18172-39A	BC369 (0-2)	7.4	-0.02	0.006	83	97.1	6.6
14	BS	18170-10A	BC369 (0-2)	2.1	-0.01	0.012	59	93.2	2.3
14	BS	18172-13A	BC369 (0-2)	9.9	0.06	0.018	96	98.3	2.2
14	BS	18172-21A	BC369 (0-2)	10.7	-0.03	0.006	42	98.3	3.1
14	BS	18172-42A	BC369 (0-2)	14.1	0.03	0.003	58	99.2	12.2
14	BS	18170-43A	BC369 (0-2)	2.1	0.02	0.004	8	102.7	12.6
14	BS	18172-23A	BC369 (0-2)	16.2	0.00	0.004	93	102.8	3.9
14	BS	18172-18A	BC369 (0-2)	10.8	0.00	0.011	71	103.3	1.6
14	BS	18172-07A	BC369 (0-2)	11.0	0.01	0.007	103	104.4	5.0
14	BS	18172-40A	BC369 (0-2)	6.1	-0.01	0.006	89	104.7	6.4
14	BS	18172-11A	BC369 (0-2)	15.3	0.09	0.003	93	104.9	12.0
14	BS	18172-08A	BC369 (0-2)	18.7	-0.05	0.003	133	105.7	11.7
14	BS	18172-36A	BC369 (0-2)	18.0	0.05	0.004	80	106.2	11.6
14	BS	18172-32A	BC369 (0-2)	16.7	0.05	0.006	47	107.3	7.4
14	BS	18172-30A	BC369 (0-2)	26.3	-0.06	0.002	93	107.5	9.9
14	BS	18172-25A	BC369 (0-2)	11.5	0.00	0.011	95	108.0	1.7
14	BS	18172-48A	BC369 (0-2)	11.2	-0.06	0.003	77	108.3	13.5
14	BS	18172-24A	BC369 (0-2)	10.3	-0.01	0.013	91	109.9	1.5
14	BS	18172-17A	BC369 (0-2)	10.9	-0.01	0.009	89	110.1	2.0
14	BS	18172-06A	BC369 (0-2)	0.0	0.00	0.060	100	110.3	0.6
14	BS	18172-22A	BC369 (0-2)	16.7	-0.01	0.004	115	112.3	4.1
14	BS	18172-12A	BC369 (0-2)	22.9	0.05	0.004	53	114.4	8.5
14	BS	18172-28A	BC369 (0-2)	9.1	0.01	0.011	92	114.7	1.6
14	BS	18172-10A	BC369 (0-2)	6.1	0.00	0.006	116	116.7	6.3
14	BS	18172-05A	BC369 (0-2)	12.9	0.01	0.005	69	117.5	7.8
14	BS	18172-37A	BC369 (0-2)	11.8	0.04	0.003	61	118.1	13.0
14	BS	18172-45A	BC369 (0-2)	9.7	-0.03	0.004	49	118.8	10.5
14	BS	18172-19A	BC369 (0-2)	13.9	-0.04	0.004	78	119.4	4.7
14	BS	18172-09A	BC369 (0-2)	15.4	0.05	0.005	106	126.8	7.2
14	BS	18172-02A	BC369 (0-2)	32.5	0.03	0.006	101	130.6	6.1
14	BS	18172-33A	BC369 (0-2)	11.1	0.09	0.003	27	133.8	14.4
14	BS	18172-31A	BC369 (0-2)	16.0	0.04	0.005	91	136.3	3.3
14	BS	18172-20A	BC369 (0-2)	10.5	0.02	0.005	56	141.8	3.5
14	BS	18172-47A	BC369 (0-2)	5.9	0.03	0.002	127	156.0	21.7
14	BS	18172-01A	BC369 (0-2)	28.7	0.02	0.003	91	203.0	11.9
15	BS	18182-48A	BC459 (Surf)	9.7	0.02	0.007	13	13.9	4.1
15	BS	18182-14A	BC459 (Surf)	17.3	0.07	0.004	13	16.2	6.1
15	BS	18182-51A	BC459 (Surf)	14.0	0.08	0.065	40	25.1	0.5
15	BS	18182-25A	BC459 (Surf)	18.1	0.05	0.006	25	31.6	3.9
15	BS	18182-33A	BC459 (Surf)	20.7	0.06	0.015	16	37.1	2.6
15	BS	18182-46A	BC459 (Surf)	16.4	0.02	0.005	33	42.9	5.1
15	BS	18182-54A	BC459 (Surf)	19.8	0.06	0.012	42	51.2	2.5
15	BS	18182-44A	BC459 (Surf)	19.2	0.05	0.023	59	57.5	1.3
15	BS	18182-39A	BC459 (Surf)	16.3	0.05	0.007	32	58.5	4.4
15	BS	18182-53A	BC459 (Surf)	22.6	0.06	0.026	60	60.0	1.2
15	BS	18179-35A	BC459 (Surf)	5.2	-0.06	0.003	13	63.9	14.0

15	BS	18182-15A	BC459 (Surf)	13.4	0.11	0.002	28	63.9	12.8	
15	BS	18182-43A	BC459 (Surf)	7.2	0.00	0.004	11	64.3	8.8	
15	BS	18182-21A	BC459 (Surf)	16.7	-0.02	0.005	28	67.1	5.3	
15	BS	18182-08A	BC459 (Surf)	13.6	0.10	0.011	81	69.3	2.5	
15	BS	18182-28A	BC459 (Surf)	10.6	0.03	0.004	42	71.5	5.9	
15	BS	18179-06A	BC459 (Surf)	12.8	0.00	0.007	10	74.4	7.9	
15	BS	18182-05A	BC459 (Surf)	19.6	0.04	0.002	41	76.9	10.9	
15	BS	18182-38A	BC459 (Surf)	16.1	0.05	0.008	65	83.7	3.1	
15	BS	18182-52A	BC459 (Surf)	26.5	0.05	0.025	52	84.0	1.3	
15	BS	18179-49A	BC459 (Surf)	1.7	-0.01	0.011	59	88.0	3.8	
15	BS	18182-50A	BC459 (Surf)	11.6	0.01	0.014	29	88.7	2.8	
15	BS	18182-16A	BC459 (Surf)	32.6	0.07	0.003	32	88.8	7.5	
15	BS	18182-29A	BC459 (Surf)	8.6	0.02	0.013	69	89.6	2.2	
15	BS	18182-13A	BC459 (Surf)	8.2	-0.02	0.009	73	90.2	2.7	
15	BS	18182-37A	BC459 (Surf)	22.2	0.12	0.008	54	90.7	3.5	
15	BS	18179-38A	BC459 (Surf)	12.8	-0.02	0.003	14	91.6	13.3	
15	BS	18182-07A	BC459 (Surf)	9.5	0.02	0.009	32	91.7	4.0	
15	BS	18182-45A	BC459 (Surf)	17.1	0.01	0.004	49	91.9	6.7	
15	BS	18179-13A	BC459 (Surf)	2.8	0.00	0.023	53	92.4	2.1	
15	BS	18182-18A	BC459 (Surf)	15.5	-0.01	0.006	60	93.3	3.9	
15	BS	18182-11A	BC459 (Surf)	9.8	0.04	0.006	57	94.5	4.7	
15	BS	18182-47A	BC459 (Surf)	6.0	0.01	0.033	88	96.7	0.9	
15	BS	18182-19A	BC459 (Surf)	10.3	0.00	0.011	54	97.4	2.7	
15	BS	18182-36A	BC459 (Surf)	14.8	0.03	0.007	68	99.4	3.7	
15	BS	18182-40A	BC459 (Surf)	9.3	0.01	0.006	54	99.5	4.1	
15	BS	18182-41A	BC459 (Surf)	17.8	0.02	0.023	61	99.6	1.4	
15	BS	18182-30A	BC459 (Surf)	34.7	0.06	0.008	33	101.3	4.3	
15	BS	18182-31A	BC459 (Surf)	16.6	0.05	0.010	76	102.7	2.7	
15	BS	18182-27A	BC459 (Surf)	11.6	0.00	0.007	40	103.0	4.2	
15	BS	18182-42A	BC459 (Surf)	12.1	0.01	0.013	25	104.6	3.3	
15	BS	18182-20A	BC459 (Surf)	14.8	0.01	0.010	52	105.3	2.9	
15	BS	18182-35A	BC459 (Surf)	11.3	0.03	0.019	88	105.9	1.6	
15	BS	18182-17A	BC459 (Surf)	14.3	-0.02	0.001	64	107.3	14.9	
15	BS	18182-32A	BC459 (Surf)	10.3	0.01	0.021	81	107.4	1.4	
15	BS	18182-06A	BC459 (Surf)	8.8	0.00	0.006	58	108.8	4.1	
15	BS	18182-24A	BC459 (Surf)	12.1	0.00	0.005	59	109.6	5.3	
15	BS	18182-02A	BC459 (Surf)	6.8	-0.06	0.002	59	114.0	12.1	
15	BS	18182-10A	BC459 (Surf)	15.7	0.03	0.009	86	115.8	3.1	
15	BS	18182-23A	BC459 (Surf)	12.2	0.02	0.016	58	120.7	2.0	
15	BS	18182-22A	BC459 (Surf)	10.1	0.00	0.070	81	120.7	0.6	
15	BS	18182-34A	BC459 (Surf)	105.1	0.07	0.008	43	138.7	3.8	
15	BS	18182-09A	BC459 (Surf)	14.0	0.02	0.005	20	143.9	7.4	
15	BS	18182-60A	BC459 (Surf)	11.4	-0.02	0.004	56	151.1	21.5	
15	BS	18182-59A	BC459 (Surf)	19.2	0.01	0.003	59	168.7	22.1	
15	BS	18182-61A	BC459 (Surf)	18.1	0.03	0.003	46	181.4	26.9	
15	BS	18182-66A	BC459 (Surf)	4.8	0.02	0.003	63	187.3	23.1	
15	BS	18182-65A	BC459 (Surf)	10.3	0.03	0.003	59	202.2	23.0	
15	BS	18182-55A	BC459 (Surf)	9.0	0.01	0.003	69	233.4	29.5	
15	BS	18182-63A	BC459 (Surf)	8.4	0.07	0.009	7	246.3	20.6	
15	BS	18182-56A	BC459 (Surf)	7.5	0.03	0.016	89	253.4	4.9	
17	AS-E	17588-26A	ELT 11-19 (0-2)	10.1	0.00	0.005	15	7.9	3.6	
17	AS-E	17588-28A	ELT 11-19 (0-2)	9.0	-0.02	0.002	26	22.4	7.0	
17	AS-E	11053-30	ELT 11-19 (0-2)	18.3			41	46.8	6.6	Roy et al., 2007
17	AS-E	11041-02	ELT 11-19 (0-2)	29.1			54	57.1	1.7	Roy et al., 2007
17	AS-E	11053-21	ELT 11-19 (0-2)	20.5			51	62.4	3.5	Roy et al., 2007
17	AS-E	17588-29A	ELT 11-19 (0-2)	17.8	0.15	0.002	24	64.6	10.8	
17	AS-E	11053-13	ELT 11-19 (0-2)	15.6			63	67.3	8.6	Roy et al., 2007
17	AS-E	11053-03	ELT 11-19 (0-2)	34.6			32	71.3	15.0	Roy et al., 2007
17	AS-E	11053-16	ELT 11-19 (0-2)	29.7			24	72.1	6.8	Roy et al., 2007
17	AS-E	11041-12	ELT 11-19 (0-2)	26.0			85	74.9	11.7	Roy et al., 2007

17	AS-E	11053-43	ELT 11-19 (0-2)	9.0			71	78.6	4.1	Roy et al., 2007
17	AS-E	11053-33	ELT 11-19 (0-2)	27.6			28	81.6	11.6	Roy et al., 2007
17	AS-E	11053-05	ELT 11-19 (0-2)	18.1			95	85.7	1.8	Roy et al., 2007
17	AS-E	11053-32	ELT 11-19 (0-2)	8.5			65	89.1	4.4	Roy et al., 2007
17	AS-E	11053-01	ELT 11-19 (0-2)	10.8			89	89.6	1.6	Roy et al., 2007
17	AS-E	17588-31A	ELT 11-19 (0-2)	7.8	0.05	0.005	44	91.0	4.2	
17	AS-E	17588-20A	ELT 11-19 (0-2)	1.8	0.08	0.002	5	93.4	16.7	
17	AS-E	11053-04	ELT 11-19 (0-2)	13.5			80	96.8	3.1	Roy et al., 2007
17	AS-E	11053-08	ELT 11-19 (0-2)	5.6			83	99.3	2.2	Roy et al., 2007
17	AS-E	11053-24	ELT 11-19 (0-2)	9.1			74	99.3	1.3	Roy et al., 2007
17	AS-E	17588-12A	ELT 11-19 (0-2)	38.6	0.14	0.006	18	99.6	5.6	
17	AS-E	11041-01	ELT 11-19 (0-2)	9.8			96	100.4	0.7	Roy et al., 2007
17	AS-E	11053-14	ELT 11-19 (0-2)	8.0			83	100.5	1.8	Roy et al., 2007
17	AS-E	17588-10A	ELT 11-19 (0-2)	8.9	0.01	0.122	94	100.7	0.3	
17	AS-E	17588-22A	ELT 11-19 (0-2)	1.9	0.01	0.001	26	101.4	14.9	
17	AS-E	11041-11	ELT 11-19 (0-2)	10.9			85	102.6	2.2	Roy et al., 2007
17	AS-E	11053-28	ELT 11-19 (0-2)	11.5			25	103.2	13.0	Roy et al., 2007
17	AS-E	11053-15	ELT 11-19 (0-2)	9.7			60	103.5	1.5	Roy et al., 2007
17	AS-E	11053-23	ELT 11-19 (0-2)	10.6			95	104.1	2.2	Roy et al., 2007
17	AS-E	11041-04	ELT 11-19 (0-2)	7.2			85	104.4	1.1	Roy et al., 2007
17	AS-E	17588-15A	ELT 11-19 (0-2)	7.0	0.02	0.025	60	106.5	1.2	
17	AS-E	17588-13A	ELT 11-19 (0-2)	5.1	0.01	0.064	65	106.5	0.6	
17	AS-E	11053-18	ELT 11-19 (0-2)	6.6			87	107.7	1.4	Roy et al., 2007
17	AS-E	11053-39	ELT 11-19 (0-2)	6.8			67	107.7	4.3	Roy et al., 2007
17	AS-E	17588-11A	ELT 11-19 (0-2)	34.3	0.10	0.002	26	108.0	17.9	
17	AS-E	11053-12	ELT 11-19 (0-2)	7.7			81	108.2	2.2	Roy et al., 2007
17	AS-E	11041-13	ELT 11-19 (0-2)	6.7			103	108.3	3.3	Roy et al., 2007
17	AS-E	11053-38	ELT 11-19 (0-2)	8.8			71	110.0	7.3	Roy et al., 2007
17	AS-E	11041-06	ELT 11-19 (0-2)	33.6			54	111.4	11.9	Roy et al., 2007
17	AS-E	17588-27A	ELT 11-19 (0-2)	11.9	0.00	0.002	58	113.9	7.8	
17	AS-E	17588-33A	ELT 11-19 (0-2)	10.1	-0.06	0.002	9	119.5	17.3	
17	AS-E	11041-07	ELT 11-19 (0-2)	18.5			93	120.8	4.5	Roy et al., 2007
17	AS-E	17588-08A	ELT 11-19 (0-2)	9.2	0.05	0.002	13	121.0	15.8	
17	AS-E	11053-29	ELT 11-19 (0-2)	13.3			82	123.3	4.8	Roy et al., 2007
17	AS-E	11053-40	ELT 11-19 (0-2)	0.6			31	127.7	18.6	Roy et al., 2007
17	AS-E	11053-34	ELT 11-19 (0-2)	14.2			68	129.3	10.2	Roy et al., 2007
17	AS-E	11053-20	ELT 11-19 (0-2)	32.3			31	132.0	10.8	Roy et al., 2007
17	AS-E	17588-09A	ELT 11-19 (0-2)	26.2	0.06	0.008	54	134.7	3.6	
17	AS-E	11053-35	ELT 11-19 (0-2)	16.6			89	135.8	10.5	Roy et al., 2007
17	AS-E	17588-35A	ELT 11-19 (0-2)	1.8	-0.01	0.009	47	140.7	4.2	
17	AS-E	11041-05	ELT 11-19 (0-2)	13.6			94	141.3	1.1	Roy et al., 2007
17	AS-E	11053-42	ELT 11-19 (0-2)	13.9			45	146.3	7.7	Roy et al., 2007
17	AS-E	17588-14A	ELT 11-19 (0-2)	23.3	0.10	0.001	41	147.6	17.9	
17	AS-E	11041-08	ELT 11-19 (0-2)	12.1			62	147.9	5.1	Roy et al., 2007
17	AS-E	11053-19	ELT 11-19 (0-2)	9.3			97	149.4	2.4	Roy et al., 2007
17	AS-E	11053-44	ELT 11-19 (0-2)	11.9			57	152.5	9.4	Roy et al., 2007
17	AS-E	11041-03	ELT 11-19 (0-2)	10.6			91	230.3	1.9	Roy et al., 2007
17	AS-E	11053-22	ELT 11-19 (0-2)	14.9			93	303.0	2.6	Roy et al., 2007
17	AS-E	11053-46	ELT 11-19 (0-2)	30.3			35	369.8	20.0	Roy et al., 2007
17	AS-E	11053-07	ELT 11-19 (0-2)	30.4			65	791.2	12.1	Roy et al., 2007
17	AS-E	11053-17	ELT 11-19 (0-2)	7.2			94	1331.8	8.1	Roy et al., 2007
17	AS-E	11053-02	ELT 11-19 (0-2)	5.2			99	1361.6	6.6	Roy et al., 2007
17	AS-E	11053-25	ELT 11-19 (0-2)	18.6			98	1726.8	11.6	Roy et al., 2007
18	AS-E	17596-10A	ELT 11-18 (2-4)	2.4	0.00	0.020	3	4.3	2.3	
18	AS-E	17596-12A	ELT 11-18 (2-4)	12.5	0.00	0.006	4	7.0	6.5	
18	AS-E	11059-23	ELT 11-18 (2-4)	19.4			17	81.4	10.9	Roy et al., 2007
18	AS-E	11059-27	ELT 11-18 (2-4)	17.3			27	85.2	14.0	Roy et al., 2007
18	AS-E	11059-22	ELT 11-18 (2-4)	16.9			63	88.4	6.9	Roy et al., 2007
18	AS-E	11059-29	ELT 11-18 (2-4)	13.2			63	91.4	11.2	Roy et al., 2007
18	AS-E	11059-17	ELT 11-18 (2-4)	9.2			97	106.8	3.9	Roy et al., 2007

18	AS-E	17596-11A	ELT 11-18 (2-4)	3.7	-0.12	0.001	24	111.1	47.6	
18	AS-E	11059-20	ELT 11-18 (2-4)	8.9			78	111.5	3.1	Roy et al., 2007
18	AS-E	17596-07A	ELT 11-18 (2-4)	13.5	0.01	0.002	60	113.5	16.2	
18	AS-E	11059-01	ELT 11-18 (2-4)	43.7			32	115.9	3.3	Roy et al., 2007
18	AS-E	11059-05	ELT 11-18 (2-4)	7.6			92	118.4	1.8	Roy et al., 2007
18	AS-E	11059-08	ELT 11-18 (2-4)	26.7			70	132.4	8.4	Roy et al., 2007
18	AS-E	11059-02	ELT 11-18 (2-4)	25.1			79	183.5	2.5	Roy et al., 2007
18	AS-E	11059-14	ELT 11-18 (2-4)	13.9			78	190.4	12.1	Roy et al., 2007
18	AS-E	11059-26	ELT 11-18 (2-4)	30.8			91	293.4	21.6	Roy et al., 2007
18	AS-E	17596-08A	ELT 11-18 (2-4)	11.9	-0.01	0.004	70	297.1	11.4	
18	AS-E	11059-28	ELT 11-18 (2-4)	16.6			82	318.5	14.6	Roy et al., 2007
18	AS-E	17596-09A	ELT 11-18 (2-4)	35.5	0.02	0.009	76	327.1	5.2	
18	AS-E	11059-24	ELT 11-18 (2-4)	12.4			74	330.7	8.5	Roy et al., 2007
18	AS-E	11059-19	ELT 11-18 (2-4)	13.4			92	354.9	2.7	Roy et al., 2007
18	AS-E	11059-07	ELT 11-18 (2-4)	28.7			88	367.0	6.9	Roy et al., 2007
18	AS-E	17596-06A	ELT 11-18 (2-4)	4.0	-0.02	0.007	95	375.6	6.4	
18	AS-E	11059-10	ELT 11-18 (2-4)	8.0			95	639.5	2.9	Roy et al., 2007
19	AS-E	11032-01	ELT11-17 (2-4)	16.6			87	56.7	0.5	Roy et al., 2007
19	AS-E	11032-10	ELT11-17 (2-4)	13.4			67	97.2	2.5	Roy et al., 2007
19	AS-E	11032-07	ELT11-17 (2-4)	14.6			92	100.2	16.0	Roy et al., 2007
19	AS-E	17590-09A	ELT11-17 (2-4)	9.4	0.02	0.024	82	101.8	1.0	
19	AS-E	17590-05A	ELT11-17 (2-4)	4.0	0.00	0.015	71	120.2	1.6	
19	AS-E	17590-07A	ELT11-17 (2-4)	19.6	-0.06	0.001	23	132.7	20.5	
20	AS-E	16408-10A	PS58/254-2 (0-2)	5.6	0.04	0.001	6	8.8	7.2	
20	AS-E	16408-11A	PS58/254-2 (0-2)	9.9	0.16	0.001	4	58.1	20.8	
20	AS-E	16408-12A	PS58/254-2 (0-2)	19.8	0.09	0.002	84	64.9	2.0	
20	AS-E	16408-13A	PS58/254-2 (0-2)	21.1	0.21	0.001	44	67.1	8.2	
20	AS-E	16408-06A	PS58/254-2 (0-2)	15.5	0.14	0.001	78	69.2	7.9	
20	AS-E	16408-02A	PS58/254-2 (0-2)	17.8	0.09	0.001	13	88.4	10.4	
20	AS-E	16412-06A	PS58/254-2 (0-2)	3.7	0.05	0.001	40	103.6	9.3	
20	AS-E	16408-15A	PS58/254-2 (0-2)	17.4	0.01	0.001	58	128.3	8.1	
20	AS-E	16408-14A	PS58/254-2 (0-2)	9.9	0.05	0.001	44	128.4	6.0	
20	AS-E	16412-01A	PS58/254-2 (0-2)	11.2	-0.02	0.001	67	154.2	8.3	
20	AS-E	16412-09A	PS58/254-2 (0-2)	9.9	0.07	0.001	37	205.5	10.1	
20	AS-E	16408-07A	PS58/254-2 (0-2)	11.3	0.01	0.003	96	249.4	2.5	
20	AS-E	16412-08A	PS58/254-2 (0-2)	3.4	0.02	0.001	92	1129.0	17.7	
20	AS-E	16408-03A	PS58/254-2 (0-2)	13.8	0.00	0.002	93	1851.8	15.6	
22	AS-E	18558-31A	PS 69/255-3 (Surf)	13.1	0.03	0.003	56	80.6	16.1	
22	AS-E	18558-14A	PS 69/255-3 (Surf)	13.0	0.02	0.005	49	87.1	9.1	
22	AS-E	18558-11A	PS 69/255-3 (Surf)	10.6	0.02	0.002	44	93.3	22.0	
22	AS-E	18558-18A	PS 69/255-3 (Surf)	7.7	0.01	0.009	70	96.4	5.0	
22	AS-E	18558-05A	PS 69/255-3 (Surf)	13.0	0.01	0.004	63	99.3	9.8	
22	AS-E	18558-20A	PS 69/255-3 (Surf)	12.7	0.03	0.004	72	102.9	10.2	
22	AS-E	18558-13A	PS 69/255-3 (Surf)	7.2	0.04	0.007	44	104.6	6.9	
22	AS-E	18558-07A	PS 69/255-3 (Surf)	8.6	0.01	0.013	48	111.8	3.6	
22	AS-E	18558-32A	PS 69/255-3 (Surf)	13.2	0.04	0.022	80	113.8	1.3	
22	AS-E	18558-15A	PS 69/255-3 (Surf)	7.3	0.01	0.023	83	115.4	2.1	
22	AS-E	18558-24A	PS 69/255-3 (Surf)	9.7	0.02	0.008	80	120.9	5.5	
22	AS-E	18558-26A	PS 69/255-3 (Surf)	9.7	0.01	0.004	76	126.0	10.0	
22	AS-E	18558-27A	PS 69/255-3 (Surf)	28.9	-0.07	0.002	29	128.9	22.8	
22	AS-E	18558-06A	PS 69/255-3 (Surf)	9.3	0.01	0.014	75	131.1	3.0	
22	AS-E	18558-03A	PS 69/255-3 (Surf)	8.5	0.01	0.028	82	152.2	1.7	
22	AS-E	18558-28A	PS 69/255-3 (Surf)	18.7	0.00	0.005	52	155.0	9.6	
22	AS-E	18558-21A	PS 69/255-3 (Surf)	12.2	0.00	0.004	60	155.3	11.5	
22	AS-E	18558-30A	PS 69/255-3 (Surf)	18.8	-0.01	0.004	72	162.9	10.9	
22	AS-E	18558-09A	PS 69/255-3 (Surf)	21.9	-0.04	0.002	29	171.6	22.8	
22	AS-E	18558-04A	PS 69/255-3 (Surf)	14.2	0.02	0.006	87	182.6	6.9	
22	AS-E	18558-22A	PS 69/255-3 (Surf)	13.3	0.00	0.004	69	192.1	12.1	

22	AS-E	18558-12A	PS 69/255-3 (Surf)	8.1	0.03	0.010	78	233.2	4.7
22	AS-E	18558-10A	PS 69/255-3 (Surf)	7.4	0.03	0.005	80	233.6	8.5
22	AS-E	18558-23A	PS 69/255-3 (Surf)	15.0	-0.02	0.003	75	239.8	14.4
22	AS-E	18558-17A	PS 69/255-3 (Surf)	21.8	0.03	0.008	76	252.5	5.7
22	AS-E	18558-25A	PS 69/255-3 (Surf)	8.5	0.01	0.009	86	258.8	5.0
22	AS-E	18558-19A	PS 69/255-3 (Surf)	30.5	-0.01	0.003	30	261.0	17.0
22	AS-E	18558-29A	PS 69/255-3 (Surf)	6.7	-0.01	0.005	78	261.4	9.3
22	AS-E	18558-16A	PS 69/255-3 (Surf)	34.2	0.01	0.003	59	296.0	15.4
22	AS-E	18558-02A	PS 69/255-3 (Surf)	8.2	0.00	0.016	82	324.2	3.8
22	AS-E	18558-08A	PS 69/255-3 (Surf)	17.8	0.06	0.007	81	361.3	7.8
24	AS-E	12650-18	DF85-109 (11-17)	1.8	0.00	0.031	1	0.5	4.4
24	AS-E	12650-14	DF85-109 (11-17)	13.4	0.01	0.045	69	100.1	3.2
24	AS-E	12650-12	DF85-109 (11-17)	11.2	0.09	0.016	35	112.7	8.3
24	AS-E	12650-19	DF85-109 (11-17)	11.3	0.04	0.036	94	118.8	3.8
24	AS-E	12650-04	DF85-109 (11-17)	11.7	0.03	0.018	85	129.4	7.0
24	AS-E	12650-30	DF85-109 (11-17)	12.3	0.02	0.024	121	132.1	5.3
24	AS-E	12650-22	DF85-109 (11-17)	16.4	0.12	0.006	33	135.9	20.8
24	AS-E	12650-20	DF85-109 (11-17)	16.2	0.10	0.010	78	138.7	13.9
24	AS-E	12650-06	DF85-109 (11-17)	17.5	0.02	0.011	69	139.9	11.8
24	AS-E	12650-10	DF85-109 (11-17)	10.4	0.10	0.018	86	141.1	7.3
24	AS-E	12650-08	DF85-109 (11-17)	6.0	0.06	0.014	87	159.0	9.4
24	AS-E	12650-16	DF85-109 (11-17)	8.8	0.02	0.078	96	166.5	2.3
24	AS-E	12650-24	DF85-109 (11-17)	9.5	0.02	0.008	106	170.5	15.6
24	AS-E	12650-25	DF85-109 (11-17)	7.0	0.01	0.007	96	173.4	16.5
24	AS-E	12650-23	DF85-109 (11-17)	7.8	0.03	0.013	51	198.2	10.2
24	AS-E	12650-29	DF85-109 (11-17)	10.7	0.00	0.021	82	202.5	6.1
24	AS-E	12650-27	DF85-109 (11-17)	10.7	-0.02	0.006	144	214.3	19.8
24	AS-E	12650-21	DF85-109 (11-17)	5.9	0.02	0.034	91	231.9	4.4
24	AS-E	12650-02	DF85-109 (11-17)	7.6	0.03	0.080	101	245.9	3.0
24	AS-E	12650-03	DF85-109 (11-17)	8.2	0.01	0.067	96	249.6	3.2
24	AS-E	12650-17	DF85-109 (11-17)	7.7	0.01	0.041	98	251.9	4.0
24	AS-E	12650-05	DF85-109 (11-17)	7.6	-0.01	0.027	100	256.7	5.3
24	AS-E	12650-13	DF85-109 (11-17)	7.5	0.03	0.049	101	259.2	3.7
24	AS-E	12650-07	DF85-109 (11-17)	13.4	0.05	0.021	114	260.3	6.4
24	AS-E	12650-11	DF85-109 (11-17)	3.9	0.08	0.017	94	262.4	8.2
24	AS-E	12650-01	DF85-109 (11-17)	10.1	0.03	0.199	99	276.3	2.9
24	AS-E	12650-15	DF85-109 (11-17)	9.7	0.06	0.045	90	276.5	4.2
24	AS-E	12650-26	DF85-109 (11-17)	5.8	-0.02	0.003	86	313.7	38.7
24	AS-E	12650-28	DF85-109 (11-17)	8.0	-0.05	0.012	63	316.7	11.3
24	AS-E	12650-09	DF85-109 (11-17)	8.6	0.10	0.021	101	506.6	7.8
25	AS-E	18177-41A	BC451 (Surf)	6.2	-0.01	0.020	87	42.6	2.5
25	AS-E	18168-25A	BC451 (Surf)	6.4	-0.01	0.009	28	85.2	4.6
25	AS-E	18168-50A	BC451 (Surf)	2.0	0.00	0.065	63	87.0	0.7
25	AS-E	18168-06A	BC451 (Surf)	1.5	0.00	0.106	34	94.6	1.6
25	AS-E	18177-28A	BC451 (Surf)	2.5	0.00	0.036	77	95.8	1.6
25	AS-E	18168-36A	BC451 (Surf)	3.1	0.00	0.053	52	98.2	1.1
25	AS-E	18168-43A	BC451 (Surf)	37.7	0.03	0.005	54	99.3	6.4
25	AS-E	18177-11A	BC451 (Surf)	3.7	0.00	0.263	84	99.4	0.5
25	AS-E	18177-45A	BC451 (Surf)	6.9	0.02	0.006	84	100.5	8.6
25	AS-E	18177-20A	BC451 (Surf)	16.0	0.02	0.007	85	110.1	6.7
25	AS-E	18168-30A	BC451 (Surf)	16.4	0.01	0.004	12	110.2	11.3
25	AS-E	18168-37A	BC451 (Surf)	10.1	0.05	0.003	76	111.9	12.3
25	AS-E	18177-03A	BC451 (Surf)	46.3	0.05	0.006	27	114.3	9.2
25	AS-E	18168-29A	BC451 (Surf)	4.6	-0.01	0.002	11	144.0	25.6
25	AS-E	18168-23A	BC451 (Surf)	1.2	0.00	0.090	87	144.7	0.7
25	AS-E	18177-31A	BC451 (Surf)	11.3	0.03	0.004	81	162.5	11.1
25	AS-E	18177-07A	BC451 (Surf)	7.9	0.03	0.011	98	170.8	3.8
25	AS-E	18177-34A	BC451 (Surf)	24.9	-0.04	0.004	80	170.9	12.8
25	AS-E	18168-24A	BC451 (Surf)	1.1	0.00	0.030	70	171.1	1.5

25	AS-E	18177-38A	BC451 (Surf)	45.5	-0.03	0.002	38	174.0	23.1
25	AS-E	18177-17A	BC451 (Surf)	6.3	0.02	0.009	73	174.6	5.8
25	AS-E	18177-32A	BC451 (Surf)	10.4	0.01	0.014	81	175.4	3.7
25	AS-E	18177-26A	BC451 (Surf)	11.7	0.02	0.015	89	178.9	3.4
25	AS-E	18177-16A	BC451 (Surf)	10.6	0.02	0.012	63	180.3	4.4
25	AS-E	18177-42A	BC451 (Surf)	25.6	0.03	0.010	81	183.3	5.1
25	AS-E	18177-15A	BC451 (Surf)	9.1	0.01	0.028	76	186.0	2.1
25	AS-E	18177-05A	BC451 (Surf)	60.6	0.01	0.002	37	191.7	23.7
25	AS-E	18177-22A	BC451 (Surf)	5.9	0.04	0.009	90	192.9	5.7
25	AS-E	18177-39A	BC451 (Surf)	21.9	0.02	0.006	87	197.0	9.0
25	AS-E	18177-04A	BC451 (Surf)	37.6	0.01	0.004	64	209.0	10.6
25	AS-E	18177-33A	BC451 (Surf)	7.8	0.02	0.013	94	237.3	3.8
25	AS-E	18177-27A	BC451 (Surf)	24.7	0.02	0.011	83	241.1	4.9
25	AS-E	18177-48A	BC451 (Surf)	9.3	-0.05	0.004	58	243.4	10.7
25	AS-E	18177-30A	BC451 (Surf)	14.1	0.04	0.004	92	244.0	12.8
25	AS-E	18177-37A	BC451 (Surf)	8.5	0.03	0.021	95	244.8	2.6
25	AS-E	18177-47A	BC451 (Surf)	9.7	0.01	0.006	89	245.5	8.2
25	AS-E	18177-29A	BC451 (Surf)	13.4	0.00	0.009	94	246.1	5.5
25	AS-E	18177-46A	BC451 (Surf)	14.4	-0.09	0.002	88	247.6	19.6
25	AS-E	18177-14A	BC451 (Surf)	14.0	0.04	0.035	74	248.6	2.0
25	AS-E	18177-40A	BC451 (Surf)	6.5	0.02	0.016	81	251.5	3.5
25	AS-E	18177-12A	BC451 (Surf)	14.2	0.01	0.052	88	255.3	1.6
25	AS-E	18177-44A	BC451 (Surf)	15.3	0.04	0.002	86	256.0	19.7
25	AS-E	18177-02A	BC451 (Surf)	8.8	0.00	0.009	76	256.3	5.5
25	AS-E	18177-10A	BC451 (Surf)	20.9	0.02	0.004	90	259.0	9.2
25	AS-E	18177-09A	BC451 (Surf)	25.3	0.01	0.063	89	263.3	1.5
25	AS-E	18177-06A	BC451 (Surf)	26.4	0.03	0.002	79	265.0	19.5
25	AS-E	18177-01A	BC451 (Surf)	14.0	0.04	0.031	79	344.0	2.7
25	AS-E	18177-13A	BC451 (Surf)	28.7	0.07	0.011	48	350.3	6.2
25	AS-E	18177-49A	BC451 (Surf)	5.1	0.00	0.011	96	522.2	4.3
26	AS-E	18175-08A	BC455 (Surf)	1.8	0.01	0.009	7	90.1	10.8
26	AS-E	18181-33A	BC455 (Surf)	18.2	0.02	0.006	55	93.2	5.1
26	AS-E	18175-01A	BC455 (Surf)	1.4	0.00	0.028	38	93.3	2.0
26	AS-E	18175-25A	BC455 (Surf)	3.7	0.00	0.047	43	95.3	1.4
26	AS-E	18181-03A	BC455 (Surf)	10.5	-0.02	0.005	70	98.4	4.5
26	AS-E	18181-11A	BC455 (Surf)	10.8	-0.01	0.010	77	99.0	2.5
26	AS-E	18181-01A	BC455 (Surf)	15.3	0.03	0.003	63	101.0	6.8
26	AS-E	18175-37A	BC455 (Surf)	1.4	0.00	0.005	50	102.2	8.5
26	AS-E	18181-47A	BC455 (Surf)	10.5	0.02	0.017	79	103.8	1.7
26	AS-E	18181-42A	BC455 (Surf)	10.2	0.05	0.026	88	104.7	1.2
26	AS-E	18181-14A	BC455 (Surf)	12.8	-0.01	0.011	51	108.9	2.5
26	AS-E	18181-44A	BC455 (Surf)	14.4	0.02	0.005	51	113.7	4.9
26	AS-E	18181-36A	BC455 (Surf)	8.2	0.02	0.036	83	119.4	0.9
26	AS-E	18181-48A	BC455 (Surf)	12.0	0.04	0.010	79	120.0	2.7
26	AS-E	18181-17A	BC455 (Surf)	9.4	0.02	0.017	54	125.7	2.0
26	AS-E	18181-45A	BC455 (Surf)	9.8	0.04	0.013	71	134.2	2.1
26	AS-E	18181-02A	BC455 (Surf)	19.4	0.06	0.003	81	135.4	8.8
26	AS-E	18175-14A	BC455 (Surf)	8.9	0.01	0.005	55	155.6	10.3
26	AS-E	18181-08A	BC455 (Surf)	23.9	0.02	0.003	55	158.0	8.4
26	AS-E	18181-23A	BC455 (Surf)	5.1	0.02	0.008	78	160.2	3.3
26	AS-E	18181-16A	BC455 (Surf)	17.8	0.01	0.048	83	169.3	0.9
26	AS-E	18175-48A	BC455 (Surf)	4.5	0.02	0.009	39	174.6	5.5
26	AS-E	18181-07A	BC455 (Surf)	11.6	-0.01	0.008	76	174.6	3.3
26	AS-E	18181-43A	BC455 (Surf)	16.3	0.00	0.004	58	174.9	6.7
26	AS-E	18181-19A	BC455 (Surf)	11.4	0.02	0.021	88	175.9	1.5
26	AS-E	18181-29A	BC455 (Surf)	22.5	0.00	0.005	72	180.2	5.2
26	AS-E	18181-05A	BC455 (Surf)	11.0	0.00	0.008	82	181.2	3.2
26	AS-E	18181-49A	BC455 (Surf)	8.1	0.01	0.067	94	187.6	0.7
26	AS-E	18181-37A	BC455 (Surf)	9.7	0.01	0.141	93	189.9	0.6
26	AS-E	18181-22A	BC455 (Surf)	7.8	0.01	0.070	83	199.9	0.9

26	AS-E	18181-21A	BC455 (Surf)	7.6	0.02	0.018	87	203.0	1.8
26	AS-E	18181-15A	BC455 (Surf)	0.8	-0.02	0.005	74	203.5	4.8
26	AS-E	18181-10A	BC455 (Surf)	12.0	0.01	0.008	74	215.3	3.7
26	AS-E	18181-18A	BC455 (Surf)	12.0	0.00	0.007	80	223.0	3.7
26	AS-E	18181-32A	BC455 (Surf)	28.1	0.00	0.013	54	228.3	3.1
26	AS-E	18181-40A	BC455 (Surf)	13.5	0.04	0.007	74	229.0	4.3
26	AS-E	18181-13A	BC455 (Surf)	9.7	0.03	0.012	96	241.2	2.2
26	AS-E	18181-12A	BC455 (Surf)	12.7	0.02	0.005	80	246.3	5.3
26	AS-E	18181-09A	BC455 (Surf)	11.2	-0.01	0.008	86	251.8	3.5
26	AS-E	18181-35A	BC455 (Surf)	9.5	0.04	0.018	94	253.1	1.9
26	AS-E	18181-20A	BC455 (Surf)	6.5	0.03	0.035	96	256.8	1.2
26	AS-E	18181-25A	BC455 (Surf)	13.8	0.01	0.018	88	258.5	2.1
26	AS-E	18181-27A	BC455 (Surf)	8.4	0.00	0.010	81	259.1	3.2
26	AS-E	18181-34A	BC455 (Surf)	9.8	0.02	0.007	90	260.3	4.1
26	AS-E	18181-24A	BC455 (Surf)	10.0	0.02	0.013	94	262.9	2.5
26	AS-E	18181-31A	BC455 (Surf)	9.6	-0.01	0.010	86	275.3	3.3
26	AS-E	18181-06A	BC455 (Surf)	14.8	-0.01	0.006	75	282.2	4.9
26	AS-E	18181-41A	BC455 (Surf)	11.7	0.03	0.011	89	287.3	3.2
26	AS-E	18175-20A	BC455 (Surf)	87.6	0.07	0.001	82	317.1	30.7
26	AS-E	18181-39A	BC455 (Surf)	24.3	0.05	0.003	61	348.3	10.6
26	AS-E	18181-28A	BC455 (Surf)	34.0	0.06	0.012	80	351.2	3.1
26	AS-E	18181-46A	BC455 (Surf)	29.2	0.05	0.003	59	416.7	9.6
26	AS-E	18175-49A	BC455 (Surf)	22.4	0.01	0.018	96	514.7	3.4
26	AS-E	18181-26A	BC455 (Surf)	34.6	-0.10	0.003	68	522.7	11.0
27	AS-E	18559-09A	BC 485 Y (0-3)	9.9	0.00	0.109	66	26.0	0.5
27	AS-E	18559-04A	BC 485 Y (0-3)	15.4	0.03	0.003	42	70.4	16.8
27	AS-E	18559-02A	BC 485 Y (0-3)	16.6	0.03	0.018	52	95.5	2.8
27	AS-E	18559-08A	BC 485 Y (0-3)	9.5	0.01	0.006	56	96.0	7.5
27	AS-E	18559-19A	BC 485 Y (0-3)	7.7	0.01	0.022	74	97.9	2.1
27	AS-E	18559-01A	BC 485 Y (0-3)	10.9	0.01	0.006	65	98.9	8.2
27	AS-E	18561-15A	BC 485 Y (0-3)	1.5	-0.02	0.004	30	110.4	6.6
27	AS-E	18559-05A	BC 485 Y (0-3)	10.2	0.01	0.003	15	152.8	18.8
27	AS-E	18561-19A	BC 485 Y (0-3)	19.1	0.06	0.002	93	175.0	13.6
27	AS-E	18559-13A	BC 485 Y (0-3)	14.8	0.01	0.013	85	228.1	3.6
27	AS-E	18559-18A	BC 485 Y (0-3)	22.2	0.01	0.006	87	240.2	7.2
27	AS-E	18559-07A	BC 485 Y (0-3)	9.9	0.01	0.013	83	241.1	3.6
27	AS-E	18559-06A	BC 485 Y (0-3)	38.4	0.04	0.002	15	264.9	31.0
27	AS-E	18559-16A	BC 485 Y (0-3)	9.7	0.00	0.007	89	289.3	6.6
27	AS-E	18559-12A	BC 485 Y (0-3)	16.3	0.03	0.007	59	343.8	6.9
28	AS-E	12652-17	DF85 96-1 (83-88)	6.1	0.12	0.010	7	12.4	12.6
28	AS-E	12652-08	DF85 96-1 (83-88)	20.3	0.10	0.012	16	36.6	9.7
28	AS-E	12652-07	DF85 96-1 (83-88)	14.3	0.05	0.023	33	45.6	5.3
28	AS-E	12652-15	DF85 96-1 (83-88)	6.4	0.23	0.006	30	60.0	17.4
28	AS-E	12652-16	DF85 96-1 (83-88)	12.2	0.09	0.016	49	62.4	7.0
28	AS-E	12652-14	DF85 96-1 (83-88)	18.0	0.12	0.012	50	69.7	9.5
28	AS-E	12652-04	DF85 96-1 (83-88)	18.2	0.04	0.030	51	81.2	4.2
28	AS-E	12652-13	DF85 96-1 (83-88)	7.0	0.13	0.012	46	88.2	9.4
28	AS-E	12652-11	DF85 96-1 (83-88)	4.2	0.02	0.016	76	91.8	7.2
28	AS-E	12530-07	DF85 96-1 (83-88)	6.3	0.02	0.042	24	92.7	2.6
28	AS-E	12652-02	DF85 96-1 (83-88)	8.8	0.03	0.117	93	94.2	1.3
28	AS-E	12652-05	DF85 96-1 (83-88)	11.3	0.04	0.045	72	95.1	2.7
28	AS-E	12530-02	DF85 96-1 (83-88)	23.9	0.16	0.019	11	96.4	5.9
28	AS-E	12530-03	DF85 96-1 (83-88)	11.3	0.01	0.342	70	98.0	1.1
28	AS-E	12530-04	DF85 96-1 (83-88)	1.7	0.00	0.128	66	98.7	1.2
28	AS-E	12530-01	DF85 96-1 (83-88)	5.7	0.01	0.308	72	102.0	1.1
28	AS-E	12652-12	DF85 96-1 (83-88)	8.1	0.06	0.029	79	102.2	3.9
28	AS-E	12652-06	DF85 96-1 (83-88)	9.9	0.02	0.127	81	103.3	1.4
28	AS-E	12530-08	DF85 96-1 (83-88)	10.2	0.00	0.006	67	104.0	5.6
28	AS-E	12530-09	DF85 96-1 (83-88)	14.4	0.04	0.079	72	106.0	1.4

28	AS-E	12652-01	DF85 96-1 (83-88)	13.4	0.03	0.072	50	112.9	2.1
28	AS-E	12652-03	DF85 96-1 (83-88)	13.4	0.00	0.041	70	119.0	2.9
28	AS-E	12530-05	DF85 96-1 (83-88)	17.7	0.02	0.043	90	120.5	1.7
28	AS-E	12652-19	DF85 96-1 (83-88)	11.2	0.07	0.015	105	122.3	7.9
28	AS-E	12652-20	DF85 96-1 (83-88)	12.8	0.05	0.011	61	124.3	11.7
28	AS-E	12652-21	DF85 96-1 (83-88)	7.2	0.03	0.007	108	126.8	16.8
28	AS-E	12652-22	DF85 96-1 (83-88)	16.9	0.02	0.008	130	149.4	13.4
28	AS-E	12652-10	DF85 96-1 (83-88)	8.7	0.40	0.003	29	160.2	37.4
28	AS-E	12652-23	DF85 96-1 (83-88)	14.1	0.07	0.005	145	196.5	22.0
28	AS-E	12652-18	DF85 96-1 (83-88)	7.0	0.00	0.007	92	210.7	15.0
29	AS-E	18165-36A	PS69/299-1 (Surf)	2.0	-0.05	0.006	21	63.5	7.1
29	AS-E	18162-06A	PS69/299-1 (Surf)	1.2	0.01	0.064	14	75.4	3.7
29	AS-E	18162-12A	PS69/299-1 (Surf)	14.6	-0.13	0.003	11	76.1	13.0
29	AS-E	18162-19A	PS69/299-1 (Surf)	6.7	-0.02	0.007	57	79.9	5.7
29	AS-E	18162-27A	PS69/299-1 (Surf)	17.4	0.02	0.006	105	87.2	5.2
29	AS-E	18162-31A	PS69/299-1 (Surf)	6.1	-0.06	0.004	46	88.9	7.9
29	AS-E	18162-02A	PS69/299-1 (Surf)	8.1	0.00	0.042	20	96.0	4.3
29	AS-E	18162-32A	PS69/299-1 (Surf)	3.2	0.00	0.018	33	97.1	2.9
29	AS-E	18162-08A	PS69/299-1 (Surf)	1.9	0.01	0.058	62	100.0	2.8
29	AS-E	18162-28A	PS69/299-1 (Surf)	2.5	-0.01	0.007	58	101.5	4.9
29	AS-E	18162-36A	PS69/299-1 (Surf)	2.0	0.01	0.018	67	102.0	2.1
29	AS-E	18162-11A	PS69/299-1 (Surf)	9.6	0.00	0.010	15	104.2	6.5
29	AS-E	18162-24A	PS69/299-1 (Surf)	1.7	-0.07	0.007	76	108.2	4.8
29	AS-E	18162-35A	PS69/299-1 (Surf)	2.0	0.00	0.011	74	109.9	3.2
29	AS-E	18162-33A	PS69/299-1 (Surf)	2.4	0.00	0.013	94	111.8	2.7
29	AS-E	18162-10A	PS69/299-1 (Surf)	2.7	0.00	0.041	35	115.3	4.2
29	AS-E	18165-39A	PS69/299-1 (Surf)	3.4	-0.01	0.005	35	115.4	4.5
29	AS-E	18162-21A	PS69/299-1 (Surf)	6.2	0.00	0.011	80	119.6	3.5
29	AS-E	18162-30A	PS69/299-1 (Surf)	8.9	-0.01	0.007	65	120.1	5.1
29	AS-E	18162-29A	PS69/299-1 (Surf)	12.5	0.00	0.002	29	133.4	17.1
29	AS-E	18162-18A	PS69/299-1 (Surf)	10.0	-0.07	0.004	70	152.1	9.0
29	AS-E	18162-25A	PS69/299-1 (Surf)	25.0	-0.06	0.002	79	163.1	18.6
29	AS-E	18162-22A	PS69/299-1 (Surf)	16.9	0.04	0.002	51	185.0	18.4
29	AS-E	18165-10A	PS69/299-1 (Surf)	4.3	0.02	0.018	45	186.7	8.5
32	AS-E	18843-01A	PS75/159-1 (0-1)	8.4	0.05	0.005	25	171.5	7.1
33	AS-E	18850-09A	PS75/168-1 (0-1)	9.2	0.00	0.001	29	69.7	27.3
33	AS-E	18850-03A	PS75/168-1 (0-1)	14.3	0.04	0.006	46	96.4	5.9
33	AS-E	18850-26A	PS75/168-1 (0-1)	15.2	-0.10	0.001	22	114.5	41.4
33	AS-E	18850-05A	PS75/168-1 (0-1)	11.2	-0.01	0.001	82	130.1	21.2
33	AS-E	18850-08A	PS75/168-1 (0-1)	9.6	-0.10	0.002	72	150.9	17.2
33	AS-E	18850-23A	PS75/168-1 (0-1)	10.3	0.04	0.001	74	165.8	25.4
33	AS-E	18850-04A	PS75/168-1 (0-1)	22.8	0.12	0.001	50	196.0	46.0
33	AS-E	18850-25A	PS75/168-1 (0-1)	15.4	-0.04	0.001	38	200.9	23.0
33	AS-E	18850-10A	PS75/168-1 (0-1)	7.8	0.07	0.001	18	271.5	47.0
34	AS-E	18164-07A	BC442 (Surf)	3.2	0.00	0.039	60	96.6	4.1
34	AS-E	18164-02A	BC442 (Surf)	6.9	0.02	0.048	36	98.0	3.5
34	AS-E	18164-06A	BC442 (Surf)	7.6	0.02	0.018	41	99.5	8.9
34	AS-E	18164-09A	BC442 (Surf)	1.6	0.00	0.041	79	103.1	3.9
34	AS-E	18164-46A	BC442 (Surf)	6.8	0.01	0.011	43	107.6	2.2
34	AS-E	18164-45A	BC442 (Surf)	2.5	0.00	0.022	73	108.1	2.2
34	AS-E	18164-49A	BC442 (Surf)	1.1	0.01	0.059	81	115.7	2.3
34	AS-E	18164-10A	BC442 (Surf)	3.1	0.00	0.033	23	119.4	5.5
34	AS-E	18173-34A	BC442 (Surf)	2.8	0.01	0.011	49	121.8	3.3
34	AS-E	18173-04A	BC442 (Surf)	4.5	-0.01	0.003	23	122.9	11.9
34	AS-E	18164-03A	BC442 (Surf)	7.5	0.00	0.021	61	132.0	7.4
34	AS-E	18164-14A	BC442 (Surf)	3.7	0.00	0.020	77	134.2	2.7
34	AS-E	18164-04A	BC442 (Surf)	5.2	0.01	0.050	88	137.8	3.1

34	AS-E	18164-12A	BC442 (Surf)	12.0	0.00	0.009	29	144.3	2.9
34	AS-E	18164-24A	BC442 (Surf)	4.7	0.00	0.102	86	148.5	3.0
34	AS-E	18164-17A	BC442 (Surf)	5.7	-0.01	0.010	35	155.4	3.1
34	AS-E	18164-40A	BC442 (Surf)	11.7	0.00	0.002	75	157.1	3.1
34	AS-E	18164-43A	BC442 (Surf)	1.0	0.00	0.060	89	158.3	3.2
34	AS-E	18164-08A	BC442 (Surf)	15.2	0.03	0.009	59	163.1	16.1
34	AS-E	18164-36A	BC442 (Surf)	10.6	0.08	0.002	86	174.1	3.5
34	AS-E	18164-32A	BC442 (Surf)	4.1	0.00	0.049	86	175.9	3.5
34	AS-E	18164-41A	BC442 (Surf)	224.5	0.03	0.002	69	183.0	3.7
34	AS-E	18164-35A	BC442 (Surf)	8.8	0.02	0.009	80	183.1	3.7
34	AS-E	18164-33A	BC442 (Surf)	5.3	0.02	0.017	89	183.9	3.7
34	AS-E	18164-23A	BC442 (Surf)	9.6	0.01	0.061	55	196.0	3.9
34	AS-E	18164-48A	BC442 (Surf)	5.1	0.01	0.013	71	199.2	4.0
34	AS-E	18164-47A	BC442 (Surf)	9.2	0.01	0.045	93	199.3	4.0
34	AS-E	18173-53A	BC442 (Surf)	6.3	0.02	0.017	33	201.1	3.1
34	AS-E	18164-11A	BC442 (Surf)	9.0	-0.03	0.010	45	205.6	4.1
34	AS-E	18164-18A	BC442 (Surf)	14.4	0.02	0.039	86	208.5	4.2
34	AS-E	18164-30A	BC442 (Surf)	13.9	0.02	0.020	94	218.0	4.4
34	AS-E	18164-16A	BC442 (Surf)	9.6	-0.03	0.006	57	225.3	4.5
34	AS-E	18164-05A	BC442 (Surf)	9.0	0.03	0.017	77	231.1	8.6
34	AS-E	18164-29A	BC442 (Surf)	14.6	0.01	0.100	92	236.9	4.7
34	AS-E	18164-28A	BC442 (Surf)	12.5	0.20	0.001	8	237.4	4.7
34	AS-E	18164-26A	BC442 (Surf)	9.9	0.01	0.006	80	238.8	4.8
34	AS-E	18164-20A	BC442 (Surf)	10.0	0.04	0.008	67	243.8	4.9
34	AS-E	18164-34A	BC442 (Surf)	7.1	0.02	0.018	93	246.9	4.9
34	AS-E	18164-19A	BC442 (Surf)	10.5	0.03	0.005	77	247.4	4.9
34	AS-E	18164-27A	BC442 (Surf)	19.3	0.02	0.004	65	248.0	5.0
34	AS-E	18164-31A	BC442 (Surf)	11.6	0.00	0.037	90	251.3	5.0
34	AS-E	18164-13A	BC442 (Surf)	11.9	0.02	0.034	87	254.9	5.1
34	AS-E	18164-25A	BC442 (Surf)	12.6	0.03	0.019	85	258.0	5.2
34	AS-E	18164-38A	BC442 (Surf)	13.1	0.01	0.015	72	259.1	5.2
34	AS-E	18164-39A	BC442 (Surf)	12.7	0.02	0.006	82	278.3	5.6
34	AS-E	18164-01A	BC442 (Surf)	45.3	0.02	0.040	69	281.6	4.0
34	AS-E	18173-10A	BC442 (Surf)	4.9	0.00	0.011	97	543.5	3.5
35	AS-E	18166-13A	BC443 (Surf)	15.0	0.09	0.016	23	18.6	2.4
35	AS-E	18167-18A	BC443 (Surf)	2.4	0.03	0.070	69	52.1	0.5
35	AS-E	18166-15A	BC443 (Surf)	20.2	0.08	0.003	69	75.4	14.3
35	AS-E	18166-39A	BC443 (Surf)	16.6	-0.08	0.003	36	76.1	12.1
35	AS-E	18166-34A	BC443 (Surf)	19.7	0.09	0.003	117	82.7	14.4
35	AS-E	18166-33A	BC443 (Surf)	1.1	0.01	0.002	66	85.5	14.2
35	AS-E	18167-14A	BC443 (Surf)	3.0	-0.03	0.002	40	86.1	7.5
35	AS-E	18167-36A	BC443 (Surf)	1.2	0.00	0.011	49	87.0	2.0
35	AS-E	18166-16A	BC443 (Surf)	11.9	0.00	0.003	28	94.8	12.3
35	AS-E	18166-53A	BC443 (Surf)	249.1	0.39	0.002	16	96.7	16.6
35	AS-E	18166-31A	BC443 (Surf)	13.8	0.03	0.008	90	97.3	4.9
35	AS-E	18167-05A	BC443 (Surf)	3.2	-0.01	0.011	59	97.9	13.2
35	AS-E	18167-19A	BC443 (Surf)	12.2	-0.01	0.003	12	99.1	10.4
35	AS-E	18166-42A	BC443 (Surf)	11.0	0.02	0.006	85	99.2	6.2
35	AS-E	18167-21A	BC443 (Surf)	5.2	0.00	0.057	56	99.4	1.0
35	AS-E	18166-41A	BC443 (Surf)	13.8	0.11	0.002	108	100.5	14.2
35	AS-E	18166-04A	BC443 (Surf)	14.9	0.02	0.039	89	103.2	4.5
35	AS-E	18166-43A	BC443 (Surf)	16.4	0.10	0.003	101	104.2	11.2
35	AS-E	18166-17A	BC443 (Surf)	35.1	0.01	0.013	71	106.2	3.6
35	AS-E	18166-05A	BC443 (Surf)	8.2	0.01	0.017	83	107.1	9.0
35	AS-E	18166-10A	BC443 (Surf)	1.4	0.01	0.031	81	107.6	5.4
35	AS-E	18166-45A	BC443 (Surf)	20.5	0.05	0.003	101	108.0	12.1
35	AS-E	18167-34A	BC443 (Surf)	2.4	0.01	0.012	95	108.2	1.6
35	AS-E	18166-19A	BC443 (Surf)	25.6	0.00	0.003	86	117.2	11.9
35	AS-E	18166-52A	BC443 (Surf)	16.5	0.02	0.002	92	119.2	14.0
35	AS-E	18166-48A	BC443 (Surf)	14.5	-0.12	0.002	83	154.3	15.3

35	AS-E	18167-17A	BC443 (Surf)	4.7	0.00	0.004	26	160.8	7.7
35	AS-E	18166-08A	BC443 (Surf)	1.3	0.01	0.055	72	168.0	4.4
35	AS-E	18166-35A	BC443 (Surf)	10.0	0.01	0.004	97	187.2	8.9
35	AS-E	18166-49A	BC443 (Surf)	7.2	-0.02	0.003	74	191.5	11.3
35	AS-E	18166-03A	BC443 (Surf)	4.1	0.01	0.057	93	207.8	4.9
35	AS-E	18166-02A	BC443 (Surf)	19.9	0.02	0.055	76	214.9	5.2
35	AS-E	18166-50A	BC443 (Surf)	26.7	-0.03	0.002	92	226.4	17.7
35	AS-E	18166-32A	BC443 (Surf)	22.2	0.02	0.007	69	231.1	6.9
35	AS-E	18166-55A	BC443 (Surf)	12.7	0.07	0.004	102	235.7	10.2
35	AS-E	18166-11A	BC443 (Surf)	15.3	0.02	0.012	86	250.8	5.9
35	AS-E	18166-22A	BC443 (Surf)	7.3	0.02	0.027	96	255.3	5.3
35	AS-E	18166-06A	BC443 (Surf)	6.7	0.01	0.127	98	255.5	5.3
35	AS-E	18166-14A	BC443 (Surf)	10.0	-0.01	0.003	89	256.2	11.7
35	AS-E	18166-01A	BC443 (Surf)	8.7	0.02	0.211	96	259.3	5.3
35	AS-E	18166-40A	BC443 (Surf)	10.1	0.00	0.006	95	261.7	7.5
35	AS-E	18166-26A	BC443 (Surf)	16.6	0.08	0.006	102	264.6	7.8
35	AS-E	18166-12A	BC443 (Surf)	21.9	0.00	0.009	85	265.8	6.6
35	AS-E	18166-25A	BC443 (Surf)	8.8	0.09	0.005	87	267.5	8.6
35	AS-E	18166-28A	BC443 (Surf)	6.0	0.03	0.006	99	269.2	7.5
35	AS-E	18166-09A	BC443 (Surf)	17.2	0.01	0.034	86	274.0	7.0
35	AS-E	18166-23A	BC443 (Surf)	31.1	0.05	0.002	64	274.0	21.8
35	AS-E	18166-44A	BC443 (Surf)	15.5	0.02	0.010	98	274.2	6.4
35	AS-E	18166-24A	BC443 (Surf)	27.6	0.05	0.013	84	284.7	6.3
35	AS-E	18166-37A	BC443 (Surf)	22.6	0.05	0.006	97	286.1	8.3
35	AS-E	18166-30A	BC443 (Surf)	32.6	0.12	0.001	98	307.4	26.8
35	AS-E	18167-07A	BC443 (Surf)	106.8	0.02	0.006	58	329.3	22.6
35	AS-E	18166-38A	BC443 (Surf)	32.1	0.06	0.004	79	359.0	11.7
35	AS-E	18166-54A	BC443 (Surf)	31.7	0.04	0.003	90	362.3	12.4
35	AS-E	18166-18A	BC443 (Surf)	143.6	0.03	0.002	65	399.7	21.1
38	AS-W	18578-07A	BC 420B (0-2)	5.4	0.00	0.001	2	13.5	27.6
38	AS-W	18578-06A	BC 420B (0-2)	1.4	0.01	0.047	35	46.0	1.0
38	AS-W	18578-20A	BC 420B (0-2)	2.4	0.00	0.033	30	56.5	1.4
38	AS-W	18578-17A	BC 420B (0-2)	2.3	0.07	0.001	10	66.4	32.0
38	AS-W	18578-14A	BC 420B (0-2)	3.3	0.00	0.001	14	72.0	24.1
38	AS-W	18578-23A	BC 420B (0-2)	104.9	0.03	0.002	8	76.2	17.6
38	AS-W	18573-08A	BC 420B (0-2)	2.6	0.01	0.004	33	77.3	8.2
38	AS-W	18578-04A	BC 420B (0-2)	8.3	-0.01	0.003	43	85.9	7.4
38	AS-W	18573-05A	BC 420B (0-2)	3.1	0.01	0.004	19	89.6	8.9
38	AS-W	18573-13A	BC 420B (0-2)	2.0	-0.01	0.009	46	91.0	3.4
38	AS-W	18573-04A	BC 420B (0-2)	4.8	-0.01	0.002	8	94.1	19.4
38	AS-W	18573-03A	BC 420B (0-2)	5.3	0.07	0.002	27	96.4	17.2
38	AS-W	18578-28A	BC 420B (0-2)	16.8	0.01	0.018	80	101.0	1.5
38	AS-W	18573-19A	BC 420B (0-2)	1.3	0.01	0.006	30	101.9	5.8
38	AS-W	18578-29A	BC 420B (0-2)	20.2	0.00	0.002	31	112.2	11.2
38	AS-W	18578-26A	BC 420B (0-2)	14.5	0.03	0.003	70	118.7	6.6
38	AS-W	18578-19A	BC 420B (0-2)	35.2	-0.04	0.002	23	226.0	15.2
38	AS-W	18578-01A	BC 420B (0-2)	29.6	0.00	0.004	60	236.7	6.8
38	AS-W	18578-24A	BC 420B (0-2)	32.1	-0.04	0.001	56	299.7	18.9
38	AS-W	18578-03A	BC 420B (0-2)	39.6	-0.01	0.004	65	308.6	8.0
38	AS-W	18578-08A	BC 420B (0-2)	28.4	0.00	0.001	80	321.1	19.9
38	AS-W	18578-11A	BC 420B (0-2)	19.8	0.03	0.003	45	321.6	9.8
38	AS-W	18578-16A	BC 420B (0-2)	25.7	-0.01	0.002	74	333.0	16.4
38	AS-W	18578-15A	BC 420B (0-2)	9.8	0.02	0.007	92	378.2	4.8
40	AS-W	18187-12A	BC421 (surf)	56.4	0.01	0.009	25	3.5	5.8
40	AS-W	18187-08A	BC421 (surf)	90.0	-0.03	0.007	15	6.5	8.1
40	AS-W	18187-23A	BC421 (surf)	30.1	0.01	0.003	18	75.2	10.8
40	AS-W	18187-26A	BC421 (surf)	8.6	0.01	0.009	91	95.3	3.5
40	AS-W	18187-13A	BC421 (surf)	20.0	0.04	0.007	36	107.0	8.2
40	AS-W	18187-06A	BC421 (surf)	14.4	0.02	0.014	64	108.4	3.8

40	AS-W	18187-16A	BC421 (surf)	18.7	0.04	0.023	51	108.5	2.5
40	AS-W	18187-09A	BC421 (surf)	11.8	0.03	0.055	77	108.9	1.1
40	AS-W	18187-01A	BC421 (surf)	13.0	0.01	0.116	52	111.2	1.1
40	AS-W	18187-19A	BC421 (surf)	14.1	0.03	0.006	67	118.6	5.6
40	AS-W	18176-02A	BC421 (surf)	7.2	0.01	0.087	44	122.8	0.9
40	AS-W	18176-11A	BC421 (surf)	6.7	0.01	0.062	66	152.4	0.9
40	AS-W	18187-25A	BC421 (surf)	14.6	0.00	0.004	66	155.3	8.2
40	AS-W	18187-04A	BC421 (surf)	12.3	0.00	0.020	91	222.8	2.7
40	AS-W	18187-35A	BC421 (surf)	30.6	0.11	0.004	69	234.3	9.6
40	AS-W	18187-11A	BC421 (surf)	9.6	0.02	0.054	81	242.5	1.5
40	AS-W	18187-32A	BC421 (surf)	26.9	0.04	0.003	68	248.6	9.4
40	AS-W	18187-18A	BC421 (surf)	28.2	0.04	0.005	86	260.2	8.6
40	AS-W	18187-20A	BC421 (surf)	22.9	0.02	0.004	70	262.9	9.8
40	AS-W	18187-31A	BC421 (surf)	12.5	0.02	0.006	94	267.3	5.8
40	AS-W	18187-34A	BC421 (surf)	19.5	0.06	0.006	91	268.2	5.7
40	AS-W	18187-14A	BC421 (surf)	30.7	0.09	0.005	69	268.6	9.7
40	AS-W	18187-17A	BC421 (surf)	13.3	0.06	0.009	66	269.7	5.9
40	AS-W	18187-33A	BC421 (surf)	20.6	0.10	0.004	96	270.4	9.0
40	AS-W	18187-29A	BC421 (surf)	21.3	0.02	0.003	99	275.9	11.5
40	AS-W	18187-10A	BC421 (surf)	12.6	0.02	0.051	72	283.8	1.8
40	AS-W	18187-30A	BC421 (surf)	16.3	-0.03	0.002	103	287.5	17.4
40	AS-W	18187-05A	BC421 (surf)	10.5	0.06	0.024	91	293.4	2.5
40	AS-W	18187-24A	BC421 (surf)	15.8	0.03	0.006	87	297.0	6.1
40	AS-W	18187-21A	BC421 (surf)	60.6	-0.16	0.002	63	298.6	25.9
40	AS-W	18176-06A	BC421 (surf)	40.3	0.03	0.003	62	309.9	15.1
40	AS-W	18187-22A	BC421 (surf)	72.6	0.25	0.002	52	471.6	21.7
41	AS-W	18188-02A	BC412 (Surf)	13.7	0.03	0.009	45	88.5	4.1
41	AS-W	18188-23A	BC412 (Surf)	12.2	0.04	0.002	76	89.8	17.4
41	AS-W	18188-14A	BC412 (Surf)	11.1	0.03	0.003	70	90.5	12.8
41	AS-W	18188-22A	BC412 (Surf)	7.7	0.08	0.002	13	100.5	19.6
41	AS-W	18188-03A	BC412 (Surf)	10.3	0.05	0.006	69	103.8	5.1
41	AS-W	18188-01A	BC412 (Surf)	14.3	0.07	0.006	87	104.1	5.6
41	AS-W	18188-07A	BC412 (Surf)	15.9	0.03	0.002	49	104.5	18.2
41	AS-W	18188-09A	BC412 (Surf)	12.9	0.07	0.008	86	110.0	4.7
41	AS-W	18188-12A	BC412 (Surf)	9.1	0.03	0.005	74	111.8	7.7
41	AS-W	18188-18A	BC412 (Surf)	12.8	0.03	0.005	63	113.0	8.4
41	AS-W	18188-04A	BC412 (Surf)	11.7	0.05	0.026	89	113.4	1.4
41	AS-W	18188-19A	BC412 (Surf)	13.9	0.00	0.002	23	118.9	19.9
41	AS-W	18188-27A	BC412 (Surf)	12.9	0.10	0.002	89	123.6	16.9
41	AS-W	18163-42A	BC412 (Surf)	4.6	0.02	0.023	50	129.3	2.6
41	AS-W	18188-25A	BC412 (Surf)	14.4	0.06	0.002	34	129.8	21.6
41	AS-W	18163-27A	BC412 (Surf)	5.5	0.02	0.004	71	144.4	7.1
41	AS-W	18163-43A	BC412 (Surf)	11.8	-0.01	0.006	31	148.2	3.0
41	AS-W	18163-41A	BC412 (Surf)	4.6	0.02	0.029	30	148.7	3.0
41	AS-W	18188-24A	BC412 (Surf)	7.7	0.04	0.010	97	259.4	4.3
43	AS-W	12649-31	NBP00-01 KC21 (5-10)	33.7	0.11	0.010	26	48.0	10.5
43	AS-W	12649-01	NBP00-01 KC21 (5-10)	10.4	0.03	0.131	63	72.2	1.4
43	AS-W	12649-38	NBP00-01 KC21 (5-10)	16.0	0.01	0.005	57	86.5	18.3
43	AS-W	12649-30	NBP00-01 KC21 (5-10)	15.9	0.04	0.020	78	89.1	5.4
43	AS-W	12649-46	NBP00-01 KC21 (5-10)	30.0	-0.16	0.003	54	91.4	29.6
43	AS-W	12649-37	NBP00-01 KC21 (5-10)	56.2	0.06	0.004	67	93.5	22.2
43	AS-W	12649-02	NBP00-01 KC21 (5-10)	14.0	0.04	0.040	95	108.0	4.2
43	AS-W	12649-03	NBP00-01 KC21 (5-10)	12.0	0.01	0.056	55	108.2	3.2
43	AS-W	12649-69	NBP00-01 KC21 (5-10)	23.1	0.17	0.007	32	108.7	13.7
43	AS-W	12649-05	NBP00-01 KC21 (5-10)	9.8	0.01	0.047	63	108.8	3.6
43	AS-W	12649-36	NBP00-01 KC21 (5-10)	11.6	0.10	0.011	106	109.8	8.6
43	AS-W	12649-40	NBP00-01 KC21 (5-10)	33.0	-0.17	0.005	76	112.6	18.7
43	AS-W	12649-42	NBP00-01 KC21 (5-10)	18.5	0.01	0.008	49	113.5	12.1
43	AS-W	12649-04	NBP00-01 KC21 (5-10)	10.7	0.03	0.040	111	115.8	3.9

43	AS-W	12649-41	NBP00-01 KC21 (5-10)	27.6	0.01	0.009	84	122.4	9.5
43	AS-W	12649-72	NBP00-01 KC21 (5-10)	13.1	0.09	0.006	47	124.0	15.0
43	AS-W	12649-66	NBP00-01 KC21 (5-10)	9.9	0.05	0.009	98	124.7	9.7
43	AS-W	12649-07	NBP00-01 KC21 (5-10)	15.5	-0.02	0.017	98	125.6	9.4
43	AS-W	12649-39	NBP00-01 KC21 (5-10)	19.3	-0.05	0.006	86	127.3	16.6
43	AS-W	12649-34	NBP00-01 KC21 (5-10)	14.1	0.09	0.011	125	143.4	8.7
43	AS-W	12649-11	NBP00-01 KC21 (5-10)	11.1	0.12	0.023	126	151.9	6.3
43	AS-W	12649-71	NBP00-01 KC21 (5-10)	50.2	0.14	0.003	23	159.8	27.0
43	AS-W	12649-06	NBP00-01 KC21 (5-10)	13.8	0.09	0.011	81	161.7	14.9
43	AS-W	12649-08	NBP00-01 KC21 (5-10)	18.6	0.04	0.019	103	164.7	8.1
43	AS-W	12649-13	NBP00-01 KC21 (5-10)	9.7	0.01	0.021	135	175.3	6.9
43	AS-W	12649-70	NBP00-01 KC21 (5-10)	2.6	0.06	0.003	55	177.9	25.8
43	AS-W	12649-43	NBP00-01 KC21 (5-10)	17.1	0.05	0.005	128	189.0	20.8
43	AS-W	12649-35	NBP00-01 KC21 (5-10)	3.7	0.01	0.005	43	190.0	21.7
43	AS-W	12649-09	NBP00-01 KC21 (5-10)	20.6	-0.04	0.010	101	223.3	14.8
43	AS-W	12649-65	NBP00-01 KC21 (5-10)	87.7	0.13	0.002	127	256.9	39.1
43	AS-W	12649-15	NBP00-01 KC21 (5-10)	3.4	0.03	0.013	251	277.3	11.4
43	AS-W	12649-10	NBP00-01 KC21 (5-10)	46.9	-0.05	0.004	259	327.2	36.7
43	AS-W	12649-14	NBP00-01 KC21 (5-10)	3.2	0.11	0.005	56	473.1	27.0
43	AS-W	12649-64	NBP00-01 KC21 (5-10)	24.3	0.06	0.002	122	663.3	46.4
43	AS-W	12649-59	NBP00-01 KC21 (5-10)	98.0	0.03	0.003	83	669.2	29.8
45	AS-W	18566-05A	PS 69/275-2 (0-1)	29.6	0.09	0.001	24	55.2	53.3
45	AS-W	18575-14A	PS 69/275-2 (0-1)	14.1	-0.02	0.001	35	67.4	13.5
45	AS-W	18566-06A	PS 69/275-2 (0-1)	15.2	0.10	0.001	41	83.7	49.0
45	AS-W	18566-02A	PS 69/275-2 (0-1)	12.6	0.02	0.007	74	102.3	4.7
45	AS-W	18566-10A	PS 69/275-2 (0-1)	13.1	0.04	0.002	53	103.1	10.1
45	AS-W	18566-04A	PS 69/275-2 (0-1)	12.7	0.01	0.006	40	105.3	6.1
45	AS-W	18566-09A	PS 69/275-2 (0-1)	11.5	0.05	0.004	65	109.8	6.3
45	AS-W	18566-11A	PS 69/275-2 (0-1)	11.1	0.02	0.011	50	111.8	2.7
45	AS-W	18566-01A	PS 69/275-2 (0-1)	13.4	0.05	0.002	74	114.3	16.3
45	AS-W	18566-08A	PS 69/275-2 (0-1)	13.7	0.05	0.003	85	119.7	11.8
45	AS-W	18566-03A	PS 69/275-2 (0-1)	12.4	-0.08	0.001	96	128.3	49.4
46	AS-W	18557-11A	BC 407 (0-2)	6.0	-0.02	0.002	8	4.8	17.2
46	AS-W	18579-03A	BC 407 (0-2)	8.0	-0.02	0.003	23	97.2	9.8
46	AS-W	18557-03A	BC 407 (0-2)	15.5	-0.06	0.001	28	98.7	37.5
46	AS-W	18579-05A	BC 407 (0-2)	4.1	0.00	0.011	42	105.6	2.9
46	AS-W	18557-04A	BC 407 (0-2)	5.6	-0.10	0.001	51	108.5	45.0
46	AS-W	18557-01A	BC 407 (0-2)	26.8	0.00	0.011	66	347.2	5.7
47	AS-W	18567-21A	PS69/283-5 (Surf)	183.1	0.01	0.002	25	26.4	10.2
47	AS-W	18570-23A	PS69/283-5 (Surf)	4.2	-0.03	0.003	12	68.8	12.1
47	AS-W	18570-32A	PS69/283-5 (Surf)	5.3	-0.01	0.010	13	83.3	7.6
47	AS-W	18570-29A	PS69/283-5 (Surf)	20.5	-0.01	0.002	17	84.3	19.2
47	AS-W	18567-02A	PS69/283-5 (Surf)	9.4	0.00	0.040	31	103.1	2.1
47	AS-W	18567-42A	PS69/283-5 (Surf)	16.2	0.02	0.007	66	104.6	3.3
47	AS-W	18567-10A	PS69/283-5 (Surf)	15.6	0.02	0.021	65	108.0	1.6
47	AS-W	18567-09A	PS69/283-5 (Surf)	16.6	0.05	0.007	68	108.1	4.1
47	AS-W	18570-43A	PS69/283-5 (Surf)	4.0	-0.04	0.001	30	141.1	29.4
47	AS-W	18567-03A	PS69/283-5 (Surf)	20.4	0.03	0.011	63	154.4	2.7
47	AS-W	18570-49A	PS69/283-5 (Surf)	10.4	0.03	0.006	66	200.4	5.9
47	AS-W	18570-37A	PS69/283-5 (Surf)	2.5	0.01	0.047	52	227.6	2.8
47	AS-W	18567-07A	PS69/283-5 (Surf)	10.5	0.02	0.061	88	228.6	1.0
47	AS-W	18567-32A	PS69/283-5 (Surf)	8.9	0.01	0.021	79	229.6	1.9
47	AS-W	18567-30A	PS69/283-5 (Surf)	8.6	0.02	0.004	88	230.3	6.8
47	AS-W	18567-19A	PS69/283-5 (Surf)	6.8	0.01	0.013	97	230.6	2.2
47	AS-W	18567-24A	PS69/283-5 (Surf)	8.8	0.01	0.017	84	231.3	2.1
47	AS-W	18567-16A	PS69/283-5 (Surf)	10.0	0.00	0.007	84	235.3	4.0
47	AS-W	18567-43A	PS69/283-5 (Surf)	14.5	0.01	0.002	85	236.4	11.1
47	AS-W	18570-45A	PS69/283-5 (Surf)	2.1	0.00	0.156	89	238.2	0.9

47	AS-W	18567-31A	PS69/283-5 (Surf)	17.5	-0.02	0.002	44	241.7	14.9
47	AS-W	18567-17A	PS69/283-5 (Surf)	39.3	0.09	0.001	48	242.1	17.3
47	AS-W	18567-34A	PS69/283-5 (Surf)	9.4	0.02	0.009	93	242.5	3.0
47	AS-W	18567-36A	PS69/283-5 (Surf)	9.1	0.01	0.024	82	243.6	1.7
47	AS-W	18567-35A	PS69/283-5 (Surf)	12.2	0.02	0.068	87	245.0	1.0
47	AS-W	18567-41A	PS69/283-5 (Surf)	7.5	0.03	0.008	67	246.2	4.1
47	AS-W	18567-13A	PS69/283-5 (Surf)	15.4	0.03	0.019	59	246.4	2.7
47	AS-W	18567-01A	PS69/283-5 (Surf)	42.5	0.04	0.011	34	246.5	5.2
47	AS-W	18567-39A	PS69/283-5 (Surf)	27.9	0.10	0.001	36	248.1	21.1
47	AS-W	18567-45A	PS69/283-5 (Surf)	8.2	0.02	0.007	94	248.6	3.8
47	AS-W	18567-15A	PS69/283-5 (Surf)	11.7	0.01	0.016	77	248.9	2.3
47	AS-W	18567-28A	PS69/283-5 (Surf)	14.2	-0.02	0.003	93	257.2	7.5
47	AS-W	18567-12A	PS69/283-5 (Surf)	22.6	0.01	0.029	58	261.5	2.5
47	AS-W	18567-23A	PS69/283-5 (Surf)	34.7	0.03	0.001	53	264.3	23.9
47	AS-W	18567-46A	PS69/283-5 (Surf)	53.1	-0.02	0.003	78	265.4	8.6
47	AS-W	18567-18A	PS69/283-5 (Surf)	6.8	0.00	0.034	88	268.9	1.4
47	AS-W	18567-22A	PS69/283-5 (Surf)	51.5	0.04	0.001	71	269.0	18.2
47	AS-W	18567-37A	PS69/283-5 (Surf)	12.2	0.01	0.006	90	269.8	4.4
47	AS-W	18567-05A	PS69/283-5 (Surf)	12.7	0.01	0.021	83	271.0	1.9
47	AS-W	18567-08A	PS69/283-5 (Surf)	24.2	0.00	0.007	83	271.3	4.5
47	AS-W	18567-20A	PS69/283-5 (Surf)	7.4	0.04	0.016	93	275.7	1.9
47	AS-W	18567-29A	PS69/283-5 (Surf)	17.2	0.04	0.017	84	276.0	2.2
47	AS-W	18567-38A	PS69/283-5 (Surf)	17.8	0.01	0.006	87	277.0	4.8
47	AS-W	18567-26A	PS69/283-5 (Surf)	33.3	0.03	0.001	78	278.6	19.3
47	AS-W	18567-14A	PS69/283-5 (Surf)	15.5	0.00	0.005	93	291.9	5.9
47	AS-W	18567-40A	PS69/283-5 (Surf)	15.6	0.05	0.047	81	293.5	1.5
47	AS-W	18567-44A	PS69/283-5 (Surf)	16.9	0.01	0.003	77	301.9	8.8
47	AS-W	18567-11A	PS69/283-5 (Surf)	19.4	0.07	0.046	73	323.0	1.8
47	AS-W	18567-27A	PS69/283-5 (Surf)	15.9	0.06	0.024	87	330.3	1.9
47	AS-W	18567-25A	PS69/283-5 (Surf)	44.3	0.00	0.003	46	332.9	10.0
47	AS-W	18567-33A	PS69/283-5 (Surf)	36.2	0.03	0.011	50	341.4	4.8
47	AS-W	18567-06A	PS69/283-5 (Surf)	10.4	0.02	0.036	79	352.0	2.0
48	AS-W	18174-11A	BC431 (Surf)	103.9	0.01	0.021	15	3.9	2.2
48	AS-W	18171-20A	BC431 (Surf)	49.9	0.03	0.009	6	66.8	9.4
48	AS-W	18174-29A	BC431 (Surf)	9.6	-0.02	0.003	73	82.4	12.5
48	AS-W	18174-30A	BC431 (Surf)	19.8	0.00	0.004	61	90.6	9.8
48	AS-W	18174-25A	BC431 (Surf)	12.4	0.05	0.008	89	96.3	4.9
48	AS-W	18174-07A	BC431 (Surf)	12.6	0.00	0.004	73	97.4	10.0
48	AS-W	18174-16A	BC431 (Surf)	11.3	0.01	0.008	89	98.8	5.3
48	AS-W	18171-41A	BC431 (Surf)	8.0	0.02	0.005	63	98.8	6.0
48	AS-W	18174-24A	BC431 (Surf)	17.6	0.00	0.011	48	99.6	4.4
48	AS-W	18174-10A	BC431 (Surf)	13.5	0.01	0.015	83	100.0	2.9
48	AS-W	18174-22A	BC431 (Surf)	9.3	0.03	0.015	95	101.0	2.8
48	AS-W	18174-05A	BC431 (Surf)	13.4	0.06	0.169	62	101.8	1.1
48	AS-W	18174-36A	BC431 (Surf)	11.1	0.02	0.012	74	102.1	3.5
48	AS-W	18174-15A	BC431 (Surf)	10.0	0.02	0.029	96	102.2	1.6
48	AS-W	18171-17A	BC431 (Surf)	1.4	0.00	0.645	81	102.4	0.4
48	AS-W	18174-21A	BC431 (Surf)	12.2	0.02	0.046	82	104.5	1.1
48	AS-W	18174-04A	BC431 (Surf)	16.8	-0.01	0.006	51	104.7	7.6
48	AS-W	18174-38A	BC431 (Surf)	17.3	0.01	0.021	81	105.3	2.2
48	AS-W	18174-02A	BC431 (Surf)	16.1	0.02	0.018	44	106.2	3.0
48	AS-W	18174-09A	BC431 (Surf)	13.4	0.00	0.011	94	106.9	3.8
48	AS-W	18174-26A	BC431 (Surf)	10.7	0.02	0.006	85	107.2	6.5
48	AS-W	18174-40A	BC431 (Surf)	15.6	0.02	0.011	84	107.3	3.9
48	AS-W	18174-01A	BC431 (Surf)	11.8	0.02	0.082	64	109.6	1.2
48	AS-W	18174-14A	BC431 (Surf)	18.0	0.01	0.022	73	110.6	2.1
48	AS-W	18174-06A	BC431 (Surf)	2.9	0.00	0.025	12	111.8	9.7
48	AS-W	18174-28A	BC431 (Surf)	15.6	-0.02	0.008	69	112.5	5.2
48	AS-W	18171-28A	BC431 (Surf)	12.3	0.02	0.012	82	112.9	2.5
48	AS-W	18174-18A	BC431 (Surf)	12.9	0.01	0.012	95	113.7	3.5

48	AS-W	18174-23A	BC431 (Surf)	9.9	0.01	0.017	73	114.7	2.6
48	AS-W	18174-31A	BC431 (Surf)	11.5	0.03	0.020	88	115.7	2.2
48	AS-W	18171-18A	BC431 (Surf)	1.4	0.00	0.079	66	116.5	0.9
48	AS-W	18174-19A	BC431 (Surf)	13.9	0.03	0.004	101	121.8	9.2
48	AS-W	18174-34A	BC431 (Surf)	9.3	0.03	0.075	76	121.9	1.1
48	AS-W	18174-13A	BC431 (Surf)	15.1	0.01	0.018	47	122.8	3.2
48	AS-W	18174-35A	BC431 (Surf)	12.7	0.02	0.021	96	123.7	2.0
48	AS-W	18174-03A	BC431 (Surf)	10.6	0.03	0.035	79	123.8	1.5
48	AS-W	18174-20A	BC431 (Surf)	9.5	0.01	0.040	92	124.6	1.2
48	AS-W	18174-37A	BC431 (Surf)	29.8	0.00	0.006	74	163.2	7.5
48	AS-W	18174-27A	BC431 (Surf)	8.6	0.01	0.030	87	201.6	1.8
48	AS-W	18174-08A	BC431 (Surf)	25.5	-0.01	0.004	84	270.9	11.1
48	AS-W	18174-17A	BC431 (Surf)	28.0	0.02	0.003	102	272.8	15.4
48	AS-W	18174-32A	BC431 (Surf)	19.3	0.03	0.032	93	280.6	1.9
48	AS-W	18174-39A	BC431 (Surf)	11.0	0.02	0.003	102	283.5	12.9
48	AS-W	18174-12A	BC431 (Surf)	18.2	0.01	0.013	76	289.3	4.0
48	AS-W	18174-33A	BC431 (Surf)	15.6	0.01	0.004	78	295.9	10.0
49	AS-W	18185-05A	BC433 (Surf)	0.2	0.01	0.581	0	0.1	0.9
49	AS-W	18184-20A	BC433 (Surf)	0.2	0.01	0.067	5	0.3	0.9
49	AS-W	18185-01A	BC433 (Surf)	0.3	0.01	1.330	22	0.5	0.0
49	AS-W	18184-05A	BC433 (Surf)	0.2	0.01	0.105	1	0.5	0.8
49	AS-W	18184-39A	BC433 (Surf)	0.3	0.01	0.058	1	0.6	1.5
49	AS-W	18184-19A	BC433 (Surf)	0.2	0.01	0.138	8	0.7	0.5
49	AS-W	18184-15A	BC433 (Surf)	0.2	0.01	0.091	12	0.7	0.7
49	AS-W	18185-03A	BC433 (Surf)	0.2	0.01	0.463	6	0.9	0.2
49	AS-W	18184-14A	BC433 (Surf)	0.4	0.00	0.062	22	0.9	1.1
49	AS-W	18184-01A	BC433 (Surf)	0.2	0.01	0.261	7	1.0	0.3
49	AS-W	18184-22A	BC433 (Surf)	0.2	0.01	0.154	50	1.1	0.4
49	AS-W	18185-02A	BC433 (Surf)	0.2	0.01	2.831	38	1.1	0.0
49	AS-W	18184-35A	BC433 (Surf)	0.2	0.00	0.070	44	1.2	0.6
49	AS-W	18184-23A	BC433 (Surf)	0.2	0.01	0.161	14	1.3	0.4
49	AS-W	18184-08A	BC433 (Surf)	0.2	0.01	0.098	8	1.4	0.7
49	AS-W	18184-26A	BC433 (Surf)	0.4	0.00	0.051	13	1.4	0.8
49	AS-W	18184-43A	BC433 (Surf)	0.1	0.00	0.034	2	1.6	1.6
49	AS-W	18185-06A	BC433 (Surf)	0.2	0.01	0.387	2	1.8	0.8
49	AS-W	18184-41A	BC433 (Surf)	0.3	0.01	0.023	14	2.0	1.7
49	AS-W	18184-25A	BC433 (Surf)	0.2	0.01	0.073	51	2.3	0.8
49	AS-W	18184-09A	BC433 (Surf)	0.3	0.00	0.056	32	2.3	1.2
49	AS-W	18184-24A	BC433 (Surf)	0.2	0.01	0.133	32	2.4	0.5
49	AS-W	18184-32A	BC433 (Surf)	0.3	0.00	0.034	51	2.6	1.2
49	AS-W	18184-04A	BC433 (Surf)	0.2	0.01	0.099	43	2.7	0.7
49	AS-W	18184-42A	BC433 (Surf)	58.4	0.00	0.004	12	3.0	10.3
49	AS-W	18184-27A	BC433 (Surf)	0.3	0.00	0.022	34	3.0	1.9
49	AS-W	18184-34A	BC433 (Surf)	0.3	0.01	0.033	9	3.6	1.3
49	AS-W	18184-31A	BC433 (Surf)	0.4	-0.01	0.021	3	3.7	2.5
49	AS-W	18184-30A	BC433 (Surf)	0.3	0.01	0.013	5	3.8	3.5
49	AS-W	18184-33A	BC433 (Surf)	0.2	0.01	0.012	33	4.2	3.5
49	AS-W	18184-07A	BC433 (Surf)	0.4	0.01	0.122	34	5.5	0.6
49	AS-W	18184-13A	BC433 (Surf)	0.4	0.00	0.054	5	6.4	1.6
49	AS-W	18184-37A	BC433 (Surf)	0.3	0.00	0.003	42	19.2	12.1
49	AS-W	18184-03A	BC433 (Surf)	25.9	0.08	0.025	21	72.1	3.7
49	AS-W	18184-16A	BC433 (Surf)	0.4	0.00	0.095	85	94.2	0.7
49	AS-W	18184-06A	BC433 (Surf)	5.4	0.02	0.030	58	97.7	2.4
49	AS-W	18184-36A	BC433 (Surf)	14.9	0.04	0.003	75	101.4	13.1
49	AS-W	18184-38A	BC433 (Surf)	0.7	0.00	0.010	51	105.0	4.2
49	AS-W	18184-11A	BC433 (Surf)	17.8	0.04	0.027	86	111.9	2.4
49	AS-W	18184-02A	BC433 (Surf)	20.3	0.19	0.012	58	120.2	6.2
49	AS-W	18184-29A	BC433 (Surf)	0.0	0.00	0.025	90	121.6	1.8
49	AS-W	18184-18A	BC433 (Surf)	0.1	0.00	0.086	97	152.3	0.8
49	AS-W	18184-12A	BC433 (Surf)	34.1	0.02	0.005	89	258.0	11.3

51	AS-W	11039-27	ELT33-12 (2-6)	6.5			112	26.5	4.2	Roy et al., 2007
51	AS-W	11081-01	ELT33-12 (2-6)	5.2			8	28.4	2.9	Roy et al., 2007
51	AS-W	17589-20A	ELT33-12 (2-6)	198.9	0.04	0.001	32	38.1	27.2	
51	AS-W	17589-19A	ELT33-12 (2-6)	384.2	-0.06	0.002	4	93.7	17.9	
51	AS-W	17589-22A	ELT33-12 (2-6)	7.5	-0.03	0.001	29	95.7	15.1	
51	AS-W	17589-18A	ELT33-12 (2-6)	6.6	0.00	0.046	80	98.6	0.7	
51	AS-W	11039-14	ELT33-12 (2-6)	10.3			79	102.5	3.1	Roy et al., 2007
51	AS-W	11039-38	ELT33-12 (2-6)	24.3			79	110.2	12.9	Roy et al., 2007
51	AS-W	11039-46	ELT33-12 (2-6)	9.2			97	116.5	8.7	Roy et al., 2007
51	AS-W	11039-02	ELT33-12 (2-6)	10.8			84	127.4	2.4	Roy et al., 2007
51	AS-W	11039-31	ELT33-12 (2-6)	9.7			79	150.5	2.3	Roy et al., 2007
51	AS-W	11039-08	ELT33-12 (2-6)	29.9			79	159.0	4.7	Roy et al., 2007
51	AS-W	17589-17A	ELT33-12 (2-6)	4.5	0.01	0.126	91	161.8	0.4	
51	AS-W	11039-01	ELT33-12 (2-6)	4.8			92	188.5	1.4	Roy et al., 2007
51	AS-W	11039-04	ELT33-12 (2-6)	13.4			94	200.1	3.2	Roy et al., 2007
51	AS-W	11039-20	ELT33-12 (2-6)	8.4			77	202.8	2.8	Roy et al., 2007
51	AS-W	11039-41	ELT33-12 (2-6)	17.7			84	208.4	3.9	Roy et al., 2007
51	AS-W	11039-34	ELT33-12 (2-6)	11.7			98	222.2	6.9	Roy et al., 2007
51	AS-W	11039-05	ELT33-12 (2-6)	21.6			77	226.0	6.1	Roy et al., 2007
51	AS-W	11017-01	ELT33-12 (2-6)	8.4			96	227.6	1.8	Roy et al., 2007
51	AS-W	11039-07	ELT33-12 (2-6)	28.2			93	240.4	6.4	Roy et al., 2007
51	AS-W	11039-10	ELT33-12 (2-6)	10.6			92	245.9	3.9	Roy et al., 2007
51	AS-W	11039-16	ELT33-12 (2-6)	12.6			85	265.5	3.8	Roy et al., 2007
51	AS-W	11039-44	ELT33-12 (2-6)	24.6			87	269.7	7.9	Roy et al., 2007
51	AS-W	11039-26	ELT33-12 (2-6)	22.5			117	312.4	13.5	Roy et al., 2007
51	AS-W	11081-08	ELT33-12 (2-6)	27.8			98	2602.1	37.7	Roy et al., 2007
51	AS-W	11079-05	ELT33-12 (2-6)	25.8			99	2804.1	20.5	Roy et al., 2007
52	AS-W	11085-10	ELT33-11 (0-2)	6.8			5	22.6	3.7	Roy et al, 2007
52	AS-W	11085-07	ELT33-11 (0-2)	4.2			11	25.7	7.1	Roy et al, 2007
52	AS-W	11085-11	ELT33-11 (0-2)	8.3			31	50.3	19.1	Roy et al, 2007
52	AS-W	11085-18	ELT33-11 (0-2)	4.7			113	90.5	17.4	Roy et al, 2007
52	AS-W	11085-05	ELT33-11 (0-2)	6.7			50	94.7	11.1	Roy et al, 2007
52	AS-W	11085-19	ELT33-11 (0-2)	6.8			65	110.7	18.0	Roy et al, 2007
52	AS-W	11085-03	ELT33-11 (0-2)	7.0			7	111.4	10.7	Roy et al, 2007
52	AS-W	11085-21	ELT33-11 (0-2)	7.1			73	131.8	19.5	Roy et al, 2007
52	AS-W	11078-01	ELT33-11 (0-2)	0.8			81	196.7	19.1	Roy et al, 2007
52	AS-W	11085-17	ELT33-11 (0-2)	3.1			246	254.6	49.4	Roy et al, 2007
55	WH	12931-11	NBP99-02 PC21 (8-13)	1.7	0.00	0.025	46	111.7	2.2	
55	WH	12931-15	NBP99-02 PC21 (8-13)	1.5	0.01	0.243	67	125.3	1.4	
55	WH	12931-13	NBP99-02 PC21 (8-13)	1.0	0.11	0.005	7	163.1	15.4	
55	WH	12931-14	NBP99-02 PC21 (8-13)	2.0	0.01	0.153	31	169.7	2.6	
55	WH	12931-16	NBP99-02 PC21 (8-13)	0.4	0.00	1.949	94	189.7	1.9	
55	WH	12931-08	NBP99-02 PC21 (8-13)	4.7	0.02	0.387	33	197.7	2.9	
55	WH	12931-10	NBP99-02 PC21 (8-13)	0.7	0.01	0.195	51	235.0	2.8	
55	WH	12931-09	NBP99-02 PC21 (8-13)	119.6	0.00	0.007	3	320.2	42.5	
55	WH	12931-07	NBP99-02 PC21 (8-13)	183.9	0.02	0.024	4	143.2	18.0	
57	WH	18841-08A	NBP00-01 PC14 (1-3)	17.0	-0.02	0.002	77	94.8	1.9	
57	WH	18841-23A	NBP00-01 PC14 (1-3)	12.2	0.04	0.003	42	96.9	1.9	
57	WH	18841-48A	NBP00-01 PC14 (1-3)	9.2	0.09	0.003	83	98.5	2.0	
57	WH	18841-10A	NBP00-01 PC14 (1-3)	8.6	0.08	0.006	97	99.0	2.0	
57	WH	18841-29A	NBP00-01 PC14 (1-3)	10.8	0.01	0.003	30	99.1	2.0	
57	WH	18841-36A	NBP00-01 PC14 (1-3)	8.7	0.02	0.009	58	99.5	2.0	
57	WH	18841-28A	NBP00-01 PC14 (1-3)	8.0	0.11	0.006	58	100.0	2.0	
57	WH	18841-03A	NBP00-01 PC14 (1-3)	12.2	0.03	0.009	79	100.5	2.0	
57	WH	18841-50A	NBP00-01 PC14 (1-3)	8.5	0.09	0.004	86	100.7	2.0	
57	WH	18841-05A	NBP00-01 PC14 (1-3)	8.1	0.09	0.016	99	100.8	2.0	
57	WH	18841-04A	NBP00-01 PC14 (1-3)	12.3	0.02	0.005	87	100.9	2.0	

57	WH	18841-26A	NBP00-01 PC14 (1-3)	9.0	0.03	0.004	43	103.9	2.1
57	WH	18841-47A	NBP00-01 PC14 (1-3)	7.3	0.14	0.004	104	103.9	2.1
57	WH	18841-51A	NBP00-01 PC14 (1-3)	10.3	0.05	0.009	72	105.9	2.1
57	WH	18841-37A	NBP00-01 PC14 (1-3)	18.6	0.01	0.002	28	106.1	2.1
57	WH	18841-06A	NBP00-01 PC14 (1-3)	12.6	0.04	0.004	75	106.6	2.1
57	WH	18841-42A	NBP00-01 PC14 (1-3)	13.0	0.04	0.002	29	106.7	2.1
57	WH	18841-41A	NBP00-01 PC14 (1-3)	17.4	0.05	0.003	40	107.6	2.2
57	WH	18841-01A	NBP00-01 PC14 (1-3)	7.8	0.01	0.013	80	108.3	2.2
57	WH	18841-13A	NBP00-01 PC14 (1-3)	11.8	0.05	0.003	82	110.0	2.2
57	WH	18841-18A	NBP00-01 PC14 (1-3)	10.7	0.01	0.006	55	111.5	2.2
57	WH	18841-15A	NBP00-01 PC14 (1-3)	15.7	0.01	0.002	98	111.5	2.2
57	WH	18841-34A	NBP00-01 PC14 (1-3)	9.8	0.00	0.006	24	111.9	2.2
57	WH	18841-07A	NBP00-01 PC14 (1-3)	16.9	0.04	0.004	79	113.0	2.3
57	WH	18841-31A	NBP00-01 PC14 (1-3)	11.1	0.02	0.006	79	113.8	2.3
57	WH	18841-17A	NBP00-01 PC14 (1-3)	11.3	0.03	0.004	106	114.0	2.3
57	WH	18841-02A	NBP00-01 PC14 (1-3)	9.7	0.03	0.006	85	114.4	2.3
57	WH	18841-39A	NBP00-01 PC14 (1-3)	12.8	0.02	0.003	76	114.8	2.3
57	WH	18841-33A	NBP00-01 PC14 (1-3)	39.6	0.08	0.002	24	115.1	2.3
57	WH	18841-14A	NBP00-01 PC14 (1-3)	19.0	0.02	0.002	87	115.6	2.3
57	WH	18841-16A	NBP00-01 PC14 (1-3)	10.6	0.01	0.007	82	117.1	2.3
57	WH	18841-40A	NBP00-01 PC14 (1-3)	8.0	0.02	0.007	84	117.3	2.3
57	WH	18841-27A	NBP00-01 PC14 (1-3)	9.8	0.09	0.005	42	118.0	2.4
57	WH	18841-49A	NBP00-01 PC14 (1-3)	11.0	0.02	0.004	101	120.2	2.4
57	WH	18841-38A	NBP00-01 PC14 (1-3)	20.0	0.04	0.004	59	122.2	2.4
57	WH	18841-11A	NBP00-01 PC14 (1-3)	11.2	0.04	0.003	76	123.0	2.5
57	WH	18841-24A	NBP00-01 PC14 (1-3)	18.3	0.02	0.002	37	124.3	2.5
57	WH	18841-32A	NBP00-01 PC14 (1-3)	12.0	0.01	0.016	83	124.7	2.5
57	WH	18841-12A	NBP00-01 PC14 (1-3)	12.5	0.01	0.004	81	124.9	2.5
57	WH	18841-20A	NBP00-01 PC14 (1-3)	13.9	-0.02	0.001	17	125.9	2.5
57	WH	18841-22A	NBP00-01 PC14 (1-3)	12.1	0.01	0.006	57	126.3	2.5
57	WH	18841-30A	NBP00-01 PC14 (1-3)	8.3	0.03	0.004	84	127.3	2.5
57	WH	18841-52A	NBP00-01 PC14 (1-3)	8.8	0.01	0.005	26	127.8	2.6
57	WH	18841-19A	NBP00-01 PC14 (1-3)	15.2	0.01	0.006	54	128.3	2.6
57	WH	18841-25A	NBP00-01 PC14 (1-3)	10.5	0.04	0.004	32	131.3	2.6
57	WH	18841-21A	NBP00-01 PC14 (1-3)	17.9	0.01	0.007	56	135.1	2.7
57	WH	18841-46A	NBP00-01 PC14 (1-3)	12.5	0.03	0.003	79	136.0	2.7
57	WH	18841-35A	NBP00-01 PC14 (1-3)	5.3	0.01	0.034	50	137.3	2.7
57	WH	18841-45A	NBP00-01 PC14 (1-3)	21.4	-0.01	0.002	21	207.6	4.2
57	WH	18841-43A	NBP00-01 PC14 (1-3)	13.9	0.17	0.003	4	299.0	6.0
57	WH	18841-44A	NBP00-01 PC14 (1-3)	23.4	0.15	0.003	6	608.6	12.2
58	WH	18563-18A	PS 75/133-1 (Surf)	2.7	0.00	0.007	3	1.2	5.0
58	WH	18563-17A	PS 75/133-1 (Surf)	6.0	0.01	0.005	4	3.4	6.4
58	WH	18563-09A	PS 75/133-1 (Surf)	3.0	-0.01	0.004	5	4.4	5.7
58	WH	18563-08A	PS 75/133-1 (Surf)	4.2	-0.03	0.003	3	5.0	8.8
58	WH	18563-28A	PS 75/133-1 (Surf)	7.2	0.07	0.002	1	7.1	19.6
58	WH	18563-29A	PS 75/133-1 (Surf)	1.9	0.00	0.005	9	9.2	8.0
58	WH	18563-13A	PS 75/133-1 (Surf)	5.6	0.04	0.002	3	11.3	16.4
58	WH	18563-06A	PS 75/133-1 (Surf)	10.0	0.00	0.004	12	14.1	5.4
58	WH	18563-01A	PS 75/133-1 (Surf)	12.8	0.03	0.003	38	86.0	8.3
58	WH	18563-27A	PS 75/133-1 (Surf)	6.9	-0.01	0.006	30	94.8	7.1
58	WH	18563-21A	PS 75/133-1 (Surf)	2.2	0.00	0.026	55	94.9	1.8
58	WH	18563-23A	PS 75/133-1 (Surf)	3.9	0.01	0.020	66	97.0	2.1
58	WH	18563-36A	PS 75/133-1 (Surf)	7.6	0.09	0.001	6	98.6	34.1
58	WH	18563-16A	PS 75/133-1 (Surf)	10.4	0.04	0.002	53	102.4	14.1
58	WH	18563-24A	PS 75/133-1 (Surf)	11.7	0.02	0.008	65	103.2	4.3
58	WH	18563-15A	PS 75/133-1 (Surf)	11.8	-0.02	0.003	51	106.3	13.3
58	WH	18563-05A	PS 75/133-1 (Surf)	7.8	0.05	0.004	86	108.7	6.0
58	WH	18563-02A	PS 75/133-1 (Surf)	18.7	0.01	0.012	53	110.4	2.3
58	WH	18563-07A	PS 75/133-1 (Surf)	12.5	0.02	0.002	89	118.0	12.1

59	WH	18562-02A	PS 75/130-2 (Surf)	2.2	0.01	0.138	12	1.0	0.2
59	WH	18562-15A	PS 75/130-2 (Surf)	5.4	0.00	0.004	6	1.8	5.2
59	WH	18562-09A	PS 75/130-2 (Surf)	5.0	-0.03	0.003	38	8.1	8.4
59	WH	18560-34A	PS 75/130-2 (Surf)	2.8	0.03	0.003	9	66.7	10.3
59	WH	18562-21A	PS 75/130-2 (Surf)	7.5	0.00	0.004	52	69.2	5.8
59	WH	18560-19A	PS 75/130-2 (Surf)	3.7	-0.06	0.003	32	88.7	15.6
59	WH	18562-12A	PS 75/130-2 (Surf)	19.2	0.01	0.003	68	90.4	7.4
59	WH	18562-24A	PS 75/130-2 (Surf)	33.8	0.04	0.006	18	92.2	5.1
59	WH	18562-10A	PS 75/130-2 (Surf)	13.3	-0.01	0.002	49	93.9	9.5
59	WH	18562-14A	PS 75/130-2 (Surf)	4.1	0.02	0.003	56	96.8	6.5
59	WH	18562-01A	PS 75/130-2 (Surf)	17.0	0.01	0.046	23	97.6	1.8
59	WH	18562-07A	PS 75/130-2 (Surf)	11.9	0.03	0.002	58	101.0	9.9
59	WH	18562-06A	PS 75/130-2 (Surf)	9.8	0.02	0.005	86	101.3	4.1
59	WH	18562-19A	PS 75/130-2 (Surf)	24.2	-0.02	0.001	24	102.1	15.9
59	WH	18562-11A	PS 75/130-2 (Surf)	7.6	0.02	0.008	73	102.9	3.0
59	WH	18562-05A	PS 75/130-2 (Surf)	10.9	0.03	0.003	86	103.7	7.4
59	WH	18562-04A	PS 75/130-2 (Surf)	11.3	0.01	0.008	66	104.6	3.0
59	WH	18562-18A	PS 75/130-2 (Surf)	8.2	0.01	0.005	82	105.7	4.1
59	WH	18562-23A	PS 75/130-2 (Surf)	14.1	0.01	0.026	78	105.7	1.1
59	WH	18562-22A	PS 75/130-2 (Surf)	13.0	-0.02	0.004	73	107.3	5.0
59	WH	18562-03A	PS 75/130-2 (Surf)	7.1	0.00	0.005	85	115.1	4.2
59	WH	18562-20A	PS 75/130-2 (Surf)	16.3	0.03	0.008	38	120.0	3.7
60	SB	18847-15A	DF83-III BC28 (2-4)	2.1	0.01	0.011	24	4.8	1.6
60	SB	18847-03A	DF83-III BC28 (2-4)	0.5	0.00	0.003	69	46.3	5.2
60	SB	18847-02A	DF83-III BC28 (2-4)	0.3	-0.01	0.005	83	46.5	3.7
60	SB	18847-22A	DF83-III BC28 (2-4)	0.3	0.05	0.001	87	57.9	13.3
60	SB	18847-27A	DF83-III BC28 (2-4)	9.1	-0.04	0.001	96	84.7	22.9
60	SB	18847-17A	DF83-III BC28 (2-4)	7.0	0.05	0.001	118	89.9	27.1
60	SB	18847-13A	DF83-III BC28 (2-4)	11.7	-0.01	0.001	98	91.8	26.4
60	SB	18847-01A	DF83-III BC28 (2-4)	8.4	0.01	0.006	94	97.2	3.4
60	SB	18847-05A	DF83-III BC28 (2-4)	0.0	0.00	0.033	99	100.6	2.1
60	SB	18847-25A	DF83-III BC28 (2-4)	11.1	0.09	0.001	71	101.6	19.9
60	SB	18847-11A	DF83-III BC28 (2-4)	7.6	0.05	0.002	100	106.6	6.4
60	SB	18847-16A	DF83-III BC28 (2-4)	10.3	0.05	0.005	92	108.9	3.7
60	SB	18847-18A	DF83-III BC28 (2-4)	9.5	0.02	0.002	102	109.2	7.3
60	SB	18847-10A	DF83-III BC28 (2-4)	8.5	0.00	0.001	63	119.2	20.4
60	SB	18847-08A	DF83-III BC28 (2-4)	11.1	-0.01	0.001	108	131.7	15.1
60	SB	18847-20A	DF83-III BC28 (2-4)	9.7	0.03	0.002	90	170.6	7.3
60	SB	18847-07A	DF83-III BC28 (2-4)	12.5	0.11	0.001	112	347.7	20.5
60	SB	18847-29A	DF83-III BC28 (2-4)	12.3	0.01	0.002	95	510.7	15.7
64	SB	18836-08A	DF83 PC31 (0-3)	17.4	0.03	0.001	12	18.8	16.9
64	SB	18836-10A	DF83 PC31 (0-3)	7.8	0.03	0.003	100	109.5	8.5
64	SB	18836-05A	DF83 PC31 (0-3)	8.7	0.04	0.003	94	117.1	9.0
64	SB	18836-06A	DF83 PC31 (0-3)	12.8	0.13	0.001	48	125.6	26.0
64	SB	18836-11A	DF83 PC31 (0-3)	9.1	0.08	0.001	54	134.3	19.4
65	SB	18845-01A	DF83-III BC26A (1-3)	2.2	0.00	0.003	63	70.5	6.5
65	SB	18845-02A	DF83-III BC26A (1-3)	0.0	0.00	0.012	99	99.6	2.5
65	SB	18845-03A	DF83-III BC26A (1-3)	1.2	0.01	0.001	105	116.8	16.3

[a]See Figure 2.2 for site location and sector. AP - Antarctic Peninsula, BS- Bellingshausen Sea, AS- Amundsen Sea (east and west), WH-

[b]This study, except when a reference is mentioned

Appendix Table 2.1.2. $^{40}Ar/^{39}Ar$ biotite data

Site[a]	Sector[a]	Lab. No.	Core name	Ca/K	Cl/K	Mol ^{39}Ar	$\%^{40}Ar^*$	Age (Ma)	±
5	AP	17592-09A	ELT05-22 (4-6)	0.3	0.00	0.042	39	27.0	1.2
5	AP	17592-47A	ELT05-22 (4-6)	0.0	0.01	0.063	87	27.2	0.6
5	AP	17592-50A	ELT05-22 (4-6)	0.0	0.01	0.015	49	27.6	2.5
5	AP	17592-44A	ELT05-22 (4-6)	0.2	0.01	0.646	72	49.4	0.2
5	AP	17592-46A	ELT05-22 (4-6)	0.1	0.00	0.035	90	54.7	1.1
5	AP	17592-49A	ELT05-22 (4-6)	0.0	0.02	0.051	92	57.2	0.8
5	AP	17592-48A	ELT05-22 (4-6)	0.0	0.01	0.079	94	77.0	0.5
8	AP	17594-40A	ELT 05-20 (2-4)	0.1	0.01	0.004	38	40.1	3.9
8	AP	17594-30A	ELT 05-20 (2-4)	0.4	0.01	0.077	73	51.2	0.4
8	AP	17594-39A	ELT 05-20 (2-4)	0.1	0.01	0.024	48	52.4	1.1
8	AP	17594-36A	ELT 05-20 (2-4)	0.1	0.01	0.068	73	58.9	0.5
8	AP	17594-38A	ELT 05-20 (2-4)	1.0	0.01	0.030	60	80.8	1.0
8	AP	17594-23A	ELT 05-20 (2-4)	0.8	0.10	0.001	62	362.8	26.8
8	AP	17594-14A	ELT 05-20 (2-4)	1.0	0.07	0.001	72	382.9	39.6
10	BS	17598-14A	ELT 42-09 (0-2)	-0.1	-0.06	0.001	63	64.0	28.2
10	BS	17598-06A	ELT 42-09 (0-2)	0.1	0.00	0.389	95	74.4	0.2
10	BS	17598-08A	ELT 42-09 (0-2)	0.0	0.00	0.090	87	74.7	0.5
10	BS	17598-09A	ELT 42-09 (0-2)	0.0	0.00	0.129	46	80.3	0.7
10	BS	17598-02A	ELT 42-09 (0-2)	0.1	0.00	0.055	88	97.3	0.8
10	BS	17598-01A	ELT 42-09 (0-2)	0.0	0.00	0.127	79	99.6	0.5
10	BS	17598-05A	ELT 42-09 (0-2)	0.6	0.01	0.026	54	100.0	1.7
10	BS	17598-10A	ELT 42-09 (0-2)	0.8	-0.01	0.007	34	106.8	5.9
10	BS	17598-13A	ELT 42-09 (0-2)	0.0	0.00	0.020	94	110.1	1.8
10	BS	17598-03A	ELT 42-09 (0-2)	0.0	-0.01	0.008	89	119.7	4.8
10	BS	17598-11A	ELT 42-09 (0-2)	0.0	0.00	0.054	99	120.6	0.8
10	BS	17598-04A	ELT 42-09 (0-2)	0.0	0.00	0.141	92	125.8	0.5
10	BS	17598-12A	ELT 42-09 (0-2)	0.0	0.00	0.054	94	127.8	0.8
10	BS	17598-21A	ELT 42-09 (0-2)	0.7	-0.03	0.001	14	134.0	18.2
10	BS	17598-23A	ELT 42-09 (0-2)	0.2	-0.01	0.005	47	136.7	4.7
10	BS	17598-20A	ELT 42-09 (0-2)	0.6	-0.08	0.001	15	170.2	24.7
10	BS	17598-18A	ELT 42-09 (0-2)	0.1	0.00	0.135	89	174.2	0.6
10	BS	17598-22A	ELT 42-09 (0-2)	0.5	-0.02	0.001	20	179.5	25.4
10	BS	17598-15A	ELT 42-09 (0-2)	0.6	0.13	0.001	10	479.0	45.0
11	BS	16076-09A	BC 361 Y (Surf)	0.1	0.01	0.007	85	22.8	0.9
11	BS	18577-16A	BC 361 Y (Surf)	0.1	0.00	0.020	55	70.1	1.4
11	BS	18577-18A	BC 361 Y (Surf)	1.0	-0.02	0.004	21	77.5	7.2
11	BS	18577-04A	BC 361 Y (Surf)	0.6	0.01	0.037	69	78.6	0.9
11	BS	18577-03A	BC 361 Y (Surf)	0.0	-0.01	0.013	58	81.1	2.2
11	BS	18577-01A	BC 361 Y (Surf)	0.3	0.01	0.035	88	82.4	0.9
11	BS	18577-17A	BC 361 Y (Surf)	-0.1	0.00	0.012	76	84.3	1.9
11	BS	18577-12A	BC 361 Y (Surf)	0.1	0.00	0.024	88	85.9	1.1
11	BS	18577-02A	BC 361 Y (Surf)	0.0	0.00	0.025	97	86.5	1.2
11	BS	18577-20A	BC 361 Y (Surf)	0.3	0.01	0.017	80	87.9	1.5
11	BS	18577-05A	BC 361 Y (Surf)	0.1	0.00	0.029	90	91.5	1.1
11	BS	18576-29A	BC 361 Y (Surf)	0.0	0.00	0.045	82	92.8	0.8
11	BS	18577-15A	BC 361 Y (Surf)	0.1	0.00	0.031	86	94.7	0.9
11	BS	18577-19A	BC 361 Y (Surf)	0.0	0.01	0.012	83	95.1	2.0
11	BS	16076-02A	BC 361 Y (Surf)	0.0	0.01	0.018	66	96.1	1.6
11	BS	16076-05A	BC 361 Y (Surf)	0.0	0.00	0.003	64	97.1	3.0
11	BS	16076-03A	BC 361 Y (Surf)	0.2	0.00	0.009	40	100.2	3.8
11	BS	16076-20A	BC 361 Y (Surf)	0.1	-0.01	0.002	51	105.9	4.0
11	BS	18577-13A	BC 361 Y (Surf)	0.2	0.00	0.005	83	106.2	4.2
11	BS	18577-14A	BC 361 Y (Surf)	0.0	0.00	0.032	74	106.5	1.0
11	BS	16076-06A	BC 361 Y (Surf)	0.0	0.00	0.005	74	110.0	2.0
11	BS	16076-19A	BC 361 Y (Surf)	0.0	0.00	0.022	97	114.5	0.8

11 BS	16076-04A	BC 361 Y (Surf)	0.0	0.00	0.007	73	115.5	1.8
11 BS	18576-31A	BC 361 Y (Surf)	0.0	-0.01	0.011	75	116.3	2.7
11 BS	16076-01A	BC 361 Y (Surf)	0.1	0.00	0.030	98	118.2	0.7
11 BS	16076-07A	BC 361 Y (Surf)	0.1	0.00	0.007	94	121.3	1.3
11 BS	16076-08A	BC 361 Y (Surf)	0.0	0.00	0.010	88	127.0	1.3
11 BS	16076-10A	BC 361 Y (Surf)	0.0	0.00	0.022	98	131.1	0.9
11 BS	16076-17A	BC 361 Y (Surf)	0.0	0.00	0.016	76	132.4	1.7
11 BS	18576-10A	BC 361 Y (Surf)	0.1	0.00	0.023	86	140.4	0.8
11 BS	16076-15A	BC 361 Y (Surf)	0.0	0.00	0.030	94	158.5	1.1
11 BS	16076-12A	BC 361 Y (Surf)	-0.1	-0.02	0.002	72	163.2	4.1
11 BS	16076-13A	BC 361 Y (Surf)	0.0	0.00	0.042	95	168.6	1.1
11 BS	16076-11A	BC 361 Y (Surf)	0.0	0.00	0.005	76	190.6	2.6
11 BS	16076-16A	BC 361 Y (Surf)	0.0	0.00	0.020	92	205.6	1.5
11 BS	18576-03A	BC 361 Y (Surf)	0.2	0.00	0.192	96	227.8	0.3
11 BS	16076-18A	BC 361 Y (Surf)	0.0	0.00	0.062	99	254.7	1.4
11 BS	16076-14A	BC 361 Y (Surf)	0.0	0.00	0.021	95	261.6	1.8
13 BS	16066-21A	BC364 (0-1)	0.1	-0.03	0.001	51	62.5	5.1
13 BS	16066-06A	BC364 (0-1)	0.2	-0.02	0.002	60	94.1	4.0
13 BS	16066-16A	BC364 (0-1)	0.1	0.00	0.004	60	98.2	2.7
13 BS	16066-11A	BC364 (0-1)	0.0	0.00	0.002	87	101.7	2.9
13 BS	16066-09A	BC364 (0-1)	0.5	0.01	0.003	67	105.2	2.7
13 BS	16066-15A	BC364 (0-1)	0.1	-0.01	0.002	89	105.8	2.9
13 BS	16066-20A	BC364 (0-1)	0.0	-0.01	0.001	50	108.9	13.3
13 BS	16066-19A	BC364 (0-1)	0.1	0.00	0.011	97	109.3	1.0
13 BS	16066-18A	BC364 (0-1)	0.1	0.00	0.303	99	109.9	0.6
13 BS	16066-13A	BC364 (0-1)	3.9	0.00	0.002	53	110.3	4.3
13 BS	16066-05A	BC364 (0-1)	0.1	0.00	0.082	99	110.9	0.6
13 BS	16066-14A	BC364 (0-1)	0.0	0.00	0.014	94	111.9	0.9
13 BS	16066-04A	BC364 (0-1)	0.0	0.01	0.008	98	111.9	1.1
13 BS	16066-17A	BC364 (0-1)	0.1	0.00	0.005	77	111.9	2.0
13 BS	16066-01A	BC364 (0-1)	0.2	0.00	0.001	85	113.0	6.5
13 BS	16066-22A	BC364 (0-1)	0.0	0.00	0.007	93	117.2	1.3
13 BS	16066-08A	BC364 (0-1)	0.4	0.00	0.015	88	118.2	1.1
13 BS	16066-07A	BC364 (0-1)	0.9	0.00	0.027	70	119.3	1.8
13 BS	16066-12A	BC364 (0-1)	0.1	0.01	0.002	94	119.5	3.0
13 BS	16066-10A	BC364 (0-1)	0.0	0.01	0.006	95	188.8	1.9
14 BS	18170-05A	BC369 (0-2)	0.2	-0.01	0.038	4	9.4	2.2
14 BS	18170-42A	BC369 (0-2)	0.2	0.00	0.031	3	10.0	2.5
14 BS	18170-08A	BC369 (0-2)	0.3	0.01	0.028	35	60.6	1.4
14 BS	18170-13A	BC369 (0-2)	1.1	0.00	0.041	39	88.8	1.6
14 BS	18170-26A	BC369 (0-2)	0.8	0.00	0.038	75	93.7	0.8
14 BS	18170-18A	BC369 (0-2)	0.3	0.00	0.090	84	95.0	0.5
14 BS	18170-16A	BC369 (0-2)	0.5	-0.01	0.014	68	96.1	1.9
14 BS	18170-02A	BC369 (0-2)	0.0	0.00	0.429	89	98.0	0.3
14 BS	18170-31A	BC369 (0-2)	0.0	0.00	0.080	95	98.2	0.4
14 BS	18170-30A	BC369 (0-2)	0.1	0.00	0.088	87	98.8	0.4
14 BS	18170-06A	BC369 (0-2)	0.0	0.00	0.079	89	100.3	0.5
14 BS	18170-47A	BC369 (0-2)	0.0	0.00	0.049	82	100.7	0.6
14 BS	18170-17A	BC369 (0-2)	0.2	0.00	0.072	96	100.7	0.5
14 BS	18170-33A	BC369 (0-2)	0.0	0.00	0.143	95	101.9	0.3
14 BS	18170-29A	BC369 (0-2)	0.1	-0.01	0.022	88	102.5	1.1
14 BS	18170-23A	BC369 (0-2)	0.1	0.00	0.570	97	102.7	0.3
14 BS	18170-14A	BC369 (0-2)	0.0	0.00	0.118	87	103.0	0.4
14 BS	18170-20A	BC369 (0-2)	0.0	0.00	0.097	73	103.5	0.6
14 BS	18170-37A	BC369 (0-2)	0.0	0.00	0.088	97	103.9	0.4
14 BS	18170-11A	BC369 (0-2)	0.0	0.00	0.235	87	105.1	0.4
14 BS	18170-36A	BC369 (0-2)	-0.1	0.00	0.044	96	105.7	0.6
14 BS	18170-25A	BC369 (0-2)	0.0	0.00	0.208	90	106.5	0.3
14 BS	18170-41A	BC369 (0-2)	0.0	0.00	0.058	86	107.2	0.6

14 BS	18170-48A	BC369 (0-2)	1.0	0.01	0.009	66	107.3	2.7
14 BS	18170-39A	BC369 (0-2)	-0.1	0.03	0.006	19	107.6	6.2
14 BS	18170-38A	BC369 (0-2)	-0.1	0.00	0.038	95	107.7	0.7
14 BS	18170-35A	BC369 (0-2)	-0.1	0.00	0.038	95	107.8	0.7
14 BS	18170-03A	BC369 (0-2)	0.1	0.00	0.035	92	108.3	0.8
14 BS	18170-15A	BC369 (0-2)	0.0	0.00	0.075	91	108.7	0.5
14 BS	18170-04A	BC369 (0-2)	-0.1	0.00	0.035	41	108.8	1.7
14 BS	18170-24A	BC369 (0-2)	0.0	0.00	0.037	91	110.2	0.8
14 BS	18170-19A	BC369 (0-2)	-0.1	0.00	0.018	91	110.6	1.4
14 BS	18170-07A	BC369 (0-2)	0.1	0.00	0.085	91	110.8	0.5
14 BS	18170-21A	BC369 (0-2)	0.3	0.01	0.025	91	110.9	1.0
14 BS	18170-27A	BC369 (0-2)	-0.4	0.00	0.016	97	111.2	1.4
14 BS	18170-45A	BC369 (0-2)	-0.1	0.00	0.061	95	112.4	0.5
14 BS	18170-12A	BC369 (0-2)	0.0	0.00	0.152	98	112.4	0.3
14 BS	18170-46A	BC369 (0-2)	-0.1	-0.01	0.039	85	112.6	0.8
14 BS	18170-22A	BC369 (0-2)	0.0	0.00	0.269	89	112.6	0.4
14 BS	18170-34A	BC369 (0-2)	0.0	0.00	0.050	63	112.8	0.9
14 BS	18170-32A	BC369 (0-2)	0.0	-0.01	0.039	95	113.1	0.7
14 BS	18170-09A	BC369 (0-2)	0.0	0.00	0.173	97	113.8	0.3
14 BS	18170-40A	BC369 (0-2)	0.1	0.00	0.040	72	114.9	0.9
14 BS	18170-01A	BC369 (0-2)	0.4	0.00	0.505	79	134.3	0.5
15 BS	18179-22A	BC459 (Surf)	0.1	0.01	0.033	27	21.8	1.4
15 BS	18179-47A	BC459 (Surf)	0.8	-0.01	0.027	16	45.9	3.0
15 BS	18179-08A	BC459 (Surf)	0.1	0.00	0.053	66	81.4	0.9
15 BS	18179-07A	BC459 (Surf)	-0.2	0.01	0.028	79	83.9	1.5
15 BS	18179-17A	BC459 (Surf)	0.3	-0.01	0.048	58	84.7	1.2
15 BS	18179-04A	BC459 (Surf)	0.5	0.01	0.260	61	87.8	0.4
15 BS	18179-29A	BC459 (Surf)	0.1	0.00	0.030	55	88.1	1.6
15 BS	18179-01A	BC459 (Surf)	0.6	0.00	0.041	84	88.3	1.1
15 BS	18179-23A	BC459 (Surf)	0.1	0.00	0.362	95	89.4	0.2
15 BS	18179-43A	BC459 (Surf)	0.4	0.00	0.017	86	90.2	2.2
15 BS	18179-50A	BC459 (Surf)	0.6	0.00	0.100	74	91.2	0.7
15 BS	18179-10A	BC459 (Surf)	0.0	0.00	0.524	96	91.6	0.2
15 BS	18179-18A	BC459 (Surf)	0.1	0.00	0.115	87	92.1	0.5
15 BS	18179-33A	BC459 (Surf)	0.3	0.00	0.083	88	92.3	0.6
15 BS	18179-11A	BC459 (Surf)	0.8	0.01	0.106	58	94.7	0.6
15 BS	18179-41A	BC459 (Surf)	-0.1	-0.01	0.018	88	95.7	2.1
15 BS	18179-31A	BC459 (Surf)	0.2	0.00	0.048	67	96.0	1.1
15 BS	18179-36A	BC459 (Surf)	0.3	0.00	0.039	92	96.2	1.1
15 BS	18179-52A	BC459 (Surf)	0.1	0.00	0.031	91	97.0	1.3
15 BS	18179-34A	BC459 (Surf)	0.0	0.00	0.047	85	97.5	1.0
15 BS	18179-28A	BC459 (Surf)	0.2	0.00	0.036	93	98.3	1.1
15 BS	18179-24A	BC459 (Surf)	0.0	0.00	0.181	95	98.6	0.4
15 BS	18179-03A	BC459 (Surf)	0.0	0.00	0.775	92	99.0	0.2
15 BS	18179-15A	BC459 (Surf)	0.0	0.00	0.087	96	99.2	0.5
15 BS	18179-45A	BC459 (Surf)	0.1	0.00	0.184	84	99.4	0.4
15 BS	18179-44A	BC459 (Surf)	0.0	0.00	0.075	96	99.9	0.6
15 BS	18179-09A	BC459 (Surf)	0.1	0.00	0.084	77	100.1	0.6
15 BS	18179-25A	BC459 (Surf)	0.0	0.00	0.045	94	100.8	1.0
15 BS	18179-05A	BC459 (Surf)	0.0	0.00	0.129	95	101.2	0.4
15 BS	18179-51A	BC459 (Surf)	0.0	0.00	0.076	91	101.2	0.6
15 BS	18179-48A	BC459 (Surf)	0.8	0.00	0.048	75	101.3	1.1
15 BS	18179-46A	BC459 (Surf)	0.0	0.00	0.051	93	101.4	0.8
15 BS	18179-40A	BC459 (Surf)	0.0	0.00	0.156	97	101.7	0.4
15 BS	18179-32A	BC459 (Surf)	0.0	0.00	0.078	96	101.9	0.6
15 BS	18179-30A	BC459 (Surf)	0.0	0.00	0.125	90	102.0	0.5
15 BS	18179-42A	BC459 (Surf)	0.3	0.00	0.069	94	102.1	0.7
15 BS	18179-21A	BC459 (Surf)	-0.3	0.00	0.020	74	102.8	2.1
15 BS	18179-19A	BC459 (Surf)	0.0	0.00	0.044	91	104.6	1.0
15 BS	18179-02A	BC459 (Surf)	0.0	0.00	0.076	83	105.4	0.6

15 BS	18179-12A	BC459 (Surf)	0.0	0.00	0.272	96	105.5	0.2
15 BS	18179-26A	BC459 (Surf)	0.0	0.00	0.047	94	107.0	0.9
15 BS	18179-14A	BC459 (Surf)	0.2	0.00	0.236	78	107.9	0.3
15 BS	18179-16A	BC459 (Surf)	0.1	0.00	0.223	86	108.3	0.3
15 BS	18182-03A	BC459 (Surf)	0.0	0.00	0.042	94	114.2	0.7
15 BS	18179-20A	BC459 (Surf)	0.0	0.00	0.032	87	119.3	1.4
15 BS	18179-39A	BC459 (Surf)	0.0	-0.01	0.065	97	282.3	1.2
17 AS-E	17588-01A	ELT 11-19 (0-2)	0.4	0.03	0.009	6	41.0	4.4
17 AS-E	17588-02A	ELT 11-19 (0-2)	0.2	0.00	0.024	44	48.2	1.3
17 AS-E	17588-03A	ELT 11-19 (0-2)	1.0	0.01	0.023	35	56.7	1.5
17 AS-E	17588-04A	ELT 11-19 (0-2)	0.2	0.01	0.072	81	58.4	0.4
17 AS-E	17588-05A	ELT 11-19 (0-2)	0.1	0.02	0.009	12	64.7	5.1
17 AS-E	17588-06A	ELT 11-19 (0-2)	0.4	0.03	0.006	32	71.7	5.0
17 AS-E	17588-07A	ELT 11-19 (0-2)	0.5	0.05	0.001	9	79.0	41.4
17 AS-E	17588-16A	ELT 11-19 (0-2)	0.3	0.06	0.002	8	88.1	13.1
17 AS-E	17588-17A	ELT 11-19 (0-2)	0.1	0.01	0.022	59	89.2	1.4
17 AS-E	17588-18A	ELT 11-19 (0-2)	0.0	0.00	0.267	94	99.5	0.2
17 AS-E	17588-19A	ELT 11-19 (0-2)	0.1	0.01	0.008	46	117.6	3.6
17 AS-E	17588-21A	ELT 11-19 (0-2)	0.9	0.01	0.006	41	133.8	6.6
17 AS-E	17588-32A	ELT 11-19 (0-2)	0.5	0.00	0.018	92	167.1	1.2
17 AS-E	17588-34A	ELT 11-19 (0-2)	0.1	0.00	0.163	96	176.7	0.3
17 AS-E	17588-36A	ELT 11-19 (0-2)	1.0	0.00	0.134	75	198.7	0.6
17 AS-E	17588-37A	ELT 11-19 (0-2)	0.1	0.01	0.007	61	213.0	4.5
18 AS-E	17596-01A	ELT 11-18 (2-4)	0.0	0.00	0.034	37	95.8	1.7
18 AS-E	17596-03A	ELT 11-18 (2-4)	0.0	-0.01	0.017	70	97.8	2.3
18 AS-E	17596-04A	ELT 11-18 (2-4)	0.0	0.00	0.053	77	99.6	0.9
18 AS-E	17596-05A	ELT 11-18 (2-4)	0.6	0.00	0.010	86	102.0	3.8
18 AS-E	17596-02A	ELT 11-18 (2-4)	0.1	0.00	0.017	92	456.3	3.2
19 AS-E	17590-06A	ELT11-17 (2-4)	0.5	-0.02	0.009	40	72.4	2.6
19 AS-E	17590-11A	ELT11-17 (2-4)	0.5	0.00	0.003	28	73.7	7.5
19 AS-E	17590-01A	ELT11-17 (2-4)	0.0	0.01	0.012	92	105.6	1.8
19 AS-E	17590-02A	ELT11-17 (2-4)	0.0	0.00	0.026	93	176.5	1.1
19 AS-E	17590-08A	ELT11-17 (2-4)	0.3	0.00	0.034	95	215.5	1.0
20 AS-E	16407-03A	PS58/254-2 (0-2)	0.0	0.00	0.011	72	91.7	1.0
20 AS-E	16407-05A	PS58/254-2 (0-2)	0.0	0.00	0.009	79	92.7	0.9
20 AS-E	16407-04A	PS58/254-2 (0-2)	0.0	0.00	0.007	79	93.2	1.0
20 AS-E	16407-01A	PS58/254-2 (0-2)	0.1	0.00	0.020	83	94.5	0.7
20 AS-E	16407-06A	PS58/254-2 (0-2)	0.0	0.00	0.023	95	99.5	0.6
20 AS-E	16407-02A	PS58/254-2 (0-2)	0.0	0.01	0.010	88	100.9	0.8
20 AS-E	16412-02A	PS58/254-2 (0-2)	0.0	0.03	0.002	93	301.0	3.1
25 AS-E	18168-32A	BC451 (Surf)	0.2	0.00	0.032	1	4.6	2.6
25 AS-E	18168-49A	BC451 (Surf)	-0.4	0.00	0.018	14	35.3	2.4
25 AS-E	18168-09A	BC451 (Surf)	0.1	0.00	0.012	32	75.5	4.3
25 AS-E	18177-25A	BC451 (Surf)	0.2	0.00	0.092	44	91.5	1.2
25 AS-E	18168-05A	BC451 (Surf)	0.5	0.00	0.046	76	94.9	1.1
25 AS-E	18168-14A	BC451 (Surf)	0.4	0.00	0.089	84	95.2	0.6
25 AS-E	18168-53A	BC451 (Surf)	0.8	0.00	0.022	82	97.2	1.4
25 AS-E	18177-08A	BC451 (Surf)	0.1	0.00	0.133	44	98.1	1.7
25 AS-E	18168-12A	BC451 (Surf)	0.2	0.00	0.199	94	99.8	0.3
25 AS-E	18168-55A	BC451 (Surf)	-0.2	0.00	0.038	100	101.0	0.8
25 AS-E	18168-19A	BC451 (Surf)	0.0	0.00	0.033	95	101.8	1.2
25 AS-E	18168-03A	BC451 (Surf)	1.0	0.00	0.020	81	108.3	2.1
25 AS-E	18168-21A	BC451 (Surf)	0.7	0.02	0.003	28	108.9	14.4
25 AS-E	18168-27A	BC451 (Surf)	0.2	0.00	0.033	89	112.3	1.1
25 AS-E	18168-44A	BC451 (Surf)	0.1	0.00	0.043	96	113.7	0.8
25 AS-E	18168-34A	BC451 (Surf)	0.6	0.00	0.041	85	114.3	0.9

25 AS-E	18168-45A	BC451 (Surf)	0.0	0.01	0.019	96	115.1	1.6
25 AS-E	18168-26A	BC451 (Surf)	0.2	0.00	0.025	48	115.9	1.7
25 AS-E	18168-18A	BC451 (Surf)	-0.6	0.02	0.002	40	116.7	21.2
25 AS-E	18168-52A	BC451 (Surf)	0.4	0.00	0.076	63	119.1	0.8
25 AS-E	18168-35A	BC451 (Surf)	0.2	0.00	0.140	74	125.8	0.6
25 AS-E	18168-13A	BC451 (Surf)	0.1	0.00	0.120	67	152.2	0.8
25 AS-E	18168-15A	BC451 (Surf)	0.1	0.00	0.179	91	155.1	0.4
25 AS-E	18168-16A	BC451 (Surf)	-0.4	0.01	0.004	44	155.6	10.8
25 AS-E	18168-56A	BC451 (Surf)	0.0	0.00	0.026	94	156.1	1.2
25 AS-E	18168-42A	BC451 (Surf)	0.1	0.00	0.108	91	156.5	0.5
25 AS-E	18168-08A	BC451 (Surf)	0.1	0.00	0.260	94	157.8	0.5
25 AS-E	18177-43A	BC451 (Surf)	0.2	0.00	0.018	91	159.3	2.8
25 AS-E	18168-48A	BC451 (Surf)	-0.2	0.00	0.021	52	164.8	2.1
25 AS-E	18168-10A	BC451 (Surf)	0.1	0.00	0.029	99	166.4	1.6
25 AS-E	18168-01A	BC451 (Surf)	0.2	0.00	0.081	98	170.0	0.6
25 AS-E	18168-47A	BC451 (Surf)	-0.1	0.00	0.010	71	174.1	3.0
25 AS-E	18168-51A	BC451 (Surf)	0.2	0.00	0.019	92	174.3	1.7
25 AS-E	18168-04A	BC451 (Surf)	0.0	0.00	0.062	78	178.1	1.0
25 AS-E	18168-22A	BC451 (Surf)	0.1	0.00	0.211	97	178.5	0.4
25 AS-E	18177-24A	BC451 (Surf)	0.1	0.00	0.047	72	184.3	1.5
25 AS-E	18168-17A	BC451 (Surf)	0.1	0.00	0.305	97	184.6	0.4
25 AS-E	18168-02A	BC451 (Surf)	0.6	0.00	0.010	77	191.5	4.1
25 AS-E	18168-11A	BC451 (Surf)	0.0	0.00	0.063	99	232.3	0.9
25 AS-E	18168-31A	BC451 (Surf)	-0.1	0.00	0.032	99	237.6	1.3
25 AS-E	18168-40A	BC451 (Surf)	-0.4	0.00	0.038	92	237.7	1.1
25 AS-E	18168-20A	BC451 (Surf)	1.0	0.00	0.080	94	238.4	0.8
25 AS-E	18168-07A	BC451 (Surf)	0.4	0.00	0.801	98	239.4	0.5
25 AS-E	18168-38A	BC451 (Surf)	0.0	0.00	0.190	99	240.5	0.5
25 AS-E	18168-33A	BC451 (Surf)	0.1	0.00	0.018	92	241.5	2.2
25 AS-E	18168-54A	BC451 (Surf)	0.1	-0.01	0.013	99	242.1	2.4
25 AS-E	18168-46A	BC451 (Surf)	0.3	0.00	0.029	97	242.1	1.3
25 AS-E	18168-39A	BC451 (Surf)	0.0	0.00	0.086	95	247.1	0.7
25 AS-E	18177-36A	BC451 (Surf)	0.0	0.00	0.017	96	250.7	3.0
25 AS-E	18168-28A	BC451 (Surf)	0.1	0.00	0.428	99	253.7	1.9
25 AS-E	18177-23A	BC451 (Surf)	0.9	0.00	0.003	51	375.4	15.4
26 AS-E	18175-21A	BC455 (Surf)	0.0	0.00	0.049	9	22.1	1.5
26 AS-E	18175-07A	BC455 (Surf)	0.0	0.00	0.192	20	34.3	0.8
26 AS-E	18175-05A	BC455 (Surf)	0.6	0.02	0.937	73	42.2	0.2
26 AS-E	18175-09A	BC455 (Surf)	0.5	0.01	0.085	73	53.5	0.8
26 AS-E	18175-10A	BC455 (Surf)	0.2	0.00	0.561	92	95.3	0.2
26 AS-E	18175-43A	BC455 (Surf)	0.1	0.00	0.119	93	96.3	0.4
26 AS-E	18175-50A	BC455 (Surf)	0.2	0.00	0.286	94	97.4	0.2
26 AS-E	18175-26A	BC455 (Surf)	0.1	0.00	0.062	96	97.6	0.7
26 AS-E	18175-24A	BC455 (Surf)	0.0	0.00	0.244	91	97.9	0.3
26 AS-E	18175-51A	BC455 (Surf)	0.2	0.00	0.061	60	98.7	0.9
26 AS-E	18175-12A	BC455 (Surf)	0.2	0.00	0.099	90	99.5	0.5
26 AS-E	18175-47A	BC455 (Surf)	0.0	0.00	0.073	94	99.8	0.6
26 AS-E	18175-17A	BC455 (Surf)	0.0	0.00	0.031	85	99.8	1.3
26 AS-E	18175-31A	BC455 (Surf)	0.1	0.00	0.046	97	99.8	0.9
26 AS-E	18175-03A	BC455 (Surf)	0.1	0.00	0.168	85	100.3	0.4
26 AS-E	18175-04A	BC455 (Surf)	0.2	0.00	0.032	59	100.6	1.6
26 AS-E	18175-13A	BC455 (Surf)	0.1	0.00	0.124	91	101.0	0.4
26 AS-E	18175-28A	BC455 (Surf)	0.1	0.00	0.042	92	102.0	0.9
26 AS-E	18175-23A	BC455 (Surf)	0.0	0.01	0.173	92	114.1	0.3
26 AS-E	18175-41A	BC455 (Surf)	0.7	0.00	0.055	81	115.7	0.9
26 AS-E	18175-39A	BC455 (Surf)	0.1	0.00	0.318	94	116.9	0.2
26 AS-E	18175-42A	BC455 (Surf)	0.1	0.00	0.088	91	130.5	0.6
26 AS-E	18175-32A	BC455 (Surf)	0.1	0.00	0.153	98	135.3	0.4
26 AS-E	18175-33A	BC455 (Surf)	0.0	0.00	0.041	67	136.5	1.4
26 AS-E	18175-22A	BC455 (Surf)	0.0	0.00	0.158	97	156.6	0.4

26 AS-E	18175-18A	BC455 (Surf)	0.1	0.00	0.115	86	160.6	0.5
26 AS-E	18175-52A	BC455 (Surf)	-0.1	0.00	0.032	84	161.1	1.4
26 AS-E	18175-35A	BC455 (Surf)	0.1	0.00	0.208	85	165.4	0.4
26 AS-E	18175-30A	BC455 (Surf)	0.7	0.01	0.094	89	170.9	0.6
26 AS-E	18175-02A	BC455 (Surf)	0.1	0.00	1.132	95	172.0	0.3
26 AS-E	18175-45A	BC455 (Surf)	0.5	-0.03	0.003	19	172.1	14.5
26 AS-E	18175-11A	BC455 (Surf)	0.1	0.00	0.121	93	175.8	0.6
26 AS-E	18175-27A	BC455 (Surf)	0.1	0.00	0.061	95	177.1	0.7
26 AS-E	18175-40A	BC455 (Surf)	0.0	0.01	0.078	97	194.6	0.7
26 AS-E	18175-44A	BC455 (Surf)	0.1	0.00	0.097	97	198.2	0.6
26 AS-E	18175-34A	BC455 (Surf)	0.0	0.00	0.139	91	230.1	0.6
26 AS-E	18175-16A	BC455 (Surf)	0.1	0.00	0.050	98	239.9	0.9
26 AS-E	18175-06A	BC455 (Surf)	0.1	0.00	0.170	97	240.1	0.5
26 AS-E	18175-15A	BC455 (Surf)	0.1	0.00	0.189	99	240.8	0.5
26 AS-E	18175-46A	BC455 (Surf)	-0.2	0.00	0.025	92	246.3	2.0
26 AS-E	18175-38A	BC455 (Surf)	0.1	0.00	0.095	92	250.3	0.7
26 AS-E	18175-29A	BC455 (Surf)	0.0	0.00	0.125	100	250.6	0.6
26 AS-E	18175-19A	BC455 (Surf)	0.1	0.00	0.127	99	257.0	0.6
26 AS-E	18175-36A	BC455 (Surf)	0.1	0.00	0.061	98	257.7	1.0
27 AS-E	18561-02A	BC 485 Y (0-3)	0.0	0.00	0.038	4	4.1	1.0
27 AS-E	18561-09A	BC 485 Y (0-3)	0.3	0.01	0.013	6	44.7	4.5
27 AS-E	18561-07A	BC 485 Y (0-3)	0.0	0.00	0.064	17	82.2	1.8
27 AS-E	18561-18A	BC 485 Y (0-3)	0.0	-0.01	0.012	70	87.6	1.9
27 AS-E	18559-20A	BC 485 Y (0-3)	0.1	0.00	0.046	71	93.1	1.1
27 AS-E	18559-14A	BC 485 Y (0-3)	0.0	0.00	0.018	69	94.8	2.6
27 AS-E	18561-10A	BC 485 Y (0-3)	0.1	0.00	0.018	90	98.3	1.3
27 AS-E	18561-21A	BC 485 Y (0-3)	0.2	0.00	0.101	76	98.8	0.4
27 AS-E	18561-12A	BC 485 Y (0-3)	0.0	0.00	0.020	86	100.0	1.3
27 AS-E	18559-10A	BC 485 Y (0-3)	0.6	0.00	0.141	92	105.0	0.4
27 AS-E	18559-11A	BC 485 Y (0-3)	0.2	0.00	0.093	46	116.8	1.3
27 AS-E	18561-04A	BC 485 Y (0-3)	0.0	0.01	0.154	93	118.5	0.3
27 AS-E	18559-17A	BC 485 Y (0-3)	0.1	0.00	0.010	77	124.5	4.6
27 AS-E	18561-13A	BC 485 Y (0-3)	0.0	0.00	0.054	82	127.2	0.7
27 AS-E	18561-22A	BC 485 Y (0-3)	0.2	0.00	0.155	80	138.9	0.5
27 AS-E	18559-03A	BC 485 Y (0-3)	0.1	0.00	0.160	89	148.6	0.5
27 AS-E	18561-08A	BC 485 Y (0-3)	0.0	0.00	0.019	73	165.7	1.7
27 AS-E	18561-17A	BC 485 Y (0-3)	0.0	0.00	0.031	98	175.9	1.0
27 AS-E	18561-16A	BC 485 Y (0-3)	0.0	0.00	0.016	96	183.8	1.8
27 AS-E	18561-01A	BC 485 Y (0-3)	0.7	0.00	0.075	67	196.3	1.0
27 AS-E	18559-15A	BC 485 Y (0-3)	0.1	0.01	0.013	76	204.4	3.5
27 AS-E	18561-05A	BC 485 Y (0-3)	0.0	0.00	0.045	91	223.7	1.0
27 AS-E	18561-06A	BC 485 Y (0-3)	0.0	0.00	0.083	86	226.2	0.8
27 AS-E	18561-14A	BC 485 Y (0-3)	0.4	0.00	0.147	97	232.3	0.6
27 AS-E	18561-03A	BC 485 Y (0-3)	0.0	0.00	0.024	96	244.9	1.5
27 AS-E	18561-11A	BC 485 Y (0-3)	0.0	0.01	0.032	99	249.7	1.2
29 AS-E	18162-07A	PS69/299-1 (Surf)	0.1	0.00	0.081	46	86.0	2.1
29 AS-E	18165-14B	PS69/299-1 (Surf)	0.4	-0.03	0.006	26	88.0	7.8
29 AS-E	18162-05A	PS69/299-1 (Surf)	0.5	0.01	0.031	22	90.6	5.5
29 AS-E	18162-14A	PS69/299-1 (Surf)	0.5	0.02	0.009	18	91.0	5.8
29 AS-E	18165-23A	PS69/299-1 (Surf)	0.3	0.00	0.013	71	93.7	3.8
29 AS-E	18162-15A	PS69/299-1 (Surf)	0.2	-0.02	0.009	42	93.9	4.5
29 AS-E	18165-31A	PS69/299-1 (Surf)	0.1	0.01	0.082	63	95.3	2.0
29 AS-E	18165-20A	PS69/299-1 (Surf)	0.0	0.00	0.005	63	95.5	7.5
29 AS-E	18165-42A	PS69/299-1 (Surf)	-0.1	0.00	0.024	24	96.1	2.8
29 AS-E	18165-17B	PS69/299-1 (Surf)	0.1	0.00	0.019	65	96.6	3.0
29 AS-E	18165-34A	PS69/299-1 (Surf)	0.1	0.00	0.038	61	96.8	2.3
29 AS-E	18165-14A	PS69/299-1 (Surf)	0.0	0.00	0.039	83	97.9	2.3
29 AS-E	18165-30A	PS69/299-1 (Surf)	0.5	0.00	0.025	28	97.9	3.3
29 AS-E	18165-35A	PS69/299-1 (Surf)	0.2	0.00	0.029	74	98.4	2.5

29 AS-E	18165-37A	PS69/299-1 (Surf)	-0.1	0.01	0.015	59	98.7	1.8
29 AS-E	18165-28A	PS69/299-1 (Surf)	0.1	0.01	0.036	73	98.7	2.3
29 AS-E	18162-37A	PS69/299-1 (Surf)	0.6	-0.02	0.008	84	98.8	3.9
29 AS-E	18165-29A	PS69/299-1 (Surf)	0.1	0.00	0.063	70	98.8	2.1
29 AS-E	18162-09A	PS69/299-1 (Surf)	0.2	0.00	0.038	64	99.0	4.2
29 AS-E	18165-43A	PS69/299-1 (Surf)	0.1	0.00	0.028	92	99.1	0.8
29 AS-E	18162-39A	PS69/299-1 (Surf)	0.7	0.06	0.003	42	99.1	12.9
29 AS-E	18165-15B	PS69/299-1 (Surf)	0.2	0.01	0.023	75	99.5	2.6
29 AS-E	18165-26A	PS69/299-1 (Surf)	0.1	-0.01	0.010	66	99.6	4.4
29 AS-E	18165-32A	PS69/299-1 (Surf)	0.1	0.00	0.036	84	99.6	2.3
29 AS-E	18162-38A	PS69/299-1 (Surf)	0.3	0.00	0.060	94	99.7	0.7
29 AS-E	18165-21A	PS69/299-1 (Surf)	0.1	0.00	0.040	85	100.6	2.3
29 AS-E	18162-06B	PS69/299-1 (Surf)	0.3	0.03	0.018	60	100.9	8.9
29 AS-E	18165-22A	PS69/299-1 (Surf)	0.1	0.01	0.019	68	101.8	3.1
29 AS-E	18165-40A	PS69/299-1 (Surf)	-0.2	0.00	0.016	57	102.5	1.7
29 AS-E	18165-07A	PS69/299-1 (Surf)	0.2	0.00	0.134	91	102.6	1.2
29 AS-E	18165-38A	PS69/299-1 (Surf)	0.3	0.01	0.012	50	103.4	2.4
29 AS-E	18165-13A	PS69/299-1 (Surf)	0.1	0.00	0.044	88	103.9	2.3
29 AS-E	18165-27A	PS69/299-1 (Surf)	0.1	0.00	0.062	85	104.9	2.2
29 AS-E	18165-18B	PS69/299-1 (Surf)	0.3	0.00	0.037	77	105.8	2.5
29 AS-E	18162-09B	PS69/299-1 (Surf)	0.1	0.03	0.008	61	107.1	20.2
29 AS-E	18162-34A	PS69/299-1 (Surf)	0.1	0.00	0.022	82	107.8	1.8
29 AS-E	18162-05B	PS69/299-1 (Surf)	0.1	0.00	0.024	68	108.6	6.5
29 AS-E	18165-03A	PS69/299-1 (Surf)	1.0	0.00	0.054	70	109.7	3.0
29 AS-E	18162-41A	PS69/299-1 (Surf)	0.1	0.00	0.025	40	109.7	2.1
29 AS-E	18165-04A	PS69/299-1 (Surf)	0.4	0.01	0.025	63	109.7	6.3
29 AS-E	18165-01A	PS69/299-1 (Surf)	0.2	0.01	0.047	29	110.6	3.8
29 AS-E	18162-40A	PS69/299-1 (Surf)	0.2	0.00	0.026	89	110.9	1.4
29 AS-E	18165-08A	PS69/299-1 (Surf)	0.1	0.00	0.098	89	111.2	1.6
29 AS-E	18162-08B	PS69/299-1 (Surf)	0.2	0.00	0.018	75	113.9	8.6
29 AS-E	18165-02A	PS69/299-1 (Surf)	0.3	0.01	0.031	54	118.5	5.0
29 AS-E	18165-09A	PS69/299-1 (Surf)	0.2	0.00	0.043	46	120.0	3.7
29 AS-E	18165-41A	PS69/299-1 (Surf)	0.0	0.01	0.017	31	123.2	3.0
29 AS-E	18165-44A	PS69/299-1 (Surf)	-0.2	0.00	0.020	85	124.7	1.1
29 AS-E	18162-07B	PS69/299-1 (Surf)	0.3	-0.01	0.011	54	125.4	13.9
29 AS-E	18165-11A	PS69/299-1 (Surf)	0.0	0.01	0.031	82	127.3	3.0
29 AS-E	18165-12A	PS69/299-1 (Surf)	0.1	0.00	0.072	87	128.2	2.7
29 AS-E	18165-33A	PS69/299-1 (Surf)	0.1	-0.01	0.025	90	129.0	3.1
29 AS-E	18162-23A	PS69/299-1 (Surf)	0.1	-0.02	0.016	70	133.4	2.5
29 AS-E	18165-05A	PS69/299-1 (Surf)	0.1	0.00	0.022	82	137.0	6.8
29 AS-E	18165-06A	PS69/299-1 (Surf)	0.1	0.00	0.067	92	141.5	2.3
29 AS-E	18165-24A	PS69/299-1 (Surf)	0.2	0.00	0.051	88	154.3	3.2
29 AS-E	18165-19A	PS69/299-1 (Surf)	0.0	0.01	0.013	91	181.2	4.9
34 AS-E	18173-11A	BC442 (Surf)	0.6	-0.01	0.008	11	42.4	4.8
34 AS-E	18173-05A	BC442 (Surf)	0.1	-0.01	0.012	58	76.7	2.7
34 AS-E	18173-09A	BC442 (Surf)	0.0	0.00	0.028	67	88.1	1.2
34 AS-E	18173-52A	BC442 (Surf)	0.2	0.00	0.029	82	90.5	1.1
34 AS-E	18173-17A	BC442 (Surf)	0.1	0.00	0.087	99	95.5	0.4
34 AS-E	18173-28A	BC442 (Surf)	0.0	-0.01	0.033	90	97.1	0.9
34 AS-E	18173-20A	BC442 (Surf)	0.0	0.00	0.088	71	99.3	0.5
34 AS-E	18173-24A	BC442 (Surf)	0.1	0.00	0.204	90	99.6	0.3
34 AS-E	18173-26A	BC442 (Surf)	0.1	0.00	0.055	98	99.7	0.6
34 AS-E	18173-43A	BC442 (Surf)	0.2	0.00	0.039	96	102.6	0.8
34 AS-E	18173-37A	BC442 (Surf)	0.3	-0.01	0.022	85	103.2	1.4
34 AS-E	18164-44A	BC442 (Surf)	0.2	0.00	0.088	88	108.0	#REF!
34 AS-E	18173-16A	BC442 (Surf)	0.0	0.00	0.208	97	116.1	0.3
34 AS-E	18164-21A	BC442 (Surf)	0.9	0.02	0.007	64	120.4	#REF!
34 AS-E	18173-40A	BC442 (Surf)	0.4	0.00	0.032	20	124.0	2.6
34 AS-E	18173-44A	BC442 (Surf)	0.3	0.01	0.142	53	125.8	0.7
34 AS-E	18173-50A	BC442 (Surf)	0.1	0.00	0.044	94	129.1	0.8

34 AS-E	18173-14A	BC442 (Surf)	0.4	0.00	0.262	88	130.6	0.3
34 AS-E	18164-15A	BC442 (Surf)	0.4	-0.01	0.035	87	155.8	#REF!
34 AS-E	18164-22A	BC442 (Surf)	0.2	0.02	0.014	74	159.2	#REF!
34 AS-E	18173-27A	BC442 (Surf)	0.6	0.01	0.008	72	162.9	4.1
34 AS-E	18173-35A	BC442 (Surf)	0.0	0.00	0.064	99	163.5	0.6
34 AS-E	18173-22A	BC442 (Surf)	0.5	0.00	0.029	92	164.6	1.1
34 AS-E	18164-50A	BC442 (Surf)	0.4	0.01	0.014	97	166.7	#REF!
34 AS-E	18173-02A	BC442 (Surf)	0.1	0.00	0.234	97	171.1	0.3
34 AS-E	18173-42A	BC442 (Surf)	0.2	0.00	0.041	96	172.0	1.0
34 AS-E	18173-15A	BC442 (Surf)	-0.1	0.00	0.012	71	177.6	2.9
34 AS-E	18173-51A	BC442 (Surf)	0.1	0.00	0.043	100	178.0	0.9
34 AS-E	18173-12A	BC442 (Surf)	0.0	0.00	0.479	72	181.9	0.6
34 AS-E	18173-25A	BC442 (Surf)	0.8	0.00	0.082	95	183.5	0.5
34 AS-E	18164-42A	BC442 (Surf)	0.8	-0.01	0.016	82	193.1	#REF!
34 AS-E	18173-33A	BC442 (Surf)	0.0	0.00	0.137	98	203.5	0.4
34 AS-E	18173-08A	BC442 (Surf)	0.1	0.00	0.049	78	208.3	1.0
34 AS-E	18173-29A	BC442 (Surf)	0.1	0.00	0.102	91	214.0	0.5
34 AS-E	18173-07A	BC442 (Surf)	-0.1	-0.01	0.033	94	216.5	1.1
34 AS-E	18173-41A	BC442 (Surf)	0.7	0.00	0.618	92	222.9	0.4
34 AS-E	18173-30A	BC442 (Surf)	-0.1	0.00	0.069	94	224.7	0.7
34 AS-E	18173-18A	BC442 (Surf)	0.1	0.00	0.365	99	228.5	0.3
34 AS-E	18173-45A	BC442 (Surf)	0.0	0.00	0.147	99	230.3	0.4
34 AS-E	18173-13A	BC442 (Surf)	0.0	0.00	0.181	95	239.0	0.5
34 AS-E	18173-19A	BC442 (Surf)	0.1	0.00	0.055	96	239.1	0.8
34 AS-E	18173-49A	BC442 (Surf)	0.2	0.01	0.028	95	239.3	1.4
34 AS-E	18173-36A	BC442 (Surf)	0.0	0.00	0.071	99	240.3	0.7
34 AS-E	18173-39A	BC442 (Surf)	0.4	0.01	0.232	91	244.0	0.5
34 AS-E	18173-01A	BC442 (Surf)	0.1	0.00	0.102	97	245.0	0.6
34 AS-E	18173-38A	BC442 (Surf)	-0.1	0.00	0.067	98	247.2	0.7
34 AS-E	18173-46A	BC442 (Surf)	0.1	0.00	0.115	93	249.4	0.6
34 AS-E	18173-03A	BC442 (Surf)	0.0	0.00	0.070	96	249.6	0.8
34 AS-E	18173-06A	BC442 (Surf)	0.0	0.00	0.034	90	252.3	1.2
34 AS-E	18173-47A	BC442 (Surf)	0.1	0.00	0.064	93	252.3	0.8
34 AS-E	18173-31A	BC442 (Surf)	-0.1	0.00	0.064	95	259.4	0.8
34 AS-E	18173-23A	BC442 (Surf)	0.0	0.00	0.158	99	264.0	0.5
34 AS-E	18173-32A	BC442 (Surf)	0.1	0.01	0.071	94	268.1	0.8
35 AS-E	18167-37A	BC443 (Surf)	-0.1	0.01	0.018	32	41.5	2.3
35 AS-E	18167-47A	BC443 (Surf)	0.3	0.00	0.062	81	74.2	0.7
35 AS-E	18167-38A	BC443 (Surf)	-0.5	-0.02	0.008	60	85.5	4.5
35 AS-E	18167-32A	BC443 (Surf)	-0.1	0.00	0.016	78	89.2	1.4
35 AS-E	18167-46A	BC443 (Surf)	0.7	0.00	0.093	73	90.2	0.6
35 AS-E	18167-16A	BC443 (Surf)	0.2	0.00	0.024	69	93.3	1.1
35 AS-E	18167-39A	BC443 (Surf)	0.2	0.00	0.024	82	94.6	1.6
35 AS-E	18167-42A	BC443 (Surf)	0.1	0.00	0.142	82	94.9	0.4
35 AS-E	18167-20A	BC443 (Surf)	0.1	0.00	0.236	92	95.5	0.3
35 AS-E	18167-24A	BC443 (Surf)	0.3	0.00	0.029	59	95.7	1.2
35 AS-E	18167-29A	BC443 (Surf)	0.1	0.00	0.142	89	97.4	0.4
35 AS-E	18167-13A	BC443 (Surf)	0.1	0.00	0.089	93	97.8	0.4
35 AS-E	18167-27A	BC443 (Surf)	0.4	0.00	0.057	85	98.4	0.6
35 AS-E	18167-30A	BC443 (Surf)	0.0	0.00	0.055	92	98.7	0.5
35 AS-E	18167-11A	BC443 (Surf)	0.1	0.00	0.026	85	99.0	0.9
35 AS-E	18167-35A	BC443 (Surf)	0.0	-0.01	0.037	89	99.0	0.7
35 AS-E	18167-22A	BC443 (Surf)	0.0	0.00	0.217	95	99.8	0.3
35 AS-E	18167-31A	BC443 (Surf)	0.2	0.00	0.041	98	99.8	0.6
35 AS-E	18167-06A	BC443 (Surf)	0.2	0.00	0.043	90	100.6	3.5
35 AS-E	18166-27A	BC443 (Surf)	0.0	0.01	0.027	97	101.0	1.3
35 AS-E	18167-09A	BC443 (Surf)	0.0	0.00	0.033	89	101.4	4.6
35 AS-E	18167-12A	BC443 (Surf)	0.3	0.00	0.048	30	103.5	2.1
35 AS-E	18167-08A	BC443 (Surf)	0.0	-0.01	0.059	96	109.5	2.5
35 AS-E	18166-29A	BC443 (Surf)	0.1	0.00	0.026	95	113.9	1.4

35 AS-E	18167-41A	BC443 (Surf)	-0.5	-0.01	0.006	71	126.7	6.2
35 AS-E	18167-25A	BC443 (Surf)	0.1	0.00	0.075	94	133.0	0.5
35 AS-E	18167-49A	BC443 (Surf)	-0.1	0.00	0.044	96	157.5	0.9
35 AS-E	18167-43A	BC443 (Surf)	-0.1	-0.01	0.014	89	172.5	3.1
35 AS-E	18166-07A	BC443 (Surf)	0.1	0.00	0.102	83	182.1	1.6
35 AS-E	18167-28A	BC443 (Surf)	0.2	0.00	0.180	95	211.9	0.6
35 AS-E	18167-01A	BC443 (Surf)	0.0	0.00	0.040	90	214.7	3.6
35 AS-E	18167-48A	BC443 (Surf)	0.1	0.00	0.099	97	215.4	0.7
35 AS-E	18167-02A	BC443 (Surf)	0.1	0.00	0.064	94	223.4	2.3
35 AS-E	18167-45A	BC443 (Surf)	0.0	0.00	0.029	97	224.8	1.6
35 AS-E	18167-26A	BC443 (Surf)	0.1	0.00	0.110	97	241.3	0.7
35 AS-E	18167-23A	BC443 (Surf)	0.2	0.00	0.046	95	242.2	1.1
35 AS-E	18167-03A	BC443 (Surf)	0.1	0.00	0.145	99	255.4	1.2
35 AS-E	18167-40A	BC443 (Surf)	-0.1	-0.01	0.022	92	273.3	2.0
35 AS-E	18167-33A	BC443 (Surf)	-0.1	0.00	0.022	100	327.0	1.9
38 AS-W	18573-11A	BC 420B (0-2)	-0.3	0.00	0.006	9	44.4	7.5
38 AS-W	18573-01A	BC 420B (0-2)	0.2	0.02	0.015	26	88.1	3.6
38 AS-W	18573-14A	BC 420B (0-2)	0.2	0.01	0.011	92	103.7	2.5
38 AS-W	18573-16A	BC 420B (0-2)	0.2	0.01	0.013	84	107.9	2.2
38 AS-W	18573-12A	BC 420B (0-2)	0.0	0.01	0.017	92	108.5	1.7
38 AS-W	18573-09A	BC 420B (0-2)	1.6	0.00	0.008	69	108.7	3.7
38 AS-W	18578-02A	BC 420B (0-2)	0.0	-0.01	0.017	85	121.4	1.6
38 AS-W	18573-06A	BC 420B (0-2)	1.2	0.00	0.054	75	123.9	1.0
38 AS-W	18578-12A	BC 420B (0-2)	0.1	0.00	0.008	64	147.4	3.4
38 AS-W	18573-02A	BC 420B (0-2)	0.9	0.00	0.009	75	193.8	3.8
38 AS-W	18573-18A	BC 420B (0-2)	0.3	-0.02	0.007	61	257.9	5.4
38 AS-W	18573-17A	BC 420B (0-2)	-0.1	0.00	0.011	96	287.5	3.3
38 AS-W	18573-10A	BC 420B (0-2)	0.3	0.01	0.005	66	331.8	7.3
38 AS-W	18573-15A	BC 420B (0-2)	0.1	0.00	0.019	94	344.5	2.5
38 AS-W	18573-07A	BC 420B (0-2)	0.0	0.00	0.035	98	357.9	1.8
40 AS-W	18187-07A	BC421 (surf)	0.2	0.01	0.066	18	1.1	0.8
40 AS-W	18176-16A	BC421 (surf)	0.4	0.02	0.040	5	25.2	2.5
40 AS-W	18176-05A	BC421 (surf)	0.2	0.00	0.057	57	101.9	0.9
40 AS-W	18176-12A	BC421 (surf)	0.5	0.00	0.075	67	103.6	0.7
40 AS-W	18176-08A	BC421 (surf)	0.3	0.00	0.413	75	104.2	0.3
40 AS-W	18176-03A	BC421 (surf)	0.1	0.00	0.122	94	105.9	0.4
40 AS-W	18176-15A	BC421 (surf)	0.1	0.01	0.080	94	108.0	0.6
40 AS-W	18176-22A	BC421 (surf)	0.2	0.01	0.022	91	108.1	2.0
40 AS-W	18176-23A	BC421 (surf)	0.0	0.01	0.099	98	108.4	0.5
40 AS-W	18176-13A	BC421 (surf)	-0.2	0.00	0.017	87	115.3	2.5
40 AS-W	18176-01A	BC421 (surf)	0.1	0.00	1.721	93	121.3	0.2
40 AS-W	18176-07A	BC421 (surf)	0.0	0.00	0.157	96	129.5	0.4
40 AS-W	18176-21A	BC421 (surf)	0.2	0.00	0.064	95	178.0	0.8
40 AS-W	18176-20A	BC421 (surf)	0.1	-0.01	0.024	89	198.1	1.9
40 AS-W	18176-04A	BC421 (surf)	0.0	0.00	0.173	98	227.1	0.4
40 AS-W	18176-25A	BC421 (surf)	0.1	0.00	0.066	98	231.5	0.8
40 AS-W	18176-24A	BC421 (surf)	0.0	-0.01	0.015	83	241.2	3.0
40 AS-W	18176-18A	BC421 (surf)	0.0	0.00	0.103	96	243.0	0.6
40 AS-W	18176-17A	BC421 (surf)	0.1	0.00	0.020	89	249.8	2.4
40 AS-W	18176-14A	BC421 (surf)	0.0	0.00	0.145	99	269.7	0.5
40 AS-W	18176-09A	BC421 (surf)	0.2	0.00	0.038	92	274.6	1.3
41 AS-W	18163-03A	BC412 (Surf)	0.1	0.00	0.317	62	97.3	0.7
41 AS-W	18163-14A	BC412 (Surf)	0.1	0.00	0.047	79	100.7	0.9
41 AS-W	18163-21A	BC412 (Surf)	0.1	0.01	0.038	94	101.6	0.9
41 AS-W	18163-16A	BC412 (Surf)	0.1	0.01	0.064	96	102.0	0.7
41 AS-W	18163-36A	BC412 (Surf)	0.2	0.00	0.003	63	102.5	10.5
41 AS-W	18163-13A	BC412 (Surf)	0.1	0.00	0.054	92	102.5	0.8
41 AS-W	18163-23A	BC412 (Surf)	1.1	0.01	0.011	93	103.0	3.3

41 AS-W	18163-15A	BC412 (Surf)	0.0	-0.01	0.033	98	103.2	1.2
41 AS-W	18163-30A	BC412 (Surf)	0.1	0.00	0.015	102	104.1	2.3
41 AS-W	18163-22A	BC412 (Surf)	0.2	0.00	0.026	96	106.2	1.4
41 AS-W	18163-12A	BC412 (Surf)	0.0	-0.01	0.018	84	106.3	2.2
41 AS-W	18163-26A	BC412 (Surf)	0.7	0.02	0.017	102	106.3	2.0
41 AS-W	18163-07A	BC412 (Surf)	0.0	0.00	0.054	88	107.8	2.9
41 AS-W	18163-24A	BC412 (Surf)	0.1	0.01	0.013	101	108.1	2.5
41 AS-W	18163-09A	BC412 (Surf)	0.5	0.00	0.114	83	108.1	1.4
41 AS-W	18163-19A	BC412 (Surf)	0.2	0.01	0.028	80	109.6	1.5
41 AS-W	18163-32A	BC412 (Surf)	-0.2	0.02	0.003	118	110.1	10.7
41 AS-W	18163-06A	BC412 (Surf)	0.0	0.00	0.077	83	110.3	2.1
41 AS-W	18163-10A	BC412 (Surf)	0.4	0.00	0.052	40	110.6	3.2
41 AS-W	18163-25A	BC412 (Surf)	0.0	0.01	0.009	111	111.2	3.4
41 AS-W	18163-11A	BC412 (Surf)	0.1	0.00	0.029	92	111.9	1.3
41 AS-W	18163-29A	BC412 (Surf)	0.3	0.01	0.014	106	112.1	2.4
41 AS-W	18163-01A	BC412 (Surf)	0.0	0.00	0.894	96	113.6	0.3
41 AS-W	18163-28A	BC412 (Surf)	0.0	0.02	0.026	102	113.7	1.3
41 AS-W	18163-04A	BC412 (Surf)	0.1	0.00	0.096	84	114.3	1.7
41 AS-W	18163-02A	BC412 (Surf)	0.1	0.00	0.336	67	115.6	0.7
41 AS-W	18163-08A	BC412 (Surf)	0.1	0.00	0.125	91	115.9	1.3
41 AS-W	18163-18A	BC412 (Surf)	0.9	0.02	0.018	49	116.7	2.6
41 AS-W	18163-20A	BC412 (Surf)	0.1	0.01	0.020	97	116.8	1.7
41 AS-W	18163-31A	BC412 (Surf)	0.1	0.04	0.008	114	117.1	4.5
41 AS-W	18163-17A	BC412 (Surf)	0.0	0.00	0.014	93	117.8	2.5
41 AS-W	18163-35A	BC412 (Surf)	0.0	0.01	0.006	75	120.6	5.5
41 AS-W	18163-05A	BC412 (Surf)	0.1	0.00	0.060	71	123.6	2.7
45 AS-W	18575-30A	PS 69/275-2 (0-1)	2.0	0.05	0.001	7	31.0	13.0
45 AS-W	18575-27A	PS 69/275-2 (0-1)	0.3	0.04	0.002	10	64.8	6.9
45 AS-W	18575-32A	PS 69/275-2 (0-1)	0.2	0.02	0.004	78	89.8	3.0
45 AS-W	18575-16A	PS 69/275-2 (0-1)	0.1	-0.01	0.019	56	89.8	1.0
45 AS-W	18575-25A	PS 69/275-2 (0-1)	0.1	0.02	0.004	64	92.6	3.0
45 AS-W	18575-18A	PS 69/275-2 (0-1)	0.7	0.03	0.001	37	92.7	12.4
45 AS-W	18575-31A	PS 69/275-2 (0-1)	0.3	0.03	0.004	72	93.2	3.5
45 AS-W	18575-01A	PS 69/275-2 (0-1)	0.1	0.00	0.528	81	94.6	0.1
45 AS-W	18575-26A	PS 69/275-2 (0-1)	-0.5	0.12	0.001	63	94.7	8.6
45 AS-W	18575-03A	PS 69/275-2 (0-1)	0.1	0.00	0.019	80	96.4	0.9
45 AS-W	18575-23A	PS 69/275-2 (0-1)	0.1	-0.01	0.014	76	97.3	1.1
45 AS-W	18575-10A	PS 69/275-2 (0-1)	0.0	-0.01	0.016	63	97.5	1.1
45 AS-W	18575-02A	PS 69/275-2 (0-1)	0.1	0.00	0.026	90	98.6	0.7
45 AS-W	18575-15A	PS 69/275-2 (0-1)	-0.2	-0.01	0.010	88	101.0	1.3
45 AS-W	18575-22A	PS 69/275-2 (0-1)	0.0	-0.02	0.010	90	101.2	1.4
45 AS-W	18575-05A	PS 69/275-2 (0-1)	0.0	-0.02	0.009	87	101.9	1.7
45 AS-W	18575-12A	PS 69/275-2 (0-1)	0.0	0.00	0.003	86	102.4	5.2
45 AS-W	18575-11A	PS 69/275-2 (0-1)	0.0	0.00	0.025	95	102.9	0.6
45 AS-W	18575-29A	PS 69/275-2 (0-1)	0.0	0.01	0.008	61	103.8	1.8
45 AS-W	18575-07A	PS 69/275-2 (0-1)	0.0	0.00	0.034	91	105.7	0.5
45 AS-W	18575-13A	PS 69/275-2 (0-1)	-0.3	-0.02	0.005	88	106.0	2.3
45 AS-W	16062-08A	PS 69/275-2 (0-1)	0.0	0.00	0.002	81	107.4	2.7
45 AS-W	18575-24A	PS 69/275-2 (0-1)	0.0	0.00	0.013	94	109.0	1.0
45 AS-W	18575-21A	PS 69/275-2 (0-1)	-0.5	-0.03	0.003	89	109.6	3.5
45 AS-W	18575-09A	PS 69/275-2 (0-1)	0.0	-0.01	0.016	80	111.5	1.0
45 AS-W	18575-20A	PS 69/275-2 (0-1)	0.1	0.00	0.010	80	112.0	1.5
45 AS-W	18575-34A	PS 69/275-2 (0-1)	-0.2	0.00	0.005	98	112.3	2.2
45 AS-W	18575-17A	PS 69/275-2 (0-1)	0.1	0.01	0.015	96	112.5	0.9
45 AS-W	18575-19A	PS 69/275-2 (0-1)	0.0	-0.01	0.012	75	112.6	1.2
45 AS-W	16062-06A	PS 69/275-2 (0-1)	0.0	0.00	0.004	97	117.4	1.8
45 AS-W	16062-03A	PS 69/275-2 (0-1)	0.0	0.00	0.008	98	117.6	1.2
45 AS-W	16062-04A	PS 69/275-2 (0-1)	0.0	0.00	0.013	91	118.9	1.1
45 AS-W	16062-07A	PS 69/275-2 (0-1)	0.0	0.00	0.004	91	120.6	1.8
45 AS-W	16062-01A	PS 69/275-2 (0-1)	0.0	0.00	0.017	87	126.1	1.2

45 AS-W	18575-04A	PS 69/275-2 (0-1)	0.0	0.01	0.108	98	127.0	0.2
45 AS-W	16062-05A	PS 69/275-2 (0-1)	0.0	0.02	0.004	98	132.5	1.8
45 AS-W	16062-02A	PS 69/275-2 (0-1)	0.1	0.00	0.002	95	141.6	3.1
46 AS-W	18579-22A	BC 407 (0-2)	0.0	0.02	0.006	3	4.2	4.3
46 AS-W	18579-08A	BC 407 (0-2)	0.8	-0.01	0.009	63	95.9	3.0
46 AS-W	18579-14A	BC 407 (0-2)	0.1	-0.01	0.001	26	97.4	24.2
46 AS-W	18579-07A	BC 407 (0-2)	0.5	0.01	0.004	75	98.6	5.9
46 AS-W	18579-10A	BC 407 (0-2)	-0.1	0.01	0.005	86	99.0	4.2
46 AS-W	18579-01A	BC 407 (0-2)	0.2	0.00	0.100	92	100.1	0.4
46 AS-W	18579-11A	BC 407 (0-2)	-0.3	0.02	0.002	67	101.7	14.0
46 AS-W	18579-19A	BC 407 (0-2)	-0.1	-0.06	0.002	34	106.3	11.8
46 AS-W	18579-18A	BC 407 (0-2)	0.0	0.01	0.004	63	108.1	5.4
46 AS-W	18579-21A	BC 407 (0-2)	-0.5	0.00	0.001	33	110.6	16.6
46 AS-W	18579-02A	BC 407 (0-2)	0.3	0.00	0.003	61	111.2	8.4
46 AS-W	18579-17A	BC 407 (0-2)	0.0	0.02	0.003	73	113.5	8.0
46 AS-W	18579-16A	BC 407 (0-2)	-0.6	-0.02	0.002	96	119.2	9.0
46 AS-W	18579-04A	BC 407 (0-2)	0.0	0.00	0.064	94	119.6	0.5
46 AS-W	18579-06A	BC 407 (0-2)	-0.3	-0.07	0.001	74	127.1	18.1
46 AS-W	18579-20A	BC 407 (0-2)	-0.3	-0.01	0.001	48	131.1	22.6
46 AS-W	18579-13A	BC 407 (0-2)	0.1	0.00	0.010	88	171.6	2.6
46 AS-W	18579-15A	BC 407 (0-2)	0.3	-0.03	0.002	87	268.8	13.6
47 AS-W	18567-04A	PS69/283-5 (Surf)	0.4	0.01	0.099	10	0.9	0.3
47 AS-W	18570-08A	PS69/283-5 (Surf)	0.4	0.01	0.132	51	93.8	0.9
47 AS-W	18570-36A	PS69/283-5 (Surf)	0.0	0.00	0.044	80	97.1	0.9
47 AS-W	18570-31A	PS69/283-5 (Surf)	0.4	0.01	0.632	85	99.7	0.4
47 AS-W	18570-02A	PS69/283-5 (Surf)	0.3	0.00	2.042	80	106.1	0.4
47 AS-W	18570-11A	PS69/283-5 (Surf)	0.0	0.00	0.103	94	106.3	0.5
47 AS-W	18570-20A	PS69/283-5 (Surf)	0.0	0.00	0.036	87	112.1	1.0
47 AS-W	18570-09A	PS69/283-5 (Surf)	0.1	0.01	0.405	94	128.9	0.3
47 AS-W	18570-17A	PS69/283-5 (Surf)	0.0	-0.01	0.021	34	146.7	3.7
47 AS-W	18570-24A	PS69/283-5 (Surf)	0.3	0.01	0.021	59	149.4	2.2
47 AS-W	18570-12A	PS69/283-5 (Surf)	0.1	0.00	0.067	71	162.6	1.2
47 AS-W	18570-10A	PS69/283-5 (Surf)	0.1	0.00	0.169	96	172.9	0.5
47 AS-W	18570-21A	PS69/283-5 (Surf)	0.9	0.00	0.143	86	173.1	0.8
47 AS-W	18570-04A	PS69/283-5 (Surf)	0.1	-0.01	0.017	64	181.9	2.4
47 AS-W	18570-06A	PS69/283-5 (Surf)	0.0	0.00	0.373	96	183.0	0.4
47 AS-W	18570-18A	PS69/283-5 (Surf)	0.1	0.00	0.042	75	190.3	1.5
47 AS-W	18570-15A	PS69/283-5 (Surf)	0.0	0.00	0.142	93	199.3	0.8
47 AS-W	18570-44A	PS69/283-5 (Surf)	0.0	0.00	0.058	96	211.9	1.0
47 AS-W	18570-26A	PS69/283-5 (Surf)	0.0	0.00	0.105	90	213.4	0.9
47 AS-W	18570-28A	PS69/283-5 (Surf)	0.0	0.00	0.048	91	214.6	1.2
47 AS-W	18570-38A	PS69/283-5 (Surf)	0.1	0.00	0.058	97	215.5	1.0
47 AS-W	18570-39A	PS69/283-5 (Surf)	0.2	0.00	0.041	96	219.2	1.2
47 AS-W	18570-13A	PS69/283-5 (Surf)	0.0	0.00	0.268	92	222.0	0.8
47 AS-W	18570-19A	PS69/283-5 (Surf)	0.0	0.00	0.045	96	223.3	1.2
47 AS-W	18570-40A	PS69/283-5 (Surf)	0.0	0.00	0.046	99	224.3	1.0
47 AS-W	18570-27A	PS69/283-5 (Surf)	0.1	0.01	0.023	78	226.4	2.0
47 AS-W	18570-03A	PS69/283-5 (Surf)	0.0	0.00	0.129	98	227.2	0.7
47 AS-W	18570-47A	PS69/283-5 (Surf)	0.0	0.00	0.035	95	228.2	1.4
47 AS-W	18570-22A	PS69/283-5 (Surf)	0.2	0.00	0.034	83	229.3	1.6
47 AS-W	18570-48A	PS69/283-5 (Surf)	0.0	0.00	0.058	95	230.0	1.0
47 AS-W	18570-14A	PS69/283-5 (Surf)	0.0	0.00	0.405	85	231.5	1.0
47 AS-W	18570-30A	PS69/283-5 (Surf)	0.0	0.01	0.015	79	232.9	2.7
47 AS-W	18570-46A	PS69/283-5 (Surf)	0.0	0.00	0.077	96	241.7	0.9
47 AS-W	18570-34A	PS69/283-5 (Surf)	0.3	0.00	0.010	65	245.0	4.0
47 AS-W	18570-35A	PS69/283-5 (Surf)	0.1	0.00	0.066	85	252.3	1.3
47 AS-W	18570-25A	PS69/283-5 (Surf)	0.0	0.00	0.127	68	257.6	1.9
47 AS-W	18570-33A	PS69/283-5 (Surf)	0.0	0.00	0.050	96	259.3	1.3
47 AS-W	18570-16A	PS69/283-5 (Surf)	0.3	0.00	0.071	85	266.2	1.4

47 AS-W	18570-41A	PS69/283-5 (Surf)	0.0	0.00	0.019	72	269.4	2.6
47 AS-W	18570-42A	PS69/283-5 (Surf)	0.1	0.00	0.046	97	273.7	1.3
47 AS-W	18570-05A	PS69/283-5 (Surf)	0.3	0.00	0.928	95	284.1	0.7
47 AS-W	18570-01A	PS69/283-5 (Surf)	0.6	0.00	2.346	91	284.9	0.7
47 AS-W	18570-07A	PS69/283-5 (Surf)	0.3	0.00	0.113	61	296.2	1.9
47 AS-W	18567-47A	PS69/283-5 (Surf)	0.8	0.00	0.005	52	435.3	7.5
48 AS-W	18171-15A	BC431 (Surf)	-0.1	0.00	0.038	36	98.5	1.8
48 AS-W	18171-32A	BC431 (Surf)	0.4	0.00	0.063	88	99.0	0.6
48 AS-W	18171-05A	BC431 (Surf)	0.3	0.00	0.260	89	99.6	0.3
48 AS-W	18171-03A	BC431 (Surf)	0.2	0.00	0.090	78	99.8	0.6
48 AS-W	18171-34A	BC431 (Surf)	0.6	0.00	0.640	76	99.8	0.3
48 AS-W	18171-01A	BC431 (Surf)	0.6	0.00	0.474	69	100.5	0.6
48 AS-W	18171-47A	BC431 (Surf)	0.0	0.00	0.104	98	100.7	0.3
48 AS-W	18171-19A	BC431 (Surf)	0.6	0.00	0.163	97	101.0	0.3
48 AS-W	18171-25A	BC431 (Surf)	0.3	0.00	0.225	82	101.2	0.3
48 AS-W	18171-31A	BC431 (Surf)	0.1	0.00	0.159	90	101.3	0.3
48 AS-W	18171-24A	BC431 (Surf)	0.0	0.00	0.311	93	101.7	0.2
48 AS-W	18171-27A	BC431 (Surf)	0.0	0.00	0.089	87	102.1	0.4
48 AS-W	18171-46A	BC431 (Surf)	0.4	0.00	0.244	86	102.4	0.2
48 AS-W	18171-26A	BC431 (Surf)	0.0	0.00	0.087	95	103.2	0.4
48 AS-W	18171-14A	BC431 (Surf)	0.0	0.00	0.292	90	103.4	0.3
48 AS-W	18171-06A	BC431 (Surf)	0.0	0.00	0.313	95	104.0	0.3
48 AS-W	18171-22A	BC431 (Surf)	0.2	0.01	0.707	91	104.3	0.2
48 AS-W	18171-16A	BC431 (Surf)	0.0	0.00	0.071	95	104.5	0.5
48 AS-W	18171-29A	BC431 (Surf)	0.0	0.00	0.084	95	104.8	0.4
48 AS-W	18171-08A	BC431 (Surf)	0.2	0.00	0.829	74	105.9	0.5
48 AS-W	18171-38A	BC431 (Surf)	0.2	0.00	0.365	98	106.0	0.2
48 AS-W	18171-42A	BC431 (Surf)	0.1	0.00	0.050	94	106.7	0.7
48 AS-W	18171-39A	BC431 (Surf)	0.0	0.00	0.114	95	106.8	0.3
48 AS-W	18171-36A	BC431 (Surf)	0.1	0.00	0.107	96	106.9	0.4
48 AS-W	18171-23A	BC431 (Surf)	0.1	0.00	0.355	97	107.2	0.2
48 AS-W	18171-10A	BC431 (Surf)	0.1	0.00	0.265	92	107.7	0.3
48 AS-W	18171-44A	BC431 (Surf)	0.0	0.00	0.044	95	107.9	0.7
48 AS-W	18171-21A	BC431 (Surf)	0.0	0.00	0.101	97	108.1	0.4
48 AS-W	18171-45A	BC431 (Surf)	-0.1	0.00	0.117	96	108.8	0.3
48 AS-W	18171-33A	BC431 (Surf)	0.0	0.00	0.089	97	109.3	0.4
48 AS-W	18171-07A	BC431 (Surf)	0.5	0.00	0.358	85	110.8	0.4
48 AS-W	18171-40A	BC431 (Surf)	0.4	0.01	0.127	82	110.9	0.4
48 AS-W	18171-12A	BC431 (Surf)	0.0	0.00	0.289	91	111.5	0.4
48 AS-W	18171-30A	BC431 (Surf)	0.0	0.00	1.003	98	112.2	0.2
48 AS-W	18171-04A	BC431 (Surf)	0.3	0.00	0.794	61	113.5	0.8
48 AS-W	18171-43A	BC431 (Surf)	0.1	0.00	0.188	93	114.2	0.3
48 AS-W	18171-02A	BC431 (Surf)	0.1	0.00	2.414	97	114.3	0.3
48 AS-W	18171-37A	BC431 (Surf)	0.2	0.00	0.052	89	120.6	0.7
48 AS-W	18171-11A	BC431 (Surf)	0.1	0.00	0.300	78	121.0	0.5
48 AS-W	18171-09A	BC431 (Surf)	0.1	0.00	0.343	97	121.4	0.3
48 AS-W	18171-13A	BC431 (Surf)	0.0	0.00	0.161	91	121.8	0.4
48 AS-W	18171-35A	BC431 (Surf)	0.0	0.00	0.275	91	122.9	0.3
49 AS-W	18183-23A	BC433 (Surf)	0.3	0.02	0.093	0	0.2	1.9
49 AS-W	18183-02A	BC433 (Surf)	0.2	0.01	0.542	1	0.3	0.4
49 AS-W	18183-01A	BC433 (Surf)	0.2	0.01	2.698	2	0.5	0.2
49 AS-W	18183-41A	BC433 (Surf)	0.3	0.01	0.062	1	0.9	1.5
49 AS-W	18183-45A	BC433 (Surf)	0.4	0.01	0.035	14	1.7	1.2
49 AS-W	18183-08A	BC433 (Surf)	0.3	0.01	0.094	11	2.2	0.8
49 AS-W	18183-05A	BC433 (Surf)	0.2	0.01	0.110	9	2.3	0.7
49 AS-W	18183-06A	BC433 (Surf)	0.3	0.01	0.047	5	2.3	1.7
49 AS-W	18183-03A	BC433 (Surf)	0.3	0.01	0.232	1	2.8	1.6
49 AS-W	18183-42A	BC433 (Surf)	0.2	0.01	0.087	42	2.9	0.5
49 AS-W	18183-43A	BC433 (Surf)	0.2	0.01	0.068	24	3.1	0.6

49	AS-W	18183-36A	BC433 (Surf)	0.1	0.01	0.099	17	3.8	0.5	
49	AS-W	18183-20A	BC433 (Surf)	0.1	0.01	0.024	4	4.1	2.5	
49	AS-W	18183-38A	BC433 (Surf)	7.7	0.01	0.007	4	5.7	6.6	
49	AS-W	18183-28A	BC433 (Surf)	0.5	0.01	0.013	7	5.9	3.7	
49	AS-W	18183-29A	BC433 (Surf)	0.0	0.01	0.058	60	34.8	0.9	
49	AS-W	18183-33A	BC433 (Surf)	5.2	0.01	0.015	38	60.3	3.4	
49	AS-W	18183-11A	BC433 (Surf)	0.0	0.00	0.992	85	95.8	0.4	
49	AS-W	18183-24A	BC433 (Surf)	0.7	0.01	0.021	25	96.7	3.9	
49	AS-W	18183-40A	BC433 (Surf)	1.1	0.00	0.018	66	97.1	2.4	
49	AS-W	18183-19A	BC433 (Surf)	0.0	0.00	0.031	91	98.4	1.6	
49	AS-W	18183-22A	BC433 (Surf)	0.3	0.00	0.011	68	98.9	4.4	
49	AS-W	18183-16A	BC433 (Surf)	9.4	0.01	0.014	37	101.4	4.3	
49	AS-W	18183-10A	BC433 (Surf)	0.0	0.00	0.164	96	102.5	0.5	
49	AS-W	18183-30A	BC433 (Surf)	-0.9	0.00	0.008	35	103.0	6.6	
49	AS-W	18183-37A	BC433 (Surf)	-0.1	0.00	0.020	62	103.2	2.2	
49	AS-W	18183-12A	BC433 (Surf)	0.2	0.00	0.058	61	103.5	1.2	
49	AS-W	18183-13A	BC433 (Surf)	0.8	0.00	0.030	60	104.5	1.9	
49	AS-W	18183-09A	BC433 (Surf)	0.2	0.00	0.077	79	104.6	1.0	
49	AS-W	18183-15A	BC433 (Surf)	0.0	0.00	0.291	90	107.2	0.4	
49	AS-W	18183-27A	BC433 (Surf)	0.1	0.00	0.075	89	117.2	0.8	
49	AS-W	18183-14A	BC433 (Surf)	0.5	-0.01	0.009	62	131.7	5.6	
49	AS-W	18183-26A	BC433 (Surf)	0.1	0.01	0.009	71	137.6	5.3	
49	AS-W	18183-34A	BC433 (Surf)	0.2	0.00	0.088	89	161.1	0.9	
49	AS-W	18183-25A	BC433 (Surf)	0.3	0.01	0.018	37	168.3	4.2	
49	AS-W	18183-18A	BC433 (Surf)	1.1	0.00	0.054	86	199.4	1.4	
49	AS-W	18183-17A	BC433 (Surf)	0.2	0.00	0.020	80	235.2	2.9	
49	AS-W	18183-39A	BC433 (Surf)	0.1	0.00	0.111	83	236.6	1.2	
49	AS-W	18183-44A	BC433 (Surf)	-0.3	0.00	0.013	90	267.0	3.3	
49	AS-W	18183-32A	BC433 (Surf)	-0.3	0.00	0.011	90	282.2	4.4	
49	AS-W	18183-07A	BC433 (Surf)	0.3	0.00	0.077	97	328.5	1.3	
50	AS-W	16135-16A	PC493 (0-1)	0.0		0.004	66	18.0	1.7	*same site as BC492*
50	AS-W	16135-24A	PC493 (0-1)	-0.3		0.002	63	83.5	4.4	*same site as BC492*
50	AS-W	16135-17A	PC493 (0-1)	1.0		0.001	71	94.1	6.2	*same site as BC492*
50	AS-W	16135-25A	PC493 (0-1)	0.1		0.011	83	94.7	0.7	*same site as BC492*
50	AS-W	16135-11A	PC493 (0-1)	0.0		0.013	95	95.2	0.6	*same site as BC492*
50	AS-W	16135-19A	PC493 (0-1)	0.1		0.015	97	95.6	0.5	*same site as BC492*
50	AS-W	16135-23A	PC493 (0-1)	0.0		0.005	86	95.6	1.5	*same site as BC492*
50	AS-W	16135-01A	PC493 (0-1)	0.0		0.037	98	95.7	0.3	*same site as BC492*
50	AS-W	16135-18A	PC493 (0-1)	0.2		0.054	97	95.8	0.3	*same site as BC492*
50	AS-W	16135-09A	PC493 (0-1)	0.0		0.009	93	97.5	0.8	*same site as BC492*
50	AS-W	16135-05A	PC493 (0-1)	0.1		0.006	84	98.5	1.1	*same site as BC492*
50	AS-W	16135-06A	PC493 (0-1)	0.1		0.045	96	99.0	0.3	*same site as BC492*
50	AS-W	16135-07A	PC493 (0-1)	0.0		0.013	98	99.2	0.6	*same site as BC492*
50	AS-W	16135-10A	PC493 (0-1)	0.0		0.016	93	99.2	0.5	*same site as BC492*
50	AS-W	16135-26A	PC493 (0-1)	0.0		0.017	96	99.4	0.5	*same site as BC492*
50	AS-W	16135-21A	PC493 (0-1)	0.0		0.025	97	99.9	0.4	*same site as BC492*
50	AS-W	16135-22A	PC493 (0-1)	0.2		0.002	67	106.2	4.3	*same site as BC492*
50	AS-W	16135-14A	PC493 (0-1)	0.0		0.012	96	112.3	0.7	*same site as BC492*
50	AS-W	16135-04A	PC493 (0-1)	0.2		0.002	56	125.6	3.8	*same site as BC492*
50	AS-W	16135-02A	PC493 (0-1)	0.0		0.018	98	157.7	0.6	*same site as BC492*
50	AS-W	16135-08A	PC493 (0-1)	0.0		0.046	99	172.8	0.4	*same site as BC492*
50	AS-W	16135-12A	PC493 (0-1)	0.1		0.048	91	173.8	0.5	*same site as BC492*
50	AS-W	16135-20A	PC493 (0-1)	0.0		0.021	98	193.1	0.7	*same site as BC492*
50	AS-W	16135-13A	PC493 (0-1)	0.0		0.018	100	219.5	0.7	*same site as BC492*
50	AS-W	16135-15A	PC493 (0-1)	0.1		0.051	99	223.8	0.6	*same site as BC492*
50	AS-W	16135-03A	PC493 (0-1)	0.0		0.012	97	240.8	1.1	*same site as BC492*
51	AS-W	17589-09A	ELT33-12 (2-6)	0.0	0.00	0.181	10	19.3	0.7	
51	AS-W	17589-12A	ELT33-12 (2-6)	0.0	0.02	0.010	32	23.4	2.3	
51	AS-W	17589-13A	ELT33-12 (2-6)	0.1	0.03	0.004	33	29.6	5.3	

51 AS-W	17589-14A	ELT33-12 (2-6)	0.1	0.01	0.005	36	40.5	4.5
51 AS-W	17589-04A	ELT33-12 (2-6)	0.1	0.01	0.003	14	47.1	8.2
51 AS-W	17589-07A	ELT33-12 (2-6)	0.1	0.00	0.055	25	57.3	1.5
51 AS-W	17589-08A	ELT33-12 (2-6)	0.3	0.01	0.015	18	64.9	2.6
51 AS-W	17589-21A	ELT33-12 (2-6)	0.3	0.00	0.003	50	89.4	6.9
51 AS-W	17589-15A	ELT33-12 (2-6)	0.5	-0.04	0.002	21	91.4	10.2
51 AS-W	17589-10A	ELT33-12 (2-6)	0.0	0.00	0.054	77	104.2	2.2
51 AS-W	17589-16A	ELT33-12 (2-6)	0.0	0.01	0.023	96	132.9	2.9
51 AS-W	17589-02A	ELT33-12 (2-6)	0.0	0.01	0.094	96	166.9	3.4
51 AS-W	17589-23A	ELT33-12 (2-6)	0.9	0.01	0.013	68	171.6	4.1
51 AS-W	17589-11A	ELT33-12 (2-6)	0.0	-0.01	0.009	91	197.1	4.9
51 AS-W	17589-24A	ELT33-12 (2-6)	0.3	0.01	0.006	87	199.2	5.3
51 AS-W	17589-03A	ELT33-12 (2-6)	0.0	0.00	0.007	92	203.7	6.0
51 AS-W	17589-06A	ELT33-12 (2-6)	0.1	0.00	0.006	57	211.3	6.2
51 AS-W	17589-01A	ELT33-12 (2-6)	0.1	0.01	0.233	99	888.5	17.8
55 WH	12931-18	NBP9902 PC21 (8-13)	0.1	0.00	0.621	72	158.9	1.7
55 WH	12931-19	NBP9902 PC21 (8-13)	0.1	0.00	0.353	96	174.9	1.8
55 WH	12931-12	NBP9902 PC21 (8-13)	0.0	0.01	0.418	73	180.2	1.9
55 WH	12931-06	NBP9902 PC21 (8-13)	0.1	0.00	0.848	46	130.9	1.6
55 WH	12931-17	NBP9902 PC21 (8-13)	0.2	0.00	0.641	86	135.6	1.4
58 WH	18563-03A	PS 75/133-1 (Surf)	0.5	-0.02	0.003	3	16.8	10.7
58 WH	18574-05A	PS 75/133-1 (Surf)	0.7	-0.02	0.002	14	24.4	16.6
58 WH	18563-25A	PS 75/133-1 (Surf)	0.1	0.01	0.003	23	25.8	12.7
58 WH	18563-33A	PS 75/133-1 (Surf)	0.2	-0.02	0.004	11	28.8	8.7
58 WH	16068-10A	PS 75/133-1 (Surf)	0.1	0.00	0.001	25	40.5	7.1
58 WH	18563-14A	PS 75/133-1 (Surf)	0.1	0.01	0.012	64	51.5	3.0
58 WH	18563-22A	PS 75/133-1 (Surf)	0.0	0.01	0.013	64	52.4	2.7
58 WH	18574-06A	PS 75/133-1 (Surf)	0.0	0.00	0.008	59	52.5	3.4
58 WH	18563-30A	PS 75/133-1 (Surf)	0.0	0.00	0.027	64	52.8	1.5
58 WH	16068-12A	PS 75/133-1 (Surf)	0.1	0.00	0.002	49	53.6	3.2
58 WH	18563-20A	PS 75/133-1 (Surf)	0.0	0.00	0.028	64	53.7	1.3
58 WH	18563-34A	PS 75/133-1 (Surf)	0.1	-0.01	0.015	56	53.8	2.4
58 WH	18574-04A	PS 75/133-1 (Surf)	0.7	-0.08	0.001	8	54.1	13.1
58 WH	18574-01A	PS 75/133-1 (Surf)	0.0	-0.01	0.015	62	58.9	1.3
58 WH	18563-31A	PS 75/133-1 (Surf)	0.8	0.01	0.008	53	59.2	4.5
58 WH	18563-26A	PS 75/133-1 (Surf)	0.0	0.00	0.033	62	60.1	1.3
58 WH	18563-04A	PS 75/133-1 (Surf)	0.0	-0.02	0.011	42	77.4	2.4
58 WH	18574-03A	PS 75/133-1 (Surf)	0.1	-0.01	0.017	67	84.5	1.2
58 WH	18574-11A	PS 75/133-1 (Surf)	-0.1	-0.02	0.003	86	94.2	7.9
58 WH	18574-09A	PS 75/133-1 (Surf)	-0.2	0.02	0.005	78	96.5	5.1
58 WH	18574-07A	PS 75/133-1 (Surf)	-0.1	0.00	0.031	95	99.1	1.0
58 WH	18574-12A	PS 75/133-1 (Surf)	0.1	0.00	0.045	94	100.0	0.7
58 WH	18574-13A	PS 75/133-1 (Surf)	0.1	0.00	0.008	95	101.1	3.0
58 WH	18574-14A	PS 75/133-1 (Surf)	0.5	0.00	0.007	97	101.1	3.5
58 WH	18574-10A	PS 75/133-1 (Surf)	0.0	0.00	0.043	97	101.7	0.7
58 WH	16068-08A	PS 75/133-1 (Surf)	0.0	0.02	0.003	65	102.6	2.7
58 WH	16068-14A	PS 75/133-1 (Surf)	0.1	0.07	0.001	70	104.8	6.5
58 WH	16068-06A	PS 75/133-1 (Surf)	0.2	-0.01	0.003	67	105.3	3.0
58 WH	18574-15A	PS 75/133-1 (Surf)	0.1	-0.02	0.005	79	107.6	5.0
58 WH	18574-02A	PS 75/133-1 (Surf)	-0.2	-0.03	0.003	87	112.0	5.6
58 WH	16068-07A	PS 75/133-1 (Surf)	0.0	0.00	0.009	90	112.4	1.2
58 WH	16068-04A	PS 75/133-1 (Surf)	0.1	-0.02	0.003	49	113.2	3.8
58 WH	16068-09A	PS 75/133-1 (Surf)	0.0	0.01	0.009	97	113.6	1.1
58 WH	16068-01A	PS 75/133-1 (Surf)	0.0	0.00	0.008	100	113.9	1.0
58 WH	16068-03A	PS 75/133-1 (Surf)	0.2	0.00	0.008	95	115.6	1.2
58 WH	18574-16A	PS 75/133-1 (Surf)	0.1	0.00	0.034	94	115.8	1.0
58 WH	16068-02A	PS 75/133-1 (Surf)	0.0	0.00	0.013	97	117.1	0.9
58 WH	16068-13A	PS 75/133-1 (Surf)	0.0	0.00	0.008	82	129.2	1.6
58 WH	16068-11A	PS 75/133-1 (Surf)	0.0	0.00	0.010	98	129.4	1.0

58 WH	16068-05A	PS 75/133-1 (Surf)	0.1	0.00	0.014	95	136.2	1.1
59 WH	18560-35A	PS 75/130-2 (Surf)	0.1	0.00	0.016	1	7.6	4.8
59 WH	18560-22A	PS 75/130-2 (Surf)	0.0	0.00	0.008	5	21.7	6.8
59 WH	16064-03A	PS 75/130-2 (Surf)	0.6	0.00	0.013	18	74.5	7.9
59 WH	18560-30A	PS 75/130-2 (Surf)	0.0	0.00	0.019	47	91.1	1.6
59 WH	18560-11A	PS 75/130-2 (Surf)	0.5	0.01	0.022	18	91.6	4.0
59 WH	18560-08A	PS 75/130-2 (Surf)	0.1	-0.01	0.016	79	94.3	2.8
59 WH	18560-25A	PS 75/130-2 (Surf)	1.0	-0.04	0.002	8	94.7	25.6
59 WH	18560-02A	PS 75/130-2 (Surf)	0.0	-0.01	0.013	30	95.5	4.1
59 WH	18560-13A	PS 75/130-2 (Surf)	0.0	0.00	0.017	90	96.9	2.6
59 WH	18560-12A	PS 75/130-2 (Surf)	0.0	0.00	0.028	84	97.3	1.7
59 WH	16064-01A	PS 75/130-2 (Surf)	0.0	0.00	0.030	76	97.7	1.2
59 WH	18560-01A	PS 75/130-2 (Surf)	0.1	-0.01	0.014	45	97.8	3.5
59 WH	18560-04A	PS 75/130-2 (Surf)	0.9	0.00	0.028	75	98.3	1.7
59 WH	18560-09A	PS 75/130-2 (Surf)	0.0	0.00	0.028	93	98.5	1.6
59 WH	18560-32A	PS 75/130-2 (Surf)	0.1	0.01	0.017	75	98.7	1.6
59 WH	18560-05A	PS 75/130-2 (Surf)	0.1	0.00	0.018	88	99.1	2.5
59 WH	18560-29A	PS 75/130-2 (Surf)	0.7	0.00	0.042	40	99.6	1.2
59 WH	18560-28A	PS 75/130-2 (Surf)	0.1	0.01	0.026	58	100.4	1.2
59 WH	18560-23A	PS 75/130-2 (Surf)	0.1	0.00	0.016	65	100.5	3.0
59 WH	18560-33A	PS 75/130-2 (Surf)	0.0	0.00	0.008	86	100.8	2.8
59 WH	18560-24A	PS 75/130-2 (Surf)	0.3	0.00	0.044	96	101.0	1.1
59 WH	18560-16A	PS 75/130-2 (Surf)	0.1	0.00	0.213	97	101.1	0.3
59 WH	18560-07A	PS 75/130-2 (Surf)	0.0	0.00	0.017	94	101.1	2.6
59 WH	18560-18A	PS 75/130-2 (Surf)	0.0	0.00	0.017	85	101.3	2.6
59 WH	18560-31A	PS 75/130-2 (Surf)	0.0	0.00	0.025	84	101.6	1.0
59 WH	18562-13A	PS 75/130-2 (Surf)	0.0	0.00	0.034	89	101.7	0.8
59 WH	18560-20A	PS 75/130-2 (Surf)	0.1	0.00	0.058	47	101.9	1.3
59 WH	18560-27A	PS 75/130-2 (Surf)	0.0	0.00	0.049	88	102.2	0.7
59 WH	16064-04A	PS 75/130-2 (Surf)	0.2	0.00	0.010	71	102.3	1.7
59 WH	18560-03A	PS 75/130-2 (Surf)	0.1	-0.01	0.023	47	102.6	2.4
59 WH	18560-36A	PS 75/130-2 (Surf)	0.0	0.00	0.037	85	102.6	0.8
59 WH	18560-26A	PS 75/130-2 (Surf)	0.1	0.01	0.006	76	103.8	7.3
59 WH	18560-17A	PS 75/130-2 (Surf)	0.8	-0.03	0.005	15	104.5	11.2
59 WH	18560-15A	PS 75/130-2 (Surf)	0.0	0.00	0.016	98	106.4	2.8
59 WH	18560-10A	PS 75/130-2 (Surf)	0.0	0.00	0.015	89	107.2	3.0
59 WH	16064-05A	PS 75/130-2 (Surf)	0.1	-0.01	0.004	58	108.4	2.9
59 WH	18560-21A	PS 75/130-2 (Surf)	0.3	0.00	0.076	39	112.2	1.5
59 WH	16064-02A	PS 75/130-2 (Surf)	0.0	0.00	0.012	95	117.0	1.0
59 WH	16064-07A	PS 75/130-2 (Surf)	0.0	-0.01	0.002	101	126.4	4.1
59 WH	16064-06A	PS 75/130-2 (Surf)	0.0	0.00	0.004	93	146.3	2.0

[a]See Figure 2.2 for site location and sector. AP - Antarctic Peninsula, BS- Bellingshausen Sea, AS- Amundsen Sea (east and west), WH-

Appendix Table 2.2. Compilation of onshore geochronological and isotopic data from the literature

Appendix table 2.2.1. Onshore geochronological data from the literature

Range[a]	Location	Latitude[b]	Longitude[b]	Sample Name	Rock type	Method	Mineral	Age	±	Ref[c]
Antarctic Peninsula	Duthiers Point	*-64.80*	*-62.82*	R.511.2	gabbro	U-Pb	zircon	93		1
Antarctic Peninsula	Mount Heogh	/	/	O.935.3	granodiorite	U-Pb	zircon	93		1
Antarctic Peninsula	Sterneck Island	*-64.18*	*-61.02*	R.4056.1	granite	U-Pb	zircon	93		1
Antarctic Peninsula	Creswick Gap	*-70.38*	*-67.73*	R.2784.1	granodiorite	U-Pb	zircon	141		1
Antarctic Peninsula	Creswick Gap	*-70.38*	*-67.73*	R.3204.3	granodiorite	U-Pb	zircon	140		1
Antarctic Peninsula	Burns Bluff	*-70.37*	*-67.93*	R.3216.2	tonalite	U-Pb	zircon	140		1
Antarctic Peninsula	Burns Bluff	*-70.37*	*-67.93*	R.3216.3	tonalite	U-Pb	zircon	140		1
Antarctic Peninsula	Creswick Peaks	*-70.48*	*-67.68*	R.5287.1	diorite	U-Pb	zircon	141		1
Antarctic Peninsula	Burns Bluff	*-70.37*	*-67.93*	R.6057.7	tonalite	U-Pb	zircon	141		1
Antarctic Peninsula	Burns Bluff	*-70.37*	*-67.93*	R.6063.5	granodiorite	U-Pb	zircon	141		1
Antarctic Peninsula	Burns Bluff	*-70.37*	*-67.93*	R.6057.16	tonalite	U-Pb	zircon	141		1
Antarctic Peninsula	Burns Bluff	*-70.37*	*-67.93*	R.6057.20	quartz-diorite	U-Pb	zircon	141		1
Antarctic Peninsula	Burns Bluff	*-70.37*	*-67.93*	R.6057.30	tonalite	U-Pb	zircon	141		1
Antarctic Peninsula	Goettel Escarpment	*-70.23*	*-66.92*	R.5270.1	diorite	U-Pb	zircon	182		1
Antarctic Peninsula	Goettel Escarpment	*-70.23*	*-66.92*	R.5271.4	granite	U-Pb	zircon	183		1
Antarctic Peninsula	Campbell Ridges	*-70.38*	*-67.58*	R.5280.2	granodiorite	U-Pb	zircon	203		1
Antarctic Peninsula	Campbell Ridges	*-70.38*	*-67.58*	R.5278.8	orthogneiss	U-Pb	zircon	227		1
Antarctic Peninsula	Mount Lepus	*-70.67*	*-67.17*	R.5297.3	paragneiss	U-Pb	zircon	210		1
Antarctic Peninsula	Mount Eissenger	*-70.03*	*-67.73*	R.5257.1	orthogneiss	U-Pb	zircon	227		1
Ellsworth Land	Mount Harry	*-74.23*	*-76.53*	R.8005.40	quartz-monzodiorite	U-Pb	zircon	105	1	2
Pine Island Bay	Wunneburger	-74.71	-113.18	356-1M	diorite	U-Pb	zircon	129	9	3
Pine Island Bay	Brownson island	-74.13	-103.37	363-8W	quartz-rich granite	U-Pb	zircon	54	35	3
Pine Island Bay	Suchland Island	-74.12	-102.45	366-1M	granite	U-Pb	zircon	127	1	3
Pine Island Bay	mcKinzie Island	-74.04	-101.82	368-1M	granodiorite	U-Pb	zircon	96	1	3
Pine Island Bay	Edwards island	-73.88	-103.10	372-2M	granodiorite	U-Pb	zircon			3
Pine Island Bay	Canisteo Peninsula	-73.02	-101.87	377-1M	granodiorite	U-Pb	zircon	47	69	3
Pine Island Bay	Lindsey Island	-73.62	-103.29	381-1M	pink granite	U-Pb	zircon	94	3	3
Pine Island Bay	Backers Island	-74.47	-102.39	385-1M	pink granite	U-Pb	zircon	114	1	3
Pine Island Bay	Backers Island	-74.35	-102.87	386-1M	gray granite	U-Pb	zircon	124	1	3
Kohler Range	Mt Petrus	-75.92	-128.62	225-7S	granodiorite	U-Pb	zircon	111	5	3
Kohler Range	mt Isherwood	-74.98	-113.70	400-1D	granodiorite	U-Pb	zircon	243	29	3
Kohler Range	Mt Wilbanks	-75.00	-112.88	402-1D	microgranite sheet	U-Pb	zircon	283.0	0.5	3
Kohler Range	Klimov Bluff	-74.87	-114.00	404-1W	granodiorite	U-Pb	zircon	113	6	3

Kohler Range	Mt Meusnier	-74.95	-113.32	412-1D	quartz-diorite/granodiorite	U-Pb	zircon	113	2	3
Kohler Range	Mt Meusnier	-74.95	-113.32	412-2D	granodiorite/monzogranite	U-Pb	zircon			3
Kohler Range	Mt Murphy	-75.25	-110.83	418-2D	gneissic intrusion	U-Pb	zircon			3
Kohler Range	kay Peak	-75.23	-110.97	422-1D	orthogneiss	U-Pb	zircon	374	13	3
Kohler Range	Early Bluff	-75.18	-113.97	426-2W	pink granite	U-Pb	zircon	103.4	0.3	3
Ruppert-Hobbs Coast	Peden Cliffs	-74.95	-136.52	160-1M	syenite	U-Pb	zircon	99.3	0.7	3
Ruppert-Hobbs Coast	Peden Cliffs	-74.95	-136.52	160-2M	quartz-syenite	U-Pb	zircon	98.4	0.8	3
Ruppert-Hobbs Coast	Holmes Bluff	-74.98	-133.72	162-1M	porphyritic granite	U-Pb	zircon	113	2	3
Ruppert-Hobbs Coast	Mt Goorhigian	-75.06	-133.72	163-1M	megacrystic granite	U-Pb	zircon	127	1	3
Ruppert-Hobbs Coast	Mt McCoy	-75.80	-141.00	201-1M	granodiorite	U-Pb	zircon	320	3	3
Ruppert-Hobbs Coast	Mt Steinfeld	-75.20	-135.87	203-1M	granodiorite	U-Pb	zircon	116	1	3
Ruppert-Hobbs Coast	Mt Goorhigian	-75.05	-133.80	204-1M	granite	U-Pb	zircon	118	5	3
Ruppert-Hobbs Coast	Mt Goorhigian	-75.05	-133.80	204-3M	leucocratic gneiss	U-Pb	zircon	128	2	3
Ruppert-Hobbs Coast	Mt Goorhigian	-75.05	-133.80	204-4M	foliated diorite	U-Pb	zircon			3
Ruppert-Hobbs Coast	Mount Prince	-74.97	-134.17	205-3V	dike	U-Pb	zircon	101	1	3
Ruppert-Hobbs Coast	Mount Prince	-74.97	-134.17	205-10M	granite	U-Pb	zircon	110	1	3
Ruppert-Hobbs Coast	Kinsey Ridge	-75.37	-139.15	212-3P	monzogranite	U-Pb	zircon	253	4	3
Ruppert-Hobbs Coast	Mount Peddie	-76.02	-145.00	218-1M	granite	U-Pb	zircon	83	13	3
Ruppert-Hobbs Coast	Mt vance	-75.47	-139.62	223-1M	syenite	U-Pb	zircon	102	1	3
Ruppert-Hobbs Coast	Adams Rock	-76.23	-145.73	226-1M	granite	U-Pb	zircon	87	17	3
Ruppert-Hobbs Coast	Wilkins Nunatak	-75.65	-139.95	302-1M	syenite	U-Pb	zircon	101.8	0.3	3
Ruppert-Hobbs Coast	Mt Langway	-75.48	-139.78	305-1M	syenite	U-Pb	zircon	102	1	3
Ruppert-Hobbs Coast	Mt Langway	-75.48	-139.78	305-2M	alkali granite	U-Pb	zircon	98.9	0.3	3
Ford Ranges	Chester Mtns	-76.66	-145.48		granodiorite	U-Pb	zircon	353		4
Ford Ranges	Mount Corey	-76.67	-145.13		granite	U-Pb	zircon	103		4
Antarctic Peninsula	Mt Eissenger	-70.92	-67.45	R.5391.4	ultramylonite	40Ar/39Ar	biotite	141	1	5
Antarctic Peninsula	Mount Sullivan	-69.67	-64.78	R.7170.12	mafic mylonite	40Ar/39Ar	biotite	102.8	3.3	6
Antarctic Peninsula	Beaumont Glacier	-72.56	-63.07	R.7629.1	quartz tonalite	40Ar/39Ar	biotite	116.5	1.5	7
Antarctic Peninsula	Beaumont Glacier	-72.5	-63.03	R.7630.4	quartz tonalite	40Ar/39Ar	biotite	107.3	1.6	7
Antarctic Peninsula	Welch Mountains	*-71.0*	*-63.5*	E.4021.1	granodiorite	K-Ar	biotite	124		1
Antarctic Peninsula	Giannini Peak	*-71.0*	*-62.8*	E.4065.1	granodiorite	K-Ar	biotite	105		1
Antarctic Peninsula	NW Palmer Land	/	/	R.5779.2	mafic dyke	K-Ar	biotite	84		29
Thurston Island	Mount Bramhall	*-72.25*	*-98.27*	R.3031.1	diorite	K-Ar	biotite	225.00	6	8
Thurston Island	Mount Bramhall	*-72.25*	*-98.27*	TI14	diorite	K-Ar	biotite	220.00	6	8
Thurston Island	Henderson Knob	*-72.15*	*-101.2*	R.3024.1	granite	K-Ar	biotite	146.00	4	8
Thurston Island	Hale Glacier	*-72.22*	*-100.55*	R.3025.1	granite	K-Ar	biotite	144.00	4	8
Thurston Island	Mount Bramhall	*-72.25*	*-98.27*	R.3030.1	granite	K-Ar	biotite	152.00	4	8
Thurston Island	Shelton Head	*-72.52*	*-97.31*	R.3039.4	granodiorite	K-Ar	biotite	152.00	4	8
Thurston Island	Langhofer Island	*-72.53*	*-93.03*	R.3034.2	granite	K-Ar	biotite	138.00	4	8

Thurston Island	Langhofer Island	*-72.53*	*-93.03*	R.3034.2	granite	K-Ar	biotite	137.00	4	8
Thurston Island	Belknap Nunatak	*-72.5*	*-97.6*	R.3037.3	granite	K-Ar	biotite	127.00	4	8
Thurston Island	McNamara Nunatak	*-72.6*	*-93.23*	R.3149.9	granite	K-Ar	biotite	125.00	3	8
Thurston Island	McNamara Nunatak	*-72.6*	*-93.23*	R.3033.1	granite	K-Ar	biotite	119.00	3	8
Thurston Island	Dustin Island	*-72.57*	*-94.8*	R.3017.5	gabbro	K-Ar	biotite	110.00	3	8
Thurston Island	Lepley Nunatak	*-73.12*	*-90.32*	R.3032.7	granodiorite	K-Ar	biotite	87.00	2	8
Pine Island Bay	Wright Island	-73.96	-116.87	PS69/277-1bts	granodiorite	40Ar/39Ar	biotite	98.4	0.3	9
Pine Island Bay	Wright Island	-73.96	-116.87	PS69/277-7bts	syeno-diorite	40Ar/39Ar	biotite	97.9	0.4	9
Pine Island Bay	Backer Island	-74.51	-74.51	PIB-1bt3	granite	40Ar/39Ar	biotite	147.0	0.6	9
Pine Island Bay	Backer Island	-74.51	-74.51	PIB-1bt4	granite	40Ar/39Ar	biotite	147.3	0.6	9
Pine Island Bay	Backer Island	-74.51	-74.51	PIB-1bt6	granite	40Ar/39Ar	biotite	151.9	0.4	9
Pine Island Bay	Bear Peninsula	-74.57	-111.89	BI-5bts, bt3, bt6	granite	40Ar/39Ar	biotite	109.8	1.3	9
Ford Ranges	Saunders Mountain	-77.92	-145.67	MB66	granodiorite	K-Ar	biotite	357	3	10
Ford Ranges	Saunders Mountain	-76.85	-145.73	MB83	granodiorite	K-Ar	biotite	367	3	10
Ford Ranges	Post Ridge	-76.92	-143.72	MB13	granodiorite	K-Ar	biotite	367	4	10
Ford Ranges	mt Morgan	-76.87	-143.60	MB21	granodiorite	K-Ar	biotite	154	2	10
Ford Ranges	Unnamed nunatak	-76.87	-143.67	MB27	granodiorite	K-Ar	biotite	165	2	10
Ford Ranges	Ranney Nunatak	-76.87	-143.87	MB28	granodiorite	K-Ar	biotite	376	3	10
Ford Ranges	Mt Edwards	-76.78	-144.22	MB154	granodiorite	K-Ar	biotite	373	3	10
Ford Ranges	Post Ridge	-76.95	-143.50	MB155	adamellite	K-Ar	biotite	350	3	10
Ford Ranges	Spauldings Rocks	-77.02	-143.27	MB156	granodiorite	K-Ar	biotite	341	3	10
Ford Ranges	Mount McCormick	-76.97	-144.40	MB15	granodiorite	K-Ar	biotite	355	3	10
Ford Ranges	5km NE Mt Ralph	-76.92	-144.27	MB29	granodiorite	K-Ar	biotite	350	5	10
Ford Ranges	Wells Ridge	-76.95	-144.57	MB34	granodiorite	K-Ar	biotite	321	4	10
Ford Ranges	Mt Gilmour	-76.92	-144.75	MB108	granodiorite	K-Ar	biotite	346	3	10
Ford Ranges	Mount Little	-77.00	-143.83	MB2	granodiorite	K-Ar	biotite	356	3	10
Ford Ranges	Mount Little	-76.98	-143.78	MB267	adamellite	K-Ar	biotite	361	3	10
Ford Ranges	Breeding Nunatak	-77.07	-142.43	MB159	diorite	K-Ar	biotite	143	1	10
Ford Ranges	Avers	-76.46	-145.52	1-1-90-3	granite	40Ar/39Ar	biotite	96.5	0.4	11
Ford Ranges	Birchall	-76.44	-146.47	12-24-89-1	pegmatite	40Ar/39Ar	biotite	97.9	0.2	11
Ford Ranges	Chester4	-76.65	-145.48	12-13-89-2	monzogranite	40Ar/39Ar	biotite	105.2	0.3	11
Ford Ranges	Getz1	-76.55	-145.23	1-10-90-3	metadiorite	40Ar/39Ar	biotite	98.3	0.3	11
Ford Ranges	Griffith	-76.26	-143.07	GB2	tonalite	40Ar/39Ar	biotite	98	0.1	11
Ford Ranges	Hutcheson	-76.26	-145.50	12-3-90-1	granite	40Ar/39Ar	biotite	99.4	0.3	11
Ford Ranges	Lewis3	-76.31	-145.39	11-29-90-2	granodiorite	40Ar/39Ar	biotite	355.9	1	11
Ford Ranges	Neptune1	-76.61	-145.28	12-14-89-4	tonalite	40Ar/39Ar	biotite	103.1	0.5	11
Ford Ranges	Richardson1	-76.55	-144.70	1-4-90-1	metadiorite	40Ar/39Ar	biotite	97.3	0.4	11
Edward VII Peninsula	Mt Nilsen	-78.05	-155.30	E7A135	hornblende-gneiss	K-Ar	biotite	100.00	2	12
Edward VII Peninsula	Scott Nunataks	-77.20	-154.55	E7A.58	biotite-gneiss	K-Ar	biotite	117.00	2	12

Edward VII Peninsula	Breckinridge Peak	-78.08	-155.48	E7A119	mica-shist	K-Ar	biotite	100.00	2	12
Edward VII Peninsula	Tennant Peak	-78.15	-155.73	E7A122	biotite-granite	K-Ar	biotite	100.00	2	12
Edward VII Peninsula	Mt Schlossbach	-78.07	-155.23	E7A106	leucogranite	K-Ar	biotite	101.00	2	12
Edward VII Peninsula	Washington Ridge	-78.13	-155.18	E7A114	leucogranite	K-Ar	biotite	101.00	2	12
Edward VII Peninsula	Mt Paterson	-78.03	-155.05	E7A137	leucogranite	K-Ar	biotite	102.00	2	12
Edward VII Peninsula	Mt Schideler	-77.92	-155.20	E7A144	biotite-granite	K-Ar	biotite	101.00	2	12
Edward VII Peninsula	Mt Fitzsimmons	-77.90	-155.28	E7A148	biotite-granite	K-Ar	biotite	100.00	2	12
Edward VII Peninsula	Bowman Pk	-77.47	-153.50	E7A30	leucogranite	K-Ar	biotite	98.00	2	12
Edward VII Peninsula	Mt Nilsen	-78.05	-153.35	E7A73	granodiorite	K-Ar	biotite	102.00	2	12
Edward VII Peninsula	Breckinridge Peak	-78.10	-155.45	E7A121	leucogranite	K-Ar	biotite	102.00	2	12
Edward VII Peninsula	Mt Swadener	-77.27	-153.78	E7A46	biotite-granite	K-Ar	biotite	103.00	2	12
Antarctic Peninsula	Mt Eissenger	-70.04	-67.76	R.5303.2	gabbro	40Ar/39Ar	hornblende	133	5	5
Antarctic Peninsula	Wade Point	-70.66	-67.53	R.5388.1	gabbro	40Ar/39Ar	hornblende	140	4	5
Antarctic Peninsula	Wade Point	-70.69	-67.45	R.5770.1	gabbro	40Ar/39Ar	hornblende	129	2	5
Antarctic Peninsula	Black Coast	-71.75	-62.00	R.4230.1	granodiorite	K-Ar	hornblende	108		1
Antarctic Peninsula	NW Palmer Land	/	/	R.5776.4	mafic dyke	K-Ar	hornblende	80		29
Thurston Island	Morgan Inlet	*-72.27*	*-95.90*	R.3127.10	gabbro	K-Ar	hornblende	286	8	8
Thurston Island	Mount Feury	*-71.83*	*-98.32*	R.3027.5	gabbro	K-Ar	hornblende	266	18	8
Thurston Island	Mount Feury	*-71.83*	*-98.32*	R.3138.6	gabbro	K-Ar	hornblende	326	35	8
Thurston Island	Guy Peaks	*-72.15*	*-98.88*	R.3139.3	diorite	K-Ar	hornblende	265	8	8
Thurston Island	Mount Bramhall	*-72.25*	*-98.27*	R.3031.1	diorite	K-Ar	hornblende	237	6	8
Thurston Island	Shelton Head	*-72.52*	*-97.31*	R.3039.4	granodiorite	K-Ar	hornblende	142	5	8
Thurston Island	McNamara Nunatak	*-72.60*	*-93.23*	R.3033.5	gabbro	K-Ar	hornblende	120	4	8
Thurston Island	McNamara Nunatak	*-72.60*	*-93.23*	TI16	gabbro	K-Ar	hornblende	111	4	8
Thurston Island	Harrison Nunatak	*-72.52*	*-96.03*	R.3021.2	gabbro	K-Ar	hornblende	121	6	8
Ford Ranges	Mt Edwards	-76.78	-144.22	MB154	granodiorite	K-Ar	hornblende	374	3	10
Ford Ranges	Post Ridge	-76.95	-143.50	MB155	adamellite	K-Ar	hornblende	360	3	10
Ford Ranges	Mount McCormick	-76.97	-144.40	MB15	granodiorite	K-Ar	hornblende	349	3	10
Ford Ranges	5km NE Mt Ralph	-76.92	-144.27	MB29	granodiorite	K-Ar	hornblende	360	3	10
Ford Ranges	Breeding Nunatak	-77.07	-142.43	MB159	diorite	K-Ar	hornblende	148	1	10
Ford Ranges	Mt Nilsen	-78.05	-155.30	E7A135	gneiss	K-Ar	hornblende	128	2	12
Ford Ranges	Chester	-76.66	-145.48	12-13-89-1	dike	40Ar/39Ar	hornblende	123.2		11
Ford Ranges	Getz	-76.55	-145.23	1-10-90-3	gneiss	40Ar/39Ar	hornblende	100.9	0.5	11
Ford Ranges	June	-76.28	-145.07	11-30-90-1	granodiorite	40Ar/39Ar	hornblende	356	1.6	11
Ford Ranges	Mutel	-76.52	-145.13	MUDUB	dike	40Ar/39Ar	hornblende	97.8	0.1	11
Ford Ranges	Neptune1	-76.61	-145.28	12-14-89-4	tonalite	40Ar/39Ar	hornblende	271.4		11
Ford Ranges	Richardson	-76.55	-144.70	1-4-90-1	metadiorite	40Ar/39Ar	hornblende	101	1.1	11
Thurston Island	Jones Mountains	*-72.53*	*-94.00*	R.3007.9	greisen	K-Ar	muscovite	183.00	5	8
Ford Ranges	Mount Little	-76.98	-143.78	MB270	leucogranite	K-Ar	muscovite	348.00	3	10

Ford Ranges	Mount Little	-76.97	-143.82	MB9	vein	K-Ar	muscovite	366.00	3	10
Ford Ranges	Avers	-76.46	-145.52	1-1-90-3	granite	40Ar/39Ar	muscovite	96.2	0.3	11
Ford Ranges	Chester4	-76.65	-145.48	12-13-89-2	monzogranite	40Ar/39Ar	muscovite	219.3		11
Ford Ranges	Getz2	-76.54	-145.18	1-10-90-2	leucogranite	40Ar/39Ar	muscovite	96.6	0.4	11
Ford Ranges	Lewis2	-76.31	-145.38	11-29-90-2	vein	40Ar/39Ar	muscovite	345.9	0.7	11
Ford Ranges	Lockhart1	-76.44	-145.17	1-2-90-2	leucogranite	40Ar/39Ar	muscovite	95.9	0.4	11
Edward VII Peninsula	Gould Peak	-78.13	-155.68	E7A128	pegmatite	K-Ar	muscovite	100.00	2	12
Antarctic Peninsula	Sterneck Island	-64.18	-61.01	R.4056.4	mafic dyke	K-Ar	whole rock	56		1
Antarctic Peninsula	Reclus Peninsula	-64.58	-61.70	O.576.4	mafic dyke	K-Ar	whole rock	56		1
Antarctic Peninsula	Reclus Peninsula	-64.58	-61.70	BBE0203	mafic dyke	K-Ar	whole rock	56		1
Antarctic Peninsula	Lemaire Channel	-65.04	-63.85	LC06	mafic dyke	K-Ar	whole rock	56		1
Antarctic Peninsula	Brabant Island	-64.40	-62.69	R.4063.15	intermediate dyke	K-Ar	whole rock	12		1
Antarctic Peninsula	Brabant Island	-64.26	-62.53	R.4063.17	intermediate dyke	K-Ar	whole rock	12		1
Antarctic Peninsula	Melchior Islands	-64.33	-63.00	MI04	intermediate dyke	K-Ar	whole rock	12		1
Antarctic Peninsula	Melchior Islands	-64.29	-62.98	R.4064.4	intermediate dyke	K-Ar	whole rock	12		1
Antarctic Peninsula	Melchior Islands	-64.29	-62.98	R.4064.9	intermediate dyke	K-Ar	whole rock	14		1
Antarctic Peninsula	Paradise Harbour	-64.90	-62.85	O.930.7	intermediate dyke	K-Ar	whole rock	56		1
Antarctic Peninsula	NW Palmer Land	/	/	R.5641.11	mafic dyke	K-Ar	whole rock	83		29
Antarctic Peninsula	NW Palmer Land	/	/	R.5784.1	mafic dyke	K-Ar	whole rock	72		29
Antarctic Peninsula	NW Palmer Land	/	/	R.5595.3	mafic dyke	K-Ar	whole rock	97		29
Antarctic Peninsula	NW Palmer Land	/	/	R.5629.2	mafic dyke	K-Ar	whole rock	90		29
Antarctic Peninsula	NW Palmer Land	/	/	R.5794.1	mafic dyke	K-Ar	whole rock	79		29
Antarctic Peninsula	NW Palmer Land	/	/	E.3515.2	mafic dyke	K-Ar	whole rock	84		29
Antarctic Peninsula	NW Palmer Land	/	/	R.5613.3	intermediate dyke	K-Ar	whole rock	85		29
Antarctic Peninsula	NW Palmer Land	/	/	R.5631.16	intermediate dyke	K-Ar	whole rock	76		29
Thurston Island	Parker Peak	*-72.30*	*-97.40*	R.3137.4	Volcanic rock	K-Ar	whole rock	144	3	8
Marie Byrd Land	Mount Petras	-76.38	-128.67	D1	Hawaiite	40Ar/39Ar	whole rock	36.11	0.22	13
Marie Byrd Land	Mount Waesche	*-77.17*	*-126.90*	41A	alkali basalt	K-Ar	whole rock	0	0.1	14
Marie Byrd Land	Mount Waesche	*-77.17*	*-126.90*	35A	alkali basalt	K-Ar	whole rock	0.17	0.03	14
Marie Byrd Land	Mount Waesche	*-77.17*	*-126.90*	39A	alkali basalt	K-Ar	whole rock	0.2	0.2	14
Marie Byrd Land	Mount Waesche	*-77.17*	*-126.90*	33C	alkali basalt	K-Ar	whole rock	1	0.1	14
Marie Byrd Land	Chang Peak	*-77.07*	*-126.63*	32C32A	alkali basalt	K-Ar	whole rock	1.6	0.2	14
Marie Byrd Land	Mount Sidley	*-77.03*	*-126.10*	53C	alkali basalt	K-Ar	whole rock	4.75	0.3	14
Marie Byrd Land	Mount Sidley	*-77.03*	*-126.10*	50A	alkali basalt	K-Ar	whole rock	4.75	0.28	14
Marie Byrd Land	Mount Sidley	*-77.03*	*-126.10*	52A	alkali basalt	K-Ar	whole rock	4.75	0.4	14
Marie Byrd Land	Mount Hartigan	*-76.87*	*-126.00*	43A	alkali basalt	K-Ar	whole rock	6.02	0.25	14
Marie Byrd Land	Mount Hartigan	*-76.87*	*-126.00*	45C	alkali basalt	K-Ar	whole rock	7.57	0.3	14
Marie Byrd Land	Mount Hartigan	*-76.87*	*-126.00*	46B	alkali basalt	K-Ar	whole rock	7.86	0.5	14
Marie Byrd Land	Mount Hartigan	*-76.87*	*-126.00*	48	alkali basalt	K-Ar	whole rock	8.36	0.41	14

Marie Byrd Land	Mount Hartigan	*-76.87*	*-126.00*	42B	alkali basalt	K-Ar	whole rock	8.5	0.33	14
Marie Byrd Land	Mount Cumming	*-76.67*	*-125.80*	28	alkali basalt	K-Ar	whole rock	10.4	0.5	14
Marie Byrd Land	Mount Hampton	*-76.48*	*-125.80*	20D	alkali basalt	K-Ar	whole rock	8.6	0.5	14
Marie Byrd Land	Mount Hampton	*-76.48*	*-125.80*	22B	alkali basalt	K-Ar	whole rock	10.1	0.4	14
Marie Byrd Land	Mount Hampton	*-76.48*	*-125.80*	25	alkali basalt	K-Ar	whole rock	10.7	0.4	14
Marie Byrd Land	Mount Hampton	*-76.48*	*-125.80*	22D	alkali basalt	K-Ar	whole rock	11.4	0.6	14
Marie Byrd Land	Mount Hampton	*-76.48*	*-125.80*	19C	alkali basalt	K-Ar	whole rock	11.7	0.5	14
Marie Byrd Land	Mount Hampton	*-76.48*	*-125.80*	23A	alkali basalt	K-Ar	whole rock	13.4	0.5	14
Marie Byrd Land	Mount Hampton	*-76.48*	*-125.80*	24A	alkali basalt	K-Ar	whole rock	13.7	0.5	14
Marie Byrd Land	Mount Hampton	*-76.48*	*-125.80*	23C	alkali basalt	K-Ar	whole rock	13.7	0.5	14
Marie Byrd Land	Mount Kaufman	*-75.62*	*-132.42*	AR39B	alkali basalt	K-Ar	whole rock	7.6	0.3	14
Marie Byrd Land	Mount Andrus	*-75.80*	*-132.30*	AR41A	alkali basalt	K-Ar	whole rock	11.3	0.4	14
Marie Byrd Land	Mount Andrus	*-75.80*	*-132.30*	AR60E	alkali basalt	K-Ar	whole rock	12.7	0.4	14
Marie Byrd Land	Mt Murphy	*-75.33*	*-110.73*	62	alkali basalt	K-Ar	Whole rock	0.82		15
Marie Byrd Land	Mt Steere	*-76.73*	*-117.82*	70	alkali basalt	K-Ar	Whole rock	1.6		15
Marie Byrd Land	Coleman N	*-75.32*	*-133.65*	77-35M	alkali basalt	K-Ar	Whole rock	2.4		15
Marie Byrd Land	Mt Cumming	*-76.67*	*-125.80*	26A	alkali basalt	K-Ar	Whole rock	3		15
Marie Byrd Land	Shibuya Pk	*-75.17*	*-133.58*	6C	alkali basalt	K-Ar	Whole rock	4.36		15
Marie Byrd Land	Kouperov Peak	*-75.10*	*-133.80*	77-47B	alkali basalt	K-Ar	Whole rock	8.26		15
Marie Byrd Land	Holmes Bluff	*-74.98*	*-133.72*	77-48B	alkali basalt	K-Ar	Whole rock	8.41		15
Marie Byrd Land	Mt Hampton	*-76.48*	*-125.80*	22D	alkali basalt	K-Ar	Whole rock	11.1		15
Marie Byrd Land	Mt Flint	*-75.73*	*-129.10*	9D	alkali basalt	K-Ar	Whole rock	13.7		15
Marie Byrd Land	Mt Petras	*-75.86*	*-128.64*	PT67D	alkali basalt	K-Ar	Whole rock	23.5		15
Marie Byrd Land	Mt Murphy	*-75.33*	*-110.73*	60AGabbro	gabbro	K-Ar	Whole rock	28		15
Ford Ranges	Drummond peak	-77.62	-153.97	E7A2	phyllite	K-Ar	whole rock	351	6	12
Ford Ranges	Drummond peak	-77.62	-153.97	E7A5	slate	K-Ar	whole rock	440	6	12
Ford Ranges	Drummond peak	-77.62	-153.97	E7A6	slate-metasiltstone	K-Ar	whole rock	363	6	12
Ford Ranges	Drummond peak	-77.62	-153.97	E7A10	slate	K-Ar	whole rock	383	7	12
Ford Ranges	Drummond peak	-77.62	-153.97	E7A11	slate-metasiltstone	K-Ar	whole rock	429	5	12
Ford Ranges	La Gorce peak	-77.62	-153.68	E7A13	phyllite	K-Ar	whole rock	317	4	12
Ford Ranges	La Gorce peak	-77.62	-153.68	E7A17	slate	K-Ar	whole rock	306	4	12
Ford Ranges	La Gorce peak	-77.62	-153.68	E7A19A	slate-metasiltstone	K-Ar	whole rock	317	7	12
Ford Ranges	La Gorce peak	-77.62	-153.68	E7A23	slate	K-Ar	whole rock	350	4	12
Ford Ranges	La Gorce peak	-77.62	-153.68	E7A26	slate	K-Ar	whole rock	361	7	12
Ford Ranges	La Gorce peak	-77.62	-153.68	E7A27A	slate	K-Ar	whole rock	346	4	12
Ford Ranges	Mt Josephine	-77.53	-153.10	E7A28	metasiltstone	K-Ar	whole rock	143	2	12
Ford Ranges	Clark Peak	-77.53	-154.18	E7A38	hornfels	K-Ar	whole rock	113	3	12
Ford Ranges	Mt Crabtree	-76.98	-145.05	MB44	slate	K-Ar	whole rock	351	3	16
Ford Ranges	Wells Ridge	-76.97	-144.87	MB55	slate	K-Ar	whole rock	377	3	16

Ford Ranges	Mt Crabtree	-76.98	-145.05	MB57	slate	K-Ar	whole rock	353	3	16
Ford Ranges	Mt Fonda	-77.98	-144.23	MB64	slate	K-Ar	whole rock	384	3	16
Ford Ranges	Mt treadwell	-77.03	-144.80	MB7	slate	K-Ar	whole rock	345	3	16
Ford Ranges	Mt treadwell	-77.00	-144.87	MB73	slate	K-Ar	whole rock	336	3	16
Ford Ranges	Greegor Peak	-77.88	-145.08	MB81	mudstone	K-Ar	whole rock	480	3	16
Ford Ranges	Mt Passel	-76.87	-145.07	MB89	slate	K-Ar	whole rock	423	3	16
Ford Ranges	Mt Passel	-76.88	-145.03	MB92	slate	K-Ar	whole rock	424	3	16
Ford Ranges	Mt Passel	-76.87	-145.10	MB93	slate	K-Ar	whole rock	428	3	16
Ford Ranges	Mt Passel	-76.88	-145.10	MB96	slate	K-Ar	whole rock	433	3	16
Ford Ranges	Mt Passel	-76.87	-145.10	MB99	slate	K-Ar	whole rock	451	3	16
Ford Ranges	Mt Passel	-76.88	-145.10	MB101	slate	K-Ar	whole rock	376	3	16
Ford Ranges	Mt Fulton	-76.90	-144.88	MBI03	slate	K-Ar	whole rock	368	3	16
Ford Ranges	Mt Fulton	-76.90	-144.88	MB105	slate	K-Ar	whole rock	368	3	16
Ford Ranges	Mt Palombo	-77.50	-143.13	MB201	slate	K-Ar	whole rock	419	3	16
Ford Ranges	Vivian Nunatak	-77.53	-143.58	MB205	slate	K-Ar	whole rock	380	2	16
Ford Ranges	Mt Monson	-77.47	-143.68	MB208	slate	K-Ar	whole rock	444	3	16
Ford Ranges	Mt Palombo	-77.47	-143.18	MB211	slate	K-Ar	whole rock	441	3	16
Ford Ranges	Mt Monson	-77.48	-143.62	MB217	slate	K-Ar	whole rock	418	3	16
Ford Ranges	Mt Palombo	-77.48	-143.22	MB216	slate	K-Ar	whole rock	450	3	16
Antarctic Peninsula	Burns Bluff	*-70.4*	*-67.9*	R.6057.10	gabbro	?		141		1
Antarctic Peninsula	Lemaire Island	*-64.8*	*-63.0*	O.942.5	granodiorite	field		93		1
Antarctic Peninsula	Leith Cove	*-64.9*	*-62.8*	O.996.1	granodiorite	field		93		1
Antarctic Peninsula	Leith Cove	*-64.9*	*-62.8*	O.989.1	granodiorite	field		93		1
Antarctic Peninsula	Curtiss Bay	*-64.0*	*-60.8*	CBA01	granodiorite	field		93		1
Antarctic Peninsula	Midas Island	*-64.2*	*-61.1*	R.4056.6	gabbro	field		93		1
Antarctic Peninsula	Cape Herschel Area	*-64.1*	*-61.0*	CHA01	granodiorite	field		93		1
Antarctic Peninsula	Cape Herschel Area	*-64.1*	*-61.0*	CHA08	granodiorite	field		93		1
Antarctic Peninsula	Scorpio Peaks	*-70.5*	*-67.4*	R.5736.1	granodiorite	field		70		1
Antarctic Peninsula	Pegasus Mountains	*-71.0*	*-67.2*	R.2414.3	granite	field		140		1
Antarctic Peninsula	Pegasus Mountains	*-71.0*	*-67.2*	R.2418.4	granodiorite	field		140		1
Antarctic Peninsula	Friedmann Nuns.	*-70.9*	*-65.5*	R.5902.8	granodiorite	field		100		1
Antarctic Peninsula	Cetus Hill	*-70.9*	*-66.1*	R.5796.4	granodiorite	field		120		1
Antarctic Peninsula	Perseus Crags	*-70.6*	*-66.2*	R.2556.1	granodiorite	field		125		1
Antarctic Peninsula	Butler Peaks	*-71.5*	*-67.2*	R.6314.9	granodiorite	field		140		1
Antarctic Peninsula	Butler Peaks	*-71.5*	*-67.2*	R.6316.4	granodiorite	field		140		1
Antarctic Peninsula	Mount Ward	*-71.6*	*-67.0*	R.6308.1	granodiorite	field		170		1
Antarctic Peninsula	Butler Peaks	*-71.5*	*-67.2*	R.6315.8	granite	field		170		1
Antarctic Peninsula	Renner Peak	*-70.3*	*-67.8*	R.5284.1	granodiorite	Pb-Pb	feldspar	140		1
Antarctic Peninsula	Auriga Nunataks	*-70.7*	*-66.6*	R.5504.2	granodiorite	Pb-Pb	feldspar	203		1

Antarctic Peninsula	Elton Hill	*-68.8*	*-66.6*	R.5506.3	granite gneiss	Pb-Pb	feldspar	210	1
Antarctic Peninsula	Reluctant island	*-67.8*	*-67.1*	R.6157.1	*GRG*	Pb-Pb	feldspar	200	1
Antarctic Peninsula	N of Werner Peak	*-68.7*	*-65.2*	R.5035.2	amphibolite	Pb-Pb	feldspar	220	1
Antarctic Peninsula	N of Werner Peak	*-68.7*	*-65.2*	R.5035.6	granite	Pb-Pb	feldspar	220	1
Antarctic Peninsula	Mount Lepus	*-70.7*	*-67.2*	R.2479.1	granite	Pb-Pb	feldspar	210	1
Antarctic Peninsula	Campbell Ridges	*-70.4*	*-67.6*	R.3239.4	orthogneiss	Pb-Pb	feldspar	227	1
Antarctic Peninsula	Sirius Cliffs	*-70.6*	*-66.9*	R.5294.1	orthogneiss	Pb-Pb	feldspar	227	1
Antarctic Peninsula	Auriga Nunataks	*-70.7*	*-66.6*	R.2436.2	paragneiss	Pb-Pb	feldspar	227	1
Antarctic Peninsula	Fomalhaut Nuns.	*-71.0*	*-66.7*	R.2535.6	orthogneiss	Pb-Pb	feldspar	227	1
Antarctic Peninsula	Fomalhaut Nuns.	*-71.0*	*-66.7*	R.2535.7	orthogneiss	Pb-Pb	feldspar	227	1
Antarctic Peninsula	Mount Eissenger	*-70.0*	*-67.7*	R.5257.2	orthogneiss	Pb-Pb	feldspar	227	1
Antarctic Peninsula	Terra Firma Islands	*-68.7*	*-67.5*	BR.138.6	granite	Pb-Pb	feldspar ?	85	1
Antarctic Peninsula	Terra Firma Islands	*-68.7*	*-67.5*	BR.138.13	gabbro	Pb-Pb	feldspar ?	85	1
Antarctic Peninsula	Terra Firma Islands	*-68.7*	*-67.5*	BR.138.17	diorite	Pb-Pb	feldspar ?	85	1
Antarctic Peninsula	Bourgeois Fjord	*-67.6*	*-67.0*	BR.132.15	granite	Pb-Pb	feldspar ?	96	1
Antarctic Peninsula	Orion Massif	*-70.4*	*-66.8*	R.5955.11	granodiorite	Pb-Pb	feldspar ?	70	1
Antarctic Peninsula	Mount Lepus	*-70.7*	*-67.2*	R.5501.1	granodiorite	Pb-Pb	feldspar ?	80	1
Antarctic Peninsula	Mount Lepus	*-70.7*	*-67.2*	R.5965.7	granodiorite	Pb-Pb	feldspar ?	80	1
Antarctic Peninsula	Goettel Escarpment	*-70.2*	*-66.9*	R.5267.1	granodiorite	Pb-Pb	feldspar ?	87	1
Antarctic Peninsula	Taurus Nunataks	*-70.9*	*-66.4*	R.2539.2	granodiorite	Pb-Pb	feldspar ?	88	1
Antarctic Peninsula	Goettel Escarpment	*-70.2*	*-66.9*	R.5271.1	porphyry	Pb-Pb	feldspar ?	91	1
Antarctic Peninsula	Bourgeois Fjord	*-67.7*	*-67.1*	BR.125.1	granodiorite	Pb-Pb	feldspar ?	100	1
Antarctic Peninsula	Bourgeois Fjord	*-67.7*	*-67.1*	BR.129.1	granite	Pb-Pb	feldspar ?	100	1
Antarctic Peninsula	Bristly Peaks	*-69.4*	*-66.3*	R.5552.1	granite	Pb-Pb	feldspar ?	98	1
Antarctic Peninsula	Aldebaran Rock	*-70.8*	*-66.7*	R.2402.1	granite	Pb-Pb	feldspar ?	140	1
Antarctic Peninsula	Sirius Cliffs	*-70.6*	*-66.9*	R.2568.2	granodiorite	Pb-Pb	feldspar ?	120	1
Antarctic Peninsula	Puppis Pikes	*-71.3*	*-66.4*	R.5904.7	granodiorite	Pb-Pb	feldspar ?	140	1
Antarctic Peninsula	Procyon Peaks	*-70.5*	*-66.5*	R.2585.1	granodiorite	Pb-Pb	feldspar ?	140	1
Antarctic Peninsula	Auriga Nunataks	*-70.7*	*-66.6*	R.5300.3	gabbro	Pb-Pb	feldspar ?	140	1
Antarctic Peninsula	Wade Point	*-70.7*	*-67.7*	R.5958.1	granodiorite	Pb-Pb	feldspar ?	140	1
Antarctic Peninsula	Mount Eissenger	*-70.0*	*-67.7*	R.5259.1	gabbro	Pb-Pb	feldspar ?	140	1
Antarctic Peninsula	Mount Eissenger	*-70.0*	*-67.7*	R.5260.2	gabbro	Pb-Pb	feldspar ?	150	1
Antarctic Peninsula	Mount Eissenger	*-70.0*	*-67.7*	R.5260.3	granite	Pb-Pb	feldspar ?	150	1
Antarctic Peninsula	Mount Ward	*-71.6*	*-67.0*	R.6309.2	granodiorite	Pb-Pb	feldspar ?	170	1
Antarctic Peninsula	Mount Pitman	*-70.2*	*-67.6*	R.5254.2	volcanic rock	Pb-Pb	feldspar ?	181	1
Antarctic Peninsula	Mount Pitman	*-70.2*	*-67.6*	R.5254.5	volcanic rock	Pb-Pb	feldspar ?	181	1
Antarctic Peninsula	Capella Rocks	*-70.7*	*-66.5*	R.2549.2	granodiorite	Pb-Pb	feldspar ?	203	1
Antarctic Peninsula	Campbell Ridges	*-70.4*	*-67.6*	R.5280.4	porphyry	Pb-Pb	feldspar ?	203	1
Antarctic Peninsula	Mount Nordhill	*-70.9*	*-63.5*	R.4920.5	granite	Pb-Pb	feldspar ?	220	1

Antarctic Peninsula	Target Hill	*-66.0*	*-63.0*	R.5511.1	orthogneiss	Pb-Pb	feldspar ?	392	1
Antarctic Peninsula	Faure Islands	*-68.1*	*-68.9*	BR.024.4	diorite	Rb-Sr	whole rock	48	1
Antarctic Peninsula	Anchorage Islands	*-67.6*	*-68.2*	R.008.1	granodiorite	Rb-Sr	whole rock	62	1
Antarctic Peninsula	Anchorage Islands	*-67.6*	*-68.2*	R.013.4	metagranite	Rb-Sr	whole rock	62	1
Antarctic Peninsula	Horseshoe Island	*-67.8*	*-67.2*	R.076.1	diorite	Rb-Sr	whole rock	67	1
Antarctic Peninsula	Horseshoe Island	*-67.8*	*-67.2*	R.079.1	gabbro	Rb-Sr	whole rock	67	1
Antarctic Peninsula	Horseshoe Island	*-67.8*	*-67.2*	R.080.1	granite	Rb-Sr	whole rock	67	1
Antarctic Peninsula	Petermann Island	*-65.2*	*-64.1*	R.503.2	granodiorite	Rb-Sr	whole rock	93	1
Antarctic Peninsula	Cape Fairweather	*-65.0*	*-61.0*	R.366.1	granite	Rb-Sr	whole rock	101	1
Antarctic Peninsula	Horseshoe Island	*-67.8*	*-67.2*	R.571.1	granite	Rb-Sr	whole rock	101	1
Antarctic Peninsula	Bildad Peak	*-65.8*	*-62.6*	R.312.2	granite	Rb-Sr	whole rock	163	1
Antarctic Peninsula	Mount Fritsche	*-66.0*	*-63.0*	R.326.2	granodiorite	Rb-Sr	whole rock	164	1
Antarctic Peninsula	Bildad Peak	*-65.8*	*-62.6*	R.302.1	diorite	Rb-Sr	whole rock	167	1
Antarctic Peninsula	Bildad Peak	*-65.8*	*-62.6*	R.310.1	granodiorite	Rb-Sr	whole rock	167	1
Antarctic Peninsula	Scharer Bluff	*-68.2*	*-65.3*	R.2605.1	gabbro	Rb-Sr	whole rock	175	1
Antarctic Peninsula	Scharer Bluff	*-68.2*	*-65.3*	R.2605.2	gabbro	Rb-Sr	whole rock	175	1
Antarctic Peninsula	Scharer Bluff	*-68.2*	*-65.3*	R.2606.1	gabbro	Rb-Sr	whole rock	175	1
Antarctic Peninsula	Scharer Bluff	*-68.2*	*-65.3*	R.2606.6	granite	Rb-Sr	whole rock	175	1
Antarctic Peninsula	Scharer Bluff	*-68.2*	*-65.3*	R.2607.4	metagranite	Rb-Sr	whole rock	175	1
Antarctic Peninsula	Trail Inlet	*-68.1*	*-65.4*	R.2624.1	granodiorite	Rb-Sr	whole rock	177	1
Antarctic Peninsula	Trail Inlet	*-68.1*	*-65.4*	R.2625.1	granodiorite	Rb-Sr	whole rock	177	1
Antarctic Peninsula	Roman Four	*-68.2*	*-66.9*	R.052.6	orthogneiss	Rb-Sr	whole rock	200	1
Antarctic Peninsula	Target Hill	*-66.0*	*-63.0*	R.321.3	granodiorite	Rb-Sr	whole rock	180	1
Antarctic Peninsula	Pylon Point	*-68.1*	*-65.1*	R.2612.3	granodiorite	Rb-Sr	whole rock	204	1
Antarctic Peninsula	Pylon Point	*-68.1*	*-65.1*	R.2612.5	granite	Rb-Sr	whole rock	204	1
Antarctic Peninsula	Curran Bluff	*-68.2*	*-65.0*	R.2614.1	granite	Rb-Sr	whole rock	204	1
Antarctic Peninsula	Curran Bluff	*-68.2*	*-65.0*	R.2614.3	granite	Rb-Sr	whole rock	204	1
Antarctic Peninsula	Cole Peninsula	*-66.8*	*-64.0*	R.280.4	granite	Rb-Sr	whole rock	209	1
Antarctic Peninsula	Mount Lepus	*-70.7*	*-67.2*	R.2480.1	granodiorite	Rb-Sr	whole rock	210	1
Antarctic Peninsula	Hope Bay	*-63.4*	*-57.0*	BR.072.1	sandstone	Rb-Sr	whole rock	250	1
Antarctic Peninsula	Hope Bay	*-63.4*	*-57.0*	BR.072.2	sandstone	Rb-Sr	whole rock	250	1
Antarctic Peninsula	Hope Bay	*-63.4*	*-57.0*	BR.072.3	sandstone	Rb-Sr	whole rock	250	1
Antarctic Peninsula	Adie Inlet	*-66.4*	*-62.3*	R.348.1A	gneiss	Rb-Sr	whole rock	246	1
Antarctic Peninsula	Adie Inlet	*-66.4*	*-62.3*	R.348.1B	gneiss	Rb-Sr	whole rock	246	1
Antarctic Peninsula	Adie Inlet	*-66.4*	*-62.3*	R.348.2	gneiss	Rb-Sr	whole rock	246	1
Antarctic Peninsula	Adie Inlet	*-66.4*	*-62.3*	R.349.1	gneiss	Rb-Sr	whole rock	246	1
Antarctic Peninsula	Adie Inlet	*-66.4*	*-62.3*	R.349.2	gneiss	Rb-Sr	whole rock	246	1
Antarctic Peninsula	Adie Inlet	*-66.4*	*-62.3*	R.349.3	amphibolite	Rb-Sr	whole rock	246	1
Antarctic Peninsula	Adie Inlet	*-66.4*	*-62.3*	R.346.5	amphibolite	Rb-Sr	whole rock	246	1

Antarctic Peninsula	Adie Inlet	*-66.4*	*-62.3*	R.350.1	amphibolite	Rb-Sr	whole rock	246	1
Antarctic Peninsula	Black Coast	*-71.7*	*-62.0*	E.4012.1	granodiorite	Rb-Sr	whole rock	120	1
Antarctic Peninsula	Black Coast	*-71.7*	*-62.0*	R.4278.1	gabbro	Rb-Sr	whole rock	120	1
Antarctic Peninsula	Black Coast	*-71.7*	*-62.0*	R.4280.2	gabbro	Rb-Sr	whole rock	120	1
Antarctic Peninsula	Mount Jackson	*-71.4*	*-63.4*	E.4178.1	granodiorite	Rb-Sr	whole rock	114	1
Antarctic Peninsula	Mount Jackson van Buren	*-71.3*	*-63.5*	R.4908.11	GRG	Rb-Sr	whole rock	206	1
Antarctic Peninsula	Mount Jackson van Buren	*-71.3*	*-63.5*	R.2109.2	GRG	Rb-Sr	whole rock	199	1
Antarctic Peninsula	Mount Nordhill	*-70.9*	*-63.5*	R.4552.2	orthogneiss	Rb-Sr	whole rock	220	1
Antarctic Peninsula	Mount Nordhill	*-70.9*	*-63.5*	R.4552.9	granite gneiss	Rb-Sr	whole rock	220	1
Antarctic Peninsula	Mount Nordhill	*-70.9*	*-63.5*	R.4920.12	granite	Rb-Sr	whole rock	220	1
Antarctic Peninsula	Hall Ridge	*-70.7*	*-63.2*	R.4942.4	granodiorite	Rb-Sr	whole rock	211	1
Antarctic Peninsula	Faure Islands	*-68.1*	*-68.9*	BR.024.3	diorite	Rb-Sr	whole rock	48	1
Antarctic Peninsula	Mount Pitman	*-70.2*	*-67.6*	R.5256.1	granodiorite	Rb-Sr	whole rock	60	1
Antarctic Peninsula	Moore Point	*-70.5*	*-67.9*	R.2793.1	gabbro	Rb-Sr	whole rock	140	1
Antarctic Peninsula	Mount Charity	*-69.9*	*-64.6*	R.1906.5	granodiorite	Rb-Sr	whole rock	120	1
Antarctic Peninsula	Mount Charity	*-69.9*	*-64.6*	R.1906.7	granodiorite	Rb-Sr	whole rock	120	1
Antarctic Peninsula	Mount Charity	*-69.9*	*-64.6*	R.1906.3	granite	Rb-Sr	whole rock	168	1
Antarctic Peninsula	Mount Charity	*-69.9*	*-64.6*	R.1907.4	porphyry	Rb-Sr	whole rock	168	1
Antarctic Peninsula	Mount Charity	*-69.9*	*-64.6*	R.1914.11	granite	Rb-Sr	whole rock	168	1
Antarctic Peninsula	Mount Charity	*-69.9*	*-64.6*	R.1905.1	diorite	Rb-Sr	whole rock	232	1
Antarctic Peninsula	Mount Charity	*-69.9*	*-64.6*	R.1905.4	granite	Rb-Sr	whole rock	232	1
Antarctic Peninsula	Mount Charity	*-69.9*	*-64.6*	R.1905.5	granite	Rb-Sr	whole rock	232	1
Antarctic Peninsula	Mount Charity	*-69.9*	*-64.6*	R.1907.2	granite	Rb-Sr	whole rock	232	1
Antarctic Peninsula	Leppard Glacier	*-66.0*	*-62.5*	R.3434.6	granite gneiss	Rb-Sr	whole rock	392	1
Antarctic Peninsula	Marsh Spur	*-65.9*	*-62.6*	R.3632.1	granite	Rb-Sr	whole rock	325	1
Antarctic Peninsula	Marsh Spur	*-65.9*	*-62.6*	R.3632.2	granite	Rb-Sr	whole rock	325	1
Antarctic Peninsula	Marsh Spur	*-65.9*	*-62.6*	R.3632.4	granite	Rb-Sr	whole rock	325	1
Antarctic Peninsula	Mount Lagado	*-66.0*	*-63.3*	R.3899.18	granite	Rb-Sr	whole rock	325	1
Antarctic Peninsula	Mount Lagado	*-66.0*	*-63.3*	R.3900.3	granite	Rb-Sr	whole rock	325	1
Antarctic Peninsula	Leppard Glacier	*-66.0*	*-62.5*	R.3431.1	granite gneiss	Rb-Sr	whole rock	392	1
Antarctic Peninsula	Leppard Glacier	*-66.0*	*-62.5*	R.3431.5	granite gneiss	Rb-Sr	whole rock	392	1
Antarctic Peninsula	Leppard Glacier	*-66.0*	*-62.5*	R.3431.17	amphibolite	Rb-Sr	whole rock	392	1
Antarctic Peninsula	Leppard Glacier	*-66.0*	*-62.5*	R.3434.1	granite gneiss	Rb-Sr	whole rock	392	1
Antarctic Peninsula	Leppard Glacier	*-66.0*	*-62.5*	R.3434.2	granite gneiss	Rb-Sr	whole rock	392	1
Antarctic Peninsula	Leppard Glacier	*-66.0*	*-62.5*	R.3434.7	granite gneiss	Rb-Sr	whole rock	392	1
Antarctic Peninsula	Leppard Glacier	*-66.0*	*-62.5*	R.4016.5	amphibolite	Rb-Sr	whole rock	392	1
Antarctic Peninsula	Solem Ridge	*-71.2*	*-63.3*	R.4293.2	paragneiss	Rb-Sr	whole rock	220	1
Antarctic Peninsula	Mount Nordhill	*-70.9*	*-63.5*	R.4294.1	paragneiss	Rb-Sr	whole rock	220	1
Antarctic Peninsula	Mount Nordhill	*-70.9*	*-63.5*	R.4920.8	paragneiss	Rb-Sr	whole rock	220	1

Antarctic Peninsula	Target Hill	*-66.0*	*-63.0*	R.3415.14	pegmatite	Rb-Sr	whole rock	321	1
Alexander Island	Arenite Ridge	*-69.7*	*-69.5*	KG.1969.1	sedimentary	Rb-Sr	whole rock	150	17
Alexander Island	Central Douglas Range	*-70.0*	*-69.6*	KG.1967.2	sedimentary	Rb-Sr	whole rock	150	17
Alexander Island	South Douglas Range	*-70.0*	*-69.6*	KG.2027.2	sedimentary	Rb-Sr	whole rock	150	17
Alexander Island	N of Lemay Range	*-70.9*	*-69.3*	KG.4822.1	sedimentary	Rb-Sr	whole rock	189	17
Alexander Island	N of Lemay Range	*-70.9*	*-69.3*	KG.4822.2	sedimentary	Rb-Sr	whole rock	189	17
Alexander Island	N of Lemay Range	*-70.9*	*-69.3*	KG.4822.3	sedimentary	Rb-Sr	whole rock	189	17
Alexander Island	Charcot Island	*-69.8*	*-75.3*	KG.4831.1	sedimentary	Rb-Sr	whole rock	120	17
Alexander Island	LeMay Range	*-69.8*	*-75.3*	KG.4836.1	sedimentary	Rb-Sr	whole rock	128	17
Alexander Island	LeMay Range	*-69.8*	*-75.3*	KG.4836.2	sedimentary	Rb-Sr	whole rock	128	17
Alexander Island	LeMay Range	*-69.8*	*-75.3*	KG.4836.3	sedimentary	Rb-Sr	whole rock	128	17
Alexander Island	LeMay Range	*-69.8*	*-75.3*	KG.4845.1	sedimentary	Rb-Sr	whole rock	128	17
Alexander Island	LeMay Range	*-69.8*	*-75.3*	KG.4845.2	sedimentary	Rb-Sr	whole rock	128	17
Alexander Island	LeMay Range	*-69.8*	*-75.3*	KG.4845.3	sedimentary	Rb-Sr	whole rock	128	17
Alexander Island	LeMay Range	*-69.8*	*-75.3*	KG.4845.5	sedimentary	Rb-Sr	whole rock	128	17
Alexander Island	LeMay Range	*-69.8*	*-75.3*	KG.4847.1	sedimentary	Rb-Sr	whole rock	128	17
Alexander Island	LeMay Range	*-69.8*	*-75.3*	KG.4847.2	sedimentary	Rb-Sr	whole rock	128	17
Alexander Island	LeMay Range	*-69.8*	*-75.3*	KG.4847.3	sedimentary	Rb-Sr	whole rock	128	17
Alexander Island	Walton Mtns.	*-71.2*	*-70.3*	KG.4869.1A	sedimentary	Rb-Sr	whole rock	234	17
Alexander Island	Walton Mtns.	*-71.2*	*-70.3*	KG.4869.1D	sedimentary	Rb-Sr	whole rock	234	17
Alexander Island	Walton Mtns.	*-71.2*	*-70.3*	KG.4869.3	sedimentary	Rb-Sr	whole rock	234	17

Appendix Table 2.2.2. Onshore strontium and neodymium isotope and concentration data from the literature

Range[a]	Location	Lat[b]	Long[b]	Sample Name	Rock type	Group[d]	Rb	Sr	$^{87}Rb/^{86}Sr$	$^{87}Sr/^{86}Sr$	Sm	Nd	$^{147}Sm/^{144}Nd$	$^{143}Nd/^{144}Nd$	ε_{Nd}	TDM	Ref
Graham Land	Camp Hill	*-63.7*	*-57.9*	R.632.5	volcanic rocks	APVG	44	304			5.0	26.5	0.1206	0.5123	-6.6	1391	18
Graham Land	Tower Peak	*-64.4*	*-59.2*	R.687.4	volcanic rocks	APVG	98	226			4.2	20.0	0.1217	0.51228	-7.0	1441	18
Graham Land	Hope Bay	*-63.4*	*-57.0*	BR.68.1	volcanic rocks	APVG	152	87			6.4	27.8	0.138	0.51233	-6.0	1650	18
Graham Land	Hope Bay	*-63.4*	*-57.0*	R.601.9	volcanic rocks	APVG	120	151			9.0	55.8	0.0928	0.51225	-7.6		18
Graham Land	Stubb Glacier	*-65.7*	*-62.2*	R.6622.4	High-Ti silicic volcanic rock	APVG	61	409	*0.432*	0.707703	5.9	28.6		0.512421	-4.2	521	19
Graham Land	Stubb Glacier	*-65.7*	*-62.2*	R.6623.3	High-Ti silicic volcanic rock	APVG	69	540	*0.370*	0.707541	5.6	26.8		0.512418	-4.3	523	19
Graham Land	Pequod Glacier	*-65.5*	*-62.1*	R.6605.4	Low-Ti silicic volcanic rock	APVG	186	204	*2.640*	0.712879	8.9	46.5					19
Graham Land	Pequod Glacier	*-65.5*	*-62.1*	R.6605.6	Low-Ti silicic volcanic rock	APVG	203	389	*1.511*	0.710374	8.4	43.9		0.512393	-4.8	541	19
Graham Land	Pequod Glacier	*-65.5*	*-62.1*	R.6607.3	Low-Ti silicic volcanic rock	APVG	150	245	*1.773*	0.711747	6.2	39.5		0.512413	-4.4	527	19
Graham Land	Pequod Glacier	*-65.5*	*-62.1*	R.6609.3	Low-Ti silicic volcanic rock	APVG	133	215	*1.791*	0.710725				0.512414	-4.4	526	19
Graham Land	Pequod Glacier	*-65.5*	*-62.1*	R.6610.3	Low-Ti silicic volcanic rock	APVG	201	143	*4.072*	0.715981	4.3	22.2					19
Graham Land	Rachel Glacier	*-65.6*	*-62.2*	R.6612.4	Low-Ti silicic volcanic rock	APVG	105	123	*2.472*	0.7115	5.9	36.6		0.512437	-3.9	510	19
Graham Land	Pequod Glacier	*-65.5*	*-62.1*	R.6614.2	Low-Ti silicic volcanic rock	APVG	133	295	*1.305*	0.710659							19
Graham Land	Rachel Glacier	*-65.6*	*-62.2*	R.6618.1	Low-Ti silicic volcanic rock	APVG	431	15						0.512457	-3.5	495	19
Graham Land	Rachel Glacier	*-65.6*	*-62.2*	R.6618.7	Low-Ti silicic volcanic rock	APVG	175	282		0.710491	4.7	25.2	0.1117	0.512432	-4.0	1074	19
Graham Land	Rachel Glacier	*-65.6*	*-62.2*	R.6619.3	Low-Ti silicic volcanic rock	APVG	80	496		0.707575	5.6	29.8					19
Graham Land	Stubb Glacier	*-65.7*	*-62.2*	R.6621.2	Low-Ti silicic volcanic rock	APVG	167	269		0.710657	4.8	24.9					19
Graham Land	Stubb Glacier	*-65.7*	*-62.2*	R.6624.1	Low-Ti silicic volcanic rock	APVG	140	246		0.710263	6.5	32.5					19
Graham Land	Stubb Glacier	*-65.7*	*-62.2*	R.6625.2	Low-Ti silicic volcanic rock	APVG	189	177		0.71407	8.0	41.0	0.1179	0.51238	-5.0	1225	19
Graham Land	Stubb Glacier	*-65.7*	*-62.2*	R.6625.3	Low-Ti silicic volcanic rock	APVG	142	446		0.708535			0.1192	0.512411	-4.4	1192	19
Graham Land	Stubb Glacier	*-65.7*	*-62.2*	R.6626.1	Low-Ti silicic volcanic rock	APVG	161	340		0.709689	7.7	37.6					19
Graham Land	Stubb Glacier	*-65.7*	*-62.2*	R.6627.3	Low-Ti silicic volcanic rock	APVG	166	223		0.711403	6.6	33.0	0.1223	0.512444	-3.8	1178	19
Graham Land	Stubb Glacier	*-65.7*	*-62.2*	R.6627.6	Low-Ti silicic volcanic rock	APVG	128	392		0.709038	6.1	31.9					19
Graham Land	Stubb Glacier	*-65.7*	*-62.2*	R.6627.7	Low-Ti silicic volcanic rock	APVG	203	167		0.714558	5.8	29.7					19
Graham Land	Stubb Glacier	*-65.7*	*-62.2*	R.6628.3	Low-Ti silicic volcanic rock	APVG	98	510		0.708296	6.4	32.6	0.1174	0.512382	-5.0	1216	19
Graham Land	Stubb Glacier	*-65.7*	*-62.2*	R.6629.4	Low-Ti silicic volcanic rock	APVG	75	276		0.70832	7.0	36.0					19
Graham Land	Stubb Glacier	*-65.7*	*-62.2*	R.6629.5	Low-Ti silicic volcanic rock	APVG	103	499		0.708046	6.2	32.3	0.1189	0.512385	-4.9	1230	19
Graham Land	Stubb Glacier	*-65.7*	*-62.2*	R.6630.2	Low-Ti silicic volcanic rock	APVG	110	269		0.709422	7.6	39.4					19
Graham Land	Stubb Glacier	*-65.7*	*-62.2*	R.6630.3	Low-Ti silicic volcanic rock	APVG	138	354		0.709191	5.7	31.8					19
Graham Land	Stubb Glacier	*-65.7*	*-62.2*	R.6630.4	Low-Ti silicic volcanic rock	APVG		217		0.711071	6.4	35.6	0.1131	0.512392	-4.8	1149	19
Graham Land	Stubb Glacier	*-65.7*	*-62.2*	R.6631.2	Low-Ti silicic volcanic rock	APVG	77	493		0.707692	6.2	32.0					19
Graham Land	Stubb Glacier	*-65.7*	*-62.2*	R.6632.2	Low-Ti silicic volcanic rock	APVG	66	353		0.707685	6.6	35.6	0.1089	0.512396	-4.7	1097	19
Graham Land	Stubb Glacier	*-65.7*	*-62.2*	R.6632.3	Low-Ti silicic volcanic rock	APVG	121	234		0.709948	6.1	32.7					19
Graham Land	Stubb Glacier	*-65.7*	*-62.2*	R.6632.7	Low-Ti silicic volcanic rock	APVG	130	422		0.708792	6.0	31.0	0.1149	0.512373	-5.2	1199	19
Graham Land	Stubb Glacier	*-65.7*	*-62.2*	R.6634.5	Low-Ti silicic volcanic rock	APVG	132	190		0.711283	5.5	25.3					19
Graham Land	Mapple Glacier	*-65.4*	*-62.3*	R.6851.3	Low-Ti silicic volcanic rock	APVG	175	139		0.715952			0.1095	0.512361	-5.4	1155	19
Graham Land	Mapple Glacier	*-65.4*	*-62.3*	R.6861.1	Low-Ti silicic volcanic rock	APVG	156	203		0.712429			0.1100	0.51237	-5.2	1147	19
Graham Land	Mapple Glacier	*-65.4*	*-62.3*	R.6911.3	Low-Ti silicic volcanic rock	APVG	100	126		0.712328	5.6	32.6					19
Graham Land	Faure Islands	*-68.1*	*-68.9*	BR.024.3	diorite	Cenozoic granitoids	113	406	0.7999	0.70461	7.8	42.8	0.1095	0.512836	3.9	461	1
Graham Land	Faure Islands	*-68.1*	*-68.9*	BR.024.4	diorite	Cenozoic granitoids	36	507	0.2043	0.70421	4.0	20.5	0.1186	0.512843	4.0	493	1
Graham Land	Anchorage Islands	*-67.6*	*-68.2*	R.008.1	granodiorite	Cenozoic granitoids	31	443	0.202	0.70405	4.9	21.6	0.1365	0.512866	4.4	562	1
Graham Land	Anchorage Islands	*-67.6*	*-68.2*	R.013.4	*MD*	Cenozoic granitoids	51	452	0.3273	0.704	5.4	23.7	0.1391	0.512888	4.9	537	1
Graham Land	Horseshoe Island	*-67.8*	*-67.2*	R.076.1	diorite	Mesozoic granitoids	10	778	0.0367	0.70414	4.9	20.3	0.1451	0.512807	3.3	764	1
Graham Land	Horseshoe Island	*-67.8*	*-67.2*	R.079.1	gabbro	Mesozoic granitoids	11	987	0.0313	0.70418	2.9	23.4	0.0746	0.512811	3.4	372	1
Graham Land	Horseshoe Island	*-67.8*	*-67.2*	R.080.1	granite	Mesozoic granitoids	45	208	0.6196	0.70467	7.7	38.4	0.1208	0.51283	3.7	526	1
Graham Land	Terra Firma Islands	*-68.7*	*-67.5*	BR.138.6	granite	Mesozoic granitoids	85	188	1.3144	0.70596	7.6	37.5	0.123	0.512765	2.5	648	1
Graham Land	Terra Firma Islands	*-68.7*	*-67.5*	BR.138.13	gabbro	Mesozoic granitoids	21	654	0.0926	0.704454	4.4	19.4	0.1364	0.512752	2.2	786	1
Graham Land	Terra Firma Islands	*-68.7*	*-67.5*	BR.138.17	diorite	Mesozoic granitoids	60	387	0.4444	0.705905	5.6	29.1	0.1151	0.512599	-0.8	853	1

Graham Land	Petermann Island	*-65.2*	*-64.1*	R.503.2	granodiorite	Mesozoic granitoids	113	256	1.2776	0.7062	7.7	40.4	0.1155	0.512706	1.3	690	1
Graham Land	Bourgeois Fjord	*-67.6*	*-67.0*	BR.132.15	granite	Mesozoic granitoids	130	113	3.315	0.71027	4.9	26.6	0.1114	0.512545	-1.8	902	1
Graham Land	Duthiers Point	*-64.8*	*-62.8*	R.511.2	gabbro	Mesozoic granitoids	8	634	0.0365	0.704653	3.6	13.2	0.1649	0.512746	2.1	1263	1
Graham Land	Lemaire Island	*-64.8*	*-63.0*	O.942.5	granodiorite	Mesozoic granitoids	58	364	0.4609	0.705058	7.1	30.2	0.1423	0.512736	1.9	885	1
Graham Land	Leith Cove	*-64.9*	*-62.8*	O.996.1	granodiorite	Mesozoic granitoids	134	267	1.4519	0.706726	3.8	18.3	0.1278	0.512691	1.0	816	1
Graham Land	Leith Cove	*-64.9*	*-62.8*	O.989.1	granodiorite	Mesozoic granitoids	140	359	1.1281	0.705881	4.8	27.9	0.1046	0.512683	0.9	654	1
Graham Land	Sterneck Island	*-64.2*	*-61.0*	R.4056.1	granite	Mesozoic granitoids	100	218	1.327	0.70621	2.0	12.8	0.0973	0.512697	1.2	594	1
Graham Land	Curtiss Bay	*-64.0*	*-60.8*	CBA01	granodiorite	Mesozoic granitoids	60	386	0.4496	0.705287	5.0	21.6	0.1414	0.512712	1.4	925	1
Graham Land	Midas Island	*-64.2*	*-61.1*	R.4056.6	gabbro	Mesozoic granitoids	7	492	0.0412	0.704846	1.7	6.4	0.1595	0.512699	1.2	1269	1
Graham Land	Cape Herschel Area	*-64.1*	*-61.0*	CHA01	granodiorite	Mesozoic granitoids	110	257	1.2382	0.706412	8.6	31.8	0.1643	0.512736	1.9	1279	1
Graham Land	Cape Herschel Area	*-64.1*	*-61.0*	CHA08	granodiorite	Mesozoic granitoids	86	176	1.4136	0.706799	3.0	15.5	0.1195	0.512699	1.2	731	1
Graham Land	Bourgeois Fjord	*-67.7*	*-67.1*	BR.125.1	granodiorite	Mesozoic granitoids	80	469	0.4947	0.706979	4.1	23.5	0.105	0.512452	-3.6	980	1
Graham Land	Bourgeois Fjord	*-67.7*	*-67.1*	BR.129.1	granite	Mesozoic granitoids	84	215	1.1323	0.706803	3.2	19.7	0.0984	0.512596	-0.8	734	1
Graham Land	Bristly Peaks	*-69.4*	*-66.3*	R.5552.1	granite	Mesozoic granitoids	122	88	4.0131	0.711047	5.0	27.0	0.1128	0.512586	-1.0	853	1
Graham Land	Cape Fairweather	*-65.0*	*-61.0*	R.366.1	granite	Mesozoic granitoids	152	61	7.2265	0.715976	5.1	26.0	0.119	0.512566	-1.4	941	1
Graham Land	Horseshoe Island	*-67.8*	*-67.2*	R.571.1	granite	Mesozoic granitoids	212	12	51.87	0.77999	7.5	37.2	0.1225	0.512548	-1.8	1007	1
Graham Land	Mount Eissenger	*-70.0*	*-67.7*	R.5260.2	gabbro	Mesozoic granitoids	64	216	0.8605	0.707769	1.8	7.6	0.1429	0.512635	-0.1	1110	1
Graham Land	Mount Eissenger	*-70.0*	*-67.7*	R.5260.3	granite	Mesozoic granitoids	76	239	0.9216	0.7088	7.1	37.6	0.1147	0.512448	-3.7	1081	1
Graham Land	Bildad Peak	*-65.8*	*-62.6*	R.312.2	granite	Mesozoic granitoids	144	348	1.1943	0.70906	6.4	35.4	0.1098	0.512404	-4.6	1095	1
Graham Land	Mount Fritsche	*-66.0*	*-63.0*	R.326.2	granodiorite	Mesozoic granitoids	76	311	0.7099	0.70845	3.7	20.0	0.1112	0.512361	-5.4	1174	1
Graham Land	Bildad Peak	*-65.8*	*-62.6*	R.302.1	diorite	Mesozoic granitoids	108	744	0.4199	0.70718	6.0	24.5	0.1479	0.512425	-4.2	1678	1
Graham Land	Bildad Peak	*-65.8*	*-62.6*	R.310.1	granodiorite	Mesozoic granitoids	172	291	1.72	0.71014	4.7	25.1	0.1121	0.512396	-4.7	1132	1
Graham Land	Scharer Bluff	*-68.2*	*-65.3*	R.2605.1	gabbro	Mesozoic granitoids	18	378	0.1402	0.70833	2.1	9.1	0.1407	0.512365	-5.3	1638	1
Graham Land	Scharer Bluff	*-68.2*	*-65.3*	R.2605.2	gabbro	Mesozoic granitoids	74	303	0.7067	0.70995	4.2	20.3	0.1244	0.512296	-6.7	1457	1
Graham Land	Scharer Bluff	*-68.2*	*-65.3*	R.2606.1	gabbro	Mesozoic granitoids	46	366	0.3638	0.70993	3.8	16.1	0.1418	0.512263	-7.3	1877	1
Graham Land	Scharer Bluff	*-68.2*	*-65.3*	R.2606.6	granite	Mesozoic granitoids	243	249	2.8286	0.7172	8.3	49.0	0.1025	0.5123	-6.6	1165	1
Graham Land	Scharer Bluff	*-68.2*	*-65.3*	R.2607.4	MG	Mesozoic granitoids	265	131	5.8885	0.72507	10.6	53.5	0.1197	0.512321	-6.2	1344	1
Graham Land	Trail Inlet	*-68.1*	*-65.4*	R.2624.1	granodiorite	Mesozoic granitoids	141	241	1.6861	0.7119	6.2	32.2	0.1157	0.512356	-5.5	1235	1
Graham Land	Trail Inlet	*-68.1*	*-65.4*	R.2625.1	granodiorite	Mesozoic granitoids	140	276	1.4672	0.71116	6.8	35.4	0.1162	0.512359	-5.4	1237	1
Graham Land	Roman Four	*-68.2*	*-66.9*	R.052.6	orthogneiss	Mesozoic granitoids	163	88	5.3428	0.721509	10.5	53.4	0.1189	0.512421	-4.2	1173	1
Graham Land	Target Hill	*-66.0*	*-63.0*	R.321.3	granodiorite	Mesozoic granitoids	120	299	1.1647	0.70931	4.5	28.2	0.0958	0.512359	-5.4	1023	1
Graham Land	Pylon Point	*-68.1*	*-65.1*	R.2612.3	granodiorite	Evolved Granitoids	175	596	0.8495	0.71004	5.0	27.9	0.1088	0.512281	-7.0	1263	1
Graham Land	Pylon Point	*-68.1*	*-65.1*	R.2612.5	granite	Evolved Granitoids	406	143	8.2413	0.73328	7.3	41.0	0.1075	0.512281	-7.0	1247	1
Graham Land	Curran Bluff	*-68.2*	*-65.0*	R.2614.1	granite	Evolved Granitoids	398	153	7.5515	0.73498	20.9	127.0	0.0997	0.512193	-8.7	1279	1
Graham Land	Curran Bluff	*-68.2*	*-65.0*	R.2614.3	granite	Evolved Granitoids	357	173	5.9919	0.7312	16.9	101.1	0.1011	0.512191	-8.7	1298	1
Graham Land	Cole Peninsula	*-66.8*	*-64.0*	R.280.4	granite	Mesozoic granitoids	120	399	0.864	0.70925	6.4	37.6	0.1035	0.512391	-4.8	1050	1
Graham Land	Elton Hill	*-68.8*	*-66.6*	R.5506.3	granite gneiss	Evolved Granitoids	186	39	13.8157	0.747093	8.3	30.6	0.1647	0.512464	-3.4	2130	1
Graham Land	Reluctant island	*-67.8*	*-67.1*	R.6157.1	granite gneiss	Mesozoic granitoids	100	188	1.5359	0.710398	9.0	54.0	0.1013	0.512382	-5.0	1042	1
Graham Land	N of Werner Peak	*-68.7*	*-65.2*	R.5035.2	amphobolite	Mesozoic granitoids	107	210	1.4675	0.713904	4.1	16.3	0.1509	0.512197	-8.6	2307	1
Graham Land	N of Werner Peak	*-68.7*	*-65.2*	R.5035.6	granite	Evolved Granitoids	474	23	60.903	0.898134	0.7	2.6	0.1687	0.512273	-7.1	2958	1
Graham Land	Hope Bay	*-63.4*	*-57.0*	BR.072.1	sandstone		72	371	0.5581	0.7095	6.8	30.8	0.1336	0.512356	-5.5	1510	1
Graham Land	Hope Bay	*-63.4*	*-57.0*	BR.072.2	sandstone		95	361	0.7574	0.7095	5.1	28.7	0.1074	0.512341	-5.8	1160	1
Graham Land	Hope Bay	*-63.4*	*-57.0*	BR.072.3	sandstone		204	138	4.3041	0.72332	7.2	35.8	0.1212	0.512301	-6.6	1399	1
Graham Land	Target Hill	*-66.0*	*-63.0*	R.3415.14	pegmatite	Paleozoic granitoids	45	211	0.6137	0.708036	1.3	2.9	0.2603	0.512703	1.3	-1471	1
Graham Land	Marsh Spur	*-65.9*	*-62.6*	R.3632.1	granite	Paleozoic granitoids	111	211	1.5168	0.713053	9.9	79.5	0.0753	0.512324	-6.1	911	1
Graham Land	Marsh Spur	*-65.9*	*-62.6*	R.3632.2	granite	Paleozoic granitoids	136	68	5.7731	0.732655	5.7	25.8	0.1336	0.512413	-4.4	1402	1
Graham Land	Marsh Spur	*-65.9*	*-62.6*	R.3632.4	granite	Paleozoic granitoids	153	36	12.299	0.76304	2.6	7.8	0.2031	0.512602	-0.7	7779	1
Graham Land	Mount Lagado	*-66.0*	*-63.3*	R.3899.18	granite	Paleozoic granitoids	135	114	3.4434	0.71988	1.7	4.9	0.2089	0.51255	-1.7	18371	1
Graham Land	Mount Lagado	*-66.0*	*-63.3*	R.3900.3	granite	Paleozoic granitoids	62	262	0.6959	0.70711	0.6	1.2	0.2994	0.512867	4.5	-505	1
Graham Land	Leppard Glacier	*-66.0*	*-62.5*	R.3431.1	granite gneiss	Paleozoic granitoids	139	232	1.7426	0.714041	3.0	19.9	0.0928	0.512495	-2.8	827	1
Graham Land	Leppard Glacier	*-66.0*	*-62.5*	R.3431.5	granite gneiss	Paleozoic granitoids	74	273	0.7796	0.70791	1.5	6.2	0.1444	0.512455	-3.6	1528	1
Graham Land	Leppard Glacier	*-66.0*	*-62.5*	R.3431.17	amphibolite	Paleozoic granitoids	39	201	0.5606	0.706805	2.7	9.0	0.1829	0.512802	3.2	1724	1
Graham Land	Leppard Glacier	*-66.0*	*-62.5*	R.3434.1	granite gneiss	Paleozoic granitoids	118	229	1.4976	0.713111	3.2	18.4	0.1043	0.512465	-3.4	955	1

Graham Land	Leppard Glacier	*-66.0*	*-62.5*	R.3434.2	granite gneiss	Paleozoic granitoids	63	171	1.0656	0.709121	1.7	5.8	0.1734	0.512566	-1.4	2205	1
Graham Land	Leppard Glacier	*-66.0*	*-62.5*	R.3434.6	granite gneiss	Paleozoic granitoids	71	272	0.7551	0.707325	4.0	18.6	0.1289	0.512519	-2.3	1135	1
Graham Land	Leppard Glacier	*-66.0*	*-62.5*	R.3434.7	granite gneiss	Paleozoic granitoids	122	183	1.9257	0.715614	3.3	19.0	0.1047	0.512478	-3.1	941	1
Graham Land	Leppard Glacier	*-66.0*	*-62.5*	R.4016.5	amphibolite	Paleozoic granitoids	61	211	0.8382	0.708063	7.3	28.9	0.1529	0.512652	0.3	1249	1
Graham Land	Target Hill	*-66.0*	*-63.0*	R.5511.1	orthogneiss	Paleozoic granitoids	39	199	0.5718	0.708604	3.0	17.5	0.1031	0.512521	-2.3	868	1
Graham Land	Adie Inlet	*-66.4*	*-62.3*	R.348.1A	gneiss	Paleozoic granitoids	174	229	2.1962	0.72277	8.1	38.8	0.1255	0.512158	-9.4	1712	1
Graham Land	Adie Inlet	*-66.4*	*-62.3*	R.348.1B	gneiss	Paleozoic granitoids	148	276	1.558	0.72093	5.4	25.7	0.127	0.512181	-8.9	1701	1
Graham Land	Adie Inlet	*-66.4*	*-62.3*	R.348.2	gneiss	Paleozoic granitoids	151	256	1.7089	0.7211	6.0	28.0	0.1283	0.512182	-8.9	1725	1
Graham Land	Adie Inlet	*-66.4*	*-62.3*	R.349.1	gneiss	Paleozoic granitoids	125	206	1.7474	0.71976	8.4	40.9	0.1236	0.512179	-9.0	1641	1
Graham Land	Adie Inlet	*-66.4*	*-62.3*	R.349.2	gneiss	Paleozoic granitoids	129	200	1.8724	0.72019	8.2	39.1	0.1268	0.512186	-8.8	1689	1
Graham Land	Adie Inlet	*-66.4*	*-62.3*	R.349.3	amphibolite	Paleozoic granitoids	99	188	1.5214	0.72056	7.1	33.8	0.1277	0.512104	-10.4	1851	1
Graham Land	Adie Inlet	*-66.4*	*-62.3*	R.346.5	amphibolite	Paleozoic granitoids	39	218	0.517	0.70765	2.1	7.2	0.1781	0.512319	-6.2	3538	1
Graham Land	Adie Inlet	*-66.4*	*-62.3*	R.350.1	amphibolite	Paleozoic granitoids	87	796	0.3274	0.70746	8.3	38.7	0.1295	0.512338	-5.9	1469	1
Graham Land	Sterneck Island	-64.18	-61.01	R.4056.4	mafic dyke	dyke	23	207	0.3213	0.702989	4.732	18.28	0.1564	0.513052	8.1	262	1
Graham Land	Reclus Peninsula	-64.58	-61.70	O.576.4	mafic dyke	dyke	38	379	0.29	0.705297	4.419	17.69	0.151	0.512721	1.6	1044	1
Graham Land	Reclus Peninsula	-64.58	-61.70	BBE0203	mafic dyke	dyke	67	322	0.6019	0.70577	3.293	14.27	0.1395	0.512839	3.9	640	1
Graham Land	Lemaire Channel	-65.04	-63.85	LC06	mafic dyke	dyke	20	429	0.1348	0.70413	3.299	12.92	0.1543	0.512867	4.5	728	1
Graham Land	Brabant Island	-64.40	-62.69	R.4063.15	intermediate dyke	dyke	20	466	0.1241	0.703963	1.874	6.22	0.1822	0.51288	4.7	1309	1
Graham Land	Brabant Island	-64.26	-62.53	R.4063.17	intermediate dyke	dyke	66	422	0.4523	0.703953	2.774	9.532	0.176	0.512886	4.8	1070	1
Graham Land	Melchior Islands	-64.33	-63.00	MI04	intermediate dyke	dyke	16	574	0.0806	0.703995	3.599	18.73	0.1161	0.512902	5.1	388	1
Graham Land	Melchior Islands	-64.29	-62.98	R.4064.4	intermediate dyke	dyke	33	448	0.213	0.70383	5.098	23.4	0.1317	0.51291	5.3	447	1
Graham Land	Melchior Islands	-64.29	-62.98	R.4064.9	intermediate dyke	dyke	15	458	0.0947	0.703802	2.02	9.163	0.1333	0.512929	5.7	420	1
Graham Land	Paradise Harbour	-64.90	-62.85	O.930.7	intermediate dyke	dyke	70	553	0.3661	0.705306	4.709	22.43	0.1269	0.5127	1.2	792	1
Palmer Land	NW Palmer Land	/	/	R.5632.11	mafic dyke	dyke	30	763	0.1138	0.70399	7	0.33	0.1296	0.51293	5.7	400	29
Palmer Land	NW Palmer Land	/	/	R.5641.11	mafic dyke	dyke	3	205	0.0385	0.70631	4.8	13.2	0.221	0.51293	5.7	-4615	29
Palmer Land	NW Palmer Land	/	/	R.5705.1	mafic dyke	dyke	6	215	0.0813	0.70647	3	8	0.1977	0.51278	2.8	3517	29
Palmer Land	NW Palmer Land	/	/	R.5784.1	mafic dyke	dyke	3	205	0.0385	0.70631	5	13	0.221	0.51293	5.7	-4615	29
Palmer Land	NW Palmer Land	/	/	R.5595.3	mafic dyke	dyke	94	410	0.6623	0.70598	4	18	0.1293	0.51268	0.8	850	29
Palmer Land	NW Palmer Land	/	/	R.5629.2	mafic dyke	dyke	110	787	0.6563	0.70578	4	25	0.0998	0.51264	0.0	684	29
Palmer Land	NW Palmer Land	/	/	R.5779.2	mafic dyke	dyke	104	403	0.7473	0.70605	9	45	0.1242	0.51269	1.0	785	29
Palmer Land	NW Palmer Land	/	/	R.5794.1	mafic dyke	dyke	151	862	0.5073	0.70518	6	29	0.1184	0.51281	3.4	545	29
Palmer Land	NW Palmer Land	/	/	E.3515.2	mafic dyke	dyke	139	404	0.9926	0.7048	4	16	0.1493	0.51279	3.0	854	29
Palmer Land	NW Palmer Land	/	/	R.5613.3	intermediate dyke	dyke	91	511	0.5158	0.70727	6	32	0.1162	0.51262	-0.4	830	29
Palmer Land	NW Palmer Land	/	/	R.5631.16	intermediate dyke	dyke	111	664	0.4841	0.70506	7	40	0.1005	0.51275	2.2	540	29
Palmer Land	NW Palmer Land	/	/	R.5776.4	mafic dyke	dyke	67	1029	0.188	0.70528	5	24	0.1141	0.51274	2.0	629	29
Palmer Land	Mount Pitman	*-70.2*	*-67.6*	R.5256.1	granodiorite	Cenozoic granitoids	103	443	0.6742	0.704968	5.5	29.0	0.1147	0.512777	2.7	576	1
Palmer Land	Scorpio Peaks	*-70.5*	*-67.4*	R.5736.1	granodiorite	Mesozoic granitoids	76	570	0.3879	0.704667	4.2	24.9	0.1034	0.512821	3.6	456	1
Palmer Land	Orion Massif	*-70.4*	*-66.8*	R.5955.11	granodiorite	Mesozoic granitoids	75	589	0.3694	0.705499	4.7	25.2	0.1136	0.512718	1.6	659	1
Palmer Land	Mount Lepus	*-70.7*	*-67.2*	R.5501.1	granodiorite	Mesozoic granitoids	86	150	1.6621	0.707292	3.2	22.7	0.0846	0.51266	0.4	580	1
Palmer Land	Mount Lepus	*-70.7*	*-67.2*	R.5965.7	granodiorite	Mesozoic granitoids	80	493	0.4718	0.705913	4.9	29.0	0.103	0.512685	0.9	642	1
Palmer Land	Goettel Escarpment	*-70.2*	*-66.9*	R.5267.1	granodiorite	Mesozoic granitoids	55	496	0.3203	0.706827	6.1	30.5	0.1209	0.512531	-2.1	1018	1
Palmer Land	Taurus Nunataks	*-70.9*	*-66.4*	R.2539.2	granodiorite	Mesozoic granitoids	31	935	0.0955	0.706768	2.7	14.5	0.1108	0.512479	-3.1	995	1
Palmer Land	Goettel Escarpment	*-70.2*	*-66.9*	R.5271.1	porphyry	Mesozoic granitoids	53	691	0.2236	0.70598	4.1	21.2	0.1155	0.512605	-0.6	847	1
Palmer Land	Pegasus Mountains	*-71.0*	*-67.2*	R.2414.3	granite	Mesozoic granitoids	84	157	1.5449	0.707309	3.9	17.8	0.1329	0.512746	2.1	764	1
Palmer Land	Pegasus Mountains	*-71.0*	*-67.2*	R.2418.4	granodiorite	Mesozoic granitoids	42	287	0.4203	0.70558	2.6	12.2	0.129	0.512625	-0.3	946	1
Palmer Land	Aldebaran Rock	*-70.8*	*-66.7*	R.2402.1	granite	Mesozoic granitoids	163	311	1.5216	0.707684	7.1	42.6	0.1015	0.512595	-0.8	755	1
Palmer Land	Friedmann Nuns.	*-70.9*	*-65.5*	R.5902.8	granodiorite	Mesozoic granitoids	58	638	0.2647	0.706755	4.1	21.8	0.1144	0.512449	-3.7	1077	1
Palmer Land	Sirius Cliffs	*-70.6*	*-66.9*	R.2568.2	granodiorite	Mesozoic granitoids	48	753	0.1855	0.707285	3.0	19.9	0.0906	0.512431	-4.0	891	1
Palmer Land	Cetus Hill	*-70.9*	*-66.1*	R.5796.4	granodiorite	Mesozoic granitoids	36	1078	0.0963	0.707003	3.2	18.8	0.1023	0.512408	-4.5	1016	1
Palmer Land	Perseus Crags	*-70.6*	*-66.2*	R.2556.1	granodiorite	Mesozoic granitoids	56	642	0.2526	0.707254	3.8	18.7	0.1223	0.512437	-3.9	1189	1
Palmer Land	Puppis Pikes	*-71.3*	*-66.4*	R.5904.7	granodiorite	Mesozoic granitoids	76	565	0.3898	0.709361	3.6	21.1	0.1034	0.512345	-5.7	1113	1
Palmer Land	Procyon Peaks	*-70.5*	*-66.5*	R.2585.1	granodiorite	Mesozoic granitoids	67	651	0.2994	0.706119	6.8	34.2	0.1202	0.512595	-0.8	906	1
Palmer Land	Creswick Gap	*-70.4*	*-67.7*	R.2784.1	granodiorite	Mesozoic granitoids	74	287	0.7412	0.706802	4.0	23.2	0.1049	0.512547	-1.8	846	1

Palmer Land	Creswick Gap	*-70.4*	*-67.7*	R.3204.3	granodiorite	Mesozoic granitoids	65	569	0.3307	0.706569	3.6	19.3	0.1121	0.51251	-2.5	961	1
Palmer Land	Burns Bluff	*-70.4*	*-67.9*	R.3216.2	tonalite	Mesozoic granitoids	18	736	0.0712	0.705693	2.0	9.4	0.1256	0.512553	-1.7	1034	1
Palmer Land	Burns Bluff	*-70.4*	*-67.9*	R.3216.3	tonalite	Mesozoic granitoids	22	612	0.1038	0.705733	2.9	14.0	0.1262	0.512539	-1.9	1065	1
Palmer Land	Renner Peak	*-70.3*	*-67.8*	R.5284.1	granodiorite	Mesozoic granitoids	31	910	0.0992	0.706244	3.6	20.0	0.1078	0.512509	-2.5	924	1
Palmer Land	Auriga Nunataks	*-70.7*	*-66.6*	R.5300.3	gabbro	Mesozoic granitoids	24	452	0.1516	0.707215	4.0	11.1	0.2183	0.512536	-2.0	-21406	1
Palmer Land	Wade Point	*-70.7*	*-67.7*	R.5958.1	granodiorite	Mesozoic granitoids	30	184	0.4787	0.705202	3.8	15.0	0.1523	0.512786	2.9	905	1
Palmer Land	Butler Peaks	*-71.5*	*-67.2*	R.6314.9	granodiorite	Mesozoic granitoids	39	573	0.1984	0.706162	3.5	19.9	0.1055	0.512479	-3.1	946	1
Palmer Land	Butler Peaks	*-71.5*	*-67.2*	R.6316.4	granodiorite	Mesozoic granitoids	28	691	0.1166	0.70596	3.2	15.3	0.1254	0.512511	-2.5	1104	1
Palmer Land	Creswick Peaks	*-70.5*	*-67.7*	R.5287.1	diorite	Mesozoic granitoids	77	383	0.5832	0.706879	3.3	16.8	0.117	0.512521	-2.3	992	1
Palmer Land	Burns Bluff	*-70.4*	*-67.9*	R.6057.7	tonalite	Mesozoic granitoids	31	153	0.5777	0.705836	4.3	18.5	0.1394	0.512781	2.8	759	1
Palmer Land	Burns Bluff	*-70.4*	*-67.9*	R.6063.5	granodiorite	Mesozoic granitoids	18	290	0.1762	0.704916	2.9	11.2	0.1563	0.512736	1.9	1101	1
Palmer Land	Burns Bluff	*-70.4*	*-67.9*	R.6057.16	tonalite	Mesozoic granitoids	56	489	0.3342	0.707202	3.3	21.5	0.092	0.512454	-3.6	873	1
Palmer Land	Burns Bluff	*-70.4*	*-67.9*	R.6057.20	quartz-diorite	Mesozoic granitoids	8	281	0.0816	0.704408	1.6	5.5	0.1773	0.512832	3.8	1334	1
Palmer Land	Burns Bluff	*-70.4*	*-67.9*	R.6057.30	tonalite	Mesozoic granitoids	36	718	0.1455	0.705706	3.0	13.4	0.1373	0.512667	0.6	965	1
Palmer Land	Moore Point	*-70.5*	*-67.9*	R.2793.1	gabbro	Mesozoic granitoids	1	236	0.013	0.704424	0.3	0.9	0.2175	0.512875	4.6	-11181	1
Palmer Land	Mount Eissenger	*-70.0*	*-67.7*	R.5259.1	gabbro	Mesozoic granitoids	3	424	0.0188	0.705195	1.5	4.5	0.2031	0.51275	2.2	5717	1
Palmer Land	Burns Bluff	*-70.4*	*-67.9*	R.6057.10	gabbro	Mesozoic granitoids	29	296	0.2832	0.704958	3.5	12.4	0.1727	0.512822	3.6	1221	1
Palmer Land	Welch Mountains	*-71.0*	*-63.5*	E.4021.1	granodiorite	Mesozoic granitoids	85	415	0.5863	0.70742	3.2	16.4	0.1163	0.512432	-4.0	1124	1
Palmer Land	Black Coast	*-71.7*	*-62.0*	E.4012.1	granodiorite	Mesozoic granitoids	81	495	0.475	0.70654	3.7	21.5	0.1054	0.512424	-4.2	1023	1
Palmer Land	Mount Charity	*-69.9*	*-64.6*	R.1906.5	granodiorite	Mesozoic granitoids	233	219	3.0858	0.711129	6.7	24.2	0.1666	0.512432	-4.0	2318	1
Palmer Land	Mount Charity	*-69.9*	*-64.6*	R.1906.7	granodiorite	Mesozoic granitoids	114	312	1.0612	0.707736	5.2	17.7	0.1778	0.512472	-3.2	2869	1
Palmer Land	Black Coast	*-71.7*	*-62.0*	R.4278.1	gabbro	Mesozoic granitoids	12	532	0.0669	0.705137	5.0	20.7	0.1473	0.512471	-3.3	1558	1
Palmer Land	Black Coast	*-71.7*	*-62.0*	R.4280.2	gabbro	Mesozoic granitoids	85	524	0.4692	0.705752	3.2	13.6	0.1425	0.512515	-2.4	1360	1
Palmer Land	Mount Jackson	*-71.4*	*-63.4*	E.4178.1	granodiorite	Mesozoic granitoids	45	455	0.289	0.70522	2.8	14.4	0.1165	0.512537	-2.0	962	1
Palmer Land	Black Coast	*-71.7*	*-62.0*	R.4230.1	granodiorite	Mesozoic granitoids	89	316	0.8153	0.707845	3.3	17.7	0.1135	0.512346	-5.7	1223	1
Palmer Land	Giannini Peak	*-71.0*	*-62.8*	E.4065.1	granodiorite	Mesozoic granitoids	155	367	1.221	0.708389	3.9	18.9	0.1261	0.512365	-5.3	1366	1
Palmer Land	Mount Ward	*-67.2*	*-51.2*	R.6308.1	granodiorite	Mesozoic granitoids	173	239	2.0899	0.71393	10.0	52.7	0.1149	0.512213	-8.3	1445	1
Palmer Land	Mount Ward	*-67.2*	*-51.2*	R.6309.2	granodiorite	Mesozoic granitoids	38	234	0.4647	0.708407	2.9	14.2	0.1216	0.512398	-4.7	1245	1
Palmer Land	Butler Peaks	*-71.5*	*-67.2*	R.6315.8	granite	Evolved Granitoids	190	27	20.7529	0.757891	9.7	34.6	0.1698	0.512358	-5.5	2740	1
Palmer Land	Mount Charity	*-69.9*	*-64.6*	R.1906.3	granite	Evolved Granitoids	190	65	8.504	0.728482	5.7	25.2	0.1364	0.512381	-5.0	1516	1
Palmer Land	Mount Charity	*-69.9*	*-64.6*	R.1907.4	porphyry	Evolved Granitoids	231	48	13.9566	0.740769	6.9	23.7	0.1759	0.512496	-2.8	2630	1
Palmer Land	Mount Charity	*-69.9*	*-64.6*	R.1914.11	granite	Mesozoic granitoids	110	659	0.4852	0.709057	5.2	31.0	0.1022	0.512242	-7.7	1241	1
Palmer Land	Mount Pitman	*-70.2*	*-67.6*	R.5254.2	volcanic rock	Mesozoic granitoids	184	69	7.7705	0.725311	10.8	49.4	0.132	0.512424	-4.2	1354	1
Palmer Land	Mount Pitman	*-70.2*	*-67.6*	R.5254.5	volcanic rock	Mesozoic granitoids	104	239	1.2557	0.712287	8.3	42.2	0.1193	0.512406	-4.5	1202	1
Palmer Land	Goettel Escarpment	*-70.2*	*-66.9*	R.5270.1	diorite	Mesozoic granitoids	46	382	0.3498	0.706802	3.9	17.6	0.1331	0.512543	-1.9	1149	1
Palmer Land	Goettel Escarpment	*-70.2*	*-66.9*	R.5271.4	granite	Mesozoic granitoids	87	447	0.5668	0.707919	11.8	64.1	0.111	0.512471	-3.3	1009	1
Palmer Land	Capella Rocks	*-70.7*	*-66.5*	R.2549.2	granodiorite	Mesozoic granitoids	36	990	0.1065	0.707215	3.5	19.6	0.1081	0.512461	-3.5	995	1
Palmer Land	Campbell Ridges	*-70.4*	*-67.6*	R.5280.2	granodiorite	Mesozoic granitoids	131	310	1.2237	0.71161	8.5	40.8	0.1261	0.512353	-5.6	1386	1
Palmer Land	Campbell Ridges	*-70.4*	*-67.6*	R.5280.4	porphyry	Mesozoic granitoids	134	94	4.1231	0.719044	6.5	31.8	0.1234	0.512356	-5.5	1340	1
Palmer Land	Auriga Nunataks	*-70.7*	*-66.6*	R.5504.2	granodiorite	Mesozoic granitoids	57	496	0.3324	0.707816	2.0	21.1	0.0566	0.512394	-4.8	735	1
Palmer Land	Mount Jackson van Buren	*-71.3*	*-63.5*	R.4908.11	granite gneiss	Evolved Granitoids	360	66	15.7498	0.76592	5.4	20.1	0.163	0.512145	-9.6	3007	1
Palmer Land	Mount Jackson van Buren	*-71.3*	*-63.5*	R.2109.2	granite gneiss	Evolved Granitoids	330	80	11.9488	0.754753	6.4	20.7	0.1853	0.512141	-9.7	5357	1
Palmer Land	Mount Lepus	*-70.7*	*-67.2*	R.2479.1	granite	Mesozoic granitoids	82	343	0.6886	0.70786	4.2	23.9	0.1069	0.512494	-2.8	937	1
Palmer Land	Mount Lepus	*-70.7*	*-67.2*	R.2480.1	granodiorite	Mesozoic granitoids	75	555	0.3911	0.70709	6.4	31.7	0.122	0.51252	-2.3	1048	1
Palmer Land	Campbell Ridges	*-70.4*	*-67.6*	R.3239.4	orthogneiss	Mesozoic granitoids	180	482	1.0827	0.71222	5.1	24.5	0.1266	0.512254	-7.5	1567	1
Palmer Land	Sirius Cliffs	*-70.6*	*-66.9*	R.5294.1	orthogneiss	Mesozoic granitoids	120	870	0.3986	0.706207	9.5	41.0	0.1406	0.512338	-5.9	1691	1
Palmer Land	Campbell Ridges	*-70.4*	*-67.6*	R.5278.8	orthogneiss	Mesozoic granitoids	139	608	0.6636	0.709655	5.0	25.1	0.1216	0.512338	-5.9	1344	1
Palmer Land	Mount Lepus	*-70.7*	*-67.2*	R.5297.3	paragneiss	Mesozoic granitoids	121	316	1.1052	0.715572	6.9	34.8	0.1202	0.512347	-5.7	1309	1
Palmer Land	Auriga Nunataks	*-70.7*	*-66.6*	R.2436.2	paragneiss	Mesozoic granitoids	188	443	1.227	0.717259	8.5	45.5	0.1124	0.512096	-10.6	1584	1
Palmer Land	Fomalhaut Nuns.	*-71.0*	*-66.7*	R.2535.6	orthogneiss	Mesozoic granitoids	114	274	1.2002	0.715872	2.6	16.0	0.0965	0.512192	-8.7	1246	1
Palmer Land	Fomalhaut Nuns.	*-71.0*	*-66.7*	R.2535.7	orthogneiss	Mesozoic granitoids	124	271	1.3198	0.716208	5.7	35.6	0.0973	0.512207	-8.4	1235	1
Palmer Land	Mount Eissenger	*-70.0*	*-67.7*	R.5257.1	orthogneiss	Mesozoic granitoids	174	189	2.6741	0.724902	0.8	3.7	0.1352	0.512543	-1.9	1179	1
Palmer Land	Mount Eissenger	*-70.0*	*-67.7*	R.5257.2	orthogneiss	Mesozoic granitoids	81	190	1.225	0.720105	13.0	62.9	0.1253	0.512548	-1.8	1039	1

Palmer Land	Mount Charity	*-69.9*	*-64.6*	R.1905.1	diorite	Mesozoic granitoids	150	770	0.5628	0.70832	7.7	35.5	0.1305	0.512361	-5.4	1445	1
Palmer Land	Mount Charity	*-69.9*	*-64.6*	R.1905.4	granite	Mesozoic granitoids	185	489	1.0911	0.710352	6.2	49.3	0.0767	0.512278	-7.0	971	1
Palmer Land	Mount Charity	*-69.9*	*-64.6*	R.1905.5	granite	Mesozoic granitoids	245	117	6.0764	0.726115	1.2	3.9	0.1799	0.51255	-1.7	2698	1
Palmer Land	Mount Charity	*-69.9*	*-64.6*	R.1907.2	granite	Mesozoic granitoids	242	113	6.2259	0.726957	1.6	4.6	0.2116	0.512503	-2.6	42856	1
Palmer Land	Mount Nordhill	*-70.9*	*-63.5*	R.4552.2	orthogneiss	Mesozoic granitoids	176	150	3.4004	0.726175	8.9	43.3	0.1248	0.512143	-9.7	1724	1
Palmer Land	Mount Nordhill	*-70.9*	*-63.5*	R.4552.9	granite gneiss	Evolved Granitoids	308	109	8.2244	0.742662	6.8	34.5	0.1201	0.512126	-10.0	1665	1
Palmer Land	Mount Nordhill	*-70.9*	*-63.5*	R.4920.5	granite	Mesozoic granitoids	201	253	2.3031	0.716426	16.3	81.5	0.1208	0.512121	-10.1	1686	1
Palmer Land	Mount Nordhill	*-70.9*	*-63.5*	R.4920.12	granite	Mesozoic granitoids	289	224	3.7368	0.724185	8.3	40.2	0.1255	0.51217	-9.1	1691	1
Palmer Land	Hall Ridge	*-70.7*	*-63.2*	R.4942.4	granodiorite	Mesozoic granitoids	77	477	0.4689	0.706893	4.9	22.9	0.1286	0.512453	-3.6	1249	1
Palmer Land	Solem Ridge	*-71.2*	*-63.3*	R.4293.2	paragneiss	Evolved Granitoids	257	102	7.3091	0.745647	10.4	50.6	0.124	0.512067	-11.1	1837	1
Palmer Land	Mount Nordhill	*-70.9*	*-63.5*	R.4294.1	paragneiss	Evolved Granitoids	144	177	2.3546	0.733153	3.4	17.5	0.1161	0.51205	-11.5	1715	1
Palmer Land	Mount Nordhill	*-70.9*	*-63.5*	R.4920.8	paragneiss	Evolved Granitoids	140	216	1.8817	0.731113	10.9	54.7	0.12	0.512035	-11.8	1811	1
Palmer Land	Werner batholith	*-73.57*	*-62.37*	V39g	granitoid	Mesozoic granitoids					0.7	4.8	0.0872	0.512502	-2.7	782	2
Palmer Land	Werner batholith	*-73.57*	*-62.37*	V71	granitoid	Mesozoic granitoids					3.2	15.6	0.1256	0.512424	-4.2	1256	2
Palmer Land	Werner batholith	*-73.57*	*-62.37*	V80c	granitoid	Mesozoic granitoids					6.2	26.1	0.1447	0.512541	-1.9	1346	2
Palmer Land	Werner batholith	*-73.57*	*-62.37*	Bo6	granitoid	Mesozoic granitoids					5.0	23.0	0.1308	0.51241	-4.4	1360	2
Palmer Land	Rath pluton	*-74.32*	*-62.5*	Ro160a	quartz monzodiorite	Mesozoic granitoids					6.2	27.3	0.1382	0.512525	-2.2	1262	2
Palmer Land	North RARE pluton	*-74.4*	*-64.08*	S54a	granodiorite	Mesozoic granitoids					2.7	14.3	0.1154	0.512593	-0.9	865	2
Palmer Land	Eklund Island	*-73.27*	*-71.83*	R.4557.4	diorite	Mesozoic granitoids					6.1	26.5	0.1386	0.512507	-2.6	1305	2
Palmer Land	North FitzGerald Bluffs pluton	*-74.05*	*-77.33*	V200a	granodiorite	Mesozoic granitoids	84	324	0.747	0.70756	6.5	34.4	0.1146	0.51242	-4.3	1123	2
Palmer Land	Mount Harry pluton	*-74.23*	*-76.53*	V201k	monzonite	Mesozoic granitoids	83	367	0.656	0.70677	3.7	20.3	0.1092	0.512431	-4.0	1049	2
Palmer Land	Mount Harry pluton	*-74.23*	*-76.53*	R.8005.4	monzonite	Mesozoic granitoids					4.4	23.4	0.1143	0.512467	-3.3	1048	2
Palmer Land	West Behrent pluton	*-75.33*	*-72.5*	Ke193d	granodiorite	Mesozoic granitoids	103	412	0.724	0.70677	2.6	12.7	0.1222	0.512384	-5.0	1276	2
Palmer Land	Edward pluton	*-75.52*	*-69.15*	Th25a	quartz monzodiorite	Mesozoic granitoids	74	825	0.259	0.70399	2.7	14.0	0.1167	0.512739	2.0	647	2
Palmer Land	Copper Nunataks pluton	*-74.37*	*-64.92*	M318a	granodiorite	Mesozoic granitoids					2.1	10.2	0.1218	0.512497	-2.8	1084	2
Palmer Land	McLaughlin pluton	*-74.58*	*-64.3*	S28b	granodiorite	Mesozoic granitoids					4.3	21.9	0.1193	0.512385	-4.9	1235	2
Palmer Land	Eklund Island	*-73.27*	*-71.83*	R.4557.2	gabbro	Mesozoic granitoids					3.1	13.0	0.146	0.512536	-2.0	1383	2
Palmer Land	Terwileger pluton	*-75.22*	*-64.73*	S47e	granite	Mesozoic granitoids					4.7	22.9	0.1246	0.51248	-3.1	1147	2
Palmer Land	Copper Nunataks pluton	*-74.37*	*-64.92*	M429c	granite	Mesozoic granitoids					5.5	37.4	0.0891	0.512428	-4.1	884	2
Palmer Land	South-west FitzGerald Bluffs pluton	*-74.05*	*-77.33*	L103a	granite	Mesozoic granitoids	101	313	0.935	0.70758	4.9	26.2	0.114	0.512467	-3.3	1045	2
Palmer Land	North FitzGerald Bluffs pluton	*-74.05*	*-77.33*	R.8003.1	granite	Mesozoic granitoids					3.4	17.2	0.12	0.51242	-4.3	1188	2
Palmer Land	North FitzGerald Bluffs pluton	*-74.05*	*-77.33*	V202j	granite	Mesozoic granitoids	82	380	0.623		5.0	27.4	0.1093	0.512437	-3.9	1042	2
Palmer Land	Hall Ridge (?)	*-70.7*	*-63.2*	E.4012.1	granodiorite	Mesozoic granitoids	81	495	0.475	0.70654	3.8	21.5	0.1054	0.512442	-3.8	997	20
Palmer Land	Giannini Peak	*-70.7*	*-63.2*	E.4065.1	granodiorite	Mesozoic granitoids	155	367	1.221	0.70835	3.9	18.9	0.126	0.512362	-5.4	1369	20
Palmer Land	S Welch Mts	*-70.7*	*-63.2*	E.4021.1	granodiodte	Mesozoic granitoids	85	415	0.5863	0.70742	3.2	16.4	0.1162	0.512432	-4.0	1123	20
Palmer Land	SE Mt Jackson	*-70.7*	*-63.2*	E.4178.1	granodiodte	Mesozoic granitoids	45	455	0.289	0.70552	2.8	14.4	0.1165	0.512537	-2.0	962	20
Palmer Land	Hall Ridge (?)	*-70.7*	*-63.2*	R.4230.1	graniodiorite	Mesozoic granitoids	89	317	0.8154	0.707812	3.3	17.7	0.1136	0.512346	-5.7	1224	20
Palmer Land	Hall Ridge (?)	*-70.7*	*-63.2*	R.4278.1	gabbro	Mesozoic granitoids	12	532	0.0669	0.705137	5.1	20.7	0.1481	0.512471	-3.3	1577	20
Palmer Land	Hall Ridge (?)	*-70.7*	*-63.2*	R.4280.2	gabbro	Mesozoic granitoids	85	524	0.4692	0.705719	3.2	13.6	0.1425	0.512453	-3.6	1492	20
Palmer Land	Mount Wasilewski	-75.17	-71.38	R.6871.3	high-Ti silicic volcanic rock	APVG	93	66	*4.066*	0.731232	9.9	49.9	0.1229	0.51216	-9.3	1660	19
Palmer Land	Sky-Hi Nunataks	-74.90	-71.50	R.6874.1	high-Ti silicic volcanic rock	APVG	215	141	*4.415*	0.73026	10.2	52.3	0.1198	0.512173	-9.1	1584	19
Palmer Land	Mount Ballard	-75.17	-70.00	R.6888.2	high-Ti silicic volcanic rock	APVG	166	150	*3.206*	0.729256	9.5	49.3	0.1221	0.512162	-9.3	1642	19
Palmer Land	Mount Ballard	-75.17	-70.00	R.6889.2	high-Ti silicic volcanic rock	APVG	187	124	*4.375*	0.730457	9.1	45.3	0.1238	0.512166	-9.2	1666	19
Palmer Land	Mount Jenkins	-75.13	-69.18	R.7111.1	high-Ti silicic volcanic rock	APVG	182	149	*3.549*	0.730546	8.5	44.1	0.1212	0.512146	-9.6	1652	19
Palmer Land	Mount Ballard	-75.17	-70.00	R.6893.1	high-Ti silicic volcanic rock	APVG	165	150	*3.190*	0.728836	9.7	48.4	0.1219	0.512151	-9.5	1657	19
Palmer Land	Mount Jenkins	-75.13	-69.18	R.7103.1	high-Ti silicic volcanic rock	APVG	180	155	*3.359*	0.728102	8.7	43.7	0.1268	0.512198	-8.6	1668	19
Palmer Land	Potter Peak	-75.15	-68.82	R.7108.2	high-Ti silicic volcanic rock	APVG	167	79	*6.138*	0.735058	8.7	42.7	0.1274	0.51217	-9.1	1729	19
Palmer Land	Mount Jenkins	-75.13	-69.18	R.7102.1	low-Ti silicic volcanic rock	APVG	203	198	*2.974*	0.723727	7.4	40.5	0.1156	0.512299	-6.6	1322	19
Palmer Land	Mount Ballard	-75.17	-70.00	R.6892.1	low-Ti silicic volcanic rock	APVG	58	200	*0.841*	0.712878	6.5	33.0	0.1253	0.51243	-4.1	1242	19
Palmer Land		/	/	R.4238.1	metavolcanic rocks	APVG					10.8	50.9	0.128	0.512206	-8.4	1677	21
Palmer Land		/	/	R.4277.1	metavolcanic rocks	APVG					10.2	50.1	0.1226	0.512138	-9.8	1691	21
Palmer Land		/	/	R.4289.l	metavolcanic rocks	APVG					15.3	73.2	0.1262	0.512146	-9.6	1746	21
Palmer Land		/	/	R.4381.6	metavolcanic rocks	APVG					9.7	46.8	0.1248	0.512185	-8.8	1653	21

Palmer Land		/	/	R.4197.2	metavolcanic rocks	APVG					9.5	47.3	0.1218	0.512115	-10.2	1714	21
Ellsworth Land	Haag Nunataks	-77	-78.3	R.2255.5	gneiss	volcanic rocks (not shown)	72	270	*0.772*	0.71579	2.7	15.0	0.1074	0.512232	-7.9	1316	22
Ellsworth Land	Haag Nunataks	-77	-78.3	R.2255.16	amphibolite	volcanic rocks (not shown)	72	494	*0.422*	0.70884	5.2	24.3	0.1296	0.512289	-6.8	1559	22
Ellsworth Land	Soholt Peaks	*-79.66*	*-84.4*	SP-3	basalt	volcanic rocks (not shown)	39	170	0.666	0.713398	2.2	6.7	0.1974	0.512831	3.8	2982	23
Ellsworth Land	Soholt Peaks	*-79.66*	*-84.28*	SP-1	basalt sill	volcanic rocks (not shown)					4.9	19.0	0.156	0.512767	2.5	1013	23
Ellsworth Land	Wilson Nunataks	*-80.01*	*-80.73*	WN-3	basalt	volcanic rocks (not shown)	30	298	0.752	0.70609	4.6	17.1	0.1635	0.512656	0.4	1500	23
Ellsworth Land	Wilson Nunataks	*-80.06*	*-80.55*	WN-4	basalt	volcanic rocks (not shown)	57	218	0.422	0.713524	22.0	108.2	0.123	0.512245	-7.7	1520	23
Ellsworth Land	Dunbar Ridge	*-79.61*	*-84.02*	DR-1	basalt	volcanic rocks (not shown)	42	286	0.856	0.709821	6.4	31.9	0.122	0.512365	-5.3	1305	23
Ellsworth Land	High Nunatak	*-80.05*	*-82.6*	HN-1	gabbro	volcanic rocks (not shown)	127	430	0.372	0.723997	4.0	18.5	0.1321	0.51232	-6.2	1549	23
Ellsworth Land	High Nunatak	*-80.08*	*-82.49*	HN-2	lamprophyre	volcanic rocks (not shown)	135	1051	0.343	0.706373	8.1	39.3	0.124	0.512465	-3.4	1165	23
Ellsworth Land	Moulder Peak	*-80.07*	*-82.91*	MP-1	basalt	volcanic rocks (not shown)	65	551	0.088	0.707885	9.2	50.0	0.1108	0.512298	-6.6	1262	23
Ellsworth Land	Moulder Peak	*-80.03*	*-83*	MP-5	basalt	volcanic rocks (not shown)	37	1211	0.121	0.707033	6.6	40.4	0.0991	0.512233	-7.9	1220	23
Ellsworth Land	Moulder Peak	*-80.13*	*-82.7*	MP-8	basalt	volcanic rocks (not shown)	18	429	*0.121*	0.705909	5.5	28.3	0.1169	0.512389	-4.9	1199	23
Alexander Island	Colbert Mountains	*-70.58*	*-70.58*	KG.4357.6B	pyroclastic	APVG	194	82	*6.850*	0.71067	3.7	23.0	0.0959	0.512705	1.3	577	24
Alexander Island	Colbert Mountains	*-70.58*	*-70.58*	KG.4361.2	plutonic	APVG	71	458	*0.449*	0.70788	5.1	24.2	0.1279	0.512633	-0.1	920	24
Alexander Island	Colbert Mountains	*-70.58*	*-70.58*	KG.4367.1A	lava	APVG	31	487	*0.184*	0.704598	5.2	23.5	0.1334	0.512715	1.5	827	24
Alexander Island	Colbert Mountains	*-70.58*	*-70.58*	KG.4374.1A	lava	APVG	56	421	*0.385*	0.705026	5.3	24.7	0.1305	0.512726	1.7	778	24
Alexander Island	Colbert Mountains	*-70.58*	*-70.58*	KG.4381.3C	pyroclastic	APVG	85	109	*2.257*	0.707698	4.9	25.1	0.1181	0.512654	0.3	792	24
Alexander Island	Colbert Mountains	*-70.58*	*-70.58*	KG.4387.1	pyroclastic	APVG	88	307	*0.829*	0.705676	3.1	13.2	0.1424	0.512687	1.0	991	24
Alexander Island	Elgar Uplands	*-69.65*	*-70.72*	KG.4400.1	lava	APVG	36	692	*0.151*	0.705887	4.7	24.3	0.1175	0.512669	0.6	763	24
Alexander Island	Elgar Uplands	*-69.65*	*-70.72*	KG.4411.2A	lava	APVG	59	431	*0.396*	0.704932	4.3	20.5	0.1269	0.51276	2.4	686	24
Alexander Island	Finlandia Foothills	*-69.93*	*-70.15*	KG.2015.1	lava	APVG	58	317	*0.529*	0.704885	3.6	16.6	0.1314	0.512787	2.9	674	24
Alexander Island	Geode Nunataks	*-69.83*	*-70.08*	KG.4402.1C	lava	APVG	60	411	*0.422*	0.70355	5.6	28.2	0.1196	0.512885	4.8	430	24
Alexander Island	Geode Nunataks	*-69.83*	*-70.08*	KG.4403.4	lava	APVG	6	496	*0.035*	0.704734	4.0	17.9	0.1343	0.512767	2.5	737	24
Alexander Island	Geode Nunataks	*-69.83*	*-70.08*	KG.4404.5A	lava	APVG	38	378	*0.291*	0.704869	4.0	16.5	0.1455	0.512762	2.4	869	24
Alexander Island	Arenite Ridge	*-69.7*	*-69.5*	KG.1969.1	metasedimentary rocks	LeMay Group	133	242	1.589	0.714746	7.7	36.4	0.1285	0.512405	-4.5	1333	17
Alexander Island	Central Douglas Range	*-70.0*	*-69.6*	KG.1967.2	metasedimentary rocks	LeMay Group	101	167	1.75	0.71472	6.5	30.7	0.1272	0.51234	-5.8	1427	17
Alexander Island	South Douglas Range	*-70.0*	*-69.6*	KG.2027.2	metasedimentary rocks	LeMay Group	206	365	1.635	0.712679	7.8	38.8	0.1214	0.512265	-7.3	1461	17
Alexander Island	N of Lemay Range	*-70.9*	*-69.3*	KG.4822.1	metasedimentary rocks	LeMay Group	242	234	2.993	0.716829	8.2	40.0	0.1235	0.512293	-6.7	1448	17
Alexander Island	N of Lemay Range	*-70.9*	*-69.3*	KG.4822.2	metasedimentary rocks	LeMay Group	209	150	4.034	0.719792	7.7	37.9	0.1228	0.512295	-6.7	1433	17
Alexander Island	N of Lemay Range	*-70.9*	*-69.3*	KG.4822.3	metasedimentary rocks	LeMay Group	180	367	1.422	0.712998	7.1	35.3	0.1211	0.512311	-6.4	1381	17
Alexander Island	Charcot Island	*-69.8*	*-75.3*	KG.4831.1	metasedimentary rocks	LeMay Group					5.1	32.1	0.0953	0.512213	-8.3	1206	17
Alexander Island	LeMay Range	*-69.8*	*-75.3*	KG.4836.1	metasedimentary rocks	LeMay Group	134	158	2.275	0.711171	5.6	28.2	0.1208	0.512437	-3.9	1170	17
Alexander Island	LeMay Range	*-69.8*	*-75.3*	KG.4836.2	metasedimentary rocks	LeMay Group	115	161	2.074	0.710633	5.7	28.7	0.1208	0.512451	-3.6	1147	17
Alexander Island	LeMay Range	*-69.8*	*-75.3*	KG.4836.3	metasedimentary rocks	LeMay Group	124	205	1.753	0.71005	5.8	29.4	0.1194	0.512427	-4.1	1169	17
Alexander Island	LeMay Range	*-69.8*	*-75.3*	KG.4845.1	metasedimentary rocks	LeMay Group	134	236	1.643	0.710014	5.8	29.0	0.1199	0.512416	-4.3	1193	17
Alexander Island	LeMay Range	*-69.8*	*-75.3*	KG.4845.2	metasedimentary rocks	LeMay Group	122	247	1.426	0.709459	5.9	29.0	0.1234	0.512475	-3.2	1140	17
Alexander Island	LeMay Range	*-69.8*	*-75.3*	KG.4845.3	metasedimentary rocks	LeMay Group	140	252	1.605	0.709811	5.4	28.1	0.1156	0.512436	-3.9	1110	17
Alexander Island	LeMay Range	*-69.8*	*-75.3*	KG.4845.5	metasedimentary rocks	LeMay Group	94	277	0.978	0.708796	5.3	26.5	0.1197	0.512443	-3.8	1147	17
Alexander Island	LeMay Range	*-69.8*	*-75.3*	KG.4847.1	metasedimentary rocks	LeMay Group	120	92	3.748	0.713807	5.5	27.0	0.123	0.512428	-4.1	1214	17
Alexander Island	LeMay Range	*-69.8*	*-75.3*	KG.4847.2	metasedimentary rocks	LeMay Group	116	97	3.445	0.71325	6.0	29.1	0.1235	0.512425	-4.2	1225	17
Alexander Island	LeMay Range	*-69.8*	*-75.3*	KG.4847.3	metasedimentary rocks	LeMay Group	81	99	2.373	0.711404	4.6	22.2	0.1247	0.512445	-3.8	1208	17
Alexander Island	Walton Mtns.	*-71.2*	*-70.3*	KG.4869.1A	metasedimentary rocks	LeMay Group	199	113	5.104	0.724089	8.5	44.5	0.1148	0.512248	-7.6	1390	17
Alexander Island	Walton Mtns.	*-71.2*	*-70.3*	KG.4869.1D	metasedimentary rocks	LeMay Group	222	65	9.853	0.740885	7.3	37.2	0.1191	0.512219	-8.2	1499	17
Alexander Island	Walton Mtns.	*-71.2*	*-70.3*	KG.4869.3	metasedimentary rocks	LeMay Group					5.7	30.6	0.1135	0.512313	-6.3	1273	17
Thurston Island	Lepley Nunatak	*-73.12*	*-90.32*	R.3032.2	granodiorite	Mesozoic granitoids	64	638	0.2888	0.706921	3.7	17.8	0.1248	0.512454	-3.6	1194	8
Thurston Island	Belknap Nunatak	*-72.5*	*-97.6*	R.3037.3	granite	Mesozoic granitoids	106	265	1.16	0.707798	5.5	26.1	0.1285	0.512556	-1.6	1064	8
Thurston Island	Belknap Nunatak	*-72.5*	*-97.6*	R.3037.9	granite	Mesozoic granitoids	158	149	3.063	0.711	4.5	24.4	0.111	0.512531	-2.1	920	8
Thurston Island	Belknap Nunatak	*-72.5*	*-97.6*	R.3038.1	granite	Mesozoic granitoids					0.2	0.8	0.1405	0.51261	-0.5	1125	8
Thurston Island	McNamara Island	*-72.6*	*-93.23*	R.3033.1	granite	Mesozoic granitoids	123	248	1.388	0.707938	2.2	13.7	0.0967	0.512568	-1.4	759	8
Thurston Island	Belknap Nunatak	*-72.5*	*-97.6*	R.3037.2	gabbro	Mesozoic granitoids	5	564	0.0254	0.705735	3.5	14.0	0.1497	0.512562	-1.5	1401	8
Thurston Island	Belknap Nunatak	*-72.5*	*-97.6*	R.3037.5	diorite	Mesozoic granitoids	31	395	0.2272	0.706069	2.9	12.2	0.1411	0.512583	-1.1	1191	8
Thurston Island	McNamara Island	*-72.6*	*-93.23*	R.3145.5	gabbro	Mesozoic granitoids	8	492	0.0443	0.705576	1.9	7.9	0.1425	0.512554	-1.6	1276	8

Thurston Island	Harrison Nunatak	*-72.52*	*-96.03*	R.3130.4	gabbro	Mesozoic granitoids	10	686	0.0417	0.705703	1.0	4.0	0.1499	0.512596	-0.8	1324	8
Thurston Island	Dustin Island	*-72.57*	*-94.8*	R.3017.1	gabbro	Mesozoic granitoids	8	628	0.0384	0.705568	1.1	4.4	0.1505	0.51265	0.2	1207	8
Thurston Island	Dustin Island	*-72.57*	*-94.8*	R.3017.5	gabbro	Mesozoic granitoids	15	420	0.1048	0.705738	2.5	9.6	0.1565	0.512575	-1.2	1532	8
Thurston Island	Landfall Peak	*-72*	*-102.02*	R.3023.1	diorite	Mesozoic granitoids	34	663	0.1473	0.705564	4.7	20.0	0.1414	0.512467	-3.3	1440	8
Thurston Island	Landfall Peak	*-72*	*-102.02*	R.3023.3	porphyry-granite	Mesozoic granitoids	82	383	0.613	0.70672	4.8	29.6	0.0988	0.512364	-5.3	1043	8
Thurston Island	Henderson Knob	*-72.15*	*-101.2*	R.3024.1	Granite	Mesozoic granitoids	103	565	0.5257	0.706029	11.1	61.4	0.1091	0.512535	-2.0	897	8
Thurston Island	Henderson Knob	*-72.15*	*-101.2*	R.3133.5	granite	Mesozoic granitoids	167	209	2.3132	0.709866	6.0	31.4	0.115	0.512532	-2.1	955	8
Thurston Island	Hale Glacier	*-72.22*	*-100.55*	R.3025.1	granite	Mesozoic granitoids	141	84	4.8443	0.715139	5.3	33.0	0.0971	0.512548	-1.8	788	8
Thurston Island	Mount Borgeson	*-72.2*	*-99*	R.3030.1	granite	Mesozoic granitoids	141	187	2.18	0.709739	5.8	37.4	0.0934	0.512485	-3.0	844	8
Thurston Island	Long Glacier	*-72.5*	*-96.72*	R.3022.2	granodiorite	Mesozoic granitoids	104	274	1.101	0.70752	4.1	23.2	0.1062	0.512461	-3.5	978	8
Thurston Island	Langhofer Island	*-72.53*	*-93.03*	R.3034.2	granite	Mesozoic granitoids	122	296	1.195	0.707768	3.3	17.1	0.1171	0.51249	-2.9	1042	8
Thurston Island	Mount Feury	*-71.83*	*-98.32*	R.3027.3	gabbro	Palaeozoic granitoids	2	178	0.0368	0.704324	0.3	1.0	0.1694	0.512564	-1.4	2014	8
Thurston Island	Mount Feury	*-71.83*	*-98.32*	R.3027.5	gabbro	Palaeozoic granitoids	2	230	0.0221	0.704169	0.6	1.6	0.2433	0.512751	2.2	-2068	8
Thurston Island	Guy Peaks	*-72.15*	*-98.88*	R.3139.3	diorite	Palaeozoic granitoids	5	692	0.019	0.705031	3.1	14.1	0.1315	0.512388	-4.9	1413	8
Thurston Island	Morgan Inlet	*-72.27*	*-95.9*	R.3019.1	gneiss	Palaeozoic granitoids					3.1	17.6	0.1082	0.512552	-1.7	865	8
Thurston Island	Morgan Inlet	*-72.27*	*-95.9*	R.3035.3	gneiss	Palaeozoic granitoids	46	864	0.1538	0.704707	3.1	16.9	0.1108	0.512466	-3.4	1014	8
Thurston Island	Morgan Inlet	*-72.27*	*-95.9*	R.3147.6	gneiss	Palaeozoic granitoids					4.2	19.0	0.1323	0.512599	-0.8	1033	8
Thurston Island	Morgan Inlet	*-72.27*	*-95.9*	R.3127.1	gabbro	Palaeozoic granitoids	3	505	0.0181	0.704761	3.0	9.2	0.1944	0.5126	-0.7	4319	8
Thurston Island	Mount Bramhall	*-72.25*	*-98.27*	R.3031.1	diorite	Palaeozoic granitoids	61	836	0.211	0.707269	7.2	36.2	0.1194	0.512321	-6.2	1340	8
Thurston Island	Mount Bramhall	*-72.25*	*-98.27*	R.3031.2	diorite	Palaeozoic granitoids	66	825	0.2294	0.707263	7.0	34.5	0.123	0.512354	-5.5	1338	8
Jones Mountains	Jones Mountains	*-73.53*	*-94*	R.3007.1	granite	Evolved Granitoids	380	93	11.92	0.743479	4.8	23.7	0.1215	0.512195	-8.6	1577	8
Jones Mountains	Jones Mountains	*-73.53*	*-94*	R.3007.7	granite	Evolved Granitoids	414	66	18.28	0.761782	3.7	18.5	0.1208	0.512253	-7.5	1471	8
Ruppert-Hobbs Coast	Milan Rock	*-76.02*	*-140.68*	MB.221.1W	metasedimentary rocks	Paleozoic metasedimentary	147	49	8.7495	0.7618	7.8	40.1	0.1175	0.511953	-13.4	1893	25
Ruppert-Hobbs Coast	Brunner Hill	*-75.57*	*-141.90*	MB.206.2P	microgranite	Evolved Granitoids	178	53	9.693	0.758429	2.2	9.6	0.1411	0.512345	-5.7	1688	25
Ruppert-Hobbs Coast	Mt McCoy	*-75.87*	*-141.17*	MB.201.5P	Granodiorite	Palaeozoic granitoids					4.0	23.9	0.1009	0.512594	-0.9	752	25
Ruppert-Hobbs Coast	Patton Bluff	*-75.22*	*-133.67*	MB.208.7P	Paragneiss enclave	Palaeozoic granitoids	164	341	1.393	0.71154	6.2	33.4	0.113	0.51238	-5.0	1166	25
Ford Ranges	Sarnoff Mountains	*-77.17*	*-145.00*	9D12-2	granite	Evolved Granitoids			21.53	0.7413	9.8	34.6	0.1713	0.5124	-4.6	2687	26
Ford Ranges	unnamed nunatak SW of Mt Iphigene	*-76.54*	*-146.10*	K6-NU01	granite	Evolved Granitoids			23.3		2.8	7.3	0.2329	0.5124	-4.6	-6060	26
Ford Ranges	Fosdick Mountains	*-76.46*	*-145.49*	K6-A21b	Granite	Palaeozoic granitoids			1.36	0.7151	6.8	38.9	0.1053	0.5122	-8.5	1335	26
Ford Ranges	Fosdick Mountains	*-76.54*	*-145.82*	C5-Is51A	Granite	Palaeozoic granitoids			7.6	0.753	7.9	38.8	0.1228	0.5121	-10.5	1758	26
Ford Ranges	Fosdick Mountains	*-76.52*	*-146.01*	K6-I60	Granite	Palaeozoic granitoids			1.37	0.7127	5.6	29.7	0.113	0.5123	-6.6	1287	26
Ford Ranges	Fosdick Mountains	*-76.05*	*-146.05*	K6-T35b	Granite	Palaeozoic granitoids			1.78	0.7151	4.3	24.3	0.1067	0.5123	-6.6	1211	26
Ford Ranges	Fosdick Mountains	*-77.16*	*-144.94*	912-2A	Granodiorite	Palaeozoic granitoids			7.1	0.7411	9.4	50.1	0.1137	0.5123	-6.6	1295	26
Ford Ranges	Fosdick Mountains	*-76.97*	*-144.55*	9N27-4	Granodiorite	Palaeozoic granitoids			0.88	0.7106	4.0	20.2	0.1198	0.5123	-6.6	1379	26
Ford Ranges		*-76.88*	*-145.70*	D1/3	Granodiorite	Palaeozoic granitoids					6.1	30.5	0.121	0.512336	-5.9	1338	27
Ford Ranges		*-76.97*	*-143.75*	R7205	Granodiorite	Palaeozoic granitoids					7.1	36.8	0.1164	0.512275	-7.1	1370	27
Ford Ranges		*-77.17*	*-145.00*	R7460	Granodiorite	Palaeozoic granitoids					5.5	31.8	0.1045	0.512282	-6.9	1212	27
Ford Ranges		*-76.66*	*-145.46*	MB.227.4P	Granodiorite	Palaeozoic granitoids	194	224	2.5089	0.720272	10.9	60.4	0.1092	0.512261	-7.4	1297	27
Ford Ranges		*-76.23*	*-143.86*	MB.219.2P	Granodiorite	Palaeozoic granitoids	89	337	0.7654	0.708903	4.0	20.1	0.1204	0.512428	-4.1	1180	27
Ford Ranges	Swanson Range	*-77.01*	*-144.88*	K6-SR29	metasedimentary rocks	Paleozoic metasedimentary	216	95	6.56	0.7585	7.6	42.8	0.107	0.512	-12.4	1641	26
Ford Ranges	Swanson Range	*-77.01*	*-144.88*	K6-SR30	metasedimentary rocks	Paleozoic metasedimentary	171	112	4.41	0.7449	7.9	38.2	0.1246	0.512	-12.4	1963	26
Ford Ranges	Swanson Range	*-77.01*	*-144.88*	K6-SR31	metasedimentary rocks	Paleozoic metasedimentary	118	136	2.5	0.732	7.2	37.9	0.1156	0.512	-12.4	1784	26
Ford Ranges	Swanson Range	*-77.01*	*-144.88*	K6-SR32	metasedimentary rocks	Paleozoic metasedimentary	135	199	1.96	0.7264	6.0	27.9	0.1304	0.5121	-10.5	1918	26
Edward VII Peninsula	Bowman Peak	*-77.48*	*-153.22*	E7W10	granite	Evolved Granitoids	391	25	45.1	0.7411			0.1352	0.512314	-6.3	1622	27
Edward VII Peninsula	Mt Schlossbach	*-78.05*	*-154.80*	E7W67	granite	Evolved Granitoids				0.784722			0.1896	0.512325	-6.1	5168	27
Edward VII Peninsula	Washington Ridge	*-78.10*	*-154.80*	E7W74	granite	Evolved Granitoids							0.1805	0.512348	-5.7	3661	27
Edward VII Peninsula	Gould Peak	*-78.12*	*-155.25*	E7W87	granite	Evolved Granitoids	372	45	24.1				0.1432	0.512233	-7.9	1979	27
Edward VII Peninsula	Mt Paterson	*-78.03*	*-154.60*	E7W90	granite	Evolved Granitoids	279	112	7.22	0.74691			0.1226	0.512196	-8.6	1595	27
Marie Byrd Land	Mt Murphy	*-75.33*	*-110.73*	62	alkali basalt	Cenozoic alkali basalt	10	548	0.054	0.70288	5.1	22.4	0.1377	0.51288	4.7	543	15
Marie Byrd Land	Mt Steere	*-76.73*	*-117.82*	70	alkali basalt	Cenozoic alkali basalt	33	713	0.1334	0.70271	7.0	37.2	0.1148	0.51298	6.7	263	15
Marie Byrd Land	Coleman Nunatak	*-75.32*	*-133.65*	77-35	alkali basalt	Cenozoic alkali basalt	37	1059	0.0999	0.70273	10.6	56.4	0.115	0.51293	5.7	341	15
Marie Byrd Land	Mt Cumming	*-76.67*	*-125.8*	26A	alkali basalt	Cenozoic alkali basalt	41	771	0.155	0.70286	8.1	40.8	0.1203	0.51298	6.7	278	15
Marie Byrd Land	Shibuya Peak	*-75.17*	*-133.58*	6C	alkali basalt	Cenozoic alkali basalt	24	873	0.0803	0.7028	6.9	34.5	0.1225	0.51295	6.1	335	15

Marie Byrd Land	Kouperov Pk	*-75.1*	*-133.8*	7-47B	alkali basalt	Cenozoic alkali basalt	24	803	0.0853	0.70268	8.0	40.2	0.1217	0.51298	6.7	283	15
Marie Byrd Land	Holmes Bluff	*-74.98*	*-133.72*	77-48B	alkali basalt	Cenozoic alkali basalt	14	558	0.0704	0.70258	5.5	26.6	0.125	0.51296	6.3	328	15
Marie Byrd Land	Mt Hampton	*-76.48*	*-125.8*	22D	alkali basalt	Cenozoic alkali basalt	41	805	0.1488	0.70278	9.4	50.3	0.114	0.51297	6.5	276	15
Marie Byrd Land	Mt Flint	*-75.73*	*-129.1*	9D	alkali basalt	Cenozoic alkali basalt	41	824	0.143	0.7029	8.7	43.0	0.1231	0.51286	4.3	489	15
Marie Byrd Land	Mt Petras	*-75.86*	*-128.64*	PT67D	alkali basalt	Cenozoic alkali basalt	46	791	0.1663	0.70309	9.4	53.2	0.1077	0.51287	4.5	404	15
Marie Byrd Land	Mt Murphy	*-75.33*	*-110.73*	60A	alkali basalt	Cenozoic alkali basalt	11	941	0.034	0.70322	2.9	13.7	0.1297	0.51285	4.1	546	15
Marie Byrd Land	Coleman Nunatak	*-75.32*	*-133.65*	46D	alkali basalt	Cenozoic alkali basalt	38	1045	*0.104*	0.702843	11.7	59.0	*0.1200*	0.512873	4.6	452	28
Marie Byrd Land	Coleman Nunatak	*-75.32*	*-133.65*	46I	alkali basalt	Cenozoic alkali basalt	37	1047	*0.101*	0.702809	11.8	58.3	*0.1227*	0.512919	5.5	388	28
Marie Byrd Land	Coleman Nunatak	*-75.32*	*-133.65*	46B	alkali basalt	Cenozoic alkali basalt	38	1076	*0.103*	0.702815	11.6	57.3	*0.1224*	0.512883	4.8	447	28
Marie Byrd Land	Coleman Nunatak	*-75.32*	*-133.65*	35E	alkali basalt	Cenozoic alkali basalt	37	1028	*0.103*	0.702858	11.9	57.7	*0.1247*	0.512908	5.3	416	28
Marie Byrd Land	Coleman Nunatak	*-75.32*	*-133.65*	35I	alkali basalt	Cenozoic alkali basalt	37	1046	*0.101*	0.70283	11.8	58.1	*0.1224*	0.512894	5.0	429	28
Marie Byrd Land	Coleman Nunatak	*-75.32*	*-133.65*	35M	alkali basalt	Cenozoic alkali basalt	39	1071	*0.106*	0.702807	11.8	57.9	*0.1232*	0.512908	5.3	409	28
Marie Byrd Land	Coleman Nunatak	*-75.32*	*-133.65*	35K	alkali basalt	Cenozoic alkali basalt	37	1040	*0.103*	0.702833	11.3	58.3	*0.1176*	0.5129	5.1	398	28
Marie Byrd Land	Cousins Rock	*-75.27*	*-133.52*	36B	alkali basalt	Cenozoic alkali basalt	36	953	*0.108*	0.702883	10.9	57.7	*0.1144*	0.512892	5.0	397	28
Marie Byrd Land	Patton Bluff	*-75.22*	*-133.67*	37A	alkali basalt	Cenozoic alkali basalt	23	652	*0.100*	0.702758	7.4	33.8	*0.1320*	0.512961	6.3	354	28
Marie Byrd Land	Shibuya Peak	*-75.17*	*-133.58*	38A	alkali basalt	Cenozoic alkali basalt	25	829	*0.087*	0.702831	8.9	42.8	*0.1252*	0.512911	5.3	413	28
Marie Byrd Land	Kouperov Peak	*-75.1*	*-133.8*	47A	alkali basalt	Cenozoic alkali basalt	24	762	*0.090*	0.7027	8.9	41.8	*0.1289*	0.512952	6.1	357	28
Marie Byrd Land	Holmes Bluff	*-74.98*	*-133.72*	48B	alkali basalt	Cenozoic alkali basalt	15	576	*0.074*	0.702535	6.5	28.5	*0.1377*	0.513008	7.2	286	28
Marie Byrd Land	Holmes Bluff	*-74.98*	*-133.72*	50A	alkali basalt	Cenozoic alkali basalt	28	900	*0.089*	0.702716	8.9	42.1	*0.1278*	0.512945	6.0	365	28
Marie Byrd Land	Scott Island	*-67.378*	*-179.911*	E-27-34c	alkali basalt	Cenozoic alkali basalt				0.702849				0.512989	6.8		28
Marie Byrd Land	Fosdick Mountains	/	/	66-D-91	alkali basalt	Cenozoic alkali basalt				0.703338				0.512859	4.3		28
Marie Byrd Land	Fosdick Mountains	/	/	66-D-30	alkali basalt	Cenozoic alkali basalt				0.703106				0.512948	6.0		28
Marie Byrd Land	Mt Siple	*-73.26*	*-126.67*	W83-5C	alkali basalt	Cenozoic alkali basalt				0.703487				0.512847	4.1		28
Marie Byrd Land	Mt Siple	*-73.26*	*-126.67*	W83-1	alkali basalt	Cenozoic alkali basalt				0.703723				0.512792	3.0		28
Marie Byrd Land	Mt Murphy	*-75.33*	*-110.73*	62	alkali basalt	Cenozoic alkali basalt				0.702917				0.512893	5.0		28
Marie Byrd Land	Mt Murphy	*-75.33*	*-110.73*	85-32B	alkali basalt	Cenozoic alkali basalt				0.703165				0.512839	3.9		28
Marie Byrd Land	Hudson Mountains	*-74.33*	*-99.42*	24-1-A	alkali basalt	Cenozoic alkali basalt				0.702904				0.51298	6.7		28
Marie Byrd Land	Hudson Mountains	*-74.33*	*-99.42*	9-1-C	alkali basalt	Cenozoic alkali basalt				0.703366				0.512859	4.3		28
Marie Byrd Land	Hudson Mountains	*-74.33*	*-99.42*	20-2B	alkali basalt	Cenozoic alkali basalt				0.703026				0.512928	5.7		28

a) see Figure 2.2

b) approximate coordinates in italics

c) 1) Ryan, 2005; 2) Flowerdew et al., 2005; 3) Mukasa and Dalziel, 2000; 4) Luyendyk et al., 1996; 5) Vaughan et al., 1998; 6) Vaughan et al., 2002; 7) Vaughan et al., 2012; 8) Pankhurst et al., 1993; 9) Kipf et al., 2012; 10) Adams et al., 1987; 11) Richard et al., 1994; 12) Adams et al., 1995; 13) Wilch and McIntosh, 2000; 14) LeMasurier and Rex, 1989; 15) Futa and LeMasurier, 1983; 16) Adams et al., 1986; 17) Adams et al., 2005; 18) Storey et al., 1984; 19) Riley et al., 2001; 20) Wever et al., 1994; 21) Wever et al., 1992; 22) Storey et al., 1994; 23) Curtis et al., 1999; 24) McCarron and Smellie, 1998; 25) Pankhurst et al., 1998; 26) Korhonen et al., 2010; 27) Weaver et al., 1992; 28) Hart et al., 1997; 29) Scarrow et al., 1998.

d) * Evolved rocks were assigned based on their distinct isotopic composition and discussion in Ryan, 2005

Appendix Table 2.3. Neodymium isotopic composition of five seafloor surface sediments ad one downcore sediment after applying a distinct leaching procedure compared to the standard procedure described in main text (e.g. Chapter 2). See Appendix Figure 2.3 for illustration of the results for the two leaching procedure on the same initial bulk sample.

Site location[a]	Core depth (cm)[b]	Size fraction	$^{143}Nd/^{144}Nd$[b]	± 2 S.E.	ε_{Nd}[d]	± 2 S.D.
BC442	0-1	< 63µm	0.512447	0.000012	-3.73	0.21
PS75/168-1	0-1	< 63µm	0.512407	0.000011	-4.51	0.21
PS58/254-1	109-110	< 63µm	0.512418	0.000013	-4.29	0.21
BC412	0-1	< 63µm	0.512499	0.000010	-2.72	0.21
BC459	0-1	< 63µm	0.512327	0.000010	-6.06	0.21
BC492X	0-1	< 63µm	0.512521	0.000012	-2.29	0.21

a) Bulk sediments were sieved at 63 micron and dried at 60°C. Approximately 1 g of <63 µm sediment was leached with buffered acetic acid to remove the biogenic carbonate. After centrifugation and decanting of the supernatant, loosely absorbed metals were extracted using 1 M $MgCl_2$ solution. After decanting, the dried residue was further leached for their authigenic (oxyhydroxide) fraction using a reducing and complexing solution consisting of 0.02 M hydroxylamine hydrochloride, 25% acetic acid and 0.03 M Na-EDTA solution, buffered with sodium acetate (based on Gutjahr et al., 2007).

b) Core depth for site PS58/254-1 is given as cm below seafloor (cmbsf)

c) All reported $^{143}Nd/^{144}Nd$ ratios are corrected to a JNdi value of 0.512115 (Tanaka et al., 2000). Average JNdi values for the analytical sessions was 0.512159 ± 0.000011 (n=21). Measurement on USGS BCR-2 standard yielded a $^{143}Nd/^{144}Nd$ value of 0.512640 ± 0.000007 (n=4), in agreement with the accepted value of 0.512637 ± 0.000014 (Weis et al., 2006).

d) ε_{Nd} values were calculated using a present day $^{143}Nd/^{144}Nd$ (CHUR) of 0.512638 (Jacobsen and Wasserburg, 1980). The error reported represents the external 2σ SD of the analytical session.

Appendix Table 3.1. $^{40}Ar/^{39}Ar$ data for ice-rafted (>150μm) hornblende and biotite grains from the Pine Island Bay, West Antarctica.

run ID	sample	Ca/K[a]	Cl/K	moles 39	%rad	Age (Ma)	err (Ma) internal
30427-01A	PS69-291-1-6cm	6.626	0.006	0.01	12.4	3.0	4.6
30429-04A	PS69-291-1-7cm	5.980	-0.039	0.005	10.6	3.3	8.1
30432-07A	PS69-291-1-9cm	0.008	0.012	0.018	82.6	110.8	2.6
30432-04A	PS69-291-1-9cm	0.437	0.005	0.007	40.3	112.4	6.4
30432-06A	PS69-291-1-9cm	0.007	0.001	0.041	91.4	113.5	1.2
30426-02A	PS69-291-1-5cm	0.090	-0.008	0.018	78.3	114.7	2.6
30426-01A	PS69-291-1-5cm	0.090	-0.015	0.018	56.5	115.0	3.0
30432-02A	PS69-291-1-9cm	0.009	-0.005	0.052	85.6	115.7	1.0
30432-05A	PS69-291-1-9cm	0.035	0.001	0.066	95.6	116.1	0.9
30429-01A	PS69-291-1-7cm	0.062	-0.034	0.008	84.9	116.8	5.2
30432-01A	PS69-291-1-9cm	0.006	-0.001	0.046	91.9	118.0	1.0
30432-08A	PS69-291-1-9cm	0.064	0.005	0.021	62.8	123.4	2.3
30427-03A	PS69-291-1-6cm	7.661	0.003	0.186	69.9	127.7	1.0
30431-03A	PS69-291-1-8cm	0.056	-0.004	0.01	85.1	143.8	4.3
30427-04A	PS69-291-1-6cm	0.529	-0.027	0.005	44.2	151.0	10.0
30431-02A	PS69-291-1-8cm	8.934	0.030	0.006	58.6	200.6	8.2
30432-03A	PS69-291-1-9cm	0.092	0.001	0.126	92.4	209.1	0.9
30427-02A	PS69-291-1-6cm	9.297	0.013	0.007	9.8	246.1	25.1
30434-04A	PS69-295-1-3cm	0.037	0.006	0.015	49.4	101.2	3.0
30438-10A	PS69-295-1-6cm	0.040	0.020	0.008	65.7	104.5	6.7
30437-02A	PS69-295-1-5cm	0.079	0.002	0.021	85	112.9	2.1
30438-03A	PS69-295-1-6cm	0.019	0.000	0.61	84	113.0	0.5
30433-02A	PS69-295-1-2cm	0.045	0.000	0.156	94.9	113.2	0.6
30434-01A	PS69-295-1-3cm	0.001	-0.001	0.067	97.1	113.8	0.8
30434-05A	PS69-295-1-3cm	-0.015	0.002	0.07	88.8	114.2	1.0
30437-03A	PS69-295-1-5cm	0.035	0.000	0.288	97.6	114.7	0.4
30438-08A	PS69-295-1-6cm	0.018	0.005	0.031	96.4	115.1	1.4
30438-02A	PS69-295-1-6cm	4.510	-0.001	0.07	59.9	116.0	1.4
30433-01A	PS69-295-1-2cm	6.614	0.003	0.068	79.6	116.5	0.9
30437-05A	PS69-295-1-5cm	1.263	0.002	0.103	83.9	116.7	0.7
30438-01A	PS69-295-1-6cm	150.308	-0.083	0.002	22.6	117.5	22.2
30438-06A	PS69-295-1-6cm	0.096	0.004	0.016	86.2	120.8	2.9
30437-04A	PS69-295-1-5cm	0.025	0.014	0.021	96.3	121.9	2.1
30434-03A	PS69-295-1-3cm	-0.046	0.004	0.024	108	122.9	3.2
30437-01A	PS69-295-1-5cm	4.512	-0.002	0.007	28.6	123.2	6.7
30438-09A	PS69-295-1-6cm	-0.025	0.007	0.022	94.2	137.5	2.2
30433-03A	PS69-295-1-2cm	-0.112	0.005	0.011	89.3	140.0	4.2
30438-05A	PS69-295-1-6cm	0.032	0.002	0.018	89.4	145.1	2.4
30436-01A	PS69-295-1-4cm	-0.011	0.016	0.023	91.6	145.2	2.0
30438-07A	PS69-295-1-6cm	10.158	-0.028	0.004	65	181.8	11.1
30436-03A	PS69-295-1-4cm	0.021	0.025	0.004	42	185.0	10.5
30438-04A	PS69-295-1-6cm	0.042	-0.020	0.016	78.7	197.5	3.0
30434-02A	PS69-295-1-3cm	0.300	0.007	0.006	82.9	217.5	7.4
30437-06A	PS69-295-1-5cm	31.445	0.001	0.005	40.5	250.9	10.9
30437-07A	PS69-295-1-5cm	0.074	-0.008	0.022	96.4	265.0	2.2
30445-03A	PS75-173-1-7cm	6.314	0.030	0.009	7.2	17.0	7.6
30442-02A	PS75-173-1-5cm	0.310	0.001	0.06	92.4	114.6	1.0
30444-01A	PS75-173-1-6cm	-0.137	0.012	0.011	97.1	116.8	3.9
30444-04A	PS75-173-1-6cm	0.212	-0.013	0.016	53.6	119.6	3.6
30440-04A	PS75-173-1-3cm	-0.049	-0.006	0.033	100.3	122.0	1.4
30440-06A	PS75-173-1-3cm	-0.005	0.002	0.011	91.1	122.2	4.0
30444-05A	PS75-173-1-6cm	-0.003	0.022	0.016	45.8	128.2	3.9
30440-03A	PS75-173-1-3cm	-0.016	0.001	0.039	95.3	128.5	1.4
30441-01A	PS75-173-1-4cm	-0.006	0.002	0.038	99.4	129.4	1.2
30442-01A	PS75-173-1-5cm	0.018	0.004	0.023	94.1	147.9	2.1
30445-01A	PS75-173-1-7cm	-0.048	-0.071	0.004	14.8	192.5	18.0
30444-02A	PS75-173-1-6cm	11.504	-0.024	0.003	91.5	251.7	15.6
30445-02A	PS75-173-1-7cm	9.880	0.041	0.003	50.1	279.6	21.9
30440-01A	PS75-173-1-3cm	15.554	-0.031	0.002	71.3	290.0	17.0
30441-02A	PS75-173-1-4cm	9.308	-0.001	0.004	90.5	300.5	10.5
30440-02A	PS75-173-1-3cm	9.784	0.008	0.004	109	325.8	10.0
30440-05A	PS75-173-1-3cm	11.652	0.075	0.003	99.5	370.6	15.2
30446-10A	PS75-177-1-4cm	6.548	0.015	0.005	1	4.9	12.1
30447-03A	PS75-177-1-5cm	5.883	0.007	0.003	9	21.4	18.2

30447-07A	PS75-177-1-5cm	4.511	0.050	0.004	3.7	30.0	15.3
30447-24A	PS75-177-1-5cm	6.413	0.025	0.039	7.3	31.3	3.2
30447-13A	PS75-177-1-5cm	5.240	0.037	0.005	11.8	35.7	11.8
30447-18A	PS75-177-1-5cm	0.254	-0.001	0.095	85.5	113.1	0.7
30446-05A	PS75-177-1-4cm	0.072	0.007	0.041	80.5	114.2	1.5
30447-20A	PS75-177-1-5cm	0.042	-0.002	0.083	62.4	115.4	1.0
30446-01A	PS75-177-1-4cm	0.005	0.000	0.21	88.5	115.6	0.4
30447-17A	PS75-177-1-5cm	0.032	0.001	0.059	58.7	118.0	1.4
30447-08A	PS75-177-1-5cm	0.093	-0.002	0.011	42.3	122.8	5.2
30446-08A	PS75-177-1-4cm	-0.079	0.001	0.016	40.1	132.5	3.9
30447-05A	PS75-177-1-5cm	-0.065	0.008	0.014	51.3	135.2	4.1
30446-07A	PS75-177-1-4cm	1.029	0.046	0.002	9.2	137.0	31.1
30447-21A	PS75-177-1-5cm	0.273	0.006	0.018	61.3	141.9	3.4
30446-12A	PS75-177-1-4cm	-0.062	0.003	0.014	61	144.6	4.1
30447-02A	PS75-177-1-5cm	0.066	0.011	0.007	67.6	155.3	8.1
30447-12A	PS75-177-1-5cm	0.015	0.069	0.005	43.5	158.7	10.3
30447-22A	PS75-177-1-5cm	-0.008	0.008	0.008	59	159.0	7.7
30447-23A	PS75-177-1-5cm	-0.155	0.028	0.01	45.4	160.7	6.0
30447-01A	PS75-177-1-5cm	-0.072	0.000	0.016	67.5	169.4	3.8
30447-14A	PS75-177-1-5cm	0.013	0.005	0.025	66.8	177.1	2.4
30446-02A	PS75-177-1-4cm	8.159	-0.020	0.004	20.6	181.8	15.8
30447-09A	PS75-177-1-5cm	0.177	0.003	0.028	65.2	188.1	2.2
30446-04A	PS75-177-1-4cm	0.071	-0.002	0.014	76.5	189.6	4.1
30447-15A	PS75-177-1-5cm	0.120	0.009	0.046	53.5	206.0	2.1
30446-06A	PS75-177-1-4cm	0.094	-0.006	0.02	66.5	209.9	3.1
30446-03A	PS75-177-1-4cm	-0.044	0.002	0.019	81.8	213.9	3.0
30447-19A	PS75-177-1-5cm	-0.010	-0.002	0.009	52	223.4	5.9
30447-16A	PS75-177-1-5cm	0.121	0.010	0.053	45.8	258.3	2.6
30446-09A	PS75-177-1-4cm	13.412	-0.030	0.003	26.2	285.3	23.0
30447-04A	PS75-177-1-5cm	8.344	0.054	0.013	71.9	287.5	4.5
30447-10A	PS75-177-1-5cm	0.019	0.000	0.018	78.3	296.9	3.4
30446-11A	PS75-177-1-4cm	8.027	0.016	0.004	46.7	311.4	13.4
30448-26A	PS104-009-1-6cm	6.552	0.019	0.022	50.2	2.0	2.7
30448-25A	PS104-009-1-6cm	6.716	0.014	0.005	-169.4	5.6	10.4
30448-13A	PS104-009-1-6cm	6.513	0.028	0.006	63.4	140.5	10.2
30448-21A	PS104-009-1-6cm	0.027	0.002	0.033	98.4	172.8	1.7
30448-03A	PS104-009-1-6cm	-0.010	0.001	0.058	89.3	178.1	1.1
30448-22A	PS104-009-1-6cm	8.151	0.025	0.005	86.8	184.2	12.1
30448-23A	PS104-009-1-6cm	15.851	-0.008	0.003	77.1	186.4	16.2
30448-08A	PS104-009-1-6cm	12.856	0.073	0.004	25	186.8	16.6
30448-36A	PS104-009-1-6cm	0.127	0.003	0.129	97.1	187.7	0.6
30448-05A	PS104-009-1-6cm	0.027	0.002	0.113	86.9	192.7	0.8
30448-01A	PS104-009-1-6cm	0.074	0.000	0.21	79.6	195.6	0.7
30448-04A	PS104-009-1-6cm	0.014	0.000	0.047	44.1	204.8	2.4
30448-16A	PS104-009-1-6cm	0.031	-0.001	0.043	85.2	206.2	1.5
30448-06A	PS104-009-1-6cm	0.085	0.010	0.026	66.9	207.0	2.5
30448-19A	PS104-009-1-6cm	13.218	0.064	0.003	84.8	208.1	15.8
30448-15A	PS104-009-1-6cm	11.562	0.011	0.006	60.7	218.2	9.5
30448-37A	PS104-009-1-6cm	8.430	0.085	0.003	78.9	225.8	22.0
30448-09A	PS104-009-1-6cm	0.056	0.026	0.025	21.3	227.9	6.2
30448-02A	PS104-009-1-6cm	0.159	0.001	0.394	91.4	229.5	0.5
30448-12A	PS104-009-1-6cm	8.529	0.013	0.006	74.4	230.5	8.8
30448-35A	PS104-009-1-6cm	8.149	0.063	0.007	72.1	234.7	8.7
30448-28A	PS104-009-1-6cm	8.937	0.019	0.005	38.3	240.6	11.9
30448-07A	PS104-009-1-6cm	11.065	0.056	0.005	56.4	241.5	9.7
30448-27A	PS104-009-1-6cm	9.094	0.060	0.005	13	245.4	15.8
30448-33A	PS104-009-1-6cm	6.826	-0.007	0.005	90.8	247.7	11.9
30448-14A	PS104-009-1-6cm	10.159	0.021	0.016	97.3	255.6	3.5
30448-34A	PS104-009-1-6cm	10.523	-0.044	0.004	84.2	263.7	15.4
30448-17A	PS104-009-1-6cm	5.916	0.087	0.005	9.6	313.2	21.6
30448-10A	PS104-009-1-6cm	6.877	0.103	0.005	6.4	543.0	45.8
12936-13	NBP99-02 53PC 24-29	0.476	0.009	0.609	27.5	19.4	0.4
12936-14	NBP99-02 53PC 24-29	27.855	0.053	0.006	16.5	57.2	6.4
12936-17	NBP99-02 53PC 24-29	57.028	0.014	0.126	17.7	58.7	1.6
12936-09	NBP99-02 53PC 24-29	3.973	0.017	0.026	11.4	90.4	4.4
12936-11	NBP99-02 53PC 24-29	13.478	0.003	0.195	20.1	90.6	2.0
12936-23	NBP99-02 53PC 24-29	3.360	0.000	0.086	28.2	95.7	1.8
12936-18	NBP99-02 53PC 24-29	4.867	0.006	0.372	55.6	96.6	1.1
12936-05	NBP99-02 53PC 24-29	5.278	0.002	0.572	79.2	98.8	1.1
12936-10	NBP99-02 53PC 24-29	0.242	0.004	0.777	52.2	99.1	1.2
12936-07	NBP99-02 53PC 24-29	0.091	0.004	0.314	81.4	99.8	1.1
12936-02	NBP99-02 53PC 24-29	27.765	0.052	0.27	55.3	100.7	1.2
12936-22	NBP99-02 53PC 24-29	0.039	0.003	1.266	95.7	100.9	1.0

12936-01	NBP99-02 53PC 24-29	10.185	0.016	0.465	40.8	101.5	1.3
12936-20	NBP99-02 53PC 24-29	0.748	-0.002	0.202	34.2	107.7	1.6
12936-04	NBP99-02 53PC 24-29	1.691	0.003	2.064	67.8	107.9	1.1
12936-24	NBP99-02 53PC 24-29	0.006	0.001	0.881	98	108.9	1.1
12936-08	NBP99-02 53PC 24-29	0.099	0.004	1.667	85.8	110.1	1.1
12936-06	NBP99-02 53PC 24-29	0.389	0.004	0.193	68.2	110.1	1.2
12936-16	NBP99-02 53PC 24-29	0.017	0.002	0.767	94.4	110.2	1.1
12936-12	NBP99-02 53PC 24-29	0.199	0.004	1.173	69.1	110.3	1.2
12936-25	NBP99-02 53PC 24-29	0.007	0.005	0.339	86.5	111.0	1.2
12936-19	NBP99-02 53PC 24-29	14.956	0.013	0.127	65.8	114.3	1.3
12936-15	NBP99-02 53PC 24-29	12.208	0.022	0.508	85.3	116.7	1.2
12936-03	NBP99-02 53PC 24-29	12.736	0.036	0.364	61.9	125.0	1.4
12936-21	NBP99-02 53PC 24-29	70.129	0.116	0.053	8.7	125.4	6.2

a) Mineral identification was primarily done based on the Ca/K ratio with hornblende grains usually > ~1 and biotite grains < 1

Appendix Table 3.2. Major and trace element data for fine (<63μm) detrital sediments from the Pine Island Bay, West Antarctica

				Major										Trace														
Number	**Site[a]**	**Depth**	**Sector**	**Na_2O**	**MgO**	**Al_2O_3**	**P_2O_5**	**K_2O**	**CaO**	**TiO_2**	**MnO**	**Fe_2O_3**	**Li**	**Sc**	**S**	**Ti**	**V**	**Cr**	**Co**	**Ni**	**Cu**	**Zn**	**Rb**	**Sr**	**Y**	**Zr**	**Nb**	**Mo**
1−1	PIG-B	2	sub-ice shelf PIG	1.22	1.41	13.6	0.06	3.86	0.46	0.77	0.05	4.25	42	10	61	4744	70	52	8	21	14	71	185	110	26	145	21.5	0.5
1−2	*PIG-B*	*52*		1.19	1.61	14.0	0.05	3.68	0.54	0.76	0.05	4.49	43	11	255	4744	74	59	9	21	17	73	173	109	28	190	19.9	0.5
2−1	PIG-A	2	sub-ice shelf PIG	1.35	1.84	15.1	0.07	3.98	0.55	0.83	0.05	4.96	51	13	47	5147	82	63	10	34	14	82	201	116	31	146	22.7	0.6
2−2	*PIG-A*	*48*		1.12	1.57	14.5	0.05	3.69	0.48	0.75	0.05	4.39	43	12	103	4642	73	58	9	19	13	66	173	103	31	161	19.3	0.5
2−3	*PIG-A*	*84*		1.11	1.67	14.5	0.05	3.85	0.51	0.77	0.05	4.66	45	12	177	4819	76	59	9	37	13	73	182	104	31	159	19.6	0.6
3−1	PIG-C	2	sub-ice shelf PIG	1.22	1.64	15.7	0.05	4.01	0.54	0.79	0.05	4.68	47	13	60	4822	77	57	9	21	15	74	192	110	31	145	21.6	0.8
3−2	*PIG-C*	*28*		1.10	1.74	15.3	0.05	3.93	0.50	0.79	0.05	4.85	47	13	226	4786	80	61	10	23	15	81	189	105	30	154	19.9	0.6
4	PS104/008-2	3.5	sub-ice shelf PIG	1.30	1.46	14.4	0.06	3.86	0.74	0.80	0.05	4.28	41	12	44	5064	73	57	8	19	12	66	182	122	30	148	21.3	0.5
5	PS104/013-2	5	eastern PIB	1.60	1.49	14.6	0.05	3.89	1.06	0.85	0.05	4.41	39	12	37	5056	76	49	9	16	11	65	183	160	31	139	21.7	0.5
6−1	PS104/012-2	5	eastern PIB	1.42	1.82	14.4	0.07	3.98	0.81	0.93	0.05	5.04	45	12	46	5555	83	70	11	24	14	78	194	124	30	154	23.7	0.5
6−2	*PS104/012-2*	*153*		1.74	3.33	14.4	0.12	3.24	1.68	1.24	0.09	7.05	41	16	49	7555	100	103	19	50	31	115	167	180	28	194	26.7	0.4
6−3	*PS104/012-2*	*173*		1.89	3.08	14.3	0.13	3.11	1.85	1.21	0.08	6.63	37	15	475	7438	101	115	16	43	24	101	156	198	27	199	25.1	1.1
6−4	*PS104/012-2*	*253*		1.83	3.11	14.2	0.13	3.04	1.90	1.21	0.08	6.58	37	15	426	7470	102	114	17	45	23	100	157	201	26	215	24.9	1.2
6−5	*PS104/012-2*	*313*		1.74	3.05	14.6	0.13	3.18	1.61	1.19	0.08	6.65	40	15	477	7210	102	106	17	45	25	104	167	180	29	201	25.4	1.1
7−1	NBP99-02 PC51	17-22	eastern PIB																									
7−2	*NBP99-02 PC51*	*30-38*																										
8−1	PS104/009-1	6	eastern PIB	1.86	1.60	15.9	0.11	4.10	0.79	0.78	0.06	4.61	48	12	40	4813	72	45	8	17	15	84	223	148	33	145	28.0	1.1
8−2	*PS104/009-1*	*223*		1.52	1.29	12.2	0.04	3.52	0.67	0.70	0.05	3.87	39	10	67	4310	62	44	8	15	11	71	185	127	28	139	22.3	0.8
8−3	*PS104/009-1*	*265*		1.83	1.26	14.3	0.05	3.85	1.01	0.79	0.06	4.06	42	11	209	4869	64	45	8	14	11	75	211	160	33	153	27.5	0.9
8−4	*PS104/009-1*	*505*		1.84	1.40	15.3	0.06	3.97	0.94	0.81	0.06	4.29	43	12	103	4642	73	58	9	19	13	66	173	103	31	161	19.3	0.5
9	NBP07-02 SMG8	Surface	eastern PIB																									
10	PS75/159-1[b]	0-1	eastern PIB										58	13		4624	81	53	10	24	18	101	213	133	30	134		
11	PS75/160-1	1	eastern PIB	1.76	1.75	15.8	0.07	4.00	0.99	0.84	0.06	5.03	45	14	73	5247	79	61	11	23	15	83	189	157	30	150	22.9	0.5
12	PS69/288-3	4	eastern PIB	1.42	1.96	15.1	0.07	4.11	0.71	0.86	0.06	5.50	51	13	126	5315	88	59	12	23	22	101	203	129	25	137	23.6	2.1
13−1	PS69/295-1	4	Central PIB	1.63	2.05	16.5	0.08	3.96	0.99	0.88	0.07	5.59	52	15	148	5354	93	57	12	32	27	111	201	157	31	165	26.8	1.9
13−2	*PS69/295-1*	*375*	*Central PIB*	1.70	2.00	14.2	0.10	3.26	1.54	0.97	0.07	5.22	35	13	95	5916	89	69	13	26	17	78	153	198	28	221	23.2	0.5
13−3	*PS69/295-1*	*474*		1.43	2.26	14.4	0.09	3.51	1.11	0.92	0.08	5.86	43	14	55	5573	89	62	15	31	22	93	169	158	29	181	24.3	0.8
14	PS69/291-1	7	*Central PIB*	1.55	1.99	16.7	0.08	4.04	0.80	0.89	0.07	5.57	53	15	134	5323	92	57	12	23	24	107	207	149	32	159	27.2	2.3
15	NBP99-02 53PC	*24-29*	*Central PIB*										50	14		4745	84	54	11	23	24	112	203	150	30	137		
16	PS69/292-2	3	western PIB	1.68	1.87	16.6	0.09	3.99	0.86	0.92	0.08	5.58	53	14	112	5754	92	52	11	21	22	107	205	166	34	197	35.6	9.0
17−1	PS75/167-1[b]	5	western PIB										58	13		5404	83	47	10	19	15	109	210	171	36	210		
17−2	*PS75/167-1*	*818*		1.61	1.83	16.2	0.07	4.31	0.64	0.86	0.07	5.44	55	12	44	5372	82	52	12	23	16	109	239	141	30	157	29.8	1.1
18	PS75/166-3	6	western PIB	1.62	1.51	16.4	0.12	3.63	0.93	0.97	0.07	5.51	47	13	138	6186	90	52	11	20	22	99	181	195	36	260	44.2	2.7
19−1	PS75/173-1	5	western PIB	1.62	2.06	16.4	0.09	3.78	0.93	0.89	0.10	5.91	52	15	180	5436	97	52	12	25	33	122	191	167	30	180	31.0	9.6
19−2	*PS75/173-1*	*195*		2.15	1.43	13.9	0.06	3.74	1.27	0.78	0.06	4.06	38	11	99	4822	67	48	8	16	12	109	197	195	30	166	25.9	0.8
20−1	PS75/177-1	5	western PIB	1.56	1.98	17.1	0.10	3.87	0.88	0.96	0.08	6.02	54	15	167	5985	97	56	13	25	25	124	202	160	33	203	36.4	5.5
20−2	*PS75/177-1*	*300*		2.28	1.93	16.3	0.09	3.48	1.41	0.92	0.09	5.84	46	14	49	5706	93	48	13	21	17	115	162	234	35	271	38.8	1.2
21	PS75/219-2	3	western PIB	1.72	1.65	15.7	0.09	3.61	0.87	0.88	0.06	5.16	52	13	171	5392	97	52	10	20	17	96	175	177	29	189	30.4	2.0
22−1	PS104/021-1	5	western PIB	1.69	2.15	17.7	0.10	3.98	0.88	0.93	0.07	6.19	55	16	115	5734	98	53	13	24	29	124	208	164	33	199	35.1	2.7
22−2	*PS104/021-1*	*77*		1.54	1.28	14.8	0.05	3.11	0.83	0.79	0.04	4.08	46	11	2447	4976	85	50	8	17	29	98	145	160	28	190	27.2	2.6
22−3	*PS104/021-1*	*103*		1.54	1.31	14.7	0.05	3.16	0.82	0.81	0.05	4.24	47	12	2243	5016	82	50	8	17	15	85	146	161	29	196	27.9	2.8
23	NBP07-02 SMG10	Surface	western PIB																									
24	NBP00-01 KC28	9-14	western PIB																									

Appendix Table 3.2. (*continued*)

Traces																						K_2O/Al_2O_3	MgO/Al_2O_3	Zr/Ti	Co/Yb
Sn	Sb	Cs	Ba	La	Ce	Pr	Nd	Sm	Eu	Gd	Tb	Dy	Ho	Ta	Er	Yb	Lu	Hf	Tl	Pb	Th	U				
6.5	0.9	9.6	656	40.3	88.3	8.6	31.8	5.8	1.0	4.6	0.7	4.2	0.9	1.6	2.5	2.4	0.4	4.1	1.3	23.9	15.9	3.2	0.284	0.104	0.030	3.34
6.4	1.0	9.1	624	40.1	85.2	8.8	32.9	6.1	1.0	4.9	0.8	4.4	0.9	1.6	2.6	2.6	0.4	5.1	1.2	20.1	15.3	3.1	0.262	0.115	0.040	3.56
7.6	1.1	11.2	675	42.2	88.3	9.5	35.3	6.7	1.2	5.3	0.9	4.9	1.0	1.6	2.9	2.9	0.4	3.9	1.3	20.7	16.8	3.1	0.263	0.122	0.028	3.33
6.4	1.0	9.0	622	41.0	84.0	9.4	35.9	6.8	1.1	5.5	0.9	5.0	1.0	1.4	3.0	2.9	0.4	4.4	1.2	18.4	15.5	2.9	0.255	0.109	0.035	3.00
6.6	1.1	9.7	634	40.5	83.8	9.2	34.6	6.6	1.1	5.2	0.8	4.8	1.0	1.5	2.9	2.9	0.4	4.3	1.2	18.7	15.5	3.1	0.266	0.115	0.033	3.31
7.1	1.0	10.5	673	43.5	88.5	9.9	36.9	7.0	1.2	5.6	0.9	5.0	1.0	1.6	3.0	3.1	0.4	4.0	1.3	22.1	16.4	3.0	0.256	0.105	0.030	2.87
6.8	1.1	10.5	663	41.6	84.9	9.4	35.4	6.7	1.1	5.2	0.8	4.7	1.0	1.4	2.8	2.8	0.4	4.3	1.3	21.0	16.4	3.4	0.257	0.114	0.032	3.47
6.3	0.9	9.0	651	42.5	86.3	9.6	35.9	6.8	1.2	5.5	0.9	4.9	1.0	1.5	2.9	2.9	0.4	4.0	1.2	24.0	14.2	2.7	0.269	0.102	0.029	2.92
6.2	0.8	8.3	674	43.2	87.6	9.7	36.5	6.9	1.3	5.6	0.9	5.0	1.0	1.6	3.0	3.1	0.4	4.1	1.2	23.2	13.6	2.6	0.267	0.102	0.028	2.79
7.1	0.9	10.3	640	41.1	86.6	9.0	34.2	6.5	1.1	5.4	0.9	4.8	1.0	1.7	2.9	3.0	0.4	4.6	1.3	28.2	15.1	2.8	0.277	0.126	0.028	3.69
6.3	0.8	12.0	482	36.8	75.1	8.1	30.5	5.9	1.0	4.7	0.8	4.5	0.9	1.7	2.7	2.6	0.4	4.9	1.1	38.9	19.0	3.3	0.225	0.231	0.026	7.11
5.8	0.8	11.1	507	34.7	69.0	7.7	29.1	5.6	1.0	4.5	0.8	4.3	0.9	1.6	2.6	2.7	0.4	5.2	1.1	32.7	17.4	3.7	0.218	0.215	0.027	6.16
5.8	0.8	11.5	486	35.0	69.9	7.7	29.0	5.6	1.0	4.5	0.7	4.2	0.9	1.6	2.6	2.5	0.4	5.0	1.1	32.2	17.1	3.5	0.215	0.219	0.029	6.63
6.4	1.2	12.8	521	36.5	74.0	8.2	31.2	6.1	1.1	5.0	0.8	4.7	1.0	1.7	2.9	2.8	0.4	5.4	1.2	38.3	19.2	4.2	0.218	0.209	0.028	6.00
9.0	1.0	12.8	622	49.1	101.4	11.2	40.6	7.7	1.2	6.1	1.0	5.4	1.1	2.1	3.2	3.3	0.5	4.4	1.5	29.2	21.1	3.6	0.257	0.100	0.030	2.53
6.8	0.8	9.3	562	39.2	78.8	8.7	32.5	6.1	1.0	4.9	0.8	4.5	1.0	1.6	2.7	2.7	0.4	3.9	1.3	23.7	18.5	3.4	0.287	0.106	0.032	2.85
8.1	0.8	9.9	585	46.2	93.9	10.3	38.3	7.2	1.1	5.6	0.9	5.2	1.1	2.0	3.1	3.3	0.5	4.5	1.5	26.3	21.4	3.9	0.270	0.088	0.031	2.30
6.4	1.0	9.0	622	41.0	84.0	9.4	35.9	6.8	1.1	5.5	0.9	5.0	1.0	1.4	3.0	2.9	0.4	4.4	1.2	18.4	15.5	2.9	0.261	0.092	0.035	3.00
		11.7	711	44.5	91.9	9.8	36.8	6.7	1.2	5.5	0.9	5.0	1.0		3.0	2.8	0.4	3.6		27.1	19.6	3.1			0.029	3.45
6.6	0.9	9.9	684	49.4	99.4	11.2	40.4	7.5	1.2	5.9	0.9	5.1	1.0	1.6	3.0	3.1	0.4	4.3	1.2	25.9	17.7	2.8	0.254	0.111	0.029	3.45
7.5	1.1	11.5	682	41.6	92.6	8.8	32.6	6.0	1.0	4.8	0.8	4.2	0.9	1.7	2.5	2.5	0.4	3.9	1.3	27.2	15.8	2.8	0.273	0.130	0.026	4.53
7.8	1.2	11.9	680	45.9	95.9	10.3	38.2	7.3	1.3	5.9	0.9	5.2	1.1	1.9	3.1	3.2	0.4	4.4	1.3	29.2	17.3	2.8	0.240	0.124	0.031	3.69
5.6	0.7	8.1	605	37.7	75.6	8.5	32.1	6.1	1.2	4.9	0.8	4.5	0.9	1.6	2.7	2.8	0.4	5.5	1.1	24.8	15.4	3.0	0.229	0.141	0.037	4.61
6.6	0.8	9.9	610	41.1	83.9	9.3	34.8	6.6	1.2	5.4	0.9	4.9	1.0	1.7	2.9	2.9	0.4	4.8	1.2	30.0	18.2	3.4	0.244	0.157	0.032	5.18
7.9	1.2	12.5	677	47.8	99.3	10.8	39.2	7.4	1.3	6.0	0.9	5.3	1.1	2.0	3.2	3.2	0.4	4.5	1.4	29.6	18.0	3.0	0.242	0.119	0.030	3.60
		12.4	732	47.0	96.7	10.3	38.6	7.1	1.2	5.7	0.9	5.0	1.0		3.0	3.0	0.4	3.9		27.6	23.9	3.5			0.029	3.54
8.1	1.5	12.5	650	50.5	103.9	11.3	41.4	7.8	1.3	6.3	1.0	5.7	1.2	2.4	3.4	3.4	0.5	5.4	1.4	29.9	20.1	3.3	0.241	0.113	0.034	3.39
		11.8	615	55.0	113.1	12.0	44.5	8.1	1.3	6.6	1.0	6.0	1.2		3.5	3.3	0.5	5.1		30.6	24.8	3.6			0.039	3.02
9.2	1.0	13.5	651	45.8	101.2	9.5	34.0	6.2	1.0	4.9	0.8	4.5	1.0	2.1	2.8	2.9	0.4	4.3	1.7	31.3	24.3	4.2	0.266	0.113	0.029	4.02
7.4	0.9	11.0	550	52.8	107.0	11.7	43.3	8.2	1.3	6.7	1.1	6.0	1.2	2.9	3.6	3.6	0.5	6.6	1.1	30.5	19.1	3.4	0.222	0.092	0.042	3.14
7.1	2.3	11.8	697	45.6	97.1	10.3	37.6	7.2	1.2	5.8	0.9	5.1	1.1	2.1	3.0	3.1	0.4	4.9	1.2	29.2	17.6	2.8	0.231	0.126	0.033	3.90
6.6	0.7	9.0	581	43.7	88.0	9.5	35.1	6.6	1.1	5.1	0.8	4.8	1.0	1.9	2.9	2.9	0.4	4.7	1.4	26.8	20.1	3.6	0.269	0.103	0.034	2.86
8.1	1.3	12.9	629	50.8	106.1	11.5	42.0	8.0	1.3	6.4	1.0	5.6	1.2	2.4	3.3	3.3	0.5	5.3	1.3	32.4	20.1	3.3	0.226	0.116	0.034	3.84
6.1	1.3	11.1	559	46.1	93.2	10.1	37.9	7.1	1.1	5.8	1.0	5.6	1.2	2.4	3.4	3.3	0.5	6.6	1.1	29.3	17.4	3.2	0.214	0.119	0.048	3.81
6.0	1.5	10.6	690	45.5	94.3	10.4	38.3	7.2	1.2	5.6	0.9	4.8	1.0	2.0	2.8	2.9	0.4	4.9	1.1	26.1	14.4	2.7	0.229	0.105	0.035	3.61
8.0	1.1	13.3	683	50.2	106.0	11.3	41.1	7.8	1.3	6.2	1.0	5.6	1.2	2.4	3.3	3.4	0.5	5.3	1.3	32.0	20.1	3.1	0.225	0.122	0.035	3.66
5.1	1.0	8.6	528	40.9	83.2	9.0	33.5	6.2	1.1	5.0	0.8	4.5	0.9	1.5	2.7	2.7	0.4	4.9	1.0	22.6	15.0	3.3	0.210	0.086	0.038	2.81
5.3	0.8	8.9	524	43.3	88.4	9.5	35.4	6.5	1.1	5.2	0.8	4.6	1.0	1.9	2.7	2.7	0.4	5.1	0.9	22.2	15.6	3.2	0.215	0.089	0.039	2.90

a) Italic: sedimentary sequences deposited below the upper muddy unit of the sediment core
b) Trace element data is from Chapter 2 (i.e. Simões Pereira et al, 2018)

Appendix Table 3.3. Clay and bulk mineral assemblages of sediments from the Pine Island Bay, West Antarctica

Number	Site[a]	Depth [cm]	Sector	Ill(%)	Sme(%)	Kln(%)	Chl(%)	Qz/std	Fld/std	K-fld/std	Plg/std	Px/std	Hnb/std	Halite/std	Fld/Qz	Px/Qz
1−1	PIG-B	2	Sub-ice shelf PIG	58	6	18	18									
1−2	*PIG-B*	*52*		*61*	*5*	*16*	*18*									
2−1	PIG-A	2	Sub-ice shelf PIG	61	4	14	19									
2−2	*PIG-A*	*48*		*61*	*4*	*16*	*19*									
2−3	*PIG-A*	*84*		*60*	*6*	*15*	*19*									
3−1	PIG-C	2	Sub-ice shelf PIG	58	8	17	17									
3−2	*PIG-C*	*28*		*61*	*5*	*15*	*18*									
4	PS104/008-2	3.5	eastern PIB	61	5	18	16	1.7	2.4	0.9	0.9	0.8	0.0	0.9	1.4	0.5
5	PS104/013-2	5	eastern PIB	61	7	17	16	1.5	2.6	0.7	1.4	1.0	0.0	0.7	1.8	0.7
6−1	PS104/012-2	5	eastern PIB	61	7	17	15	1.2	4.0	1.3	2.4	1.1	bdl.	0.6	3.5	1.0
6−2	*PS104/012-2*	*153*		*41*	*31*	*13*	*15*	*1.1*	*5.6*	*1.7*	*3.4*	*1.1*	*bdl.*	*0.3*	*5.0*	*0.9*
6−3	*PS104/012-2*	*173*		*33*	*43*	*10*	*14*	*1.0*	*3.8*	*1.2*	*1.8*	*1.7*	*bdl.*	*bdl.*	*3.8*	*1.8*
6−4	*PS104/012-2*	*253*		*32*	*43*	*10*	*14*	*1.0*	*3.3*	*1.0*	*1.2*	*1.4*	*bdl.*	*bdl.*	*3.2*	*1.3*
6−5	*PS104/012-2*	*313*		*35*	*39*	*13*	*14*	*1.0*	*4.0*	*1.3*	*2.1*	*1.4*	*0.0*	*bdl.*	*3.9*	*1.3*
7−1	NBP99-02 PC51	17-22	eastern PIB													
7−2	*NBP99-02 PC51*	*30-38*														
8−1	PS104/009-1	6	eastern PIB	56	2	26	17	1.7	3.0	0.8	1.7	1.0	bdl.	0.5	1.8	0.6
	repeat							*1.4*	*3.3*	*1.1*	*1.8*	*1.0*	*bdl.*	*1.1*	*2.3*	*0.7*
8−2	*PS104/009-1*	*223*		*58*	*5*	*21*	*16*	*1.4*	*4.1*	*1.9*	*2.0*	*0.9*	*0.0*	*0.5*	*2.9*	*0.7*
8−3	*PS104/009-1*	*265*		*55*	*7*	*25*	*12*	*1.9*	*4.5*	*2.2*	*1.8*	*1.2*	*bdl.*	*bdl.*	*2.4*	*0.6*
8−4	*PS104/009-1*	*505*		*55*	*7*	*25*	*13*	*1.5*	*5.8*	*3.0*	*1.6*	*1.2*	*0.2*	*bdl.*	*4.0*	*0.8*
9	NBP07-02 SMG8	Surface	eastern PIB													
10	PS75/159-1a	0-1	eastern PIB	59	6	19	16	1.0	2.7	1.1	0.8	0.7	bdl.	13.5	2.7	0.7
11	PS75/160-1	1	eastern PIB	60	8	16	16	1.2	6.2	2.4	3.4	1.2	0.1	0.5	5.1	1.0
12	PS69/288-3	4	eastern PIB	62	10	14	14	1.1	2.3	0.7	1.0	0.7	0.0	1.2	2.1	0.7
13−1	PS69/295-1	4	central PIB	53	13	17	17	1.0	2.4	0.8	0.8	0.8	0.0	5.4	2.4	0.8
13−2	*PS69/295-1*	*375*		*45*	*20*	*19*	*15*	*1.5*	*5.4*	*2.0*	*3.0*	*1.1*		*0.6*	*3.6*	*0.8*
13−3	*PS69/295-1*	*474*		*45*	*20*	*19*	*16*	*1.7*	*4.9*	*1.6*	*2.7*	*bdl.*	*bdl.*	*bdl.*		
14	PS69/291-1	7	central PIB	59	10	17	14	1.0	2.5	0.7	1.0	bdl.	bdl.	bdl.		
15	NBP99-02 53PC	*24-29*	central PIB													
16	PS69/292-2	3	western PIB	54	12	23	12	1.1	2.2	0.6	0.9	bdl.	bdl.	bdl.		
17−1	PS75/167-1a	5	western PIB	45	12	31	12	1.2	2.6	0.8	1.4	bdl.	bdl.	bdl.		
17−2	*PS75/167-1*	*818*		*56*	*5*	*23*	*17*	*1.2*	*2.5*	*1.0*	*0.9*	*1.0*	*0.0*	*1.1*	*2.1*	*0.8*
18	PS75/166-3	6	western PIB	36	20	37	8	1.2	2.8	1.0	1.0	1.0		1.1	2.4	0.8
19−1	PS75/173-1	5	western PIB	48	15	23	14	0.9	2.8	0.7	1.2	0.7	0.0	0.9	3.2	0.8
19−2	*PS75/173-1*	*195*		*50*	*10*	*23*	*17*	*1.5*	*4.8*	*2.0*	*2.2*	*0.8*	*0.1*	*0.3*	*3.1*	*0.5*
20−1	PS75/177-1	5	western PIB	50	9	27	13	0.9	2.3	0.6	0.9	0.8	0.0	1.1	2.6	0.9
20−2	*PS75/177-1*	*300*		*38*	*20*	*27*	*16*	*1.2*	*3.6*	*0.9*	*1.6*	*1.1*	*0.0*	*0.8*	*3.0*	*0.9*
21	PS75/219-2	3	western PIB	53	14	19	14	1.2	3.1	0.8	1.4	0.7	0.0	4.4	2.6	0.6
22−1	PS104/021-1	5	western PIB	50	14	21	15	0.9	2.9	0.7	1.4	0.9	0.0	1.4	3.3	1.0
22−2	*PS104/021-1*	*77*		*30*	*32*	*26*	*11*	*1.5*	*3.4*	*1.3*	*1.4*	*0.9*	*bdl.*	*bdl.*	*2.2*	*0.6*
22−3	*PS104/021-1*	*103*		*30*	*32*	*28*	*11*	*1.6*	*4.0*	*1.7*	*1.6*	*0.9*	*0.0*	*bdl.*	*2.5*	*0.5*
23	NBP07-02 SMG10	Surface	western PIB													
24	NBP00-01 KC28	9-14	western PIB													

a) Italic: sedimentary sequences deposited below the upper muddy unit of the sediment core
Abbreviatons: Qtz: Quartz; Fld: Feldspar; K-fld: K-feldspar; Plg: Plagioclase; Px: Pyroxene; Hnb: Hornblende; std: standard

Appendix Table 3.4. Clay and bulk mineral assemblages of sediments from the Pine Island Bay, West Antarctica

Number	Sitea	Depth [cm]	Sector	ARM [mA/m]	(S)IRM [mA/m]@700mT	IRM [mA/m]@100mT	IRM [mA/m]@300mT	HIRM [mA/m]	MDFarm [mT]	Sus [10E-6)	kARM [10E-6 SI]	KARM/ SUS	ARM_100mT/ IRM_100mT	S-ratio
1−1	PIG-B	2	sub-ice shelf PIG											
1−2	*PIG-B*	*52*												
2−1	PIG-A	2	sub-ice shelf PIG											
2−2	*PIG-A*	*48*												
2−3	*PIG-A*	*84*												
3−1	PIG-C	2	sub-ice shelf PIG											
3−2	*PIG-C*	*28*												
4	PS104/008-2	3.5	western PIB	158	12866	8675	12347	519	24	409	3983	10	0.018	0.960
5	PS104/013-2	5	western PIB	186	18438	13571	17903	535	24	1089	4680	4	0.014	0.971
6−1	PS104/012-2	5	western PIB	257	21645	14412	20826	819	25	775	6469	8	0.018	0.962
6−2	*PS104/012-2*	*153*		287	29144	19172	28081	1063	26	1258	7205	6	0.015	0.964
6−3	*PS104/012-2*	*173*		437	29482	23857	28596	886	28	1462	10976	8	0.018	0.970
6−4	*PS104/012-2*	*253*		568	30791	25374	29927	864	22	1813	14272	8	0.022	0.972
6−5	*PS104/012-2*	*313*		393	26481	21200	25630	851	27	1396	9876	7	0.019	0.968
7−1	NBP99-02 PC51	17-22	western PIB											
7−2	*NBP99-02 PC51*	*30-38*												
8−1	PS104/009-1	6	western PIB	159	15408	9562	14832	576	27	726	4004	6	0.017	0.963
8−2	*PS104/009-1*	*223*		166	12386	9463	11898	488	28	667	4184	6	0.018	0.961
8−3	*PS104/009-1*	*265*		215	21360	15057	20628	732	26	1543	5414	4	0.014	0.966
8−4	*PS104/009-1*	*505*		222	27172	18368	26223	949	25	2135	5569	3	0.012	0.965
9	NBP07-02 SMG8	Surface	western PIB											
10	PS75/159-1a	0-1	western PIB	180	11452	6658	10964	488	28	330	4529	14	0.027	0.957
11	PS75/160-1	1	western PIB	174	14204	10111	13633	571	26	1133	4376	4	0.017	0.960
12	PS69/288-3	4	western PIB	126	7315	4816	7029	286	28	229	3171	14	0.026	0.961
13−1	PS69/295-1	4	central PIB	187	9891	6001	9522	369	28	287	4713	16	0.031	0.963
13−2	*PS69/295-1*	*375*		461	61260	42424	59340	1920	23	2151	11599	5	0.011	0.969
13−3	*PS69/295-1*	*474*		452	22724	31376	32397	1021	24	1342	11366	8	0.020	0.968
14	PS69/291-1	7	central PIB	178	6372	9998	10399	401	28	296	4469	15	0.028	0.961
15	NBP99-02 53PC	*24-29*	central PIB											
16	PS69/292-2	3	eastern PIB	251	9193	14534	15080	546	27	447	6299	14	0.027	0.964
17−1	PS75/167-1a	5	eastern PIB	272	14101	20375	21062	687	26	1020	6841	7	0.019	0.967
17−2	*PS75/167-1*	*818*		143	12769	9659	12310	459	28	595	3601	6	0.015	0.964
18	PS75/166-3	6	eastern PIB	326	22819	14580	22106	713	27	699	8185	12	0.022	0.969
19−1	PS75/173-1	5	eastern PIB	252	10210	6012	9791	419	27	278	6338	23	0.042	0.959
19−2	*PS75/173-1*	*195*		270	21810	18145	21277	533	26	1593	6787	4	0.015	0.976
20−1	PS75/177-1	5	eastern PIB	241	12410	7581	11917	493	26	353	6047	17	0.032	0.960
20−2	*PS75/177-1*	*300*		326	29851	16986	28644	1207	28	1048	8184	8	0.019	0.960
21	PS75/219-2	3	eastern PIB	202	10975	7247	10565	410	26	414	5075	12	0.028	0.963
22−1	PS104/021-1	5	eastern PIB	263	11284	6305	10774	510	26	283	6623	23	0.042	0.955
22−2	*PS104/021-1*	*77*		288	11903	9995	11619	284	25	678	7235	11	0.029	0.976
22−3	*PS104/021-1*	*103*		221	9057	7938	8879	177	25	593	5551	9	0.028	0.980
23	NBP07-02 SMG10	Surface	eastern PIB											
24	NBP00-01 KC28	9-14	eastern PIB											

a) Italic: sedimentary sequences deposited below the upper muddy unit of the sediment core

Appendix Table 4.1. Age model of sediment profile PS58/254 (Hillenbrand et al., 2009)

Depth [m]	Event	Depth comp [mcd]	Age model [ka]	Comm
0	PS58/254-2	0	0	top
0.12	PS58/254-2	0.12	14	2-4
0.37	PS58/254-1	0.55	71	4/5
0.89	PS58/254-1	1.07	130	5/6
2.25	PS58/254-1	2.43	191	6/7
3.57	PS58/254-1	3.75	243	7/8
4.24	PS58/254-1	4.42	300	8/9
5.07	PS58/254-1	5.25	337	9/10
5.9	PS58/254-1	6.08	374	10/11
6.82	PS58/254-1	7	424	11/12
8.28	PS58/254-1	8.46	478	12/13
9.09	PS58/254-1	9.27	533	13/14
9.47	PS58/254-1	9.65	563	14/15
10.31	PS58/254-1	10.49	621	15/16
12.12	PS58/254-1	12.3	676	16/17
12.77	PS58/254-1	12.95	712	17/18
13.49	PS58/254-1	13.67	761	18/19
14.19	PS58/254-1	14.37	780	C1n (base)
14.22	PS58/254-1	14.4	790	19/20
14.39	PS58/254-1	14.57	814	20/21
14.82	PS58/254-1	15	866	21/22
16.32	PS58/254-1	16.5	900	22/23
16.99	PS58/254-1	17.17	990	C1r.1n (top)
17.59	PS58/254-1	17.77	1070	C1r.1n (base)

Appendix Table 4.2. Age model of sediment profile PC493 (Williams et al., submitted)

Depth [m]	Age model [ka]	Description	Linear sed. rate (cm/kyr)
5.25	14	MIS 1/2 transition	0.38
40	71	MIS 4/5 transition	0.61
58.5	123	MIS 5e δ18O minimum	0.36
66	130	MIS 5/6 transition	1.07
71.5	140	MIS 6 δ18O maximum	0.55
99	191	MIS 6/7 transition	0.53
110.5	240	MIS 7.5 δ18O minimum	0.23
112.5	252	MIS 8.2 δ18O maximum	0.17
116	286	MIS 8.5 δ18O minimum	0.1
118.5	294	MIS 8.6 δ18O maximum	0.31
122	300	MIS 8/9 transition	0.58
148	337	MIS 9/10 transition	0.7
156.25	374	MIS 10/11 transition	0.22
166	424	MIS 11/12 transition	0.2
181	478	MIS 12/13 transition	0.28
193.5	533	MIS 13/14 transition	0.23
195.5	565	MIS 15 youngest δ18O minimum	0.06
209	621	MIS 15/16 transition	0.24
250	676	MIS 16/17 transition	0.75
261	712	MIS 17/18 transition	0.31
269	761	MIS 18/19 transition	0.16
282-287*	780	Brunhes-Matuyama boundary	n/a*
283	790	MIS 19/20 transition	0.48
323.5	990	Jaramillio top	0.20
328.5	1070	Jaramillio base	0.06
*: not used as fixed tie point			

Appendix Table 4.3. $^{40}Ar/^{39}Ar$ data for hornblende and biotite grains from sediment profile PS58/254.

Run ID	Status	Ca/K[a]	Cl/K	Mol 39Ar	%40Ar*	Age (Ma)	± Age
30008-02A	PS58/254-1 88-89	0.637	0.01	0.014	8.90	1.2	1.3
30008-13A	PS58/254-1 88-89	1.094	0.02	0.031	18.30	2.5	0.6
30008-03A	PS58/254-1 88-89	33.423	0.01	0.011	29.50	3.0	1.6
30008-06A	PS58/254-1 88-89	1.546	-0.01	0.002	32.60	6.0	6.8
30008-12A	PS58/254-1 88-89	78.287	0.01	0.007	36.90	7.1	2.4
30008-09A	PS58/254-1 88-89	17.129	0.09	0.005	71.30	47.3	3.4
30008-14A	PS58/254-1 88-89	0.147	0.00	0.027	79.70	55.4	0.7
30008-04A	PS58/254-1 88-89	27.203	-0.01	0.001	18.80	107.9	31.5
30008-01A	PS58/254-1 88-89	5.784	-0.01	0.007	74.90	136.45	2.74
30002-06A	PS58/254-1 109-110	22.485	0.06	0.002	22.40	79.4	7.8
30002-03A	PS58/254-1 109-110	0.131	0.01	0.025	40.20	88.2	1.6
30002-04A	PS58/254-1 109-110	4.638	0.00	0.052	50.60	90.9	1.1
30002-02A	PS58/254-1 109-110	0.058	0.00	0.007	26.90	90.9	3.9
30002-15A	PS58/254-1 109-110	0.036	0.00	0.025	76.10	94.1	0.9
30002-16A	PS58/254-1 109-110	7.737	0.01	0.003	36.60	97.7	4.9
30002-01A	PS58/254-1 109-110	6.505	0.02	0.030	52.90	98.3	1.3
30002-14A	PS58/254-1 109-110	0.365	-0.01	0.018	81.20	100.7	1.0
30002-12A	PS58/254-1 109-110	0.085	0.01	0.005	88.30	100.8	2.7
30002-17A	PS58/254-1 109-110	0.134	0.00	0.013	79.40	101.6	1.4
30002-19A	PS58/254-1 109-110	8.498	-0.01	0.001	27.20	102.9	10.2
30002-08A	PS58/254-1 109-110	0.033	0.00	0.043	95.90	160.8	0.7
30002-10A	PS58/254-1 109-110	0.390	0.13	0.001	39.10	182.1	20.9
30002-11A	PS58/254-1 109-110	0.062	-0.01	0.004	66.00	183.5	3.7
30002-07A	PS58/254-1 109-110	26.532	0.12	0.001	65.80	193.9	19.1
30002-05A	PS58/254-1 109-110	16.667	0.01	0.029	79.40	333.7	2.0
30002-09A	PS58/254-1 109-110	0.004	0.01	0.021	98.10	344.5	2.0
30002-13A	PS58/254-1 109-110	0.006	-0.01	0.009	98.60	344.6	2.6
30002-18A	PS58/254-1 109-110	14.155	0.08	0.001	96.00	356.0	10.4
16061-13A	PS58-254-1 593 603 663 673 cm	0.57738	-0.0571	0.001	5.1	10.2	13.0
16061-05A	PS58-254-1 593 603 663 673 cm	0.09143	0.00277	0.002	14	35.6	6.5
16061-06A	PS58-254-1 593 603 663 673 cm	0.04259	0.0333	0.002	70.2	84.1	3.8
16061-01A	PS58-254-1 593 603 663 673 cm	0.00339	-0.01295	0.003	40	84.9	4.0
16061-18A	PS58-254-1 593 603 663 673 cm	0.07455	-0.01821	0.001	83.4	90.6	6.5
16061-21A	PS58-254-1 593 603 663 673 cm	0.04154	-0.02621	0.005	31	104.0	5.7
16061-02A	PS58-254-1 593 603 663 673 cm	-0.01288	0.01459	0.002	64.3	104.0	4.2
16061-20A	PS58-254-1 593 603 663 673 cm	0.05258	0.01355	0.003	81.9	111.5	2.6
16061-12A	PS58-254-1 593 603 663 673 cm	0.01143	-0.00019	0.006	86.5	128.0	1.7
16061-15A	PS58-254-1 593 603 663 673 cm	0.32824	-0.08029	0.001	47.5	131.9	8.9
16061-22A	PS58-254-1 593 603 663 673 cm	0.04002	-0.00924	0.01	86.1	142.6	1.5
16061-11A	PS58-254-1 593 603 663 673 cm	-0.0001	0.00152	0.001	80.6	143.2	5.3
16061-17A	PS58-254-1 593 603 663 673 cm	0.0013	-0.00625	0.005	95.9	156.0	1.8
16061-09A	PS58-254-1 593 603 663 673 cm	0.01209	0.00194	0.013	85.6	158.8	1.6
16061-19A	PS58-254-1 593 603 663 673 cm	0.09428	-0.00409	0.011	96.8	161.5	1.3
16061-04A	PS58-254-1 593 603 663 673 cm	0.00392	-0.00624	0.003	93.9	172.2	2.4
16061-08A	PS58-254-1 593 603 663 673 cm	0.05761	0.03834	0.003	94.3	225.7	3.2
16061-07A	PS58-254-1 593 603 663 673 cm	0.08458	0.03291	0.002	84.3	228.8	4.4
16061-14A	PS58-254-1 593 603 663 673 cm	0.00884	-0.00804	0.002	88.4	245.7	4.7
16061-10A	PS58-254-1 593 603 663 673 cm	0.00763	-0.00373	0.003	93.7	253.1	3.3
16061-03A	PS58-254-1 593 603 663 673 cm	0.00821	0.00386	0.01	97.3	276.9	1.9
30005-04A	PS58/254-1 667-668	0.144	0.01	0.013	10.10	0.9	0.9
30005-02A	PS58/254-1 667-668	23.230	0.00	0.020	25.10	1.7	0.6
30005-07A	PS58/254-1 667-668	0.504	0.02	0.004	36.60	4.1	2.4
30005-12A	PS58/254-1 667-668	14.914	0.03	0.002	12.10	8.4	5.1
30005-11A	PS58/254-1 667-668	15.191	0.06	0.001	41.30	55.1	10.5
30005-05A	PS58/254-1 667-668	18.893	0.05	0.001	42.10	99.2	8.2
30005-06A	PS58/254-1 667-668	13.763	0.11	0.001	53.80	108.5	14.1
30005-10A	PS58/254-1 667-668	31.416	0.02	0.001	91.20	340.1	10.5
30006-29A	PS58/254-1 759-760	-0.015	-0.05	0.001	13.30	59.7	13.3
30006-01A	PS58/254-1 759-760	4.656	0.01	0.013	42.40	84.8	2.0
30006-08A	PS58/254-1 759-760	10.308	0.01	0.001	54.30	87.6	16.0
30006-15A	PS58/254-1 759-760	0.016	0.00	0.012	45.00	89.3	2.2

30006-10A	PS58/254-1 759-760	0.028	0.00	0.065	43.60	90.4	1.1
30006-27A	PS58/254-1 759-760	9.367	0.02	0.003	72.50	91.8	4.5
30006-21A	PS58/254-1 759-760	8.642	-0.01	0.009	43.00	92.2	2.4
30006-17A	PS58/254-1 759-760	8.618	0.03	0.002	85.30	94.5	8.3
30006-11A	PS58/254-1 759-760	0.009	0.00	0.023	86.40	95.0	1.0
30006-06A	PS58/254-1 759-760	18.402	-0.02	0.002	44.10	95.9	10.9
30006-05A	PS58/254-1 759-760	0.097	0.02	0.010	92.90	96.7	1.7
30006-25A	PS58/254-1 759-760	-0.076	0.00	0.011	79.30	97.3	1.4
30006-23A	PS58/254-1 759-760	8.374	0.04	0.003	88.20	97.5	3.4
30006-38A	PS58/254-1 759-760	-0.019	0.00	0.008	98.10	98.2	1.6
30006-31A	PS58/254-1 759-760	-0.008	0.00	0.032	94.40	98.8	0.6
30006-09A	PS58/254-1 759-760	0.028	0.01	0.010	80.20	98.9	1.9
30006-24A	PS58/254-1 759-760	0.296	0.00	0.213	97.40	99.1	0.3
30006-33A	PS58/254-1 759-760	0.021	0.00	0.034	82.50	99.5	0.7
30006-16A	PS58/254-1 759-760	0.548	0.00	0.013	89.80	100.2	1.4
30006-30A	PS58/254-1 759-760	-0.024	0.00	0.015	95.60	100.3	1.0
30006-14A	PS58/254-1 759-760	10.243	0.02	0.005	70.90	100.5	3.8
30006-37A	PS58/254-1 759-760	9.056	0.01	0.005	88.10	100.7	2.2
30006-34A	PS58/254-1 759-760	-0.041	0.00	0.009	97.60	101.2	1.4
30006-04A	PS58/254-1 759-760	0.007	0.01	0.010	89.80	101.2	1.7
30006-07A	PS58/254-1 759-760	0.021	-0.01	0.034	92.10	101.6	0.7
30006-32A	PS58/254-1 759-760	7.820	0.02	0.005	93.30	102.1	2.3
30006-18A	PS58/254-1 759-760	10.192	0.01	0.003	79.90	102.6	6.3
30006-26A	PS58/254-1 759-760	8.125	0.01	0.019	92.80	106.9	0.9
30006-20A	PS58/254-1 759-760	0.128	0.00	0.119	73.40	112.3	0.7
30006-22A	PS58/254-1 759-760	21.123	0.01	0.012	69.40	114.3	1.6
30006-13A	PS58/254-1 759-760	0.140	0.00	0.013	68.80	117.0	1.7
30006-02A	PS58/254-1 759-760	0.094	0.00	0.011	61.50	117.1	2.0
30006-35A	PS58/254-1 759-760	13.412	0.02	0.002	82.90	121.3	6.8
30006-12A	PS58/254-1 759-760	5.007	0.02	0.005	74.60	121.4	3.8
30006-28A	PS58/254-1 759-760	9.848	-0.01	0.005	82.30	127.2	2.3
30006-03A	PS58/254-1 759-760	0.106	-0.02	0.006	90.80	153.9	3.0
30009-04A	PS58/254-1 988-989	1.351	0.01	0.017	12.10	1.0	1.0
30009-03A	PS58/254-1 988-989	9.718	0.02	0.004	4.20	4.1	4.2
30009-02A	PS58/254-1 988-989	3.392	0.06	0.001	39.30	15.6	28.1
30009-10A	PS58/254-1 988-989	8.212	-0.03	0.001	8.60	15.7	23.6
30009-08A	PS58/254-1 988-989	-0.078	-0.01	0.007	83.80	25.3	2.4
30009-13A	PS58/254-1 988-989	0.202	0.00	0.008	93.00	30.3	2.2
30009-06A	PS58/254-1 988-989	18.398	0.09	0.001	14.50	77.7	17.6
30009-05A	PS58/254-1 988-989	9.015	0.00	0.002	87.50	115.9	7.6
30009-14A	PS58/254-1 988-989	11.534	0.02	0.001	52.60	125.9	16.5
30009-11A	PS58/254-1 988-989	7.527	0.05	0.001	73.00	129.2	25.2
30009-09A	PS58/254-1 988-989	24.260	0.11	0.001	77.70	135.4	12.5
30009-07A	PS58/254-1 988-989	17.179	0.03	0.001	75.70	231.0	11.2
30003-12A	PS58/254-1 1116-1117	0.102	-0.10	0.001	22.90	30.6	12.0
30003-27A	PS58/254-1 1116-1117	0.028	0.00	0.018	98.20	102.8	0.9
30003-04A	PS58/254-1 1116-1117	13.439	0.04	0.004	89.70	103.3	3.1
30003-25A	PS58/254-1 1116-1117	7.537	0.02	0.003	48.00	103.5	5.2
30003-31A	PS58/254-1 1116-1117	0.033	0.00	0.038	95.70	109.9	0.6
30003-17A	PS58/254-1 1116-1117	0.074	0.00	0.021	94.70	149.0	1.1
30003-01A	PS58/254-1 1116-1117	7.919	0.02	0.015	41.00	149.7	2.5
30003-05A	PS58/254-1 1116-1117	3.748	0.00	0.024	72.40	179.2	1.4
30003-35A	PS58/254-1 1116-1117	16.541	-0.04	0.002	92.60	190.9	5.5
30003-32A	PS58/254-1 1116-1117	0.052	0.00	0.062	87.50	210.5	0.8
30003-28A	PS58/254-1 1116-1117	0.090	-0.01	0.008	84.70	214.5	2.5
30003-10A	PS58/254-1 1116-1117	4.949	-0.04	0.003	96.20	219.4	4.2
30003-16A	PS58/254-1 1116-1117	9.832	0.01	0.004	85.20	222.4	4.1
30003-29A	PS58/254-1 1116-1117	9.996	0.02	0.007	95.90	231.9	2.8
30003-34A	PS58/254-1 1116-1117	9.414	0.01	0.002	91.40	233.1	6.1
30003-15A	PS58/254-1 1116-1117	6.555	0.01	0.009	89.30	233.1	2.3
30003-03A	PS58/254-1 1116-1117	0.027	0.00	0.054	98.70	240.0	0.9
30003-38A	PS58/254-1 1116-1117	0.004	0.00	0.008	98.60	246.4	2.5
30003-02A	PS58/254-1 1116-1117	11.061	0.02	0.003	89.00	249.8	5.4
30003-06A	PS58/254-1 1116-1117	17.762	0.05	0.003	69.70	249.8	6.3
30003-14A	PS58/254-1 1116-1117	9.751	0.01	0.009	96.10	252.1	2.3
30003-30A	PS58/254-1 1116-1117	0.003	-0.01	0.012	99.50	253.2	2.1
30003-09A	PS58/254-1 1116-1117	17.739	0.10	0.002	89.00	257.3	8.0
30003-20A	PS58/254-1 1116-1117	9.742	0.03	0.002	100.60	258.3	6.6
30003-18A	PS58/254-1 1116-1117	8.389	0.03	0.003	92.70	258.6	4.7
30003-22A	PS58/254-1 1116-1117	0.003	0.00	0.006	97.80	258.8	3.1

30003-23A	PS58/254-1 1116-1117	10.422	0.01	0.003	83.70	260.7	6.2
30003-33A	PS58/254-1 1116-1117	9.396	0.00	0.003	96.00	262.3	5.3
30003-24A	PS58/254-1 1116-1117	15.991	0.01	0.003	90.60	264.3	5.0
30003-37A	PS58/254-1 1116-1117	7.509	0.05	0.003	99.30	268.1	5.0
30003-39A	PS58/254-1 1116-1117	7.148	0.04	0.006	96.80	269.0	3.2
30003-19A	PS58/254-1 1116-1117	7.658	0.01	0.008	99.00	269.3	2.5
30003-36A	PS58/254-1 1116-1117	29.347	-0.05	0.001	86.50	275.0	11.7
30003-11A	PS58/254-1 1116-1117	0.897	0.00	0.005	95.10	277.4	3.1
30003-07A	PS58/254-1 1116-1117	29.116	0.01	0.001	82.30	283.4	11.9
30003-13A	PS58/254-1 1116-1117	34.116	0.02	0.001	77.80	294.4	17.9
30003-21A	PS58/254-1 1116-1117	37.261	-0.02	0.001	76.70	331.6	20.2
16055-04A	PS58-254 1223 1233 1253 1263 cm	-0.00429	-0.04046	0.004	52.5	81.5	5.8
16055-07A	PS58-254 1223 1233 1253 1263 cm	0.07986	-0.01305	0.003	88.3	117.1	7.9
16055-02A	PS58-254 1223 1233 1253 1263 cm	0.07389	-0.00151	0.018	95.4	121.4	1.5
16055-09A	PS58-254 1223 1233 1253 1263 cm	0.02129	-0.00321	0.005	54.1	131.2	5.6
16055-03A	PS58-254 1223 1233 1253 1263 cm	0.09855	-0.00429	0.038	98.5	186.9	0.8
16055-05A	PS58-254 1223 1233 1253 1263 cm	0.08622	0.00449	0.004	81.7	201.1	6.0
16055-08A	PS58-254 1223 1233 1253 1263 cm	0.06105	0.01494	0.002	78.9	250.2	11.5
16055-06A	PS58-254 1223 1233 1253 1263 cm	0.0142	-0.01095	0.005	90.7	267.1	4.7
16055-01A	PS58-254 1223 1233 1253 1263 cm	0.00248	0.00937	0.03	95.7	284.0	1.5
30004-35A	PS58/254-1 1415-1416	0.420	0.01	0.026	28.90	1.1	0.4
30004-17A	PS58/254-1 1415-1416	3.211	-0.03	0.003	22.40	6.0	4.2
30004-08A	PS58/254-1 1415-1416	-0.006	0.00	0.003	6.20	29.1	8.0
30004-02A	PS58/254-1 1415-1416	200.202	-0.03	0.001	17.00	31.2	11.7
30004-24A	PS58/254-1 1415-1416	11.517	0.06	0.002	59.90	50.4	4.8
30004-13A	PS58/254-1 1415-1416	14.033	0.07	0.001	7.70	51.8	21.9
30004-27A	PS58/254-1 1415-1416	2.174	-0.03	0.002	36.60	53.5	7.2
30004-15A	PS58/254-1 1415-1416	1.040	0.00	0.003	26.10	55.2	5.1
30004-12A	PS58/254-1 1415-1416	25.859	0.20	0.001	23.80	59.1	15.3
30004-04A	PS58/254-1 1415-1416	11.243	-0.03	0.002	12.80	62.2	8.0
30004-11A	PS58/254-1 1415-1416	-0.016	0.01	0.008	10.00	88.5	8.0
30004-03A	PS58/254-1 1415-1416	29.004	0.25	0.008	43.70	92.0	2.5
30004-23A	PS58/254-1 1415-1416	-0.005	-0.01	0.014	89.00	93.7	1.0
30004-36A	PS58/254-1 1415-1416	0.667	0.00	0.034	73.80	95.0	0.8
30004-32A	PS58/254-1 1415-1416	25.116	0.13	0.001	63.40	96.6	9.1
30004-28A	PS58/254-1 1415-1416	0.096	0.01	0.019	95.10	98.2	0.8
30004-33A	PS58/254-1 1415-1416	0.020	0.00	0.009	99.00	100.7	1.3
30004-01A	PS58/254-1 1415-1416	14.107	0.02	0.072	62.70	101.3	0.9
30004-31A	PS58/254-1 1415-1416	6.639	0.05	0.003	83.30	103.4	4.1
30004-21A	PS58/254-1 1415-1416	22.616	0.01	0.001	47.20	104.0	16.4
30004-26A	PS58/254-1 1415-1416	10.998	0.10	0.001	92.20	126.2	9.1
30004-19A	PS58/254-1 1415-1416	0.244	0.00	0.020	90.90	142.5	1.0
30004-09A	PS58/254-1 1415-1416	3.977	0.06	0.001	25.10	147.1	17.2
30004-18A	PS58/254-1 1415-1416	1.007	-0.01	0.004	52.90	152.0	3.8
30004-06A	PS58/254-1 1415-1416	8.275	-0.06	0.001	35.90	161.5	10.3
30004-16A	PS58/254-1 1415-1416	0.666	0.01	0.002	78.90	170.9	5.9
30004-22A	PS58/254-1 1415-1416	0.015	0.00	0.016	82.40	187.5	1.4
30004-05A	PS58/254-1 1415-1416	22.023	-0.04	0.001	79.10	214.1	12.3
30004-29A	PS58/254-1 1415-1416	0.091	0.02	0.004	100.70	224.6	3.6
30004-07A	PS58/254-1 1415-1416	8.461	0.02	0.003	75.80	236.4	4.3
30004-14A	PS58/254-1 1415-1416	0.076	0.00	0.007	82.30	268.2	2.7
30004-30A	PS58/254-1 1415-1416	20.148	0.05	0.001	86.00	293.8	14.3
16052-05A	PS58-254 1463 and 1473 cm	0.16399	-0.06515	0.002	15.6	24.5	13.7
16052-09A	PS58-254 1463 and 1473 cm	0.06677	-0.01639	0.004	13.3	31.2	6.2
16052-01A	PS58-254 1463 and 1473 cm	0.21954	0.00896	0.29	83.6	62.1	0.3
16052-02A	PS58-254 1463 and 1473 cm	0.00568	0.01393	0.02	90.3	71.0	1.4
16052-03A	PS58-254 1463 and 1473 cm	0.08418	0.00405	0.007	84.9	112.1	3.3
16052-10A	PS58-254 1463 and 1473 cm	0.11	0.03681	0.004	44.6	112.2	6.3
16052-11A	PS58-254 1463 and 1473 cm	0.01057	0.01801	0.009	101.2	113.3	2.5
16052-06A	PS58-254 1463 and 1473 cm	0.11626	-0.06767	0.002	68.6	120	13.7
16052-13A	PS58-254 1463 and 1473 cm	-0.02636	-0.06241	0.001	74.5	145.1	17.5
16052-08A	PS58-254 1463 and 1473 cm	0.03037	-0.00559	0.023	97.7	160.1	1.4
16052-04A	PS58-254 1463 and 1473 cm	0.12783	-0.00758	0.005	87.6	220.9	5.2
16052-12A	PS58-254 1463 and 1473 cm	-0.00372	0.0163	0.003	96.3	245.9	7.2

a) Mineral identification was primarily done based on the Ca/K ratio with hornblende grains usually > ~1 and biotite grains < 1

Appendix Table 4.3. $^{40}Ar/^{39}Ar$ data for biotite grains from sediment profile PC493.

Sample	Run ID	Ca/K	Mol 39Ar	%Ar40*	Age (Ma)	±
PC493 25-26	16137-12A	0.022	0.002	23.3	51.9	4.2
PC493 25-26	16137-06A	0.156	0.002	42.8	93.0	2.8
PC493 25-26	16137-10A	0.042	0.002	86.4	106.3	2.7
PC493 25-26	16137-14A	0.088	0.002	73.0	107.5	3.6
PC493 25-26	16137-11A	0.130	0.003	85.4	110.8	2.2
PC493 25-26	16137-01A	0.576	0.001	91.2	115.2	5.1
PC493 25-26	16137-05A	1.307	0.001	55.8	116.5	4.8
PC493 25-26	16137-02A	0.160	0.002	79.6	117.8	3.5
PC493 25-26	16137-03A	0.291	0.004	82.4	201.7	2.0
PC493 25-26	16137-08A	0.075	0.028	90.5	211.8	0.7
PC493 25-26	16137-07A	0.117	0.004	93.9	242.3	1.8
PC493 25-26	16137-15A	0.492	0.001	91.0	248.0	8.4
PC493 25-26	16137-09A	0.166	0.004	94.3	256.9	2.2
PC493 25-26	16137-13A	0.092	0.004	91.7	280.9	2.6
PC493 57-58	16138-05A	-0.021	0.004	12.4	47.6	3.0
PC493 57-58	16138-12A	0.092	0.006	64.2	81.6	1.2
PC493 57-58	16138-11A	0.380	0.013	80.0	83.4	0.6
PC493 57-58	16138-04A	0.030	0.010	99.4	96.1	0.8
PC493 57-58	16138-14A	0.269	0.002	89.3	97.2	3.6
PC493 57-58	16138-15A	0.045	0.009	91.7	97.4	0.8
PC493 57-58	16138-02A	0.075	0.073	80.3	97.8	0.3
PC493 57-58	16138-03A	-0.018	0.003	56.7	104.4	2.6
PC493 57-58	16138-18A	0.139	0.002	115.9	129.2	3.9
PC493 57-58	16138-10A	0.126	0.005	95.3	141.2	1.5
PC493 57-58	16138-13A	0.072	0.003	86.5	163.2	2.6
PC493 57-58	16138-09A	0.096	0.011	72.4	172.5	1.2
PC493 57-58	16138-19A	-0.054	0.001	88.2	197.8	8.1
PC493 57-58	16138-07A	0.149	0.001	107.0	213.3	5.5
PC493 57-58	16138-16A	0.174	0.004	102.5	217.8	2.1
PC493 57-58	16138-08A	-0.011	0.009	99.2	261.4	1.3
PC493 73-74	16139-17A	0.091	0.003	23.8	6.3	2.0
PC493 73-74	16139-08A	0.565	0.001	20.2	78.2	6.3
PC493 73-74	16139-12A	0.091	0.013	84.6	86.1	0.7
PC493 73-74	16139-01A	0.192	0.007	57.6	99.2	1.2
PC493 73-74	16139-11A	0.403	0.002	75.2	99.9	2.9
PC493 73-74	16139-04A	0.108	0.014	65.1	100.1	0.8
PC493 73-74	16139-02A	0.079	0.018	86.1	104.3	0.6
PC493 73-74	16139-03A	0.054	0.007	82.1	109.0	1.1
PC493 73-74	16139-19A	0.042	0.068	96.8	109.6	0.3
PC493 73-74	16139-09A	0.039	0.015	77.7	117.4	0.7
PC493 73-74	16139-15A	0.024	0.003	82.9	128.4	2.5
PC493 73-74	16139-06A	0.060	0.004	78.8	143.7	2.0
PC493 73-74	16139-21A	0.027	0.036	50.9	145.2	1.1
PC493 73-74	16139-13A	0.384	0.001	73.7	192.9	6.0
PC493 73-74	16139-18A	0.130	0.002	77.6	201.2	4.4
PC493 73-74	16139-07A	0.117	0.029	93.9	205.7	0.6
PC493 73-74	16139-16A	0.040	0.007	75.5	205.9	1.5
PC493 73-74	16139-05A	0.609	0.001	95.7	211.4	6.7
PC493 73-74	16139-10A	0.005	0.010	96.5	225.9	1.1
PC493 73-74	16139-20A	0.059	0.020	95.2	226.1	0.8
PC493 73-74	16139-14A	0.110	0.002	95.8	238.5	3.6
PC493 100-101	16140-07A	1.308	0.001	3.1	15.2	9.2
PC493 100-101	16140-09A	0.147	0.001	96.6	26.9	12.0
PC493 100-101	16140-15A	5.955	0.001	23.8	61.4	8.5

PC493 100-101	16140-05A	1.737	0.015	4.5	79.8	10.1
PC493 100-101	16140-16A	0.552	0.137	57.5	80.8	0.5
PC493 100-101	16140-17A	0.421	0.013	40.1	92.8	1.4
PC493 100-101	16140-02A	0.039	0.007	72.6	99.7	1.2
PC493 100-101	16140-06A	0.153	0.240	86.0	102.2	0.3
PC493 100-101	16140-12A	0.060	0.005	94.0	102.8	1.5
PC493 100-101	16140-03A	0.131	0.003	82.7	103.5	2.6
PC493 100-101	16140-18A	0.004	0.004	31.9	109.9	2.6
PC493 100-101	16140-14A	-0.031	0.012	86.4	118.1	0.7
PC493 100-101	16140-23A	0.104	0.002	86.4	119.8	3.0
PC493 100-101	16140-01A	0.110	0.007	77.8	128.3	1.2
PC493 100-101	16140-10A	0.328	0.002	79.4	140.9	3.4
PC493 100-101	16140-13A	-0.317	0.002	81.6	151.0	4.1
PC493 100-101	16140-22A	0.170	0.004	88.1	181.3	1.9
PC493 100-101	16140-11A	0.148	0.015	97.4	188.2	0.8
PC493 100-101	16140-24A	0.756	0.001	91.5	205.9	5.7
PC493 100-101	16140-20A	0.112	0.003	71.0	209.5	3.1
PC493 100-101	16140-19A	-0.071	0.005	73.5	227.0	2.1
PC493 100-101	16140-21A	-0.001	0.009	94.5	240.0	1.3
PC493 100-101	16140-08A	0.093	0.008	96.6	250.1	1.6
PC493 100-101	16140-04A	0.066	0.010	97.3	254.5	1.2
PC493 113-114	16141-15A	0.091	0.003	76.9	54.9	2.3
PC493 113-114	16141-01A	0.135	0.002	18.0	85.7	4.2
PC493 113-114	16141-17A	0.232	0.017	73.3	97.8	0.7
PC493 113-114	16141-10A	0.094	0.015	89.6	105.6	0.7
PC493 113-114	16141-13A	0.412	0.002	63.5	121.2	3.4
PC493 113-114	16141-11A	0.065	0.006	93.2	139.1	1.3
PC493 113-114	16141-16A	0.015	0.001	94.0	149.0	4.4
PC493 113-114	16141-19A	-0.161	0.003	96.2	150.6	2.0
PC493 113-114	16141-03A	0.094	0.006	94.5	167.0	1.4
PC493 113-114	16141-09A	0.041	0.008	93.6	171.6	1.1
PC493 113-114	16141-02A	0.032	0.012	95.5	171.9	0.8
PC493 113-114	16141-14A	0.153	0.004	91.9	172.1	1.8
PC493 113-114	16141-05A	0.017	0.057	98.1	175.7	0.4
PC493 113-114	16141-07A	-0.001	0.007	97.1	178.8	1.3
PC493 113-114	16141-06A	-0.079	0.004	90.8	201.7	2.2
PC493 113-114	16141-18A	-0.219	0.003	97.2	206.7	2.7
PC493 113-114	16141-12A	1.043	0.001	81.1	228.1	6.5
PC493 113-114	16141-08A	0.081	0.013	97.9	229.6	0.9
PC493 113-114	16141-04A	0.002	0.007	99.6	235.2	1.5
PC493 139-140	16142-03A	0.084	0.003	80.2	87.4	1.8
PC493 139-140	16142-07A	0.005	0.031	99.0	100.2	0.4
PC493 139-140	16142-05A	0.061	0.020	96.7	106.1	0.5
PC493 139-140	16142-10A	0.030	0.003	97.1	124.3	1.9
PC493 139-140	16142-09A	0.500	0.005	87.7	127.3	1.5
PC493 139-140	16142-13A	0.087	0.031	87.2	128.6	0.5
PC493 139-140	16142-12A	0.162	0.009	92.3	140.6	0.9
PC493 139-140	16142-15A	0.096	0.003	93.2	156.2	2.5
PC493 139-140	16142-01A	0.087	0.019	87.2	167.9	0.7
PC493 139-140	16142-06A	0.269	0.002	86.2	199.5	3.7
PC493 139-140	16142-08A	-0.319	0.002	92.4	201.1	2.9
PC493 139-140	16142-16A	-0.134	0.002	92.5	209.4	3.5
PC493 139-140	16142-02A	0.079	0.006	88.8	233.5	1.7
PC493 139-140	16142-14A	0.079	0.010	94.9	240.1	1.1
PC493 139-140	16142-04A	-0.011	0.012	98.7	255.9	1.1
PC493 150-151	16143-06A	0.044	0.011	84.3	90.8	0.7
PC493 150-151	16143-09A	1.329	0.003	84.5	95.6	2.1
PC493 150-151	16143-07A	0.057	0.032	80.0	108.8	0.5

PC493 150-151	16143-10A	0.700	0.001	74.6	116.2	8.5
PC493 150-151	16143-12A	0.356	0.001	71.6	121.5	5.2
PC493 150-151	16143-01A	-0.401	0.001	86.3	127.9	8.9
PC493 150-151	16143-02A	0.114	0.003	47.4	129.8	3.0
PC493 150-151	16143-08A	0.165	0.024	96.3	133.0	0.4
PC493 150-151	16143-05A	0.028	0.002	32.6	144.8	4.0
PC493 150-151	16143-11A	0.077	0.002	89.1	228.3	4.2
PC493 150-151	16143-03A	-0.026	0.002	97.5	230.6	3.4
PC493 150-151	16143-04A	0.506	0.003	95.2	234.8	2.7
PC493 163-164	16144-17A	0.024	0.004	80.9	88.3	1.8
PC493 163-164	16144-04A	0.067	0.096	97.7	96.6	0.2
PC493 163-164	16144-15A	0.188	0.032	96.6	98.1	0.4
PC493 163-164	16144-11A	-0.253	0.001	73.1	112.6	9.6
PC493 163-164	16144-12A	0.126	0.007	93.8	119.0	1.1
PC493 163-164	16144-05A	0.017	0.018	94.5	120.3	0.5
PC493 163-164	16144-14A	0.158	0.003	97.1	130.1	2.4
PC493 163-164	16144-03A	0.248	0.005	88.3	153.5	1.7
PC493 163-164	16144-13A	0.132	0.007	97.4	171.6	1.2
PC493 163-164	16144-06A	-0.278	0.001	74.3	181.4	4.9
PC493 163-164	16144-07A	0.163	0.002	80.5	187.0	3.8
PC493 163-164	16144-02A	-0.119	0.001	98.3	188.3	5.8
PC493 163-164	16144-01A	0.221	0.003	83.3	210.3	2.8
PC493 163-164	16144-08A	-0.190	0.003	93.2	235.0	2.5
PC493 163-164	16144-09A	0.021	0.009	98.9	235.9	1.3
PC493 163-164	16144-10A	0.213	0.005	97.9	273.5	2.0
PC493 163-164	16144-16A	0.163	0.004	95.3	292.4	2.5
PC493 172-173	16145-16A	0.293	0.001	58.0	38.9	4.4
PC493 172-173	16145-08A	0.144	0.004	19.1	60.5	2.8
PC493 172-173	16145-05A	0.034	0.002	92.6	91.9	4.1
PC493 172-173	16145-14A	0.082	0.013	90.2	91.9	0.6
PC493 172-173	16145-23A	0.193	0.015	82.7	93.3	0.6
PC493 172-173	16145-10A	0.231	0.012	90.5	96.0	0.6
PC493 172-173	16145-11A	0.376	0.004	92.7	96.0	1.4
PC493 172-173	16145-03A	-0.664	0.001	71.3	96.2	11.6
PC493 172-173	16145-09A	0.095	0.008	94.0	97.7	0.9
PC493 172-173	16145-19A	-0.481	0.001	60.2	97.9	4.5
PC493 172-173	16145-01A	0.075	0.003	98.3	98.2	2.2
PC493 172-173	16145-21A	0.265	0.004	96.6	100.9	1.6
PC493 172-173	16145-13A	1.502	0.001	98.1	109.4	4.2
PC493 172-173	16145-20A	-0.107	0.004	99.5	124.1	1.9
PC493 172-173	16145-07A	0.640	0.002	80.8	137.9	4.1
PC493 172-173	16145-06A	0.508	0.002	96.2	148.8	2.6
PC493 172-173	16145-02A	-0.520	0.002	81.9	153.0	4.3
PC493 172-173	16145-04A	0.031	0.006	93.9	155.2	1.4
PC493 172-173	16145-18A	0.143	0.004	95.9	156.4	2.0
PC493 172-173	16145-22A	0.195	0.010	93.5	165.6	1.0
PC493 172-173	16145-17A	1.002	0.001	94.3	191.1	7.4
PC493 172-173	16145-15A	1.129	0.002	93.8	206.8	3.9
PC493 172-173	16145-12A	3.838	0.001	84.1	222.7	5.9
PC493 184-185	16146-07A	0.184	0.005	44.5	71.7	1.7
PC493 184-185	16146-18A	-0.700	0.001	70.6	73.9	4.4
PC493 184-185	16146-01A	0.185	0.006	92.6	94.9	1.1
PC493 184-185	16146-20A	7.584	0.001	11.2	96.4	14.2
PC493 184-185	16146-02A	0.086	0.012	95.1	97.3	0.6
PC493 184-185	16146-17A	-0.227	0.001	89.8	99.3	4.1
PC493 184-185	16146-13A	0.462	0.002	93.0	99.6	2.8
PC493 184-185	16146-15A	-0.054	0.003	54.0	101.2	2.4
PC493 184-185	16146-09A	1.348	0.001	75.6	113.5	5.7

PC493 184-185	16146-21A	2.107	0.001	22.8	116.7	7.3
PC493 184-185	16146-16A	-1.110	0.002	66.9	118.7	4.2
PC493 184-185	16146-05A	-0.761	0.003	83.1	125.8	2.5
PC493 184-185	16146-08A	-0.130	0.003	73.1	136.7	2.2
PC493 184-185	16146-03A	-0.241	0.002	75.3	146.0	3.3
PC493 184-185	16146-06A	-0.096	0.005	94.5	146.0	1.5
PC493 184-185	16146-10A	-0.330	0.002	100.6	152.8	3.0
PC493 184-185	16146-11A	0.067	0.015	93.9	185.7	0.8
PC493 184-185	16146-19A	0.495	0.004	90.0	198.6	2.1
PC493 184-185	16146-12A	0.370	0.003	97.5	205.8	2.2
PC493 184-185	16146-14A	-0.122	0.003	98.2	207.4	2.7
PC493 184-185	16146-04A	-0.504	0.003	97.2	321.8	3.3
PC493 194-195	16147-05A	0.905	0.003	35.2	83.2	2.8
PC493 194-195	16147-07A	-1.999	0.001	78.4	84.3	5.8
PC493 194-195	16147-17A	0.597	0.004	77.3	91.0	1.6
PC493 194-195	16147-16A	0.065	0.010	92.8	94.0	0.7
PC493 194-195	16147-04A	0.167	0.004	88.4	95.1	1.6
PC493 194-195	16147-18A	0.405	0.003	83.4	97.2	1.7
PC493 194-195	16147-14A	-0.366	0.002	91.4	102.4	3.2
PC493 194-195	16147-13A	0.212	0.004	96.9	103.2	1.7
PC493 194-195	16147-21A	0.156	0.004	86.3	105.6	1.7
PC493 194-195	16147-08A	-1.087	0.002	89.1	114.2	3.7
PC493 194-195	16147-09A	-0.969	0.002	3.1	130.1	25.3
PC493 194-195	16147-12A	0.692	0.001	129.9	135.0	5.6
PC493 194-195	16147-11A	-0.384	0.001	64.2	151.0	7.3
PC493 194-195	16147-02A	2.504	0.001	54.3	164.9	11.9
PC493 194-195	16147-10A	0.232	0.006	95.4	166.7	1.3
PC493 194-195	16147-15A	-0.039	0.005	93.6	175.5	1.4
PC493 194-195	16147-01A	-0.088	0.006	91.2	218.3	1.6
PC493 194-195	16147-03A	-0.104	0.004	93.1	223.5	2.2
PC493 194-195	16147-19A	-1.052	0.001	38.5	256.2	11.7
PC493 205-206	16148-17A	-1.082	0.002	51.2	26.5	2.9
PC493 205-206	16148-04A	0.058	0.002	95.6	95.2	2.8
PC493 205-206	16148-07A	-0.331	0.004	95.7	96.1	1.6
PC493 205-206	16148-06A	-0.216	0.004	100.9	97.5	1.4
PC493 205-206	16148-03A	-0.429	0.004	84.9	98.3	7.0
PC493 205-206	16148-01A	0.650	0.004	69.4	101.8	1.7
PC493 205-206	16148-13A	-0.831	0.002	99.1	102.1	2.3
PC493 205-206	16148-15A	-0.488	0.002	102.7	105.1	3.6
PC493 205-206	16148-11A	-1.126	0.001	51.5	110.2	4.7
PC493 205-206	16148-08A	-0.321	0.006	97.6	114.6	1.1
PC493 205-206	16148-05A	-1.215	0.001	109.1	146.2	4.6
PC493 205-206	16148-12A	-0.642	0.002	83.8	161.2	2.7
PC493 205-206	16148-16A	0.061	0.003	94.6	220.9	2.5
PC493 205-206	16148-02A	0.258	0.004	95.3	243.4	2.1
PC493 216-217	16150-16A	0.038	0.028	2.4	7.5	1.9
PC493 216-217	16150-09A	-1.151	0.002	61.4	86.1	4.5
PC493 216-217	16150-24A	-0.008	0.006	31.5	91.6	2.1
PC493 216-217	16150-05A	0.031	0.213	66.7	96.2	0.4
PC493 216-217	16150-23A	0.186	0.002	85.3	98.5	2.9
PC493 216-217	16150-02A	0.035	0.286	89.7	105.8	0.2
PC493 216-217	16150-03A	0.362	0.008	78.4	108.1	1.0
PC493 216-217	16150-01A	0.028	0.117	94.6	108.7	0.2
PC493 216-217	16150-04A	-0.008	0.004	83.1	111.0	2.0
PC493 216-217	16150-14A	-1.153	0.002	106.7	111.1	3.7
PC493 216-217	16150-21A	0.330	0.011	62.1	112.6	1.0
PC493 216-217	16150-06A	-0.005	0.019	89.8	112.9	0.6
PC493 216-217	16150-25A	0.032	0.008	80.7	122.2	1.1

PC493 216-217	16150-08A	-0.188	0.004	93.1	143.9	1.9
PC493 216-217	16150-12A	-0.004	0.004	80.6	145.0	2.0
PC493 216-217	16150-22A	0.044	0.005	86.9	149.0	1.4
PC493 216-217	16150-10A	-0.113	0.006	97.0	166.7	1.6
PC493 216-217	16150-13A	-1.107	0.003	96.6	183.8	2.2
PC493 216-217	16150-17A	-0.053	0.015	97.0	190.6	0.8
PC493 216-217	16150-07A	-0.023	0.018	89.1	195.4	0.8
PC493 216-217	16150-11A	-0.045	0.029	98.0	217.2	0.7
PC493 216-217	16150-15A	-0.775	0.004	99.4	224.8	2.3
PC493 216-217	16150-18A	-0.024	0.012	98.6	251.8	1.0
PC493 216-217	16150-20A	2.745	0.009	83.7	494.5	2.6
PC493 255-256	16151-20A	0.350	0.009	83.2	75.1	0.8
PC493 255-256	16151-23A	0.280	0.001	61.8	82.2	4.5
PC493 255-256	16151-02A	0.185	0.099	36.5	89.2	1.1
PC493 255-256	16151-31A	-0.096	0.007	94.5	95.7	1.0
PC493 255-256	16151-09A	0.264	0.008	87.6	98.1	1.0
PC493 255-256	16151-28A	0.146	0.005	90.0	101.8	1.3
PC493 255-256	16151-07A	0.109	0.025	69.3	103.4	0.6
PC493 255-256	16151-10A	0.625	0.003	63.0	104.7	2.6
PC493 255-256	16151-13A	-0.009	0.003	81.4	105.1	2.1
PC493 255-256	16151-17A	-0.049	0.012	97.1	107.1	0.7
PC493 255-256	16151-05A	0.215	0.009	96.5	107.6	0.9
PC493 255-256	16151-11A	0.182	0.005	92.9	109.4	1.5
PC493 255-256	16151-03A	0.065	0.016	93.9	110.4	0.6
PC493 255-256	16151-29A	-0.167	0.006	91.6	112.0	1.2
PC493 255-256	16151-14A	0.530	0.005	96.3	131.3	1.5
PC493 255-256	16151-26A	-0.382	0.005	97.9	136.5	1.5
PC493 255-256	16151-08A	0.479	0.004	83.9	140.4	1.8
PC493 255-256	16151-30A	0.615	0.002	94.8	157.7	3.0
PC493 255-256	16151-19A	0.266	0.002	95.8	160.4	3.1
PC493 255-256	16151-01A	-0.258	0.002	87.6	163.4	3.2
PC493 255-256	16151-22A	0.034	0.013	96.9	166.8	0.8
PC493 255-256	16151-27A	0.100	0.002	50.8	170.0	4.4
PC493 255-256	16151-24A	-1.550	0.001	92.4	171.9	5.1
PC493 255-256	16151-25A	-0.003	0.030	98.6	174.7	0.6
PC493 255-256	16151-04A	0.007	0.037	98.5	214.6	0.6
PC493 255-256	16151-12A	0.210	0.005	91.5	214.9	1.7
PC493 255-256	16151-15A	0.146	0.003	98.1	222.8	2.8
PC493 255-256	16151-16A	-0.563	0.003	97.6	235.8	2.9
PC493 255-256	16151-06A	0.226	0.010	98.7	240.6	1.2
PC493 255-256	16151-32A	0.324	0.001	83.0	314.7	7.6
PC493 266-267	16153-01A	0.098	0.002	31.9	77.8	4.0
PC493 266-267	16153-04A	1.560	0.001	25.9	102.1	6.4
PC493 266-267	16153-10A	0.499	0.002	97.5	108.5	2.7
PC493 266-267	16153-14A	0.254	0.002	89.5	115.7	2.9
PC493 266-267	16153-16A	-0.613	0.002	94.3	121.7	2.6
PC493 266-267	16153-07A	1.409	0.001	72.7	137.1	8.7
PC493 266-267	16153-03A	0.689	0.001	85.9	149.4	4.1
PC493 266-267	16153-15A	-0.398	0.005	21.0	161.0	4.5
PC493 266-267	16153-17A	-0.512	0.003	91.9	165.9	2.2
PC493 266-267	16153-09A	0.239	0.007	99.0	193.8	1.1
PC493 266-267	16153-11A	-0.126	0.003	92.8	195.5	2.4
PC493 266-267	16153-05A	0.791	0.002	90.8	209.5	3.8
PC493 266-267	16153-12A	0.011	0.006	93.9	213.9	1.5
PC493 266-267	16153-06A	1.485	0.001	59.8	228.3	7.6
PC493 266-267	16153-02A	0.159	0.002	97.3	228.7	3.5
PC493 266-267	16153-08A	-0.021	0.002	100.0	229.5	2.9
PC493 266-267	16153-13A	-1.431	0.001	105.2	235.8	10.7
PC493 266-267	16153-18A	-0.447	0.001	95.2	255.7	5.4

PC493 279-280	16154-17A	1.828	0.002	78.2	8.8	2.7
PC493 279-280	16154-01A	0.500	0.001	35.6	69.8	5.8
PC493 279-280	16154-06A	0.481	0.004	93.7	99.6	1.6
PC493 279-280	16154-05A	0.732	0.004	100.5	114.2	1.5
PC493 279-280	16154-07A	0.687	0.002	93.4	114.5	3.3
PC493 279-280	16154-16A	0.793	0.001	92.1	128.2	7.0
PC493 279-280	16154-02A	-0.743	0.002	90.7	162.5	3.4
PC493 279-280	16154-08A	2.421	0.001	1.9	165.7	55.7
PC493 279-280	16154-10A	0.222	0.004	96.2	171.9	1.9
PC493 279-280	16154-15A	-1.467	0.001	99.0	203.5	6.0
PC493 279-280	16154-11A	0.536	0.004	98.6	228.0	2.2
PC493 279-280	16154-12A	-0.047	0.014	100.0	233.4	1.0
PC493 279-280	16154-03A	-0.081	0.003	100.2	234.6	2.5
PC493 279-280	16154-04A	0.186	0.008	93.9	236.2	1.3
PC493 279-280	16154-21A	1.570	0.001	30.3	251.9	9.7
PC493 279-280	16154-14A	1.054	0.001	98.8	271.2	6.2
PC493 279-280	16154-22A	5.631	0.007	98.2	290.7	1.6
PC493 279-280	16154-23A	7.801	0.028	94.4	465.9	1.4
PC493 279-280	16154-25A	7.774	0.007	91.7	469.0	2.4